

# Precision luminosity measurement at LHCb with beam-gas imaging

Von der Fakultät für Mathematik, Informatik und Naturwissenschaften  
der RWTH Aachen University zur Erlangung des akademischen Grades  
eines Doktors der Naturwissenschaften genehmigte Dissertation

vorgelegt von

Diplom-Physiker

**Colin Barschel**

aus Brockville, Kanada

CERN-THESIS-2013-301  
05/03/2014



Berichter: Univ.-Prof. Dr. Thomas Hebbeker  
Univ.-Prof. Dr. Stefan Schael

Tag der mündlichen Prüfung: 05.03.2014

Diese Dissertation ist auf den Internetseiten der Hochschulbibliothek online verfügbar.

## ABSTRACT

The luminosity is the physical quantity which relates the cross-section to the production rate in collider experiments. The cross-section being the particle physics observable of interest, a precise determination of the luminosity is required. This work presents the absolute luminosity calibration results performed at the Large Hadron Collider beauty (LHCb) experiment at CERN using a novel method based on beam-gas interactions with data acquired at a center of mass energy  $\sqrt{s} = 8$  TeV and  $\sqrt{s} = 2.76$  TeV.

Reconstructed beam-gas interaction vertices in LHCb are used to measure the beam profiles, thus making it possible to determine the beams overlap integral. An important element of this work was to install and use a neon gas injection system to increase the beam-gas interaction rate. The precision reached with the beam-gas imaging method relies on the two-dimensional beam shape determination developed in this work. For such precision, the interaction vertex resolution is an important ingredient. Therefore, a new method has been developed using all reconstructed vertices in order to improve the understanding of the vertex resolution.

In addition to the overlap integral, the knowledge of the colliding bunch populations is required to measure the luminosity. The determination of the bunch populations relies on LHC instruments to measure the bunch population fractions and the total beam intensity. Studies performed as part of this work resulted in a reduction of the bunch current normalization uncertainty from  $\pm 2.7\%$  to  $\pm 0.2\%$  and making it possible to achieve precision luminosity measurements at all LHC experiments. Furthermore, information on beam-gas interactions not originating from nominally filled bunches was analyzed to determine the charge fraction not participating in bunch collisions. The knowledge of this fraction is required to correct the total beam intensity.

The reference cross-section of  $pp$  interactions with at least two tracks in the vertex detector was measured with the beam-gas imaging method. The result is  $\sigma_{\text{Track}} = 60.6 \pm 0.9$  mb at a center-of-mass energy of  $\sqrt{s} = 8$  TeV. The same measurement performed at  $\sqrt{s} = 2.76$  TeV results in a cross-section of  $\sigma_{\text{Track}} = 52.7 \pm 1.2$  mb.

The luminosity measurement at  $\sqrt{s} = 8$  TeV presented here, with an uncertainty of 1.4%, is to date the most precise luminosity calibration performed at the LHC and at any other bunched-beam proton collider.

# ZUSAMMENFASSUNG

Die Luminosität beschreibt das Verhältnis zwischen dem Wirkungsquerschnitt und der erzeugten Ereignisrate in Experimenten mit Teilchenbeschleunigern. Von physikalischem Interesse ist die Messung von Wirkungsquerschnitten; dafür ist die genaue Kenntnis der Luminosität des Teilchenstrahls Voraussetzung. Diese Arbeit beschreibt die Bestimmung der Luminosität für das LHCb Experiment – eines der vier Experimente am Large Hadron Collider (LHC) – für Schwerpunktsenergien von  $\sqrt{s} = 8$  TeV und  $\sqrt{s} = 2.76$  TeV. Dafür wurde eine neue Methode angewendet, die das Abbild der LHC Strahlen beim Passieren des LHCb Detektors misst. Hierfür werden die Wechselwirkungsorte der LHC Strahlen mit Restgas in der LHC Vakuumröhre rekonstruiert; dies ermöglicht eine Messung der transversalen Strahlenprofile und die Bestimmung des Überlappungsintegrals der beiden Strahlen. Zur Erhöhung des Restgases im LHC Vakuum wurde ein Gaseinspritzsystem in den LHCb Detektor eingebaut.

Die erreichte Genauigkeit des Strahlen-Gas Abbildungsverfahrens beruht auf der zweidimensionalen Modellierung der Strahlenprofile. Die präzise Kenntnis der Ortsauflösung der Wechselwirkungsorte ist ein wichtiger Bestandteil des Verfahrens. Zusätzlich zur Bestimmung des Überlappungsintegrals ist auch die Kenntnis der Protonenzahl pro Strahlenbündel nötig. Dafür werden die gesamte Strahlungsintensität und der Bruchteil der Strahlungsintensität pro Strahlenbündel mit zwei LHC Instrumenten getrennt gemessen. Im Rahmen dieser Arbeit wurde eine Methode erarbeitet, die die Unsicherheit der Messung der gesamten Strahlungsintensität von  $\pm 2.7\%$  auf  $\pm 0.2\%$  reduziert. Erst damit wird eine präzise Messung der Luminosität an allen LHC Experimenten ermöglicht. Weiterhin wird die Strahlen-Gas Methode verwendet, um Informationen über Ladungen zu gewinnen, die sich außerhalb der nominell gefüllten Protonenbündel befinden, welche zur Korrektur der Gesamtstrahlungsintensität nötig sind.

Zusammen mit der Messung der Luminosität wurden auch Raten von sogenannten Kalibrationsereignissen aufgezeichnet, die es erlauben, die Luminosität des gesamten Datensatzes zu bestimmen.

Der Wirkungsquerschnitt von  $pp$  Ereignissen mit wenigstens zwei Spuren im Vertex-Detector liegt bei  $\sigma_{\text{Track}} = 60.6 \pm 0.9$  mb für  $\sqrt{s} = 8$  TeV mit einer Unsicherheit von 1.4%. Dies ist die präziseste Kalibrierung der Luminosität am LHC und in jeder gebündelten Protonenstrahlen Maschine. Die gleiche Messung wurde auch bei  $\sqrt{s} = 2.76$  TeV durchgeführt mit einem Ergebnis von  $\sigma_{\text{Track}} = 52.7 \pm 1.2$  mb.

# CONTENTS

<b>1</b>	<b>Introduction</b>	<b>2</b>
<b>2</b>	<b>LHCb experiment</b>	<b>4</b>
2.1	Overview . . . . .	4
2.2	Tracking and VELO detector . . . . .	5
2.3	Large Hadron Collider . . . . .	6
<b>3</b>	<b>Luminosity of colliding beams</b>	<b>8</b>
3.0.1	Luminosity in the case of pure Gaussian beams . . . . .	9
3.1	Luminosity with the van der Meer method . . . . .	12
3.2	Luminosity with the beam-gas imaging method . . . . .	13
<b>4</b>	<b>Beam-gas imaging measurements</b>	<b>15</b>
4.1	Data-taking conditions and event selection . . . . .	15
4.1.1	LHC fills with BGI measurements . . . . .	15
4.1.2	Trigger conditions . . . . .	16
4.1.3	Data selection . . . . .	19
4.2	Gas injection . . . . .	21
4.3	Vertex Resolution . . . . .	22
4.3.1	Resolution unfolding . . . . .	23
4.3.2	Resolution for beam-beam interaction vertices . . . . .	24
4.3.3	Resolution for beam-gas interaction vertices . . . . .	28
4.4	Measurement of beam parameters . . . . .	38
4.4.1	Crossing angles . . . . .	38
4.4.2	Transverse shape in one-dimensional fit . . . . .	39
4.4.3	Transverse shape in two-dimensional fit . . . . .	45
4.4.4	Bunch length and longitudinal crossing point . . . . .	50
4.5	Generic Monte Carlo simulation . . . . .	52
4.6	Overlap integral . . . . .	55
4.6.1	Corrections to the fit . . . . .	57
4.6.2	Evidence for beam shape non-factorizability . . . . .	59
<b>5</b>	<b>Interaction rate</b>	<b>66</b>
5.1	Luminosity propagation . . . . .	66
5.2	Background for the zero counting method . . . . .	69
5.3	Systematic uncertainties . . . . .	71
<b>6</b>	<b>Bunch population measurements</b>	<b>74</b>
6.1	Measurements with LHC instrumentation . . . . .	74
6.2	Ghost Charge . . . . .	76
6.2.1	Definitions . . . . .	76
6.2.2	Event selection . . . . .	78
6.2.3	Trigger efficiency correction . . . . .	81
6.2.4	ghost charge distribution over the ring circumference . . . . .	82
6.2.5	Ghost charge measurements and results . . . . .	85

6.3	Satellite charges . . . . .	88
6.4	Total uncertainty . . . . .	88
<b>7</b>	<b>Cross-section measurement</b>	<b>90</b>
7.1	Beam-gas imaging results . . . . .	90
7.1.1	FBCT non-linearity effects . . . . .	92
7.1.2	Factorizability of longitudinal bunch coordinate . . . . .	93
7.1.3	Correlation checks . . . . .	94
7.2	Systematic uncertainties . . . . .	95
7.2.1	Beam-beam vertex resolution . . . . .	95
7.2.2	Beam-gas vertex resolution . . . . .	98
7.2.3	Measurement spread . . . . .	99
7.2.4	Detector alignment and crossing angle . . . . .	100
7.2.5	Fit model . . . . .	101
7.2.6	Bunch length and reconstruction efficiency . . . . .	103
7.2.7	Additional checks . . . . .	104
7.3	Final results . . . . .	108
<b>8</b>	<b>Luminosity for central exclusive production</b>	<b>109</b>
<b>9</b>	<b>Conclusion</b>	<b>113</b>
<b>Appendices</b>		
<b>A</b>	<b>Luminosity measurements at intermediate energy</b>	<b>115</b>
<b>B</b>	<b>Single interaction detector response</b>	<b>121</b>
<b>C</b>	<b>VELO detector alignment studies</b>	<b>124</b>
<b>D</b>	<b>Additional plots and tables</b>	<b>129</b>
<b>E</b>	<b>Generic Monte Carlo simulation parameters</b>	<b>142</b>
<b>F</b>	<b>SMOG characterization and commissioning</b>	<b>144</b>
<b>G</b>	<b>Results of the LHC DCCT calibration studies</b>	<b>164</b>
<b>List of Figures</b>		<b>233</b>
<b>List of Tables</b>		<b>242</b>
<b>Bibliography</b>		<b>245</b>

# 1 INTRODUCTION

Luminosity is a key quantity in accelerator-based particle physics experiments. It relates the production rate of a reaction to its cross-section. Therefore, a precision luminosity determination is of general interest. In the LHCb physics programme several cross-section measurements can benefit from a reduced luminosity uncertainty, which was at the 3.5% level for data acquired in 2010 and 2011. Examples of such measurements are weak boson production, heavy flavor production and inelastic cross-section determination. The primary motivations for making precision cross-section measurements are to test the Standard Model and to constrain the theoretical parton distribution functions (PDF) [1, 2]. As an example, theoretical predictions of electroweak boson production are now known to next-to-next-to-leading-order and the uncertainties are often limited in precision by the PDFs [3]. Theoretical uncertainties depend on the pseudorapidity  $\eta$  of the final state lepton. The LHCb detector covers the pseudorapidity range  $2 < \eta < 5$ , which overlaps with ATLAS and CMS in the range  $2 < \eta < 2.5$ , and extends to the forward region  $\eta > 2.5$ . In this range, the theoretical uncertainties are larger and the PDFs are less constrained by experimental data and have therefore higher uncertainties.

Theoretical predictions are in good agreement with present analyses such as  $W/Z \rightarrow \mu\mu$  [4],  $Z \rightarrow ee$  [5],  $Z \rightarrow \tau\tau$  [6],  $Z \rightarrow (\mu\mu) + \text{jet}$  [7] or Drell-Yan  $Z/\gamma^* \rightarrow \mu\mu$  [8]. However, those measurements have for the most part comparable uncertainties to that of the luminosity, and in future or updated analyses, the luminosity will become the dominating uncertainty if its precision is not improved. Accordingly, a level of luminosity precision of 2% or better is necessary for ongoing and future cross-section measurements for their uncertainty not to be dominated by the luminosity accuracy. Furthermore, such precision would lead to new information on the proton PDF [9]. Many studies can benefit from a higher precision in the luminosity, for example, reduced uncertainties in the PDF are required to improve the  $W$  mass measurement at the LHC [10].

Methods to measure the absolute luminosity can be separated in indirect and direct methods. Indirect methods are based on measuring the rate of a process with a known cross-section. For example the large and small scattering angles of Bhabha scattering  $e^+e^- \rightarrow e^+e^-$ , which are theoretically known to 0.05%, were used at LEP to measure the luminosity to a similar precision [11, 12, 13]. At the LHC, the elastic dilepton production  $pp \rightarrow pp + l^+l^-$  is known to about 1% [14], but an indirect luminosity measurement is experimentally difficult. Another approach taken by the TOTEM-CMS and ALFA-ATLAS experiments at the LHC is to make use of the optical theorem that relates the forward scattering amplitude to the total cross-section [15]. Those experiments are dedicated to measure the total elastic and inelastic  $pp$  cross-section.

Direct methods are based on the determination of the colliding beam geometries and their particle distributions. The main direct method used at the LHC is the van der Meer (VDM) method explained in Sec. 3.1, which is used by the four main experiments. The present work uses an alternative direct method that consists of measuring the beam geometries using interaction vertices between the beams and the residual gas present in the beam-pipe vacuum. A visualization of beam-gas interactions is shown in Fig. 1.1 for illustration purposes.

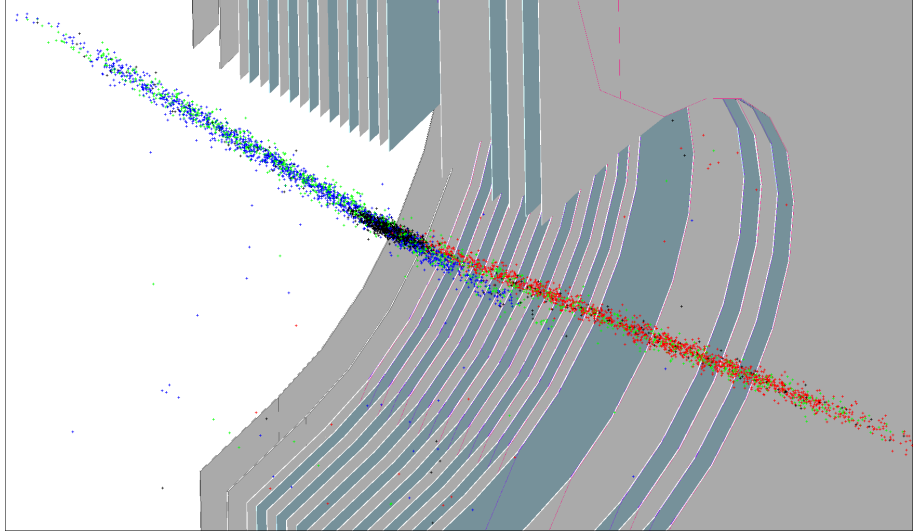


**Fig. 1.1:** Beam-gas interaction vertices visualized with the LHCb event display. The first 1500 vertices per bunch crossing type are shown (LHC fill 3563 at  $\sqrt{s} = 2.76$  TeV). The vertex colors green, blue, red and black denote interaction vertices in empty, beam 1, beam 2 and beam-beam crossing types. The longitudinal  $z$ -axis along the nominal beam-line is compressed by a factor 100 for a better visualization. The sensors of the vertex detector are visible in alternating colors. Only the left half of the detector is shown.

The thesis is structured according to the ingredients required to determine the absolute luminosity. The chapters 2 and 3 introduce the LHCb experiment and the luminosity concepts, respectively. Chapter 4 provides a description of the beam-gas imaging method including all measurements leading to the overlap integral determination. Chapter 5 focuses on the measurement of the interaction rate, while Chapter 6 describes the bunch population measurements. Results combining all previous measurements are presented in Chapter 7 where the uncertainties are also discussed. Chapter 8 discusses the special treatment of the luminosity required for central exclusive production analyses.

Studies directly related to this work and referred to in the text are provided in appendices. The intermediate energy luminosity calibration at  $\sqrt{s} = 2.76$  TeV is provided in Appendix A. An alternative method to measure the interaction rate is discussed in Appendix B. A summary of the VELO alignment studies is provided in Appendix C. Additional plots and simulation parameters referred in the text are provided in Appendix D and E, respectively. Finally, two pillars of this work are provided in Appendices F and G detailing the SMOG laboratory studies and the calibration studies to measure the beam intensity, respectively.

## 2 LHCb EXPERIMENT

### 2.1 Overview

The LHCb<sup>1</sup> experiment is one of the four main experiments at the Large Hadron Collider (LHC) at CERN [16, 17] (European Organization for Nuclear Research). The experiment is dedicated to heavy-flavor physics, mainly to study CP violation and rare decays of charm and beauty hadrons; it is located in the former Delphi cavern at the LHC intersection point 8. The relatively small mass of charm and beauty mesons compared to the center of mass energy at the LHC, results in particle production concentrated in the forward or backward regions in a cone close to the beam pipe. To optimize the study of their decays, the detector is a single-arm spectrometer covering a forward angle of about 300 mrad. The acceptance covers the pseudorapidity interval  $1.8 < \eta < 4.9$ , where  $\eta = -\ln(\tan(\theta/2))$ , and  $\theta$  is the polar angle with respect to the beam direction.

An overview of the detector layout and its components is shown in Fig. 2.1. The VErtex LOcator (VELO) surrounds the interaction point (on the left in Fig. 2.1). The detector components with increasing distance to the collision point are the first Ring-imaging Cherenkov (RICH) detector (RICH1), the Tracker Turicensis (TT), the magnet, the tracking stations (T1-T3), the second RICH detector (RICH2), the calorimeter system, which is composed of the scintillating pad detector (SPD), the pre-shower detector (PS) and the electromagnetic and hadronic calorimeters (ECAL and HCAL), and finally the muon stations (M1-M5).

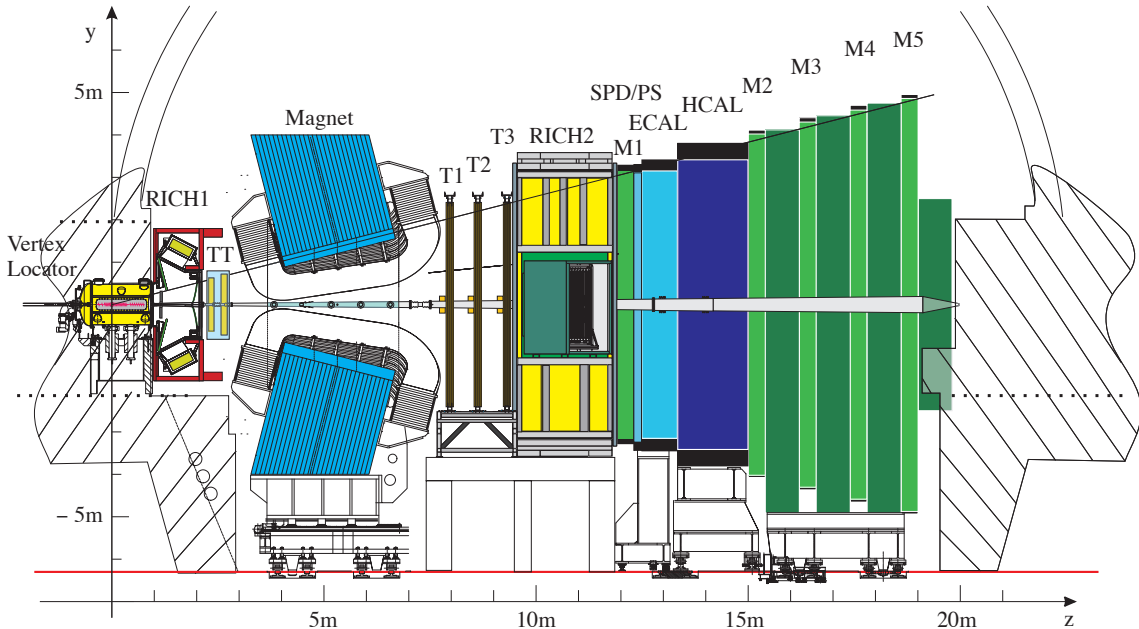


**Fig. 2.1:** Vertical cross section through the LHCb detector. The different detector components are indicated in the figure (drawing from Ref. [16]).

Next, a brief description is given of the components that are essential for the understanding of this thesis.

<sup>1</sup>Large Hadron Collider beauty experiment.

## 2.2 Tracking and VELO detector

The tracking system consists of the VELO, the TT upstream of the magnet and the tracking stations T1 to T3 located downstream of the magnet. The charge and momentum of particles are inferred from the particle trajectories bent in the magnetic field and the measurement of the transverse position of particles in the tracking detectors. The trajectory associated with a candidate particle and hits in the tracking system form a ‘track’. Tracks which start at the VELO and end in the tracking stations are called ‘long’ tracks and can be reconstructed with about 96% efficiency and a momentum resolution  $\Delta p/p$  of 0.4 to 0.6% for particles with a momentum in the range of 5 to 100  $\text{GeV}/c$ , respectively. The detector geometry, which is optimized in the high pseudorapidity range mentioned above, provides an almost ideal configuration to analyze beam-gas interactions with particles in the forward direction.

The VELO, TT and inner part of the tracking stations (IT) use silicon microstrip sensors, whereas the outer region of the tracking stations (OT) makes use of straw-tubes. The TT and IT stations are called the silicon tracker (ST) system and are based on silicon microstrip sensors with a pitch of about 200  $\mu\text{m}$ . Each station has four detection layers, the first and last layers have vertical strips, while the second and third layers are rotated by a stereo angle of  $-5^\circ$  and  $5^\circ$ , respectively.

The VELO detector comprises two halves, each holding 21 modules of silicon microstrip detectors placed almost perpendicular to the beam line. The VELO halves are retracted during the beam injection and acceleration and are closed when the beams are in the mode “stable beams” as declared by the LHC control center. When the VELO is in its closed position, the edge of the active region of the sensors is located at 8.2 mm from the beam line. To provide a full azimuthal coverage, the VELO detector of the left and right side overlap and are displaced in  $z$  by 1.5 cm. A drawing of the cross section of the VELO is shown in Fig. 2.2.

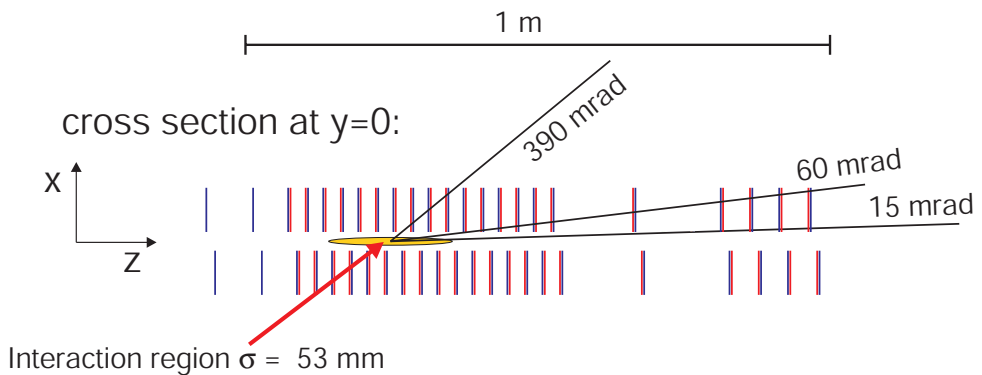


**Fig. 2.2:** Cross section of the VELO in the  $(x,z)$  plane, at  $y = 0$ . The position of the sensors is shown in the fully closed position (drawing from Ref. [17]).

The detectors are enclosed in a vacuum vessel separating the beam pipe vacuum by a 0.3 mm thin aluminum foil called ‘RF foil’, which protects the sensors from the RF pickup from the beams. Each module is composed of one  $R$ -sensor and one  $\phi$ -sensor providing an  $r, \phi, z$  spatial position in cylindrical coordinates. The  $R$ -sensors provide the radial distance from the beam axis and the  $\phi$ -sensors provide the azimuthal coordinate around the beam. To limit the occupancy in each strip, the  $\phi$ -sensors are separated into inner and outer sections. Two stations on both sides, consisting exclusively of 4  $R$ -sensors, are placed upstream and form the Pile-Up (PU) system [16].

The precision of the VELO transverse scale is about 0.05% and originates from the difference between the temperature during manufacturing process and the temperature during the operation.

## 2.3 Large Hadron Collider

The LHC is installed in the tunnel originally constructed for the LEP (Large Electron–Positron) collider at CERN [18, 19]. In the LHC two proton beams collide at a center-of-mass energy  $\sqrt{s}$  of up to 14 TeV; the LHC was operated at a  $\sqrt{s} = 7$  TeV in 2010 and 2011 and at  $\sqrt{s} = 8$  TeV in 2012 and also at lower energies for short special runs. The LHC brings the beams into collision at four interaction points around the ring for the ATLAS [20], CMS [21], ALICE [22] and LHCb [16] experiments.

The LHC uses radio frequency (RF) cavities operated at about 400 MHz to accelerate both beams, to longitudinally confine charges in RF buckets and to compensate for energy loss from synchrotron radiation. The resulting harmonic number segments the ring circumference in exactly 35640 RF buckets of about 2.5 ns length. Charged particles are contained in an RF bucket and nominally only 1 out of 10 buckets is filled. A bunch crossing identifier (BCID), also called bunch slot, spans 10 RF buckets over about 25 ns; BCIDs are numbered from 1 to 3564.

The operation of the LHC at  $\sqrt{s} = 7$  TeV began in 2010 with a large fraction of time dedicated to machine commissioning and development. The increase in luminosity was achieved by way of higher bunch intensities, lower  $\beta^*$ , then by a higher number of colliding bunches. Since 2011 the LHC had to provide different instantaneous luminosities to the experiments depending on the physics goals and capacities of each detector. While ATLAS and CMS received the highest luminosities with up to  $7.5 \times 10^{33} \text{ cm}^{-2}\text{s}^{-1}$  in 2012, ALICE requested a luminosity of about  $1 \times 10^{31} \text{ cm}^{-2}\text{s}^{-1}$ . A luminosity leveling scheme was developed for LHCb, which allowed the delivery of mostly constant luminosity throughout each fill with a value of about  $4 \times 10^{32} \text{ cm}^{-2}\text{s}^{-1}$ . The LHCb experiment recorded a total integrated luminosity of  $1.0 \text{ fb}^{-1}$  in 2011 and  $2 \text{ fb}^{-1}$  in 2012. The delivered integrated luminosity by the LHC as a function of time for 2011 and 2012 for the four experiments is shown in Fig. 2.3.

The LHC is made of eight arcs and eight straight sections for a total circumference of about 27 km. A schematic view of the LHC with the four experiments is shown in Fig. 2.4. The beam instruments DCCT, FBCT and LDM, referred to in Sec. 6, are located in point 4. The LHCb detector is located in point 8.

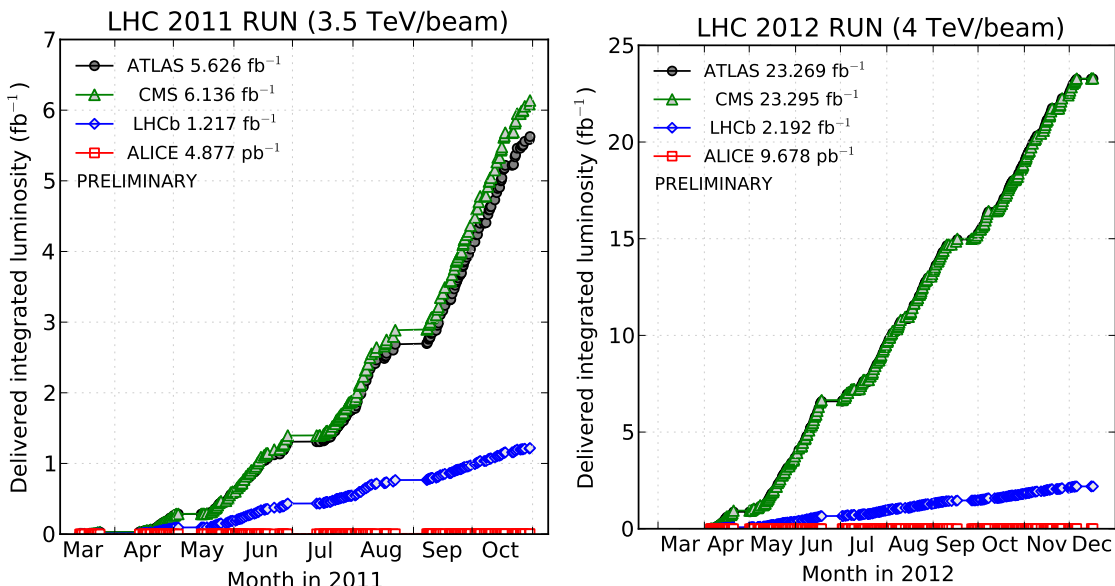


**Fig. 2.3:** Delivered integrated luminosity to the four LHC experiments for 2011 (left) and 2012 (right). The plots are generated with data provided by each experiment.

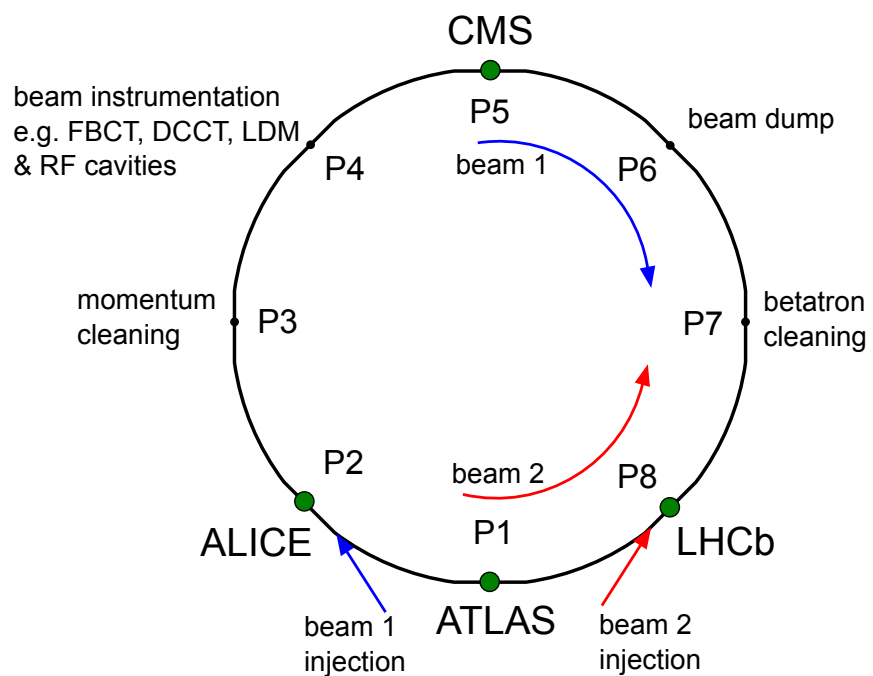


**Fig. 2.4:** Schematic view of the LHC. The LHC is composed of eight arcs and eight straight sections. The eight straight sections dividing the collider are denoted with P1 to P8 and are used by the experiments or for the machine instrumentation and operation. Beam 1 circulates clockwise and beam 2 counterclockwise.

### 3 LUMINOSITY OF COLLIDING BEAMS

The number of reactions  $N$  per unit of time  $dt$  and volume  $dV$  of a beam with particle density  $n_1$  and velocity vector  $\mathbf{v}_1$  colliding with a target with particle density  $n_2$  is given by [23]

$$\frac{d^2N}{dVdt} = \sigma |\mathbf{v}_1| n_1 n_2, \quad (3.1)$$

with  $\sigma$  the total cross-section. Equation (3.1) can be transformed to an arbitrary reference frame either by transforming Eq. (3.1) in a moving frame where the target is moving with a velocity  $\mathbf{v}_2$  as derived in reference [23], or by deriving directly a relativistic invariant formulation of Eq. (3.1) [24]. The general expression becomes

$$\frac{d^2N}{dVdt} = \sigma n_1 n_2 \sqrt{(\mathbf{v}_1 - \mathbf{v}_2)^2 - \frac{(\mathbf{v}_1 \times \mathbf{v}_2)^2}{c^2}}, \quad (3.2)$$

with  $\mathbf{v}_{1,2}$  the velocity vectors of the colliding particle groups and  $c$  the speed of light. The volume  $dV$  denotes the interaction region where both beams overlap. In the ultra-relativistic case we can assume  $|\mathbf{v}_1| \approx |\mathbf{v}_2| \simeq c$  and simplify (3.2) to

$$\frac{d^2N}{dVdt} \simeq \sigma n_1 n_2 \cdot 2c \cos^2 \phi, \quad (3.3)$$

with  $\phi$  the half crossing angle between the beams.

The luminosity  $\mathcal{L}$  relates a process cross-section to its rate with

$$\frac{dN}{dt} = \sigma \mathcal{L} \quad (3.4)$$

and is obtained from (3.3) by the volume integration

$$\mathcal{L} = 2c \cos^2 \phi \int n_1 n_2 dV. \quad (3.5)$$

The LHC being a bunched beam collider, the particle densities  $n_j$  (for beam  $j = 1, 2$ ) can be expressed, per bunch, as

$$n_j = N_j \rho_j(x, y, z, t), \quad (3.6)$$

with  $N_j$  the number of particles in a bunch in beam  $j$  and  $\rho_j$  the unit-normalized particle density function. The small half crossing angle present at the LHCb interaction point of about 500  $\mu$ rad allows setting  $\cos^2 \phi \simeq 1$ . With Eq. (3.6), the luminosity for one colliding bunch pair is then expressed as

$$\mathcal{L} = 2c \nu_{\text{rev}} N_1 N_2 \int \rho_1(x, y, z, t) \rho_2(x, y, z, t) dx dy dz dt, \quad (3.7)$$

with  $\nu_{\text{rev}}$  the collider revolution frequency. The indices 1 and 2 denote the bunch from beam 1 and 2, respectively. This expression for the luminosity of one colliding bunch pair can be written as

$$\mathcal{L} = \nu_{\text{rev}} N_1 N_2 \mathcal{O} \quad (3.8)$$

with  $\mathcal{O}$  the overlap integral defined as

$$\mathcal{O} = 2c \int \rho_1(x, y, z, t) \rho_2(x, y, z, t) dx dy dz dt. \quad (3.9)$$

The kinematic factor  $2c$  is here included in  $\mathcal{O}$  for dimensional reasons and thus  $\mathcal{O}$  has the unit of a surface-area $^{-1}$ .

The calibration consists of determining the luminosity on an absolute scale with Eq. (3.8). Knowing the luminosity, the rate  $R_{\text{ref}}$  of a reference process measured by a sub-detector is associated to a reference cross-section  $\sigma_{\text{ref}}$  with

$$\sigma_{\text{ref}} = \frac{R_{\text{ref}}}{\mathcal{L}}. \quad (3.10)$$

Once a reference cross-section has been calibrated to its rate, this reference process can be used at any time to measure the absolute luminosity.

The coordinate definition and beam crossing geometry used for the coming equations are shown in Fig. 3.1. The velocity vectors are defined according to the main axis with  $\mathbf{v}_1 + \mathbf{v}_2$  in the  $x$ -direction,  $\mathbf{v}_1 \times \mathbf{v}_2$  in the  $y$ -direction and  $\mathbf{v}_1 - \mathbf{v}_2$  in the  $z$ -direction. With the half crossing angle  $\phi$  between both beam trajectories in the  $xz$  plane, defined as  $\phi = (\alpha_{1,x} - \alpha_{2,x})/2$  with  $\alpha_{j,x}$  the individual beam angles for beam  $j$  in the coordinate  $x$ , the velocity vectors are  $\mathbf{v}_1 = c \cdot (\sin \phi, 0, \cos \phi)$  and  $\mathbf{v}_2 = c \cdot (\sin \phi, 0, -\cos \phi)$ . The half crossing angle  $\phi$  is a relevant quantity to measure the overlap integral.

The LHCb coordinate system is chosen as a right-handed coordinate system with its origin at the nominal  $pp$  interaction point. The  $z$ -axis points towards the LHCb dipole magnet along the nominal beam-line, the  $x$ -axis points roughly towards the center of the LHC and lies in the horizontal plane, and the  $y$ -axis points roughly upwards. This coordinate system almost coincides with the definition given above and is used in the BGI analysis. The directions of both beams are not perfectly symmetric and a tilt of about 95  $\mu\text{rad}$  is present in the  $xz$  plane and about 20  $\mu\text{rad}$  in  $yz$  plane. Those tilts have no influence on the measurement of the overlap integral as only the crossing angles are relevant, not the individual beam directions.

The LHC ring is tilted by 13 mrad with respect to the LHCb  $x, y$  axes [25]. However, the LHCb  $z$ -axis is aligned to the tangent of the LHC ring and points counter-clockwise. The beam reference frames  $\hat{x}_j, \hat{y}_j, \hat{z}_j$  are right-handed systems with the  $\hat{z}_j$ -axis pointing in the direction of motion of beam  $j$  ( $\mathbf{v}_j$ ) and with  $\hat{y} = y$ .

In addition to the known tilt of the LHC with respect to the LHCb coordinate system, each beam can also be tilted with respect to the LHC plane, for example due to different magnet alignments. Nevertheless, a coordinate rotation around the  $z$ -axis of  $\theta \approx 13$  mrad can be neglected.

### 3.0.1 Luminosity in the case of pure Gaussian beams

It is useful to consider the ideal case of pure Gaussian beams. In this case Eq. (3.9) can be developed analytically when the single beam distributions  $\rho_j$  are Gaussian functions [26, 27]. Here we assume bunches centered at  $\mathbf{r}_j = (\xi_{xj}, \xi_{yj}, \xi_{zj})$  at the time  $t = 0$ , with a particle density function described by a normalized Gaussian function

$$\rho_{mj}(m) = \frac{1}{\sqrt{2\pi}\sigma_{mj}} e^{-\frac{1}{2}\left(\frac{m-\xi_{mj}}{\sigma_{mj}}\right)^2} \quad \text{for beam } j = 1, 2 \text{ and plane } m = x, y, z, \quad (3.11)$$

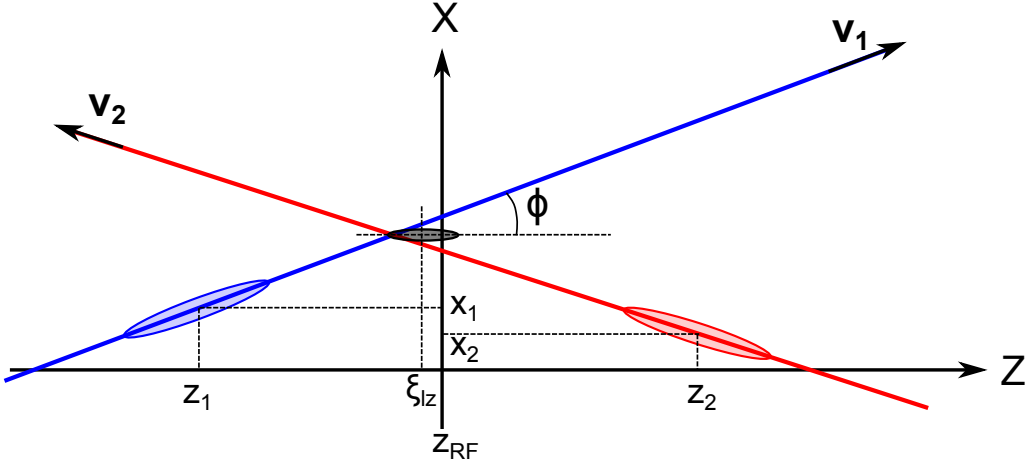


**Fig. 3.1:** Definition of coordinates and beam geometry in the  $xz$  plane. The  $y$  plane is not shown and  $y = 0$  can be assumed for all quantities. At time  $t$  the bunches are centered at  $(x_1, y_1, z_1)$  and  $(x_2, y_2, z_2)$  for beam 1 and 2, respectively. Beam 1 (blue) comes from the left and beam 2 (red) comes from the right. The luminous region is indicated by a black ellipse. At the time  $t = 0$ , the bunches cross in position  $Z_{RF}$ , which is arbitrarily set at  $z = 0$ . In this example, both beams have a different offset in  $x$ , shifting the geometrical crossing point in the  $-z$  direction. The  $z$ -center of the luminous region is denoted by  $\xi_{lz}$ .

where  $\sigma_{mj}$  denotes the distribution width. The single beam density function is given by

$$\rho_j(x, y, z, 0) = \frac{\exp\left(-\frac{(\pm \cos\phi \cdot (x - \xi_{xj}) - \sin\phi \cdot (z - \xi_{zj}))^2}{2\sigma_{\hat{x}_j}^2} - \frac{(y - \xi_{yj})^2}{2\sigma_{\hat{y}_j}^2} - \frac{(\pm \cos\phi \cdot (z - \xi_{zj}) + \sin\phi \cdot (x - \xi_{xj}))^2}{2\sigma_{\hat{z}_j}^2}\right)}{\sqrt{2\pi}\sigma_{\hat{x}_j}\sqrt{2\pi}\sigma_{\hat{y}_j}\sqrt{2\pi}\sigma_{\hat{z}_j}}, \quad (3.12)$$

with  $\sigma_{\hat{x}_j}$ ,  $\sigma_{\hat{y}_j}$  and  $\sigma_{\hat{z}_j}$  the variance in the beam reference frame; the upper signs are for beam 1 and the lower signs for beam 2.

If one assume a bunch density time evolution given by

$$\rho_j(\mathbf{r}, t) = \rho_j(\mathbf{r} - \mathbf{v}_j t, 0), \quad (3.13)$$

with  $\mathbf{r} = (x, y, z)$ , the time-dependent bunch density function becomes

$$\begin{aligned} \rho_j(x, y, z, t) &= \frac{1}{\sqrt{2\pi}\sigma_{\hat{x}_j}} \exp\left(-\frac{(\pm \cos\phi \cdot (\Delta x_j - ct \sin\phi) - \sin\phi \cdot (\Delta z_j \mp ct \cos\phi))^2}{2\sigma_{\hat{x}_j}^2}\right) \\ &\times \frac{1}{\sqrt{2\pi}\sigma_{\hat{y}_j}} \exp\left(-\frac{\Delta y_j^2}{2\sigma_{\hat{y}_j}^2}\right) \\ &\times \frac{1}{\sqrt{2\pi}\sigma_{\hat{z}_j}} \exp\left(-\frac{(\pm \cos\phi \cdot (\Delta z_j \mp ct \cos\phi) + \sin\phi \cdot (\Delta x_j - ct \sin\phi))^2}{2\sigma_{\hat{z}_j}^2}\right), \end{aligned} \quad (3.14)$$

with  $\Delta m_j = m - \xi_{mj}$  for beam  $j = 1, 2$  and plane  $m = x, y, z$ . Note that Eq. (3.13) assumes that the beam shapes are constant and neglects the hourglass effect [28]. With  $\beta_{x,y}^* \gg \sigma_{z1,2}$ <sup>1</sup> as is the case for the measurements described here, the hourglass effect can be neglected for luminosity calibration. However, the hourglass effect will be used for single beam profiles measurements versus  $z$ , see Sec. 4.3.3.2.

Introducing the quantities

$$\begin{aligned} \Sigma_x^2 &= 2\sigma_{\hat{z}}^2 \sin^2\phi + 2\sigma_{\hat{x}}^2 \cos^2\phi & 2\sigma_{\hat{x}}^2 &= \sigma_{\hat{x}_1}^2 + \sigma_{\hat{x}_2}^2 \\ \Sigma_y^2 &= 2\sigma_{\hat{y}}^2 & \text{with} & \quad 2\sigma_{\hat{y}}^2 = \sigma_{\hat{y}_1}^2 + \sigma_{\hat{y}_2}^2 \\ \Sigma_z^2 &= 2\sigma_{\hat{z}}^2 & & \quad 2\sigma_{\hat{z}}^2 = \sigma_{\hat{z}_1}^2 + \sigma_{\hat{z}_2}^2, \end{aligned} \quad (3.15)$$

<sup>1</sup>The quantity  $\beta^*$  is the value of the beta function  $\beta(s)$  evaluated at the interaction point [29].

and the beam separation terms  $\Delta_m = \xi_{m1} - \xi_{m2}$  (with  $m = x, y$ ), the overlap integral in Eq. (3.9) is integrated over space and time with the single bunch density distributions defined in Eq. (3.14) and can be expressed as [26]

$$\mathcal{O} = \frac{e^{-\frac{\Delta_x^2}{2\Sigma_x^2} - \frac{\Delta_y^2}{2\Sigma_y^2}}}{2\pi \Sigma_x \Sigma_y}. \quad (3.16)$$

In the presence of small half crossing angles less than 1 mrad, as is the case at LHCb, the bunch variances can be expressed in the laboratory frame with  $\sigma_m^2 \simeq \sigma_m^2$  for the planes  $m = x, y, z$ . The formulation is based on results taken from [27, 28, 30]. In the presence of a crossing angle in both  $xz$  and  $yz$  planes and expressing Eq. (3.16) in terms of single bunch observables, the overlap integral is given by

$$\begin{aligned} \mathcal{O} = & \left( 2\pi \sqrt{(\sigma_{x1}^2 + \sigma_{x2}^2)(\sigma_{y1}^2 + \sigma_{y2}^2)} \right)^{-1} \\ & \times \left( 1 + \frac{\sigma_{z1}^2 + \sigma_{z2}^2}{\sigma_{x1}^2 + \sigma_{x2}^2} \tan^2(\phi_x) + \frac{\sigma_{z1}^2 + \sigma_{z2}^2}{\sigma_{y1}^2 + \sigma_{y2}^2} \tan^2(\phi_y) \right)^{-1/2} \\ & \times \exp \left( -\frac{\Delta_x^2}{2(\sigma_{x1}^2 + \sigma_{x2}^2)} - \frac{\Delta_y^2}{2(\sigma_{y1}^2 + \sigma_{y2}^2)} \right) \\ & \times \exp \left[ S^2 \frac{\sigma_{z1}^2 + \sigma_{z2}^2}{2} \left( \frac{\Delta_x \tan(\phi_x)}{\sigma_{x1}^2 + \sigma_{x2}^2} + \frac{\Delta_y \tan(\phi_y)}{\sigma_{y1}^2 + \sigma_{y2}^2} \right)^2 \right], \end{aligned} \quad (3.17)$$

with

$$S = \left( 1 + \frac{\sigma_{z1}^2 + \sigma_{z2}^2}{\sigma_{x1}^2 + \sigma_{x2}^2} \tan^2(\phi_x) + \frac{\sigma_{z1}^2 + \sigma_{z2}^2}{\sigma_{y1}^2 + \sigma_{y2}^2} \tan^2(\phi_y) \right)^{-1/2}.$$

The beam offset terms  $\Delta_m = \xi_{m1} - \xi_{m2}$  (with  $m = x, y$ ) are evaluated at the point  $Z_{\text{RF}}$  where the bunch pairs cross in time. The  $Z_{\text{RF}}$  position is defined by the LHC RF timing and need not coincide with the  $z = 0$  of the LHCb laboratory frame nor with the geometrical crossing point of the two beams.

The longitudinal position  $\xi_{lz}$  of the luminous region is related to the beam offset  $\Delta m$  in the crossing plane  $m$  and bunch crossing point  $Z_{\text{RF}}$  with [26]

$$Z_{\text{RF}} = \xi_{lz} - \delta z_{l,0,m}, \quad (3.18)$$

where  $\delta z_{l,0,m}$  is the longitudinal offset created by a crossing angle in the  $mz$  plane ( $m = x, y$ ). Assuming single Gaussian beams, with a crossing angle in the  $xz$  plane only, the longitudinal offset is given by

$$\delta z_{l,0} = -\frac{\sin 2\phi_x}{4} \cdot \frac{\sigma_{z1}^2 + \sigma_{z2}^2 - \sigma_{x1}^2 + \sigma_{x2}^2}{(\sigma_{x1}^2 + \sigma_{x2}^2) \cos^2 \phi_x + (\sigma_{z1}^2 + \sigma_{z2}^2) \sin^2 \phi_x} \cdot \Delta x. \quad (3.19)$$

In the presence of two crossing angles (in  $xz$  and  $yz$ ), the offset has two contributions  $\delta z_{l,0} = \delta z_{l,0,x} + \delta z_{l,0,y}$ , replacing  $x$  by  $y$  in the above equation for the second term.

The longitudinal width  $\sigma_{lz}^2$  of the luminous region is related to the bunch length convolution  $\sigma_{z1}^2 + \sigma_{z2}^2$  by [26]:

$$\frac{1}{\sigma_{lz}^2} = \frac{\Sigma_x^2}{\sigma_{\hat{x}}^2 \sigma_{\hat{z}}^2} = \frac{2 \sin^2 \phi_x \sigma_{\hat{z}}^2 + 2 \cos^2 \phi_x \sigma_{\hat{x}}^2}{\sigma_{\hat{x}}^2 \sigma_{\hat{z}}^2}, \quad (3.20)$$

with the index  $l$  indicating a luminous region quantity and  $\sigma_{\hat{x}}^2$  and  $\sigma_{\hat{z}}^2$  as defined in Eq. 3.15. In the presence of a crossing angle in both  $xz$  and  $yz$  planes, the above equation can be written as

$$\frac{1}{\sigma_{lz}^2} = \frac{4 \cos^2 \sqrt{\phi_x^2 + \phi_y^2}}{\sigma_{z1}^2 + \sigma_{z2}^2} + \frac{4 \sin^2(\phi_x)}{\sigma_{x1}^2 + \sigma_{x2}^2} + \frac{4 \sin^2(\phi_y)}{\sigma_{y1}^2 + \sigma_{y2}^2}. \quad (3.21)$$

### 3.1 Luminosity with the van der Meer method

The luminosity as defined in Eq. (3.8) requires evaluations for the bunch population products  $N_1 N_2$  and the overlap integral  $\mathcal{O}$ . One method to measure the overlap was introduced by S. van der Meer to measure the luminosity of the coasting beams in the Intersecting Storage Rings collider [31]. The method was further extended to measure the luminosity of a collider with bunched beams [32] and is the main method used to determine the luminosity at the other LHC experiments [33]. The key principle of the van der Meer scan method (VDM) is to express the overlap integral in terms of rates that are experimental observables as opposed to measure the bunch density functions. Experimentally, the method consists in moving the beams across each other in the vertical and horizontal directions. The overlap integral can be inferred from the rates measured at different beam positions. The formalism of the method is described below.

Starting with Eq. (3.7), under the assumption that the beam densities are independent in the  $x$  and  $y$  variables, and assuming vanishing crossing angle between the beams, the integration over  $dz dt$  in Eq. (3.7) results in

$$\int \rho_{z1}(z - ct) \rho_{z2}(z + ct) dz dt = \frac{1}{2c},$$

canceling the factor  $2c$  in Eq. (3.7). It follows that the luminosity can be expressed as

$$\mathcal{L} = \nu_{\text{rev}} N_1 N_2 \int \rho_{1x}(x) \rho_{1y}(y) \rho_{2x}(x) \rho_{2y}(y) dx dy. \quad (3.22)$$

Displacing beam 2 by an offset  $\Delta x$  and  $\Delta y$  in the transverse directions, the luminosity becomes

$$\mathcal{L}(\Delta x, \Delta y) = \nu_{\text{rev}} N_1 N_2 \int \rho_{1x}(x) \rho_{1y}(y) \rho_{2x}(x + \Delta x) \rho_{2y}(y + \Delta y) dx dy. \quad (3.23)$$

Since the  $x$  and  $y$  variables are assumed to be decoupled, the integrals over  $dx$  and  $dy$  can be replaced by a constant term  $A_x$  and  $A_y$ , respectively with

$$\begin{aligned} \mathcal{L}(\Delta x, \Delta y) &= \nu_{\text{rev}} N_1 N_2 \int \rho_{1x}(x) \rho_{2x}(x + \Delta x) dx \int \rho_{1y}(y) \rho_{2y}(y + \Delta y) dy \\ \mathcal{L}(\Delta x, \Delta y) &= \nu_{\text{rev}} N_1 N_2 A_x(\Delta x) A_y(\Delta y). \end{aligned} \quad (3.24)$$

Considering only the integration over  $dx$

$$\mathcal{L}(\Delta x, \Delta y) = \nu_{\text{rev}} N_1 N_2 A_y(\Delta y) \int \rho_{1x}(x) \rho_{2x}(x + \Delta x) dx, \quad (3.25)$$

and integrating both sides over the displacement  $d(\Delta x)$  yields

$$\int \mathcal{L}(\Delta x, \Delta y) d(\Delta x) = \nu_{\text{rev}} N_1 N_2 A_y(\Delta y) \int \rho_{1x}(x) \rho_{2x}(x + \Delta x) d(\Delta x) dx. \quad (3.26)$$

Using the integral property

$$\int \rho_{2x}(x + \Delta x) d(\Delta x) = \int \rho_{2x}(x) dx, \quad (3.27)$$

and the fact that the bunch density functions are normalized to unity,

$$\int \rho_{1x}(x) dx = \int \rho_{2x}(x) dx = 1, \quad (3.28)$$

the constant term  $A_y(\Delta y)$  can be expressed with

$$A_y(\Delta y) = \frac{\int \mathcal{L}(\Delta x, \Delta y) d(\Delta x)}{\nu_{\text{rev}} N_1 N_2}. \quad (3.29)$$

Substituting Eq. (3.29) in Eq. (3.24) provides a value for  $A_x(\Delta x)$  for a fixed displacement  $\Delta y_0$  in the  $y$  coordinate

$$A_x(\Delta x) = \frac{\mathcal{L}(\Delta x, \Delta y_0)}{\int \mathcal{L}(\Delta x, \Delta y_0) d(\Delta x)}. \quad (3.30)$$

The measurement of  $A_x(\Delta x)$  in Eq. (3.30) is performed by moving the beams in the  $x$  axis over  $d(\Delta x)$ , while the displacement in  $y$  is kept at a constant separation  $\Delta y_0$ . The same substitution procedure in the  $y$  direction is used to evaluate the term  $A_y(\Delta y)$ , which is given by

$$A_y(\Delta y) = \frac{\mathcal{L}(\Delta x_0, \Delta y)}{\int \mathcal{L}(\Delta x_0, \Delta y) d(\Delta y)} \quad (3.31)$$

for a fixed displacement  $\Delta x_0$  in the  $x$  direction.

The luminosity is not directly measurable in Eqs. (3.30) and (3.31). Instead, the interaction rate  $R$ , which is linear with the luminosity, is used as observable. Accordingly, using Eq. (3.24) with Eqs. (3.30) and (3.31), the absolute luminosity at a given beam displacement  $\Delta x_0, \Delta y_0$  is given by

$$\mathcal{L}(\Delta x_0, \Delta y_0) = \nu_{\text{rev}} N_1 N_2 \frac{R(\Delta x_0, \Delta y_0) R(\Delta x_0, \Delta y_0)}{\int R(\Delta x, \Delta y_0) d(\Delta x) \cdot \int R(\Delta x_0, \Delta y) d(\Delta y)}. \quad (3.32)$$

The pair of displacements  $(\Delta x_0, \Delta y_0)$  is called the working point and is typically chosen to be as close as possible to  $(0,0)$ , that is, head-on beams. The VDM formula (3.32), however, is valid for any  $\Delta x_0$  and  $\Delta y_0$  positions. It can be shown that Eq. (3.32) is valid also in the presence of non-zero crossing angles [34].

The VDM method has the advantage to use a detector rate as its only observable, which is experimentally simple. Additionally, the method does not assume a particular beam shape.

The experimental difficulties of the VDM method arise mostly from the fact that the beams must be moved to perform the measurement. The exact displacements  $\Delta x, \Delta y$  in Eq. (3.32) steered by the LHC magnets are calibrated by the LHC experiments in a so-called length scale calibration (LSC) [35]. While the resulting corrections are typically of the order of 1%, some larger non-reproducibilities have been observed between two consecutive scans without being able to identify the cause. Another difficulty originates from beam-beam effects. When the beams are displaced, a change in  $\beta^*$  (dynamic beta) and a beam deflection may be produced, which influences the observed rate [36]. The resulting corrections to the visible cross-section depend on the LHC optics, the beam parameters and filling scheme, and must be evaluated at each interaction point.

In addition, the VDM method as performed in only one vertical and one horizontal scan, is valid only under the assumption that the transverse directions  $x$  and  $y$  are independent, i.e., that the  $x$  ( $y$ ) shape measured at a working point  $\Delta y_0$  ( $\Delta x_0$ ) does not depend on the working point position. As will be seen in Sec. 4.6.2, the beams can only be considered factorizable in  $x$  and  $y$  for the measurements performed in Nov 2012, in all other measurements a time dependence was observed in the cross-section measurements traced back to the non-factorizable shape of the beams.

## 3.2 Luminosity with the beam-gas imaging method

A direct luminosity measurement alternative to the VDM method is the Beam-Gas Imaging (BGI) method [37] which is used in this work and is, to date, a unique capability of the LHCb experiment. The principle of this method is to evaluate the overlap integral by measuring all required observables in Eq. (3.17) using beam-gas interaction vertices. Measuring stationary beams allows avoiding changes of beam-beam effects and other non reproducible effects due to beam

steering. Furthermore, the measurements are made parasitically while other experiments perform VDM scans and can therefore be made in all dedicated luminosity calibration fills.

On the other hand, while the  $\beta^*$  and crossing angles used at the LHC did not impact the VDM method, the BGI measurement relies on the vertex measurement to determine the bunch shape. Therefore, an increased<sup>2</sup>  $\beta^*$  is preferable such as to avoid being limited by the detector resolution. Also the knowledge of the crossing angle is important since the luminosity reduction due to the crossing angle can be as large as 20%. Furthermore, the crossing angle is necessary to avoid interactions between the main bunch and out-of-time charges captured in the next RF bucket (see Sec. 6). Such displaced collisions, centered at  $z = \pm 37.5$  cm, can not be all disentangled cleanly from beam-gas interactions. They can be avoided by introducing a crossing angle. On the other hand, the VDM measurement can exclude interactions occurring away from the interaction point and is therefore not affected by these so-called “satellite” collisions.

A single Gaussian model does not describe the bunch shape well enough and a precision luminosity measurement requires a shape description with a superposition of two Gaussian functions (“double Gaussian model”). Furthermore, as will be seen in Sec. 4.4, an additional factorizability parameter is required in case of double Gaussian beams to describe the relation between the description in  $x$  and  $y$ . While the overlap integral with double Gaussian beams can be written as the sum of partial single Gaussian overlap integrals resulting from the combination of all partial double Gaussian widths, the individual weights depend on the factorizability parameter and will be explained in Sec. 4.4.2 and 4.4.3. The non Gaussian shape and factorizability have also to be taken into account with the VDM method.

The VDM and BGI methods are complementary in the sense that they have different experimental difficulties. The systematic uncertainties on the overlap integral are highly uncorrelated and a luminosity calibration performed with both methods in the same fill permits the systematic uncertainties to be constrained further. At present this can only be done by LHCb.

---

<sup>2</sup>At LHCb, in 2012, normal physics fills were operated at  $\beta^* = 3$  m, while most luminosity calibrations fills were operated at  $\beta^* = 10$  m.

## 4 BEAM-GAS IMAGING MEASUREMENTS

This chapter describes the beam-gas imaging method starting with the data-taking conditions and event selection (Sec. 4.1) and followed by the gas injection (Sec. 4.2). The measurement of the vertex resolution, which is required to determine the physical beam shapes, is discussed in Sec. 4.3. The measurements of all beam parameters required to measure the overlap integral are treated in Sec. 4.4 and follow the order in which the parameters are measured: first the crossing angles, then the transverse beam shapes and finally the convolved bunch length. A generic simulation method used to validate the fit model is described in Sec. 4.5. Finally, Sec. 4.6 describes the measurement of the overlap integral which combines all beam parameters.

### 4.1 Data-taking conditions and event selection

Three important configuration sets are described here. First, the experimental configuration of the beam during the luminosity calibration measurements. Second, the LHCb trigger configuration during those same measurements. Third, the data selection configuration.

#### 4.1.1 LHC fills with BGI measurements

Since the start of LHC operation a series of dedicated luminosity calibration measurements have been carried out by the main LHC experiments at each interaction point (IP). Those measurements are usually performed in dedicated LHC fills, which, whenever possible, use a special machine setup and filling scheme optimized according to the requirements of each experiment. While the Beam-Gas Imaging (BGI) method has been used before 2012 to measure the visible cross-section [35], limitations in the bunch current normalization accuracy did not justify dedicated LHC optics and optimizations in the beam-gas method. The drastic improvement of the beam intensity measurement accuracy, obtained in early 2012 (see Chap. 6), opened the way to a full exploitation of the method’s potential by using special beam optics, new trigger schemes and by increasing the event rate by degrading the vacuum or at a later stage by injecting gas into the beam pipe. The first step was to switch off the VELO vacuum pumps, while the second step consisted in installing a new gas injection system called SMOG (see next Sec. 4.2 and Appendix F). Since 2012 all  $pp$  fills dedicated to luminosity calibration benefited from SMOG gas injection and from a new trigger selection (described below).

The list of dedicated luminosity calibration fills for 2012 and 2013 is provided in Table 4.1. A total of eight  $pp$  fills were dedicated to luminosity calibrations at  $\sqrt{s} = 8$  TeV in 2012. The LHCb experiment recorded data during all fills, allowing the BGI method to be used parasitically while other experiments carried out their measurement. The gas injection used for the BGI method was interrupted only for the VDM measurements at LHCb, which were performed in fills 2523 and 2853.

In addition to the data acquired parasitically, two periods of 40 minutes were dedicated to the LHCb experiment for the BGI method in fills 2852 and 2853. During those dedicated periods the

beams were left untouched at every LHC interaction point (IP) to avoid a possible parasitic beam movement at LHCb while another experiment would perform a VDM scan.

Fills 2520 and 2523 in April 2012 were performed with the normal physics optics at IP8 with  $\beta^* = 3$  m and a crossing angle in both  $xz$  and  $yz$  planes (see Fig. 4.2 left). Those two fills are therefore suboptimal for the BGI method and are only used to evaluate the systematic uncertainty as will be discussed in Sec. 7.2.1. Additionally, BGI measurements with displaced beams have been performed in fills 2852 and 2853 and are discussed in Sec. 7.2.7.2. In addition, the LHCb luminosity calibration relied on the BGI method alone for intermediate energy  $pp$  fills at  $\sqrt{s} = 2.76$  TeV in 2013.

Luminosity calibrations in January 2013 with lead ions in one beam were performed in normal physics fills and LHCb provided a ghost charge measurement for the other LHC experiments that performed luminosity calibrations. Those fills were acquired with the normal trigger dedicated to physics data taking. The VELO vacuum was degraded only by switching off the vacuum pumps instead of operating the SMOG gas injection such as to limit the amount of beam-gas background. The BGI method has not been used for the  $p\text{Pb}$  fills in 2013, but was used in the  $p\text{Pb}$  pilot fill 3056 in September 2012. This measurement suffered from very low beam intensities. Its results were reported elsewhere [38] and are not part of this work.

Finally, the LHCb experiment provided a beam width measurement as function of time with the beam-gas method in the scope of an LHC machine development period during fill 3160.

### 4.1.2 Trigger conditions

The LHCb trigger system is devised in two stages: a hardware trigger is implemented in dedicated electronics, then a software based High Level Trigger (HLT) running on a computing farm analyses events which passed the hardware trigger decision. The purpose of the hardware trigger is to reduce the events rate down to 1 MHz while keeping a high efficiency for the different physics channels [39].

Performing luminosity calibration measurements with beam-gas interactions during dedicated fills permits the optimization of the trigger requirements for beam-gas interactions in both hardware and HLT stages. All luminosity calibration fills acquired in 2012 and 2013 benefited from a simplified trigger on activity in all bunch crossing types. For these fills the hardware trigger used information from the SPD and PU sensors, and from the calorimeters. The relevant hardware trigger channels with their trigger conditions are described in Table 4.2. The HLT trigger dedicated to the BGI measurement accepted events based on the vertex position and track multiplicity. The full HLT requirements are described in Table 4.3. The top rows describe the conditions present for both April 2012 fills, while the second set of rows describes the condition used for all subsequent fills. In April 2012 the hardware trigger requirements were different depending on the bunch crossing type, while no such distinction was made for later fills, the strategy being to trigger on any activity on all bunch crossings and only prescale the large beam-beam rate. As a consequence, the trigger requirements used as of July 2012 are more uniform in all bunch-crossing types and are simpler.

While beam-gas interactions in non-colliding and empty bunches are used for the ghost charge measurement (see Sec. 6.2) and for resolution measurements (Sec. 4.3), only beam-gas events originating from colliding bunch pairs are relevant for the overlap integral measurement with the BGI analysis. The measurement of the beam crossing angles uses a combination of both colliding and non-colliding bunches. The last two columns show the requirements for  $bb$  crossings. To select beam-gas events in  $bb$  crossings, any hardware triggered event having a vertex  $z$ -position at least 300

**Table 4.1:** Dedicated luminosity measurement fills used for BGI analysis or fills for which LHCb provided related beam-gas measurements as a service to other experiments. Fills 2520 to 3316 were dedicated to  $pp$  luminosity measurements at  $\sqrt{s} = 8$  TeV, while  $pp$  calibrations in fills 3555 to 3563 were performed at  $\sqrt{s} = 2.76$  TeV. January 2013  $Pbp$  and  $pPb$  fills at  $\sqrt{s} = 5.02$  TeV/nucleon were analysed for ghost charge measurements. LHCb provided a beam width measurement in fill 3160 for an LHC machine development (MD). The number of colliding bunches at LHCb is indicated in parenthesis. The vacuum state “SMOG” indicates an acquisition performed with gas injection (see Sec.4.2), “pumps off” indicates that the vacuum was degraded by switching the pumps off, without gas injection.

Period	Fill	angle $\phi_x(\phi_y)$	$\beta^*$	Bunches per beam	Vacuum state	Remarks
Fills with BGI luminosity calibration; $pp$ at $\sqrt{s} = 8$ TeV						
Apr 2012	2520	236(90) $\mu$ rad	3 m	48 (6)	SMOG	VDM for ATLAS, CMS LHCb trigger efficiency
Apr 2012	2523	236(90) $\mu$ rad	3 m	52 (24)	SMOG	VDM for LHCb, ALICE
Jul 2012	2852	456(0) $\mu$ rad	10 m	50 (16)	SMOG	VDM for ALICE BGI with beam offset in $y$
Jul 2012	2853	456(0) $\mu$ rad	10 m	35 (16)	SMOG	VDM for LHCb BGI with beam offset in $y$
Jul 2012	2855	456(0) $\mu$ rad	10 m	48 (6)	SMOG	VDM for ATLAS, CMS
Jul 2012	2856	456(0) $\mu$ rad	10 m	48 (6)	SMOG	VDM for ATLAS, CMS
Nov 2012	3311	456(0) $\mu$ rad	10 m	39 (6)	SMOG	VDM for ATLAS
Nov 2012	3316	456(0) $\mu$ rad	10 m	39 (6)	SMOG	VDM for ATLAS CMS, ALICE
Oct 2012	3160	236(0) $\mu$ rad	3 m	24 (1)	SMOG	emittance MD
Fills with BGI luminosity calibration; $pp$ at $\sqrt{s} = 2.76$ TeV						
Feb 2013	3555	885(0) $\mu$ rad	10 m	100 (22)	SMOG	LHCb BGI analysis
Feb 2013	3562	885(0) $\mu$ rad	10 m	39 (6)	SMOG	VDM for ATLAS
Feb 2013	3563	885(0) $\mu$ rad	10 m	39 (6)	SMOG	VDM for CMS and ATLAS
Fills with beam-gas analysis; $pPb$ at $\sqrt{s_{NN}} = 5.02$ TeV						
Sep 2012	3056	456(0) $\mu$ rad	10 m	15 (8)	SMOG	pilot run $p$ - $Pb$
Jan 2013	3503	456(0) $\mu$ rad	2 m	272+338 (38)	pumps off	VDM for ATLAS, CMS
Jan 2013	3505	456(0) $\mu$ rad	2 m	272+338 (38)	pumps off	VDM for ALICE
Fills with beam-gas analysis; $Pbp$ at $\sqrt{s_{NN}} = 5.02$ TeV						
Jan 2013	3537	456(0) $\mu$ rad	2 m	314+272 (22)	pumps off	VDM for ALICE, CMS
Jan 2013	3540	456(0) $\mu$ rad	2 m	314+272 (22)	pumps off	VDM for ATLAS

mm away from the interaction point but within  $\pm 2$  m is acquired without prescaling (as long as the track multiplicity and transverse position requirement are also met). The central region is excluded in order to reject  $pp$  interactions; instead, to select beam-beam events, all vertices within  $\pm 2$  m are selected with a prescale factor.<sup>1</sup> This way the total event accept rate is kept within the online writing speed capability. The highest hardware trigger rate observed for dedicated luminosity calibration fills was about 300 kHz all of which can be reconstructed by the HLT. The prescale for beam-beam events is selected such as to keep the total accept rate below 15 kHz which is close to the maximal rate which can be recorded.

**Table 4.2:** Hardware trigger channel definitions used for dedicated BGI luminosity measurement fills.  $\sum E_T$  is the total transverse energy deposited in the calorimeters  $N_{PU}$  is the hit multiplicity in the Pile-Up system,  $N_{SPD}$  is the hit multiplicity in the Scintillating Pad Detector.

Channel name	Logical operation	$\sum E_T$	Trigger conditions	$N_{PU}$	$N_{SPD}$	Remarks
L0B1gas	AND		$> 250$ MeV	$< 40$ hits	—	Dedicated to select beam-gas interactions from beam 1
L0B2gas	AND		$< 300$ MeV	$> 9$ hits	—	Dedicated to select beam-gas interactions from beam 2
L0BB	OR	—		$> 5$ hits	$> 5$ hits	Triggers on any beam-beam interaction

**Table 4.3:** High level trigger requirements for dedicated luminosity measurement fills. The first half of the table shows the requirements used in April 2012, while the second half shows the requirements used later as of July 2012. Relevant differences are emphasized in bold.

Filter type	Beam-gas in ee	Beam-gas in ee	Beam-gas in be	Beam-gas in eb	Beam-gas in bb	Beam-beam in bb
Apr 2012						
Prescale	1	1	1	1	1	1, 20 or 50
Bunch crossing	<i>ee</i>	<i>ee</i>	<i>be</i>	<i>eb</i>	<i>bb</i>	<i>bb</i>
Longitudinal position $z$ (mm)	$[-2000,400]$	$[0,2000]$	$[-2000,400]$	$[-2000,400]$	$[-2000,-300] \cup [300,2000]$	$[-2000,2000]$
Hardware line	L0B1gas	L0B2gas	L0B1gas	L0B2gas	L0BB	L0BB
Hardware rate limit				10 MHz		
Tracks in vertex					$> 6$	
Transverse position					$< 4$ mm	
Postscale					10 MHz	
Filter type from Jul 2012	Beam-gas in ee	Beam-gas in ee	Beam-gas in be	Beam-gas in eb	Beam-gas in bb	Beam-beam in bb
Prescale	1	1	1	1	1	0, 1, 3.5, 5, 7 10, 15 or 20
Bunch crossing	<i>ee</i>	<i>ee</i>	<i>be</i>	<i>eb</i>	<i>bb</i>	<i>bb</i>
Longitudinal position $z$ (mm)	$[-2000,400]$	$[0,2000]$	$[-2000,400]$	$[-2000,400]$	$[-2000,-300] \cup [300,2000]$	$[-2000,2000]$
Hardware line					Any hardware trigger decision	
Hardware rate limit					none	
Tracks in vertex					$> 10$	
Transverse position					$< 4$ mm	
Postscale					none	

<sup>1</sup>The prescale factor can be changed during data taking.

### 4.1.3 Data selection

All events acquired are reconstructed offline with a standard LHCb set of algorithms. A vertex has a number of tracks  $N_{\text{tracks}}$  associated to it, each track having either a forward or backward direction with respect to beam 1. Their quantities are defined as  $N_{\text{bwd tr}}$  and  $N_{\text{fwd tr}}$ . Forward tracks are created by particles moving towards the LHCb spectrometer and benefit from additional information such as energy and transverse momentum which can improve the vertex resolution. The acceptance for forward tracks falls to zero at  $z \gtrsim 600$  mm. Backward tracks are only seen by the VELO and can be detected when they originate with values of  $z \gtrsim -95$  mm. The longitudinal vertex distribution for all bunch-crossing types is shown in Fig. 4.1 before applying further selection criteria. The acceptance limits for beam-gas events from beam 1 (blue) and beam 2 (red) are visible as a sharp drop. It can be seen that the acceptance drops in two stages for beam 1 at about 200 mm and 400 mm; this effect is related to the positions of VELO sensors in the forward region. The distribution of  $pp$  events in the luminous region is reduced due to the prescale factor, which also affects beam-gas interactions in  $bb$  crossings located in  $|z| < 300$  mm. The longitudinal vertex distribution for non-colliding bunches are shown in Fig. 4.2 for the first 1000 vertices per beam. The same data are shown as a 3 dimensional scatter plot in Fig. 4.3.

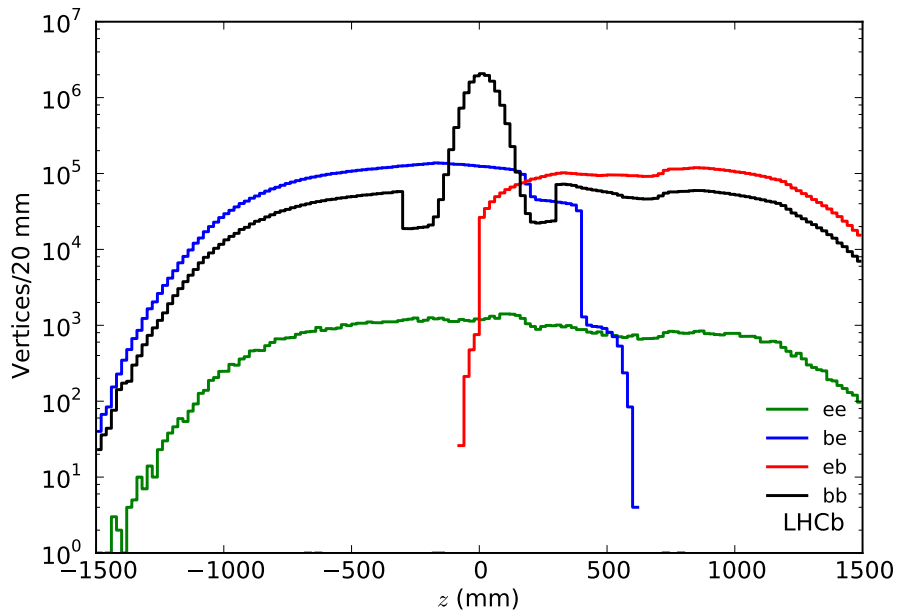


**Fig. 4.1:** Distribution of longitudinal  $z$ -position vertices for the various bunch crossing types acquired in 40 minutes (fill 2852). Crossing types  $ee$ ,  $be$  and  $eb$  contain only beam-gas events while  $bb$  crossing types contain beam-beam vertices in the central region and beam-gas vertices away from  $z = 0$ . The effect of the trigger prescale reducing  $pp$  events is visible. Also the exclusion region of  $\pm 300$  mm for beam-gas events in  $bb$  crossings is visible.

The BGI method relies on an unambiguous differentiation of beam-gas and beam-beam vertices to measure the single beam and luminous region shapes. The vertices are selected according to the following criteria:

1. The transverse position of a vertex must be within a 2 mm distance from the beam-line ( $\sqrt{x^2 + y^2} < 2$  mm) to exclude material interactions (in the VELO RF foil).
2. The vertex must be in the longitudinal range  $-1000 \text{ mm} \leq z \leq 500 \text{ mm}$  for beam1-gas and  $0 \text{ mm} \leq z \leq 1000 \text{ mm}$  for beam2-gas.
3. Beam-gas interaction vertices from colliding bunch pairs ( $bb$  crossing type) are excluded in the central region  $-250 \text{ mm} < z < 250 \text{ mm}$  as they cannot be unambiguously differentiated

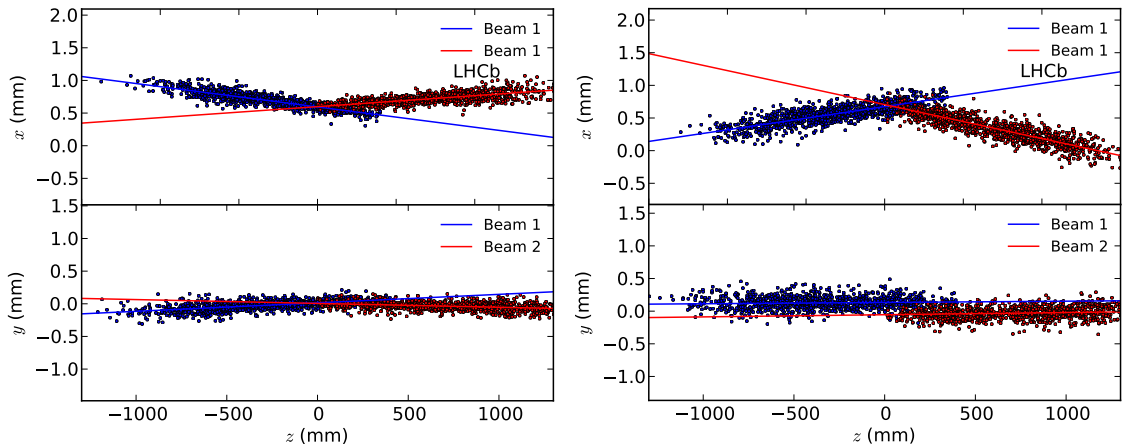


**Fig. 4.2:** Position of beam-gas vertices projected in the  $xz$  and  $yz$  planes for fill 2520 on the left plot and fill 2852 on the right plot. The first 1000 vertices per beam are shown. The effect of the crossing angle in both planes for fill 2520 (left) and on the  $xz$  plane only in fill 2852 (right) are visible. The angles are measured by fitting a straight line through all vertices and indicated as solid lines. The beams were offset in the  $yz$  plane during this period of fill 2852; beam 1 is slightly above beam 2 in the  $y$  plane (right plot, bottom).

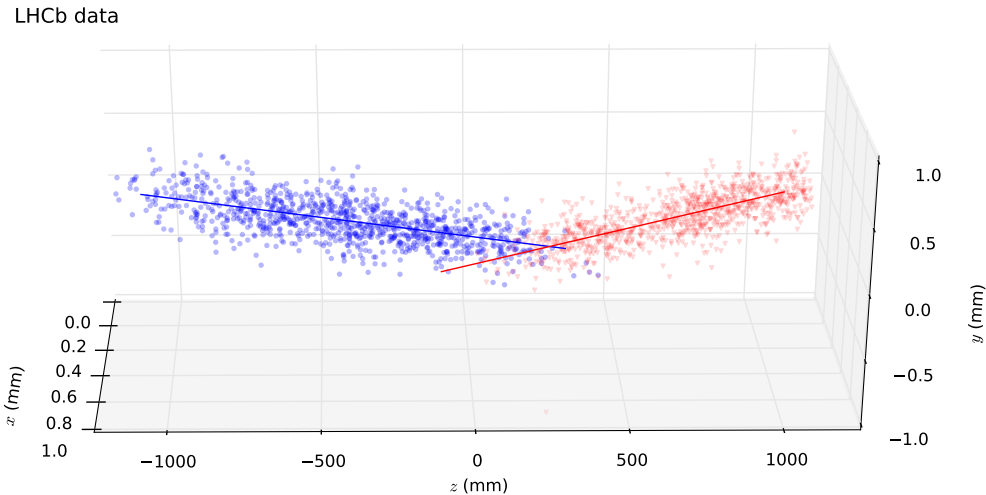


**Fig. 4.3:** Reconstructed beam-gas interaction vertices view in 3 dimensions for illustration purpose showing the first 1000 vertices per beam acquired during fill 2852. The effect of the crossing angle is visible. The angles are measured by fitting a straight line through all vertices and indicated as solid lines. The beam were offset in the  $yz$  plane during this period of fill 2852, it can be seen that beam 1 is slightly above beam 2 in the  $y$  plane.

from beam-beam vertices.

4. Beam-beam interaction vertices are required to originate from the central region  $-250 \text{ mm} < z < 250 \text{ mm}$ .
5. The reconstructed vertex must have at least 10 tracks:  $N_{\text{tracks}} \geq 10$ .
6. Finally, a forward-backward track asymmetry is required to separate beam-gas interactions originating from beam 1 or beam 2: vertices are required to have zero backward track for beam 1 and respectively zero forward track for beam 2. This requirement, however, is effective only in the VELO region  $-95 \text{ mm} < z < 600 \text{ mm}$  where both backward and forward tracks can be detected. For beam-gas events originating in a  $bb$  crossing where beam-gas interaction vertices are excluded in the central region, this asymmetry cut is only effective for beam 2 in the region  $300 \text{ mm} < z < 600 \text{ mm}$ . It is nevertheless an important requirement for ghost charge measurements as explained in Sec. 6.2.2.

7. Beam-gas vertices are excluded by the trigger in  $bb$  crossing in the central region  $-300 \text{ mm} < z < 300 \text{ mm}$ , effectively allowing a negligible fraction of the order of  $5 \times 10^{-8}$   $pp$  events to be triggered as beam-gas.<sup>2</sup> The above selection list rejects beam-beam interaction vertices in the narrower central region  $-250 \text{ mm} < z < 250 \text{ mm}$  to accept the fraction of beam-gas interactions which occurred in a triggered  $pp$  event. Beam-beam interaction vertices selected for the transverse luminous region measurements are required to have at least two forward and two backward tracks.

## 4.2 Gas injection

Dedicated luminosity calibration fills are operated with a low number of bunches of about 50 per beam or less. Under these conditions the normal vacuum pressure at the interaction point is of the order of  $10^{-9}$  mbar, producing an HLT and hardware triggered beam-gas rate of about 0.3 and 0.5 Hz per bunch with the nominal intensity<sup>3</sup> for beam 1 and beam 2, respectively. The beam-gas rate is directly proportional to the bunch population. Performing a BGI measurement with such low beam-gas rates necessitates integration of a measurement over a period of up to 8 hours. Previous measurements [35], if they would not have been limited by the DCCT precision, would have been limited by event rate, by the beam drift and by emittance growth over the integration time of many hours. In 2011 the VELO vacuum pumps placed close to the interaction point were switched off, increasing the beam-gas rate by about a factor of 4. To increase the beam-gas rate further and to take full advantage of the BGI capabilities, a gas injection system (SMOG<sup>4</sup>) was proposed and developed for LHCb [37].

Since a precise luminosity measurement with beam-gas imaging was only possible with the help of an increased beam-gas interaction rate, a central part of this work was to commission and operate the SMOG system to bring the BGI method to its full potential. All laboratory measurements and commissioning work and final in-situ tests are documented in Appendix F. The results permitted the approval by the CERN vacuum group and convinced the LHCb collaboration and the LHC machine committee of its usefulness and safe operation. The SMOG has been installed in the LHCb detector environment in November 2011 during a technical stop. A first gas injection test with circulating beams was performed on 10 November 2011.

When activating the SMOG system, neon gas is injected in the VELO, thus raising the pressure from about  $10^{-9}$  mbar to slightly above  $10^{-7}$  mbar. The beam-gas rate is increased proportionally to the pressure. Once the injection is stopped, the nominal pressure below  $10^{-9}$  mbar is reached within 20 minutes. The effect of the SMOG gas injection on the pressure and beam-gas rate is shown in Fig. 4.4. An example of SMOG operation for a BGI measurement is shown in Fig. 4.5 for fill 2853 where the different measurements and gas injection sequences can be seen. Fill 2853 acquired in July 2012 was dedicated to a luminosity calibration for LHCb and allowed a BGI measurement to be performed together with a VDM scan in the same fill.

With the July trigger configuration for  $pp$  collisions at  $\sqrt{s} = 8 \text{ TeV}$ , the selected beam-gas rates are about 98 Hz/ $10^{11}$  protons and 82 Hz/ $10^{11}$  protons for beam 1 and 2, respectively. The corresponding rates of the hardware trigger lines L0B1gas and L0B2gas (described in Table 4.2) are respectively about 2.1 kHz/ $10^{11}$  protons and 1.3 kHz/ $10^{11}$ .

<sup>2</sup> Assuming a luminous region longitudinal Gaussian length of  $\sigma_{lz} = 55 \text{ mm}$ , the fraction of the tail distribution is  $\int_{\infty}^{-300} (\sqrt{2\pi} \sigma_{lz})^{-1} e^{-\frac{1}{2}(z/\sigma_{lz})^2} \approx 2.5 \times 10^{-8}$  per side.

<sup>3</sup> Proton bunches injected for  $pp$  luminosity calibration fills have an intensity in the order of  $10^{11}$  charges.

<sup>4</sup> SMOG stands for System to Measure the Overlap integral with Gas.

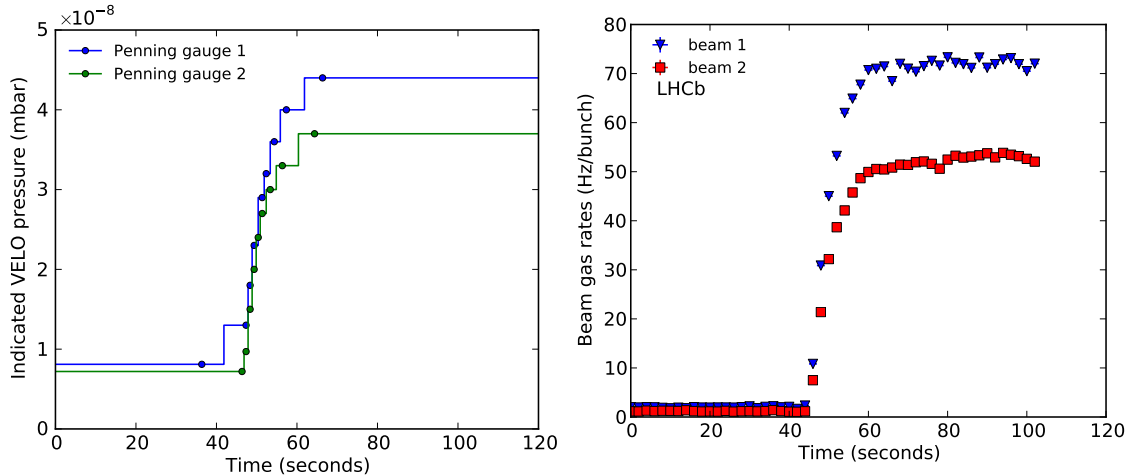


**Fig. 4.4:** Beam-gas event rate increase with SMOG injection (fill 2520). Left: Pressure increase in VELO with gas injection. The pressure is measured with Penning gauges (VGPC.PE411 and VGPC.PE412) in the vacuum vessel within 50 cm of the interaction point. The indicated value when neon is injected is to be multiplied by 4.1 to account for the neon gauge sensitivity. Right: selected beam-gas rate increase with SMOG operation. The rate increases from about 2 to 72 Hz/bunch for beam 1 and 1.3 to 41 Hz/bunch for beam 2 compared to the “pumps off” situation.

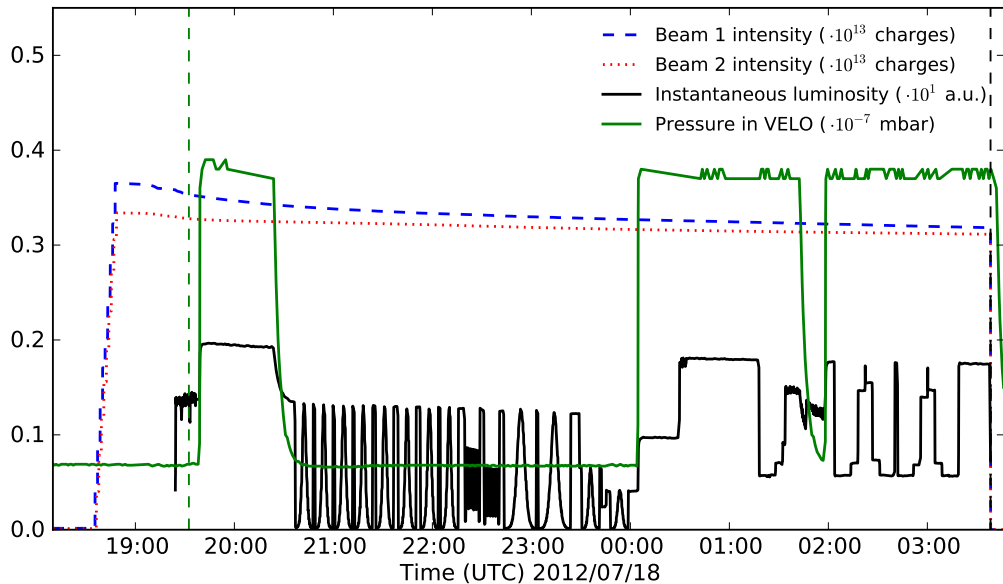


**Fig. 4.5:** Dedicated luminosity measurement fill with gas injection (fill 2853). The different measurement activities can be inferred from the instantaneous luminosity and pressure values. A first BGI period at about 19:40-20:20 was followed by a VDM measurement without gas injection (from about 20:30 to 24:00). After the VDM measurement, gas injection was resumed to perform a BGI measurement with offset beams (see lower luminosity step) and then with head-on beams ending at about 01:30. The last part of the fill was used to perform a special length scale calibration using beam-gas data. The pressure drop just before 02:00 was due to a technical problem which necessitated to stop the SMOG for a short time. The vertical dashed lines denote the stable beam period as defined by the LHC operation.

### 4.3 Vertex Resolution

The knowledge of the vertex resolution is a central ingredient for the measurement of the absolute beam shapes as the observed vertex distribution is a convolution of the physical beam with the detector resolution. While it is desirable to obtain a resolution as small as possible compared to the beam size, the intrinsic resolution is mostly dictated by the detector and sensor geometry and to some extent by the reconstruction algorithms and detector alignment. To reduce the impact of the

resolution on the overlap integral measurement, most dedicated luminosity calibration fills were operated at a  $\beta^*$  value of 10 m (larger than the value of 3 m used for physics runs). This resulted in increasing the beam width to about twice the resolution. While the larger beam size compared to the resolution reduces the uncertainties related to it, a good resolution description and understanding of additional effects influencing the beam width remains crucial for a precision measurement of the luminosity.

The vertex resolution as defined here and used for the BGI analysis is understood as the standard deviation of the distribution of the distance  $\Delta v$  (for  $v = x, y$ ) between the true vertex position and its measured position, i.e. a small resolution implies a more accurate vertex position. The resolution depends on the number of tracks associated with a vertex, the longitudinal  $z$ -position and whether the vertex originates from a beam-gas collision with only forward or only backward tracks, or from a beam-beam collision with both forward and backward tracks. Although the longitudinal resolution of about 100  $\mu\text{m}$  in the  $z$  plane is about 10 times larger than the resolution in the transverse plane, its effect can be neglected when measuring the comparatively large beam spot  $z$ -length of about 50 to 60 mm. Consequently, only resolution values in the transverse  $x$  and  $y$  planes are considered here. The measurement is performed on an event-by-event basis using the same data as for the BGI analysis.

The resolution is measured separately for beam-beam and beam-gas interactions. In all cases a correction factor as function of  $z$  is evaluated to take the  $z$ -dependence of the resolution into account. While the resolution measurements are not statistically limited and the parametrization functions appear to describe the data without bias, consistency checks shown in Sec. 4.3.3.2 and performed on the single beam width revealed the presence of additional factors broadening the beam which are not explained by the measured detector resolution. The last section 4.3.3.2 is dedicated to the measurement of correction factors applied to the beam-gas interaction vertex resolution. The combined effect of all resolution correction factors on the cross-section will be added as systematic uncertainty.

### 4.3.1 Resolution unfolding

The observed vertex distribution of a sample  $M(m)$  (for  $m = x, y$ ) is a convolution of the physical beam distribution with the detector vertex resolution. The vertex resolution is described with an effective resolution function  $R(m)$  per coordinate  $m = x, y$ . All vertices of a sample have an assigned resolution that is evaluated with the vertex properties such as, for example, the number of tracks and the  $z$ -position. The function  $R(m)$  is typically non-Gaussian, but can be described with the sum of  $K$  Gaussian functions, with each function having a width  $\sigma_{\text{res},k}$  weighted with the relative occupancy  $c_k$

$$R(m) = \sum_{k=1}^K c_k g_k(m; \sigma_{\text{res},k}). \quad (4.1)$$

The weight  $c_k$  is the fraction of vertices from the sample to be measured which lie within a resolution range with an average  $\sigma_{\text{res},k}$ . Per definition,  $\sum^K c_k = 1$ . Defining  $\rho(x)$  as the physical beam shape distribution, the measured distribution  $M(x)$  is a convolution of the physical beam with the detector resolution

$$M(x) = \int_{-\infty}^{+\infty} \sum_{k=1}^K c_k g(x; \sigma_{\text{res},k}) \rho(x - \tau) d\tau. \quad (4.2)$$

The case is considered where the physical beam shape can be described with a Gaussian function  $\rho(x; \xi_{x,j}, \sigma_{x,j})$  centered at  $\xi_{x,j}$  with a width  $\sigma_{x,j}$  (in the  $x$  plane for beam  $j = 1, 2$ ). Using the

fact that the convolution of two Gaussian distributions  $f \otimes g$  is again Gaussian [40] with a width  $\sigma_{f \otimes g} = \sqrt{\sigma_f^2 + \sigma_g^2}$ , the measured distribution  $M(x)$  can be expressed as

$$M(x) = \sum_{k=1}^K c_k \rho(x; \xi_{x,j}, \sigma_{x,j}^*), \quad (4.3)$$

with  $\sigma_{x,j}^* = \sqrt{\sigma_{\text{res},k}^2 + \sigma_{x,j}^2}$ . The values of  $\sigma_{\text{res},k}^2$  depend on the track multiplicity  $N_{\text{Tr},1}$  and  $z$ .

The resolution deconvolution can be applied in the same way when the beam shape  $\rho(x)$  is defined as a sum of Gaussian functions. One advantage to use Gaussian functions to describe the physical beam shape and the resolution is that the equations remain analytical.

### 4.3.2 Resolution for beam-beam interaction vertices

Vertices used to measure the resolution are selected using the same criteria as for the beam-gas analysis as discussed in Sec. 4.1.3. Selected beam-beam interaction vertices used for the resolution analysis and corresponding distribution of number of tracks per vertex are shown in Fig. 4.6 using fill 2520 as an example.

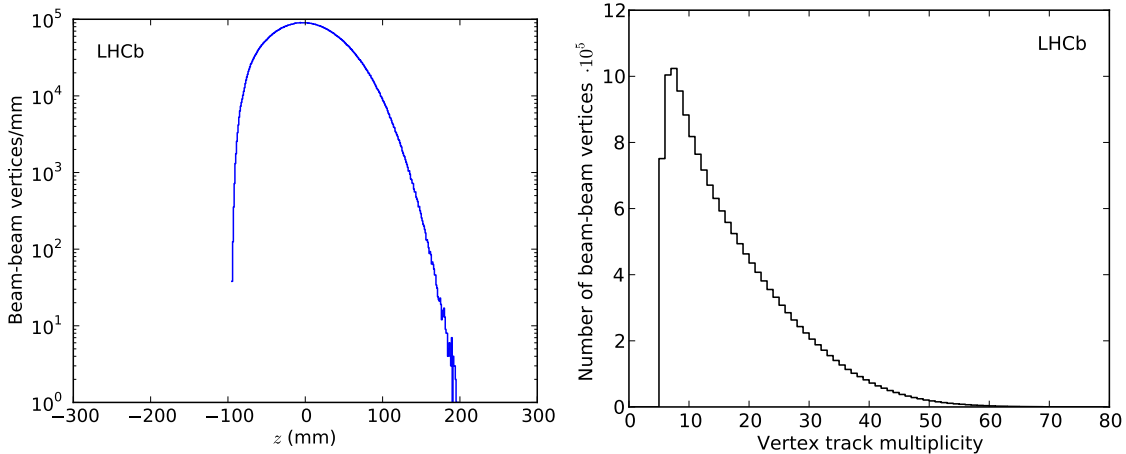


**Fig. 4.6:** Selected beam-beam vertices for resolution measurement (fill 2520). Left: primary (unsplit) vertex longitudinal  $z$ -position distribution of all beam-beam vertices used for resolution measurement. The requirement to have at least two forward and two backward tracks in each vertex causes the sharp efficiency drop close to  $z = -100$  mm. Right: distribution of vertex track multiplicity for all split vertices.

Without external knowledge of the true position of a primary vertex, the residual distance to the true position and therefore the resolution cannot be measured directly. Instead, one can measure the residual distance between two reconstructed vertices originating from the same collision with the following method. Tracks associated with a primary vertex are split into two sets. The same standard LHCb reconstruction algorithm attempts to find the corresponding vertex in each set as if it were originating from different events, resulting into two split vertices for one primary vertex. If more than one primary vertex is found, two track sets and split vertices are created per primary vertex. A vertex is discarded in case only one split vertex could be reconstructed. This requirement is also applied to the BGI analysis that uses the split vertices to measure the beam shapes. The primary vertex tracks are randomly selected and assigned to either one set such that the total number of tracks per set is similar or equal. Equalizing the number of tracks per set is not required but improves the statistical accuracy for vertices with a large number of tracks.

Defining the absolute vertex position as  $v$  (in the plane  $v = x, y$ ), and  $\Delta v$  the distance between both split vertices ( $v_1, v_2$ ) of a primary vertex, the Gaussian width  $\sigma_{\Delta v}$  of all  $\Delta v$  residuals is a

convolution of each vertex resolution and depends only on the number of tracks in each split vertex

$$\Delta v = v_1 - v_2$$

$$\sigma_{\Delta v} = \sqrt{\sigma_{\text{res},v1}^2(N_{\text{Tr},1}) + \sigma_{\text{res},v2}^2(N_{\text{Tr},2})}, \quad (4.4)$$

where  $\sigma_{\text{res},v}(N_{\text{Tr}})$  is the vertex resolution for the track multiplicity  $N_{\text{Tr}}$ . Indices 1, 2 denote here the first and second split vertex. Equation (4.4) is also valid when the vertex track multiplicities  $N_{\text{Tr}}$  are not equal in both split vertices. In addition to the above, due to the longitudinally asymmetric geometry of the VELO and the varying acceptance for forward and backward tracks along  $z$ , the resolution also depends on the  $z$ -position. This  $z$ -dependence will be addressed in the next section, numbers and plots in this section are based on a resolution measurement using the full beam spot data ignoring the  $z$ -position.

Measured residuals  $\Delta v$  are sorted according to the possible  $i$  combinations  $(N_{\text{Tr},1}, N_{\text{Tr},2})$  of the two number of tracks per set  $N_{\text{Tr},1}$  and  $N_{\text{Tr},2}$ . For each combination  $i = (N_{\text{Tr},1}, N_{\text{Tr},2})$ , the distribution of all  $\Delta v_i$  measurements are fitted with a Gaussian function to measure the width of the distribution  $\sigma_{\Delta v_i}$ ; an example of such a distribution and fit is shown in Fig. 4.7 (left). In this particular case, the number of tracks in both sets being equal, the measured distribution width  $\sigma_{\Delta v_i}$  is directly related to the vertex resolution (here with 48 tracks per split vertex) using Eq. (4.4):

$$\sigma_{\text{res},x_1}(N_{\text{Tr},1} = 48) = \sigma_{\text{res},x_2}(N_{\text{Tr},2} = 48) = \sigma_{\Delta x_i}(N_{\text{Tr}} = 48)/\sqrt{2}.$$

All measured distribution widths  $\sigma_{\Delta x_i}$  as function of  $(N_{\text{Tr},1}, N_{\text{Tr},2})$  combinations are shown in Fig. 4.7 (right).

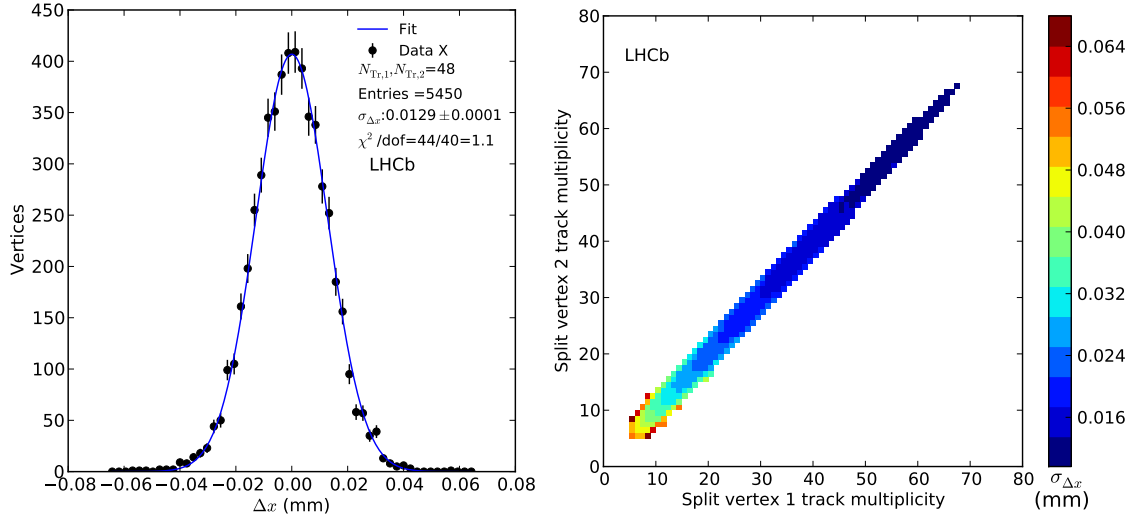


**Fig. 4.7:** Measurement of the residuals between two split vertices from beam-beam interactions (fill 2520). Left: Gaussian fit to measure the distance  $\Delta x$  between two split vertices with 48 tracks per vertex (as an example). Right: Measured distance between two split vertices as function of number of tracks per vertex. Each colored square represents the Gaussian width of the distance between split vertices sorted according to the number of tracks per split vertex. The measured width of 0.013 mm for two vertices with 48 tracks as shown on the left plot as example corresponds to the blue square at a multiplicity of 48 number for set 1 and 2.

The resolution per number of tracks  $\sigma_{\text{res},v}(N_{\text{Tr}})$  is measured by fitting all distributions widths  $\sigma_{\Delta v_i}$  simultaneously with a least squares minimization

$$\chi^2 = \frac{\left[ \sqrt{\sigma_{\text{res},v1}^2(N_{\text{Tr},1}) + \sigma_{\text{res},v2}^2(N_{\text{Tr},2})} - \sigma_{\Delta v_i} \right]^2}{\delta_{\sigma_{\Delta v_i}}^2}, \quad (4.5)$$

with  $\delta_{\sigma_{\Delta v_i}}$  the fit uncertainty obtained in the  $\sigma_{\Delta v_i}(N_{\text{Tr}})$  measurement. The fit parameters are the values of the resolution per number of tracks  $\sigma_{\text{res},v}(N_{\text{Tr}})$  with  $N_{\text{Tr}}$  ranging from 5 to about 65 depending on the available number of entries. As can be seen in Fig. 4.6 (right), the number of split vertices with more than 60 tracks is vanishing, limiting a resolution measurement up to about 60 to 65 tracks per split vertex. Results for the resolution as function of tracks per vertex are shown in Fig. 4.8 as individual data points. An advantage of this direct method is that the results are independent of a parametrization function, but has the disadvantage of having statistical fluctuations for high track multiplicity or when the number of available vertices is small.

Alternatively, the resolution can be parametrized as function of track multiplicity  $N_{\text{Tr}}$  with

$$\sigma_{\text{res},v}(N_{\text{Tr}}) = \frac{A}{N_{\text{Tr}}^B} + C. \quad (4.6)$$

The factor  $A$ , the power term  $B$  and constant  $C$  are measured by fitting all  $\sigma_{\Delta v_i}$  measurements in the same way as in Eq. (4.5) where the values for  $\sigma_{\text{res},v1}(N_{\text{Tr},1})$  and  $\sigma_{\text{res},v2}(N_{\text{Tr},2})$  are given by Eq. (4.6). The terms  $A$ ,  $B$  and  $C$  are fit parameters, reducing the number of parameters from about 65 to 3. Results for the resolution parametrization functions are shown in Fig. 4.8 as dashed lines and are in good agreement with results from the direct determination of individual resolutions per track multiplicity. The residuals between the parametrization functions and individual resolution are shown in Fig. 4.9 (left). While statistical fluctuations are higher with larger track multiplicity, there is no discernible structure in the residuals. However, more important is the distribution of residuals weighted by number of vertices per track multiplicity (taken from Fig. 4.6 right) as shown in Fig. 4.9 (right). The residuals being centered at zero, a possible bias introduced by the parametrization can be excluded and the statistical fluctuations are less than 0.1  $\mu\text{m}$ . Beam-beam resolution parametrization results for all dedicated luminosity calibration fills are shown in Table 4.4.

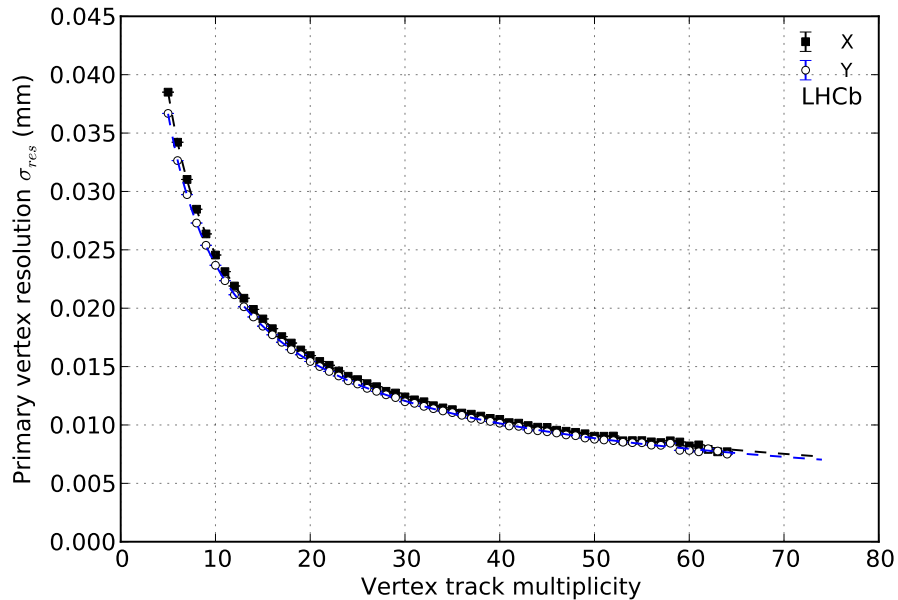


**Fig. 4.8:** Beam-beam resolution as function of track multiplicity (fill 2520). Open and closed markers are direct determination of individual resolution per track multiplicity for the  $y$  and  $x$  axes, respectively. Dashed lines are results of resolution parameterization using Eq. (4.6). Both methods are in agreement.

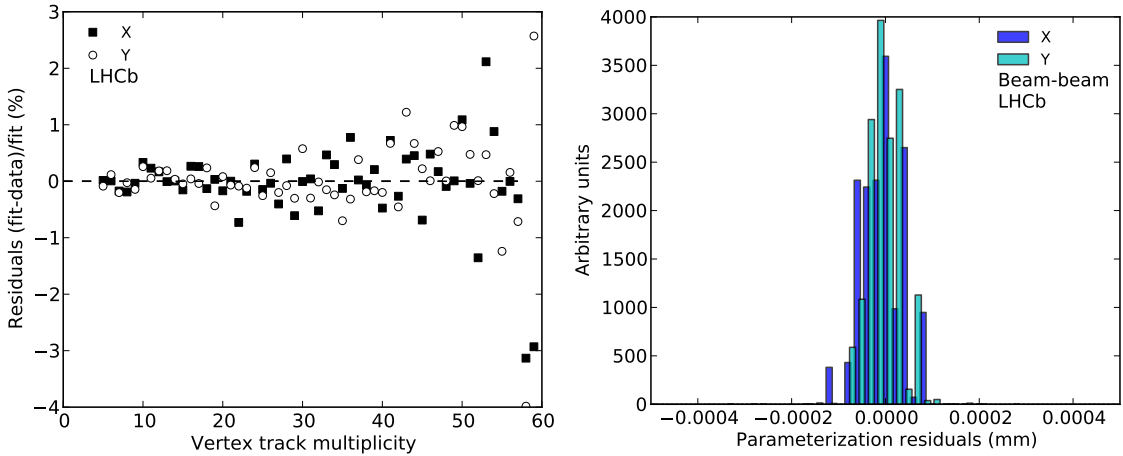


**Fig. 4.9:** Left: residuals between parameterization fit and direct resolution measurement for beam-beam interactions (fill 2520). The direct measurement is less precise above about 50 tracks per split vertex where the single Gaussian fits start to be statistically limited. Right: distribution of residuals (in mm) weighted according to the number of events participating in a given track multiplicity as taken from right Fig.4.6.

**Table 4.4:** Beam-beam resolution parameters for Eq. 4.6 for the  $x$  and  $y$  plane. The statistical uncertainty is in the order of  $10^{-8}$  and can be neglected.

Fill	$A_x$ (mm)	$B_x$	$C_x$ (mm)	$A_y$ (mm)	$B_y$	$C_y$ (mm)
2520	0.110	0.669	0.0011	0.101	0.640	0.0006
2523	0.110	0.671	0.0013	0.103	0.655	0.0011
2852	0.122	0.719	0.0017	0.112	0.696	0.0014
2853	0.119	0.704	0.0014	0.110	0.682	0.0011
2855	0.118	0.701	0.0014	0.109	0.679	0.0010
2856	0.121	0.711	0.0014	0.111	0.689	0.0011
3311	0.124	0.725	0.0017	0.113	0.698	0.0013
3316	0.123	0.722	0.0017	0.113	0.696	0.0013
3555	0.121	0.709	0.0013	0.112	0.692	0.0010
3562	0.122	0.711	0.0013	0.113	0.698	0.0011
3563	0.121	0.704	0.0011	0.112	0.689	0.0009

#### 4.3.2.1 Correction for longitudinal position

The vertex resolution for beam-beam interactions is not constant along  $z$ . To account for this dependence, a correction factor  $F_z$  is applied to the resolution depending on the vertex  $z$ -position. The ratio  $\Delta F$  of the distance between both split vertices to the convolved resolution of the split vertices,

$$\Delta F = \frac{v_1 - v_2}{\sqrt{\sigma_{\text{res},v1}^2(N_{\text{Tr},1}) + \sigma_{\text{res},v2}^2(N_{\text{Tr},2})}}, \quad (4.7)$$

is used to evaluate the resolution correction for a given  $z$ -position. Here  $v$  indicate the axis  $x, y$  and the indices 1, 2 denote the first and second split vertex. The correction factor to the resolution is the width of the distribution  $F_z = \sigma_{\Delta F}$  and is applies to a specific resolution parametrization. Here, the resolution values in (4.7) result from a parametrization based on vertices centered at  $z = \pm 5$  mm instead of the full  $z$ -range. Because  $F_z$  is close to unity, the final  $z$ -corrected resolution values obtained by correcting a resolution parametrization based on the full  $z$ -range or only a central  $z$ -range are equal as long as the  $F_z$  correction is based on the corresponding parametrization. The incentive to use a limited central  $z$ -range to measure the resolution is that all vertices share a similar acceptance to forward and backward tracks and the resolution does not depend on the  $z$ -position.

The correction is evaluated for a large sample of vertices (about  $10^7$ ). All  $\Delta F$  values are binned in  $z$  per 20 mm and fitted with a Gaussian function to measure the overall correction  $F_z$ . Results for  $F_z$  corrections are shown in Fig. 4.10 for fill 2520 as example with  $\beta^* = 3$  m. Values for  $F_z$  corrections can vary between fills and are evaluated for each fill. An additional example can be found in Appendix D showing results for fill 2855 with  $\beta^* = 10$  m in Fig. D.1. The correction at  $z = 0$  can be slightly larger than unity due to a binning effect and also because the distribution of corrections evaluated with Eq. (4.7) contain a wide range of resolution values leading to non-perfect Gaussian shapes.

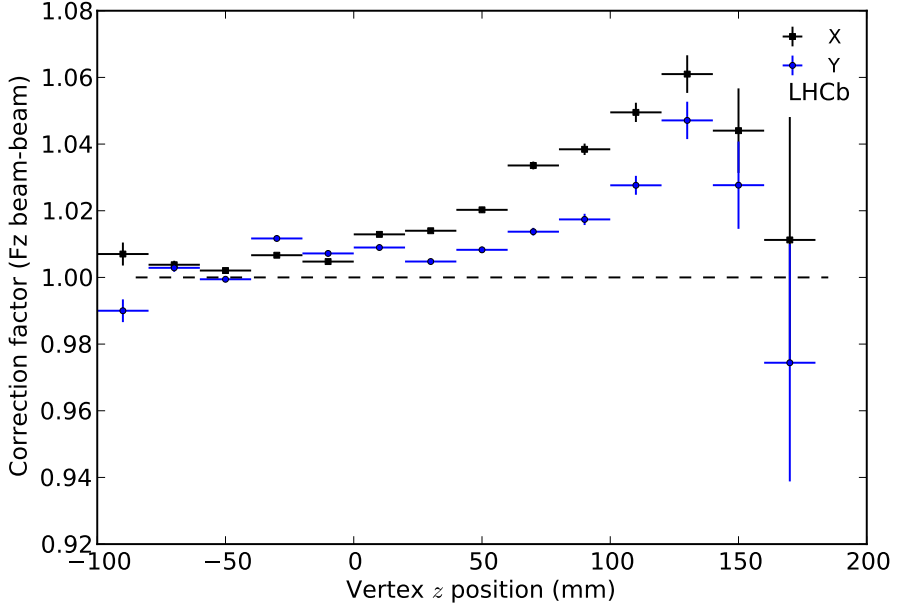


**Fig. 4.10:** Beam-beam resolution  $z$ -dependent correction factor  $F_z$  based on a resolution parametrization measured in the central  $z$ -range  $z = \pm 5$  mm (fill 2520 with  $\beta^* = 3$  m).

### 4.3.3 Resolution for beam-gas interaction vertices

Owing to the SMOG gas injection system, the increased beam-gas event rate allows not only a dedicated resolution measurement to be performed per fill, but also the beam-gas interaction vertex resolution to be measured directly from beam-gas events instead of using the beam-beam resolution with correction factors as performed in previous measurements [35]. Furthermore, the resolution measurement of beam-gas interaction vertices is independent for each beam. The measurement principle is similar to the beam-beam method as described above. The sole difference resides in the vertex selection for each beam and in the segmentation of resolution parametrization for different  $z$ -bins.

Beam-gas interaction vertices from both beams are selected according to the same criteria used for the BGI analysis as described in Sec. 4.1.3. In addition to beam-gas interaction vertices originating from colliding bunch pairs ( $bb$  crossing type), all vertices from non-colliding bunch crossings are also used to provide a resolution measurement down to  $z = 0$  and to improve the statistical precision. Vertices in  $be$  and  $eb$  crossings are assigned to beam 1 and beam 2, respectively.

The detector acceptance and resolution vary within the  $\pm 1$  m  $z$ -range used for the BGI analysis, leading to different distributions of track multiplicity per vertex and different parametrization curves. Consequently, basing the resolution parametrization on events covering the full  $z$ -range (or only a central part thereof) and correcting for the  $z$ -dependence with a single factor raised the following two problems. First, the distributions used to measure the correction factors  $F_{z,j}$  per

beam  $j$  and individual  $\sigma_{\Delta v_i}$  values (as shown in left Fig. 4.7) were no longer Gaussian due to the mixing of vertices with dissimilar characteristics. Secondly, the beam width measurements showed an unexpected  $z$  dependence (as discussed in the next section).

Therefore, beam-gas interaction vertex resolutions are measured separately in 5  $z$ -bins for beam 1 and 4  $z$ -bins for beam 2, namely [-1200,-800], [-800,-500], [-500,-250], [-250,0], [0,250] mm and [0,250], [250,500], [500,800], [800,1200] mm for beam 1 and 2, respectively. The number and size of these  $z$ -bins are limited by the available number of events and to some extent by computing limitations.

Distributions of track multiplicity for beam 1 and beam 2 for all  $z$ -bins are shown in Fig. 4.11. Beam-gas resolution results are shown in Fig. 4.12. As for beam-beam results, individual data points indicate a resolution measurement for a given number of tracks per vertex and are independent of the parametrization; the solid lines show the parametrization results for each  $z$ -bin. It can be seen that not only each resolution curve corresponds to a higher average value for a  $z$ -bin away from  $z = 0$ , but also the shape differs between bins. Histograms for weighted residuals for beam-gas resolution measurements are shown in Fig. 4.13. The residuals are weighted by the number of vertices per track multiplicity according to the distributions in Fig. 4.11. There is no significant bias in the parametrization and the statistical spread of about 0.2  $\mu\text{m}$  can be neglected.

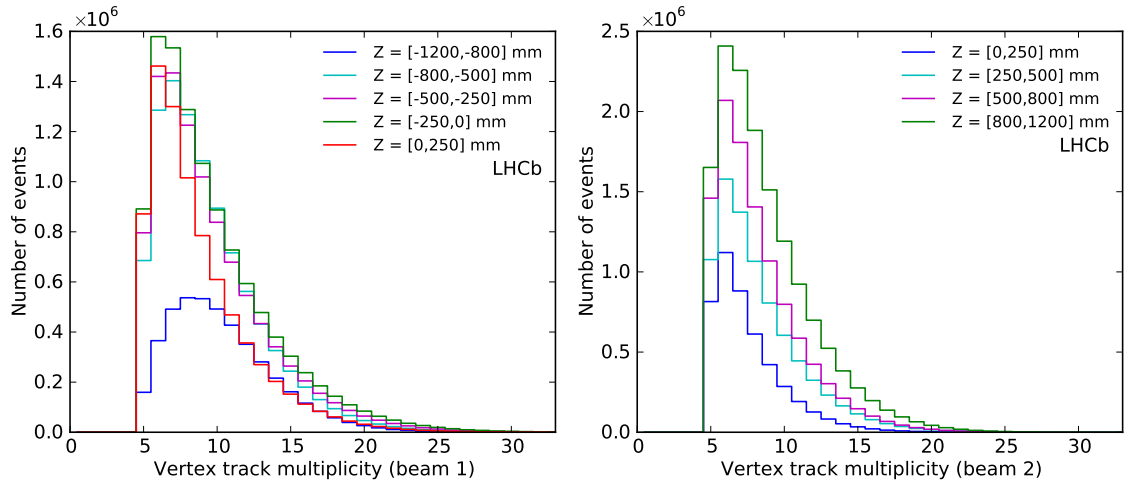


**Fig. 4.11:** Vertex track multiplicity distribution for different- $z$  bins for beam-gas interactions (for fill 2855 as example). Left: beam 1 split in 5  $z$ -bins. Right: beam 2 split in 4  $z$ -bins. The  $z$ -bins are indicated in the legend.

#### 4.3.3.1 Correction for longitudinal position for beam-gas results

Measurements of the  $z$ -dependent correction factors are performed similar to those for beam-beam interactions explained in the previous section. A correction factor is evaluated for each beam, axis and  $z$ -bin using Eq. (4.7) in 25 mm  $z$ -bins. Results for both beams are shown in Fig. 4.14. The correction factors apply only to resolution values of the corresponding  $z$ -bin explaining the sawtooth shape in the plot.

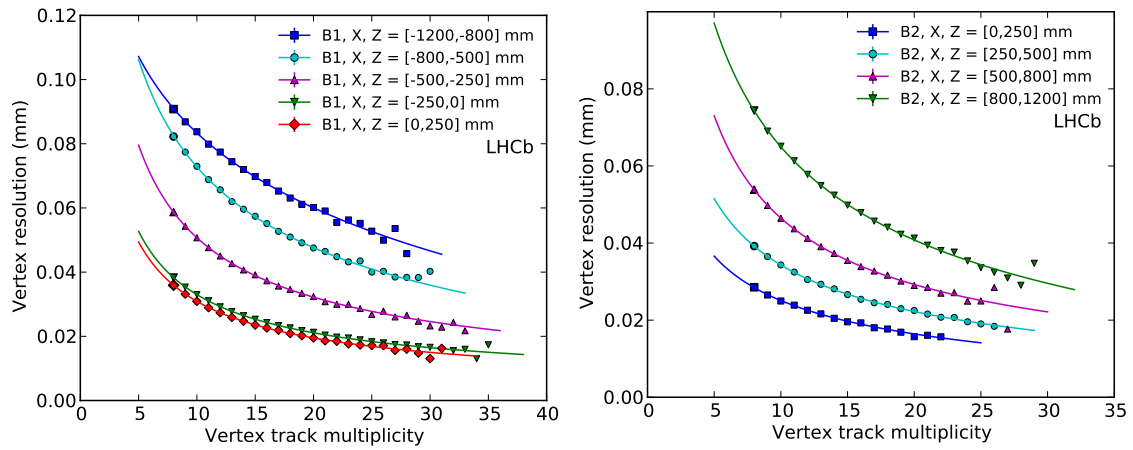


**Fig. 4.12:** Parameterization of beam-gas vertex resolution for both beams and different  $z$ -bins in the  $x$  plane (for fill 2855 as example). Results in the  $y$  plane are visually equal. Left: beam 1 resolution for 5  $z$ -bins. Right: beam 2 resolution for 4  $z$ -bins. Single markers indicate a resolution measurement per vertex track multiplicity. Continuous lines indicate the parameterization result for the corresponding  $z$  bin.

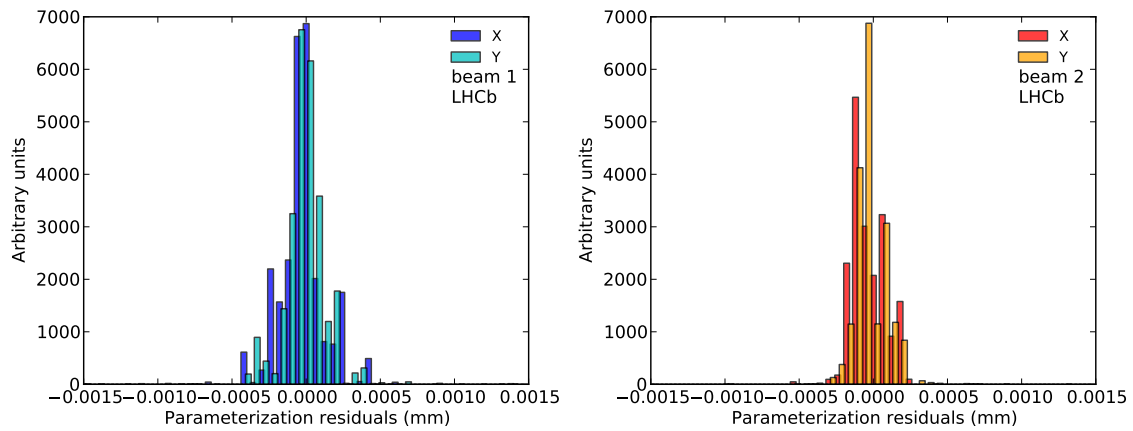


**Fig. 4.13:** Weighted residuals in mm between the direct beam-gas resolution measurement and the parameterization for (left) beam 1 and (right) beam 2 (for fill 2855 as example).

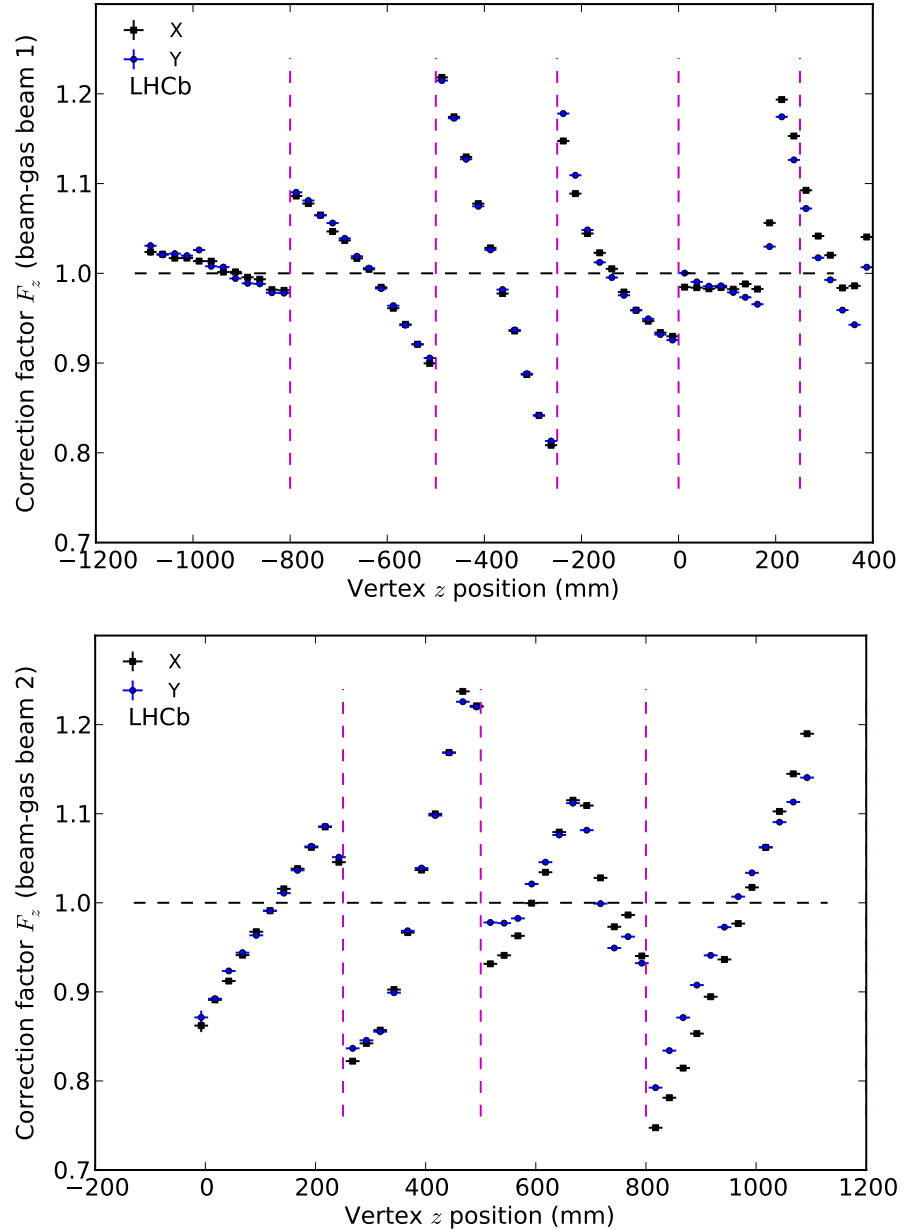


**Fig. 4.14:** Beam-gas resolution correction factors as function of  $z$ -position for (top) beam 1 and (bottom) beam 2 for fill 2855. Corrections are applied to the corresponding resolution parameterization, the boundaries between bins are indicated by a vertical dashed line. The shape asymmetry seen in the region  $z > 180$  mm are due to the specific positions of the VELO sensors. The differences between the  $x$  and  $y$  values can be related to the VELO sensors alignment.

### 4.3.3.2 Additional correction factors

The beam-gas vertex resolution can be tested by measuring the single beam width at different  $z$ -positions. While the physical beam width is unknown, its relative change as a function of  $z$  can be predicted from the machine optics with [28]

$$\sigma_{\text{beam}}(z) = \sigma_{\text{beam}}(0) \sqrt{1 + \frac{z^2}{\beta^{*2}}}, \quad (4.8)$$

assuming the waist position is at  $z = 0$ . This is called the “hourglass” effect [41]. Some measurements were performed (in fill 2520) with  $\beta^* = 3$  m optics, providing smaller beam sizes and a stronger hourglass effect than in other luminosity calibration fills. Therefore, the beam width measurements are more sensitive to the resolution.

Single beam widths are measured with the four methods described below. In all cases the beam shape is assumed to be a single Gaussian function. Even though the beams have double Gaussian shape in this fill, this simplification allows results from different methods to be compared. The resolution unfolding method described in Sec. 4.3.1 is used in the first three methods below.

1. The observed distributions from primary beam-gas interaction vertices are fitted using Eq. (4.3). The different resolution width components  $\sigma_{\text{res},k}$  entering in the effective resolution function Eq. (4.1) are based on the track multiplicity of the primary vertex. It is therefore assumed that the resolution measured with split vertices also applies to the primary vertex. This method indicated here as “Primary Vertex” does not use the split vertices, but uses the resolution parametrization.
2. The distribution is based on the average position of both split vertices instead of the primary vertex and is fitted as before using Eq. (4.3). However, each resolution value  $\sigma_{\text{res},k}$  associated to a vertex average is a convolution of both split vertex resolutions:  $\sigma_{\text{res},k} = \sqrt{\sigma_{\text{res},k,1}^2 + \sigma_{\text{res},k,2}^2}$ . The indices 1, 2 indicate the first and second vertex. This method is referred to as “Split Average”.
3. The beam distribution is based on the average position of both split vertices and is fitted as above. However, the resolution function Eq. (4.1) is not generated with the resolution parametrization, but instead is directly measured from the same sample of split vertices. The distribution of half distances  $\Delta v/2$  between two split vertices is fitted with a double Gaussian function and used as resolution function  $R(x)$ . This method is therefore independent of resolution parametrization and relies only on the split vertices of the measured sample. This method is referred to as “Split Data”.
4. Finally the beam RMS is measured from the covariance of split vertices in the following way. The beam shape in one dimension is a distribution of  $N$  vertices with physical position  $x_0$ . As explained before, the tracks forming a vertex are split into two groups and reconstructed into two split vertices  $x_{1,2}$  with a deviation from the true vertex  $\delta_{1,2}$

$$\begin{aligned} x_1 &= x_0 + \delta_1 \\ x_2 &= x_0 + \delta_2. \end{aligned}$$

Only the positions  $x_{1,2}$  of the reconstructed split vertices can be measured, the true position  $x_0$  and deviations  $\delta_{1,2}$  are unknown.

The covariance of both split vertices gives

$$\text{cov}(x_1, x_2) = \text{cov}(x_0 + \delta_1, x_0 + \delta_2) \quad (4.9)$$

$$= \text{cov}(x_0, x_0) + \text{cov}(x_0, \delta_1) + \text{cov}(x_0, \delta_2) + \text{cov}(\delta_1, \delta_2). \quad (4.10)$$

The first term  $\text{cov}(x_0, x_0)$  from the above equation is per definition the variance of the true vertex:  $\text{cov}(x_0, x_0) = \text{var}(x_0)$ . The second and third terms are the covariance between the true position and the deviation from the true position. It is difficult to see how those values could be correlated and we can assume those terms to be close to zero. The last term  $\text{cov}(\delta_1, \delta_2)$  is the covariance of the deviations  $\delta_1$  and  $\delta_2$ ; ideally, those values are uncorrelated and the split vertices are independent. However, it is possible that a systematic bias in the reconstruction, VELO geometry or mis-alignment affects both deviations in the same way and thus introduces a correlation between split vertices. Nevertheless, supposing the correlation between the deviations is small and therefore  $\text{cov}(\delta_1, \delta_2) \approx 0$ , the true beam RMS is then given by

$$\text{RMS} = \sqrt{\text{var}(x_0)} = \sqrt{\text{cov}(x_0, x_0)} \approx \sqrt{\text{cov}(x_1, x_2)}. \quad (4.11)$$

The covariance of  $x_{1,2}$  is calculated with

$$\text{cov}(x_1, x_2) = \frac{1}{N} \sum_{i=1}^N (x_{i1} - \bar{x}_1)(x_{i2} - \bar{x}_2). \quad (4.12)$$

This method is referred here as “Split Covariance”.

Both beam widths have been measured using the four methods described above for all non-colliding bunches. The measurements are performed in 100 mm  $z$ -bins in  $x$  and  $y$ . Because bunches have different width, all measured values per bunch are normalized to their beam width measured at  $z = 0$  using the second method (Split Average). The statistical fluctuations per  $z$ -bin and bunch reach about 10%. Therefore, for each method all normalized values are averaged over all bunches. Results for fill 2520 are shown in Fig. 4.15, while an example with  $\beta^* = 10$  m is shown in Fig. D.4 in Appendix D for fill 2855. Solid blue lines indicate the expected relative beam width evolution due to the hourglass effect assuming  $\beta^* = 3 \pm 0.3$  m [42]. Results using the third method described above (Split Data) using a resolution function measured directly from the data sample are not shown as they cannot be distinguished from the Split Average results.

For the Primary Vertex method, the resolution measured by splitting the primary vertex into two split vertices does not describe the primary vertex resolution well enough. Consequently, the primary vertices will not be used for the BGI analysis. Except for the  $x$  plane of beam 2, both Split Average and Split Covariance methods behave similarly and underestimate the resolution away from the detector center. Ideally the resolution would describe the distance between a split vertex and the true vertex position. However, the method as performed above provides the resolution of the average position of two split vertices and cannot take possible correlations between the two split vertex deviations  $\delta_{1,2}$  into account. Indeed, a correlation between both vertex deviations would not change the measured resolution, but would affect the observed beam width and therefore bias the measured beam width after resolution unfolding. To take this unseen correlation into account, a set of  $z$ -dependent and global resolution correction factors are measured as described below. The full effect of the correction factors with  $\beta^* = 10$  m is about 0.5% as discussed in Sec. 7.2.2 and will be taken as systematic uncertainty to the luminosity.

#### 4.3.3.3 Resolution correction factors as function of $z$

The normalized values labeled Split Covariance in Fig. 4.15 represent a way to evaluate the beam width independent of a resolution and fit model. Setting aside the absolute scale, those  $z$ -dependent beam widths do not agree with the hourglass prediction. A set of  $z$ -dependent correction factors  $f_z$  are evaluated with a fit to take the correlations between the two split vertex deviations  $\delta_{1,2}$  into account and bring the Split Covariance measurements in agreement with the expectation  $\beta^*$ . The

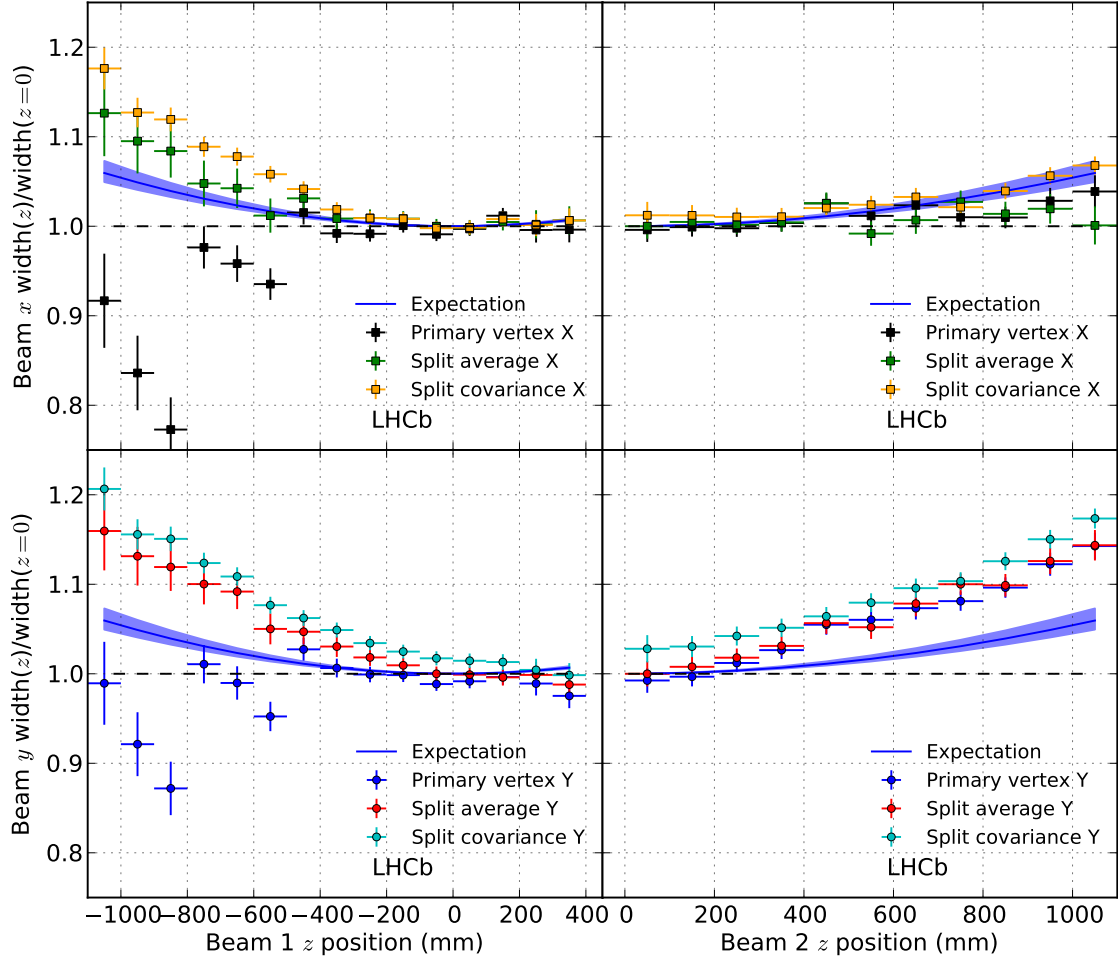


**Fig. 4.15:** Measurement of the single beam width along  $z$  normalized to the width at  $z = 0$  for fill 2520 ( $\beta^* = 3$  m). Each data point for a given  $z$ -position and measurement method is an average of all normalized widths from non-colliding bunches. The curved blue lines indicate the expected beam width evolution in  $z$  due the 3 m  $\beta^*$  hourglass effect. The shaded blue surface indicates the 10% uncertainty on  $\beta^*$ .

following measurement is only based on the variance and covariance of split vertices and is therefore independent of the resolution parametrization, resolution unfolding and fit model. As the absolute beam width and consequently the resolution scale is unknown, the correction factors are set to one at  $z = 0$  and only change the measured beam width away from  $z = 0$ .

For all  $N$  non-colliding bunches  $i$  per beam, the fit minimizes the  $\chi_z^2$  function for each 100 mm  $z$ -slice. The  $\chi_z$  function for one  $z$ -slice is defined as

$$\chi_z = \sqrt{1 + \frac{z^2}{\beta^{*2}}} - \sum_{i=1}^N \frac{1}{N} \left( \frac{\sqrt{\sigma_{\text{var},i,z}^2 - (\sigma_{\text{var},i,z}^2 - \sigma_{\text{cov},i,z}^2) f_z^2}}{\sigma_{\text{cov},i(z=0)}} \right), \quad (4.13)$$

with  $\sigma_{\text{cov},i,z}^2 = \text{cov}(x_1, x_2)$  the beam width squared, and  $\sigma_{\text{var},i,z}^2 = \text{var}(x_1, x_2)$  the variance of all split vertices, which is a measurement of the raw beam width squared. The first term in (4.13) describes the relative beam width change due to the hourglass effect. The fit parameters are the  $f_z$  factors. The fit is performed independently for both  $x$  and  $y$  axes and both beams. Note that the  $f_z$  corrections are different per  $z$ -slice but common for all bunches; however, the average of all normalized widths per bunch is taken after  $f_z$ -correction per bunch to account for the differences in width per bunch. Results of the fit showing the  $z$ -dependent resolution correction factors are given in Fig. 4.16. These  $f_z$  corrections factors are measured for each fill separately. With a 10 m  $\beta^*$ , not only the hourglass effect is negligible (less than 1% at  $z = 1$  m), but also the beam width to

resolution ratio is larger and the correction factors have a smaller impact on the measured width after resolution deconvolution. The resolution correction factors for fill 2855 ( $\beta^* = 10$  m) are shown in Fig. D.2 in Appendix D as example.

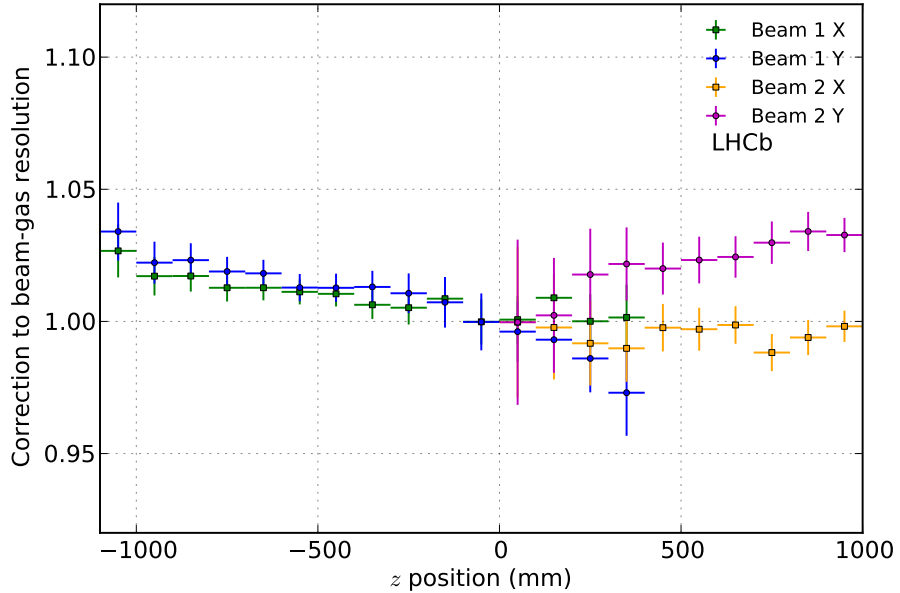


**Fig. 4.16:** Beam-gas resolution correction factors  $f_z$  as function of  $z$  (for fill 2520 with  $\beta^* = 3$  m).

#### 4.3.3.4 Global resolution correction factors

The resolution correction factors  $f_z$  measured above are applied to the resolution function (4.1) and the resolution convolved beam width in Eq. (4.3) becomes now  $\sigma_{x,j}^* = \sqrt{f_z^2 \sigma_{\text{res},k}^2 + \sigma_{x,j}^2}$ .

Whilst applying the resolution correction factors described above improves the consistency of beam width with respect to the hourglass effect, those factors only act on vertices with large  $|z|$ . An additional global resolution scaling per beam and axis is evaluated by a fit based on the residuals between the beam width measured after resolution unfolding and the hourglass effect resulting from the  $\beta^*$  optic. Further away from the origin, the resolution values are larger and the unfolded beam width is more sensitive to a global resolution scale. Consequently, scaling the resolution by a global factor  $f_g$  affects each measured width differently as function of  $z$  and makes the data consistent with the hourglass effect.

For  $N$  non-colliding bunches  $i$  per beam, the  $n$ -dimensional vector fit function  $\chi_z = (\chi_{z_1}, \dots, \chi_{z_n})$  has one  $z$ -slice measurement and corresponding  $f_z$  value per vector component allowing to fit all  $z$ -slices simultaneously. The fit function for one  $z$ -slice is defined as

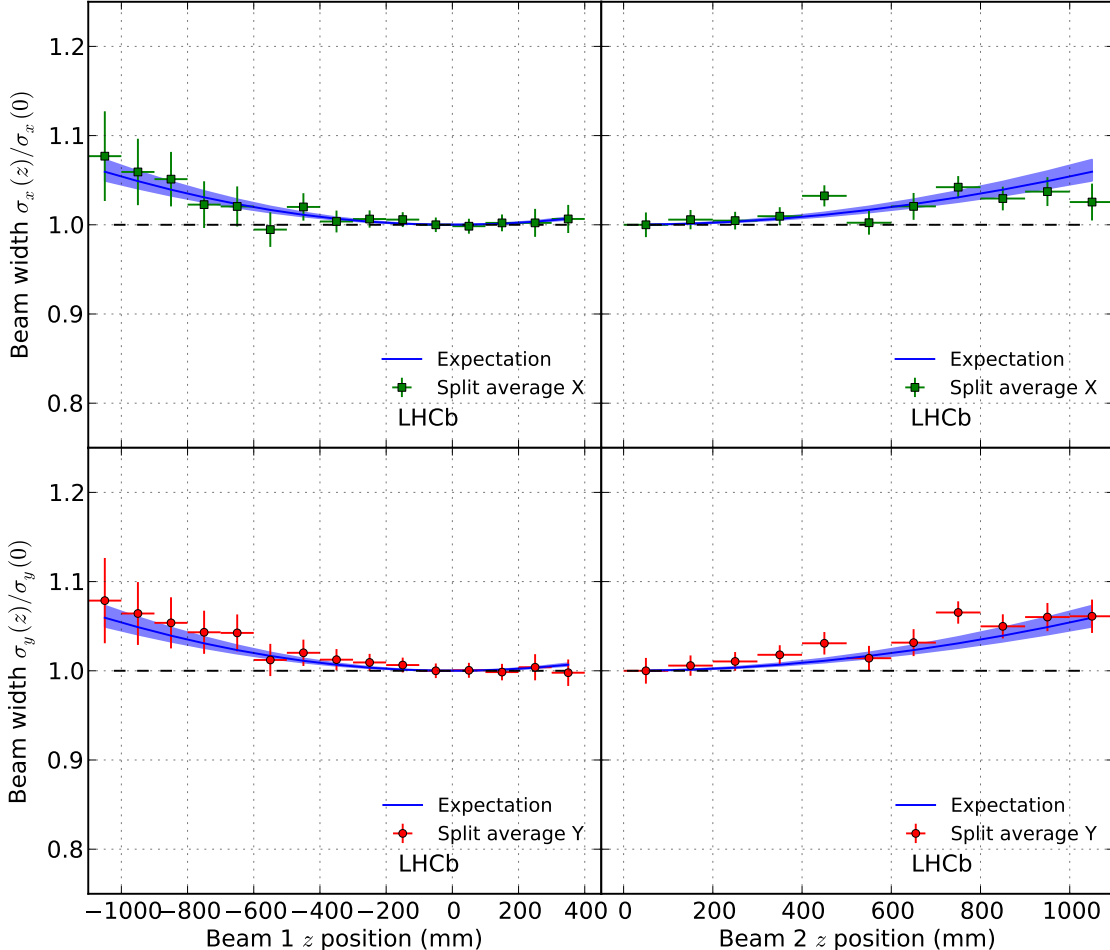
$$\chi_{z_n} = \sqrt{1 + \frac{z^2}{\beta^{*2}}} - \sum_{i=1}^N \frac{1}{N} \left( \frac{\sqrt{\sigma_{\text{raw},i,z}^2 - (f_z f_g \sigma_{\text{res},i,z})^2}}{\sigma_{\text{avg},i(z=0)}} \right), \quad (4.14)$$

with  $\sigma_{\text{res},i,z}$  the resolution value for this  $z$ -slice and bunch  $i$ ,  $\sigma_{\text{avg},i(z=0)}$  the beam width at center of the VELO after resolution unfolding using the average position of both split vertices, and finally  $\sigma_{\text{raw},i,z}$  the measured raw beam width of the average split vertices before resolution unfolding. The factor  $f_g$  is the sole fit parameter per beam and axis, while the factors  $f_z$  are taken from the previous fit described above. Results for all global correction factors are given in Table 4.5 for all fills. The results are different per fill due to the VELO movement and due to the different beam lattice and crossing angle.

The beam width  $\sigma_v$  is measured with the scaled resolution using the resolution unfolding method described in Sec. 4.3.1. The transverse beam distribution  $\rho(v)$  is fitted in the coordinate  $v = x, y$  with the function

$$M(v) = \sum_{k=1}^K c_k \rho(v; \xi_{v,j}, \sigma_{v,j}^*) \quad (4.15)$$

with the resolution convolved width  $\sigma_{v,j}^* = \sqrt{(f_g f_z \sigma_{\text{res},k})^2 + \sigma_{v,j}^2}$ . A final verification of single beam width measurements as function of  $z$  is shown in Fig. 4.17 for fill 2520 as example. Both correction factors  $f_z$  and  $f_g$  have been applied to the resolution.

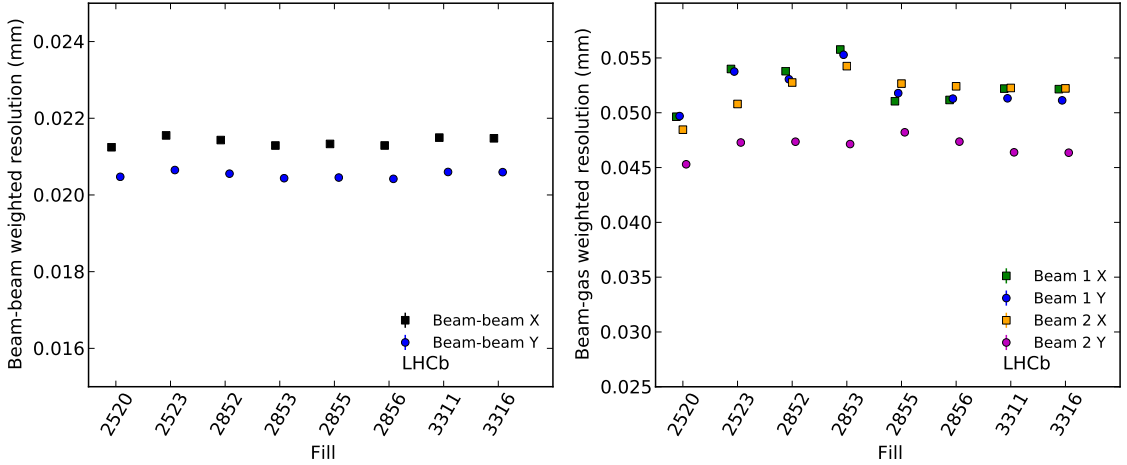
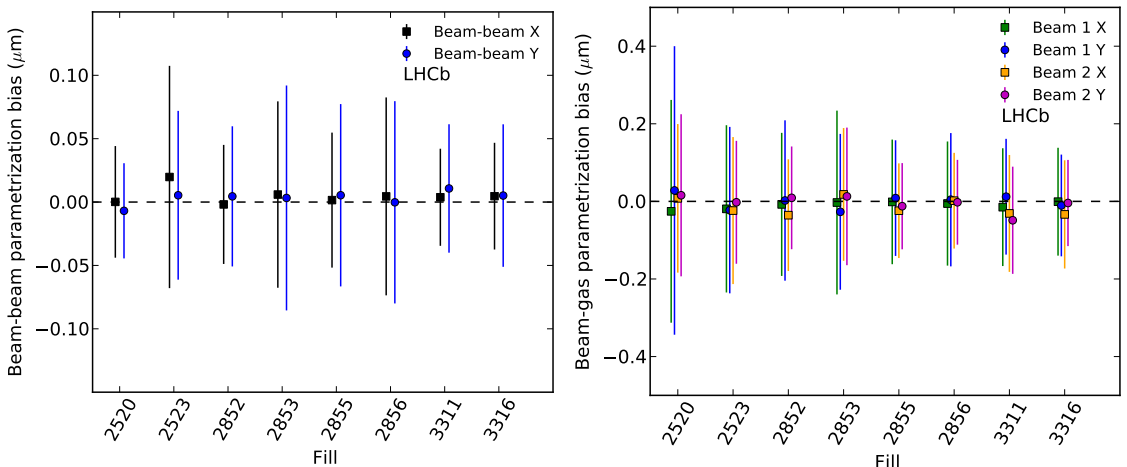


**Fig. 4.17:** Measurement of single beam width  $\sigma_v$  along  $z$  for fill 2520 ( $\beta^* = 3$  m). The beam widths are measured with the resolution deconvolution including all resolution correction factors. Each data point for a given  $z$ -position is an average of all normalized widths from non-colliding bunches. The curved blue line show the expected beam width evolution in  $z$  due to the  $\beta^*$  hourglass effect, the shaded blue surface indicates the 10% uncertainty boundaries on the  $\beta^*$ .

The resolution has been measured independently for all dedicated luminosity calibration fills. While the resolution is not expected to change within fills, it can still vary due to the VELO closing at different positions per fill. The average resolution, obtained by weighing the resolution value of each vertex multiplicity bin by the number of vertices in that bin, is shown for every fill at  $\sqrt{s} = 8$  TeV in Fig. 4.18 including the correction factors discussed here for the beam-gas resolution. The resolution parametrization bias (for which examples were shown already in Fig. 4.9 (right) and Fig. 4.13) is summarized for all fills in Fig. 4.19.

**Table 4.5:** Resolution global correction factors  $f_g$  per beam and axis for all luminosity calibration fills.

Fill	Beam 1 $x$	Beam 1 $y$	Beam 2 $x$	Beam 2 $y$
2520	$0.998 \pm 0.004$	$1.014 \pm 0.004$	$0.986 \pm 0.005$	$1.041 \pm 0.005$
2523	$0.998 \pm 0.004$	$1.004 \pm 0.004$	$0.991 \pm 0.006$	$1.045 \pm 0.006$
2852	$1.03 \pm 0.01$	$1.03 \pm 0.01$	$1.05 \pm 0.01$	$1.07 \pm 0.01$
2853	$1.03 \pm 0.01$	$1.03 \pm 0.01$	$1.07 \pm 0.01$	$1.05 \pm 0.02$
2855	$1.019 \pm 0.008$	$1.050 \pm 0.009$	$1.07 \pm 0.01$	$1.11 \pm 0.01$
2856	$1.025 \pm 0.008$	$1.044 \pm 0.009$	$1.07 \pm 0.01$	$1.09 \pm 0.01$
3311	$1.038 \pm 0.008$	$1.038 \pm 0.008$	$1.05 \pm 0.01$	$1.06 \pm 0.01$
3316	$1.036 \pm 0.008$	$1.033 \pm 0.008$	$1.051 \pm 0.009$	$1.06 \pm 0.01$
3555	$1.02 \pm 0.01$	$1.04 \pm 0.01$	$1.06 \pm 0.01$	$1.12 \pm 0.02$
3562	$1.03 \pm 0.01$	$1.06 \pm 0.01$	$1.06 \pm 0.01$	$1.14 \pm 0.02$
3563	$1.03 \pm 0.01$	$1.07 \pm 0.01$	$1.07 \pm 0.01$	$1.14 \pm 0.02$

**Fig. 4.18:** Weighted resolution for dedicated luminosity calibration fills. Left: beam-beam resolution weighted by number of vertices as function of tracks per vertex. Right: beam-gas resolution weighted by number vertices and including global correction factors per beam and axis.**Fig. 4.19:** Resolution parametrization bias for dedicated luminosity calibration fills. Left: beam-beam parametrization bias. Right: beam-gas parametrization bias. The error bars indicate the standard deviation of parametrization bias.

## 4.4 Measurement of beam parameters

The knowledge of the three-dimensional bunch shapes  $\rho_j(x, y, z)$  are required to evaluate the overlap integral defined in Eq. (3.17). It is assumed that the  $z$  component can be factorized allowing the transverse shapes to be described independently of  $z$ . This factorizability will be discussed in Sec. 7.1.2. The bunch position as function of  $z$  is determined with the beam directions, which also define the crossing angle. A first measurement of the transverse bunch shape assuming the  $x$  and  $y$  coordinates are factorizable is performed with a one-dimensional measurement and described in Sec. 4.4.2. A two-dimensional measurement of the bunch shape is described in Sec. 4.4.3 where the factorizability of the  $x$  and  $y$  axes can be measured. The measurement of the convolved bunch length  $\sigma_{z1}^2 + \sigma_{z2}^2$  is described in Sec. 4.4.4.

In light of the resolution results presented in the previous section, the transverse beam shape measurements are performed with the distribution of the average position of split vertices instead of using the primary vertex. The vertex position entering the beam-gas and beam-beam distributions is given by  $v = (v_1 + v_2)/2$  for  $v = x, y$ . The resolution assigned to the average vertex position is evaluated from the resolution of both split vertices and is given by  $\sigma_{\text{res},v} = \sqrt{\sigma_{\text{res},v1}^2 + \sigma_{\text{res},v2}^2}/2$ .

### 4.4.1 Crossing angles

The angles  $\alpha_{m,j}$  for beam  $j = 1, 2$  and axis  $m = x, y$  are measured in the laboratory reference frame independently for both beams and planes. While only colliding bunch pairs can be used for a luminosity measurement, vertices originating from non-colliding bunch crossings are used to measure the crossing angles as they cover the full  $z$ -range providing a longer lever arm. It has been verified that the colliding and non-colliding bunches share the same angles by measuring the crossing angle of both groups. Since the angles are constant over time, they are measured over a period of about 1 hour to increase the statistical accuracy. The measurement is performed in two stages. First, a least square fit of a line is performed using all beam-gas interaction vertices (up to  $9 \times 10^6$  vertices per beam) for one beam and plane, the resolution attributed to each vertex is used as uncertainty for the fit. An example of crossing angle measurement using vertices directly is shown in Fig. 4.2. In a second stage, single beam positions are measured every 50 mm with a Gaussian fit to the vertex position distribution. For each 50 mm  $z$ -bin centered at  $z_c$ , the vertex transverse position  $v_{j,m}$  is projected to  $v'_{j,m} = v_{j,m} - \alpha_{m,j} \cdot (z - z_c)$ . Here the directions  $\alpha_{m,j}$  are used to project the vertices along the beam direction in a  $z$ -bin. All single beam positions are then fitted with a line using the position error from the fit as uncertainty. An example of angle measurement is shown in Fig. 4.20 for fill 2852; during this period beams were offset by 180  $\mu\text{m}$  in  $y$ .

Both measurement methods provide the same result and have a negligible statistical uncertainty of about  $10^{-8}$  rad. The second stage proved to be necessary in some rare cases where the straight line fit performed using all vertices can be biased by outliers. The second stage is more robust. The half crossing angle which is of interest to measure the overlap integral is defined as

$$\phi_m = (\alpha_{m,1} - \alpha_{m,2})/2. \quad (4.16)$$

The half crossing angle  $\phi_y$  in the  $yz$  plane is close to zero ( $|\phi_y| \leq 8 \mu\text{rad}$ ) for all calibrations fills but those of April 2012.

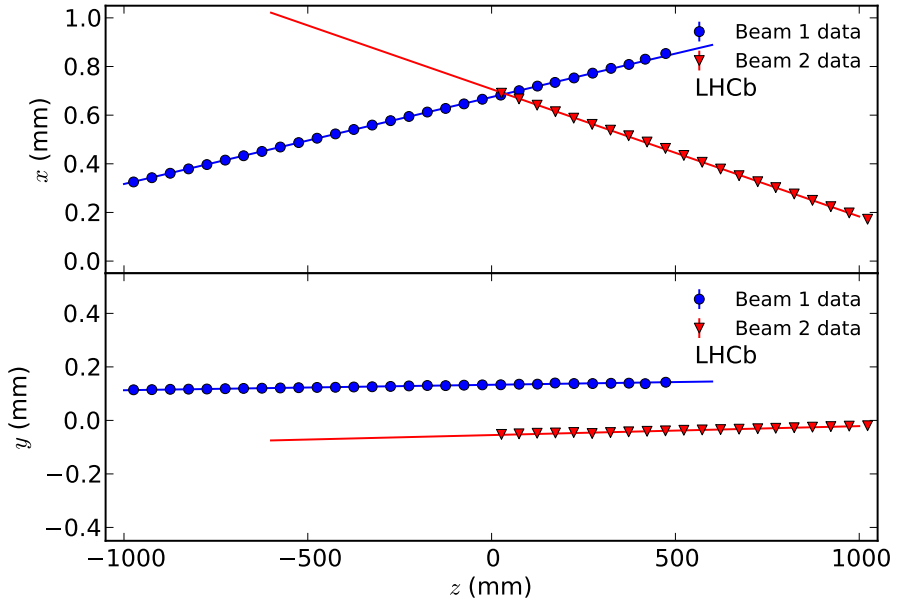


**Fig. 4.20:** Crossing angle measurement by fitting beam positions along  $z$ . The single beam positions are measured every 50 mm with a Gaussian fit to beam-gas interaction vertices using the cumulation of all bunches. Top: angles fit in the  $xz$  crossing plane. Bottom: angles fit in the  $yz$  crossing plane. In this particular measurement period the beams were offset by 180  $\mu\text{m}$  in  $y$  and the offset effect is clearly visible.

#### 4.4.2 Transverse shape in one-dimensional fit

A first approach to measure the beam shape which is also the only available method when confronted with limited statistics, is to measure the beam shapes in the  $x$  and  $y$  directions independently. Single beam transverse profiles are described with a double Gaussian function. For the axis  $m = x, y$  and in the LHCb laboratory frame, the Gaussian distribution with mean  $\xi_m$  and width  $\sigma_m$  is defined as:

$$g(m; \xi_m, \sigma_m) = \frac{1}{\sqrt{2\pi}\sigma_m} e^{-\frac{1}{2}\left(\frac{m-\xi_m}{\sigma_m}\right)^2}. \quad (4.17)$$

For a given  $z$ -range, all vertices are projected along the beam direction  $\alpha_{j,m}$  onto the  $xy$  plane at the center  $z_c$  of the  $z$ -range with

$$m' = m - \alpha_{j,m} \cdot (z - z_c) \quad (4.18)$$

for  $m = x, y$ . The double Gaussian beam shape is defined as

$$\rho_m(m'; \xi'_m, \sigma_{m,n}, \sigma_{m,w}) = w_m g(m', \xi'_m, \sigma_{m,n}) + (1 - w_m) g(m', \xi'_m, \sigma_{m,w}), \quad (4.19)$$

with  $\sigma_{m,n}$  and  $\sigma_{m,w}$  the narrow and wide widths and  $w_m$  the weight of the narrow Gaussian. The mean position  $\xi'_m$  depends on  $z$  and the beam angle and is related to the beam position  $\xi_m$  at  $z = 0$  with  $\xi'_m = \xi_m - \alpha_{j,m} \cdot z_c$ .

All vertices in a selected  $z$ -range are binned in the axis  $m$  ( $x$  or  $y$ ) and form the observed distribution  $M(m')$  which is a convolution of the beam with the detector resolution as described in Sec. 4.3.1. The required effective resolution function  $R(m)$  from Eq. (4.1) is obtained from the resolution distribution of all vertices from the sample described by  $M(m')$ . The resolution distribution is split in  $K$  bins each having an average resolution  $\sigma_{\text{res},k}$  and population fraction  $c_k$ . An example of such a resolution distribution is shown in Fig. 4.21 left. The resulting effective resolution function  $R(m)$  using 6 bins is shown in Fig. 4.21 right as a solid green line.

With the effective resolution function, the observed vertex distribution is defined as

$$M(m') = \sum_k c_k w_m g(m', \xi'_m, \sigma_{m,n}^*) + c_k (1 - w_m) g(m', \xi'_m, \sigma_{m,w}^*), \quad (4.20)$$

with

$$\sigma_{m,n}^* = \sqrt{\sigma_{\text{res},k}^2 + \sigma_{m,n}^2}$$

$$\sigma_{m,w}^* = \sqrt{\sigma_{\text{res},k}^2 + \sigma_{m,w}^2}.$$

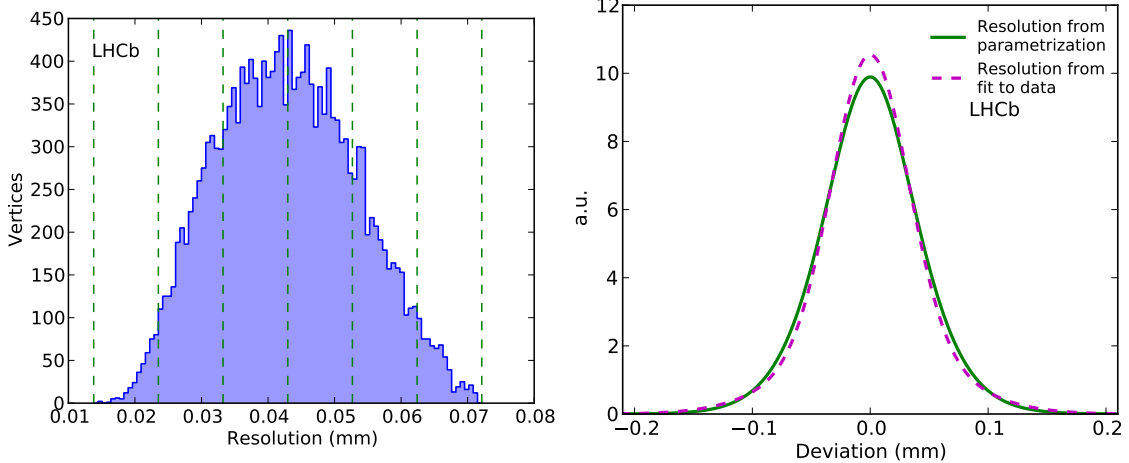


**Fig. 4.21:** Left: distribution of a vertex resolution from the data sample to be measured. The sample is divided in  $K$  bins indicated by vertical dashed lines (here  $K = 6$ ). Right: effective resolution function  $R(m)$  resulting from the distribution on the left (solid line). Alternatively the effective resolution function is also obtained with a double Gaussian fit to the split vertices separation and is indicated with a dashed line. The difference between both results is due to the beam-gas correction factors applied to the parametrization, without correction both functions are similar.

The observed transverse vertex distribution per single beam  $j$  and axis  $m$  is fitted to Eq. (4.20) with a least square minimization to measure the double Gaussian beam widths, weights and position at  $z = 0$ . The observables  $w_{m,j}$ ,  $\xi_{m,j}$ ,  $\sigma_{m,n,j}$ ,  $\sigma_{m,w,j}$  are the fit parameters. An amplitude  $A_{m,j}$  is also added as a parameter to the fit. Two examples of single beam resolution deconvolution are shown in Fig. 4.22 for beam 1 using beam-gas interaction vertices in the longitudinal range  $-500 < z < -250$  mm. It can be seen that for the smaller  $\beta^* = 3$  m (left plot), the true beam width is similar in size to the resolution, while for the  $\beta^* = 10$  m (right plot) case, the resolution is smaller than the true beam width and therefore plays a less important role.

To avoid mixing beam-gas interaction vertices with too different resolutions in the same distribution, the beam shape is fitted in 3  $z$ -regions simultaneously. The  $z$ -ranges in mm are  $[\mp 1000, \mp 750]$ ,  $[\mp 750, \mp 500]$  and  $[\mp 500, \mp 250]$ ; the  $-$  and  $+$  signs are for beam 1 and beam 2, respectively. All 3 regions are described by a different distribution (4.20) but share the same fit parameters (besides the amplitudes).

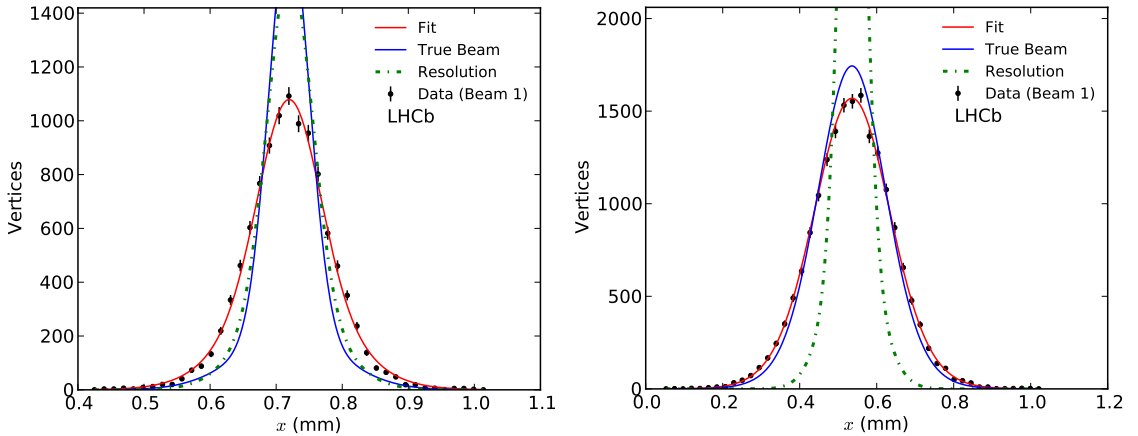


**Fig. 4.22:** Resolution deconvolution examples. Left: single beam shape measurement of beam 1 in  $x$  for fill 2520 with  $\beta^* = 3$  m. The true beam width is about 45  $\mu$ m. Right: single beam shape measurement of beam 1 in  $x$  for fill 2852 with  $\beta^* = 10$  m. The true beam width is about 93  $\mu$ m. Both measurements assume a double Gaussian beam shape and are performed on the most central  $z$  slice using vertices in the range  $-500 < z < -250$  mm. The SMOG gas injection was active; the number of vertices in the distributions is about  $10^4$  and  $1.4 \times 10^4$  for the left and right plot, respectively.

The overlap integral using this 1-d model assumes that  $x$ ,  $y$  and  $z$  can be factorized and is given by

$$\mathcal{O} = 2c \int \rho_{x1}(x') \rho_{y1}(y') \rho_{z1}(z - ct) \rho_{x2}(x') \rho_{y2}(y') \rho_{z2}(z + ct) dx dy dz dt$$

and will be discussed in Sec. 4.6.

The luminous region transverse shape is fully determined by the single beam distributions and therefore the observed  $pp$  collision vertices are used as an additional constrain to the single beam fit without adding new parameters besides the individual amplitudes. The luminous region benefits from about 10 times more vertices and also a smaller resolution of about half that from beam-gas. Given a  $z_c$ -position (center of a  $z$ -bin), the luminous region shape in the transverse directions ( $m = x, y$ ) is defined by the product of the two beam distributions evaluated at the same  $z_c$ -position

$$\rho_{bb}(m') = \rho_{m1}(m') \rho_{m2}(m'). \quad (4.21)$$

With Eq. (4.18), the single beam positions  $m'$  depend on the projection point  $z_c$ . The beam-beam interaction vertex positions  $m$ , entering the distribution  $\rho_{bb}(m')$ , are projected along the average direction of both beams with  $m' = m - (z - z_c)(\alpha_{1,m} + \alpha_{2,m})/2$ .

With double Gaussian shaped beams, the luminous region distribution is the sum of four Gaussian function products per axis. As the product of two Gaussians has again a Gaussian shape, we can simplify the description of the luminous region with the sum of four Gaussian function whose mean  $\xi_{hi}$ , width  $\sigma_{hi}$  and normalization  $A_{hi}$  are inferred from the single beam parameters. The indices  $h, i$  represent each the narrow or wide Gaussian width indices  $n, w$  for beam 1 and 2, respectively. The four  $h, i$  combinations being  $nn, nw, wn$  and  $ww$ . In the direction  $m = x, y$ , the luminous region distribution in the laboratory reference frame is described by

$$\begin{aligned} \rho_{bb}(m') = & A_{nn,m} w_{m1} w_{m2} \cdot g(m'; \xi_{nn,m}, \sigma_{nn,m}) \\ & + A_{nw,m} w_{m1} (1 - w_{m2}) \cdot g(m'; \xi_{nw,m}, \sigma_{nw,m}) \\ & + A_{wn,m} (1 - w_{m1}) w_{m2} \cdot g(m'; \xi_{wn,m}, \sigma_{wn,m}) \\ & + A_{ww,m} (1 - w_{m1})(1 - w_{m2}) \cdot g(m'; \xi_{ww,m}, \sigma_{ww,m}), \end{aligned} \quad (4.22)$$

with the Gaussian product normalization factor

$$A_{hi,m} = \frac{1}{\sqrt{2\pi(\sigma_{mh}^2 + \sigma_{mi}^2)}} e^{-\frac{1}{2} \frac{((\xi_{m1} - \alpha_{m1} \cdot z_c) - (\xi_{m2} - \alpha_{m2} \cdot z_c))^2}{\sigma_{m1h}^2 + \sigma_{m2i}^2}}, \quad (4.23)$$

the mean

$$\xi_{hi,m} = \frac{(\xi_{m1} - \alpha_{m1} \cdot z_c)\sigma_{m2i}^2 + (\xi_{m2} - \alpha_{m2} \cdot z_c)\sigma_{m1h}^2}{\sigma_{m1h}^2 + \sigma_{m2i}^2}, \quad (4.24)$$

and width

$$\sigma_{hi,m} = \sqrt{\frac{\sigma_{m1h}^2 \sigma_{m2i}^2}{\sigma_{m1h}^2 + \sigma_{m2i}^2}}, \quad (4.25)$$

with  $h = n, w$  and  $i = n, w$ . The indices 1, 2 denote here beam 1 and 2, respectively.

As for the single beam distributions, the observed luminous region distribution is a convolution of (4.22) with the beam-beam resolution. The observed luminous region transverse distribution can be described as

$$M_{bb}(m') = \sum_k c_k \rho_{bb}(m'; \xi_{h,i}, \sigma_{h,i}^*), \quad (4.26)$$

with the width components

$$\sigma_{h,i}^* = \sqrt{\sigma_{\text{res},k}^2 + \sigma_{h,i}^2}. \quad (4.27)$$

The effective resolution function is evaluated in the same way as for the single beam measurement described above.

Beam parameters are measured with a global fit combining both single beams and the luminous region. The fit is performed in the  $x$  and  $y$  directions independently. Beam-gas interaction vertices are divided in 3  $z$ -slices as to not mix vertices with too dissimilar resolutions, but still keep enough statistic per  $z$ -slice. Each single beam  $z$ -slice distribution is described with Eq. 4.20. The luminous region is divided in 18  $z$ -slices as Eq. 4.26 is  $z$ -dependent in the crossing plane. The  $z$ -slices are 10 mm wide in  $z$  in the central region and 15 mm wide in the outer region ( $|z| > 50$  mm). Each luminous region  $z$ -slice distribution is described with Eq. 4.26. The  $z$ -range selection and longitudinal vertex distribution are shown in Fig. 4.23 for 20 minutes of data acquisition during fill 2852 as an example. The asymmetric longitudinal shape of the luminous region is due to the requirement of having at least two forward and two backward tracks in each vertex which affects the VELO acceptance in the  $-z$  region. A three-dimensional view of vertices for the first BCID in the same fill is shown in Fig. 4.24 before the binning in  $z$ .

Single beam observables are measured first by fitting the 3  $z$ -slices per beam simultaneously and independently of the luminous region. Fit results are used as starting parameters for the global fit where all 24  $z$ -slices are fitted simultaneously combining both single beams and the luminous region. Both fits use 8 parameters describing the beam shapes, plus one amplitude per distribution. Global fit results for a colliding bunch pair are shown in Fig. 4.25 as example.<sup>5</sup>

---

<sup>5</sup>Showing the first measurement and first bunch of fill 2852.

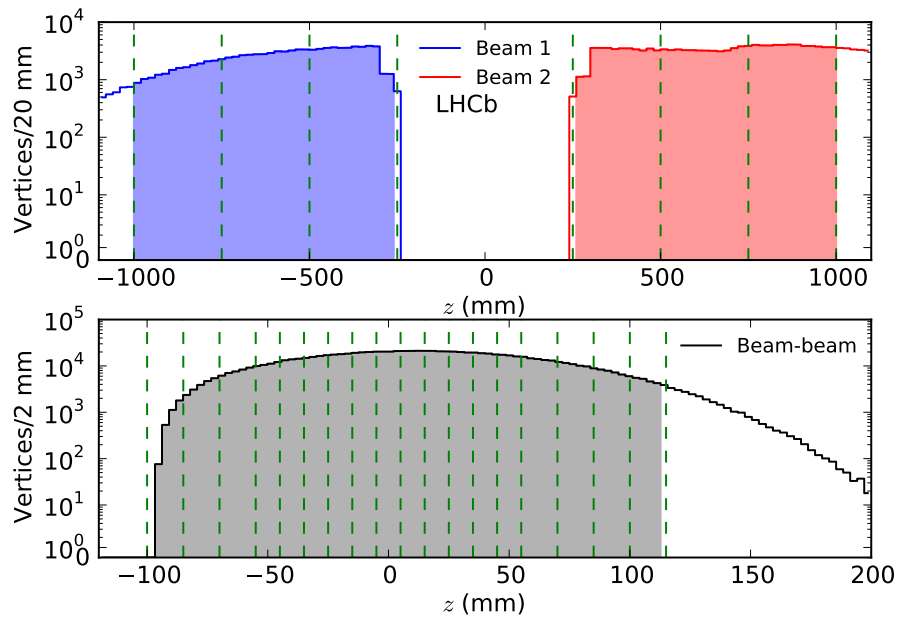


**Fig. 4.23:** Selected  $z$ -regions used for global fit. Top panel: longitudinal distribution of selected beam-gas interaction vertices for a colliding bunch pair over 20 minutes with beam 1 on the left and beam 2 on the right. The single beams are split in 3  $z$ -regions starting 250 mm away from  $z = 0$ , the boundaries are indicated by a vertical dashed line. Bottom panel: longitudinal distribution of selected beam-beam interactions requiring at least two forward and two backward tracks to exclude beam-gas background. The luminous region is split in 18  $z$  slices indicated by vertical dashed lines. The asymmetrical shape of the luminous region is due to the reduced VELO acceptance of backward tracks in the negative  $z$ -region.

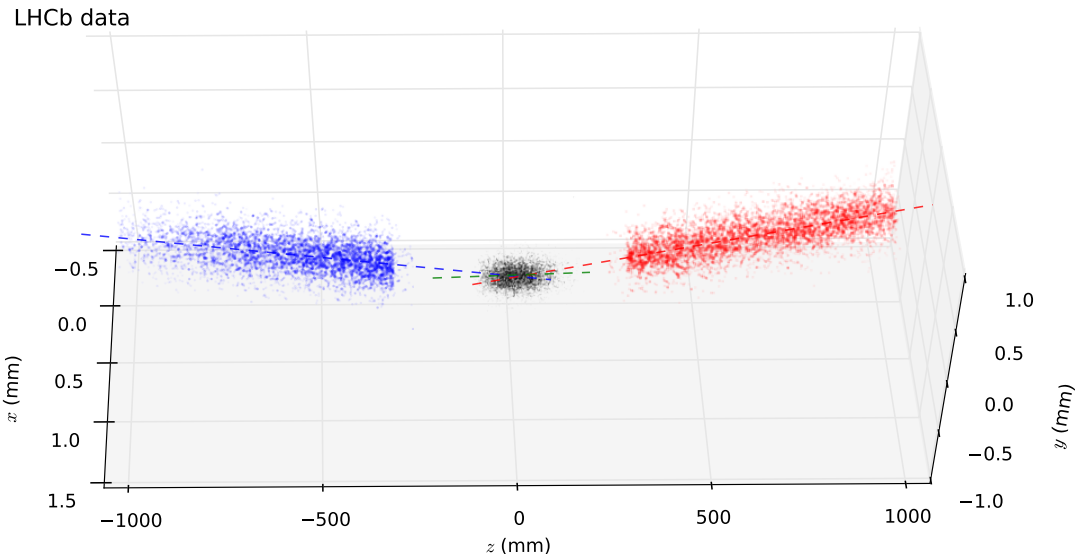


**Fig. 4.24:** Reconstructed beam-gas interaction vertices view in 3 dimensions for fill 2852 and BCID 1989. Only the first 5000 vertices per beam and in the luminous region are shown.

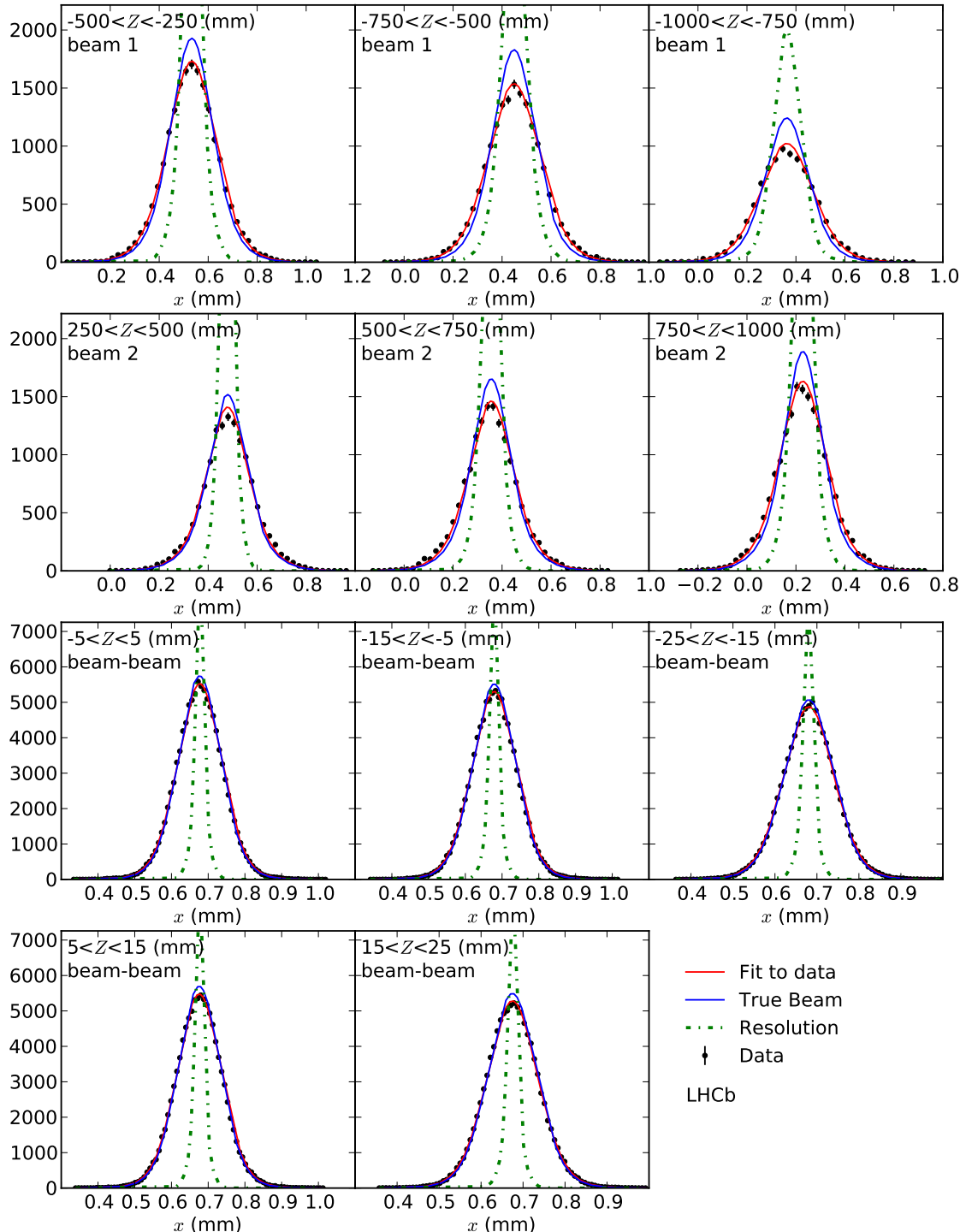


**Fig. 4.25:** Global fit results of a colliding bunch pair in 1-dimension, the  $z$ -range and collision type of each distribution is indicated in the plots. The first three panels show the fit results of the three beam 1  $z$ -slices, the next three slices are for beam 2, the remaining five distributions show the central beam-beam slices (the remaining 13 slices used in the fit are not shown for better readability). The double Gaussian fit is shown as a solid red line together with the effective resolution function as dashed green line. The unfolded true beam shape is shown as solid blue line.

### 4.4.3 Transverse shape in two-dimensional fit

While the one-dimensional fit model described above implicitly assumes that both axis  $x$  and  $y$  are independent, that is, the transverse shape in one axis does not depend on the other axis position, the beam shapes observed since 2012 with the larger amount of events gained with the SMOG system showed that the beam shapes are not exactly factorizable in  $x$  and  $y$  as will be shown in Sec. 4.6.2. To obtain a precision better than  $\approx 2.5\%$ , a two dimensional ( $x$   $y$ ) fit model is therefore needed. The single beam density function is defined in terms of a double Gaussian distributions per axis with a factorizable term  $f_j$  and is the sum of four Gaussian products:

$$\begin{aligned} \rho(x', y') = & [f_j w_x w_y & + (1 - f_j)(w_x + w_y)/2] \cdot g(x'; \xi'_x, \sigma_{xn}) g(y'; \xi'_y, \sigma_{yn}) \\ & + [f_j w_x (1 - w_y)] & \cdot g(x'; \xi'_x, \sigma_{xn}) g(y'; \xi'_y, \sigma_{yw}) \\ & + [f_j (1 - w_x) w_y] & \cdot g(x'; \xi'_x, \sigma_{xw}) g(y'; \xi'_y, \sigma_{yn}) \\ & + [f_j (1 - w_x) (1 - w_y) & + (1 - f_j)(1 - (w_x + w_y)/2)] \cdot g(x'; \xi'_x, \sigma_{xw}) g(y'; \xi'_y, \sigma_{yw}) \end{aligned} \quad (4.28)$$

with

$$x'_j = x_j - (z - z_c)\alpha_{xj} \text{ and } y'_j = y_j - (z - z_c)\alpha_{yj},$$

and

$$\xi'_m = \xi_m - z_c \alpha_{jm}.$$

Here  $z_c$  is the longitudinal position of the  $xy$  projection plane and all vertices with position  $(x_j, y_j)$ ,  $z$  are projected onto the  $xy$  plane at  $z_c$ . This coordinate translation excludes the hourglass effect by assuming a constant beam shape along the beam axis. With  $\beta^* = 10$  m, the hourglass effect broadens the beam by 0.5% at 1 m and its effect is neglected.

Setting  $f_j = 1$  in Eq. (4.28) is equivalent to the previous 1-d model where the beam is fully factorizable in  $x$  and  $y$ . With  $f_j = 0$ , the cross terms between the narrow and wide components vanish leaving only a narrow-narrow and wide-wide Gaussian product. Explicitly, the density function  $\rho_j = \rho_j(x, y, z)$  defined at a longitudinal position  $z_c$  for beam  $j$  in the LHCb reference frame is given by

$$\begin{aligned} \rho_j = & w_{nn,j} \cdot g(x - (z - z_c)\alpha_{x,j}; \xi_{x,j} - z_c\alpha_{x,j}, \sigma_{xn,j}) g(y - (z - z_c)\alpha_{y,j}; \xi_{y,j} - z_c\alpha_{y,j}, \sigma_{yn,j}) \\ & + w_{nw,j} \cdot g(x - (z - z_c)\alpha_{x,j}; \xi_{x,j} - z_c\alpha_{x,j}, \sigma_{xn,j}) g(y - (z - z_c)\alpha_{y,j}; \xi_{y,j} - z_c\alpha_{y,j}, \sigma_{yw,j}) \\ & + w_{wn,j} \cdot g(x - (z - z_c)\alpha_{x,j}; \xi_{x,j} - z_c\alpha_{x,j}, \sigma_{xw,j}) g(y - (z - z_c)\alpha_{y,j}; \xi_{y,j} - z_c\alpha_{y,j}, \sigma_{yn,j}) \\ & + w_{ww,j} \cdot g(x - (z - z_c)\alpha_{x,j}; \xi_{x,j} - z_c\alpha_{x,j}, \sigma_{xw,j}) g(y - (z - z_c)\alpha_{y,j}; \xi_{y,j} - z_c\alpha_{y,j}, \sigma_{yw,j}) \end{aligned} \quad (4.29)$$

with the weights

$$\begin{aligned} w_{nn,j} &= f_j w_{x,j} w_{y,j} + (1 - f_j)(w_{x,j} + w_{y,j})/2 \\ w_{nw,j} &= f_j w_{x,j} (1 - w_{y,j}) \\ w_{wn,j} &= f_j (1 - w_{x,j}) w_{y,j} \\ w_{ww,j} &= f_j (1 - w_{x,j}) (1 - w_{y,j}) + (1 - f_j)(1 - (w_{x,j} + w_{y,j})/2). \end{aligned} \quad (4.30)$$

The sum of all weights equals one per construction, regardless of  $f_j$ .

The overlap integral using this 2-d model is only factorized in  $z$  and is defined as

$$\mathcal{O} = 2c \int \rho_1(x, y, \alpha_{x1}, \alpha_{y1}) \rho_{z1}(z - ct) \rho_2(x, y, \alpha_{x2}, \alpha_{y2}) \rho_{z2}(z + ct) dx dy dz dt,$$

and will be discussed in Sec. 4.6.

The observed beam distribution is a convolution of (4.29) with the detector resolution and can be written as

$$M_j(x, y) = \sum_{k_x} \sum_{k_y} c_{k_x} c_{k_y} \rho_j(x, y, z, \alpha_x, \alpha_y, \sigma_{k_x, h}^*, \sigma_{k_y, h}^*). \quad (4.31)$$

As in the 1-d case, each beam width in (4.29) is replaced by a resolution convolved width in the plane  $m = x, y$ :

$$\sigma_{k_m, h}^* = \sqrt{\sigma_{\text{res}, k_m}^2 + \sigma_{m, h}^2} \quad (4.32)$$

with  $m = x, y$ . The indices  $h = n, w$  stand for the narrow and wide Gaussian components and the weights  $c_{k_x}$  and  $c_{k_y}$  are the relative resolution weights of the effective resolution functions for  $x$  and  $y$ , respectively. To keep the computing time of the fit below a few hours, the effective resolution functions  $R(x)$  and  $R(y)$  from Eq. (4.1) are generated with the sum of 3 Gaussian functions instead of 6 as for the 1-d case. This simplification, however, has no effect on the results.

The observed transverse vertex distribution per beam for a given  $z$ -range is fitted to Eq. (4.31). Fit parameters are the observables per beam  $j$  which are the Gaussian parameters  $w_{m,j}$ ,  $\xi_{m,j}$ ,  $\sigma_{m,n,j}$  and  $\sigma_{m,w,j}$  for both  $x$  and  $y$  axes and a factorizability parameter  $f_j$ . A free amplitude  $A_j$  per distribution is added as fit parameter. An examples of single beam resolution deconvolution in 2 dimension using the above model is shown in Fig. 4.26 for beam 1 using beam-gas interaction vertices in the longitudinal range  $-500 < z < -250$  mm. Results of the 1-d fit described before are used as starting parameters for the 2-d single beam fit. The pulls are defined as

$$\text{pulls}_{i,j} = \frac{N_{i,j} - f(x_i, y_i)}{\sqrt{N_{i,j}}}, \quad (4.33)$$

with  $N_{i,j}$  the data for bin  $i$  in  $x$  and bin  $j$  in  $y$  and  $f(x_i, y_i)$  the fit prediction.

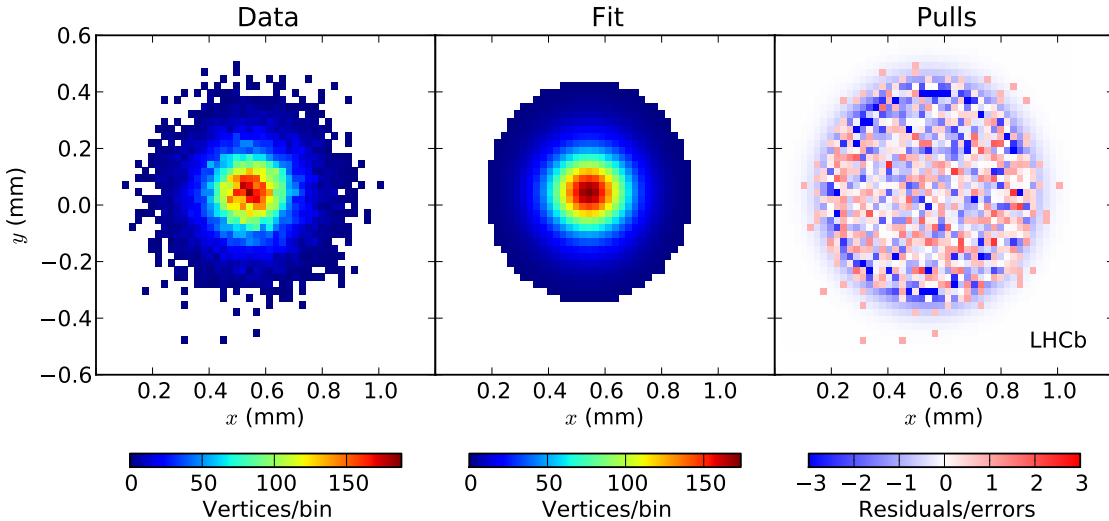


**Fig. 4.26:** Example of a  $z$ -slice fit result in 2-dimensions showing a single beam transverse projection for BCID 1909 in fill 2853. Left panel: raw beam transverse distribution; each square has a color proportional to the number of vertices within its  $x$ - $y$  position. Central panel: fit predictions including resolution convolution. Right panel: Pulls of the fit in the range  $[-3, 3]$  as defined by Eq. (4.33).

As in the 1-d case, the transverse luminous region shape is predicted by single beams parameters and is defined as the product of both beam density functions

$$\rho_{bb}(x, y, z) = \rho_1(x, y, z, \alpha_{x1}, \alpha_{y1}) \rho_2(x, y, z, \alpha_{x2}, \alpha_{y2}). \quad (4.34)$$

The coupling of  $x$  and  $y$  in each beam density function leads to a total of 16 Gaussian function combinations to describe the luminous region transverse shape. In a similar way to Eq. (4.22), we

define the individual Gaussian products per plane  $m$  with

$$\begin{aligned} p_{nn}(m) &= A_{nn,m} w_{m1} w_{m2} \cdot g(m; \xi_{nn,m}, \sigma_{nn,m}) \\ p_{nw}(m) &= A_{nw,m} w_{m1} (1 - w_{m2}) \cdot g(m; \xi_{nw,m}, \sigma_{nw,m}) \\ p_{wn}(m) &= A_{wn,m} (1 - w_{m1}) w_{m2} \cdot g(m; \xi_{wn,m}, \sigma_{wn,m}) \\ p_{ww}(m) &= A_{ww,m} (1 - w_{m1}) (1 - w_{m2}) \cdot g(m; \xi_{ww,m}, \sigma_{ww,m}). \end{aligned}$$

The amplitudes  $A_{hi,m}$  are defined in equation (4.23) and the luminous region mean position  $\xi_{hi,m}$  and width  $\sigma_{hi,m}$  are defined in equations (4.24) and (4.25), respectively. The  $h, i$  indices indicates either a narrow  $n$  or wide  $w$  Gaussian component. Note that the  $z$ -dependence of the luminous region transverse shape and position enters through the factors  $A_{hi,m}$  and  $\xi_{hi,m}$  and is dictated by the single beam positions and angles.

As for the 1-d case and to account for different angles per beams, the beam-beam interaction vertex positions  $m$  (for  $m = x, y$ ), entering the luminous region distribution, are projected along the average direction of both beams:  $m' = m - z(\alpha_{1,m} + \alpha_{2,m})/2$ . Using the weights  $w_{hi,j}$  per beam  $j$  defined in Eq. (4.30), the true luminous region transverse distribution is described by

$$\begin{aligned} \rho_{bb}(x', y', z) = & w_{nn,1} w_{nn,2} \cdot p_{nn}(x'; \xi_{nn,x}, \sigma_{nn,x}) \cdot p_{nn}(y'; \xi_{nn,y}, \sigma_{nn,y}) \\ & + w_{nn,1} w_{nw,2} \cdot p_{nn}(x'; \xi_{nn,x}, \sigma_{nn,x}) \cdot p_{nw}(y'; \xi_{nn,y}, \sigma_{nn,y}) \\ & + w_{nn,1} w_{wn,2} \cdot p_{nw}(x'; \xi_{nw,x}, \sigma_{nw,x}) \cdot p_{nn}(y'; \xi_{nw,y}, \sigma_{nw,y}) \\ & + w_{nn,1} w_{ww,2} \cdot p_{nw}(x'; \xi_{nw,x}, \sigma_{nw,x}) \cdot p_{nw}(y'; \xi_{nw,y}, \sigma_{nw,y}) \\ & + w_{nw,1} w_{nn,2} \cdot p_{nn}(x'; \xi_{nn,x}, \sigma_{nn,x}) \cdot p_{wn}(y'; \xi_{nn,y}, \sigma_{nn,y}) \\ & + w_{nw,1} w_{nw,2} \cdot p_{nn}(x'; \xi_{nn,x}, \sigma_{nn,x}) \cdot p_{ww}(y'; \xi_{nn,y}, \sigma_{nn,y}) \\ & + w_{nw,1} w_{wn,2} \cdot p_{nw}(x'; \xi_{nw,x}, \sigma_{nw,x}) \cdot p_{wn}(y'; \xi_{nw,y}, \sigma_{nw,y}) \\ & + w_{nw,1} w_{ww,2} \cdot p_{nw}(x'; \xi_{nw,x}, \sigma_{nw,x}) \cdot p_{ww}(y'; \xi_{nw,y}, \sigma_{nw,y}) \\ & + w_{wn,1} w_{nn,2} \cdot p_{wn}(x'; \xi_{wn,x}, \sigma_{wn,x}) \cdot p_{nn}(y'; \xi_{wn,y}, \sigma_{wn,y}) \\ & + w_{wn,1} w_{nw,2} \cdot p_{wn}(x'; \xi_{wn,x}, \sigma_{wn,x}) \cdot p_{nw}(y'; \xi_{wn,y}, \sigma_{wn,y}) \\ & + w_{wn,1} w_{wn,2} \cdot p_{ww}(x'; \xi_{wn,x}, \sigma_{wn,x}) \cdot p_{nn}(y'; \xi_{ww,y}, \sigma_{ww,y}) \\ & + w_{wn,1} w_{ww,2} \cdot p_{ww}(x'; \xi_{wn,x}, \sigma_{wn,x}) \cdot p_{nw}(y'; \xi_{ww,y}, \sigma_{ww,y}) \\ & + w_{ww,1} w_{nn,2} \cdot p_{wn}(x'; \xi_{wn,x}, \sigma_{wn,x}) \cdot p_{wn}(y'; \xi_{wn,y}, \sigma_{wn,y}) \\ & + w_{ww,1} w_{nw,2} \cdot p_{wn}(x'; \xi_{wn,x}, \sigma_{wn,x}) \cdot p_{ww}(y'; \xi_{wn,y}, \sigma_{wn,y}) \\ & + w_{ww,1} w_{wn,2} \cdot p_{ww}(x'; \xi_{ww,x}, \sigma_{ww,x}) \cdot p_{wn}(y'; \xi_{ww,y}, \sigma_{ww,y}) \\ & + w_{ww,1} w_{ww,2} \cdot p_{ww}(x'; \xi_{ww,x}, \sigma_{ww,x}) \cdot p_{ww}(y'; \xi_{ww,y}, \sigma_{ww,y}). \end{aligned} \quad (4.35)$$

Note that the means  $\xi_{hi,m}$  and widths  $\sigma_{hi,m}$  describe luminous region quantities, but are defined by the single beam parameters.

The observed luminous region distribution after resolution convolution is defined by

$$M_{bb}(x', y') = \sum_{k_x} \sum_{k_y} c_{k_x} c_{k_y} \rho_{bb}(x', y', z, \xi_{hi,x}, \sigma_{hi,k_x}^*, \xi_{hi,y}, \sigma_{hi,k_y}^*). \quad (4.36)$$

Each luminous region width component  $\sigma_{hi,m}$  in (4.35) is convolved with the detector resolution for beam-beam interaction vertices with

$$\sigma_{hi,k_m}^* = \sqrt{\sigma_{\text{res},k_m}^2 + \sigma_{hi,m}^2} \quad \text{for } m = x, y. \quad (4.37)$$

The weights  $c_{k_x}$  and  $c_{k_y}$  are the relative resolution weights of the beam-beam effective resolution functions for  $x$  and  $y$ , respectively.

The bunch shape measurement is performed in a similar way as in the 1-d case. Beam-gas interaction vertices are projected along the beam direction at the center of the  $z$ -slice and binned in  $x$ - $y$ . The single beams are measured individually with (4.31) using the same 3  $z$ -slices per beam as described in Fig. 4.23. Then the beam parameters are measured again in a global fit including single beams and luminous region distributions using the same  $z$ -slices as described previously for the 1-d measurement. Observables are fit parameters, namely the Gaussian parameters  $w_{m,j}$ ,  $\xi_{m,j}$ ,  $\sigma_{m,n,j}$  and  $\sigma_{m,w,j}$  for both  $x$  and  $y$  axis and beam  $j$  and one factorizability parameter  $f_j$  per beam. Additionally one free amplitude per  $z$ -slice is added as fit parameter. The increased number of parameters (18 beam parameters + 24 amplitudes) for the global fit requires starting values reasonably close to the final result. Accordingly, results of the 1-d single beam fit are used as starting parameters for the single beam 2-d fit, the results of which are used as starting values for the global fit. The starting values for the factorizability parameters  $f_j$  are set to 0.5. Bunch pairs with the largest statistics have up to 50k bins in the global fit.

An example of global fit result showing one slice per beam and one luminous region slice is shown in Fig. 4.27 for the first bunch and first measurement performed with SMOG and a  $\beta^* = 10$  m lattice. Pulls of the 2-d global fit results are shown in Fig. 4.28 for BCID 1909 in fill 2852. This example uses the same BCID and time period as shown in the 1-d measurement in Fig. 4.25.

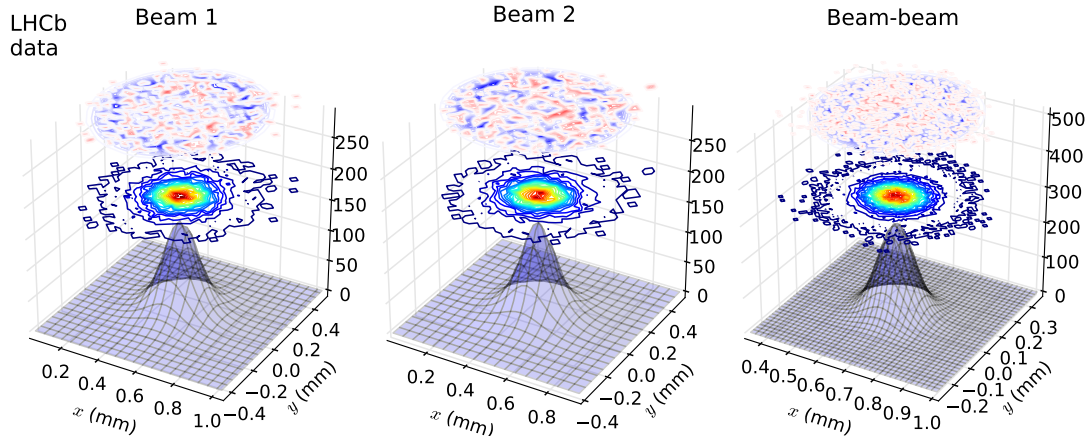


**Fig. 4.27:** Global fit in 2-dimensions for fill 2853 as example. Left: central  $z$ -slice of beam 1. Middle: central  $z$ -slice of beam 2. Right: central  $z$ -slice of the luminous region. The remaining 19  $z$ -slices are not shown for better readability. The fit result of the true beam shape including resolution convolution is shown as a 3-dimensional shape, the data is shown as a contour plot above the fit result. The pulls of the fit are shown on top. The color codes are the same as in Fig. 4.26.

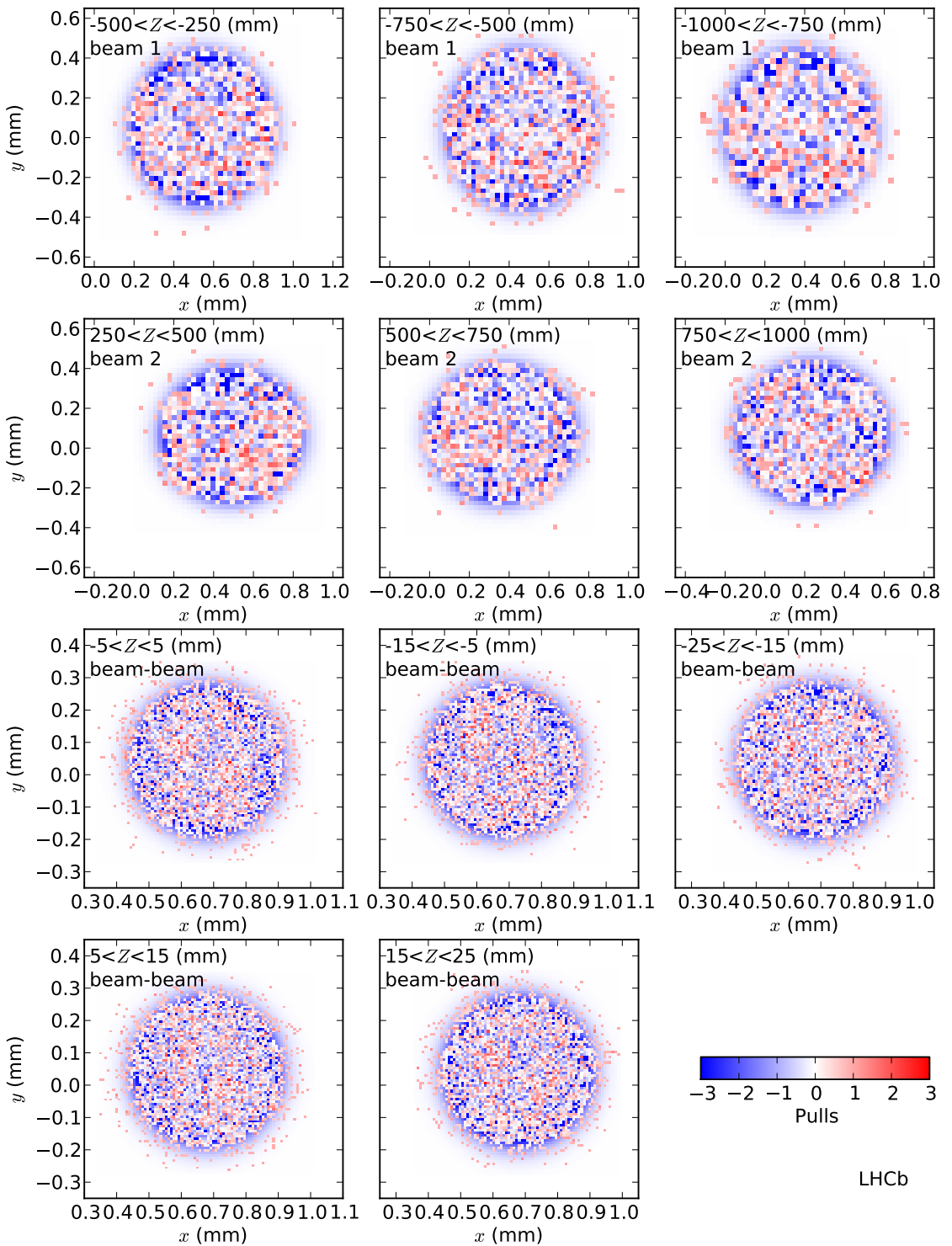


**Fig. 4.28:** Global fit results of a colliding bunch pair in 2-dimensions showing the fit pulls for fill 2853. The same  $z$ -slices as shown in Fig. 4.25 are shown here with the two-dimensional fit. The  $z$ -range and collision type of each distribution is indicated in the plots. The first three panels show the fit results of the three beam 1  $z$ -slices, the next three slices are for beam 2, the remaining five distribution show the central beam-beam slices (the remaining 13 slices used in the fit are not shown for better readability). The pulls are evaluated with Eq. (4.33).

#### 4.4.4 Bunch length and longitudinal crossing point

The beam offsets  $\Delta_m$  required in Eq. (3.17) are measured at the longitudinal position  $Z_{\text{RF}}$  where the bunches cross in time (see Fig. 3.1 in Sec. 3). In the crossing plane, the beams collide head-on (zero offset) when the  $z$ -mean of the luminous region coincides with the geometrical crossing point, which is the  $z$ -position where the beam velocity vectors intersect, and the  $Z_{\text{RF}}$  position. The position  $Z_{\text{RF}}$  is defined by the LHC RF phase. A transverse beam drift in the crossing plane will shift the luminous region center as well as the geometrical crossing point. The  $Z_{\text{RF}}$  position can be measured once during the fill when the beams have been optimized in both planes, and then used for all overlap integral measurements for the fill. While the beam positions are normally optimized by the LHC operators at the beginning of a stable beam period or at another time during the fill, this optimization does not guarantee perfect head-on positions. Furthermore, the optimization can be performed at a time when the LHCb detector is not active in which case the luminous region cannot be measured. Instead, the  $Z_{\text{RF}}$  position can be measured with the luminous region longitudinal shape and position using Eq. (3.19) for each colliding bunch pair.

In addition to the beam offsets  $\Delta_m$  discussed above, also the individual bunch length  $\sigma_{z1}$  and  $\sigma_{z2}$  required in Eq. (3.17) are not directly measurable. However, the convolved bunch length  $\sigma_{z1}^2 + \sigma_{z2}^2$  is related to the luminous region shape and can be measured with the luminous region longitudinal vertex distribution with Eq. (3.21).

Considering the case where the beams have a three-dimensional Gaussian distribution, the longitudinal luminous region distribution  $\rho_{bb} = B \cdot g(z)$  can be described with a Gaussian function  $g(z; \xi_{lz}, \sigma_{lz})$  with a mean position  $\xi_{lz}$  and width  $\sigma_{lz}$ . The amplitude  $B$  is proportional to the luminosity and therefore to the overlap integral. The observables  $\xi_{lz}$  and  $\sigma_{lz}$  can be described in terms of  $Z_{\text{RF}}$  and  $\sigma_{z1}^2 + \sigma_{z2}^2$  using Equations (3.19) and (3.20), and are given by

$$\sigma_{lz} = \left[ \frac{1}{\sigma_{lz}^2} = \frac{4 \cos^2 \sqrt{\phi_x^2 + \phi_y^2}}{\sigma_{z1}^2 + \sigma_{z2}^2} + \frac{4 \sin^2(\phi_x)}{\sigma_{x1}^2 + \sigma_{x2}^2} + \frac{4 \sin^2(\phi_y)}{\sigma_{y1}^2 + \sigma_{y2}^2} \right]^{-1/2} \quad (4.38)$$

and

$$\xi_{lz} = Z_{\text{RF}} + \delta z_{l,0,m}, \quad (4.39)$$

with

$$\delta z_{l,0} = -\frac{\sin 2\phi_x}{4} \cdot \frac{\sigma_{z1}^2 + \sigma_{z2}^2 - \sigma_{x1}^2 + \sigma_{x2}^2}{(\sigma_{x1}^2 + \sigma_{x2}^2) \cos^2 \phi_x + (\sigma_{z1}^2 + \sigma_{z2}^2) \sin^2 \phi_x} \cdot \Delta x. \quad (4.40)$$

Because the beams are described with double Gaussian transverse shapes, the luminous region distribution  $\rho_{bb}(z)$  has 16 Gaussian contributions instead of one. Each contributing Gaussian function is allowed to have a different length  $\sigma_{lz}$  and longitudinal offset  $\delta z_{l,0,m}$  depending on the single beam parameters entering in (4.40) and (4.38); however, the quantities  $Z_{\text{RF}}$  and  $\sigma_{z1}^2 + \sigma_{z2}^2$  are common to all. Additionally, each Gaussian function is weighted according to the fraction of luminosity it carries. The longitudinal distribution is then defined as

$$\rho_{bb}(z) = \sum_{i,j,k,l} B_{i,j,k,l} \cdot g_{i,j,k,l}(z) \quad (4.41)$$

$$\text{with } B_{i,j,k,l} = w_{i,j} w_{k,l} O_{i,j,k,l}.$$

The indices  $i, j, k, l$  define the beam parameters combination  $i \in \{x_{1n}, x_{1w}\}$ ,  $j \in \{y_{1n}, y_{1w}\}$ ,  $k \in \{x_{2n}, x_{2w}\}$ ,  $l \in \{y_{2n}, y_{2w}\}$ . The fractions  $w_{i,j}$  and  $w_{k,l}$  are the product defined in (4.30), and the individual partial overlap integrals  $O_{i,j,k,l}$  are evaluated with Eq. (3.17) (see next Sec. 4.6 for the explicit expressions of the individual overlaps). Note that  $Z_{\text{RF}}$  depends on the beam offsets

$\Delta_m$  which themselves depend on the  $Z_{\text{RF}}$  position. Furthermore, each individual overlap  $O_{i,j,k,l}$  in (4.41) also depends on the unknown values  $Z_{\text{RF}}$ ,  $\Delta_m$  and  $\sigma_{z1}^2 + \sigma_{z2}^2$  and must be evaluated in each fit iteration with the changing fit parameters. The three parameters of the fit (per BCID and 20 minutes) are the  $Z_{\text{RF}}$  position, the convolved length  $\sigma_{z1}^2 + \sigma_{z2}^2$  and an amplitude.

The VELO reconstruction efficiency is not exactly constant with varying  $z$ . This distorts the luminous region longitudinal shape and possibly biases the  $Z_{\text{RF}}$  and  $\sigma_{z1}^2 + \sigma_{z2}^2$  measurements described above. Therefore, the relative vertex reconstruction efficiency has been evaluated with a Monte Carlo simulation. The simulation generates minimum bias  $pp$  interactions at  $\sqrt{s} = 8$  TeV in the range  $-200 \text{ mm} < z < 200 \text{ mm}$  [43]. The simulated data are then reconstructed with the LHCb algorithms to evaluate the efficiency that is applied to the raw distribution before fitting. The reconstruction efficiency  $\epsilon_v$  as function of  $z$  is shown in Fig. 4.29 (left). Each raw bin value  $h_i$  in the longitudinal distribution is corrected with  $h'_i = h_i / \epsilon_{vi}$  and fitted with function (4.41). A fit result is shown in Fig. 4.29 (right) for a colliding bunch pair (BCID 1335) measurement in fill 2855 as an example. In this example only 4 out of 16 contributions are visible as the beams are non-factorizable, leaving only 4 non-zero contributions (see Sec. 4.6.2 for the evidence for beam shape non-factorizability).

The deconvolution of the detector resolution, which is about 100  $\mu\text{m}$  in  $z$  has no effect on the measurements and is not applied. As the efficiency  $\epsilon_v$  depends on the track requirements per vertex, the simulation is performed with the same requirement as used to select the vertices. In this measurement the vertices are required to have at least 10 tracks. However, no further selection is made on the track direction to exclude beam-gas interactions. All vertices in the range  $[-250, 250]$  mm per BCID are used for this measurement which includes a fraction of beam-gas events of about 0.7%. The same measurement is performed with a cut on forward and backward track such as to exclude beam-gas events and is discussed in Sec. 7.2.6.

The  $Z_{\text{RF}}$ ,  $\Delta_m$  and  $\sigma_{z1}^2 + \sigma_{z2}^2$  measurements described above are made under the assumption that the longitudinal bunch shape is Gaussian and its width and center is common to both partial Gaussian components for bunches with double Gaussian transverse shapes. While the observed longitudinal distribution is Gaussian-like and its shape would not allow to fit a double Gaussian function, BGI measurements performed with offset beams permit to evaluate the  $\sigma_{z1}^2 + \sigma_{z2}^2$  value of the wide bunch component and is discussed in Sec. 7.1.2.

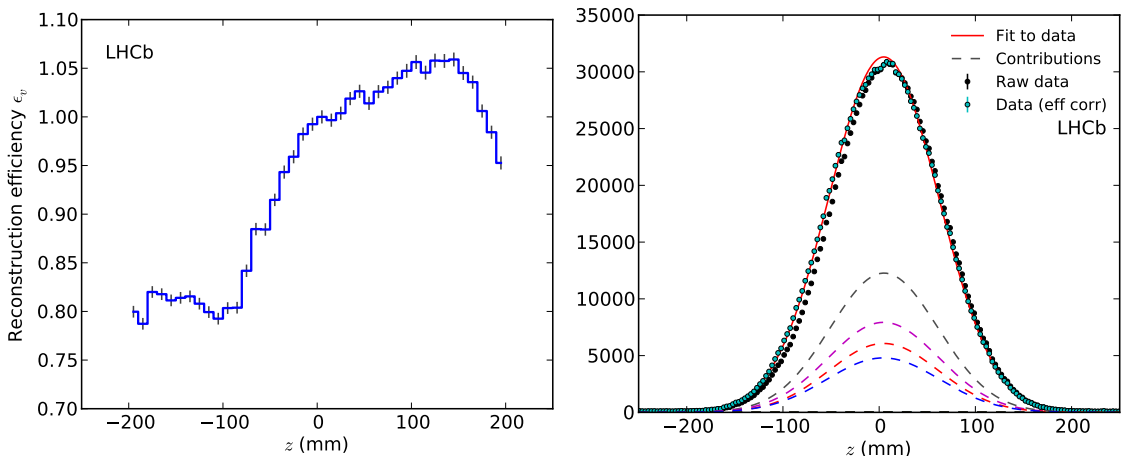


**Fig. 4.29:** Left: relative vertex reconstruction efficiency as function of  $z$  for  $pp$  collisions at  $\sqrt{s} = 8$  TeV. The 100% efficiency is set at  $z = 0$  as to keep the amplitudes between raw and corrected data similar; however, the absolute scale of the correction does not change the fit results. Right: fit of the longitudinal vertex distribution of a colliding bunch pair (BCID 1335) after reconstruction efficiency correction for fill 2855. The solid red line is the fit result. The different contributions to the final fit shape are shown as dashed lines.

## 4.5 Generic Monte Carlo simulation

Beams measured during dedicated luminosity calibration fills have varying sizes, shapes and available statistics; transverse sizes range from about 40  $\mu\text{m}$  for Apr 2012 fills at  $\beta^* = 3$  m to about 90  $\mu\text{m}$  for  $\beta^* = 10$  and above 150  $\mu\text{m}$  for intermediate energy fills in 2013. Beams observed in Apr and Jul had a double Gaussian shape, while beams observed in Nov 2012 had a shape close to being single Gaussian but with a lower peak amplitude which can be described by allowing one Gaussian component of a double Gaussian shape to carry a negative weight. Additionally, some intermediate energy bunches acquired in 2013 had a factor 10 lower statistics in both beam-gas and luminous region data.

The BGI method relies on the accurate beam shape description regardless of the bunch shapes, sizes and statistics. Therefore, simulated data sets have been created with a generic Monte Carlo method to test the fit models described in the previous section and to assess the capability to describe the beam shapes with various parameters and statistics. The systematic uncertainties related to the fit model will be discussed in Sec. 7.2.5.

The development of the more complex two dimensional fit model described in Sec. 4.4.3 was motivated by the possible non-factorizability of the beams in the  $x$  and  $y$  directions which could in principle be measured with beam-gas interactions. The capability to measure the beam factorizability was first tested with simulated data. Results showing evidence for beam non-factorizability are presented in Sec. 4.6.2. Datasets of simulated vertices are generated for single beams and luminous region in the following way.

Single beam vertices positions  $v'_m$  (in the axis  $m = x, y$ ) are generated by sampling eq. (4.29) within  $\pm 2$  mm for a fixed  $z = 0$  position for both beams. A random  $z$ -position  $v_{z,j}$  is then assigned to each vertex in the range  $-1000 < z < -250$  mm for beam 1 and  $250 < z < 1000$  mm for beam 2. The crossing angles are applied to each vertex with  $v_m = v'_m + (v_{z,j} \alpha_{m,j})$  with  $\alpha_{m,j}$  the crossing angle for beam  $j$  and transverse axis  $m$ . To simulate the lower statistics away from  $z = 0$ , a simple linear  $z$ -dependent exclusion criteria is applied to each vertex, keeping all vertices at  $z = 0$  and reducing the statistics to about 10% at  $|z| = 1.1$  m. About  $5 \times 10^4$  vertices are generated per beam which is similar to 20 minutes beam-gas data for a bunch pair.

The luminous region shape is defined by the overlap integral and is sampled over space-time using

$$\mathcal{O} = 2c \int \rho_1(x, y, z) \rho_{z1}(z - ct) \rho_2(x, y, z) \rho_{z2}(z + ct) dx dy dz dt \quad (4.42)$$

with the single beam distributions  $\rho_j$  defined in eq. (4.29) and  $\rho_{z,j}$  a single Gaussian function to describing the longitudinal bunch shape. While the integration of (4.42) is defined with infinite boundaries, in practice it is sufficient that the sampling volume  $S_{\text{vol}} = dx dy dz dt$  encompasses the full luminous region dimensions without cutting the distribution tails. A sampling over  $\pm 0.8$  mm in the transverse axes, and  $\pm 250$  mm in  $z$ , and  $\pm 1.2$  ns proved to be conservative enough for most beam parameters while keeping the required computing time below 24 hours per dataset. A number  $N_s$  of random samples of  $(x, y, z, t) \in S_{\text{vol}}$  are evaluated with

$$\rho_{bb}^s(x, y, z, t) = \rho_1(x, y, z) \rho_{z1}(z - ct) \rho_2(x, y, z) \rho_{z2}(z + ct). \quad (4.43)$$

At each iteration  $s$ , a vertex is kept in the dataset if a sampled number  $A_{bb}^s$  satisfies  $A_{bb}^s \leq \rho_{bb}^s$ , where  $A_{bb}^s$  is a random number in the range  $[0, A_{bb}]$ . The maximal amplitude  $A_{bb}$  is chosen such that  $A_{bb} \geq \max(\rho_{bb})$ .

The numerical value of a generated overlap integral is calculated using the fraction  $N_{bb}$  of vertices kept compared to the total number of samples  $N_s$  tested in the volume  $S_{\text{vol}}$  with

$$\mathcal{O} = 2c \cdot \frac{N_{bb}}{N_s} S_{\text{vol}} \cdot A_{bb}. \quad (4.44)$$

The statistical uncertainty is taken as  $\sqrt{N_{bb}}$ .

Each primary MC vertex as generated with the above method is assigned a track multiplicity ranging from 10 to 30 for single beams vertices and from 10 to 40 for luminous region vertices. Two split vertices are generated for each primary MC vertex, each with the track multiplicity of the primary vertex split in two. In case of an odd number of tracks, the first split vertex will have one more track. Using a resolution parametrization measured with data, each vertex is assigned a resolution in  $x$  and  $y$  by sampling a normal Gaussian distribution. The resolution distribution width  $\sigma_{\text{res}}$  is given by the vertex resolution and depend on the vertex track multiplicity,  $z$ -position and beam type as described in Sec. 4.3.

The generated datasets have the same format and are processed with the same algorithms as used for the data. The simulations permitted to verify the analytical formulas for the overlap integral defined in (3.17) for single Gaussian beams and (4.46) for double Gaussian beam. Also the two dimensional shape description with resolution convolution defined in (4.35) (4.36) could be tested. An example of data generated with non realistic beam parameters is shown in Fig. 4.30 using double Gaussian beams. It can be seen on the bottom right plot that the predicted lines agree well with the simulated data also with such non realistic test case. An example generated with data-like beam parameters is shown in Fig. 4.31.

The binning and fitting algorithms have been tested with different beam parameters and are first validated with simulated datasets before being applied to data. Systematic uncertainties related to the fit model or fit bias will be addressed in Sec. 7.2.5.

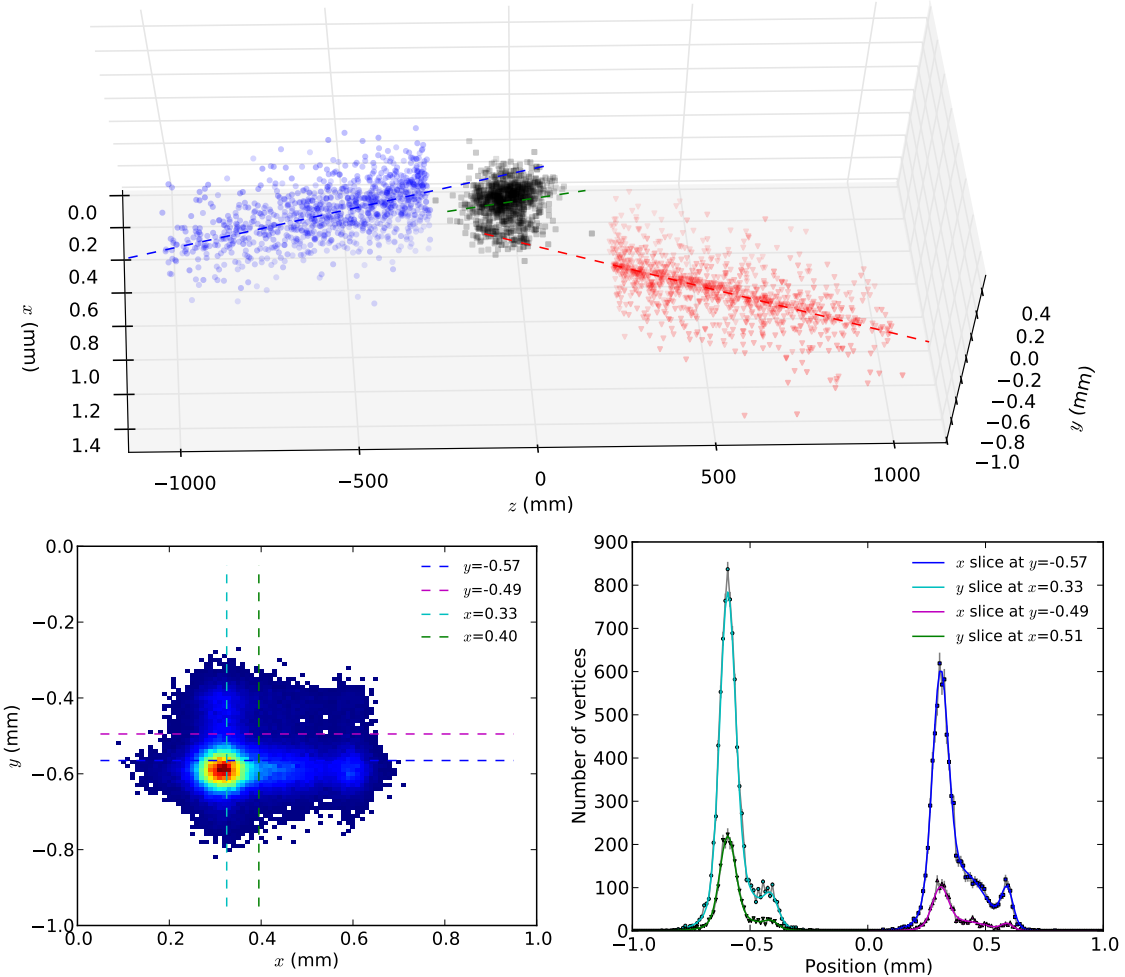


**Fig. 4.30:** Fit model test with extreme non-realistic beam parameters. Top panel: scatter plot of simulated beam-gas interaction vertices (left for beam 1 and right for beam 2) and beam-beam interaction vertices (center). Bottom left: transverse view of vertices density of the central  $z$ -slice at  $z = 0$ . The color scale is similar to 4.26 with red indicating the highest number of vertices per bin. Dashed lines indicate  $x$  and  $y$  slices in the distribution shown on the right plot. Bottom right: Comparison of simulated data with predictions for different  $x$  and  $y$  slices of the luminous region central  $z$ -slice. Markers indicate the simulated data while solid lines show the prediction. Both simulated data and predictions are convolved with the resolution.

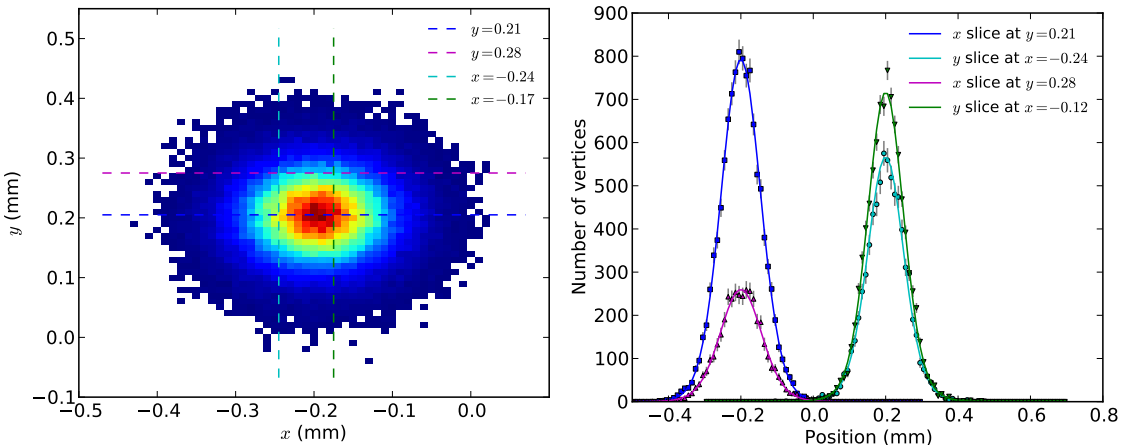


**Fig. 4.31:** Fit model test with data-like beam parameters. Same plots as in Fig. 4.30 but with beam parameters similar to observed values in Jul 2012.

## 4.6 Overlap integral

All beam parameters required to measure the overlap integral of colliding bunch pairs are measured with the methods described in Sec. 4.4 for all dedicated luminosity calibration fills listed in Table 4.1 with  $pp$  interactions (excluding MD fill 3160). The beam-gas and beam-beam interaction vertices for each colliding bunch pair is integrated over 20 minutes per measurement. The available statistics can vary depending on the bunch intensity, the beam offset and trigger prescale. Furthermore, detector dead-time or occasional technical difficulties can reduce the available data. An overview of the number of vertices per measurement is shown in Fig. D.6 in appendix D.

The measurement is performed in stages using vertices passing the selection described in Sec. 4.1.3: first, the crossing angles are measured per plane and beam as described in Sec. 4.4.1. Secondly, all vertices per BCID are binned in  $z$ -slices and fitted with the 1-d and 2-d fit models described in Sec. 4.4.2 and 4.4.3, respectively. The reduced  $\chi^2$  per degree of freedom for the 2-d fit is typically between 1 and 1.1 as shown in Fig. D.7 in appendix D. The crossing angles are measured over an acquisition run which lasts typically one hour and are assumed to be constant over time. To test this assumption, one measurement using the 2-d fit model is performed with the crossing angles as free fit parameters and only uses the measured angles as starting values. The resulting angles are unchanged within  $\pm 1 \mu\text{rad}$  and are shown in Fig. D.9 in appendix D for all fills in 2012. Finally, the convolved bunch length  $\sigma_{z1}^2 + \sigma_{z2}^2$  and bunch crossing point  $Z_{\text{RF}}$  are measured as described in Sec. 4.4.4. The measured  $\sigma_{z1}^2 + \sigma_{z2}^2$  values are shown in Fig. D.8 in appendix D.

The overlap integral defined by eq. (3.17) is valid for Gaussian shaped bunches in  $x$ ,  $y$  and  $z$ . In the presence of double Gaussian beam shapes in all three axes, each beam having 8 Gaussian widths, the overlap integral can be described as the sum of 64 partial single Gaussian overlaps resulting from the combination of all partial double Gaussian widths between both bunches and all axes. A double Gaussian shaped bunch can be visualized as the superposition of two bunches in one having different widths. In practice, a double Gaussian shape in  $z$  is not observed (or the double Gaussian strength is too small) in the luminous region longitudinal distribution and the assumption is made that the  $z$  distribution has a single Gaussian shape for both bunches and is therefore factorizable when evaluating the overlap integral. The uncertainty related to the bunch length is discussed in Sec. 7.2.6.

As previously described, the transverse bunch shape  $\rho_m$  (in the direction  $m = x, y$ ) is described by a double Gaussian function with a narrow and wide component denoted with indices  $n$  and  $w$ , respectively:

$$\rho_m(m; \xi_m, \sigma_{m,n}, \sigma_{m,w}) = w_n g(m, \xi_m, \sigma_{m,n}) + w_w g(m, \xi_m, \sigma_{m,w}). \quad (4.45)$$

Here  $g(m, \xi_m, \sigma_m)$  is a normalized Gaussian function with mean  $\xi_m$  and width  $\sigma_m$  and  $w_n$  and  $w_w$  are the corresponding weights for the narrow and wide component with  $w_n + w_w = 1$  per definition. Assuming the bunches have a single Gaussian shape in  $z$ , the overlap integral  $\mathcal{O}_d$  with double Gaussian beams in the transverse direction can be written as the sum of partial single Gaussian overlaps resulting from the combination of all partial double Gaussian width. It is furthermore assumed that the narrow and wide components share the same mean. The overlap integral of double Gaussian beams can be described with the sum of 16 components:

$$\mathcal{O}_d = \sum_{i,j,k,l} w_{i,j} w_{k,l} \mathcal{O}_{i,j,k,l}, \quad (4.46)$$

with the  $i, j, k, l$  indices defining the beam parameters combination:  $i \in \{x_{1n}, x_{1w}\}$ ,  $j \in \{y_{1n}, y_{1w}\}$ ,  $k \in \{x_{2n}, x_{2w}\}$  and  $l \in \{y_{2n}, y_{2w}\}$ . The individual overlaps  $\mathcal{O}_{i,j,k,l}$  are evaluated with eq. (3.17) and the fractions  $w_{i,j} w_{k,l}$  are the product of each weight  $w_i w_j w_k w_l$ . As seen in

sec. 4.4.3, correlation between the  $x$  and  $y$  axes with double Gaussian beam shapes changes the weight products  $w_{i,j}w_{k,l}$ .

For each partial overlap integral  $\mathcal{O}_{i,j,k,l}$ , only the width per beam and axis are different, other parameters like the means, offsets, angles and bunch length are common for all partial overlap integrals of the given bunch pair. Using the notation  $\mathcal{O}_{i,j,k,l} = \mathcal{O}(\sigma_i, \sigma_j, \sigma_k, \sigma_l)$ , the overlap integral  $\mathcal{O}_d$  with double Gaussian beams can be described as

$$\begin{aligned}
\mathcal{O}_d = & w_{nn,1} w_{nn,2} \cdot \mathcal{O}(\sigma_{x1n}, \sigma_{y1n}, \sigma_{x2n}, \sigma_{y2n}) \\
& + w_{nn,1} w_{nw,2} \cdot \mathcal{O}(\sigma_{x1n}, \sigma_{y1n}, \sigma_{x2n}, \sigma_{y2w}) \\
& + w_{nw,1} w_{nn,2} \cdot \mathcal{O}(\sigma_{x1n}, \sigma_{y1w}, \sigma_{x2n}, \sigma_{y2n}) \\
& + w_{nw,1} w_{nw,2} \cdot \mathcal{O}(\sigma_{x1n}, \sigma_{y1w}, \sigma_{x2n}, \sigma_{y2w}) \\
& + w_{nn,1} w_{wn,2} \cdot \mathcal{O}(\sigma_{x1n}, \sigma_{y1n}, \sigma_{x2w}, \sigma_{y2n}) \\
& + w_{nn,1} w_{ww,2} \cdot \mathcal{O}(\sigma_{x1n}, \sigma_{y1n}, \sigma_{x2w}, \sigma_{y2w}) \\
& + w_{nw,1} w_{wn,2} \cdot \mathcal{O}(\sigma_{x1n}, \sigma_{y1w}, \sigma_{x2w}, \sigma_{y2n}) \\
& + w_{nw,1} w_{ww,2} \cdot \mathcal{O}(\sigma_{x1n}, \sigma_{y1w}, \sigma_{x2w}, \sigma_{y2w}) \\
& + w_{wn,1} w_{nn,2} \cdot \mathcal{O}(\sigma_{x1w}, \sigma_{y1n}, \sigma_{x2n}, \sigma_{y2n}) \\
& + w_{wn,1} w_{nw,2} \cdot \mathcal{O}(\sigma_{x1w}, \sigma_{y1n}, \sigma_{x2n}, \sigma_{y2w}) \\
& + w_{ww,1} w_{nn,2} \cdot \mathcal{O}(\sigma_{x1w}, \sigma_{y1w}, \sigma_{x2n}, \sigma_{y2n}) \\
& + w_{ww,1} w_{nw,2} \cdot \mathcal{O}(\sigma_{x1w}, \sigma_{y1w}, \sigma_{x2n}, \sigma_{y2w}) \\
& + w_{wn,1} w_{wn,2} \cdot \mathcal{O}(\sigma_{x1w}, \sigma_{y1n}, \sigma_{x2w}, \sigma_{y2n}) \\
& + w_{wn,1} w_{ww,2} \cdot \mathcal{O}(\sigma_{x1w}, \sigma_{y1n}, \sigma_{x2w}, \sigma_{y2w}) \\
& + w_{ww,1} w_{wn,2} \cdot \mathcal{O}(\sigma_{x1w}, \sigma_{y1w}, \sigma_{x2w}, \sigma_{y2n}) \\
& + w_{ww,1} w_{ww,2} \cdot \mathcal{O}(\sigma_{x1w}, \sigma_{y1w}, \sigma_{x2w}, \sigma_{y2w}),
\end{aligned} \tag{4.47}$$

with the weights per beam  $j$

$$\begin{aligned}
w_{nn,j} &= f_j w_{x,j} w_{y,j} + (1 - f_j)(w_{x,j} + w_{y,j})/2 \\
w_{nw,j} &= f_j w_{x,j} (1 - w_{y,j}) \\
w_{wn,j} &= f_j (1 - w_{x,j}) w_{y,j} \\
w_{ww,j} &= f_j (1 - w_{x,j}) (1 - w_{y,j}) + (1 - f_j)(1 - (w_{x,j} + w_{y,j}))/2.
\end{aligned} \tag{4.48}$$

The statistical uncertainty is evaluated by sampling the multivariate normal  $\mathcal{O}_i(\mathbf{x})$  using the fit results  $\boldsymbol{\mu}$  as mean values and the covariance matrix  $\boldsymbol{\Sigma}$  provided by the last fit iteration. The index  $i$  denotes the sampling number. About 1000 values of  $\mathcal{O}_i(\mathbf{x})$  with  $i = 1, \dots, 1000$  are sampled with a random  $\mathbf{x}$  parameter vector with

$$\mathcal{O}_i(\mathbf{x}) = \frac{1}{\sqrt{(2\pi)^n |\boldsymbol{\Sigma}|}} \exp\left(-\frac{1}{2}(\mathbf{x} - \boldsymbol{\mu})^T \boldsymbol{\Sigma}^{-1} (\mathbf{x} - \boldsymbol{\mu})\right). \tag{4.49}$$

Here  $n$  is the number of parameters required to evaluate the overlap  $\mathcal{O}$ . The standard deviation of all  $\mathcal{O}_i$  are taken as statistical uncertainty on the overlap integral per bunch pair, and it is typically less than 0.5% in the 2-d global fit model.

The longitudinal luminous region  $z$ -position  $\xi_{lz}$  and bunch crossing point  $Z_{RF}$  measured for all 2012 fills with  $\beta^* = 10$  m are shown in Fig. 4.32 left. The measurements are sorted by time and BCID. The fill boundaries are indicated by a vertical dashed line. It can be seen that the luminous region moves throughout the fill as the beams drift in the crossing plane. The bunch crossing point  $Z_{RF}$ , however, remains stable within about  $\pm 2$  mm in each fill as expected. The beam

transverse offsets are evaluated at the  $Z_{RF}$  position for each measurement. The offset values for all measurements in 2012 are shown in Fig. 4.32 right. Note that the beams were nominally head-on during all measurements, the non-zero offsets are due to beam drifts.

A series of corrections applied to the fit due to the detector alignment or beam drift are described in Sec. 4.6.1. While the corrections improved the fit  $\chi^2$ , the impact on the overlap integral is negligible. The non-factorizability of the beams in the  $x$  and  $y$  axes can affect the overlap integral up to 4%. The evidence and measurements results for beam shape non-factorizability is discussed in Sec. 4.6.2.

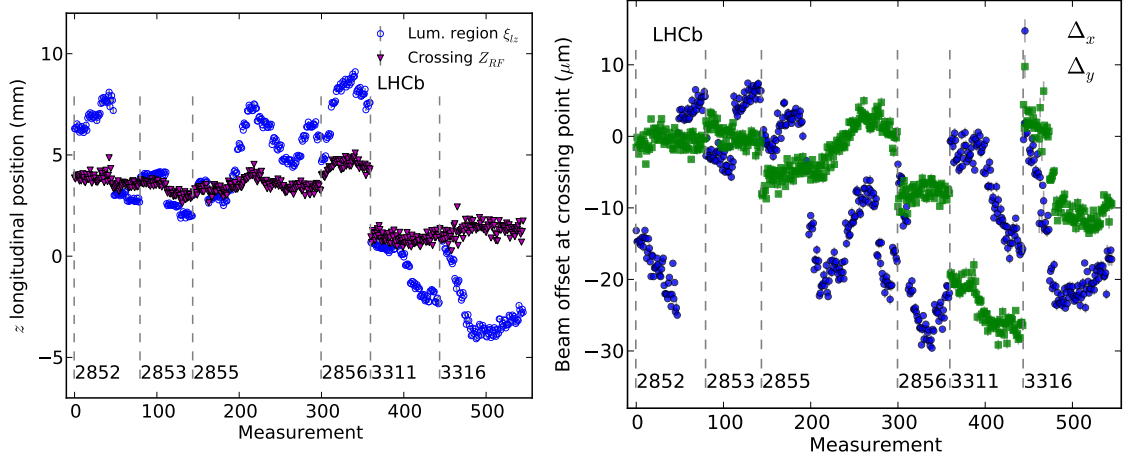


**Fig. 4.32:** Left: Longitudinal  $z$ -position of the luminous region center and bunch crossing point  $Z_{RF}$ . Each data point is one measurement period for one colliding BCID. The measurements are sorted by time and BCID. While the luminous region  $z$ -position will move as beams drift in the crossing plane, the crossing point  $Z_{RF}$  is determined by the stability of the LHC RF cavities and is expected to be constant within  $\pm 2$  mm within a fill but can have larger differences over a longer period as is seen between the first 4 fills in July and the last 2 fills in November. The statistical uncertainty is smaller than the marker. Right: beam offset in  $x$  and  $y$  at the crossing point  $Z_{RF}$ .

#### 4.6.1 Corrections to the fit

The beam parameter measurements presented in Sec. 4.4 and the resulting overlap integral evaluation assume stationary beams and a perfect detector alignment. This section describes the corrections applied to the beam shape measurement to take those two effects into account.

##### 4.6.1.1 Detector alignment corrections

The VELO sensors alignment is not perfect and affects the measurement of the luminous region position. The luminous region transverse shape and position enters into the global fit as an additional constrain and is split into 18  $z$ -slices in the  $z$ -region  $[-100, 115]$  mm. Small offsets in the transverse position induce tensions in the fit between the different  $z$ -slices and can degrade the fit convergence as well as the  $\chi^2$ . The luminous region transverse position  $\xi_{lm}(z)$  (for  $m = x, y$ ) as function of  $z$  are measured for each fill. The expected luminous region position  $\tilde{\xi}_{lm}(z)$  is evaluated from the beam parameters measured in a previous fit. The offset  $\delta\xi_{lm}(z)$  between the predicted position  $\tilde{\xi}_{lm}(z)$  and the measured one  $\xi_{lm}(z)$  originating from a non-perfect alignment are defined as

$$\delta\xi_{lm}(z) = \xi_{lm}(z) - \tilde{\xi}_{lm}(z). \quad (4.50)$$

An example of position measurements with predictions and offset measurements are shown in Fig. 4.33 for fill 2853. In the measurements described in Sec. 4.4.2 and Sec. 4.4.3, an offset  $\delta\xi_{lm}(z)$  is

added to the individual positions  $\xi_{hi}$  in Equations (4.22) and (4.35). The offset  $\delta\xi_{lm}(z)$  is evaluated per luminous region  $z$ -slice by taking the average offset of the  $z$ -range. This procedure effectively corrects the known alignment artifacts affecting the position measurement. The expected positions, however, require to know all beam parameters. Therefore, all transverse beam shape measurements are performed twice, a first measurement allows to predict the luminous region positions per BCID and to evaluate the alignment offsets for the fill. The final measurement makes use of the offset values to improve the fit.

An example of improvement in the pulls due to the alignment correction is shown in Fig. 4.34 for BCID 1949 in fill 2853. The alignment corrections applied in the fit improve the  $\chi^2$  and the fit convergence, but have a negligible impact on the overlap integral.

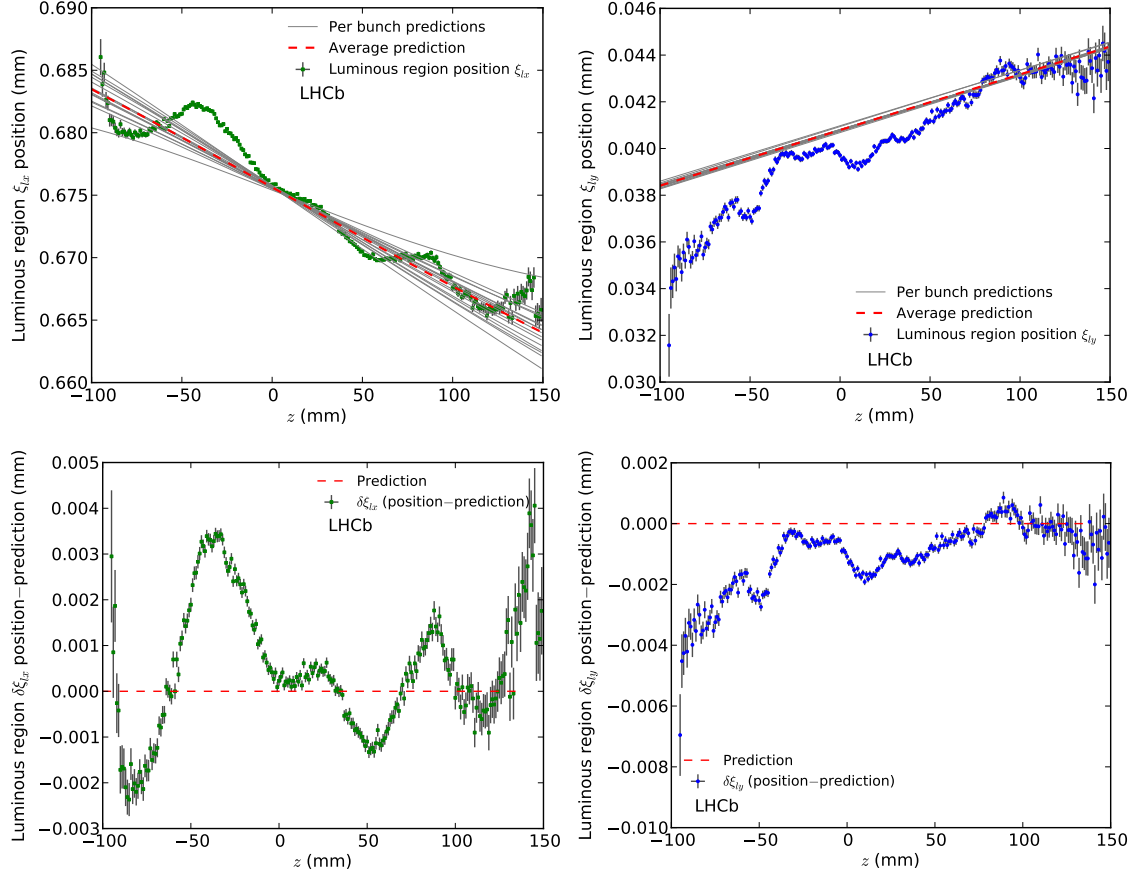


**Fig. 4.33:** Detector alignment corrections for fill 2852. Top: measurement of luminous region  $\xi_{lx}(z)$  (left plot) and  $\xi_{ly}(z)$  (right plot) transverse position as function of longitudinal  $z$ -position. Each data point is a Gaussian fit of beam-beam interaction vertices using all colliding bunches. The indicated error bar is statistical. Solid grey lines show the luminous region position  $\tilde{\xi}_{lm}(z)$  for the different colliding bunches as expected from the beam parameters. The expected position can vary between bunches in the crossing plane  $xz$ . The dashed red line shows the expected average position of the luminous region and can be compared to the measured values. Bottom: difference between expected and measured luminous region position in  $\delta\xi_{lx}(z)$  (left plot) and  $\delta\xi_{ly}(z)$  (right plot) as function of longitudinal  $z$ -position.

#### 4.6.1.2 Beam orbit drift correction

The beam transverse positions drift with time and fluctuations of 20  $\mu\text{m}$  are not uncommon during a fill. Beam-gas imaging measurements are integrated over 20 minutes and a beam drift during this period will affect the beam shapes and offset. The beam positions used to evaluate the offsets are based on vertices acquired over 20 minutes and are therefore an average of the beam position over

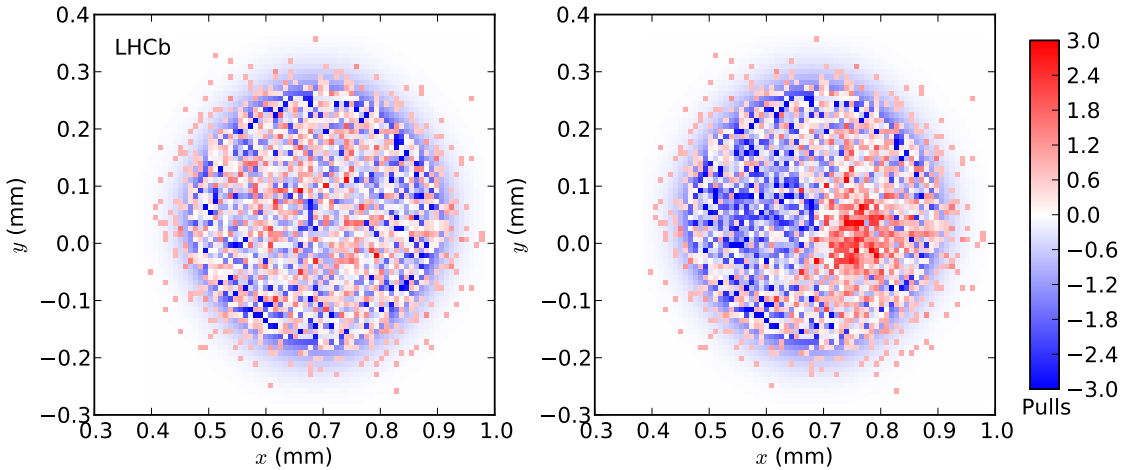


**Fig. 4.34:** Alignment offset correction improvement on the fit quality. Left: fit pulls of one  $z$ -slice measurement where the expected alignment offset is included in the fit. Right: fit pulls of the same  $z$ -slice measurement as on the left plot without taking the alignment offset into account.

this time period. The transverse shapes are a convolution of the beam with the detector resolution and beam movement over 20 minutes. An example of beam drift is shown in Fig. 4.35 for fill 2855.

To take into account the beam image broadening due to the position drift, the standard deviation  $\delta m_t$  of the relative beam positions  $m$  in a measurement  $t$  over 20 minutes are added in quadrature to the resolution in (4.20) and (4.28). The beam positions are measured with beam-gas interaction vertices over 30 s and use vertices from all bunches. Each data point is the mean position of a Gaussian fit. The error shown in Fig. 4.35 are the statistical uncertainties of the fit and are typically about 0.3  $\mu\text{m}$ . In a 20 minutes period, the standard deviation of the drift is typically 1  $\mu\text{m}$  and is therefore negligible with  $\beta^* = 10$  m.

#### 4.6.2 Evidence for beam shape non-factorizability

Discrepancies in the order of 2% have been observed in the visible cross-section measurements performed with the BGI method in the four July 2012 fills when fitted with the 1-d model. Also cross-sections measured with the van der Meer method performed by ATLAS and CMS in July 2012 revealed a time dependence in the cross-section which could not be explained by systematic uncertainties or by the bunch intensity measurement or ghost charges. Both issues faced by either the BGI or VDM method could be explained by an inaccurate beam shape description. Indeed, both BGI 1-d model or VDM model assume the beam shape to be factorizable in  $x$  and  $y$ , that is, the measured beam shape in  $x$  is independent of  $y$  and vice versa. Since the beam-gas interaction vertices provide a complete transverse view of the beams, the factorizability of  $x$  and  $y$  can be measured with the BGI method.

The difference in the transverse beam shape due to the factorizability is shown in Fig. 4.36 with simulated data using the generic Monte Carlo method described in Sec. 4.5 and showing a central beam 1  $z$ -slice:  $-500 < z < -250$  mm. The beam parameters are similar to the ones observed in July 2012 and correspond to the simulation set 2170 described in Table E.1 in appendix D. Only the factorizability parameter  $f_1$  changes between both figures, all other beam parameters are equal. With about 15k vertices in a  $z$ -slice as shown here the difference between both transverse sections is clearly visible. Note that the square-like shape in the factorizable beam is only present with double Gaussian beam parameters, a single Gaussian beam would be round or elliptical in shape.

A set of simulated data with non-factorizable beams ( $f_{1,2} = 0$ ) has been fitted with the 2-d global fit model described in Sec. 4.4.3. The effect of the pulls showing the difference between a factorizable

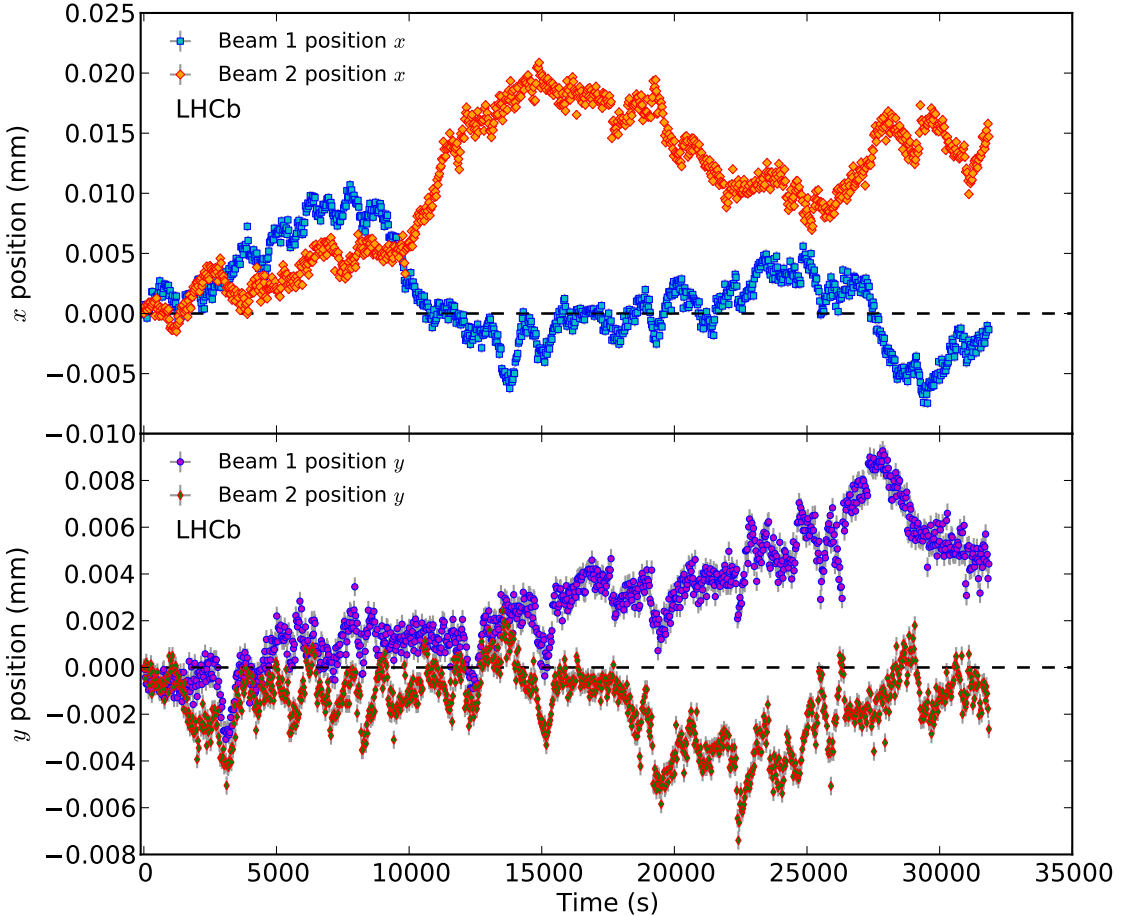


**Fig. 4.35:** Single beam orbit drift measurement measured during fill 2855 which stayed about 9 hours in Stable Beams. The absolute position is set at zero on the first measurement to better compare the relative drift over time. Each point is measured over a time period of 30 seconds using beam-gas interaction vertices from all bunches. Top panel: measured  $x$  position. Bottom panel: measured  $y$  position. The indicated errors are statistical only with a typical accuracy of about  $0.3 \mu\text{m}$ .

and non-factorizable model is shown in Fig. 4.37, the top row shows the pulls with the factorization parameter set to one, while the bottom row shows pulls when allowing the factorization parameter to take any value between zero and one. Not only does the fit converge towards the correct  $f_j = 0$  parameter showing that this factor can be measured with statistics and beam parameters similar to data, but also the difference induced by the beam factorizability is clearly visible in the pulls, even in the single beam slices. The same dataset simulated with non-factorizable beams fitted with the 1-d model is shown in Fig. 4.38 for the  $x$  plane. The fit appears to describe the data correctly when the data is projected in one plane showing that a 2-d treatment is important to describe the beam shape. The same measurement performed on data acquired in July 2012 is shown in Fig. 4.39 as an example. The 2-d fit model converges towards non-factorizable beams (bottom row) and the pulls of the fit assuming a factorizable beam (top row) display the same cross-like structure as in the simulated data.

All simulated beams generated with double Gaussian parameters listed in Table E.1 in appendix D (all sets with ID 2100 to 2190 excluding 2150) have been measured with the 2-d model to verify that the factorizability parameter could be correctly measured as those parameters are similar to the one observed in data. Some of those sets have also been generated with factorizable beams. Results of the measured factorizability parameter  $f_j$  are shown in Fig. 4.40. In most cases the fit can reliably measure the  $f_j$  parameter and converges to either one or zero corresponding to the value used to generate the data. In some cases when the beams shape are close to being single Gaussian, the  $f_j$

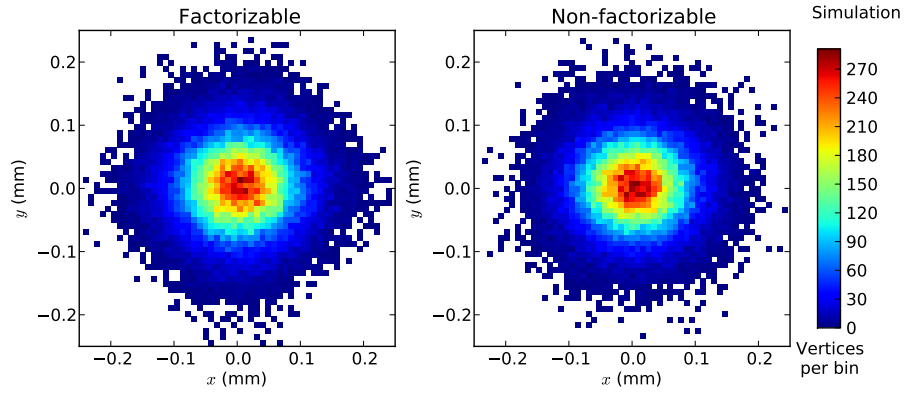


**Fig. 4.36:** Effect of beam factorizability seen on a single beam double-Gaussian 2-d transverse distribution using simulated data. Left: factorizable beam with  $f_j = 1$ . Right: non-factorizable beam with  $f_j = 0$ . The factorizable beam has a more square-like shape.

value don't converge to exactly one or zero but are still within about 10% of the correct value and are compatible with the uncertainty on the parameter.

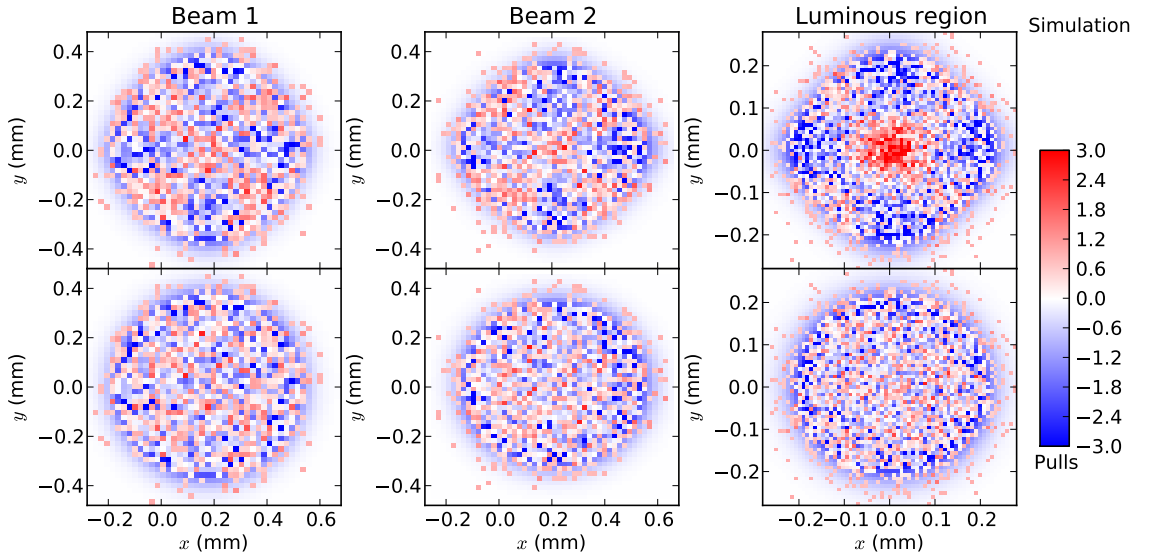


**Fig. 4.37:** Measurement of beam factorizability with simulated beams. From left to right: fit pulls of a beam  $z$ -slice for beam 1, beam 2 and luminous region, respectively. For better readability only the  $z$ -slices  $[-500, -250]$  mm for beam 1,  $[250, 500]$  mm for beam 2 and  $[-5, 5]$  mm for beam-beam are shown here out of the 24  $z$ -slices. The beams are generated assuming non-factorizability:  $f_{1,2} = 0$ ; the same dataset is used in both rows but the data are fitted with two different models. Top row: fit assumes fully factorizable beams:  $f_{1,2} = 1$  (equivalent to the 1-d model which is not sensitive to factorizability). The pulls show a clear cross-like structure as the model can not fully describe the beam shape. Bottom row: fit with the additional beam factorizability parameters  $f_{1,2}$ . The fit correctly describes the beam shapes and the fit pulls are more uniform. The fit converges to a non-factorizable beam shape  $f_{1,2} = 0$  as set in the simulation parameters for this example.

The factorizability parameter is only meaningful if the beam has a double Gaussian shape in both  $x$  and  $y$  transverse planes. If the beam shape is single Gaussian in one plane only, that is, the projection in  $x$  or  $y$  is Gaussian, the beam is factorizable per definition and the  $f_j$  parameter can not be measured. It follows that the capability to measure the factorizability parameter  $f_j$  depends on the “strength” of the double Gaussian shape of the beams. The double Gaussian strength factor is defined here as

$$S_{j,m} = 1 - \frac{\sigma_{\text{main},j,m}}{\sigma_{\text{rms},j,m}}, \quad (4.51)$$

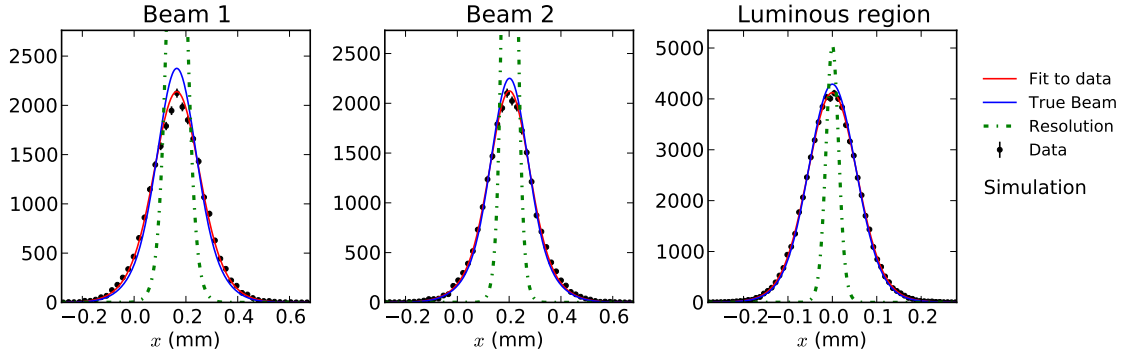


**Fig. 4.38:** Non-factorizable beam shape measurement in  $x$  using a 1-d fit on simulated data. From left to right: fit of a beam  $z$ -slice for beam 1, beam 2 and luminous region, respectively. For better readability only the  $z$ -slices  $[-500, -250]$  mm for beam 1,  $[250, 500]$  mm for beam 2 and  $[-5, 5]$  mm for beam-beam are shown here out of the 24  $z$ -slices. The beams are generated assuming non-factorizability:  $f_{1,2} = 0$  (same data as in Fig. 4.37). In a 1-d fit the shape appears properly described showing that a 2-d description of the beams is crucial.

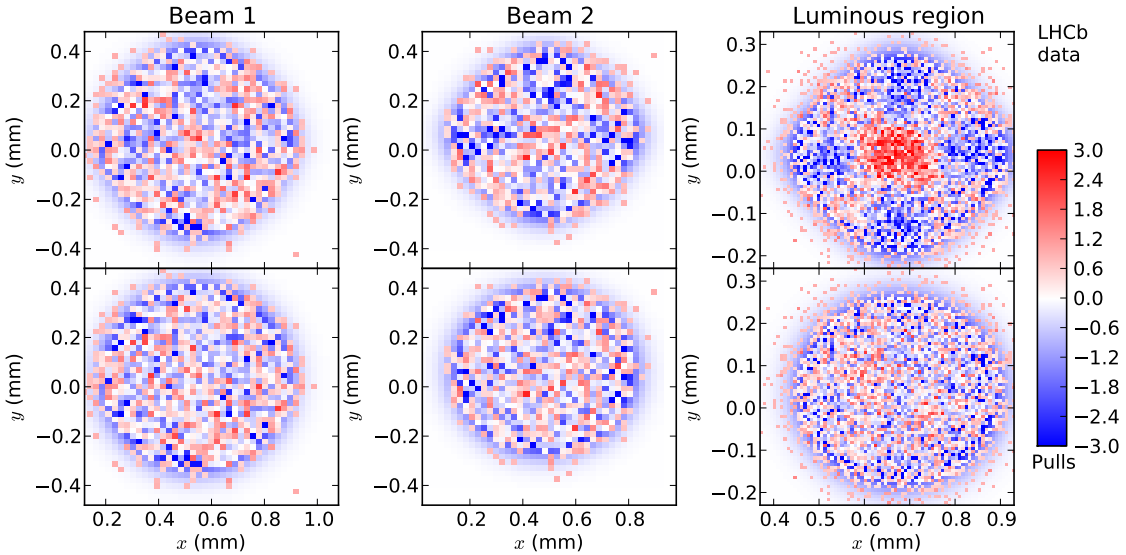


**Fig. 4.39:** Measurement of beam factorizability on real data for fill 2855, bunch 1335. From left to right: fit pulls of a beam  $z$ -slice for beam 1, beam 2 and luminous region, respectively. For better readability only the  $z$ -slices  $[-500, -250]$  mm for beam 1,  $[250, 500]$  mm for beam 2 and  $[-5, 5]$  mm for beam-beam are shown here out of the 24  $z$ -slices. Top row: fit assumes factorizable beams with  $f_{1,2} = 1$  (equivalent to a 1-d model). The pulls show a clear cross-like structure as the model can not fully describe the beam shape similarly to simulated data, see Fig. 4.37. Bottom row: fit with the additional beam factorizability fit parameters  $f_{1,2}$ . The fit correctly describes the beam shapes showing more uniform pull distribution. In this example with real data the fit converges to non-factorizable beam shape.

with

$$\sigma_{\text{rms},j,m} = \sqrt{w_{j,m}\sigma_{j,m,n}^2 + (1 - w_{j,m})\sigma_{j,m,w}^2} \quad (4.52)$$

for beam  $j = 1, 2$  and plane  $m = x, y$ . Indices  $n$  and  $w$  denote the narrow and wide width Gaussian component, respectively. The width  $\sigma_{\text{main}}$  is the dominant Gaussian width which carries the largest weight. A single Gaussian shape has therefore a strength parameter of zero. The parameter  $S_{j,m}$  has been measured for all colliding bunch pairs in 2012 and is shown in Fig. 4.41. Both November fills 3311 and 3316 are clearly different from the previous fills. Those bunches have single Gaussian-like shape but have a smaller than Gaussian peak value and are therefore not well described by a single Gaussian function. This shape, however, can be described by the same double Gaussian function from Eq. (4.19) by allowing the narrow component to have a negative weight. In this case, the factorizability parameter has little effect on the shape and carries a large uncertainty which

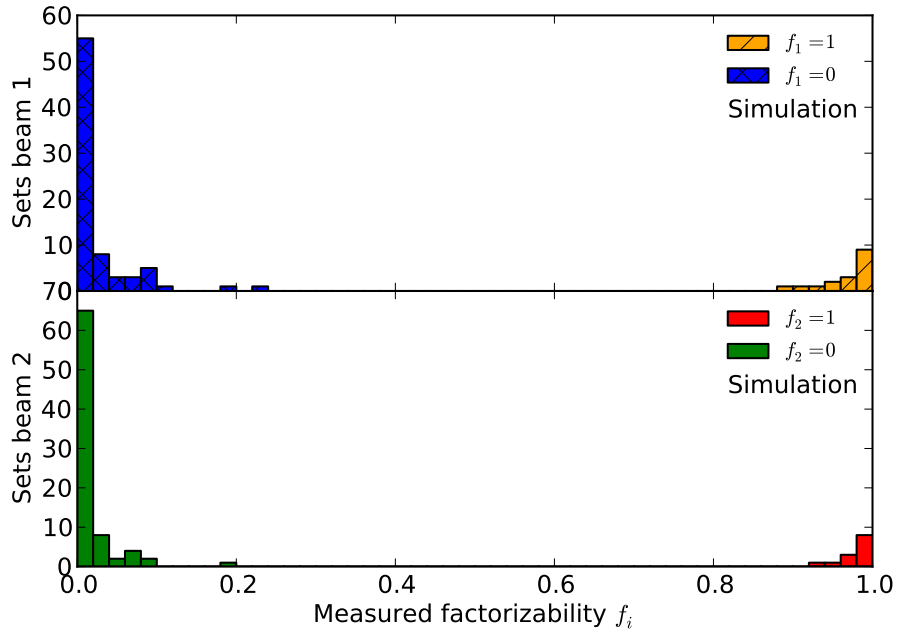


**Fig. 4.40:** Measurement of beam factorizability with different beam parameters using simulated data. A simulation set is generated with different double Gaussian beam parameters and with a factorizability factor  $f_{1,2}$  set to either one or zero, its value is indicated in the legend. Each set is measured in the same way as real data with a global 2-d fit and the measured factorizability value is reported in the histograms. Top panel: beam 1. Bottom panel: beam 2. In general the fit algorithm can reliably measure the  $f_{1,2}$  factor except in cases where the beams are close to a single Gaussian shape where the  $f_{1,2}$  has less or no meaning.

makes the fit less stable. A constrain is added to the fit function that favors a values of  $f_j = 0$  when a Gaussian component is negative. This constrain stabilize the fit for the shapes observed in November 2012, but the factorizability parameter has no meaning in those fills.

With few exceptions, all bunch pairs measured in April and July 2012 have a double Gaussian shape and  $S_{j,m}$  is larger than zero for both beams and planes. The lowest value of  $S_{j,m}$  at which the factorizability can still be measured depends on the available statistics. The factorizability parameters per beam measured for all colliding bunch pairs in 2012 is shown in Fig. 4.42 for bunch pairs with a double Gaussian strength  $S_{j,m} > 0.02$  and with a fit uncertainty on the factorizability parameter of  $\delta(f_j) < 1$ . Except for some rare exceptions, all bunch pairs are non-factorizable, so long as the parameters can be measured. The same data is presented in a histogram in Fig. 4.43.

The difference in the overlap integral measurement between the 1-d and 2-d models is shown in Fig. 4.44 for the July and November fills performed at  $\beta^* = 10$  m. The 1-d fit model assumes factorizable beam shapes while the 2-d fit model can measure the factorizability. Both fits use the same full dataset. While the difference is negligible or  $< 1\%$  for the November fills, it can account for up to 3% in the July fills. The 1-d model tends to overestimate the overlap integral and therefore underestimate the visible cross-section.

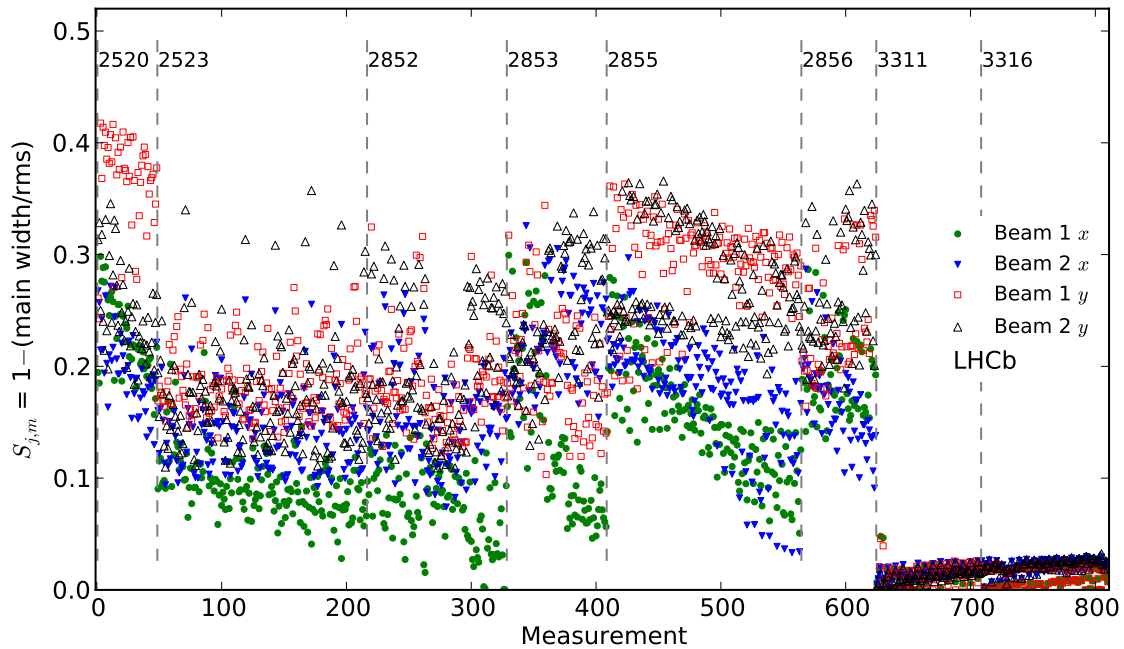


**Fig. 4.41:** Strength of double Gaussian beam shape for all measurements performed in 2012 at  $\sqrt{s} = 8$  TeV sorted by time and BCID. The different fills are indicated by a vertical dashed line. A single Gaussian shape would have a strength of zero. Both November fills (3311 and 3316) are described with the same double Gaussian function as for the other fills (see Eq. (4.19)) but the narrow component can have a negative weight.

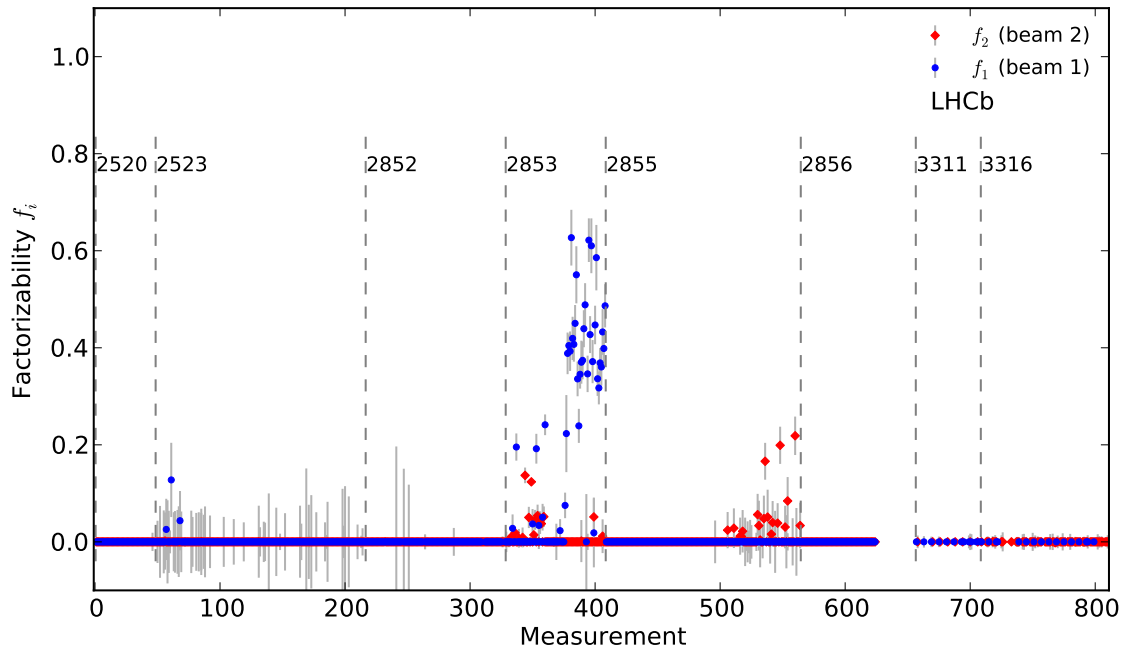


**Fig. 4.42:** Measurement of beam factorizability for all measurements performed in 2012 at  $\sqrt{s} = 8$  TeV sorted by time and BCID. Only  $f_j$  values are shown for which the double Gaussian strength  $S_{j,m}$  was larger than 0.02 and the uncertainty on the factorizability parameter  $\delta(f_j)$  was smaller than 1.

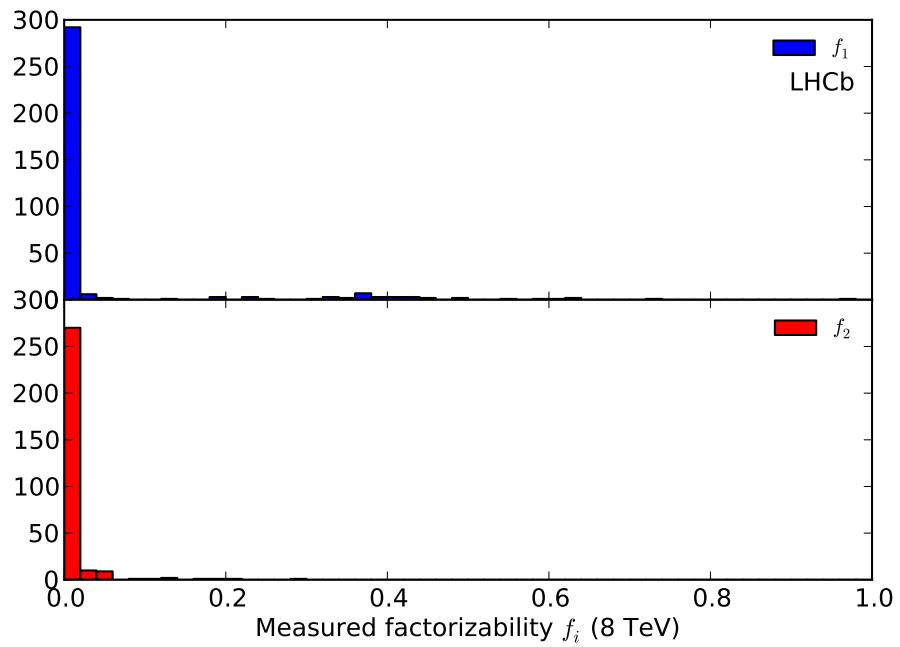


**Fig. 4.43:** Measurement of beam factorizability for all measurements performed in 2012 at  $\sqrt{s} = 8$  TeV projected as histograms. Top panel: beam 1, bottom panel: beam 2.

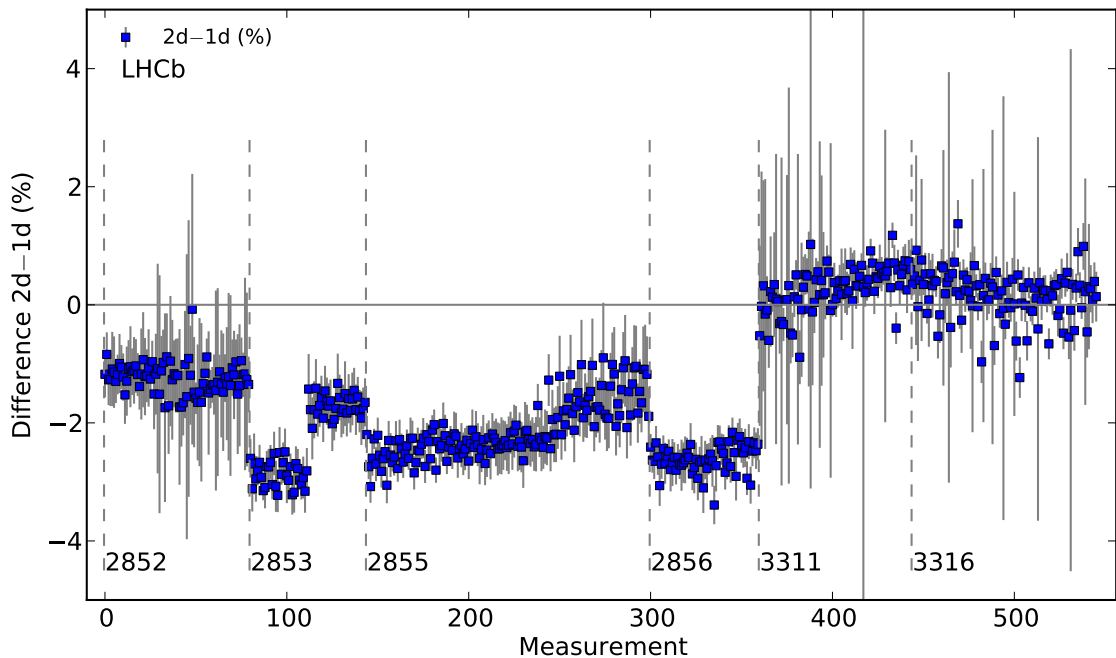


**Fig. 4.44:** Difference in the overlap integral between 1-dimensional and 2-dimensional fits. The difference of up to 3% shows the importance to measure and take the beam factorizability into account.

## 5 INTERACTION RATE

The interaction rate of a given process relates its cross-section to the luminosity and is a central part of a luminosity calibration measurement. The measured rate, however, depends on the detector and selection algorithm used for the measurement. This chapter introduces how the instantaneous luminosity is propagated to the full data set using the calibration of a counter definition. The methods used to measure the interaction rate are presented and the systematic uncertainty relative to the rate measurement is discussed in the last section.

### 5.1 Luminosity propagation

The absolute instantaneous luminosity varies during a fill and is therefore evaluated in a short period of time during which the beam parameters are sufficiently constant. To be able to measure a cross-section of any process during normal data taking periods, the relative luminosity must be determined during the acquisition period. The relative luminosity is proportional to the interaction rate, therefore, a set of luminosity counters suited to measure the rate are acquired together with normal physics data. The absolute luminosity measured in dedicated luminosity calibration fills permits the interaction rate  $R_c = dN/dt$  of a reference counter  $c$  to be related to its cross-section  $\sigma_{\text{ref},c}$  by

$$\sigma_{\text{ref},c} = \frac{R_c}{\mathcal{L}}, \quad (5.1)$$

where  $dN$  is the total number of interactions seen by the counter  $c$  in the time interval  $dt$  and with

$$\mathcal{L} = N_1 N_2 \nu_{\text{rev}} \mathcal{O}, \quad (5.2)$$

as defined in chapter 3. Accordingly, each counter corresponds to reference cross-section.

While the instantaneous (and integrated) luminosity is independent of the counter definition, the reference cross-section and its rate are directly related to a given counter. For a colliding bunch pair, the interaction rate is the average number of visible interactions per crossings  $\mu_{\text{ref},c}$  seen by a counter, times the revolution frequency  $\nu_{\text{rev}}$ :  $R_c = \mu_{\text{ref},c} \nu_{\text{rev}}$ .

The counter rate  $R_c$  is determined by using the fraction of colliding bunch pair crossings that had no visible event (called empty events) denoted  $P_c(0)$ . The measured rate of a counter depends on the threshold set to separate an empty event from a non-empty one. An event is considered empty when a counter-specific quantity is below the chosen threshold. Given a number of crossings  $\tilde{N}_{\text{xing}}$ , a subsample of those crossings  $\tilde{N}_{\text{ref},c}$  will be non-empty. The remaining crossings  $\tilde{N}_{0,c} = \tilde{N}_{\text{xing}} - \tilde{N}_{\text{ref},c}$  are empty. An interaction could still have occurred in an empty event, for example due to limits in the detector acceptance or response; however, because such interaction is not visible, the crossing is counted as an empty event. The fraction  $P_c(0)$  of empty events is therefore given by

$$P_c(0) = \frac{\tilde{N}_{0,c}}{\tilde{N}_{\text{xing}}} = 1 - \frac{\tilde{N}_{\text{ref},c}}{\tilde{N}_{\text{xing}}}. \quad (5.3)$$

In the remainder of the chapter, the suffix  $c$  to denote a counter is dropped for simplicity. The main luminosity counters corresponding to reference cross-sections are listed in Table 5.1.

**Table 5.1:** Main luminosity counters recorded in parallel to data. The threshold column defines the condition required for which the event is considered empty.

Name	Threshold	Description
SPD	< 2 hits	Hit multiplicity on the SPD sub-detector
PU	< 2 hits	Hit multiplicity on the Pile-Up sensors in the VELO
SumEt	< 15 MeV	Sum of transverse energy deposited in the calorimeters
RzVelo	< 2 tracks	VELO track multiplicity (as defined in [44])
Track	< 2 tracks	VELO track multiplicity with the point of closest approach to the beam line inside a cylinder with $ z  < 300$ mm and $x^2 + y^2 < 4$ mm
Vertex	< 1 vertex	Number of reconstructed vertices <sup>1</sup> inside a cylinder with $ z  < 300$ mm and $x^2 + y^2 < 4$ mm
PV3D	< 1 vertex	Number of reconstructed vertices (regardless of its position)
muon	< 1 muon	Number of detected muons

In practice, instead of counting the true number of bunch crossings  $\tilde{N}_{\text{xing}}$ , dedicated luminosity events are randomly triggered on  $bb$  crossings at a fixed rate  $\nu_{\text{rnd}}$  and include all counters from Table 5.1. Accordingly, the number of crossings is then related to the number of triggered luminosity events  $N_{\text{rnd}}$  with

$$\tilde{N}_{\text{xing}} = N_{\text{rnd}} \frac{\nu_{\text{rev}}}{\nu_{\text{rnd}}}. \quad (5.4)$$

It follows that the fraction  $P(0)$  of empty events is based on the number  $N_{\text{ref}}$  of observed events in a given number  $N_{\text{rnd}}$  of luminosity events

$$P(0) = 1 - \frac{N_{\text{ref}}}{N_{\text{rnd}}}. \quad (5.5)$$

During normal data taking periods the total rate  $\nu_{\text{rnd}}^{\text{tot}}$  is 1 kHz with the proportions 14:3:2:1 assigned to  $bb$ ,  $be$ ,  $eb$  and  $ee$  crossings, respectively. For dedicated luminosity calibration fills the total rate  $\nu_{\text{rnd}}^{\text{tot}}$  is increased to 2.8125 kHz with proportions 40:2:2:1 assigned to  $bb$ ,  $be$ ,  $eb$  and  $ee$  crossings, respectively. Note that, in the presence of more than one colliding bunch pair, the sampling rate  $\nu_{\text{rnd}}$  is shared among all bunches. Nevertheless, Eq. 5.5 remains valid per crossing bunch pair. The number of random luminosity triggers  $N_{\text{rnd}}$  available for a given bunch pair is then statistically reduced and  $N_{\text{ref}}$  is the number of visible events for this bunch pair seen in  $N_{\text{rnd}}$ .

The number of interactions per crossing,  $n$ , follow a Poisson probability distribution  $P(n, \mu)$

$$P(n, \mu) = \frac{e^{-\mu} \mu^n}{n!}, \quad (5.6)$$

with  $\mu$  the average number of interactions per crossing. As only visible interactions can be detected, the average number of visible interactions  $\mu_{\text{ref}}$  must be used instead of  $\mu$ . The probability  $P_{\text{ref}}$  to observe a visible event in a crossing is the sum of all crossings with a visible interaction and thus the sum of all Poisson probabilities with  $n > 0$

$$P_{\text{ref}} = \sum_{n=1} P(n, \mu_{\text{ref}}) = 1 - e^{-\mu_{\text{ref}}} = \frac{N_{\text{ref}}}{N_{\text{rnd}}}. \quad (5.7)$$

Alternatively to Eq. (5.7), one can take the probability to *not* see an event

$$\begin{aligned} P(0, \mu_{\text{ref}}) &= 1 - P_{\text{ref}} \\ &= e^{-\mu_{\text{ref}}} = 1 - \frac{N_{\text{ref}}}{N_{\text{rnd}}}. \end{aligned} \quad (5.8)$$

<sup>1</sup>A vertex has at least 5 associated tracks

From Eq. (5.7), the average number of visible interactions per bunch crossing  $\mu_{\text{ref}}$  is

$$\mu_{\text{ref}} = -\ln \left( 1 - \frac{N_{\text{ref}}}{N_{\text{rnd}}} \right) = -\ln \left( \frac{N_0}{N_{\text{rnd}}} \right), \quad (5.9)$$

with  $N_0 = N_{\text{rnd}} - N_{\text{ref}}$ . This method used to calculate  $\mu_{\text{ref}}$  is called “zero counting” method.

The visible cross-section  $\sigma_{\text{ref}}$  of a counter is calibrated using its rate  $\mu_{\text{ref}}$  during a dedicated experiment with

$$\sigma_{\text{ref}} = \frac{\mu_{\text{ref}} \nu_{\text{rev}}}{\mathcal{L}} = \frac{\mu_{\text{ref}}}{\mathcal{O} N_1 N_2}, \quad (5.10)$$

with  $\mathcal{L}$  the absolute instantaneous luminosity inferred from beam parameters and  $\mathcal{O}$  as defined in Eq. (3.9) in Sec. 3. As different counters have different sensitivities, each counter has its own cross-section calibration, and since  $\sigma_{\text{ref}}$  is a physical observable, the luminosity of any data taking period can be determined by measuring  $\mu_{\text{ref}}$  for this period using the corresponding counter definition.

The integrated luminosity of a data sample is the quantity of interest for physics analysis and is evaluated by integrating the relative luminosity recorded by a counter. The luminosity events are triggered independently of the physics trigger or detector activity, but are acquired together with the full physics-event data stream. It follows that some events will be triggered by both the physics trigger and the luminosity trigger and that the integrated luminosity can be evaluated from any data sample. During data taking, multiple files are acquired in parallel each containing about 1 minute of data and therefore one fraction of the luminosity events  $N_{\text{rnd}}$ . The luminosity is integrated per data file  $f$  as it represents the smallest acquisition time granularity with self contained luminosity and physics events while retaining enough luminosity events. Furthermore, with a typical beam lifetime of about 15 hours, the rate decays by less than 0.2% during one minute and can therefore be considered constant over this time period.

The integrated luminosity of a data file for a colliding bunch pair  $i$  is given by

$$\int_f \mathcal{L}^i dt = \frac{\tilde{N}_{\text{xing}} \mu_{\text{ref}}}{\sigma_{\text{ref}}} = -\ln \left( \frac{N_0}{N_{\text{rnd}}} \right) \frac{N_{\text{rnd}}}{\sigma_{\text{ref}}} \frac{\nu_{\text{rev}}}{\nu_{\text{rnd}}}, \quad (5.11)$$

where  $\sigma_{\text{ref}}$  is the calibrated reference cross-section for this counter,  $\tilde{N}_{\text{xing}}$  the number of crossings of this pair that occurred during the acquisition of this file  $f$  and  $N_{\text{rnd}}$  is the number of luminosity events for this pair. This procedure takes into account the periods when the detector is not ready to acquire data (dead time).

The  $bb$  sampling frequency of 0.7 kHz is shared among all colliding bunches (up to 1262 in 2011 and 2012) and typically 12 files were acquired in parallel. It is therefore not possible to measure  $\mu_{\text{ref}}$  per colliding bunch pair and per file in a one minute period. Instead, the  $\mu_{\text{ref}}$  value is evaluated per file using all luminosity events  $N_{\text{rnd},f}$  from all colliding bunches. Consequently, the number of bunch crossings  $\tilde{N}_{\text{xing},f}$  seen in each file depends on the number  $n_b$  of colliding bunches

$$\tilde{N}_{\text{xing},f} = n_b N_{\text{rnd},f} \frac{\nu_{\text{rev}}}{\nu_{\text{rnd}}}. \quad (5.12)$$

Then, the integrated luminosity associated to a file is

$$\int_f \mathcal{L} dt = -\ln \left( \frac{N_0}{N_{\text{rnd},f}} \right) \frac{N_{\text{rnd},f}}{\sigma_{\text{ref}}} \frac{n_b \nu_{\text{rev}}}{\nu_{\text{rnd}}}. \quad (5.13)$$

Strictly speaking, Eq. (5.13) is only valid if all bunches have the same interaction rate. The usual rate spread between colliding bunch pairs introduces a systematic uncertainty of about 0.5% in the  $\mu_{\text{ref}}$  measurement, but can be corrected for and is described elsewhere [45].

Finally, the total integrated luminosity contained in a dataset of  $F$  files ( $f = 1, \dots, F$ ) is then

$$\int_F \mathcal{L} dt = \sum_{f=1}^F \int_f \mathcal{L} dt. \quad (5.14)$$

## 5.2 Background for the zero counting method

For each colliding bunch pair in dedicated luminosity calibration fills, the average visible interaction rate  $\mu_{\text{ref}}^{\text{raw}}$  is measured with Eq. (5.9) in periods of 4 minutes for each counter. The value of  $\mu_{\text{ref}}^{\text{raw}}$  measured over time in fill 2855 is shown in Fig. 5.1 for the 6 colliding bunches for the *Track* and *Vertex* counters. The bunches are labeled by an identifier, BCID (bunch crossing identifier).<sup>2</sup> The *Vertex* counter being more restrictive in defining a visible event, its  $\mu_{\text{ref}}^{\text{raw}}$  values are lower than for the *Track* counter. Note, however, that this average rate includes also a background contribution from beam-gas interactions which can be significant when SMOG gas injection is active. Accounting for the background, the average number of visible interactions is

$$\mu_{\text{ref}} = -\ln P_{bb}(0) - [-\ln P_{bkg}(0)], \quad (5.15)$$

with the background contribution

$$-\ln P_{bkg}(0) = -\ln P_{be}(0) - \ln P_{eb}(0). \quad (5.16)$$

Here the indices *bb*, *be* and *eb* denote the bunch crossing type. Background independent of beam is neglected. The uncertainty on  $\mu_{\text{ref}}$  is calculated for both the beam-beam and background rates using the binomial error for  $P(0)$  with

$$\delta_{\mu} = \delta(\ln P_{bb}(0)) = \delta P_{bb}(0)/P_{bb}(0), \quad (5.17)$$

$$\text{with } \delta P_{bb}(0) = \sqrt{\frac{P(0)(1 - P(0))}{N_{\text{ref}}}}, \text{ and } P(0)N_{\text{ref}} = N_0, \quad (5.18)$$

$$\text{leading to } \delta_{\mu} = \sqrt{\frac{1}{N_0} - \frac{1}{N_{\text{ref}}}}. \quad (5.19)$$

The statistical uncertainties are dominated by the background subtraction. The background contribution from both beams in Eq. (5.15) is proportional to the pressure in the beam pipe and bunch intensities of the colliding bunches. The background correction per BCID must therefore take the colliding bunch intensities into account. The background contribution normalized per particle (i.e. per charge)  $\mu_{\text{ref},j}^c$  is evaluated for both beams  $j$ . Using a total of  $n_j$  non-colliding bunches  $i$ , the background contribution per particle  $\mu_{\text{ref},j}^c$  is measured with

$$\mu_{\text{ref},j}^c = \sum_{i=1}^{n_{k,j}} \frac{1}{n_{k,j}} \frac{\mu_{\text{ref},ij}}{N_{ij}}, \quad (5.20)$$

with the average rate  $\mu_{\text{ref},ij} = -\ln P_{ij}(0)$  of a non colliding bunch  $i$  in beam  $j$  with intensity  $N_{ij}$ . Equation (5.15) can now be written as

$$\mu_{\text{ref}} = \mu_{\text{ref}}^{\text{raw}} - \mu_{\text{ref},1}^c N_1 - \mu_{\text{ref},2}^c N_2. \quad (5.21)$$

Here  $\mu_{\text{ref}}^{\text{raw}}$  is the raw interaction rate observed for the colliding bunch pair including beam-gas background, and  $N_1, N_2$  are the colliding bunch populations for beam 1 and 2, respectively.

<sup>2</sup>For beam 1 the standard LHC BCID is used, while for beam 2 the BCID is shifted by 894 such that the same BCID number collide at LHCb.

The background per charge  $\mu_{\text{ref},j}^c$  for both *Track* and *Vertex* counters is shown in Fig. 5.2 for fill 2855. The *Vertex* counter has about 10-20 times less background. The final average number of interactions per crossing after background subtraction as defined in (5.21) is shown in Fig. 5.3 for fill 2855 and both *Track* and *Vertex* counters. The  $\mu_{\text{ref}}$  values for all 2012 measurements are shown in Fig. 5.4 for the *Track* counter.

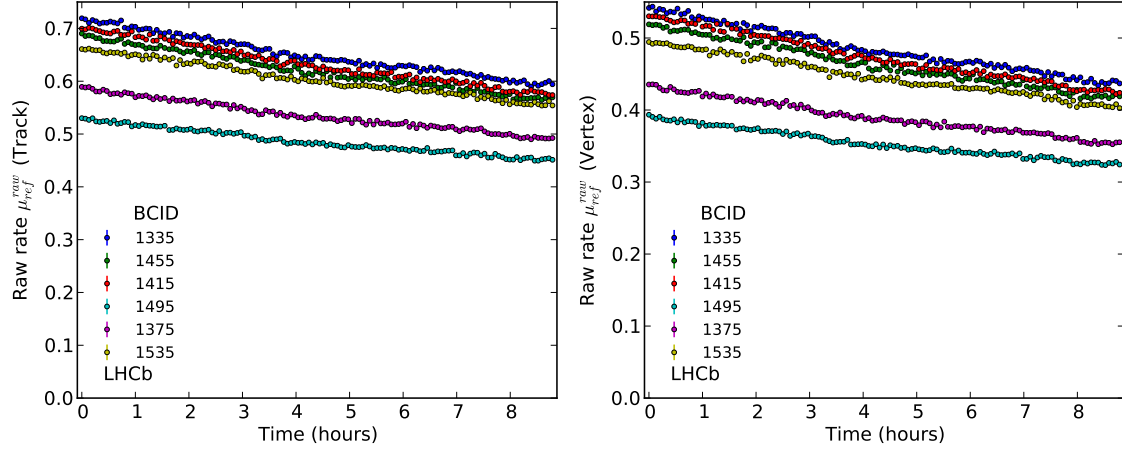


**Fig. 5.1:** Average raw interaction rate per bunch crossing  $\mu_{\text{ref}}^{\text{raw}}$  for the 6 colliding bunch pairs of fill 2855 in 4 minutes time bins. The data points show the raw rate before background correction. Left: counter *Track*. Right: counter *Vertex*. The BCIDs are indicated in the legend.

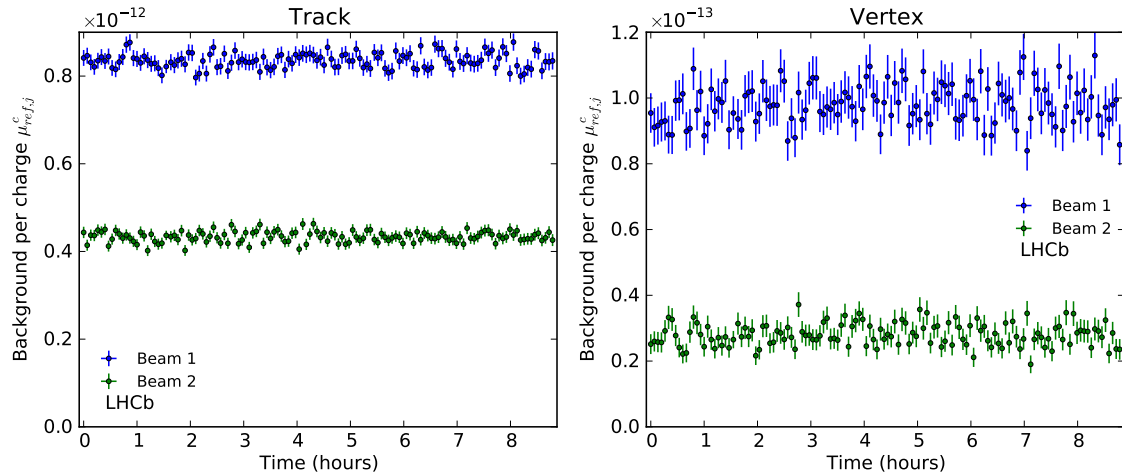


**Fig. 5.2:** Background rate per charge  $\mu_{\text{ref},j}^c$  and beam for fill 2855. Left: counter *Track*. Right: counter *Vertex*. The vertex counter has about ten times less background than the track counter. The pressure decay of about 1% per 24h is not visible and is neglected.

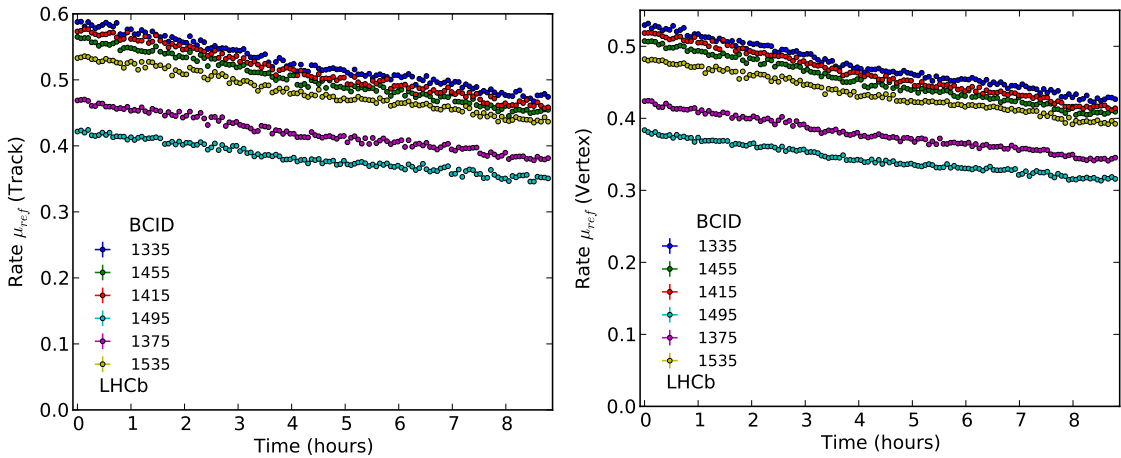


**Fig. 5.3:** Background corrected average interaction rate per bunch crossing  $\mu_{ref}$  for the 6 colliding bunch pairs of fill 2855 in 4 minutes time bins. Left: counter *Track*. Right: counter *Vertex*.

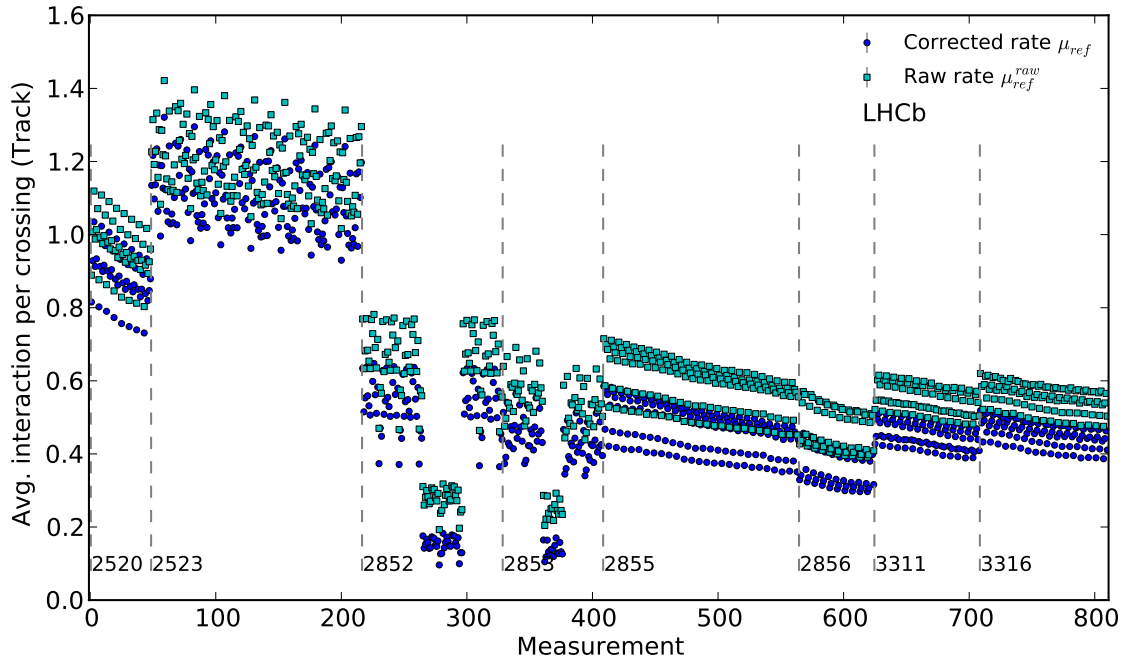


**Fig. 5.4:** Average interaction rate per bunch crossing for the *Track* counter. The substantial background correction required for this counter is clearly visible as the difference between the blue and cyan points and can account for up to 50% for low luminosity periods as in fills 2852 and 2853. Measurements are sorted per time and BCID (using LHC naming and beam 1). Fill numbers are indicated in the plot and the fill boundaries are shown with dashed vertical lines.

### 5.3 Systematic uncertainties

Counters based on the VELO detector proved to have the highest time stability throughout the full physics data taking period [35]. However, those counters are affected by the luminous region position (and to a smaller extend its width). As previously mentioned, the luminosity leveling scheme used at LHCb induces a longitudinal displacement of the luminous region during normal data taking fills. Furthermore, rates measured during a VDM scan are also affected by the movement of the luminous region position in the crossing plane. To take this displacement into account, the counter efficiency as function of the luminous region  $z$ -position for both *Track* and *Vertex* counters has been evaluated with a Monte-Carlo simulation [45] and is shown in Fig. 5.5.

Owing to its time stability and limited  $z$ -dependence on the luminous region position during

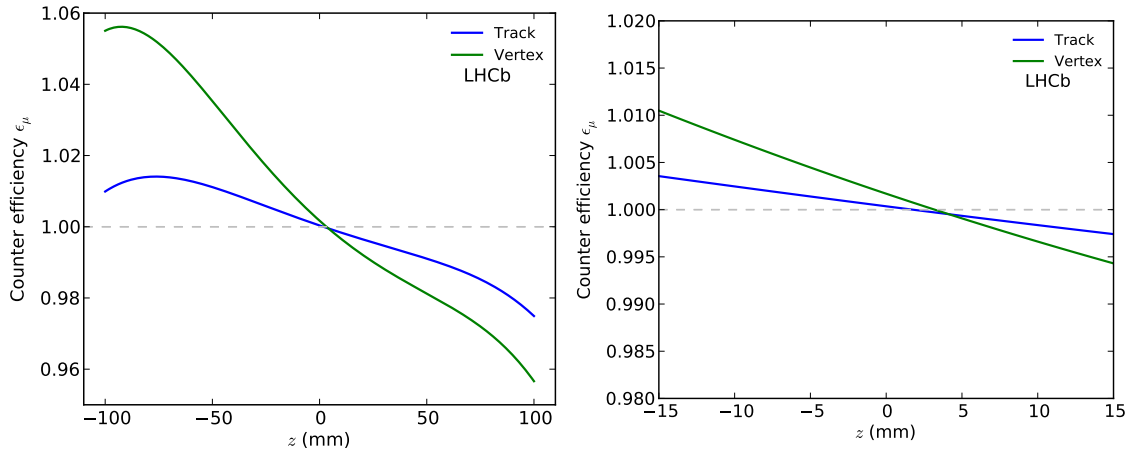


**Fig. 5.5:** Counter efficiency as function of  $z$  for the *Track* and *Vertex* counters. The right plot shows a narrower  $z$ -range of the left plot. In normal physics data taking periods, the luminous region  $z$ -position stays within  $[-10 \text{ mm}; +10 \text{ mm}]$ .

normal physics data taking and VDM measurements, the luminosity propagation to the full dataset (as described in Sec. 5.1) is based on the cross-section calibration of the *Track* counter. As seen in Sec. 5.2, the *Track* counter, however, is affected by a significant beam-gas background during the BGI measurements due to the SMOG gas injection. The background correction can be as high as 50% for low  $\mu_{\text{ref}}$  periods and relies on the background rate per charge.

Both *Track* and *Vertex* counters are limited to events originating near the interaction point, while the similar *RzVelo* and *PV3D* counters are also sensitive to events originating away from the interaction point. The amount of background correction required for those counters is shown in Fig. 5.6 by plotting the ratios of the raw rate compared to the background corrected rate. As expected, the least restrictive counter *RzVelo* (top left) is affected by the largest background, while the more restrictive *Vertex* counter requires the smallest background correction.

Nevertheless, besides the larger background sensitivity of the *RzVelo* and *PV3D* counters, the corresponding rates should be equal to the *Track* and *Vertex* counters, respectively, once the background has been subtracted. The ratio of background corrected counters *RzVelo/Track* and *PV3D/Vertex* are shown in Fig. 5.7 for all dedicated measurements in 2012 at  $\sqrt{s} = 8 \text{ TeV}$ .

The ratio of background corrected rates for the *Track* and *Vertex* counters compared respectively to the *RzVelo* and *PV3D* counters is not consistent in the beam offset periods in fills 2852 and 2853. Additionally, a difference of 0.5% is observed between the ratios *Track/Vertex* measured with and without SMOG gas injection. Accordingly, the BGI measurements are based on the *Vertex* counter which requires the smallest background correction and is the most reliable counter when using the SMOG gas injection. The overall ratio *PV3D/Vertex* of 1.002 indicates a systematic effect not accounted for in the background subtraction of one or both of those counters. Therefore, a systematic uncertainty of 0.02% is assigned to the counter background subtraction when using the *Vertex* counter. The statistical uncertainty on the rate using all cross-section measurements is negligible. The final cross-section of the *Track* counter is inferred from the *Vertex* counter with

$$\sigma_{\text{Track}} = \sigma_{\text{Vertex}} \frac{\mu_{\text{Track}}}{\mu_{\text{Vertex}}}. \quad (5.22)$$

The ratio  $\mu_{\text{Track}}/\mu_{\text{Vertex}}$  can be measured with high accuracy in background-free conditions during a VDM measurement and can be verified throughout the year with normal data taking conditions. The ratio is measured to be  $\mu_{\text{Track}}/\mu_{\text{Vertex}} = 1.106$  for  $\sqrt{s} = 8 \text{ TeV}$  beams.

A different method to measure  $\mu_{\text{ref}}$  has been studied with the goal to better understand the background correction required with SMOG gas injection. The method uses the full detector

response spectrum instead of counting empty and non-empty events and is described in Appendix B. This method can be further developed and used in future analysis of the luminosity counters.

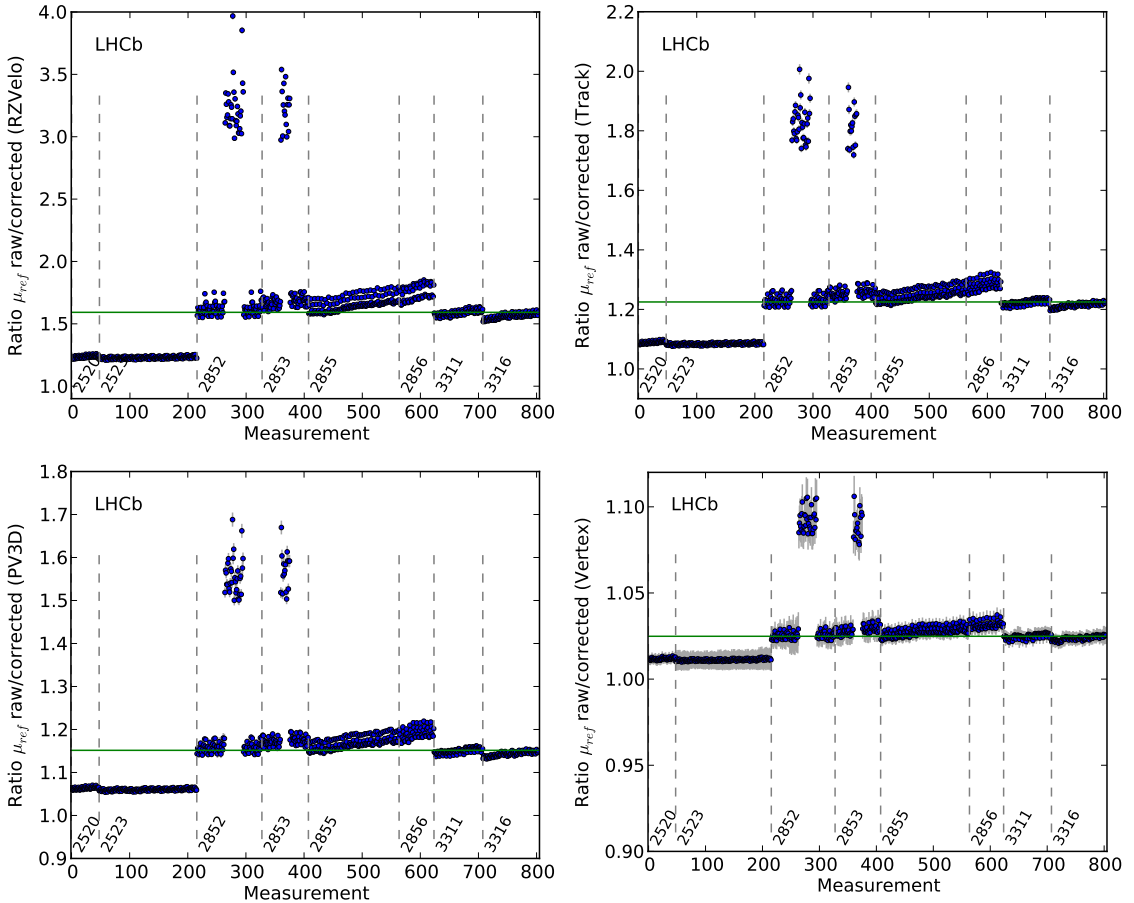


**Fig. 5.6:** Ratio of raw rates compared to background corrected rates. Top left: counter *RzVelo*. Top right: counter *Track*. Bottom left: counter *PV3D*. Bottom right: counter *Vertex*. Fill numbers are indicated in the plot and the fill boundaries are shown with dashed vertical lines. The first two fills had a higher rate due to the  $\beta^* = 3$  m optics. The effect of a larger relative background contribution due to the beam offset measurements in fill 2852 and 2853 is clearly visible.

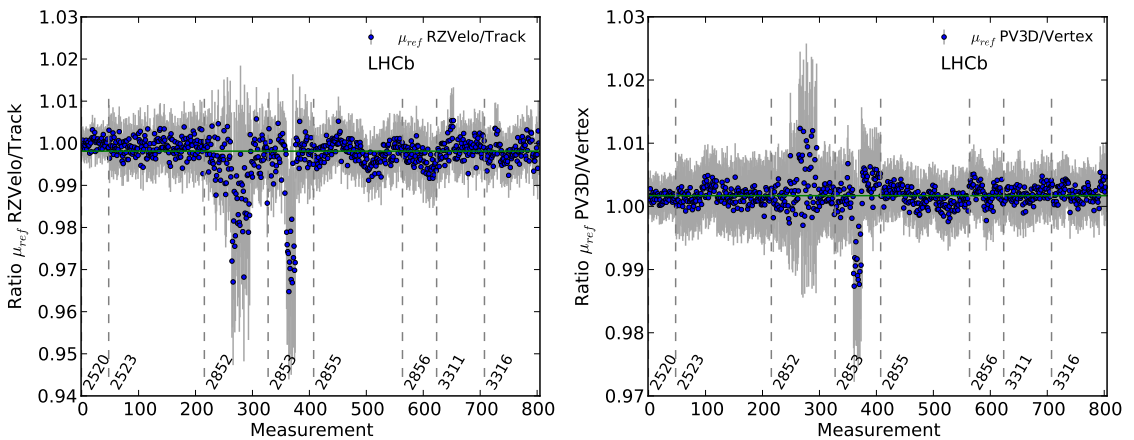


**Fig. 5.7:** Ratio of counters after background correction. Left: ratio of  $\mu_{\text{ref}}$  *RzVelo*/*Track*. Right: ratio of  $\mu_{\text{ref}}$  *PV3D*/*Vertex*. Fill numbers are indicated in the plot with boundaries denoted with dashed vertical lines.

## 6 BUNCH POPULATION MEASUREMENTS

### 6.1 Measurements with LHC instrumentation

Each colliding bunch pair has a different shape and bunch population product  $N_1 N_2$ . This imposes that the luminosity measurement is carried out individually for each colliding bunch pair. The analysis and procedures required for the bunch population measurement have been performed by the LHC Bunch Current Normalization Working Group (BCNWG) in a joint effort between the LHC experiments and the LHC instrumentation group. Results and procedures are described in Refs. [46, 47, 48, 49]. The bunch populations are measured with Bunch Current Transformers (BCTs) in a two-step process exploiting the individual capabilities of each instrument [50, 51]. Each beam is equipped with two DC current transformers (DCCT) and two fast beam-current transformers (FBCT), the two transformers per BCT type, called system A and B, are technically identical but operated independently. Both A and B systems were operational for the DCCT, while only system A was used for the FBCT.

The DCCT measures the total current circulating in each ring irrespective of the time structure of the beam. The FBCT [52, 53] measures the intensity of all 3564 nominal 25 ns slots, but provides a relative intensity determination and needs to be normalized to the DCCT measurement. The total bunch populations  $N_{\text{main},j}$  for beam  $j$  is the sum of all bunches intensities  $N_{j,i}$

$$N_{\text{main},j} = \sum_{i \in \mathcal{M}_j} N_{j,i}, \quad (6.1)$$

where  $\mathcal{M}_j$  is the set of all nominal bunches in beam  $j$ . The measured population fractions are thus defined as

$$P_{j,i} = \frac{N_{j,i}}{N_{\text{main},j}} \text{ with } \sum_{i \in \mathcal{M}_j} P_{j,i} = 1. \quad (6.2)$$

The total  $N_{\text{main},j}$  is normalized to the total intensity measured by the DCCT  $N_{\text{tot},j}$  up to small corrections (“ghost charge” and “satellite”), which are discussed later.

The relative population fractions measured by the FBCT have been checked against other instruments sensitive to the bunch intensity such as the ATLAS beam pick-up timing system (BPTX) as described in Ref. [48]. It has been found that both instruments present a non linearity. Nevertheless, the systematic uncertainty related to the FBCTs is of the order of 0.1% with beam conditions observed since 2012. Furthermore, an analysis combining all bunch-by-bunch cross-sections per fill allows to reduce this uncertainty further as will be discussed in Sec. 7.1.1.

The DCCT, described in Refs. [50, 51, 54, 55], is the only device providing an absolute scale of the circulating beam intensity and plays a central role in the luminosity measurement. In 2010 the luminosity calibration measurements were limited by the DCCT uncertainty on the bunch current product of  $\pm 2.7\%$ . This uncertainty was mostly determined from the observation of the peak-to-peak variation of the absolute calibration made in 2010 with a precision current source.

As part of this work and to be able to perform precise luminosity measurements with beam-gas and SMOG gas injection, a measurement campaign was carried out in the 2010 winter shutdown

and throughout 2011. The purpose was to evaluate all possible sources of uncertainty affecting the DCCT and provide a final uncertainty determination for all LHC experiments based on this measurement campaign. The measurements have been carried out either in the LHC beam instrumentation laboratory or in-situ in the tunnel. Some analyses have also been performed with data stored during normal operation. Results of the DCCT calibration studies have been published in Ref. [56], which is added as appendix to this document in Sec. G. The uncertainties depend on the total intensity and reach about 0.3% on the beam current product for dedicated luminosity calibration fills; however, the total uncertainty depends on the beam intensity and acquisition conditions and must be evaluated on a fill-by-fill basis. The summary of all uncertainties associated with the DCCT is listed in Tables G.8 and G.9, relevant quantities which are fill dependent are the lowest intensity observed at the end of a fill, the ADC acquisition range, the baseline before injection and after the beam dump.

Taking fill 2855 as example, the final uncertainty on the current product is evaluated as follows. The lowest intensity for beam 1 and 2 was  $3.8 \cdot 10^{12}$  and  $4.1 \cdot 10^{12}$  protons, respectively. Both beams were acquired with the DCCT blocked on range 3 for the whole fill,<sup>1</sup> including the periods without beam. To be valid for the whole fill, the relative uncertainty is based on the lowest intensity of  $3.8 \cdot 10^{12}$  protons, using Eq. (G.12) (from Sec. G.7), the relative error of one least significant bit is 0.08%. The absolute value of the baseline before and after the fill is smaller than  $10^9$  protons, a dedicated correction is therefore not warranted and the smaller error of  $10^9$  protons can be used as if the baseline was manually corrected. The relative error of the baseline is  $10^9 / (3.8 \cdot 10^{12}) = 0.03\%$ . If the normalization is done with a time average shorter than 1 minute, then the error from the long term stability of baseline for range 3 is  $2.4 \cdot 10^9$  protons corresponding to a relative error of 0.08%. The smaller error of  $1.1 \cdot 10^9$  can be used if the normalization is performed over a period of 1 hour or more. The summary of all uncertainties for fill 2855 is presented in Table 6.1. As shown in Table G.9, all uncertainties are given as an interval that contains all values (envelope error).

**Table 6.1:** Summary of uncertainties on the total beam intensity for fill 2855 in July 2012

Source of uncertainty (per beam)	Relative error (%)	Correlated btw. beams
Current source precision	$\pm 0.05$	yes
Bunch pattern dependence (laboratory test)	$\pm 0.1$	yes
Non-linearity of 12-bit ADC	$\pm 0.07$	yes
Baseline correction	$\pm 0.03$	no
Long term stability of baseline on range 3	$\pm 0.06$	no
Long term stability of calibration on range 3	$\pm 0.07$	no
Difference between system A and B on range 3	$\pm 0.08$	no
Total uncertainty per beam	$\pm 0.174$	
Correlated error per beam	( $\pm 0.130$ )	yes
Uncorrelated error per beam	( $\pm 0.116$ )	no
Total uncertainty on intensity product	$\pm 0.31$	

The total uncertainty on the beam current product is 0.31% assuming the first three listed errors are correlated between beams. This uncertainty is understood as an envelope error (100% confidence level), to interpret the envelope uncertainty in terms of a one standard deviation confidence level, the uncertainty should be multiplied by 0.683.

The beam intensity evolution over time for fill 2855 measured by the DCCT is shown in Fig. 6.1 as example. Individual bunch intensities measured by the FBCT are shown in Fig. 6.2 for the same fill. A spread in bunch intensities of up to 40% is not uncommon.

<sup>1</sup>The acquisition ADC can operate with four amplification ranges (see Sec. G.2.3)

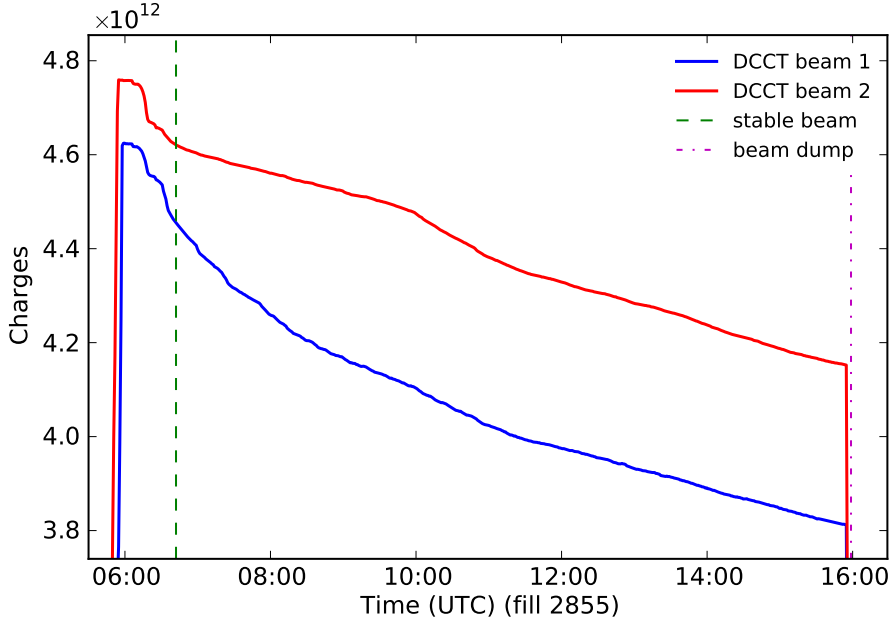


**Fig. 6.1:** Total beam intensity measured with the DCCT for fill 2855 as function of time. The vertical dashed lines indicate the stable beams and beam dump times.

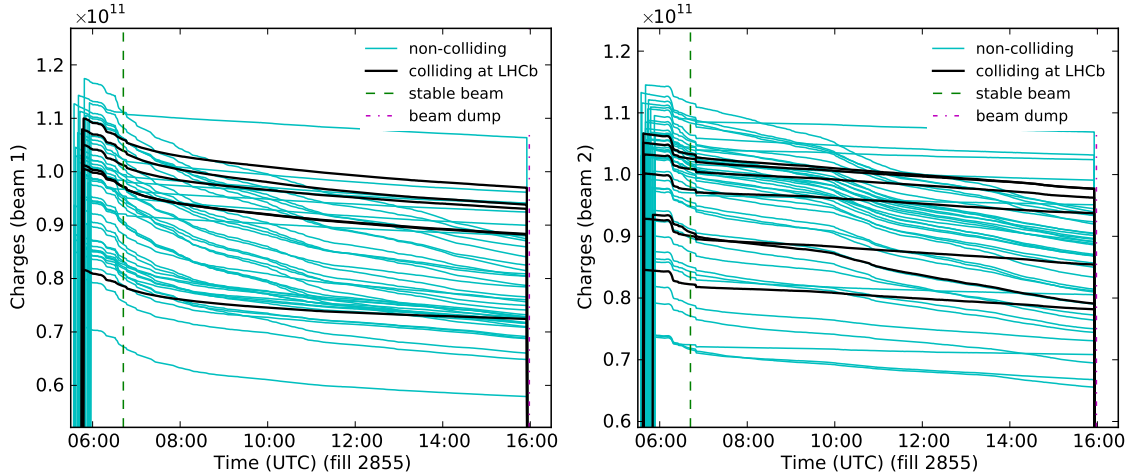


**Fig. 6.2:** Single bunch intensities measured with the FBCT (fill 2855) as function of time. Black lines indicate bunches colliding at LHCb. Left: beam 1; right: beam 2. Bunches colliding at LHCb experienced a smaller intensity decay compared to most other bunches.

## 6.2 Ghost Charge

### 6.2.1 Definitions

As seen in 2.3, a BCID spans 10 RF buckets and about 25 ns and they are numbered from 1 to 3564. The charge contained in each nominal RF bucket of colliding bunch pairs is the relevant quantity required for luminosity calibration measurements. As illustrated in Fig. 6.3, particles are captured in all RF buckets and not only inside the nominally filled bucket. Charges captured outside of the 25 ns bunch slot are called “ghost charges”, while those charges captured within  $\pm 12.5$  ns of the main filled bucket but not in the main bucket are called “satellite” charges. Definitions and variable-naming conventions used here follow the study in Ref. [49]. Ghost charge evaluations for luminosity calibration have been performed in 2010 and 2011 [57, 49] and 2012 which is described here. While the measurement principle has not changed, the following measurement profits from

a larger number of beam-gas events obtained with the SMOG gas injection which permits the reduction of the uncertainty and provides a more detailed charge distribution determination over the ring.

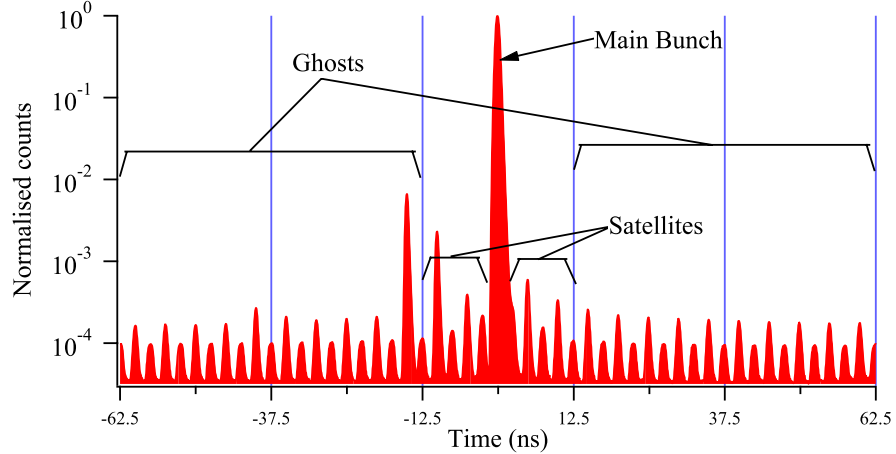


**Fig. 6.3:** Example of a longitudinal profile measured with the Longitudinal Density Monitor (LDM) instrument to illustrate the ghost charge definition. This example measured with an ion beam shows significantly more satellite and ghost charge than what is normally seen in typical  $pp$  beams. Source: A. Jeff [49]

The total population of beam  $j$  can be expressed as the population sum over all nominally filled slots plus the ghost charge

$$N_{\text{tot},j} = N_{\text{main},j} + N_{\text{ghost},j}. \quad (6.3)$$

Ultimately, the populations  $N_{j,i}$  of all colliding bunches are of interest for the luminosity measurement. The importance of the ghost charge measurement arises from the beam current measurement instrumentation. The total beam intensity  $N_{\text{tot},j}$  (which includes ghost charge) is measured by the DCCT, while filled bunch populations are measured with the FBCT. Since the sum of all bunch populations measured by the FBCT is normalized to the DCCT, the ghost charge fraction must be subtracted from the DCCT measurement.

All bunches  $i$  are part of either set  $\mathcal{M}_j$  of all main filled bunch slots or part of set  $\mathcal{E}_j$  of all nominally empty slots where the buckets of both beams are nominally empty (called *ee* crossings). Bunches from set  $\mathcal{M}_j$  also contain unpaired bunch crossings called *be* crossings where a nominally filled beam 1 bunch crosses a nominally empty bunch from beam 2 or *eb* crossing when a filled beam 2 bunch crosses a nominally empty bunch from beam 1. The sum of all main bunch populations  $N_{\text{main},j}$  and ghost charge  $N_{\text{ghost},j}$  are then defined as

$$N_{\text{main},j} = \sum_{i \in \mathcal{M}_j} N_{j,i}; \quad N_{\text{ghost},j} = \sum_{i \in \mathcal{E}_j} N_{j,i}, \quad (6.4)$$

with  $N_{j,i}$  the bunch population of a single slot  $i$  for beam  $j$ . Accordingly, the ghost charge fraction is defined as

$$\nu_{\text{ghost},j} = \frac{N_{\text{ghost},j}}{N_{\text{tot},j}}. \quad (6.5)$$

Assuming the beam-gas rate of a bunch slot is proportional to its population, the ghost charge fraction could be directly measured with the ratio  $\sum_{i \in \mathcal{E}_j} R_{j,i} / \sum_{i \in \mathcal{M}_j} R_{j,i}$ . To exclude contamination from satellite collisions in *bb* crossings, the ghost charge fraction per beam is determined by comparing beam-gas rates seen in unpaired bunch slots and empty bunch slots and is then

normalized to the total beam intensity

$$\nu_{\text{ghost},j} = \frac{\sum_{i \in \mathcal{E}_j} R_{j,i}}{\sum_{i \in \mathcal{U}_j} R_{j,i}} \cdot \frac{\sum_{i \in \mathcal{U}_j} N_{j,i}}{\sum_{i \in \mathcal{M}_j} N_{j,i}} \cdot \epsilon_j^{-1}, \quad (6.6)$$

with  $\epsilon_j$  the trigger efficiency discussed below in Sec. 6.2.3 and  $\mathcal{U}_j$  the set of unpaired (non-colliding) bunches.

### 6.2.2 Event selection

The ghost charge measurement is based on the same data sample as used for the BGI analysis. The trigger requirements are described in Sec. 4.1.2.

To ensure that each vertex is a result of a beam-gas interaction and is associated to the correct beam, vertices used for ghost charge analysis are selected according to the following offline criteria.

1. The transverse position of a vertex must lie inside a 2 mm radius along the beam-line:  $\sqrt{x^2 + y^2} < 2$  mm to exclude material interactions.
2. The vertex must be within in the longitudinal  $z$  range  $-1000$  mm  $\leq z \leq 300$  mm for beam 1 and  $0$  mm  $\leq z \leq 1000$  mm for beam 2.
3. The reconstructed vertex must have at least 10 tracks  $N_{\text{tracks}} \geq 10$ .
4. Finally, a forward-backward track asymmetry is required to separate beam-gas interactions originating from beam 1 or beam 2. While the previous criteria are sufficient to unambiguously identify an interaction as originating from a beam-gas collision when associated with a  $be$  or  $eb$  crossing, an interaction seen in an  $ee$  crossing can be attributed to beam 1 or beam 2 in the central VELO region. The direction of tracks associated with a vertex are either forward or backward with respect to beam 1, their quantities are defined as  $N_{\text{backward tracks}}$  and  $N_{\text{forward tracks}}$ . Therefore, due to the fact that the center of mass is moving, all vertices are required to have zero backward track for beam 1 and respectively zero forward track for beam 2.

To exclude any beam-beam contamination in beam-gas counts, the distribution of all vertices passing the requirements listed above are analyzed. An example of distributions accumulating 20 minutes of data<sup>2</sup> is shown in Fig. 6.4 for the  $z$  distribution, in Fig. 6.5 for the  $x$ - $z$  projection and in Fig. 6.6 for the  $x$ - $y$  transverse profiles. Since the beams are not perpendicular to the  $x$ - $y$  laboratory frame due to the crossing angle and also a global detector tilt in  $x$  and  $y$ , transverse vertex distributions are projected along the corresponding beam angle  $\theta_{j,m}$  (with beam  $j = 1, 2$  and plane  $m = x, y$ ) to an  $x$ - $y$  plane at  $z = 0$  in the laboratory frame. Explicitly, each vertex transverse position  $v_{j,m}(z)$  is projected to  $v'_{j,m} = v_{j,m}(z) - \alpha_{j,m} \cdot z$ .

---

<sup>2</sup>First 20 minutes of fill 2852

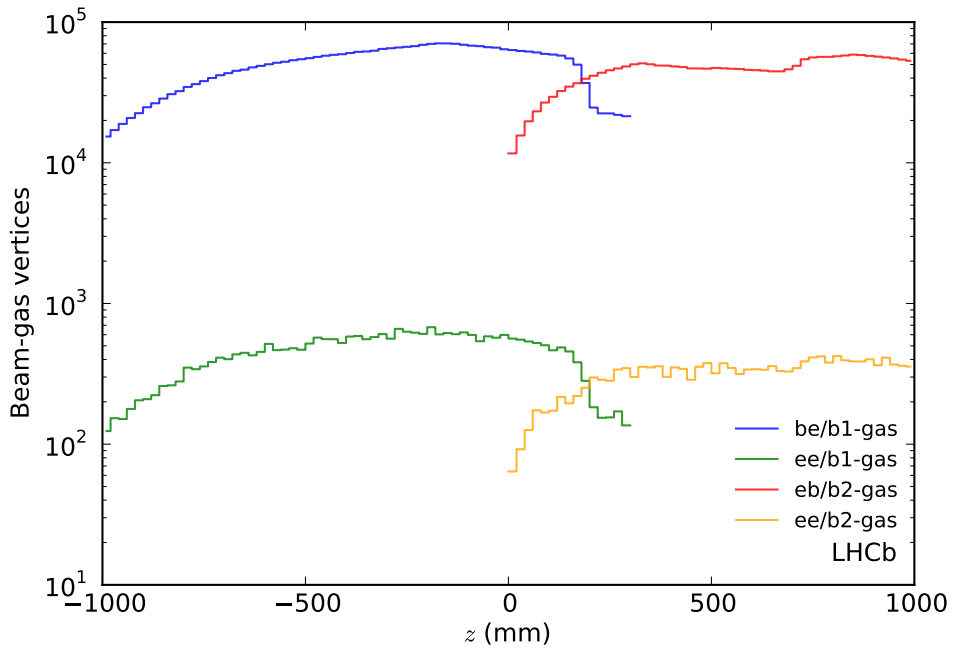


**Fig. 6.4:** Distribution of selected beam-gas events along  $z$  used for the ghost charge measurement. Both top curves are from unpaired bunches, with beam 1 selection criteria on the left and beam 2 selection criteria on the right. Bottom curves are from  $ee$  crossings.

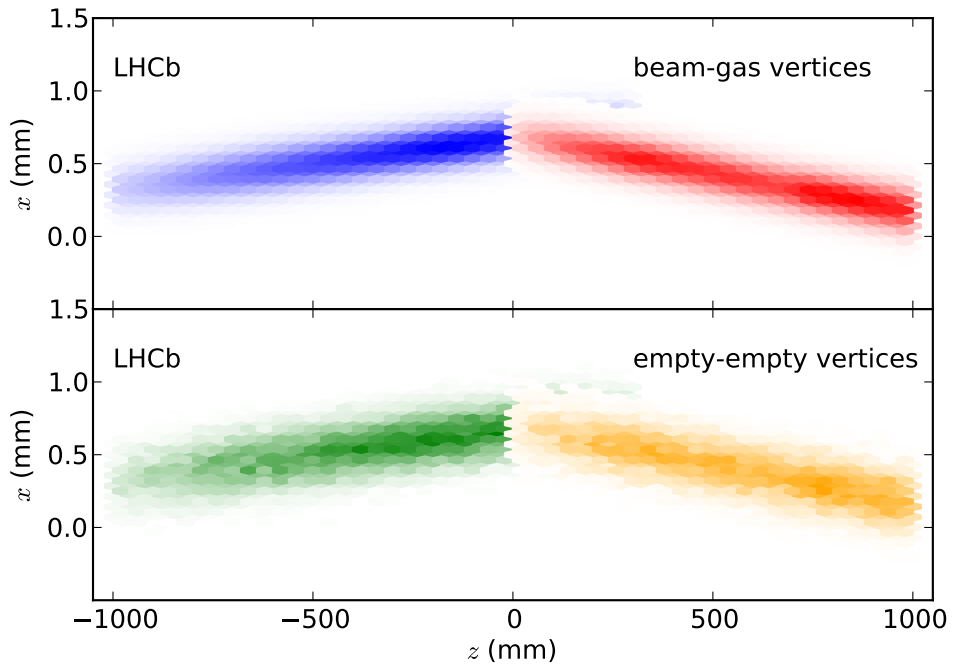


**Fig. 6.5:** Selected beam-gas  $x$ - $z$  vertex density profile used for a ghost charge measurement. Regions with stronger plain color have a higher beam-gas density compared to regions with weaker color. The top panel shows the sum of all unpaired bunch crossings  $be$  in blue from beam 1 selection criteria on the left and  $eb$  in red from beam 2 selection criteria on the right. The bottom panel shows all vertices from  $ee$  crossings with beam 1 on the left and beam 2 on the right.

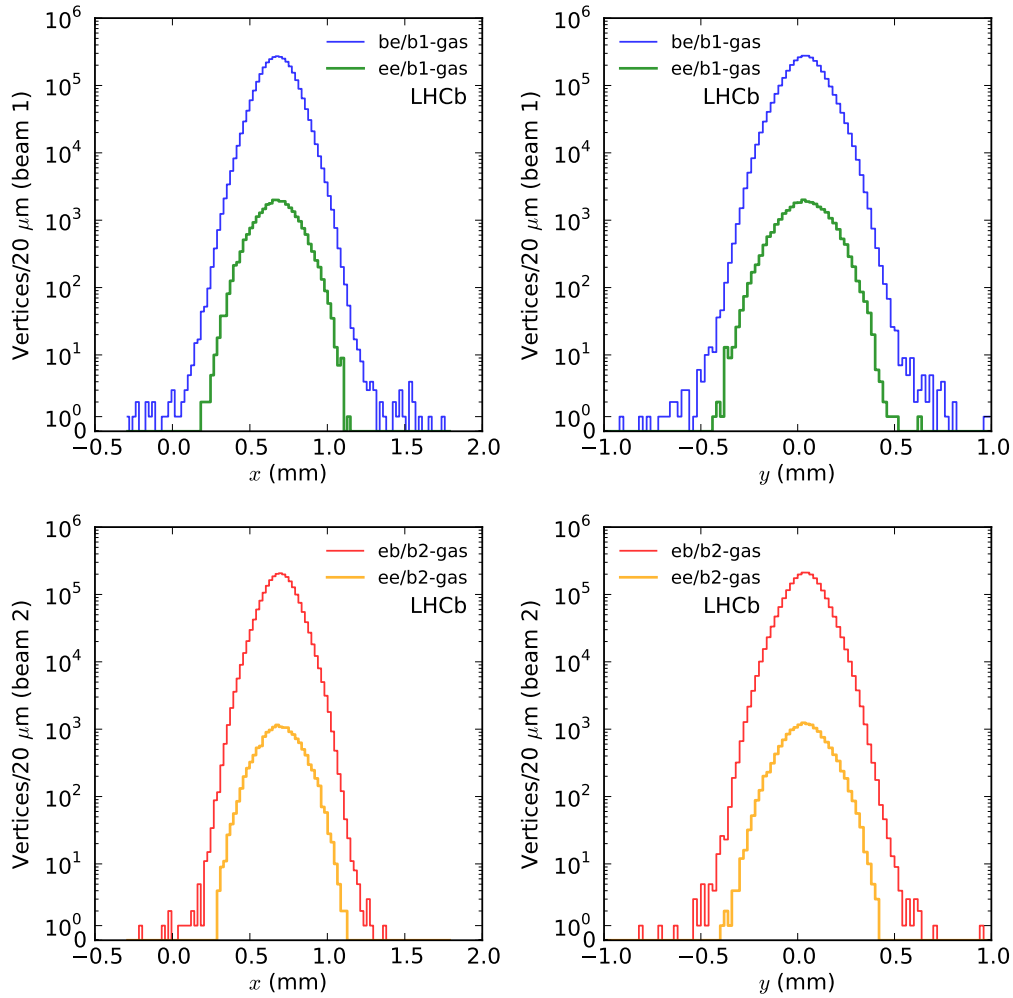


**Fig. 6.6:** Transverse distribution of selected beam-gas events for ghost charge analysis. All vertices are projected along the corresponding beam direction onto the  $x$ - $y$  plane. Histograms from beam 1 vertices are on both top panels and from beam 2 on both bottom panels. The less populated histograms are from  $ee$  events of the corresponding beam.

### 6.2.3 Trigger efficiency correction

The LHCb detector has a timing granularity of 25 ns and its trigger clock phase relative to the LHC timing is optimized to provide the highest efficiency for nominally filled RF buckets. The trigger efficiency is not constant across the 25 ns bunch slot and depends on the interaction time with respect to the nominal detector clock phase. A first efficiency measurement was performed in 2010 [57, 49], resulting in a ghost charge uncertainty of about 20% per beam. The new measurement presented here was performed with the aim to reduce this uncertainty by acquiring more data points and by using the SMOG gas injection to increase the statistical accuracy.

The efficiency is determined by measuring beam-gas rates at different clock shifts and comparing them with the nominal value observed at zero shift. Per definition, the efficiency is set to unity for a zero clock shift. Any detector dead time during which the acquisition rate is reduced is accounted for by monitoring the so-called “Lumi Triggers” which are randomly sampled at a fixed frequency  $\nu_{\text{rnd}} = 2.8125$  kHz with a ratio between beam crossings  $bb:be:eb:ee$  of 20:1:1:0.5. The rate  $\nu_{\text{rnd}}$  is independent of detector dead time or clock shift, while the observed rate  $\nu_{\text{lumi}}$  of “Lumi Triggers” is reduced by dead time. Therefore, the trigger efficiency for a given clock shift  $k$  on beam  $j$  is given by

$$\epsilon_{j,k} = \frac{\sum_{i \in \mathcal{U}_j} R_{j,i,k}}{\sum_{i \in \mathcal{U}_j} R_{j,i,0}} \cdot \frac{\nu_{\text{rnd}}}{\nu_{\text{lumi}}} \quad (6.7)$$

with  $R_{j,i,0}$  the beam-gas rate at the nominal LHCb clock shift.

A proper dead time correction is critical for this measurement as some sub-detectors can induce a large dead time of over 50% when the clock shift is larger than 5-10 ns. Furthermore, as the analysis compares absolute rates, it is important to make sure that all recorded raw files and events have been fully reconstructed. The efficiency has been measured as function of clock shift in 2.5 ns intervals and each step was acquired for about 4-5 minutes. The beam intensity decay observed during the measurement which lasted about 1h20, has been taken into account.

If a beam-gas interaction occurs near the bunch slot edges, that is, the originating charge was near the previous or next BCID, the resulting VELO sensor signals might last long enough to be also acquired in the neighboring BCID. Therefore, depending on where the charges are located within the 25 ns bunch slot, some vertices will be counted twice and thus bias the ghost charge or trigger efficiency measurement. To take this double-counting effect into account, the efficiency is measured once including all beam-gas events regardless if some vertices are counted twice, and once excluding double-counted vertices. double-counted vertices in non-colliding bunch slots are detected when two events have both a consecutive BCID and event ID. The latter is incremented for each accepted trigger. In addition, the efficiency is measured for different cuts requiring at least 8, 10 and 12 tracks per vertex, respectively, to account for the slightly different trigger used for this measurement performed in April compared to later measurements (see Table 4.3). The difference in trigger requirements between this measurement and later ones is expected to be negligible. Apart from the requirement on the number of tracks per vertex, the same selection as described in 6.2.2 is also applied to this measurement.

The results determined are shown in Fig. 6.7 and summarized in Table 6.2. The average values in Table 6.2 are with the assumption that the charge distribution within a bunch slot is constant and not concentrated in one RF bucket. Measurements performed with the LDM [58] confirmed that the ghost charge tend to be spread within all RF buckets. Vertices originating from beam 1 interactions are more prone to be counted twice near the bunch edge as can be seen on the left plot which includes double-counted vertices.

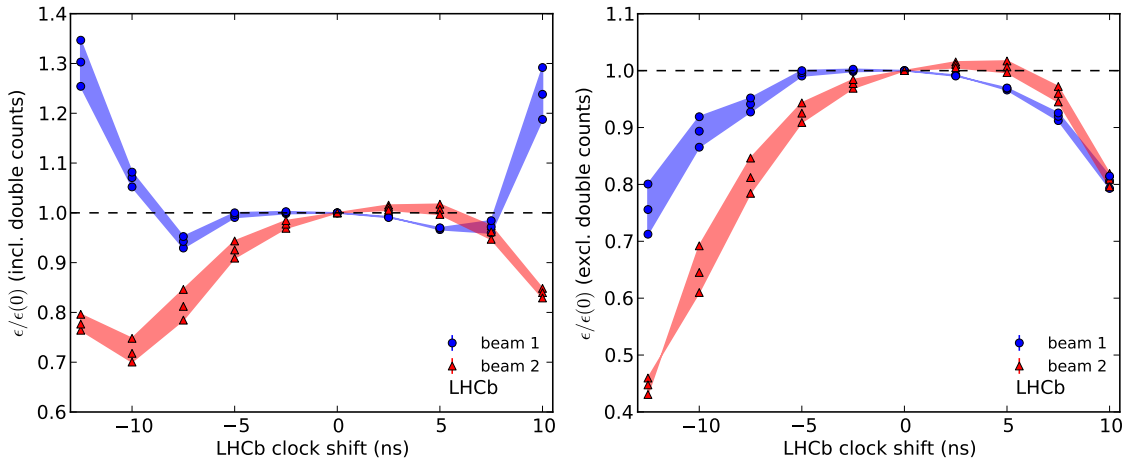


**Fig. 6.7:** Relative beam-gas trigger efficiency as function of LHCb detector-clock shift with respect to the LHC reference timing. Left/right plots: trigger efficiency including/excluding double-counted beam-gas vertices. The efficiency is shown relative to the value at the nominal clock setting (zero shift). For each clock shift and beam the efficiency is measured requiring at least 8, 10 and 12 tracks per vertex, respectively, the surface between the 8 and 12 tracks values is filled for better readability.

**Table 6.2:** Relative beam-gas trigger efficiency for the ghost charge measurement assuming a constant charge distribution within a bunch slot.

Beam	Efficiency average $\epsilon_j$ including double-counting	Efficiency average $\epsilon_j$ excluding double-counting
1	$1.05 \pm 0.03$	$0.93 \pm 0.02$
2	$0.90 \pm 0.01$	$0.86 \pm 0.01$

#### 6.2.4 ghost charge distribution over the ring circumference

The increased rate of beam-gas data acquired with SMOG gas injection allows not only for a more accurate ghost charge measurement, but also permits a better observation of its distribution over the ring circumference. The ghost charge distribution is shown as function of BCID in Fig. 6.8 as an example using data from fill 2520. This was the first fill dedicated to luminosity calibration and was acquired in combination with SMOG gas injection. Ghost charges are concentrated around nominally filled bunches and are mostly absent about 20 BCIDs away from filled bunches. Also the ghost charge amplitude is different around each bunch.

Ghost charges have also been measured with the Longitudinal Density Monitor (LDM) [58] instrument. The LDM counts synchrotron radiation photons emitted by particles bent in a magnetic field. While the ghost charge measurement performed with the LDM presents different sources of uncertainties, such as a necessary noise background subtraction or possible presence of internal reflections, the measured ghost charge fractions are typically within 20% of the LHCb values. A comparison of the ghost charge distribution between LHCb and LDM as function of BCID is shown in Fig. 6.10 for fill 2853, the correlation of both measurements is shown in Fig. 6.9. A zoomed-in selection of BCIDs between 1500 and 2000 is shown in Fig. 6.11. In all comparison plots with the LDM, the LDM data has been subtracted for background and therefore contains bins with negative contents in which case the lower axis limit has been set to zero for better readability. Both measurements show a similar pattern of ghost charge distribution concentrated around filled bunches. Also the general shape preceding and following each peak as seen in the enlarged plot is comparable between both methods. The peak amplitudes are different between both measurements. However, this difference could be due to the noise subtractions applied to the LDM data or also due to the different time integration of 60 minutes for LHCb and 5 minutes for the LDM.

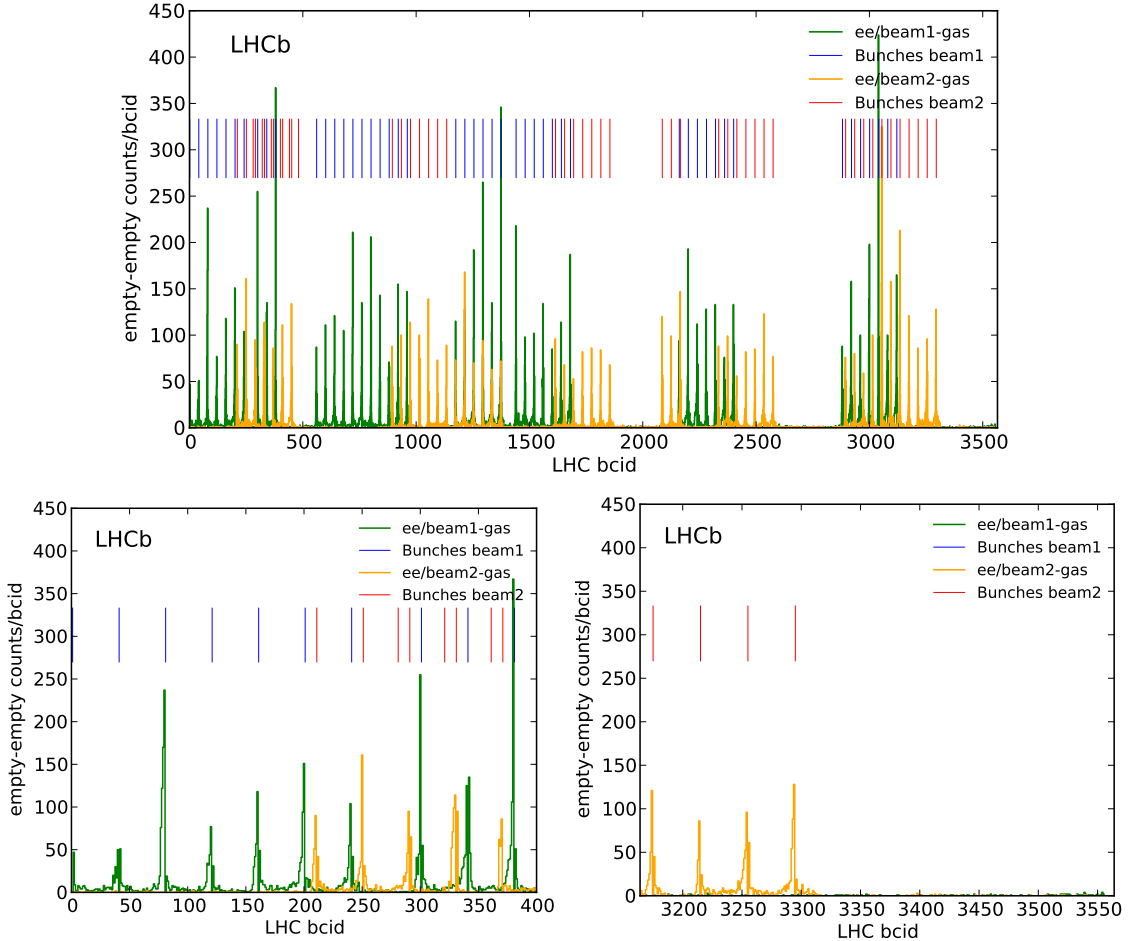


**Fig. 6.8:** Ghost charge distribution over the ring circumference as function of LHC BCID for fill 2520. Top: histogram of ghost charge for beam 1 (green) and beam 2 (yellow) as function of LHC BCID. The BCID position of nominally filled bunches is indicated as small vertical blue and red lines for beam 1 and 2, respectively. Bottom left (right): ghost charge distribution for the first (last) 400 BCIDs using the same data as above. Ghost charges are mostly absent in regions without nominally filled bunches. Note that the ghost charge is only measured in  $ee$  BCIDs.

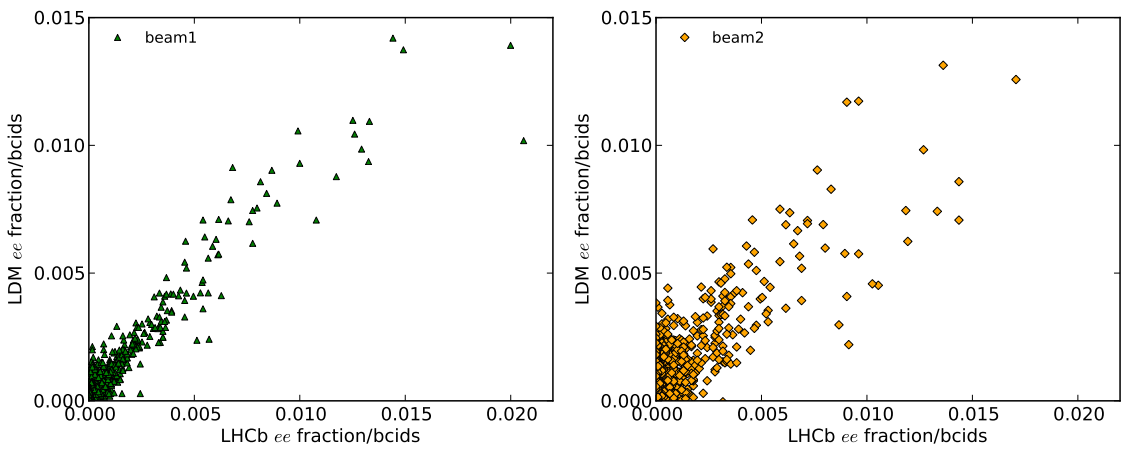


**Fig. 6.9:** Correlation between ghost charge fractions measured by the LDM and LHCb for fill 2853. Each data point corresponds to one BCID measurement, the values are normalized such that the sum of all data points per beam is equal to one.

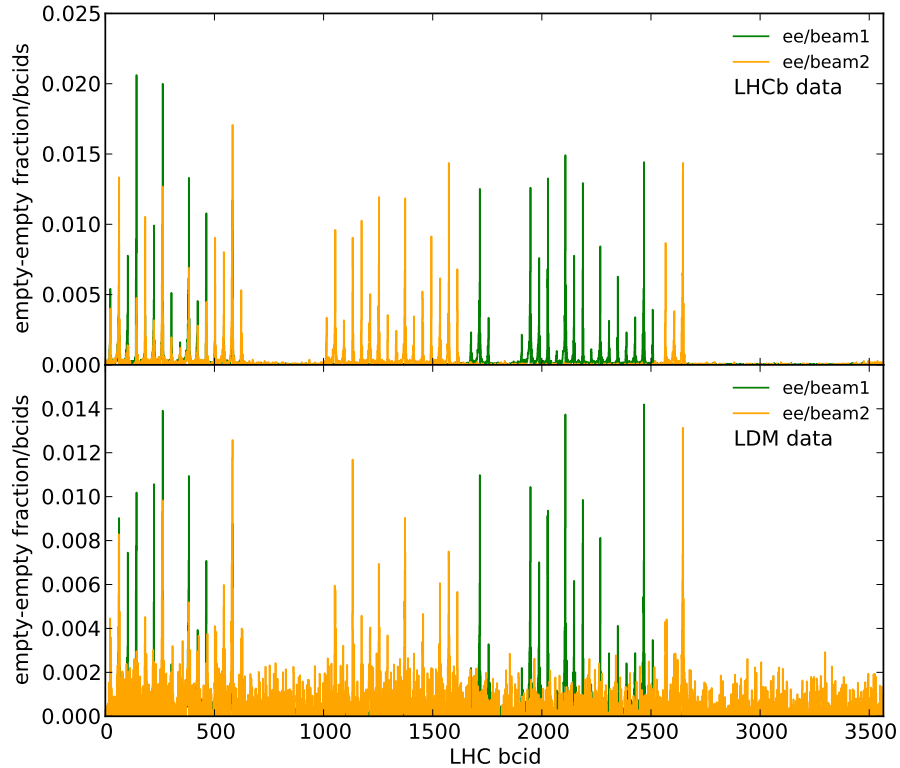


**Fig. 6.10:** Ghost charge distribution measured with LHCb (top panel) and with the LDM (bottom panel) for fill 2853. The distributions are normalized such that the sum of all bins per beam is equal to one.

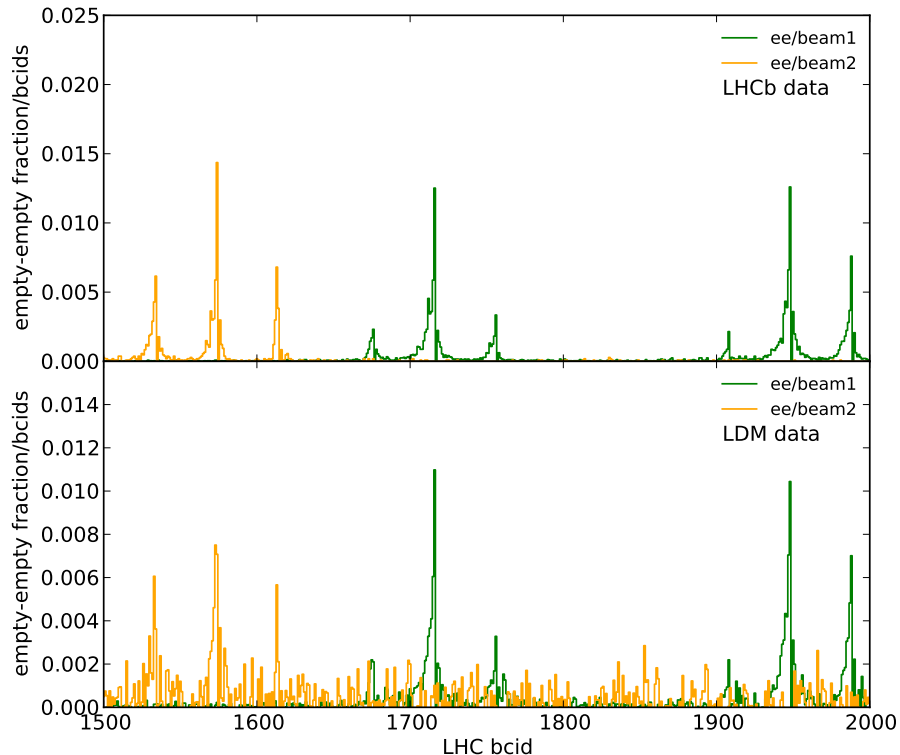


**Fig. 6.11:** Ghost charge distribution measured with LHCb (top panel) and with the LDM (bottom panel) selecting the BCID region of 1500 to 2000 for fill 2853.

### 6.2.5 Ghost charge measurements and results

Ghost charge fractions are measured in 4 minutes time bins. For each time bin the ghost charge fraction is evaluated with both counting methods: including and excluding double-counted vertices and applying the corresponding efficiency. If all charges are on average evenly spread within their bunch slot, both measurements would provide a different value before efficiency correction, but the same result after efficiency correction. On the other hand, if all or most charges are concentrated in the central RF bucket of each empty bunch slot, the results between both counting methods will be identical before efficiency correction, but will differ after correction due to the different efficiency treatment. Since the charge distribution within the 25 ns bunch slots is considered unknown,<sup>3</sup> the full difference after efficiency correction between both counting methods is taken as systematic uncertainty. The trigger efficiency uncertainty taken from Table 6.2 is added in quadrature to the systematic uncertainty. The central value is taken as an average of both measurements.

A change in ghost charge spread within the 25 ns bunch slot will affect the difference between single and double-count measurements; this effect can be observed in fill 2852 as shown in Fig. 6.12. A summary of all ghost charge measurements performed for the special luminosity fills in 2012 and 2013 is provided in Table 6.3.

With the exception of intermediate energy fills at  $\sqrt{s} = 2.76$  TeV, ghost charge fractions are stable within  $\pm 10\%$  during a fill and the total beam intensity can be corrected within a good approximation using an average value for a fill. In this case the RMS over the fill given in Table 6.3 should be taken into account in the uncertainty. In the contrary, for intermediate energy fills, an increase in the ghost charge fraction over time warrants a time dependent correction to the total beam intensity. The difference in ghost charge evolution seen between high and intermediate energy fills is shown for example in Fig. 6.13 comparing the long fill 2855 at to  $\sqrt{s} = 8$  TeV and fill 3563 at to  $\sqrt{s} = 2.76$  TeV. Due to the evolution of the ghost charge fraction in fills 3562 and 3563, results for the ghost charge are provided as function of time for those fills in Appendix D in Tables D.1 and D.2, respectively.

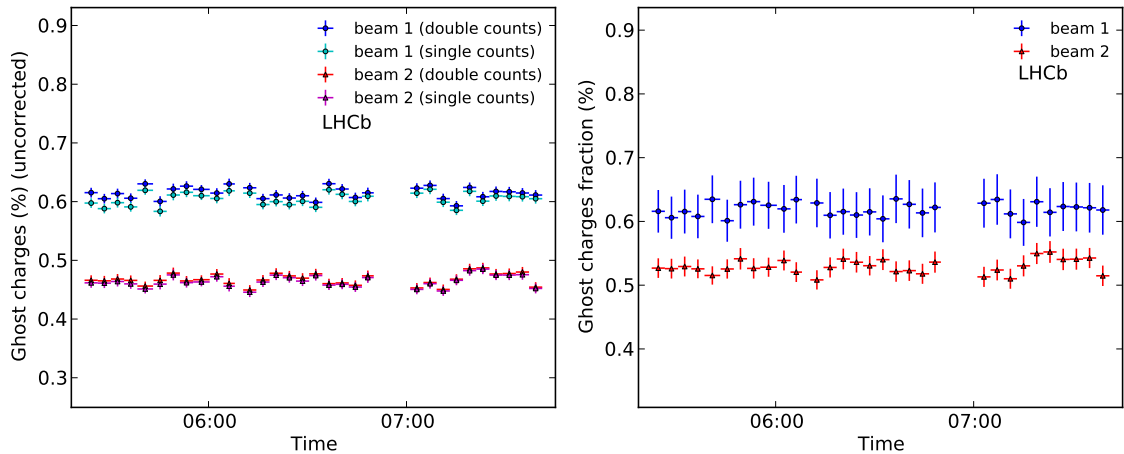


**Fig. 6.12:** Ghost charge fraction for fill 2852. Left: ghost charge fractions not corrected for trigger efficiency; only the statistical uncertainty is shown as error bar. For beam 1 a difference between single and double-counting methods can be observed at the start of the fill, while this difference is reduced towards the end of the fill. Right: Ghost charge fractions corrected for trigger efficiency; the data points are an average of both counting methods. Indicated error bars include the systematic uncertainty related to the two counting methods, the trigger uncertainty and the statistical uncertainty.

In addition to the previously discussed trigger efficiency, some  $ee$  events can be missed due to two trigger artifacts, affecting the measurement. First, the hardware trigger can not acquire any events

<sup>3</sup>LDM measurements [58] shown that the ghost charge tend to be spread among the RF buckets in a BCID.

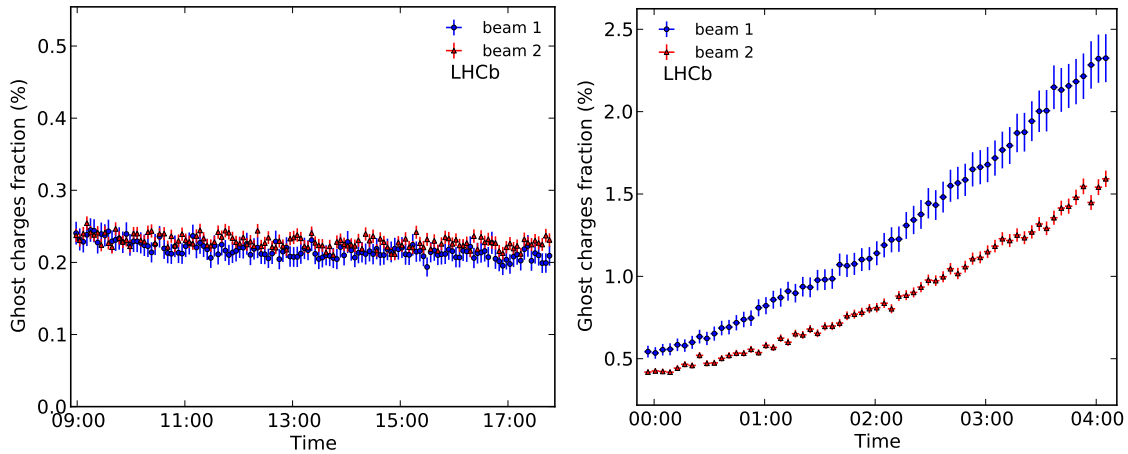


**Fig. 6.13:** Ghost charge fractions for fills 2855 and 3563. Left: fill 2855 operated at  $\sqrt{s} = 8$  TeV shows a constant or slightly decreasing ghost charge fraction throughout the fill lasting about 9 hours. Right: fill 3563 operated at  $\sqrt{s} = 2.76$  TeV shows an important increase of ghost charge over a period of 4 hours.

in a window of 15 consecutive BCIDs normally located closely after BCID 1000. A light pulse is used during this blind spot to calibrate the calorimeters. Most fills are affected. The BCID location depends on the LHC filling pattern and is automatically placed in a region without nominally filled bunches on either beam. The effect of the missing BCID events can be seen in Fig. 6.14 as an example for two different filling schemes. In case of evenly distributed ghost charge around the ring, missing  $ee$  events would account for  $15/3564 \approx 0.4\%$ . However, as most ghost charges are located near filled bunches, this effect can be neglected.

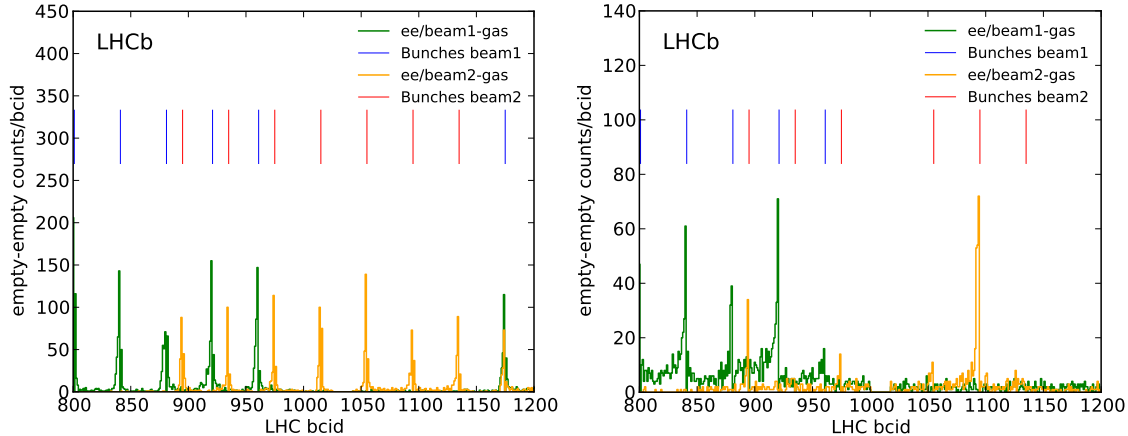


**Fig. 6.14:** Missing  $ee$  events for 15 consecutive BCIDs between BCIDs 1000 and 1050 for (left) fill 2520 and (right) fill 3311. The trigger blind spot is automatically placed in a region without nominally filled bunches. The low ghost charge fraction of fill 3311 makes the gap more visible.

The second trigger artifact affects beam-gas rates acquired with a normal physics trigger, which includes both RICH detectors. In this case, the detector can not be triggered in the bunch slot directly following a triggered event and a ghost charge event timely located in this slot would not be seen. Only Pb ion fills in 2013 are affected as beam-gas events were acquired in parallel to normal physics data taking. All other fills dedicated to luminosity calibration excluded both RICH detectors and could trigger on all 25 ns slots. The missing ghost charge fraction can be calculated as the probability to get an interaction from a colliding bunch pair times the fraction of colliding bunch slots. During lead fills in 2013 the average number of interactions per crossing  $\mu_{\text{ref}}$  was ranging from 0.01 to 0.02 with a total of 38 colliding bunches. The untriggered ghost charge fraction is then  $1 - e^{-0.02} \cdot 38/3564 \approx 0.02\%$  which is negligible.

**Table 6.3:** Measurements of ghost charge fractions for all luminosity calibration fills in 2012 and 2013. The systematic uncertainty is to be assumed fully correlated between both beams. Therefore, the final systematic uncertainty on the beam intensity product due to the ghost charge correction is a linear sum of the ghost charge systematic uncertainties from both beams. Lead fills (3503 to 3540) were acquired without SMOG and have a larger statistical uncertainty, all other fills were acquired with SMOG. See Tables D.1 and D.2 in Appendix D for fills 3562 and 3563, respectively.

Fill	Description	beam	Ghost charges (%)	RMS over fill (%)	Systematic uncertainty (%)	Statistical uncertainty (%)
2520	$pp \sqrt{s} = 8 \text{ TeV}$	1	0.30	0.01	0.02	0.001
		2	0.35	0.01	0.01	0.002
2523	$pp \sqrt{s} = 8 \text{ TeV}$	1	0.50	0.02	0.03	0.001
		2	0.44	0.01	0.01	0.001
2852	$pp \sqrt{s} = 8 \text{ TeV}$	1	0.62	0.01	0.04	0.002
		2	0.53	0.01	0.01	0.002
2853	$pp \sqrt{s} = 8 \text{ TeV}$	1	0.40	0.01	0.02	0.002
		2	0.28	0.01	0.01	0.002
2855	$pp \sqrt{s} = 8 \text{ TeV}$	1	0.22	0.01	0.01	0.001
		2	0.23	0.01	0.01	0.001
2856	$pp \sqrt{s} = 8 \text{ TeV}$	1	0.24	0.01	0.01	0.001
		2	0.22	0.02	0.01	0.001
3311	$pp \sqrt{s} = 8 \text{ TeV}$	1	0.15	0.03	0.01	0.001
		2	0.06	0.01	0.01	0.001
3316	$pp \sqrt{s} = 8 \text{ TeV}$	1	0.19	0.01	0.01	0.001
		2	0.06	0.01	0.01	0.001
3503	$pPb \sqrt{s} = 8 \text{ TeV}$	1	0.18	0.04	0.01	0.005
		2	0.50	0.13	0.01	0.011
3505	$pPb \sqrt{s} = 8 \text{ TeV}$	1	0.29	0.05	0.02	0.007
		2	0.66	0.12	0.02	0.015
3537	$Pbp \sqrt{s} = 8 \text{ TeV}$	1	0.50	0.12	0.03	0.010
		2	0.88	0.11	0.02	0.015
3540	$Pbp \sqrt{s} = 8 \text{ TeV}$	1	0.73	0.09	0.05	0.019
		2	0.17	0.05	0.01	0.014
3555	$pp \sqrt{s} = 2.76 \text{ TeV}$	1	0.58	0.14	0.04	0.001
		2	0.33	0.03	0.01	0.001
3562	$pp \sqrt{s} = 2.76 \text{ TeV}$	1	0.78	0.30	0.05	0.003
		2	0.52	0.22	0.01	0.003
3563	$pp \sqrt{s} = 2.76 \text{ TeV}$	1	1.28	0.55	0.08	0.002
		2	0.88	0.35	0.02	0.002

### 6.3 Satellite charges

In addition to the ghost charge discussed above, the total population of all main filled bunches (6.1) is affected by out-of-time charges captured in an RF bucket within the nominally filled 25 ns bunch slot, but outside the main RF bucket. Those so-called “satellite charges” are counted by the FBCT but don’t contribute to the luminosity of the colliding bunch pairs. In 2012, the Longitudinal Density Monitor (LDM) instrument provided a measurement of satellite charges per bunch slot. The measurement of satellite charges is detailed in Refs. [49, 58].

The ghost charge fraction affects the total beam intensity, while the satellite fraction affects the bunch intensity and is different for each bunch slot. The final bunch population  $N'_{j,i}$  of the bunch slot  $i$  in beam  $j$  including corrections for the ghost charge fraction  $f_{\text{ghosts},j}$  and satellite fraction  $f_{\text{sat},j,i}$  is evaluated with

$$N'_{j,i} = N_{j,i} \cdot \frac{N_{\text{tot},j}(1 - f_{\text{ghosts},j})}{\sum_{i \in \mathcal{M}} N_{j,i}} \cdot (1 - f_{\text{sat},j,i}), \quad (6.8)$$

where  $\mathcal{M}$  is the set of all nominal bunches in beam  $j$  and  $N_{j,i}$  the bunch population measured by the FBCT.

A summary of uncertainties related to the bunch population measurement is provided in Table 6.4 for all fills with a BGI measurement. The individual uncertainties are explained in the following.

The satellite fractions provided by the LDM [58] are measured at the beginning and at the end of the fill. The fractions per BCID  $f_{\text{sat},j,i}$  used in this analysis are the averages of both measurements. The average satellite fractions for all colliding bunches and fills with  $\beta^* = 10$  m at  $\sqrt{s} = 8$  TeV are 0.25% and 0.18% for beam 1 and 2, respectively. The uncertainty on the satellite fraction correction is taken as the difference between the fractions measured at the beginning and end of fill:  $\delta f_{\text{sat},j,i} = |f_{\text{sat},j,i}^{\text{begin}} - f_{\text{sat},j,i}^{\text{end}}|$ . Assuming the uncertainties are fully correlated between both beams, the uncertainty on the cross-section related to the satellite fraction correction is taken as the sum of the average uncertainties per beam:  $\delta f_{\text{sat}} = <\delta f_{\text{sat},1,i}> + <\delta f_{\text{sat},2,i}>$  and is given as average per fill in Table 6.4. The average satellite correction uncertainty over all BGI measurements per BCID amounts to 0.06% for all  $\sqrt{s} = 8$  TeV measurements and 0.08% for  $\sqrt{s} = 2.76$  TeV.

### 6.4 Total uncertainty

Systematic uncertainties for the ghost charge (as seen in Sec. 6.2.5) are assumed to be fully correlated per beam and the final uncertainty listed in Table 6.4 is the direct sum of the systematic uncertainties for both beams. The single beam RMS is not included in Table 6.4. For the measurements taken in 2012 at  $\sqrt{s} = 8$  TeV, the average uncertainty on the ghost charge fraction, weighted by the number of measurements amounts to 0.022% and to 0.072% for the measurements taken in 2013 at  $\sqrt{s} = 2.76$  TeV.

The beam population product normalization uncertainty is driven by the DCCT measurement following the example given in Table 6.1 for fill 2855. All fills listed in Table 6.4 follow the same procedure to evaluate the beam population product uncertainty. For fills with  $\beta^* = 10$  m and  $\sqrt{s} = 8$  TeV, the average uncertainty on the beam intensity product weighted by the number of measurements amounts to 0.31% as a uniformly distributed error and 0.22% as a one standard deviation confidence level uncertainty.

**Table 6.4:** Summary of bunch population uncertainties for all fills where the BGI method was applied. Uncertainties on the beam population product normalization (measured by the DCCT as in Table 6.1) are understood as a uniformly distributed error and should be multiplied by 0.683 to be interpreted in terms of a one standard deviation confidence level. Fill 3555 was acquired with the ADC range 2 that was not blocked. The ghost charge uncertainties are described in Sec. 6.2.5 and assumed to be fully correlated between beams. The number of BGI measurements is used to weight the uncertainties when results from multiple fills are combined.

Fill	Ghost charge uncertainty (%)	Intensity product uncertainty (%)	Satellite charge uncertainty	Number of BGI measurements
2520	0.029	0.28	not av.	not used
2523	0.043	0.35	not av.	not used
2852	0.049	0.28	$9.7 \times 10^{-4}$	80
2853	0.032	0.35	$1.9 \times 10^{-4}$	64
2855	0.019	0.31	$2.1 \times 10^{-4}$	156
2856	0.020	0.31	$3.1 \times 10^{-4}$	60
3311	0.011	0.32	$1.1 \times 10^{-4}$	84
3316	0.013	0.33	$1.1 \times 10^{-4}$	102
3555	0.047	0.74	$2.3 \times 10^{-3}$	76
3562	0.062	0.38	$2.0 \times 10^{-4}$	30
3563	0.101	0.34	$2.4 \times 10^{-4}$	78

## 7 CROSS-SECTION MEASUREMENT

### 7.1 Beam-gas imaging results

Instantaneous luminosity values for each colliding bunch pair are evaluated with  $\mathcal{L} = \nu_{\text{rev}} N_1 N_2 \mathcal{O}$ , with  $N_1 N_2$  the colliding bunch pair population product as described in Sec. 6 and  $\mathcal{O}$  the overlap integral values presented in Sec. 4.6 measured with data integrated over about 20 minutes. The luminosity measurements per colliding bunch pair are used to evaluate the visible cross-section of each counter definition listed in Sec. 5.1 with

$$\sigma_{\text{ref}} = \frac{\mu_{\text{ref}} \nu_{\text{rev}}}{\mathcal{L}} = \frac{\mu_{\text{ref}}}{N_1 N_2 \mathcal{O}}, \quad (7.1)$$

where  $\mu_{\text{ref}}$  is the visible average interaction rate for a given counter, as described in Sec. 5. The *Vertex* counter is used here due to its time stability and low background. Cross-section results for the *Vertex* counter for all dedicated luminosity calibration fill in 2012 at  $\sqrt{s} = 8$  TeV with  $\beta^* = 10$  m and nominally head-on are shown in Fig. 7.1 (left) for the one-dimensional fit and (right) for the two-dimensional fit. Those results include the bunch population corrections as discussed in Sec. 6.3, the background subtraction on the rate  $\mu_{\text{ref}}$  and the  $z$ -dependence of  $\mu_{\text{ref}}$  (see Sec. 5.2). Comparing results from both fit methods clearly shows the importance to measure the beam shapes in two dimensions to take the non-factorizability of the beams into account. In both cases, the fit to the transverse bunch shapes typically have a reduced  $\chi^2 \approx 1.1$ . The one-dimensional fit has a larger statistical uncertainty when the bunch shape is nearly single Gaussian. In this case, the weight linking both Gaussian widths has a small impact on the shape and the covariance matrix used to evaluate the uncertainty is almost singular leading to a larger uncertainty. In the two-dimensional fit, the weights of both  $x$  and  $y$  axis are constrained by the factorizability parameter, stabilizing the fit and reducing the uncertainty.

The bunch shapes change over the course of a fill due to emittance growth and other factors, such as beam-beam effects, or beam position drifts (as seen in Sec. 4.6). Any change in the beam shape influence the overlap integral. Furthermore, the bunch population products decay over time, reducing the luminosity. The cross-section is a particle physics observable and its measurement, which combines those variables, must be stable over time. The time evolution of the measured cross-sections, together with the corresponding overlap integrals, rates and bunch intensity products are shown in Fig. 7.2 for one colliding bunch pair for two different fills. While the intensity product decay is typically smooth, the rate fluctuations follow the variations of the overlap integral. Time evolution measurements for fills 2852, 2853, 2856 and 3316 are shown in Fig. D.12 in Appendix D.

The measurements of cross-sections as function of time for all six colliding bunch pairs in fill 2855 are shown in Fig. 7.3. There is no systematic trend visible and the cross-section measurements are scattered around the central value. The same plots for fills 2856, 3311 and 3316 are shown in Appendix D in Figs. D.13, D.14 and D.15, respectively.

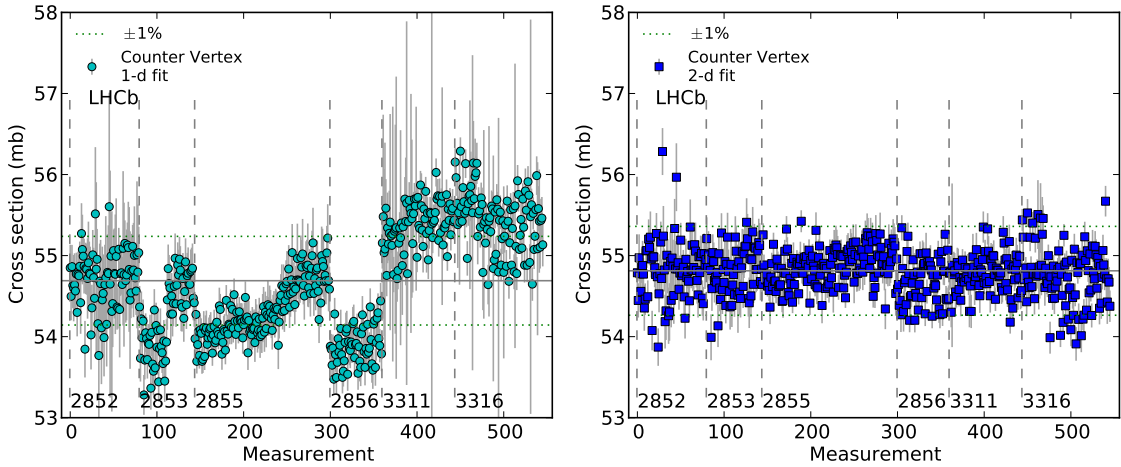


**Fig. 7.1:** Cross-section results for head-on beams with  $\beta^* = 10$  m at  $\sqrt{s} = 8$  TeV using the *Vertex* counter. Left: one-dimensional fit. Right: two-dimensional fit. Each data point is a cross-section measurement from a colliding bunch pair using integrated data over about 20 minutes. The measurements are sorted by time and BCID (using the LHC naming). The fills are indicated in the figure and are separated by a dashed vertical line. Two dotted horizontal lines indicate a  $\pm 1\%$  deviation from the central value. The error bars are the statistical uncertainty of the overlap integral.

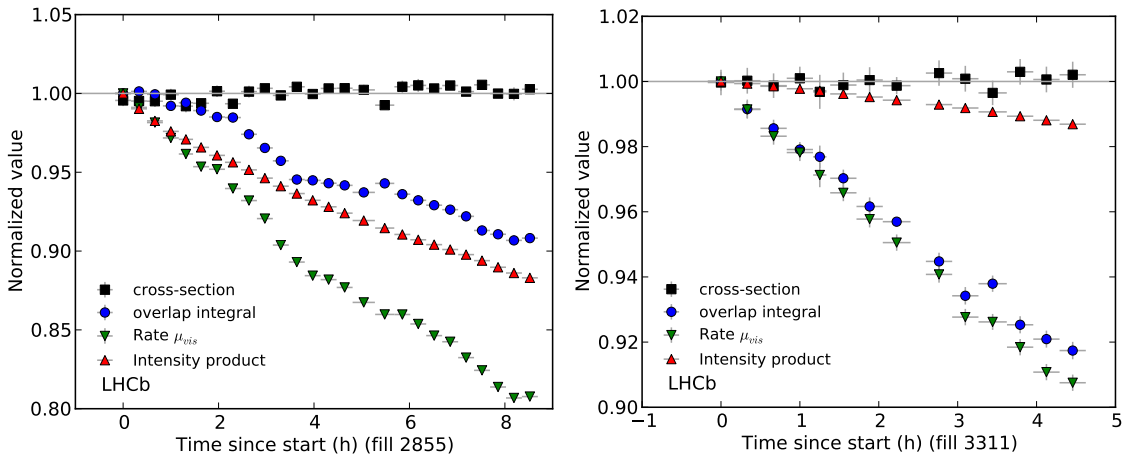


**Fig. 7.2:** Normalized cross-section and related values evolution for a colliding bunch pair. Left: first bunch pair of fill 2855 (BCID 1335). Right: first bunch pair of fill 3311 (BCID 1335). Cross-section values are normalized to their average while other parameters are normalized to the first data point. Fill 2855 lasted more than 8 hours with a beam intensity product decrease by about 10%. Fill 3311 lasted about 4h30 with a beam intensity product decrease by less than 2%; in this fill the luminosity reduction is mostly attributed to the emittance growth.

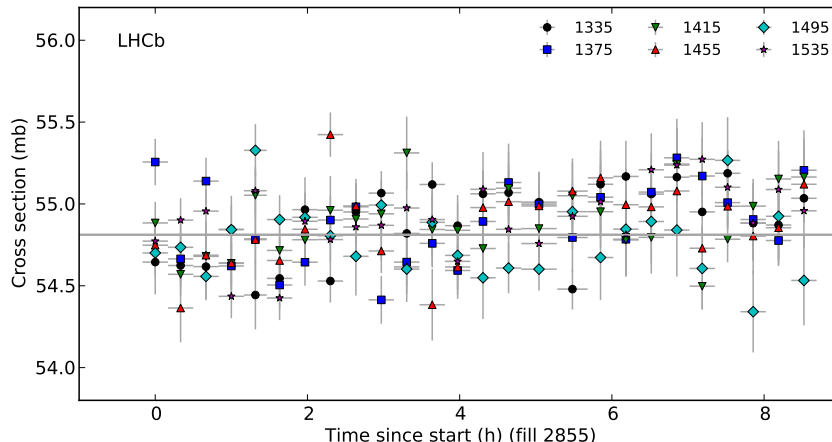


**Fig. 7.3:** Cross-section trend of the six colliding bunch pairs (indicated in the legend) for fill 2855. The central value combining all measurements and fills is shown as solid horizontal line.

### 7.1.1 FBCT non-linearity effects

Comparing the relative bunch populations measured with the FBCT and with the ATLAS beam pick-up timing system (BPTX) revealed a possible non-linearity in both instruments [48]. In the measurements presented above, a non-linearity or local curvature of the FBCT signal would be difficult to assess without low intensity bunches and with only six colliding bunch pairs in most fills. However, previous measurements showed that the non-linearity effects on the cross-section were small when all bunches have a population around  $10^{11}$  protons. Only the presence of pilot bunches next to high intensity bunches revealed a possible non-linearity [48].

Under the assumption that the FBCT has a locally linear response with respect to the bunch intensities, the presence of a curvature in the FBCT response can be described by an affine line which introduces an offset at zero bunch intensity. This offset can be inferred from the combination of all cross-sections measured during a fill. Under the supposition that the FBCT instruments have a non-zero offset  $N_1^0$  and  $N_2^0$  for beam 1 and 2, respectively, the offsets should be subtracted from the individual bunch populations  $N_{1,2}^j$  of all bunches present in a beam (denoted with indices 1, 2). The correction  $\rho_i$  per colliding bunch pair  $i$  that is applied to the cross-section can be defined as

$$\rho_i = \prod_{b=1,2} \left( \frac{N_b^i - N_b^0}{N_b^i} \cdot \frac{\sum_{j \in \mathcal{M}} N_b^j}{\sum_{j \in \mathcal{M}} (N_b^j - N_b^0)} \right), \quad (7.2)$$

where  $i$  runs over all colliding bunches at LHCb forming the set  $\mathcal{C}$ , and  $j$  runs over all bunches circulating in beam  $b = 1, 2$  forming the set  $\mathcal{M}$ . The bunch population fractions are always renormalized such that their sum is one.

For a given fill, all measured cross-sections  $\sigma_{\text{ref},i}$  are combined in a three parameter fit. The parameters are the FBCT offsets for each beam  $N_1^0$  and  $N_2^0$ , and the effective cross-section  $\sigma_{\text{eff}}$  common to all colliding bunch pairs. The fit minimizes the function

$$\chi^2 = \sum_{i \in \mathcal{C}} \frac{(\sigma_{\text{ref},i} - \sigma_{\text{eff}} \cdot \rho_i)^2}{\delta \sigma_{\text{ref},i}^2}, \quad (7.3)$$

with  $\delta \sigma_{\text{ref},i}^2$  the statistical uncertainty of each cross-section measurement, which is typically less than 0.5%, and  $\rho_i$  the correction given in Eq. (7.2).

The resulting FBCT offsets and effective cross-sections obtained with the fit are given in Table 7.1 for all 2012 fills with  $\beta^* = 10$  m. The reduced  $\chi^2/\text{ndof}$  values are typically above one and are an indication for additional systematic uncertainties not covered by the uncertainties  $\delta \sigma_{\text{ref},i}$  nor by the FBCT offsets. The effect of the FBCT offset correction on each cross-section measurement is shown in Fig. 7.4 for fill 2852 as an example. Plots for the FBCT offset correction of the remaining fills are shown in Appendix D.

All cross-section results obtained after applying the FBCT offset corrections are shown in Fig. 7.5 for fills with  $\beta^* = 10$  m and  $\sqrt{s} = 8$  TeV. While the distribution of all cross-sections has a smaller RMS of 0.48% instead of 0.54%, the central value remains essentially unchanged, as already observed in the past [48], with a deviation of 0.04%. This small correction is not applied to the final result, but is taken as systematic uncertainty related to the FBCT offset. The values in Fig. 7.5 (left) can be compared to those in Fig. 7.1 (right) to see the effect of the FBCT offset fit.

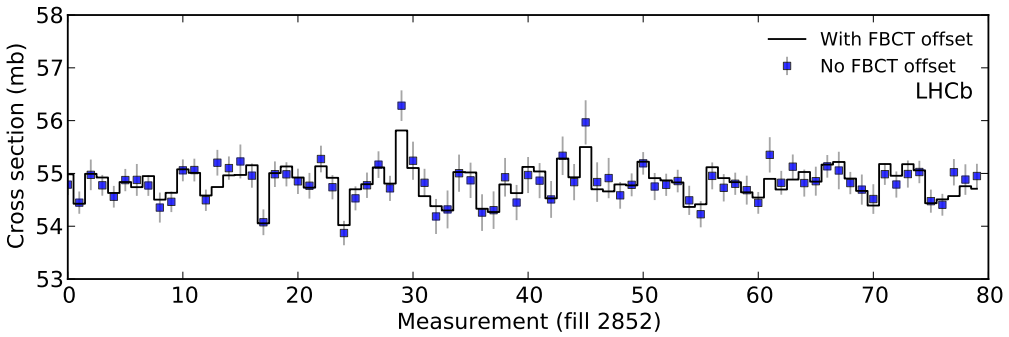


**Fig. 7.4:** Cross-section with and without FBCT offset correction for fill 2852. The data points are cross-section measurements per colliding bunch pair without FBCT offset correction. The measurements are sorted by time and BCID. The horizontal bars show the offset-corrected cross-sections.

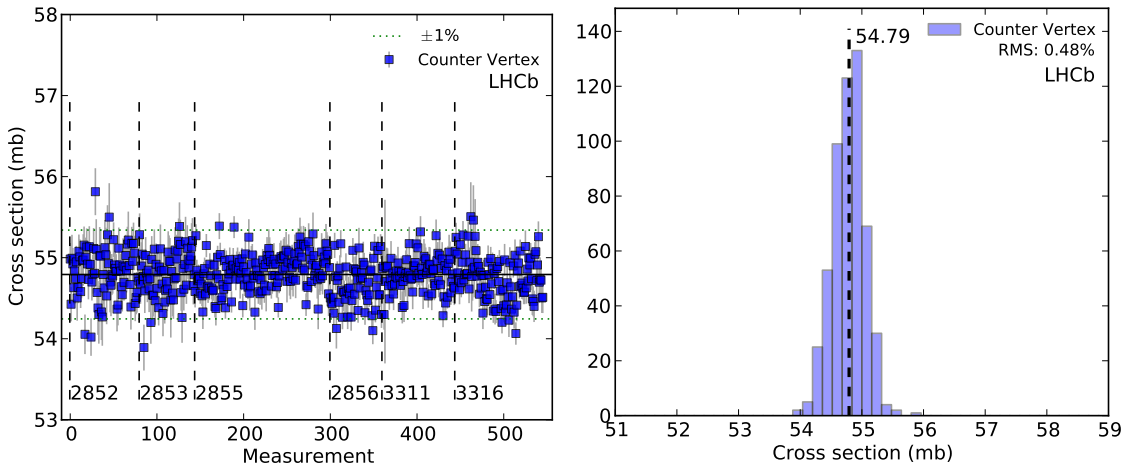


**Fig. 7.5:** Cross-section results for head-on beam periods with  $\beta^* = 10$  m fills at  $\sqrt{s} = 8$  TeV after FBCT offset correction. Left: cross-section measurement per colliding bunch pair and 20 minutes time integration. The measurements are sorted by time and BCID; the different fills are separated by a dashed vertical line and indicated in the figure. Two dotted horizontal lines show the  $\pm 1\%$  deviation from the central value. Right: histogram of all cross-section measurement from the left plot, the measurement spread is reduced from 0.54% to 0.48% after FBCT offset correction; however, the cross-section is not changed significantly by the FBCT offset fit. The median value is indicated by a dashed vertical line.

**Table 7.1:** FBCT offset results for all luminosity calibration fills at  $\sqrt{s} = 8$  TeV. The average cross-section column shows the measured average cross-section  $\pm$  the RMS per fill prior to the FBCT offset fit.

Fill	Average cross-section $\sigma_{\text{avg}}$ (mb)	Fitted cross-section $\sigma_{\text{eff}}$ (mb)	Beam 1 offset $N_1^0$ ( $\times 10^9$ charges)	Beam 2 offset $N_2^0$ ( $\times 10^9$ charges)	$\chi^2/\text{ndof}$
2852	$54.71 \pm 0.40$	$54.82 \pm 0.03$	$-1.4 \pm 0.3$	$-2.4 \pm 0.6$	$233/93 = 2.5$
2853	$54.63 \pm 0.27$	$54.79 \pm 0.03$	$-1.0 \pm 0.4$	$-1.0 \pm 0.5$	$67/61 = 1.1$
2855	$54.61 \pm 0.28$	$54.81 \pm 0.02$	$0.7 \pm 0.2$	$0.5 \pm 0.3$	$262/153 = 1.7$
2856	$54.33 \pm 0.33$	$54.65 \pm 0.02$	$-1.5 \pm 0.3$	$-0.1 \pm 0.6$	$154/57 = 2.7$
3311	$54.34 \pm 0.40$	$54.78 \pm 0.02$	$0.4 \pm 0.5$	$2.8 \pm 0.5$	$106/81 = 1.3$
3316	$54.54 \pm 0.38$	$54.72 \pm 0.02$	$2.3 \pm 0.4$	$6.5 \pm 0.7$	$233/93 = 2.5$

### 7.1.2 Factorizability of longitudinal bunch coordinate

Two periods in fills 2852 and 2853 dedicated to the BGI method were acquired with displaced beams by 180  $\mu\text{m}$  in  $y$ . The convolved bunch length  $\sigma_{z1}^2 + \sigma_{z2}^2$  measured during those fills is shown in Fig. 7.6. Periods where the beams were offset show the same  $\sigma_{z1}^2 + \sigma_{z2}^2$  values as when the beams

were head-on.

The beams had a double Gaussian transverse shape during those fills with a narrow Gaussian width ranging from 40 to 80  $\mu\text{m}$ , and a wide component of about 100  $\mu\text{m}$  or more. With a displacement of 180  $\mu\text{m}$ , the luminosity is dominated by the interaction of the wide beam components of both beams. On the other hand, the luminosity would be dominated by the interaction of the narrow beam components when the beams would collide head-on. The convolved bunch length values being unchanged for head-on and offset collisions, is an indication that the wide and narrow bunch components share the same length. It indicates that the  $z$  coordinate is factorizable, as is assumed for the BGI measurement.

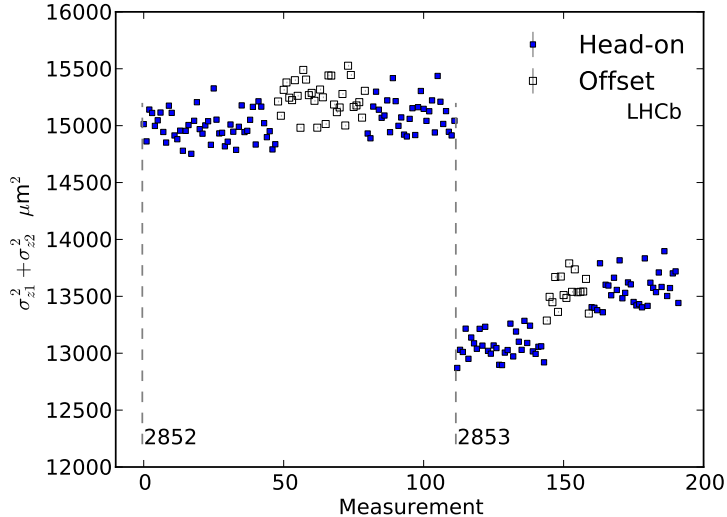


**Fig. 7.6:** Measurement of convolved bunch length  $\sigma_{z1}^2 + \sigma_{z2}^2$  with displaced beam during fills 2852 and 2853. The fills are indicated in the plot and denoted by a dashed vertical line. The measurements are sorted by time and BCID. About 3.5 hours separate the first head-on period in fill 2853 from the offset period explaining the higher values observed during offset. The next head-on period is adjacent.

Assuming that the wide bunch components can have a larger convolved bunch length by 10% in the other fills, the effect on the cross-section is estimated as follows. The beams are non-factorizable for those fills and the overlap integral is therefore composed of four contributions, namely

$$\begin{aligned} \mathcal{O}_d = & w_{nn,1} w_{nn,2} \cdot \mathcal{O}(\sigma_{x1n}, \sigma_{y1n}, \sigma_{x2n}, \sigma_{y2n}) \\ & + w_{nn,1} w_{ww,2} \cdot \mathcal{O}(\sigma_{x1n}, \sigma_{y1n}, \sigma_{x2w}, \sigma_{y2w}) \\ & + w_{ww,1} w_{nn,2} \cdot \mathcal{O}(\sigma_{x1w}, \sigma_{y1w}, \sigma_{x2n}, \sigma_{y2n}) \\ & + w_{ww,1} w_{ww,2} \cdot \mathcal{O}(\sigma_{x1w}, \sigma_{y1w}, \sigma_{x2w}, \sigma_{y2w}), \end{aligned} \quad (7.4)$$

using the nomenclature defined in Sec. 4.6. To estimate the impact of the larger convolved bunch length of the wider component, all overlap integrals have been re-evaluated with a scaling of 1.1 applied to the  $\sigma_{z1}^2 + \sigma_{z2}^2$  values in the last line in Eq. (7.4), which is the partial overlap integral attributed to the wide bunch component. The observed difference of 0.05% in the cross-section is taken as systematic uncertainty related to the convolved bunch length  $\sigma_{z1}^2 + \sigma_{z2}^2$  measurement.

### 7.1.3 Correlation checks

Some structure remains visible in the measurement shown in Fig. 7.5 (left) pointing towards additional systematic uncertainties or a less than perfect bunch shape description. Correlations between the cross-sections and the major variables entering into the cross-section measurement

have been checked. Correlations with the interaction rate and bunch population product are shown in Fig. 7.7 for all fills with  $\beta^* = 10$  m. While a linear fit to all data points is not fully compatible with zero, a possible correlation with those variables is negligible. Furthermore, some fills have an inverted correlation compared to others. Correlations with the overlap integral and luminous region  $z$ -position are shown in Fig. 7.8 and are compatible with zero. Correlations with the crossing angle corrections are shown in Fig. D.18 in Appendix D.

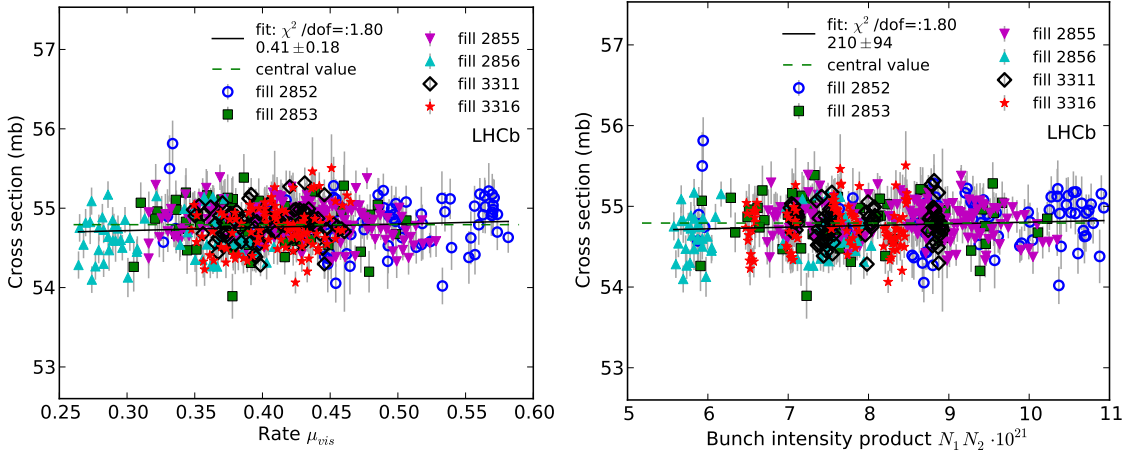


**Fig. 7.7:** Left: cross-section correlation with the average interaction rate per crossings  $\mu_{\text{ref}}$ . Right: cross-section correlation with the bunch intensity product  $N_1 N_2$ . The central value is indicated as dashed horizontal line. A straight line fit through all data points is shown as solid black line.

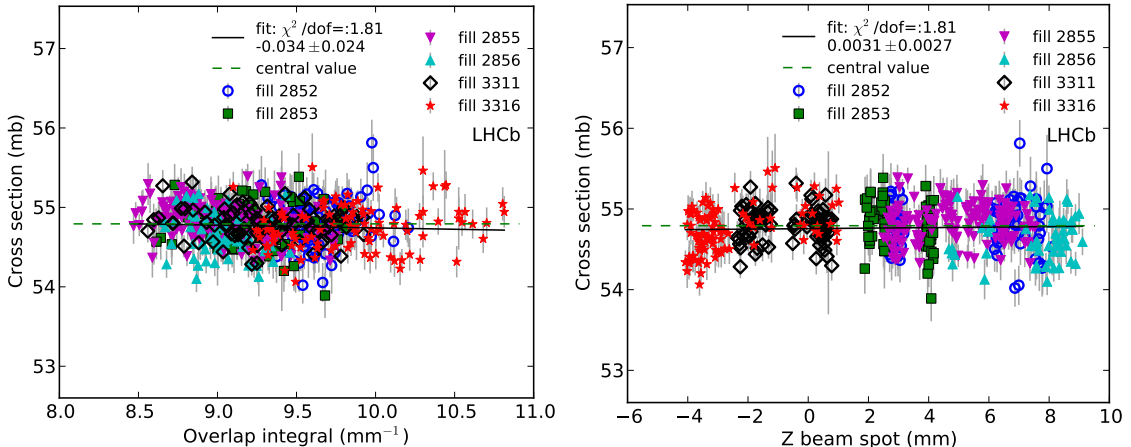


**Fig. 7.8:** Left: cross-section correlation with the overlap integral. Right: cross-section correlation with the luminous region  $z$ -center. The central value is indicated as dashed horizontal line. A straight line fit through all data points is shown as solid black line.

## 7.2 Systematic uncertainties

### 7.2.1 Beam-beam vertex resolution

The impact of the beam-beam interaction vertex resolution on the cross-section depends on the transverse size of the luminous region. Comparing the results obtained with different ratios of the resolution to the luminous region size permits the evaluation of the systematic uncertainty related to the resolution measurement. The measurement of the luminous region width can be biased by an effect not directly related to the resolution. For example, a mis-alignment in the VELO sensors would correlate the position of both split vertices (see resolution Sec. 4.3) and broaden the beam

without affecting the measured resolution. Considering head-on beams by setting  $\Delta_x = \Delta_y = 0$  in Eq. 3.16 from Sec. 3, one sees that

$$\mathcal{L} \propto \frac{1}{\Sigma_x \Sigma_y}, \quad (7.5)$$

with the definitions

$$\begin{aligned} \Sigma_x^2 &= 2\sigma_z^2 \sin^2 \phi + 2\sigma_x^2 \cos^2 \phi \\ \Sigma_y^2 &= 2\sigma_y^2 \\ 2\sigma_x^2 &= \sigma_{x_1}^2 + \sigma_{x_2}^2 \\ 2\sigma_y^2 &= \sigma_{y_1}^2 + \sigma_{y_2}^2 \\ 2\sigma_z^2 &= \sigma_{z_1}^2 + \sigma_{z_2}^2. \end{aligned} \quad (7.6)$$

The quantities  $\sigma_{xj}$ ,  $\sigma_{yj}$ ,  $\sigma_{zj}$  for beam  $j = 1, 2$  are the physical beam sizes after resolution deconvolution. The luminous region widths  $\sigma_{lx,y}$  in the coordinates  $x$  and  $y$ , respectively, are related to the single beam widths by

$$\frac{1}{\sigma_{lx}^2} = \cos^2 \phi \left( \frac{1}{\sigma_{x_1}^2} + \frac{1}{\sigma_{x_2}^2} \right) \quad \text{and} \quad \frac{1}{\sigma_{ly}^2} = \frac{1}{\sigma_{y_1}^2} + \frac{1}{\sigma_{y_2}^2}. \quad (7.7)$$

Assuming equal beam sizes for both beams  $\left| \frac{\sigma_{m1} - \sigma_{m2}}{(\sigma_{m1} + \sigma_{m2})/2} \right| \ll 1$ , this leads to

$$\Sigma_x^2 = 2\sigma_z^2 \sin^2 \phi + 4\sigma_{lx}^2 \quad \text{and} \quad \Sigma_y^2 = 4\sigma_{ly}^2. \quad (7.8)$$

The presence of an additional factor  $k$  scaling the beam-beam resolution would bias the measured beam widths and the  $\Sigma_{x,y}$  values. With  $\Sigma'_{x,y}$  and  $\sigma'_{x,y}$  defined as the biased measurements of  $\Sigma_{x,y}$  and  $\sigma_{x,y}$ , respectively, and  $\sigma_{\text{res},lx,y}^2$  the beam-beam resolutions, the biased luminous region width can be written as

$$\sigma'_{lm}^2 = \sigma_{lm}^2 + k \sigma_{\text{res},lm}^2 \quad (7.9)$$

for the axis  $m = x, y$ . The widths  $\sigma'_{lm}^2$  are the luminous region sizes after resolution deconvolution and the term  $k \sigma_{\text{res},lm}^2$  takes the non-perfect deconvolution into account. With Eq. (7.9) and Eq. (7.8), the unbiased  $\Sigma_{x,y}$  values can be expressed in terms of

$$\Sigma_x^2 = 2\sigma_z^2 \sin^2 \phi + 4(\sigma'_{lx}^2 - k \sigma_{\text{res},lx}^2) \quad \text{and} \quad \Sigma_y^2 = 4(\sigma'_{ly}^2 - k \sigma_{\text{res},ly}^2). \quad (7.10)$$

Eq. (7.10) can be transformed to

$$\Sigma_x^2 = 4\sigma'_{lx}^2 \left( 1 - \frac{k \sigma_{\text{res},lx}^2}{\sigma'_{lx}^2} + \frac{2\sigma_z^2 \sin^2 \phi}{4\sigma'_{lx}^2} \right) \quad \text{and} \quad \Sigma_y^2 = 4\sigma'_{ly}^2 \left( 1 - \frac{k \sigma_{\text{res},ly}^2}{\sigma'_{ly}^2} \right). \quad (7.11)$$

The  $x$  and  $y$  indices denote the axes. For small values of  $k$  and of  $\frac{\sigma_z^2 \sin^2 \phi}{2\sigma'_{lx}^2}$ ,<sup>1</sup> the  $\Sigma_{x,y}$  values can be expressed to first order with

$$\Sigma_x \approx 2\sigma'_{lx} \left( 1 - \frac{k \sigma_{\text{res},lx}^2}{2\sigma'_{lx}^2} + \frac{\sigma_z^2 \sin^2 \phi}{4\sigma'_{lx}^2} \right) \quad \text{and} \quad \Sigma_y \approx 2\sigma'_{ly} \left( 1 - \frac{k \sigma_{\text{res},ly}^2}{2\sigma'_{ly}^2} \right). \quad (7.12)$$

The biased  $\Sigma'_{x,y}$  values are inferred from Eq. (7.8) by substituting the unbiased widths  $\sigma_{lx,y}^2$  with the biased widths  $\sigma'_{lx,y}^2$ . As for Eq. (7.12), the first order approximation of  $\Sigma'_{x,y}$  are given by

$$\Sigma'_x \approx 2\sigma'_{lx} \left( 1 + \frac{\sigma_z^2 \sin^2 \phi}{4\sigma'_{lx}^2} \right) \quad \text{and} \quad \Sigma'_y = 2\sigma'_{ly}. \quad (7.13)$$

<sup>1</sup>With  $\sigma_z \approx 80$  mm,  $\phi \approx 450$   $\mu$ rad,  $\sigma'_{lx} \approx 60$   $\mu$ m one get  $\frac{\sigma_z^2 \sin^2 \phi}{2\sigma'_{lx}^2} \approx 0.2$ .

The ratio of the  $\Sigma_{x,y}$  values to the biased  $\Sigma'_{x,y}$  values is then given by

$$\frac{\Sigma_x}{\Sigma'_x} = 1 - \frac{2k \sigma_{\text{res},lx}^2}{4\sigma_{lx}^{\prime 2} + \sigma_z^2 \sin^2 \phi} \quad \text{and} \quad \frac{\Sigma_y}{\Sigma'_y} = 1 - \frac{k \sigma_{\text{res},ly}^2}{2\sigma_{ly}^{\prime 2}}. \quad (7.14)$$

Substituting  $\frac{\Sigma_x}{\Sigma'_x} = 1 - \epsilon_x$  and  $\frac{\Sigma_y}{\Sigma'_y} = 1 - \epsilon_y$  in (7.14), the ratio between the visible cross-section  $\sigma_{\text{ref}}$  and its resolution biased value  $\sigma'_{\text{ref}}$  can be expressed as

$$\frac{\sigma_{\text{ref}}}{\sigma'_{\text{ref}}} = (1 - \epsilon_x)(1 - \epsilon_y) \approx 1 - \epsilon_x - \epsilon_y \quad \text{or} \quad \frac{\sigma'_{\text{ref}}}{\sigma_{\text{ref}}} \approx 1 + \epsilon_x + \epsilon_y. \quad (7.15)$$

It follows that

$$\frac{\sigma'_{\text{ref}}}{\sigma_{\text{ref}}} - 1 \approx k \left( \frac{2\sigma_{\text{res},lx}^2}{4\sigma_{lx}^{\prime 2} + \sigma_z^2 \sin^2(\phi_x)} + \frac{\sigma_{\text{res},ly}^2}{2\sigma_{ly}^{\prime 2}} \right) = k \cdot R. \quad (7.16)$$

The quantity

$$R = \left( \frac{2\sigma_{\text{res},lx}^2}{4\sigma_{lx}^{\prime 2} + \sigma_z^2 \sin^2(\phi_x)} + \frac{\sigma_{\text{res},ly}^2}{2\sigma_{ly}^{\prime 2}} \right) \quad (7.17)$$

is representative of the importance of the beam-beam resolution in the cross-section measurement. A value of  $R = 0$  means that the resolution is negligible compared to the beam size. A value  $k = 0$  in Eq. (7.16) indicates that the result is independent of the value of  $R$ , i.e. the result does not depend on the average resolution corresponding to the selection made. A dependence of the cross-section with  $R$  is therefore a direct indication of the presence of factors affecting the beam shape that are not taken into account with the resolution deconvolution.

Measurements with different  $R$  values are obtained by using different cuts on the vertex track multiplicity and by using data acquired with a  $\beta^*$  of 3 and 10 m. All cross-section measurements are performed with 3 vertex track multiplicity cuts on both beam-gas and beam-beam vertices in order to perform a BGI analysis with different resolutions. The three cut selections are listed in Table 7.2 for beam-gas and beam-beam interaction vertices. The full data sample is split into two roughly equal size samples, one with a low track multiplicity and therefore larger resolution and one with a high track multiplicity and consequently a lower resolution. The analysis is also performed with the full data sample to provide a measurement with an intermediate resolution value. For every measurement, the resolution is unfolded.

The luminous region has about 20 times more vertices than the single beam distributions. Accordingly, the cross-section measurements are dominated by the constraints imposed by the beam-beam distributions and by the beam-beam resolution.

**Table 7.2:** Track multiplicity cuts used to change the resolution. Vertices are selected based on the track sum of both split vertices. The approximate weighted resolution is provided as indication.

Selection	Beam-gas vertices		Beam-beam vertices	
	Cut criteria	Weighted resolution	Cut criteria	Weighted resolution
Low track multiplicity	$10 < \sum_{i=1,2} N_{\text{Tr},i} < 16$	$\approx 50 \mu\text{m}$	$10 < \sum_{i=1,2} N_{\text{Tr},i} < 28$	$\approx 28 \mu\text{m}$
All vertices	$\sum_{i=1,2} N_{\text{Tr},i} > 10$	$\approx 46 \mu\text{m}$	$\sum_{i=1,2} N_{\text{Tr},i} > 10$	$\approx 21 \mu\text{m}$
High track multiplicity	$\sum_{i=1,2} N_{\text{Tr},i} \geq 16$	$\approx 41 \mu\text{m}$	$\sum_{i=1,2} N_{\text{Tr},i} \geq 28$	$\approx 15 \mu\text{m}$

Cross-section measurements performed with the three track multiplicity cuts listed above and for the six fills with  $\beta^* = 10 \text{ m}$  and two fills with  $\beta^* = 3 \text{ m}$  are combined in Fig. 7.9. Measurements

performed with the larger  $\beta^* = 10$  m and the best resolution (high track multiplicity cut) provide the smallest  $R$  value, while a larger resolution combined with the smaller  $\beta^* = 3$  m results in a larger  $R$  value. The clear correlation between the cross-section and the  $R$  value visible in Fig. 7.1 is an indication that the resolution is not perfectly understood.

The leftmost group of data points are the results presented in (right) Fig. 7.1. Those results are obtained with the high track multiplicity cut that offer the best resolution and with a  $\beta^* = 10$  m beam optics. This combination provides the best measurement conditions and those measurements, called here  $\sigma_c$  are used as central value in the final results. The cross-section  $\sigma_e$  obtained by extrapolating the cross-section to  $R = 0$  based on the  $\beta^* = 10$  m fills with the low and high track multiplicity cuts (blue and magenta leftmost measurement groups) is used to evaluate the uncertainty. The difference of  $\Delta\sigma = \sigma_c - \sigma_e = 0.93\%$  between the central value  $\sigma_c$  and the extrapolated value  $\sigma_e$  is taken as systematic uncertainty due to the beam-beam resolution. The fills with  $\beta^* = 3$  m confirm the findings with  $\beta^* = 10$  m but are not used otherwise.

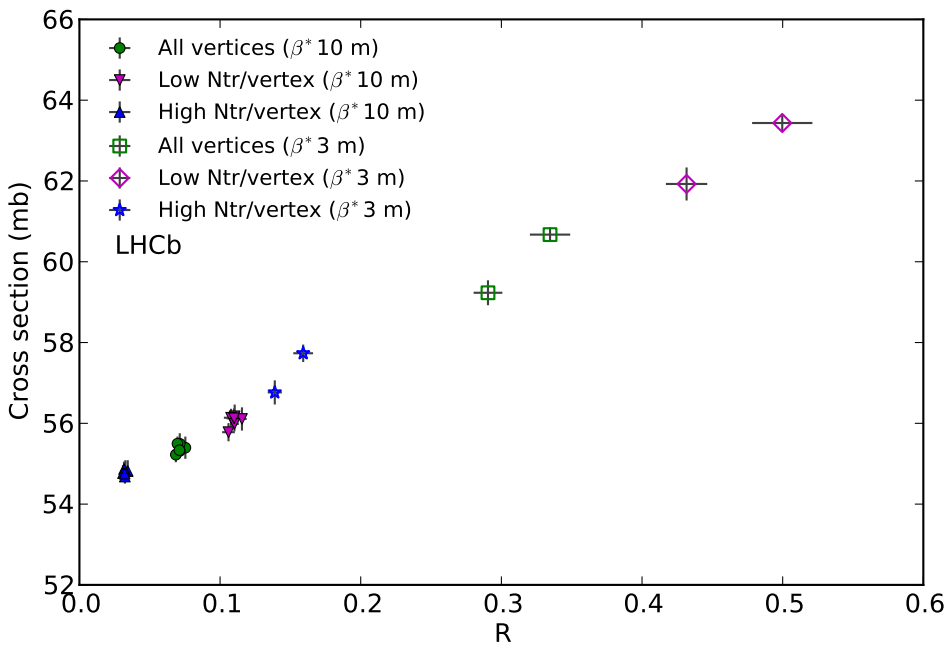


**Fig. 7.9:** Cross-section dependence on beam-beam resolution compared to the squared ratios of the resolution and luminous region width. The  $R$  parameter is calculated with Eq. (7.17). Each data point is an average of all measurements from a fill. The error bars are the RMS of the cross-section and  $R$  values per fill. Plain markers are measurements performed with  $\beta^* = 10$  m (6 fills) and open markers are performed with  $\beta^* = 3$  m (2 fills). Note that the data points including all vertices contain data from both the low and high track multiplicities.

### 7.2.2 Beam-gas vertex resolution

As discussed in Sec. 4.3.3.2, a set of correction factors to the beam-gas interaction vertex resolution have been measured to take unseen correlations between split vertices into account. While the resolution appears to be well measured with enough statistics, the necessity to include correction factors to reach consistent beam width measurements at different  $z$ -positions is an indication of additional systematic uncertainties. Conservatively assuming 100% uncertainty on the correction factors, the overlap integrals have also been measured without any beam-gas resolution correction factor. Results of cross-section measurements performed with and without correction factors are shown in Fig. 7.10 for all  $\beta^* = 10$  fills. The full difference of 0.55% is taken as systematic uncertainty due to the beam-gas interaction vertex resolution.

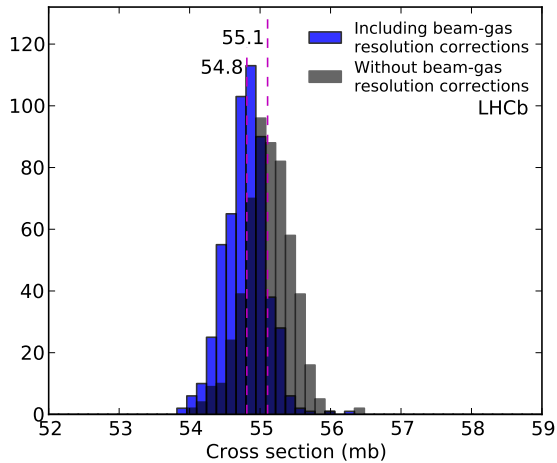


**Fig. 7.10:** Cross-sections measured with and without beam-gas resolution correction factors. Dashed vertical lines indicate the median value of the measurements.

### 7.2.3 Measurement spread

Measurements of cross-sections for all 2012 colliding bunch pairs with  $\beta^* = 10$  m are shown in Fig. 7.11 (left) as histogram. The measurement spread has an RMS of 0.54% with the *Vertex* counter. Cross-section results per fill are shown in Fig. 7.11 (right); the indicated error is the RMS of all measurements of the corresponding fill. The statistical uncertainty per colliding bunch pair measurement being typically less than 0.5%, the observed spread of 0.54% is due to the statistical fluctuations and also includes additional systematic effects such as the non-perfect bunch shape description.

Conservatively, the full RMS is taken as systematic uncertainty on the cross-section. This uncertainty covers uncorrelated bunch-by-bunch uncertainties such as the shape description, which is influenced by the fit model and detector resolutions, or the FBCT bunch population measurements.

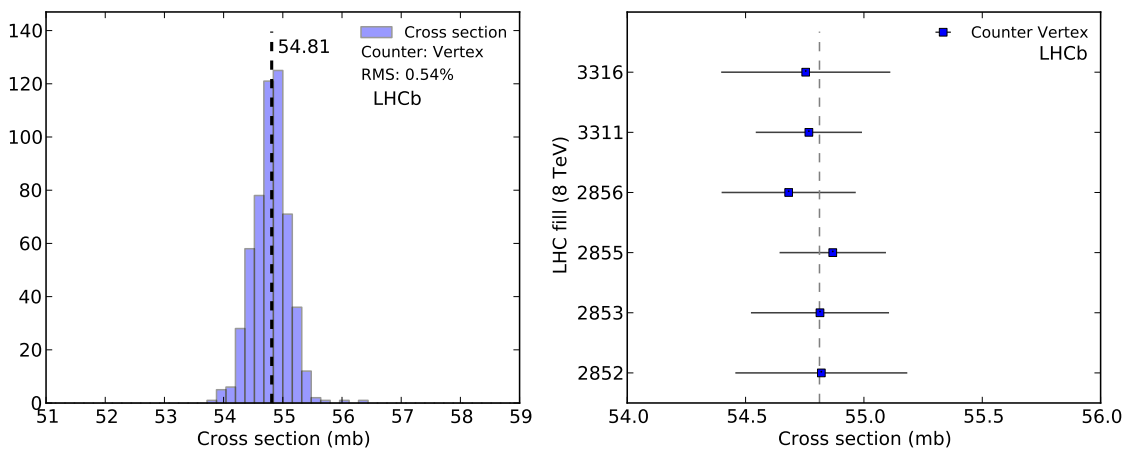


**Fig. 7.11:** Cross-section overview for head-on periods with  $\beta^* = 10$  m fills at  $\sqrt{s} = 8$  TeV showing the same data as in Fig. 7.1 (right). The dashed vertical line indicate the median value of all measurements. Left: results presented as histogram combining all data from Fig. 7.1 (right). Right: central value of cross-sections per fill for the same data as shown on the left plot. The error bar is the standard deviation of all measurements from a fill. The statistical uncertainty of each average is smaller than the marker.

### 7.2.4 Detector alignment and crossing angle

The alignment of the VELO detector can correlate the split vertices and degrade the vertex resolution and also broaden the beam image width. Those two effects are covered by the resolution systematic uncertainties seen above (Sec. 7.2.1 and 7.2.2). However, the detector alignment can also affect the crossing angle measurement which is an important observable for the evaluation of the overlap integral. Various detector alignments have been produced and tested using data from fill 2520 with the goal to improve the overall alignment for beam-gas events (see Appendix C). A set of 47 different alignments have been selected all of which provide acceptable and comparable results in the overall alignment quality. The same raw dataset has been reconstructed with all alignments and the half crossing angle measurements performed with those selected alignments are shown in left Fig. 7.12 in a histogram. The difference between the main peaks in the histogram is about 10  $\mu\text{rad}$  which is about ten times larger than the statistical uncertainty. The expected uncertainty on the luminosity due to the crossing angle correction for the single Gaussian case can be expressed as

$$\frac{d\mathcal{L}}{\mathcal{L}} = \frac{d\mathcal{O}}{\mathcal{O}} = \frac{1}{\mathcal{O}} \frac{\partial \mathcal{O}}{\partial \phi_x} d\phi_x = -\frac{(\sigma_{z1}^2 + \sigma_{z2}^2) \cos^{-2}(\phi_x) \tan(\phi_x)}{(\sigma_{x1}^2 + \sigma_{x2}^2) \left(1 + \frac{(\sigma_{z1}^2 + \sigma_{z2}^2)}{\sigma_{x1}^2 + \sigma_{x2}^2} \tan^2(\phi_x)\right)} d\phi_x. \quad (7.18)$$

The crossing angle uncertainty on the  $y$  axis is about 3  $\mu\text{rad}$  and has a negligible impact on the luminosity uncertainty due to the zero angle in this plane. Equation (7.18) is plotted in Fig. 7.12 (right) for various angle uncertainties  $d\phi$  and typical beam parameters as observed in 2012. The relative uncertainty on the overlap integral is plotted against the crossing angle  $\phi_x$ . A systematic uncertainty of about 0.35% is to be expected with a crossing angle of about 500  $\mu\text{rad}$  and with an uncertainty of 10  $\mu\text{rad}$  in the crossing angle. However, this uncertainty also depends on the bunch width and length and is different for each bunch pair.

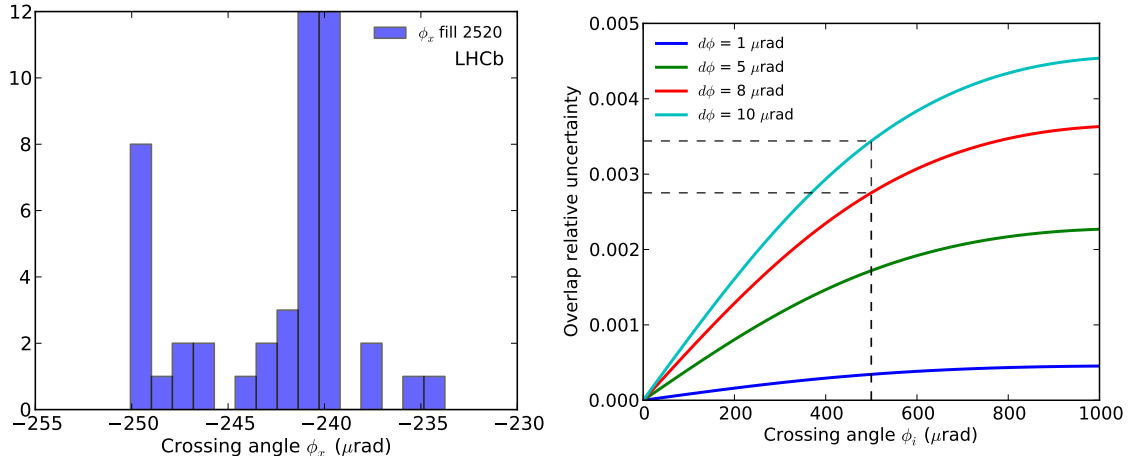


**Fig. 7.12:** Effect of detector alignment on crossing angle and overlap uncertainty. Left: different detector alignments result in different crossing angle measurements with the same data. Right: assuming a crossing angle uncertainty of 8 to 10  $\mu\text{rad}$  results in an overlap relative uncertainty of about 0.3% using beam conditions similar to July 2012.

A dedicated VELO alignment is used for all luminosity calibration fills in 2012 and is different from the default one used for physics analyses. One acquisition run containing about an hour of data has also been reconstructed with the default alignment to evaluate the systematic uncertainty directly related to the alignment. The ratio of the overlap integral results between the overlaps measured with the dedicated alignment and the default alignment is shown in Fig. 7.13. The left panel shows the ratio of the overlap integral, while the right panel shows the ratio of the overlap integral without crossing angle correction, that is, only the transverse beam shape and offset enters in the overlap

integral evaluation. The three different markers denote the different track multiplicity cuts that affect the resolution (discussed in Sec. 7.2.1). The difference between both alignments is due to the crossing angle correction only and the alignment does not affect the bunch shape directly. The full difference of 0.45% between both alignments is taken as systematic uncertainty related to the VELO alignment.

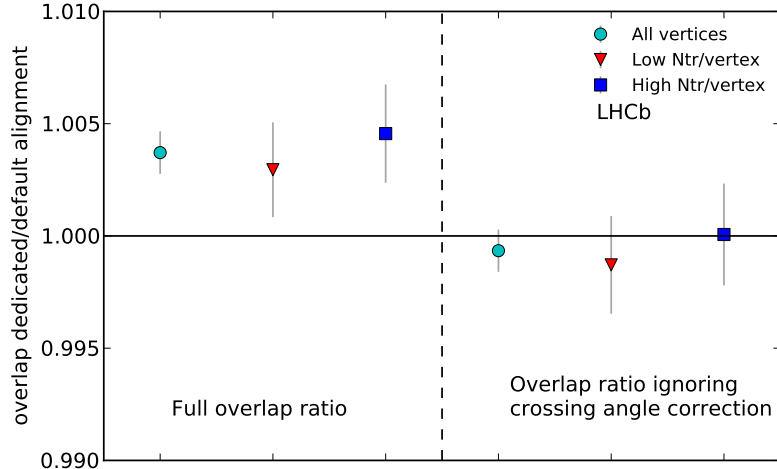


**Fig. 7.13:** Overlap integral difference using two different alignments with the same data. The left half-panel shows the overlap integral ratio of the overlap measured with the dedicated alignment over the overlap measured with the default alignment. Here the dedicated alignment shows a larger overlap integral by 0.45%. The right half-panel shows the same ratio but ignoring the crossing angle correction.

### 7.2.5 Fit model

The bunch shapes observed throughout 2012 and 2013 are different, ranging from a strongly double Gaussian shape to single Gaussian-like shape. Furthermore, bunches observed in November 2012 require a negative component to describe the lower peak of the distribution. The fit model used to describe the bunch shapes uses a double Gaussian function in  $x$  and  $y$  with an additional parameter to describe the factorizability of both axes. In addition, the narrow Gaussian component can have a negative weight. While this model can describe all observed bunch shapes with a  $\chi^2/\text{dof}$  close to one, the accuracy of the fit procedure as well as the capacity to describe different shapes has been verified with generic Monte-Carlo simulations. The simulation procedure developed to test the BGI method as described in Sec. 4.5 is used to generate datasets of vertex distributions with different shape models.

The simulation tests are twofold: first, to test the capability of the binning and fitting procedure to measure beam parameters generated with a double or single Gaussian model, including double Gaussian shape with a negative component. In those cases, the fit model is the same as the Monte-Carlo model used to create the datasets. Second, to evaluate the systematic uncertainty arising from fitting a non-double Gaussian shape with the double Gaussian model.

A given set of beam parameters is generated 10 times in statistically independent datasets, each of which is measured using the same algorithms as for real data. The true overlap integral from Monte-Carlo datasets is either evaluated analytically as described in Sec. 3 and Sec. 4.6 for double Gaussian shapes, or numerically with Eq. (4.44). The ratios between the true Monte-Carlo overlap integrals and the measured overlap integrals for different shapes are shown in Fig. 7.14. Each point is an average of 10 datasets with identical input parameters, the indicated error is the standard deviation of the measurements. Identical markers share a similar shape family (single, double or triple Gaussian for example) and are indicated in the legend. However, each marker represents datasets with different beam parameters. The beam parameters used to create each dataset, which

are referenced by the simulation set number, are listed in Table E.1 for the single and double Gaussian shapes, in Table E.2 for the triple Gaussian shapes and in Table E.3 for the super Gaussian shapes in Appendix E.

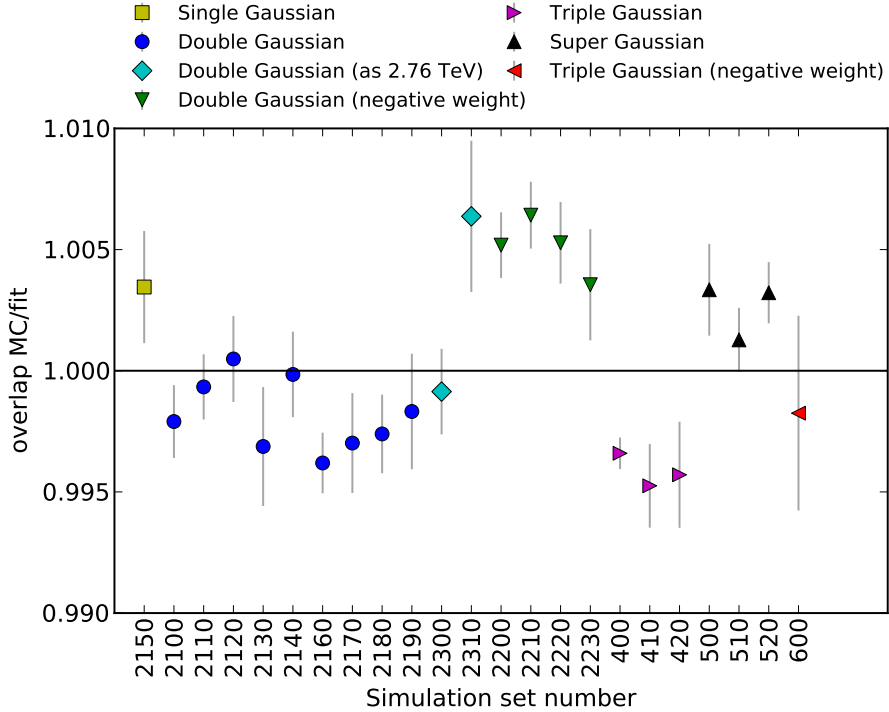


**Fig. 7.14:** Evaluation of double Gaussian fit model applied to different simulation sets. The comparison is done on the basis of the overlap integral. Each point is an average of overlap integral ratios between ten simulation sets measurements compared to their theoretical value. Each of the ten simulation set is statistically independent but generated with the same beam parameters. Identical markers share a common general shape but have different input parameters. The parameters of the different simulation sets are provided in Tables E.1, E.2 and E.3.

The triple Gaussian beam shape is defined as the sum of normalized Gaussian distributions  $g(x; \xi, \sigma)$  for the direction  $x$  and with mean  $\xi$  and width  $\sigma$ , the distribution is defined as

$$\rho_x(x; \xi_x, \sigma_{x,n}, \sigma_{x,m}, \sigma_{x,w}) = w_n g(x, \xi_x, \sigma_{x,n}) + w_m g(x, \xi_x, \sigma_{x,m}) + (1 - w_n - w_m) g(x, \xi_x, \sigma_{x,w}), \quad (7.19)$$

with  $\sigma_{x,n}$ ,  $\sigma_{x,m}$  and  $\sigma_{x,w}$  the narrow, medium and wide widths and  $w_n$  and  $w_m$  the weight of the narrow and medium Gaussian components, respectively. All Gaussian widths share the same mean  $\xi_x$ . Simulated datasets with a triple Gaussian shape are similar to the double Gaussian shape and assume fully non-factorizable beams ( $f_j = 0$ ) as observed in the data. For the case of triple Gaussian beams with negative component, the narrow width has a negative weight.

Simulated datasets with super Gaussian shapes are meant to reproduce bunch shapes observed in November 2012 where the transverse shape is Gaussian-like, but the peak of the distribution is lower than that predicted by a single Gaussian function. The super Gaussian function [59] adds a value  $\epsilon$  to the power two exponent of the normal Gaussian and is described by

$$sg(x; \mu, \sigma, \epsilon) = A e^{-\frac{1}{2} \left( \frac{|x-\mu|}{\sigma} \right)^{2+\epsilon}}. \quad (7.20)$$

The normalization factor  $A$  in Eq. (7.20) is given by

$$A = \frac{2^{-\frac{3+\epsilon}{2+\epsilon}}}{\sigma \Gamma \left( 1 + \frac{1}{2+\epsilon} \right)}, \text{ with the gamma function } \Gamma(z) = \int_0^\infty t^{z-1} e^{-t} dt. \quad (7.21)$$

All shapes shown in Fig. 7.14 are measured with a  $\chi^2$  per degree of freedom close to one and can be considered as well described by the fit model. In light of the different simulation results presented in Fig. 7.14, a systematic uncertainty of 0.5% is taken as uncertainty related to the fit model and fit accuracy.

### 7.2.6 Bunch length and reconstruction efficiency

As described in Sec. 4.4.4, the convolved bunch length  $\sigma_{z1}^2 + \sigma_{z2}^2$  and bunch crossing position  $Z_{\text{RF}}$  are measured with a fit to the longitudinal distribution of the luminous region. For each colliding bunch pair measurement, all vertices in the range  $|z| < 250$  mm are selected, regardless of the track directions. This selection reduces the effect of the  $z$ -dependence in the VELO aperture, and limits the distortion of the luminous region shape. On the other hand, some beam-gas interaction vertices can be included in the distribution.

An additional measurement of  $\sigma_{z1}^2 + \sigma_{z2}^2$  and  $Z_{\text{RF}}$  is performed by requiring asymmetric tracks on each vertex entering the luminous region vertex distributions as to exclude beam-gas interactions. The luminous region distribution is based on vertices with at least two forward and two backward tracks per vertex. This requirement excludes any beam-gas background in the luminous region distribution but distorts its longitudinal shape as backward tracks with an origin  $z \gtrsim -95$  mm are not detected by the VELO. The reconstruction efficiency  $\epsilon_v$  corresponding to this requirement is shown in left Fig. 7.15 and is used to correct the raw distribution as seen in Sec. 4.4.4. An example of a fit to the longitudinal luminous region distribution with the assymetric track requirement is shown in Fig. 7.15 (right) for BCID 1335 in fill 2855 (same BCID and period as shown in Fig. 4.29 in Sec. 4.4.4). All cross-section measurements have been measured with both track requirements. The difference between the methods is 0.04% and is taken as systematic uncertainty related to the reconstruction efficiency.

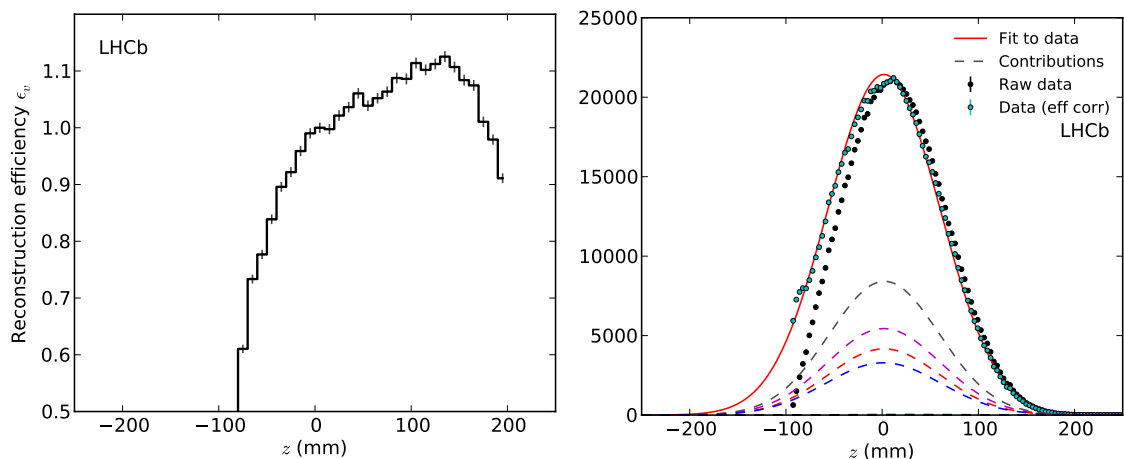


**Fig. 7.15:** Left: vertex reconstruction efficiency as function of  $z$  requiring at least two forward and two backward tracks per vertex. The 100% efficiency is set at  $z = 0$  to keep similar amplitudes between the raw and corrected data; however, the absolute scale of the correction does not change the fit results. Right: Fit of the longitudinal vertex distribution of a colliding bunch pair after efficiency correction. The raw data (black dots) shows a distortion resulting from requiring backward tracks.

### 7.2.7 Additional checks

#### 7.2.7.1 Description of distribution tails

The double Gaussian fit model used to describe the transverse bunch shapes does not allow a description of a possible third component. For example a fraction of the protons measured in a bunch could be present in a wider Gaussian shape that would not be measured with a double Gaussian function. In this case, the tails of the measured distributions would have a larger population fraction than expected.

The fraction of vertices in the tails beyond the double-sided 99 percentile predicted by the fit, is shown in Fig. 7.16 (left) for all measurements with  $\beta^* = 10$  m and (right) for simulated datasets. The measured distributions have a larger population in the tails of the distribution than expected. The tail population is about 2% for the single beams and about 1.5% for the luminous region, while 1% is expected. This higher than expected tail population, however, is also observed when fitting the simulated datasets with comparable fractions, indicating that the higher tail population is a result of the fit instead of a physical property of the beams. Therefore, no additional systematic uncertainty is assigned.

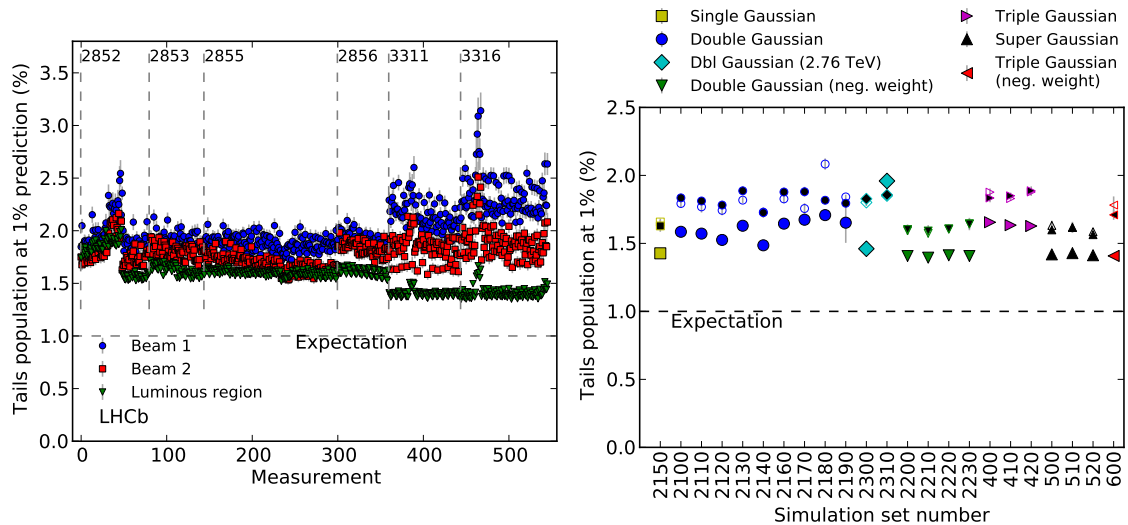


**Fig. 7.16:** Fraction of vertices in the tails beyond the double-sided 99 percentile predicted by the fit. Left: tails populations measured on data at the 1% prediction boundaries. In general the single beam (luminous region) distributions contain about 2% (1.5%) of the population instead of the expected 1%. Right: tails populations measured on simulated datasets at the 1% prediction boundaries. The tails have a population fraction larger than the expected 1% similar to that observed in the data. Open markers denote beam 1, plain black markers denote beam 2 and larger colored markers denote the luminous region.

#### 7.2.7.2 Cross-section measurement with offset beams

Two dedicated BGI measurements have been performed with beams displaced by 180  $\mu$ m in fills 2852 and 2853 with a  $\beta^* = 10$  m optics and were preceded and followed by periods with head-on beams. The offset was performed on the  $y$  axis where the beams have no crossing angle. The beam offset reduced the overlap integral by a factor of about 4. The reduced luminosity and therefore the rate was compensated by changing the trigger prescale. As can be seen from Eq. (3.17), with the presence of a large offset, such that  $\Delta_m^2$  is similar in size to  $\sigma_{m1}^2 + \sigma_{m2}^2$ , the overlap integral is similarly sensitive to the beam position and to the transverse beam size in the offset plane. While the relative beam positions can be measured with a sub-micron accuracy, the uncertainty on the

transverse beam size is larger. Furthermore, the accuracy of the offset measurement depends on the determination of the crossing point  $Z_{RF}$  that is also affected by the transverse beam sizes.

The overlap integral measurements performed in fills 2852 and 2853 are shown in Fig. 7.17 (left) where the periods with head-on and offset beams, and therefore a reduced overlap, can be seen. The crossing point  $Z_{RF}$  and longitudinal position  $\xi_{lz}$  of the luminous region for the same periods are shown in Fig. 7.17 (right). In both fills the movement of the  $\xi_{lz}$  position is attributed to beam drift or beam optimization performed by the LHC operators. The  $Z_{RF}$  position, however, is displaced by 2-3 mm during the offset measurement, which cannot be due to the LHC RF timing. This displacement is not fully understood; it can result from the change in the  $\sigma_{x,j}$  widths due to the different constrain imposed by the luminous region or by the non-perfect model, particularly in the presence of the double Gaussian shapes.

The cross-sections measured with displaced beams in fills 2852 and 2853 are shown in Fig. 7.18, the acquisition run numbers 12264 and 122474 were acquired with offset beams. The other runs are with head-on beams. The cross-section is up to 7% higher with offset beams compared to the central value measured with head-on beams (square blue markers). Setting the  $Z_{RF}$  position to a value of 4 mm, which is consistent with other head-on periods, brings down the cross-section measured during offset beams (triangle cyan marker). Finally, scaling the beam-gas resolution by 1.05 in the  $x$  axis and by 0.95 in the  $y$  axis brings the cross-section down to about the same level as the central value measured with head-on beams without affecting the measurements performed with head-on beams. The measurements performed with displaced beams are highly sensitive to the position measurements and to the beam width ratio in  $x$  and  $y$ , and have a larger sensitivity to the beam-gas resolution. This beam-gas resolution scaling of 5% is within the expected beam-gas resolution uncertainty and beam-gas correction factors. Consequently, the measurements with displaced beams do not reveal additional uncertainties.

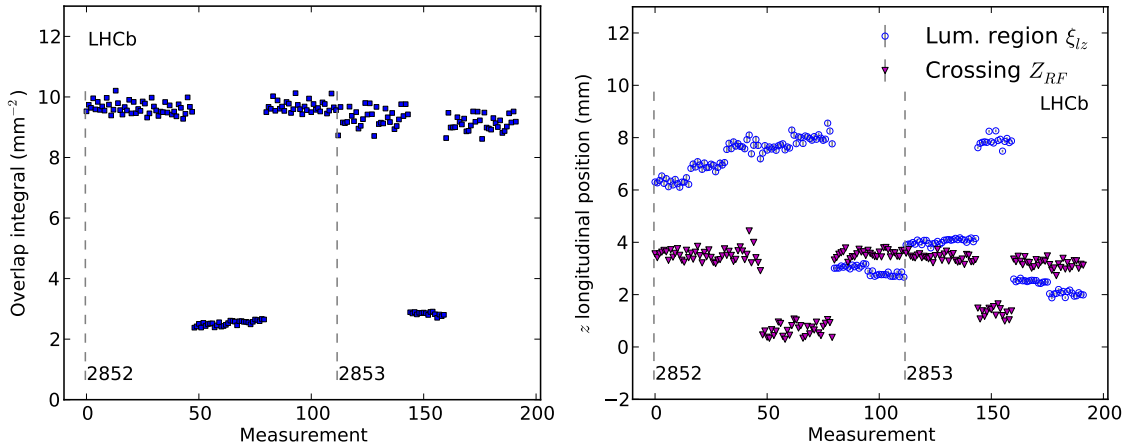


**Fig. 7.17:** Left: overlap integral measured with displaced beams in fills 2852 and 2853. The overlap is smaller when the beams are displaced. Right:  $Z_{RF}$  measurements in fills 2852 and 2853. The position of the luminous region  $\xi_{lz}$  is attributed to beam drift or position adjustments performed by the LHC operators. About 3.5 hours separate the first head-on period in fill 2853 from the offset period explaining the higher values observed during offset. The next head-on period is adjacent. The crossing point  $Z_{RF}$  should not be affected by the beam offset. However, it can be seen that the evaluated  $Z_{RF}$  position is shifted during the beam offset periods. This shift is not physical. For both plots the measurements are sorted by time and BCID. Fills are indicated in the figures and a dashed vertical line denotes the fill boundaries.

### 7.2.7.3 Pressure gradient

The beam-gas interaction rate is proportional to the residual gas pressure at the interaction point. The BGI method measures the beam shapes with beam-gas interaction vertices, and therefore

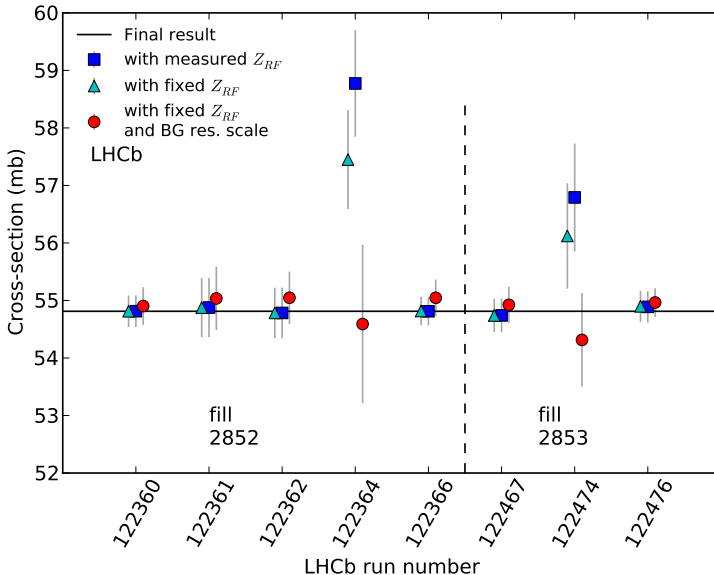


**Fig. 7.18:** Cross-section measurement with displaced beams. Beams were offset in  $y$  by about 180  $\mu\text{m}$  during LHCb run number 122364 (fill 2852) and 122474 (fill 2853), other measurement runs were performed with nominally head-on beams. Markers indicate the average value of all measurements performed in a run, the error bars indicate the RMS of those measurements. Square markers show the default measurement method using the measured  $Z_{RF}$  position as described in Sec. 4.4.4. Cyan upper triangles show measurements with a fixed  $Z_{RF}$  position of 4 mm inferred from the luminous region position when the beams are optimized for maximal luminosity and therefore head-on. Red circles are cross-section measurements with the same fixed  $Z_{RF}$  position of 4 mm and a beam-gas resolution scaling of 1.05 in  $x$  and 0.95 in  $y$ .

assumes that the pressure is uniform in the transverse directions. A pressure gradient orthogonal to the beam would distort the measured bunch transverse shape. The relative error induced by a pressure gradient is estimated by evaluating the effect of a distortion on the overlap integral with

$$\delta_{\mathcal{O}} = \frac{\mathcal{O}(\text{no gradient})}{\mathcal{O}(\text{with gradient})} - 1. \quad (7.22)$$

Assuming beams with a Gaussian transverse shape, in head-on collisions and centered at  $\xi = 0$ , the overlap integral is the convolution of both beams

$$\mathcal{O} = \int g_{1x}(x)g_{1y}(y)g_{2x}(x)g_{2y}(y) dx dy, \quad (7.23)$$

with the Gaussian functions per beam  $j$  and axis  $m = \{x, y\}$  defined as

$$g_{jm}(m) = \frac{1}{\sqrt{2\pi}\sigma_{jm}} e^{-\frac{1}{2}\frac{m^2}{\sigma_{jm}^2}}. \quad (7.24)$$

Considering a constant pressure along the  $y$  axis and a pressure gradient along the  $x$  axis, the true Gaussian beam shapes  $g_{jm}$  are distorted by the pressure gradient into visible beam shapes  $\hat{g}_{jm}$ . The observed beam shapes  $\hat{g}_{jm}$  are defined by

$$\hat{g}_{jx} = (b + a x) g_{jx} \quad (7.25)$$

for a pressure gradient along the  $x$  axis, and with

$$\hat{g}_{jy} = b g_{jy}, \quad (7.26)$$

assuming a constant pressure along the  $y$  axis. The constant parameter  $b$  has units of Hz and the gradient  $a$  has units of Hz/mm.

Assuming beams of equal size:  $\sigma_{1x} = \sigma_{2x}$  and  $\sigma_{1y} = \sigma_{2y}$ , the integration over the  $y$  coordinate in Eq. (7.23), with a constant pressure, is given by

$$\int_{-\infty}^{\infty} \hat{g}_{1y}(y) \hat{g}_{2y}(y) dy = \int_{-\infty}^{\infty} \left( \frac{1}{\sqrt{2\pi} \sigma_{1y}} e^{-\frac{1}{2} \left( \frac{y}{\sigma_{1y}} \right)^2} \cdot b \right)^2 dy = \frac{b^2}{2\sqrt{\pi} \sigma_{1y}}. \quad (7.27)$$

With a pressure gradient, the integration of Eq. (7.23) over  $x$  is given by

$$\int_{-\infty}^{\infty} \hat{g}_{1x}(x) \hat{g}_{2x}(x) dx = \int_{-\infty}^{\infty} \left( \frac{1}{\sqrt{2\pi} \sigma_{1x}} e^{-\frac{1}{2} \left( \frac{x}{\sigma_{1x}} \right)^2} \cdot (b + a x) \right)^2 dx = \frac{a^2 \sigma_{1x}^2 + 2b^2}{4\sqrt{\pi} \sigma_{1x}}. \quad (7.28)$$

The overlap integrals with a pressure gradient  $\mathcal{O}(a \neq 0)$  and without pressure gradient  $\mathcal{O}(a = 0)$  are calculated by solving Eq. (7.23) using the modified Gaussians (7.25) and (7.26)

$$\mathcal{O}(a = 0) = \frac{b^4}{4\pi \sigma_{1x} \sigma_{1y}}, \text{ and} \quad (7.29)$$

$$\mathcal{O}(a \neq 0) = \frac{1}{4\pi^2 \sigma_{1x}^2 \sigma_{1y}^2} \int (a x + b)^2 e^{-\frac{x^2}{\sigma_{1x}^2}} b^2 e^{-\frac{y^2}{\sigma_{1y}^2}} dx dy \quad (7.30)$$

$$= \frac{a^2 b^2 \sigma_{1x}^2 + 2b^4}{8\pi \sigma_{1x} \sigma_{1y}}. \quad (7.31)$$

The relative error introduced by the pressure gradient is then given by

$$\delta_{\mathcal{O}} = \frac{\mathcal{O}(a = 0)}{\mathcal{O}(a \neq 0)} - 1 = \frac{a^2 \sigma_{1x}^2}{2b^2}. \quad (7.32)$$

A measurement has been performed in 2012 during fill 1422 to verify the homogeneity of the pressure in the  $x$  direction by displacing the beams by 0.3 mm and has been used in the luminosity measurement for 2010 [35]. The beam-gas rates measured at different positions are shown in Fig. 7.19 (left). The  $\chi^2$  value per degree of freedom is shown for different slopes in Fig. 7.19 (right) and is used to set a limit of  $a = 0.62$  Hz/mm at 95% CL for a base rate of  $b = 2.14 \pm 0.05$  Hz. With a beam width of about  $\sigma_{1x} \approx 60 \mu\text{m}$ , the uncertainty on the overlap is given by

$$\delta_{\mathcal{O}} = \frac{0.62^2 0.06^2}{2 \cdot 2.1^2} = 0.03\%. \quad (7.33)$$

This uncertainty due to a possible pressure gradient is included in the final results.

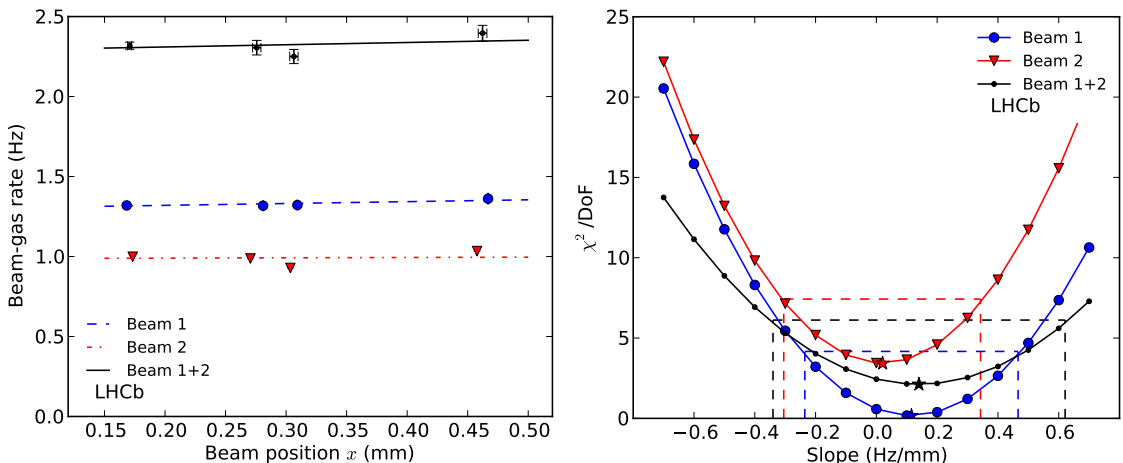


**Fig. 7.19:** Left: measurement of pressure gradient in the VELO. Right:  $\chi^2$  analysis on the gradient to set a limit on a transverse pressure gradient.

### 7.3 Final results

The reference cross-section for  $pp$  collisions at  $\sqrt{s} = 8$  TeV for the *Vertex* counter is measured to be  $54.81 \pm 0.78$  mb. The list of uncertainties affecting this measurement is provided in Table 7.3. During physics data taking the reference cross-section is based on the *Track* counter (see Sec. 5.1). The rate ratio of the *Vertex* to *Track* counter has been determined with data acquired throughout the year and have a value of  $\mu_{\text{Track}}/\mu_{\text{Vertex}} = 1.106$ . An uncertainty of 0.2% is assigned to this factor, which comes from the largest difference observed in physics and VDM data [45]. Systematic uncertainties related to the counter rate have been discussed in Sec. 5.3. Using the relation between the *Vertex* and *Track* counter, the final result

$$\sigma_{\text{Track}} = 60.6 \pm 0.9 \text{ mb}$$

is obtained.

The same luminosity measurement using BGI with data acquired at  $\sqrt{s} = 2.76$  TeV results in a cross-section of  $\sigma_{\text{Track}} = 52.7 \pm 1.2$  mb and is discussed in Appendix A.

**Table 7.3:** Systematic uncertainties on the luminosity calibration using the beam-gas imaging method. The fourth column indicate whether this uncertainty is correlated with the VDM measurements.

Source of uncertainty	Section	Uncertainty (%)	Correlated with VDM
Beam-beam resolution	7.2.1	0.93	No
Beam-gas resolution	7.2.2	0.55	No
Measurement spread (RMS)	7.2.3	0.54	No
Detector alignment	7.2.4	0.45	No
Fit model	7.2.5	0.50	Yes
Longitudinal reconstruction efficiency	7.2.6	0.04	Yes
Pressure gradient	7.2.7.3	0.03	No
Convolved bunch length	7.1.2	0.05	No
Counter background subtraction	5.3	0.20	Yes
Ratio of counter <i>Track</i> to <i>Vertex</i>	7.3	0.20	Yes
FBCT offset	7.1.1	0.04	Yes
Intensity product normalization	6.4	0.22	Yes
Ghost charge	6.2.5	0.02	Yes
Satellites charge	6.3	0.06	Yes
VELO transverse scale	2.2	0.05	Yes
Total uncertainty on the luminosity calibration		1.43	

## 8 LUMINOSITY FOR CENTRAL EXCLUSIVE PRODUCTION

Central exclusive production (CEP) are events resulting from collisions where the colliding particles remain intact and only a “central” system is produced. The exclusive production cross-section is measured with all final state particles except the colliding one. The LHCb detector is well suited to study CEP production. In addition to the intrinsic detector capabilities, such as the acceptance to high rapidities  $\eta$  with  $2 < \eta < 5$ , the flexible trigger system, and particle identification, which makes it possible to distinguish final state decays in  $K$ ,  $\pi$ ,  $p$  and  $\mu$ , the low average number of interaction per crossing ( $\mu < 2$ ) permits the analysis of exclusive events in single interaction events.

Non-resonant  $pp \rightarrow \mu\mu$  and vector boson  $J/\psi \rightarrow \mu\mu$  and  $\psi(2S) \rightarrow \mu\mu$  exclusive production has been measured with data acquired in 2010 [60, 61] and are being updated with 2011 data. In addition, CEP analyses with hadronic decays such as,  $\chi_c \rightarrow \pi\pi$  (and  $\chi_c \rightarrow KK$ ),  $\psi(2S) \rightarrow J/\psi\pi\pi$  and  $X \rightarrow J/\psi\pi\pi$  are ongoing with data acquired in 2011 and 2012. The CEP analyses require the absence of detector activity except for the signal process. This requirement excludes events with multiple interactions and therefore affects the efficiency with which the integrated luminosity is available to the analysis. The determination of the useful integrated luminosity ( $\epsilon_L \int \mathcal{L}$ ) available in CEP analyses is explained in the following.

The integrated luminosity contained in a file (see Sec. 5.1) is given by

$$\int_f \mathcal{L} dt = \frac{\mu_{\text{ref}}}{\sigma_{\text{ref}}} \frac{n_b N_{\text{rnd},f} \nu_{\text{rev}}}{\nu_{\text{rnd}}}, \quad (8.1)$$

with  $\mu_{\text{ref}}$  the average number of interaction per crossing evaluated with all colliding bunches and  $\sigma_{\text{ref}}$  the calibrated cross-section of the counter corresponding to the  $\mu_{\text{ref}}$  measurements. With  $n_b$  the number of colliding bunches,  $N_{\text{rnd},f}$  the number of luminosity events present in the file,  $\nu_{\text{rnd}}$  the sampling frequency of luminosity events and  $\nu_{\text{rev}}$  the LHC revolution frequency, the number of bunch crossings  $N_{\text{xing},f}$  seen in each file is given by

$$N_{\text{xing},f} = \frac{n_b N_{\text{rnd},f} \nu_{\text{rev}}}{\nu_{\text{rnd}}}. \quad (8.2)$$

The total integrated luminosity contained in a dataset of  $F$  files ( $f = 1, \dots, F$ ) is the luminosity sum over all files

$$\int_F \mathcal{L} dt = \sum_{f=1}^F \int_f \mathcal{L} dt. \quad (8.3)$$

The probability  $P_{\text{sig}}$  to get a signal in one interaction is

$$P_{\text{sig}} = \frac{\sigma_{\text{sig}}}{\sigma_{\text{vis}}}, \quad (8.4)$$

with  $\sigma_{\text{vis}}$  the visible cross-section which includes events within the LHCb acceptance. At this stage, it is assumed that the signal interactions are a sub-sample of all visible interactions. For  $n$  visible interactions, the probability to get at least one signal event is given by

$$P_{\text{sig},n} = \left(1 - \left(1 - \frac{\sigma_{\text{sig}}}{\sigma_{\text{vis}}}\right)^n\right). \quad (8.5)$$

The number of signal events  $N_{\text{sig}}$  per bunch crossing, is the sum of all Poisson probabilities  $P(n, \mu_{\text{vis}})$  multiplied with the corresponding probability  $P_{\text{sig},n}$ :

$$\frac{N_{\text{sig}}}{N_{\text{xing}}} = \sum_n \frac{e^{-\mu_{\text{vis}}} \mu_{\text{vis}}^n}{n!} \cdot \left(1 - \left(1 - \frac{\sigma_{\text{sig}}}{\sigma_{\text{vis}}}\right)^n\right) \quad (8.6)$$

$$= 1 - e^{-\mu_{\text{vis}} \frac{\sigma_{\text{sig}}}{\sigma_{\text{vis}}}} \quad (8.7)$$

$$\simeq \mu_{\text{vis}} \frac{\sigma_{\text{sig}}}{\sigma_{\text{vis}}} \quad \text{for } \sigma_{\text{sig}} \ll \sigma_{\text{vis}}. \quad (8.8)$$

The signal cross-section is then given by

$$\sigma_{\text{sig}} = \frac{N_{\text{sig}}}{N_{\text{xing}}} \frac{\sigma_{\text{vis}}}{\mu_{\text{vis}}}. \quad (8.9)$$

In Eq. (8.9), the cross-section  $\sigma_{\text{vis}}$  and its corresponding rate  $\mu_{\text{vis}}$  have been measured in a luminosity calibration fill. Any luminosity counter with a linear response to the luminosity can be used to propagate the relative luminosity as in Eq. (8.1). With Eq. (8.9) and Eq. (8.2), the cross-section  $\sigma_{\text{sig}}$  of a signal process depends therefore on the number  $N_{\text{sig}}$  of signal events observed in a given integrated luminosity  $\int \mathcal{L} dt$

$$\sigma_{\text{sig}} = \frac{N_{\text{sig}}}{\int \mathcal{L} dt}. \quad (8.10)$$

The cross-section determination as described above assumes that the signal selection (cuts) do not affect the Poisson distribution of visible interactions next to the signal interaction. That is, Eq. (8.6) remains valid for any  $n$  visible interactions per crossing. In a central exclusive production analysis, the identification of an exclusive event requires a selection that changes the Poisson distribution in Eq. (8.6). The CEP selection requirement is such that there are no backward VELO tracks in an event, and exactly  $m$  forward tracks all originating from a common vertex. All other bunch crossings with more than one visible interaction ( $n \neq 1$ ) are suppressed.

The total integrated luminosity available to the analysis does not depend on the signal selection of the analysis. However, because the specific CEP analysis cannot clearly identify exclusive events in crossings with more than one interactions, only bunch crossings with a single interaction are considered. It follows that CEP signals occurring in crossings with more than one interaction are not considered, which reduces the available integrated luminosity by a factor  $\epsilon_L$ . Setting ( $n = 1$ ) for single interactions in Eq. (8.6) yields

$$\frac{N_{\text{sig}}}{N_{\text{xing}}} \stackrel{n=1}{=} \mu_{\text{vis}} e^{-\mu_{\text{vis}}} \cdot \frac{\sigma_{\text{sig}}}{\sigma_{\text{vis}}}. \quad (8.11)$$

The integrated luminosity is therefore reduced by the CEP luminosity factor  $\epsilon_L = e^{-\mu_{\text{vis}}}$ . The CEP signal cross-section becomes

$$\sigma_{\text{CEP}} = \frac{N_{\text{CEP}}}{\epsilon_L \int \mathcal{L} dt}. \quad (8.12)$$

A requirement for Eq. (8.12) to be valid is that the rate  $\mu_{\text{vis}}$  is constant over time. To account for the rate variations during data acquisition throughout the year, the rate values  $\mu_{\text{vis},f}$  are evaluated

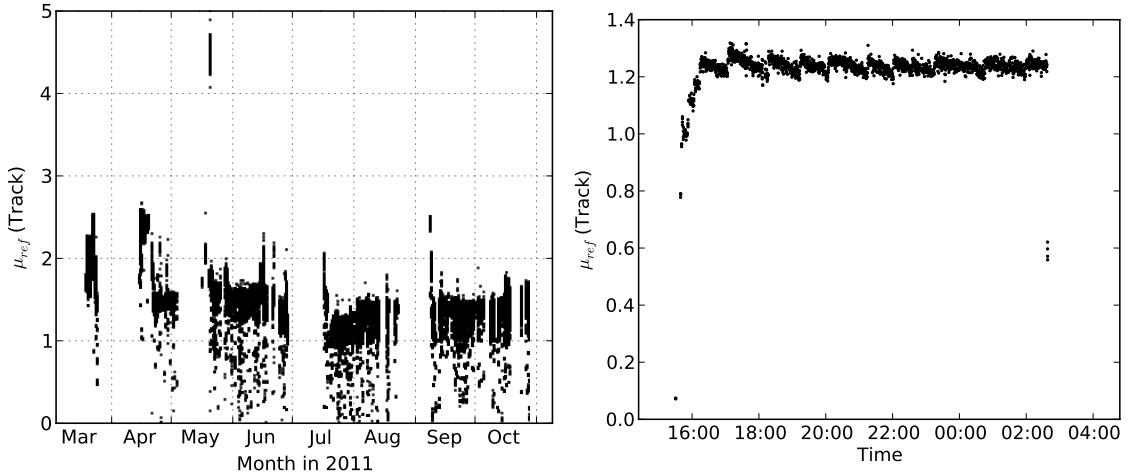
per acquisition file using the luminosity counters stored therein. Each factor  $\epsilon_L$  per file is weighted by the luminosity contained in the file. The final CEP luminosity factor used to scale the integrated luminosity is given by

$$\epsilon_L = \frac{e^{-\mu_{\text{vis},f}} \cdot \sum_{f=1}^F \int \mathcal{L} dt}{\sum_{f=1}^F \int \mathcal{L} dt}, \quad (8.13)$$

where  $\mu_{\text{vis},f}$  is the average visible interaction rate per crossing measured in one acquisition file  $f$ , and  $\int_f \mathcal{L} dt$  the integrated luminosity contained in the file.

The counter *Track* is used to define a visible interaction. All  $\mu_{\text{ref}}$  values per acquisition file are shown in Fig. 8.1 for the counter *Track* in 2011 for  $pp$  collisions at  $\sqrt{s} = 7$  TeV. Rate values for 2012 are shown in Fig. 8.2.

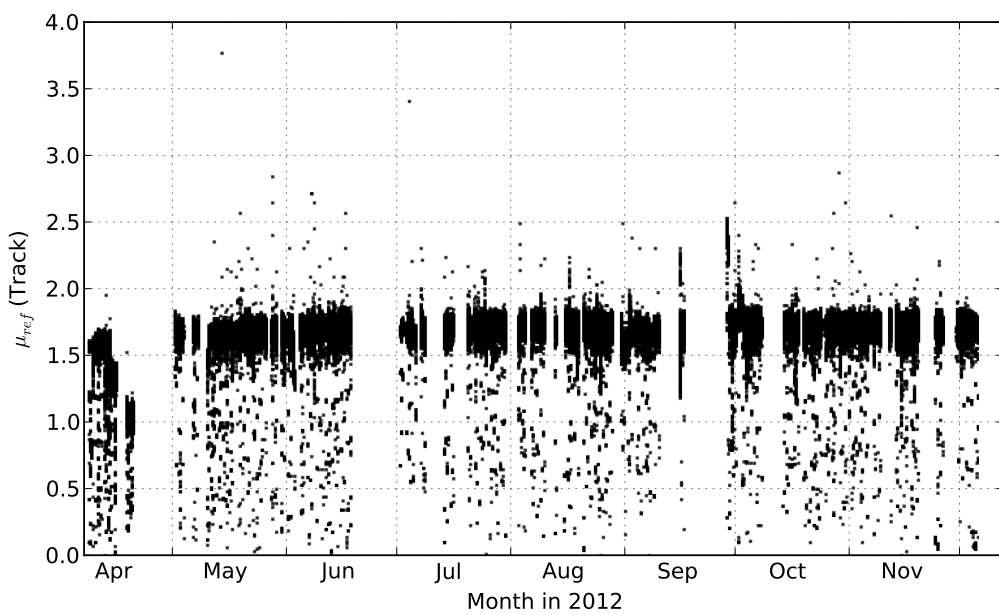
Two tracks are required for an event to be considered non-empty, this threshold is chosen to avoid possible “ghost” tracks when a track is reconstructed with noise in the VELO sensors. However, in the CEP analysis, no extra VELO tracks are allowed in an event. Accordingly, the values for  $\mu_{\text{ref}}$  have been evaluated using a threshold of one track to define a visible event instead of the usual two tracks required. Defining non-empty events with one or more tracks raises the  $\mu_{\text{ref}}$  values by 2.3% in 2011 and by 2.4% in 2012. This difference is taken as systematic uncertainty on the luminosity reduction factor  $\epsilon_L$ . Integrated luminosity values for one interaction per crossing are shown in Table 8.1 for 2011 and 2012 data. Those numbers apply to the full dataset and  $\epsilon_L$  must be evaluated consistently for each analysis according to the data used.



**Fig. 8.1:** Average interaction rate per crossing  $\mu_{\text{ref}}$  from counter *Tracks* in 2011 for  $pp$  collisions at  $\sqrt{s} = 7$  TeV. Left: Measurements of  $\mu_{\text{ref}}$  for all acquisition files in 2011 as function of time. Right: Measurements of  $\mu_{\text{ref}}$  for fill 1982 as example. The visible steps are results of the luminosity leveling.

**Table 8.1:** Integrated luminosity for CEP analysis.

Year	Measurement	Magnet polarity UP	Magnet polarity Down
2011	Total integrated luminosity	$432 \pm 15 \text{ pb}^{-1}$	$582 \pm 20 \text{ pb}^{-1}$
	Integrated luminosity in single interaction crossings	$102.8 \pm 4.4 \text{ pb}^{-1}$	$141.0 \pm 6.1 \text{ pb}^{-1}$
	CEP luminosity factor $\epsilon_L$	$0.238 \pm 0.006$	$0.242 \pm 0.006$
2012	Total integrated luminosity	$1014 \pm 15 \text{ pb}^{-1}$	$1013 \pm 15 \text{ pb}^{-1}$
	Integrated luminosity in single interaction crossings	$188.5 \pm 5.7 \text{ pb}^{-1}$	$196.3 \pm 5.9 \text{ pb}^{-1}$
	CEP luminosity factor $\epsilon_L$	$0.186 \pm 0.005$	$0.194 \pm 0.005$

**Fig. 8.2:** Average interaction rate per crossing  $\mu_{\text{ref}}$  from *Track* counter in 2012 for  $pp$  collisions at  $\sqrt{s} = 8$  TeV.

## 9 CONCLUSION

The absolute luminosity calibration at LHCb was performed with the novel beam-gas imaging method with data acquired in 2012 and 2013. The obtained reference cross-sections of the *Track* counter are  $\sigma_{\text{Track}} = 60.6 \pm 0.9 \text{ mb}$  and  $\sigma_{\text{Track}} = 52.7 \pm 1.2 \text{ mb}$  for  $\sqrt{s} = 8 \text{ TeV}$  and  $\sqrt{s} = 2.76 \text{ TeV}$ , respectively.

The precision reached in the beam-gas imaging measurements of the overlap integral relies on two crucial aspects. First, the SMOG gas injection system not only allowed the reduction of the integration time, but also the increased number of events permitted a two-dimensional shape analysis to be performed and provided a better accuracy in the resolution and ghost charge determination. The full characterization of the SMOG system in the vacuum lab and its commissioning in the LHCb environment was an important part of this work. The laboratory measurements were a prerequisite to gain the support of the CERN vacuum group and later of the LHCb collaboration and of the LHC machine committee to be able to install and use the system. The SMOG gas injection has been a success and results such as ghost charge, beam factorizability and beam size measurements obtained with its operation have been used by the LHC experiments (ATLAS, ALICE, CMS, LHCb) and by the LHC machine. Second, the two-dimensional beam shape determination, including the beam factorizability, was paramount to reach consistent fill-to-fill measurements with an RMS of 0.5%. The developed generic beam simulation was used to assess the capacity of the beam-gas imaging method to measure the beam factorizability and also to validate the fit model.

A vertex resolution determination was developed that uses all available vertices instead of selecting only the fraction of split vertices with equal number of tracks as was the case prior to this work. This new analysis allowed the determination of the resolution up to a higher number of track multiplicity and to decouple the measurement of the beam-beam interaction resolution from the beam-gas resolution. Also, this method provided a measurement of the resolution parametrization independent of the individual resolution measurements per track multiplicity.

The central role played by the DCCT instrument in the bunch population determination led to a measurement campaign dedicated to characterize its uncertainties. As a result of the DCCT calibration studies, which were an important part of this work, the uncertainty on the bunch-current product normalization was reduced from  $\pm 2.7\%$  to  $\pm 0.2\%$ , to the benefit of all LHC experiments. The ghost charge analysis presented here reached a precision such that the ghost charge uncertainty is negligible in the final results. The improved precision is the result of the better statistical precision reached with SMOG and of a new trigger efficiency measurement as function of the LHCb clock shift.

The reference cross-section measured with the beam-gas imaging method has an uncertainty of 1.4% at  $\sqrt{s} = 8 \text{ TeV}$ . This is, to date, the most precise luminosity calibration at the LHC and in any other bunched-beam proton collider. The BGI precision can be further improved with a better VELO alignment and by using a larger  $\beta^*$ . In addition, using a heavier gas (such as argon, krypton or xenon) in the SMOG would provide a larger track multiplicity and improve the resolution. The absolute luminosity calibration measured in 2012 will be combined with VDM measurements to further reduce the uncertainty. Ongoing electroweak production analyses will profit from this luminosity precision, leading to more accurate probes of the Standard Model and stronger constraints on the theoretical parton distribution models.

# **Appendices**

## A LUMINOSITY MEASUREMENTS AT INTERMEDIATE ENERGY

A total of three dedicated luminosity calibration fills (3555, 3562 and 3563) has been performed in 2013 at an intermediate energy of  $\sqrt{s} = 2.76$  TeV. The filling scheme conditions are listed in Table 4.1 (Sec. 4.1). While those fills were dedicated to VDM measurements at ATLAS and CMS, the LHCb experiment used the BGI method parasitically to measure the luminosity using colliding bunch pairs at LHCb. Trigger conditions were identical to those in July and November 2012 and the SMOG gas injection was active. The luminosity measurement and evaluation of systematic uncertainties follows the same procedure as with  $\sqrt{s} = 8$  TeV data.

Due to the expected larger emittance combined with a  $\beta^* = 10$  m optics, a transverse beam size of about 150  $\mu\text{m}$  was expected. A half crossing angle of 885  $\mu\text{rad}$  was chosen to avoid collisions between satellite and main bunches. The reconstruction of the data was performed with the standard VELO alignment as opposed to 2012 where a dedicated fill-by-fill VELO alignment was used. Differences observed in the data as compared to 2012 data are discussed below.

Bunches colliding in fill 3555 form two distinct groups with highly different intensities and sizes as can be seen in Fig. A.1 (left) for the interaction rates  $\mu_{\text{ref}}$  and the overlap integral (right). The comparatively low rate produced by the low luminosity bunch group in fill 3555 results in lower number of beam-beam interactions by a factor of about eight compared to the majority of measurements performed at  $\sqrt{s} = 8$  TeV. The number of vertices per measurement is shown in Fig. A.8. The effect of limited number of vertices has been tested with simulated datasets showing a difference of 0.5% on the overlap integral measurement when reducing the available data by this factor. As seen in Fig. 7.14 in Sec. 7.2.5, the simulation set number 2300, which has a similar shape as that observed in fill 3555, can be measured with a 0.1% accuracy with about 900k beam-beam events. Datasets based on the same beam parameters, but having ten times less data (simulation set number 2310), show a bias of 0.5% when measured with the same algorithms. One can therefore expect a larger measurement spread in fill 3555 due to the fit model.

As explained in Sec. 4.6.2, the beam factorizability parameter  $f_j$  is only meaningful in the presence of a double Gaussian beam shape in both  $x$  and  $y$  transverse planes. The strength of the double Gaussian shape is defined with the parameter  $S_{j,m}$  (see Eq. (4.51)). The measured values of  $S_{j,m}$  and the parametrization  $f_j$  are shown in Fig. A.2. The beams have a double Gaussian shape and are for the most part non-factorizable ( $f_j$  is close to zero). However, the factorizability is not as clearly defined as with as with  $\sqrt{s} = 8$  TeV data and the uncertainties on the  $f_j$  parameter are larger. See Fig. 4.42 for comparison.

The convolved bunch length  $\sigma_{z1}^2 + \sigma_{z2}^2$  measurement plays a more important role compared to the  $\sqrt{s} = 8$  TeV data due to the larger crossing angle correction. As in 2012, the  $\sigma_{z1}^2 + \sigma_{z2}^2$  values are measured with two different track requirements for vertices located in the luminous region (see Sec. 7.2.6). One measurement uses all vertices within the  $z$ -range  $[-250, 250]$  mm, while a second measurement requires each vertex to contain at least two forward and at least two backward tracks to exclude beam-gas interactions. Both selections are corrected with a corresponding reconstruction efficiency inferred from simulation. A constant background term is added to the fit to model the beam-gas contribution. A fit example with both vertex selections is shown in Fig. A.3. Both

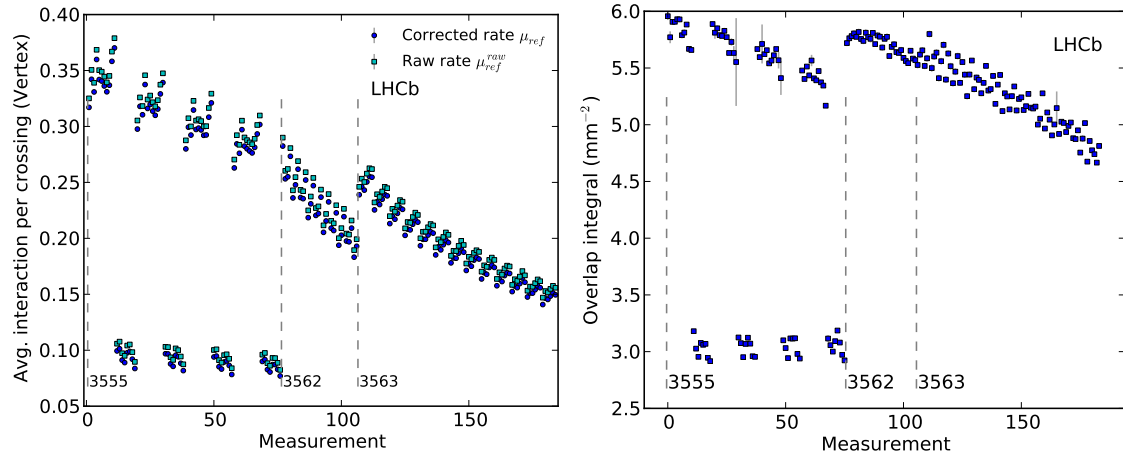


**Fig. A.1:** Average interaction rate and overlap integral for fills at  $\sqrt{s} = 2.76$  TeV. Measurements are sorted by time and BCID. Fill number are indicated in the plots and fill boundaries are indicated with a dashed vertical line. Left: Average number of interaction per crossing  $\mu_{\text{ref}}$  with and without background correction for the *Vertex* counter. Two groups of bunches are present in Fill 3555. Right: overlap integral for fills at  $\sqrt{s} = 2.76$  TeV. In fill 3555, a factor of about two separates both bunch groups.

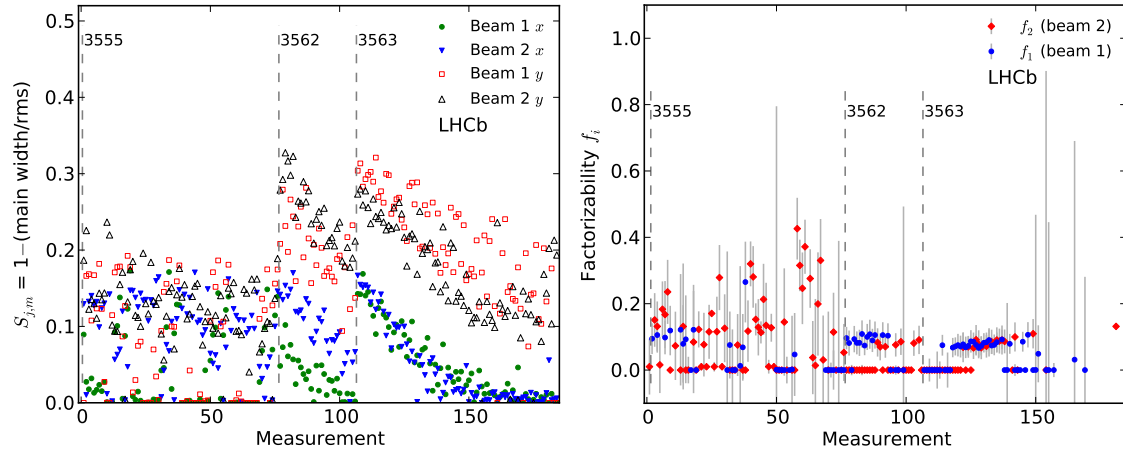


**Fig. A.2:** Left: Strength  $S_{j,m} = 1 - (\text{main width}/\text{rms})$  of double Gaussian beam shape for all measurements performed at  $\sqrt{s} = 2.76$  TeV. Right: measurement of beam factorizability  $f_j$  for all measurements performed at  $\sqrt{s} = 2.76$  TeV. For both plots the measurements are sorted by time and BCID. The different fills are indicated in the plot and separated by a vertical dashed line.

measurements of  $\sigma_{z1}^2 + \sigma_{z2}^2$  for all colliding bunch pairs are shown in Fig. A.4 (left) and are similar. The median cross-section result for the *Vertex* counter using the default “no cut” selection is 46.41 mb, while the median result using the “bb cut” asymmetric requirement is 46.32 mb. An uncertainty of 0.2%, which covers the measurement difference is assigned to the determination of  $\sigma_{z1}^2 + \sigma_{z2}^2$  and  $Z_{\text{RF}}$ , and to the reconstruction efficiency.

The crossing angle correction to the overlap integral is shown in Fig. A.4 right, it shows the ratio of the measured overlap with the overlap evaluated without crossing angle. The two bunch groups are clearly visible in fill 3555 and it has been verified that the beam angles are equal for both groups. The difference in the crossing angle correction is due to the different values of  $\sigma_{z1}^2 + \sigma_{z2}^2$  and the different transverse shapes. The luminous region position  $\xi_{lz}$  and crossing point position  $Z_{\text{RF}}$  are shown in Fig. A.5 left. The offset measured at the  $Z_{\text{RF}}$  crossing point is shown in Fig. A.5 right; in fill 3555 the two bunch groups have a different offset.

Cross-sections results for  $\sqrt{s} = 2.76$  TeV evaluated using the same two-dimensional fit and track multiplicity cuts as for the  $\sqrt{s} = 8$  TeV are shown in Fig. A.6. The left figure shows the measurements per BCID, while the right plot shows a histogram of all results; the RMS

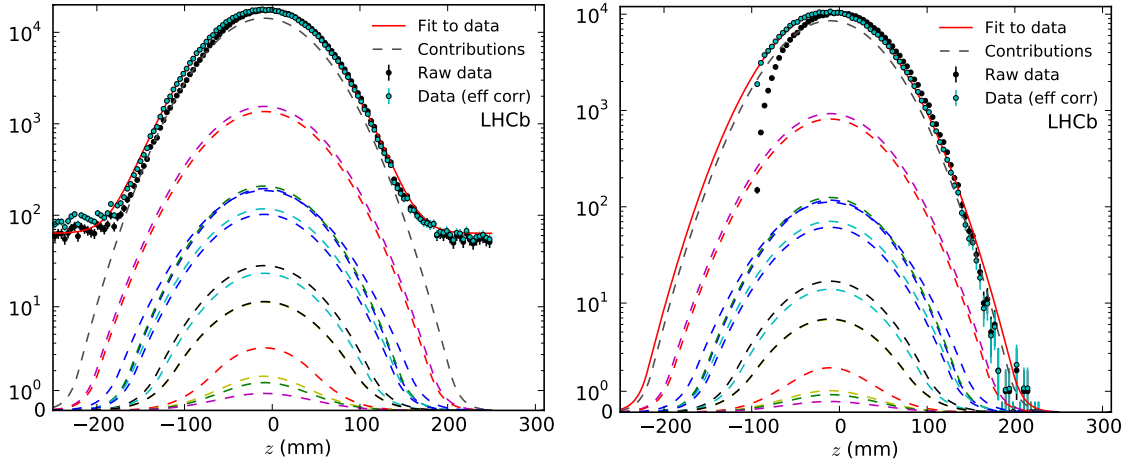


**Fig. A.3:** Bunch length and  $Z_{RF}$  fit example at  $\sqrt{s} = 2.76$  TeV (BCID 1535, fill 3563). The solid red line is the fit result. The different contributions to the final fit shape are shown as dashed lines. Left: fit of the longitudinal vertex distribution using the default “no cut” selection. Right: fit of the longitudinal vertex distribution using the “bb cut” asymmetric requirement.

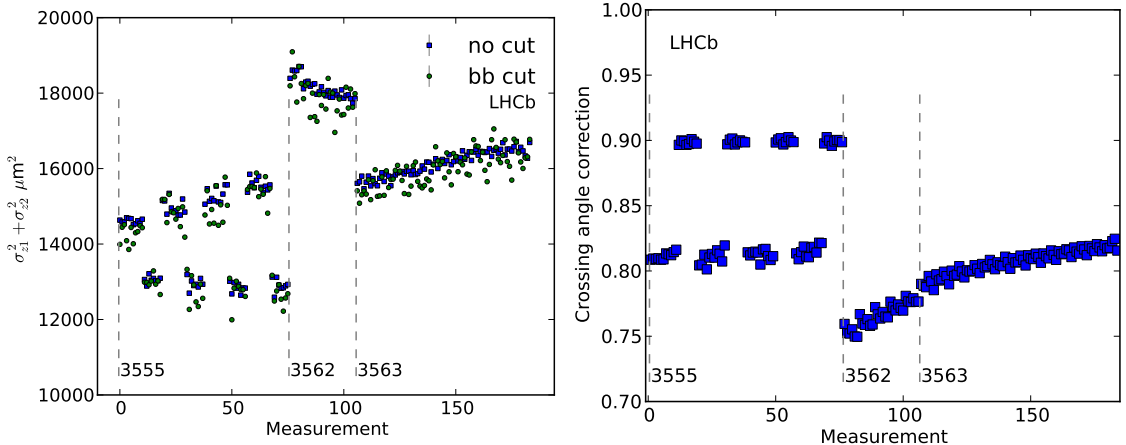


**Fig. A.4:** Convolved bunch length and beam position for fills at  $\sqrt{s} = 2.76$  TeV. Measurements are sorted by time and BCID. Fill boundaries are indicated with a dashed vertical line. Left: convolved bunch length  $\sigma_{z1}^2 + \sigma_{z2}^2$  measurement without track direction requirement (square blue markers “no cut” label) and with asymmetric track direction requirement (circle green markers “bb cut” label). Right: crossing angle correction compared to an overlap integral evaluated without crossing angle.

of the measurements is 1.3%. As described in Sec. 7.2.1, the uncertainty related to the beam-beam interaction vertex resolution is evaluated by measuring the cross-section with different track multiplicities. Here the beam-beam resolution has a small impact on the cross-section compared to 2012, possibly due to the comparatively large transverse bunch size and the lower number of vertices in the luminous region, see left Fig. A.7

On the other hand, the uncertainty related to the beam-gas resolution is significantly larger than in 2012. The cross-section difference measured with and without all beam-gas resolution correction factors (see Sec. 4.3.3.2) amounts to 1.3%. The histograms of both results with and without the resolution correction factors are shown in right Fig. A.7. The global correction factors are larger for fills at  $\sqrt{s} = 2.76$  TeV (see Table 4.5 in Sec. 4.3) and the  $z$ -dependent correction factor are also larger as can be seen in Fig. D.3 in Appendix D.

The FBCT offset fit as described in Sec. 7.1.1 changes the cross-section by 0.05% and reduces the overall RMS to 1.1%. The resulting FBCT offsets and effective cross-sections obtained by the fit are given in Table A.1 for all luminosity calibration fills at  $\sqrt{s} = 2.76$  TeV.

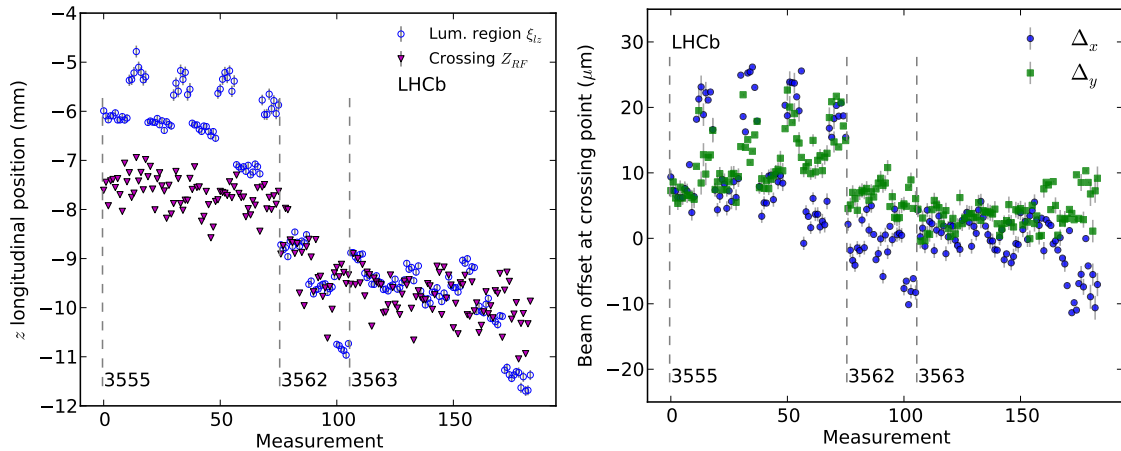


**Fig. A.5:** Left: luminous region position  $\xi_{lz}$  and crossing point position  $Z_{RF}$ . Right: transverse bunch offset measured at the  $Z_{RF}$  crossing point. In fill 3555, the two bunch groups have a different position in the crossing plane  $xz$  leading to a different offset. Measurements are sorted by time and BCID. Fill boundaries are indicated with a vertical dashed line.

**Table A.1:** FBCT offset results for all luminosity calibration fills at  $\sqrt{s} = 2.76$  TeV.

Fill	Fitted cross-section $\sigma_{\text{eff}}$ (mb)	Beam 1 offset $N_1^0$ ( $\times 10^9$ charges)	Beam 2 offset $N_2^0$ ( $\times 10^9$ charges)	$\chi^2/\text{ndof}$
3555	$46.63 \pm 0.06$	$-2.1 \pm 1.8$	$-1.8 \pm 1.3$	$215/72 = 3.0$
3562	$46.30 \pm 0.06$	$-3.7 \pm 1.6$	$-0.6 \pm 2.7$	$74/27 = 2.7$
3563	$46.30 \pm 0.02$	$-3.8 \pm 3.4$	$-6.5 \pm 2.6$	$381/75 = 5.1$

Ghost charge corrections are more important compared to 2012 as can be seen in Sec. 6.2.5; however, the systematic uncertainty related to the ghost charge is negligible and amounts to 0.07%.

The uncertainty related to the detector alignment of 0.9% is estimated at twice the value obtained in 2012 because the crossing angle correction is about twice as large here.

Uncertainties for the counter background subtraction and fit model are taken from the 2012 measurements. The reference cross-section for the *Vertex* counter is  $46.4 \pm 1.0$  mb. A summary of all uncertainties is provided in Table A.2. As for the  $\sqrt{s} = 8$  TeV data, the reference cross-section used for physics data taking is based on the *Track* counter. Using the relation between the *Vertex* and *Track* counter of  $\mu_{\text{Track}}/\mu_{\text{Vertex}} = 1.135$ , the final calibration result is

$$\sigma_{\text{Track}} = 52.7 \pm 1.2 \text{ mb}.$$

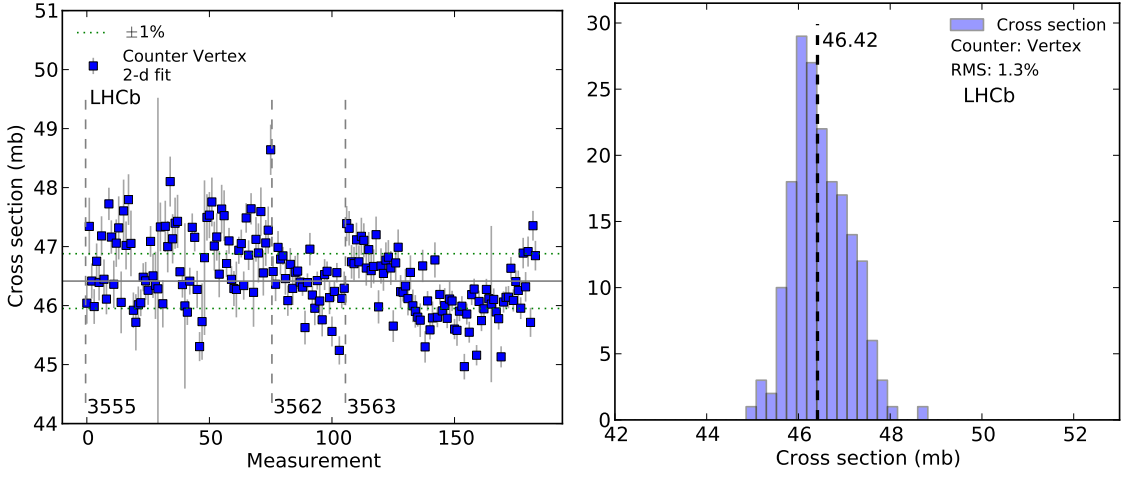


**Fig. A.6:** Cross-section results with head-on beams with  $\beta^* = 10$  m at  $\sqrt{s} = 2.76$  TeV for the *Vertex* counter. Left: cross-section measurement per colliding bunch pair and 20 minutes time integration. The measurements are sorted by time and BCID; the different fills are separated by a dashed vertical line and indicated in the figure. Two dotted horizontal lines show the  $\pm 1\%$  deviation from the central value. Right: histogram of all cross-section measurement from the left plot, the measurement spread has a 1.3% RMS. The median value is indicated by a dashed vertical line.

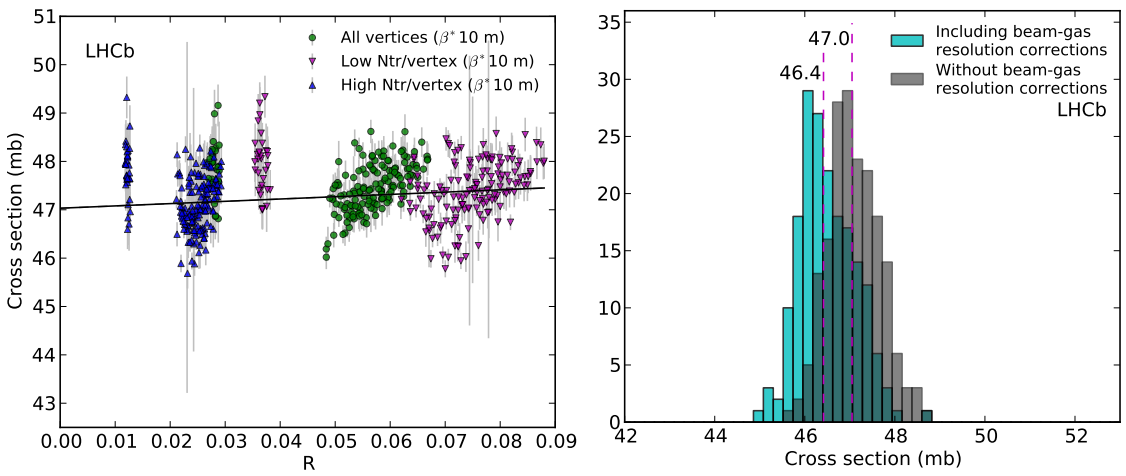


**Fig. A.7:** Uncertainties related to resolution for fills at  $\sqrt{s} = 2.76$  TeV. Left: cross-section dependence on beam-beam resolution compared to beam width for luminosity calibration fills at  $\sqrt{s} = 2.76$  TeV. The  $R$  parameter is calculated with (7.17) (Sec. 7.2.1). Right: cross-section measured with and without beam-gas resolution correction factors (see Sec. 4.3.3.2).

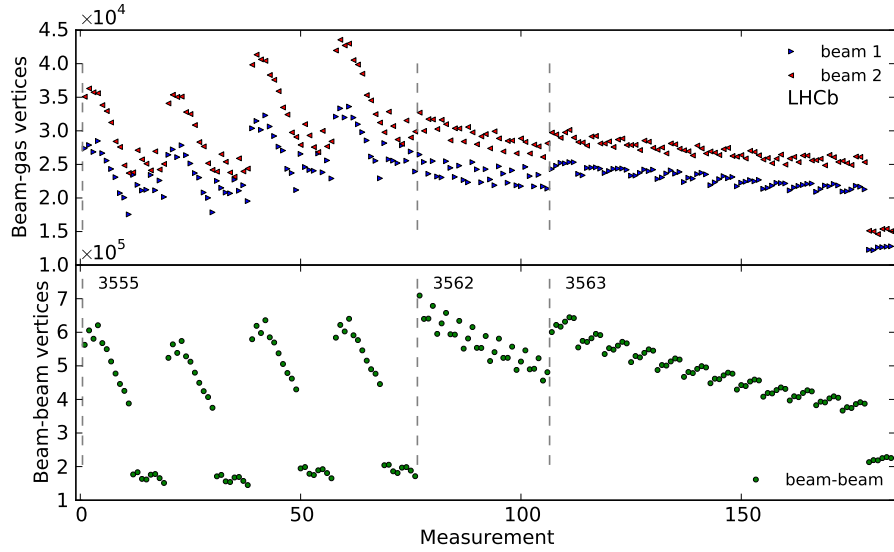


**Fig. A.8:** Number of vertices per measurement at  $\sqrt{s} = 2.76$  TeV for beam-gas and beam-beam vertices. The measurements are sorted by time and BCID. The fill is indicated in the figure and the fill boundaries are denoted with a vertical dashed line.

**Table A.2:** Beam-gas imaging systematic uncertainties on the visible cross-section at  $\sqrt{s} = 2.76$  TeV.

Source of uncertainty	Uncertainty (%)
Beam-beam resolution	0.40
Beam-gas resolution	1.31
Measurement spread (RMS)	1.30
Detector alignment	0.90
Fit model	0.50
Bunch length, crossing point and reconstruction efficiency	0.20
Counter background subtraction	0.20
FBCT offset	0.05
Intensity product normalization	0.28
Ghost charge	0.07
Satellite charge	0.08
VELO transverse scale	0.05
Total uncertainty	2.20

## B SINGLE INTERACTION DETECTOR RESPONSE

Each counter or sub-detector has a characteristic response to a single  $pp$  interaction. This multiplicity response, denoted  $I(N)$ , is a probability density function (PDF) of its multiplicity  $N$ , for example for the *Track* (*Vertex*) counter,  $N$  is the number of VELO tracks (reconstructed vertices) and  $I(N)$  is the distribution of this quantity over many observations. The response  $I$  of a single interaction cannot be observed directly as multiple interactions are bound to occur even at low  $\mu_{\text{ref}}$ . In the presence of multiple interactions  $n$ , the detector response is an  $n$ -convolution of its single interaction PDF  $I$  [62]. The convolution of the response spectrum can be calculated with the use of the Fourier transform, using the fact that the Fourier transform of the convolution is the product of the individual Fourier transforms

$$S_{12}^F = S_1^F \cdot S_2^F. \quad (\text{B.1})$$

The superscript  $F$  and  $F^{-1}$  denote the Fourier and inverse Fourier transform

$$S^F(k) = \int_{-\infty}^{\infty} S(n) e^{-2\pi i nk} dn, \text{ and} \quad (\text{B.2})$$

$$S^{F^{-1}}(n) = \int_{-\infty}^{\infty} S(k) e^{2\pi i kn} dk. \quad (\text{B.3})$$

Using the above equations, the Fourier transform PDF response of  $n$  interactions is  $(I^F)^n$ . The number of  $pp$  interactions per bunch crossing follow a Poisson distribution with  $\mu_{\text{ref}}$  as average number of visible interactions. Therefore, the Fourier transform of the observed detector spectrum  $S$  for a given  $\mu_{\text{ref}}$  is

$$S^F = \sum_{n=0}^{\infty} \frac{e^{-\mu_{\text{ref}}} \mu_{\text{ref}}^n}{n!} (I^F)^n = e^{\mu_{\text{ref}}(I^F - 1)}, \quad (\text{B.4})$$

with  $n$  the number of  $pp$  interactions.

In the presence of background from beam-empty (*be*) and empty-beam (*eb*) crossings, the actual beam-beam (*bb*) spectrum is given by

$$S_{bb}^F = S_{be}^F S_{eb}^F e^{\mu_{\text{ref}}(I^F - 1)}. \quad (\text{B.5})$$

The single interaction response is found by inverting (B.5)

$$I = \left( \frac{1}{\mu_{\text{ref}}} \ln \left( \frac{S_{bb}^F}{S_{be}^F S_{eb}^F} \right) + 1 \right)^{F^{-1}}, \quad (\text{B.6})$$

with  $S_{bb}$ ,  $S_{be}$  and  $S_{eb}$  the normalized detector spectra such that  $\sum_N S(N) = 1$  for *bb*, *be* and *eb* crossings. The  $\mu_{\text{ref}}$  value is evaluated from data and calculated using the zero probability to get an interaction in a crossing as discussed in the previous section

$$\mu_{\text{ref}} = -\ln P_{bb}(0) + \ln P_{be}(0) + \ln P_{eb}(0). \quad (\text{B.7})$$

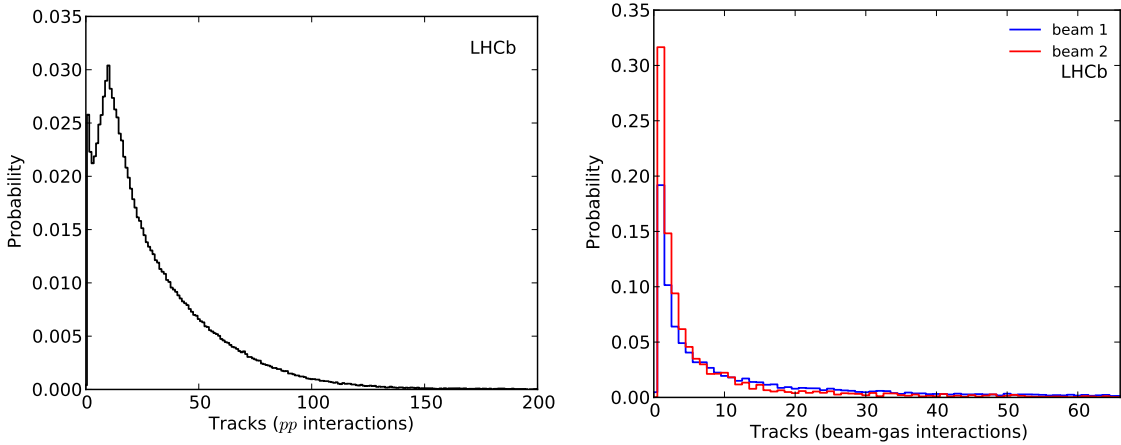
Note that  $P(0)$  is the probability to get an empty event in a crossing.

The single interaction spectra for beam-beam and beam-gas interactions are shown in Fig. B.1 for the *Track* counter. The beam-beam spectrum (left plot) has been measured with data acquired during VDM scans combining different datasets with different  $\mu_{\text{ref}}$  values in mostly background free conditions. Furthermore, the presence of only 16 colliding bunches spread over the LHC ring permits the exclusion of any detector saturation or spill-over and to measure the response  $I$  under ideal conditions. The beam-gas responses (right plot) have been measured with fill 2855 using non-colliding bunches and taking advantage of the SMOG gas injection to improve the statistical accuracy.

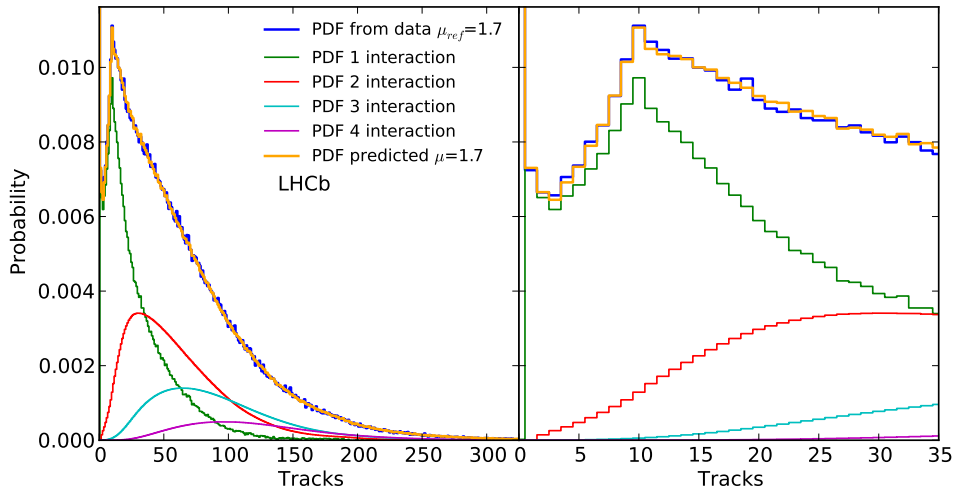
Knowing the single interaction response  $I$ , the  $\mu_{\text{ref}}$  value can be fitted to Eq. (B.5) using the observed spectra  $S$ . In principle, this method is more accurate than the zero counting method described in the previous section because the full detector spectrum is used as information instead of using only the zero bin to count empty events. The large background contribution (10% to 50%) due to the SMOG gas injection during BGI measurements could be better treated by reducing the statistical accuracy and possibly improve the consistency of counter ratios as seen in Sec. 5.3; however, the simpler method used in this work does not degrade the final result.

Figure B.2 shows the detector spectrum  $S$  of the counter *Tracks* acquired during a normal physics fill (3034) superimposed with the predicted spectrum for the observed  $\mu_{\text{ref}}$  value. The predicted spectrum is in good agreement with the data. The same measurement performed in a subsequent fill (3110) with a similar  $\mu_{\text{ref}}$  value is shown in Fig. B.3; in this case the predicted spectrum does not agree with the data. This problem is understood by the  $z$ -dependence of the detector response. The detector acceptance varies with the vertex  $z$ -position of an interaction, and is therefore sensitive to the position and width of the luminous region. The acceptance affects the vertex track multiplicity and its spectrum  $I$ .

Since 2011, the LHC operates a luminosity leveling scheme at LHCb by displacing the beams such as to keep an almost constant luminosity at LHCb of about  $\mathcal{L} \approx 4 \cdot 10^{32} \text{ cm}^{-2}\text{s}^{-1}$ . During normal data taking periods, the beams have a crossing angle in both  $x$  and  $y$  directions and the beams are displaced in both coordinates during the leveling to minimize the longitudinal displacement of the luminous region. Nevertheless, the luminous region longitudinal  $z$ -position is not constant leading to a change in acceptance and therefore in the observed detector response and  $\mu_{\text{ref}}$  value. While the *Track* counter is only affected to the extent of about 0.3% when using the zero count method, the determination of  $\mu_{\text{ref}}$  using the Fourier transform of the detector spectrum as described here would require to evaluate the single interaction response  $I$  for multiple  $z$ -positions. The detector PDF method described in this section, while promising and potentially superior to the zero count method, could not be used for the BGI analysis in this work and further studies of the detector response are needed.



**Fig. B.1:** Single interaction detector response  $I$  for the *Track* counter. Left: response for  $pp$  collisions. Right: response for beam-gas collisions.



**Fig. B.2:** Detector response spectrum during normal physics data taking with  $\mu_{\text{ref}} = 1.6$  (fill 3034). Left panel: measured (blue histogram) and predicted spectrum (orange histogram) agree well over the full track multiplicity range. The PDF contributions for 1, 2, 3 and 4 interactions are also shown. The prediction includes spectra up to  $n = 20$  interactions. Right panel: same data showing a smaller tracks range.

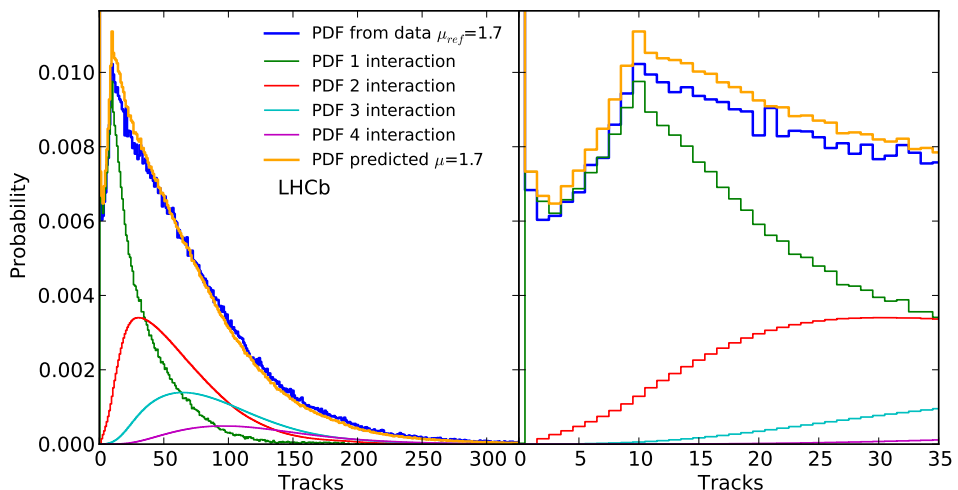


**Fig. B.3:** Same plot as in Fig. B.2 but using data from a different fill (3110). While  $\mu_{\text{ref}}$  is similar to fill 3034 and the background is negligible in both cases, the prediction does not agree well with data in this example.

## C VELO DETECTOR ALIGNMENT STUDIES

Sensors in the VELO detector are aligned with tracks and vertices originating from interactions acquired with collision data [63, 64]. The VELO has two retractable halves, each with 21 modules. The modules have two semi-circular silicon sensors measuring  $r$  and  $\phi$  coordinate with microstrips. Therefore, a total of 84 sensors have to be aligned. The alignment of the sensors and modules within a VELO half is called a local alignment. As the VELO halves are retracted and closed in every fills for physics, their final position can vary by about  $\pm 5 \mu\text{m}$  between fills. Each half has 6 degrees of freedom and the positions and orientations of both halves are called a global alignment.

The alignment can be performed in two parts; first the relative sensors and modules are aligned with tracks using the so-called MILLEPEDE [65] algorithm. Second, the global alignment uses hits on the sensors overlapping part between both VELO halves to align them to each other. Primary vertices, which provide tracks in both halves can also be used for the global alignment.

The BGI method presented in this work relies on the knowledge of the vertex resolution, on the beam directions and also on the positions of the single beams and the luminous region. All those quantities can be affected by the alignment. For the BGI analysis, the alignment is evaluated by measuring the vertex position seen by both VELO halves independently. Tracks belonging to a primary vertex reconstructed with standard LHCb algorithms are split in two sets corresponding to each VELO half. Each track set per VELO half is then reconstructed again to provide a vertex. The beam positions  $m_{\text{left}}$  or  $m_{\text{right}}$  (for the axis  $m = x, y$ ) seen by each VELO half are determined with a double Gaussian function fit on the vertex position distribution and for a given  $z$ -range. The difference in vertex position  $dm = m_{\text{left}} - m_{\text{right}}$  is shown in Fig. C.1 for the default alignment and using beam-gas interactions only.

Using only beam-gas data makes it possible to disentangle vertices originating from each beam and to cover the large  $z$ -range of  $\pm 1 \text{ m}$  used for the BGI analysis. A perfect agreement between the VELO halves would result in a flat distribution scattered around the zero-line. A global shift of the detector halves in  $x$  or  $y$  will shift all measured values shown in Fig. C.1 such that the average difference is vanishing. A global rotation around a transverse axis of the VELO halves will rotate all values in Fig. C.1 around the zero point. However, a modification of the global alignment will not affect the structures seen.

Residuals between the vertex position per VELO half and a straight line fit to the average beam position seen by both halves is shown in Fig. C.2. Ideally, the residuals should be scattered around zero and be independent of  $z$ . The structures seen close to  $z = 0$  distort the luminous region shape and its position. While some effects can be corrected for when fitting the luminous region (as explained in Sec. 4.6.1), the observed discrepancies also affect the measured beam directions and the resolution.

Attempts to improve the alignment with a dedicated algorithm remained unsuccessful for beam-gas data. Instead, the individual sensor positions were modified in the alignment database such as to reduce the position difference  $dm$  at larger  $z$  ( $|z| > 500 \text{ mm}$ ) and to reduce the residuals to a straight line. Results for the local alignment used for the BGI analysis are shown in Fig. C.3 for the left-right difference  $dm$  and in Fig. C.4 for the residuals to a straight line. Since multiple incremental improvements were needed, the alignments test were performed with less vertices to

reduce the computing time, explaining the lower number of datapoints in Figs. C.3 and C.4. In addition, a global alignment has been evaluated for each dedicated luminosity calibration fill in 2012, such as to minimize the left–right difference. Accordingly, the dedicated alignment consist of a local and a global alignment. The local alignment is the same for all fills, while the global alignment is adapted on a fill-by-fill basis.

This dedicated alignment appears only marginally better that the default one. The difference observed in the cross-section between the low and high number of tracks cuts is about 2.3% in both the dedicated and standard alignments. A special version of the global fit described in Sec. 4.4.3 allows the beam directions to be fitted together with the beam parameters. When performed on data reconstructed with the dedicated alignment, this fit provides the same result as with fixed beam directions. On the other hand, a cross-section difference of about 1% was observed with the default alignment, which revealed tensions between the single beam and the luminous region measurements.

At this stage, the alignment accuracy is taken into account by a systematic uncertainty of 0.45%. In addition the alignment affects the detector resolution, which accounts for systematic uncertainties of 0.9% and 0.5%, for the beam-beam and beam-gas resolutions respectively. More work is ongoing for the detector alignment and future BGI measurements might reach a higher precision with an improved alignment.

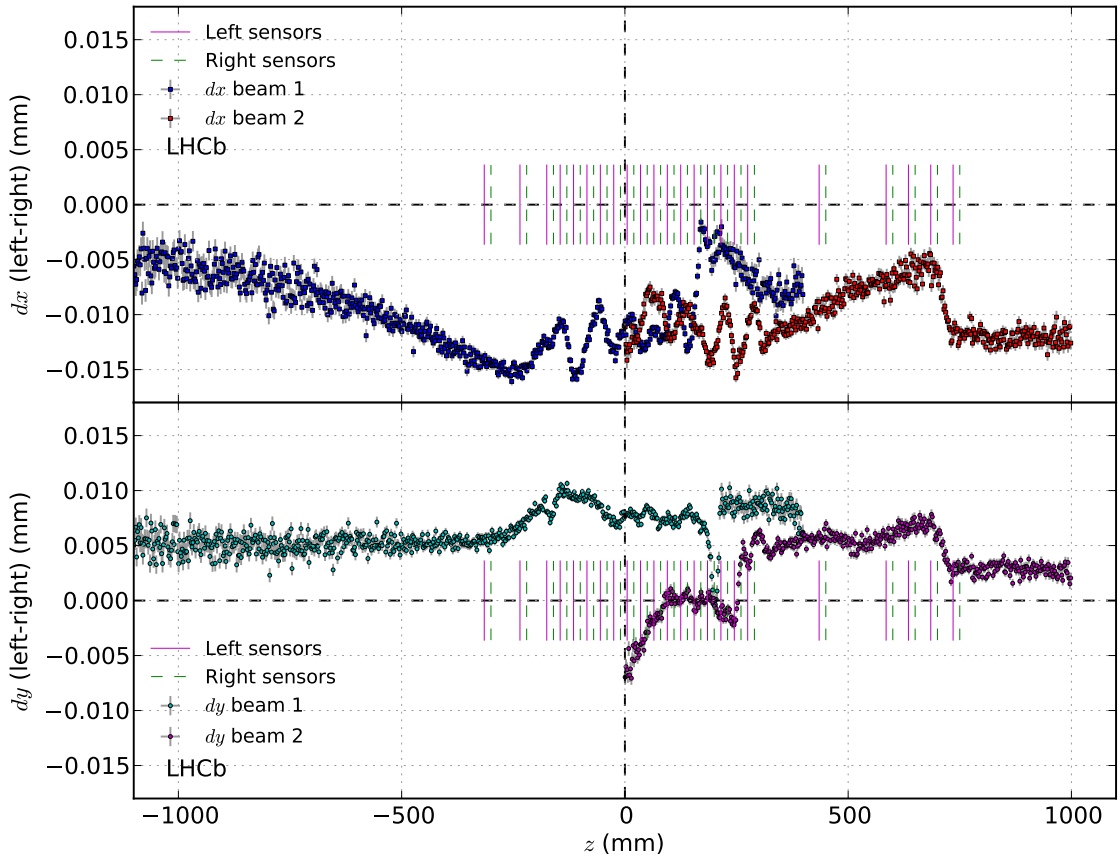


**Fig. C.1:** Difference in transverse vertex position as seen from VELO left and right halves with default alignment in 2012 (fill 2520 as example). The position of the sensors is indicated by vertical lines in the figure. Each data point is the mean of a double Gaussian function fit to the vertex distribution  $dx$  or  $dy$  in a  $z$ -range. The errors are the statistical uncertainties of the fits.

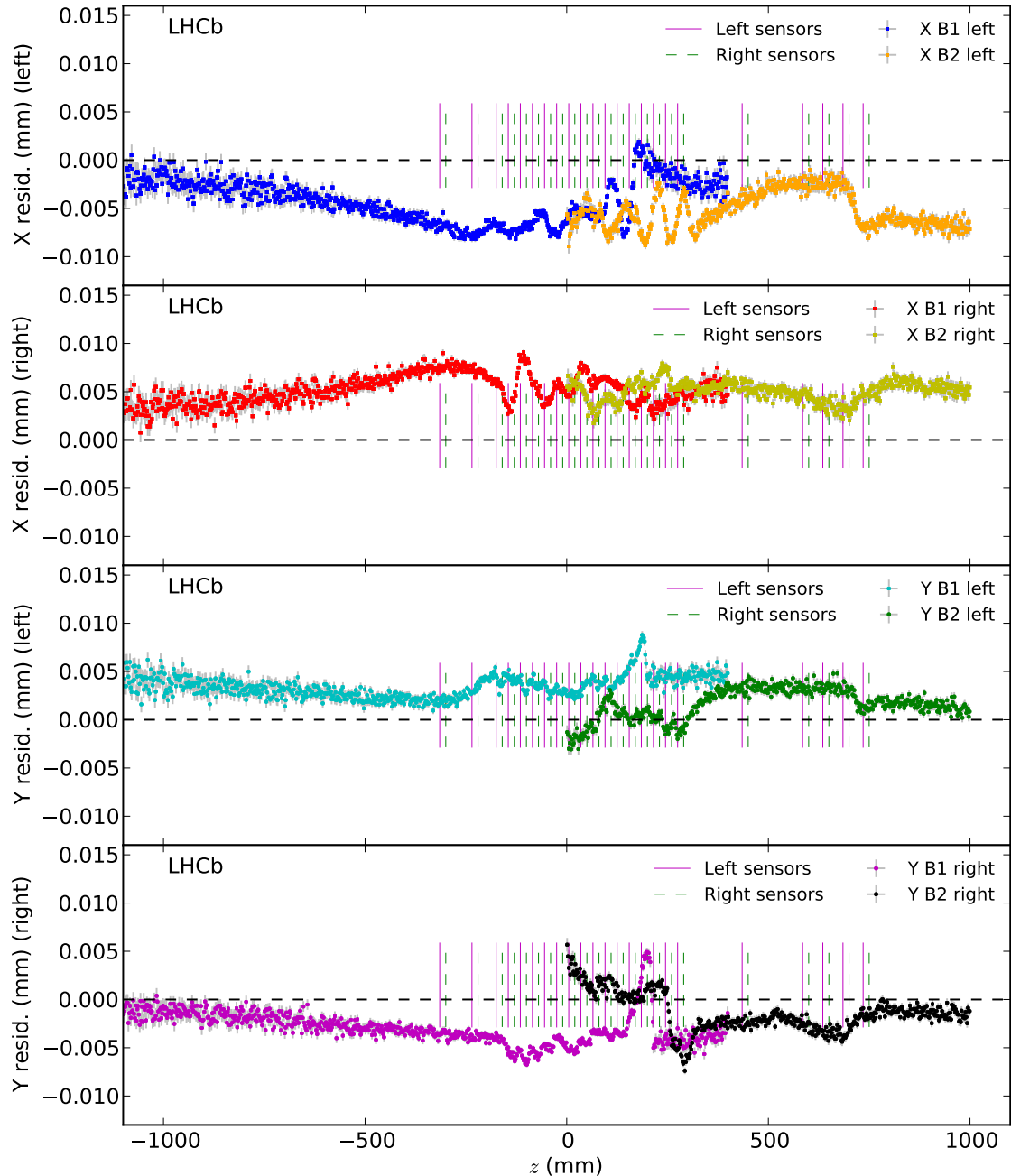


**Fig. C.2:** Residuals between a straight line fit to the average beam position and the beam seen by a VELO half using the default alignment in 2012 (fill 2520 as example). The position of the sensors is indicated by vertical lines in the figure. The errors are the statistical uncertainties of the fits.

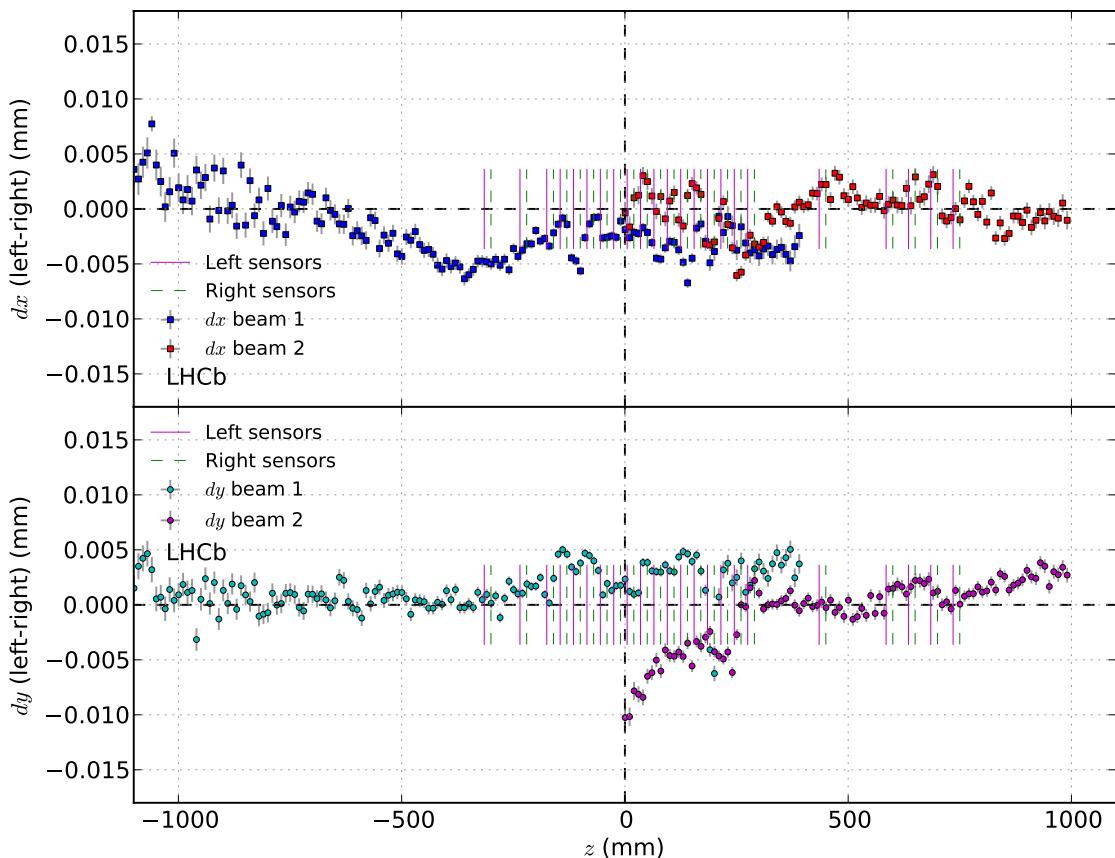


**Fig. C.3:** Difference in transverse vertex position as seen from VELO left and right halves with dedicated alignment in 2012 (fill 2520 as example). The position of the sensors is indicated by vertical lines in the figure. Each data point is the mean of a double Gaussian function fit to the vertex distribution  $dx$  or  $dy$  in a  $z$ -range. The errors are the statistical uncertainties of the fits.

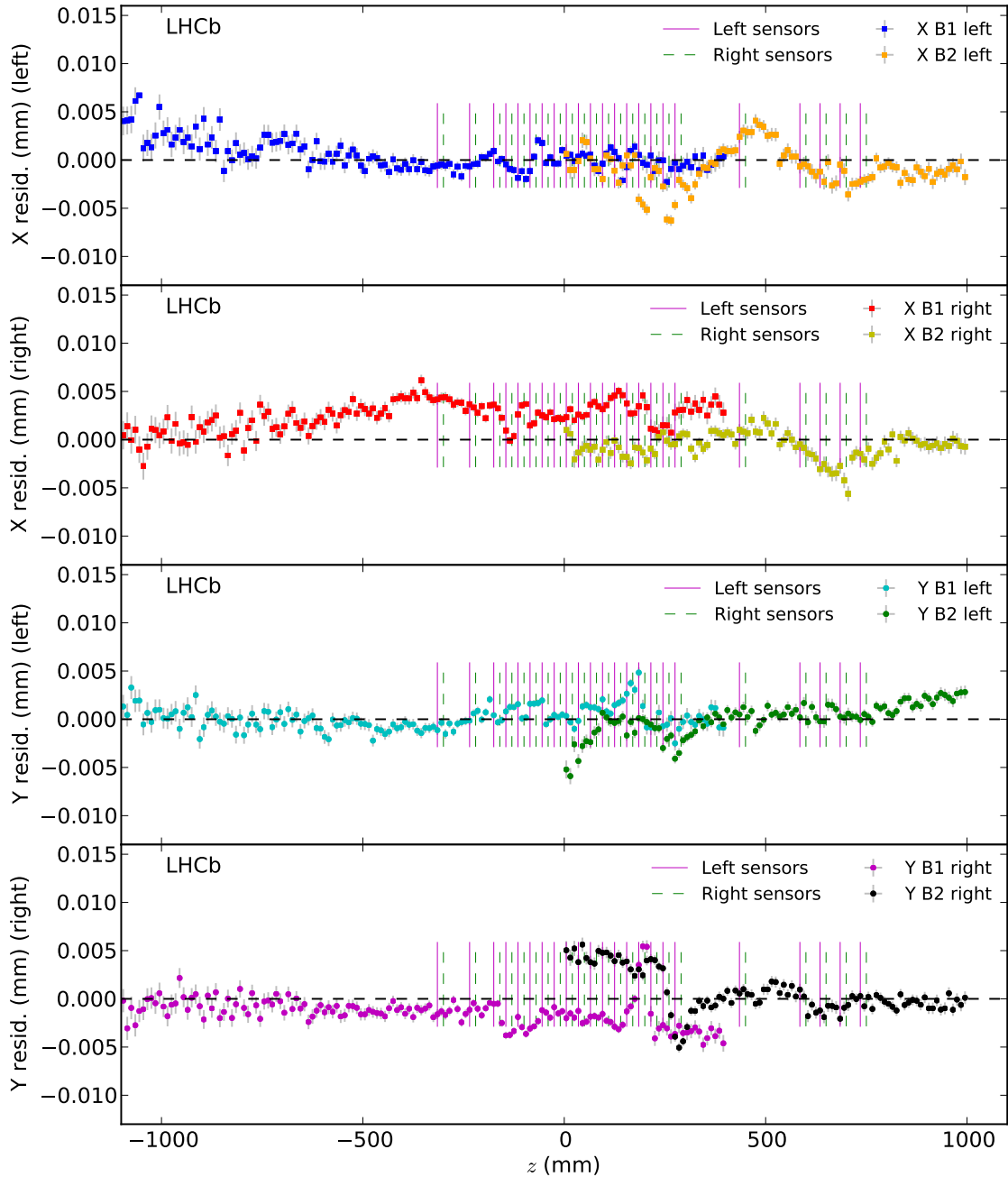


**Fig. C.4:** Residuals between a straight line fit to the average beam position and the beam seen by a VELO half using the dedicated alignment in 2012 (fill 2520 as example). The position of the sensors is indicated by vertical lines in the figure. The errors are the statistical uncertainties of the fits.

## D ADDITIONAL PLOTS AND TABLES

This Appendix contains tables and plots, which are not essential to the understanding of the method. The figures give additional information and are referred to in the text.

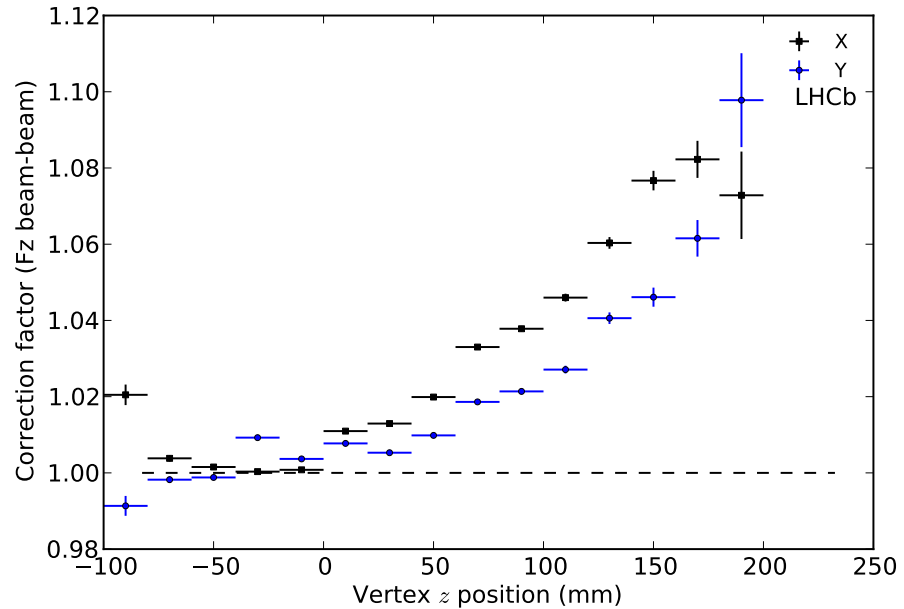


**Fig. D.1:** Correction function describing the  $z$ -dependence of the beam-beam resolution based on a resolution parametrization measured in the central  $z$ -range  $z = \pm 5$  mm (fill 2855).

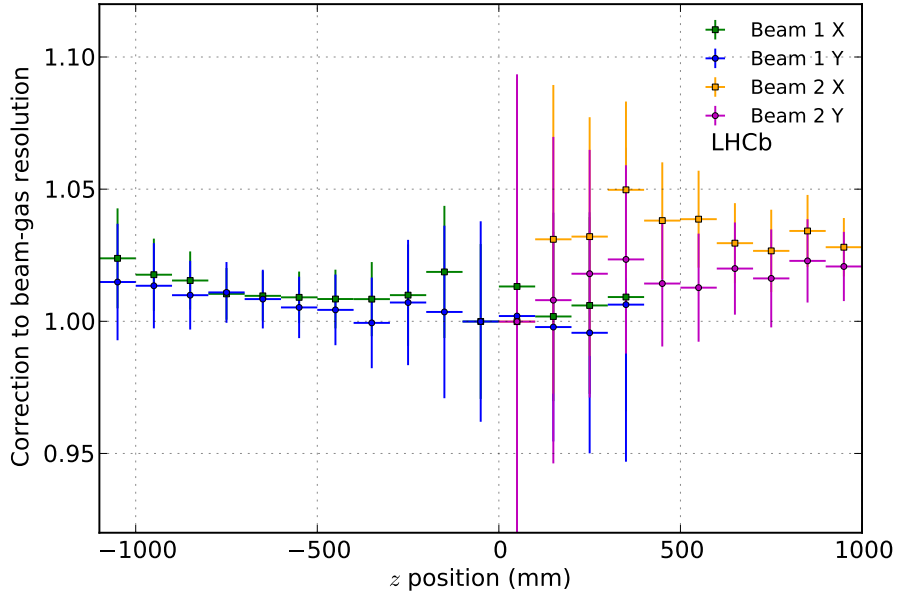


**Fig. D.2:** Correction factors  $f_z$  to the beam-gas resolution as function of  $z$ -position (for fill 2855 with 10 m  $\beta^*$  optics) at  $\sqrt{s} = 8$  TeV. The large fit uncertainties reflect the smaller influence of the  $f_z$  factors compared to Fig. 4.16 with  $\beta^* = 3$  m.

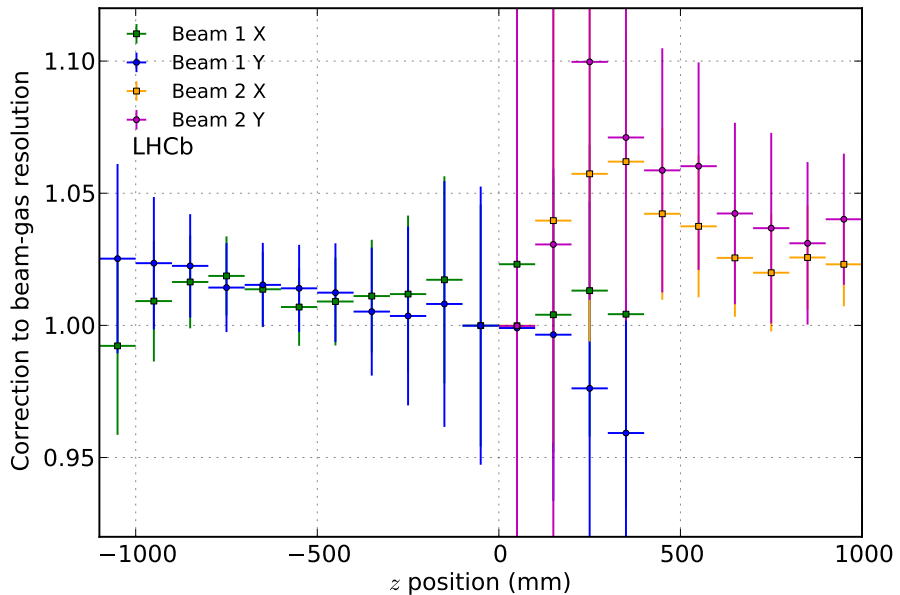


**Fig. D.3:** Correction factors  $f_z$  to the beam-gas resolution as function of  $z$ -position (for fill 3563 with 10 m  $\beta^*$  optics) at  $\sqrt{s} = 2.76$  TeV. The large fit uncertainties reflect the smaller influence of the  $f_z$  factors compared to Fig. 4.16 with  $\beta^* = 3$  m.

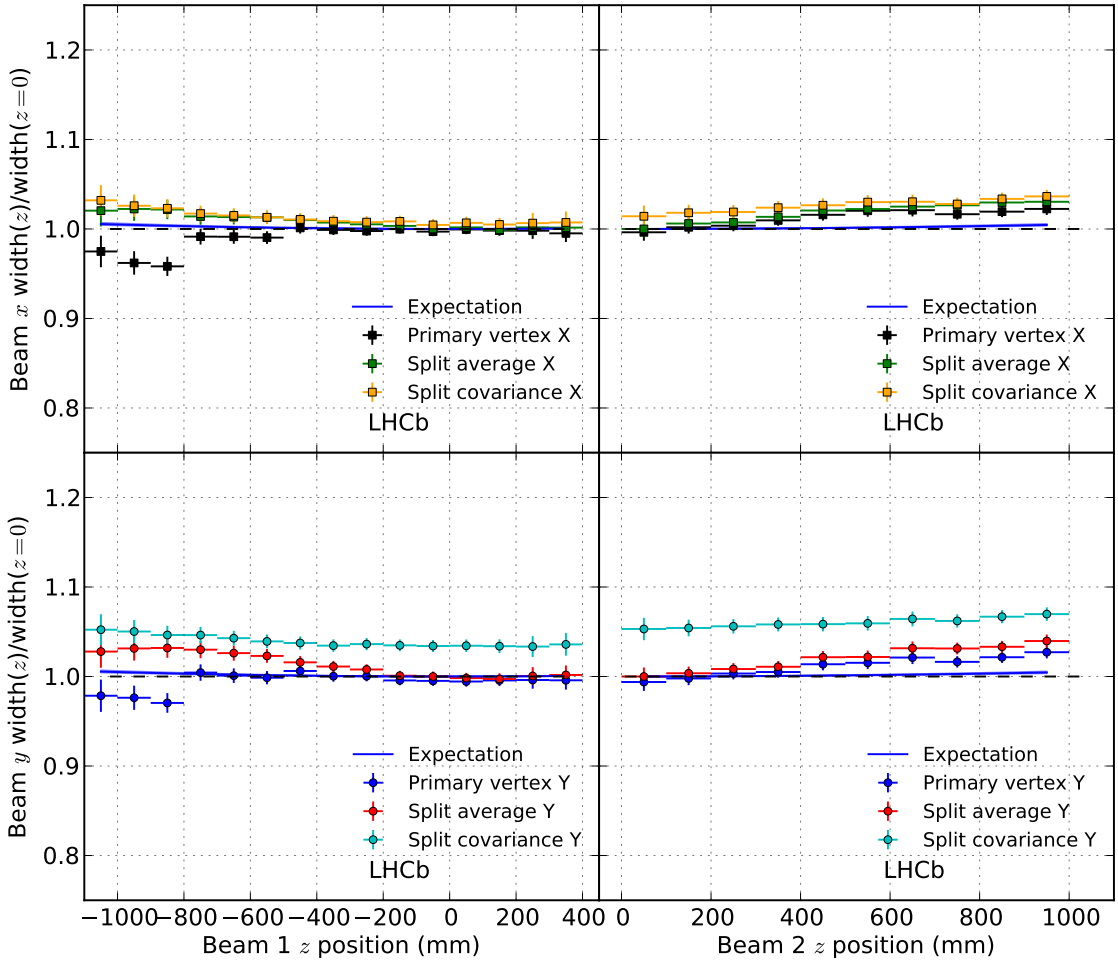


**Fig. D.4:** Measurement of single beam width along  $z$  normalized to the width at  $z = 0$  for fill 2855 ( $\beta^* = 10$  m). Each data point for a given  $z$ -position and measurement method is an average of all normalized width from non-colliding bunches. The curved blue lines indicate the expected beam width evolution in  $z$  due the 3 m  $\beta^*$  hourglass effect, the shaded blue surface indicate the 10% uncertainty on the  $\beta^*$ .

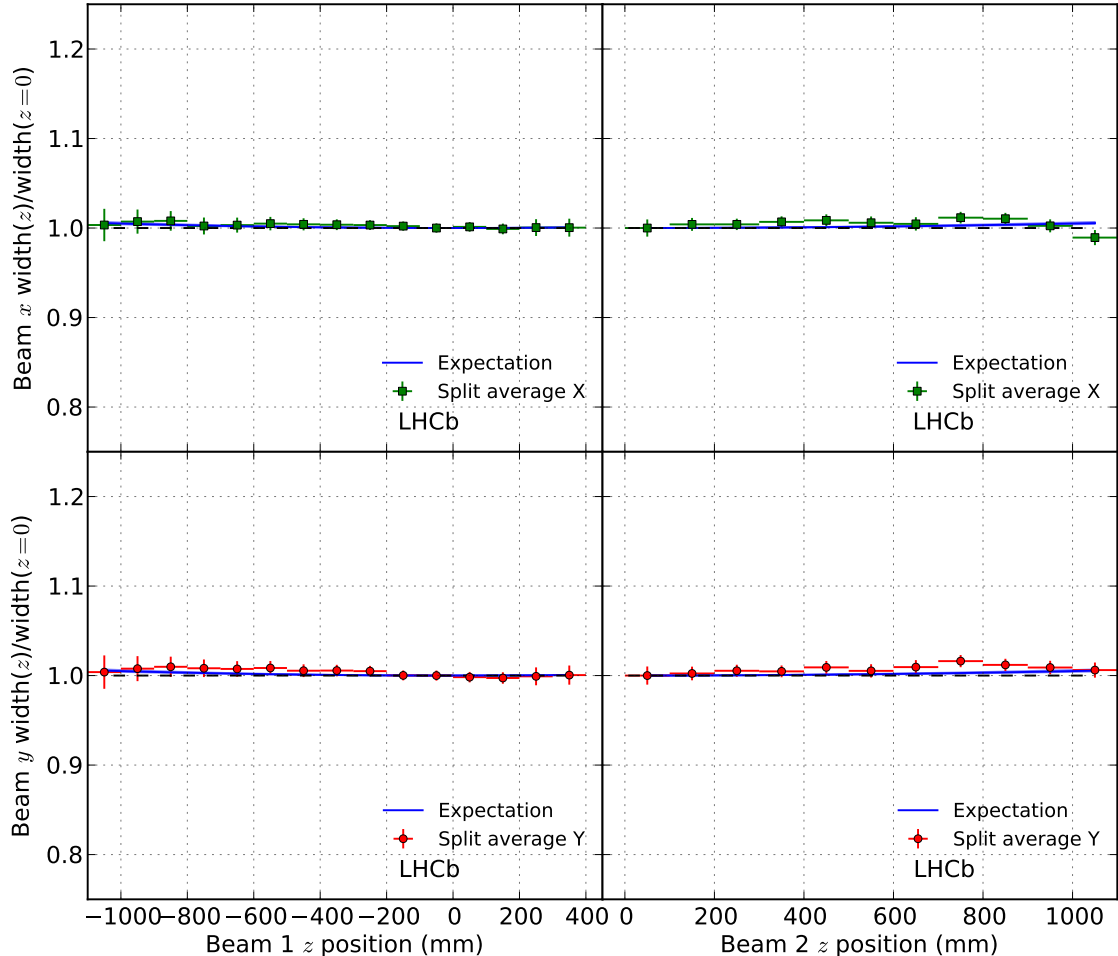


**Fig. D.5:** Measurement of single beam width along  $z$  for fill 2855 ( $\beta^* = 10$  m). The beam widths are measured with the resolution deconvolution including all resolution correction factors. Each data point for a given  $z$ -position is an average of all normalized width from non-colliding bunches. The curved blue line indicate the expected beam width evolution in  $z$  due the  $\beta^*$  hourglass effect, the shaded blue surface indicate the 10% uncertainty on the  $\beta^*$ .

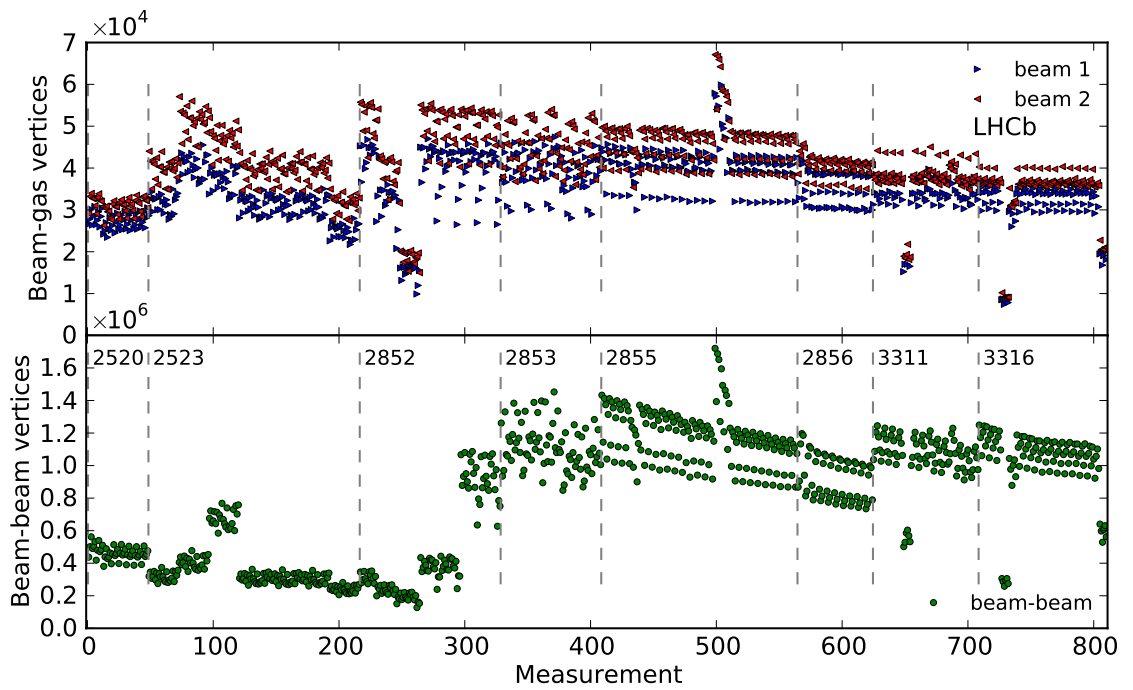


**Fig. D.6:** Number of vertices per measurement. The measurements are sorted by time and BCID. The fill is indicated in the figure and the fill boundaries are denoted with a vertical dashed line.

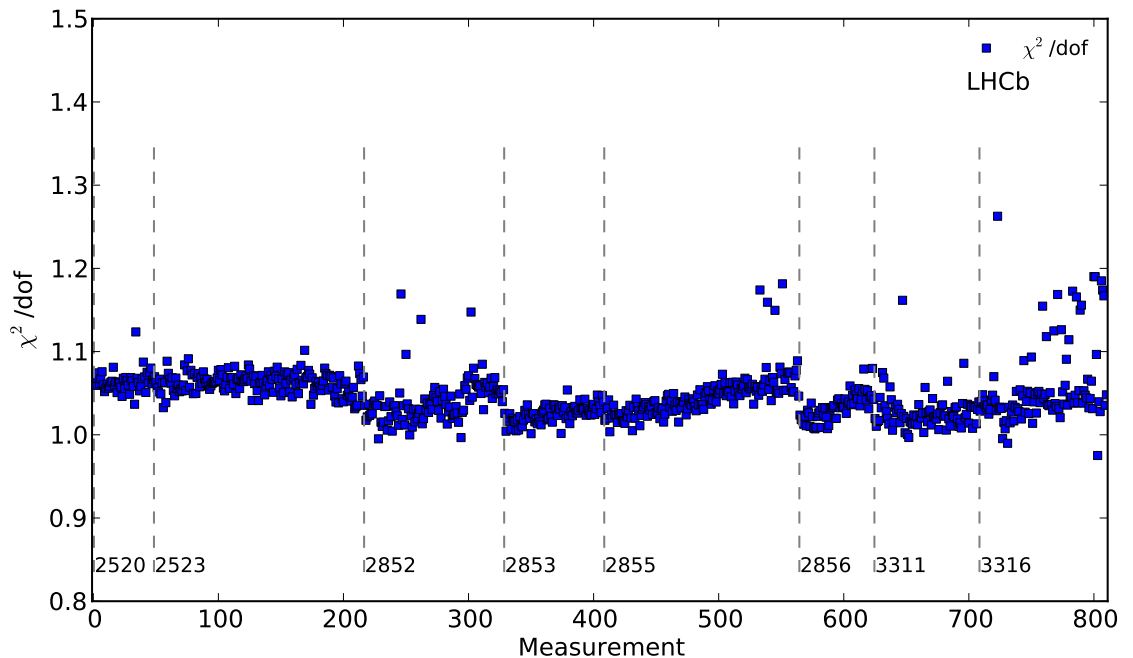


**Fig. D.7:** Fit  $\chi^2/\text{dof}$  of the 2-d global fit. The measurements are sorted by time and BCID. The fill is indicated in the figure and the fill boundaries are denoted with a vertical dashed line.

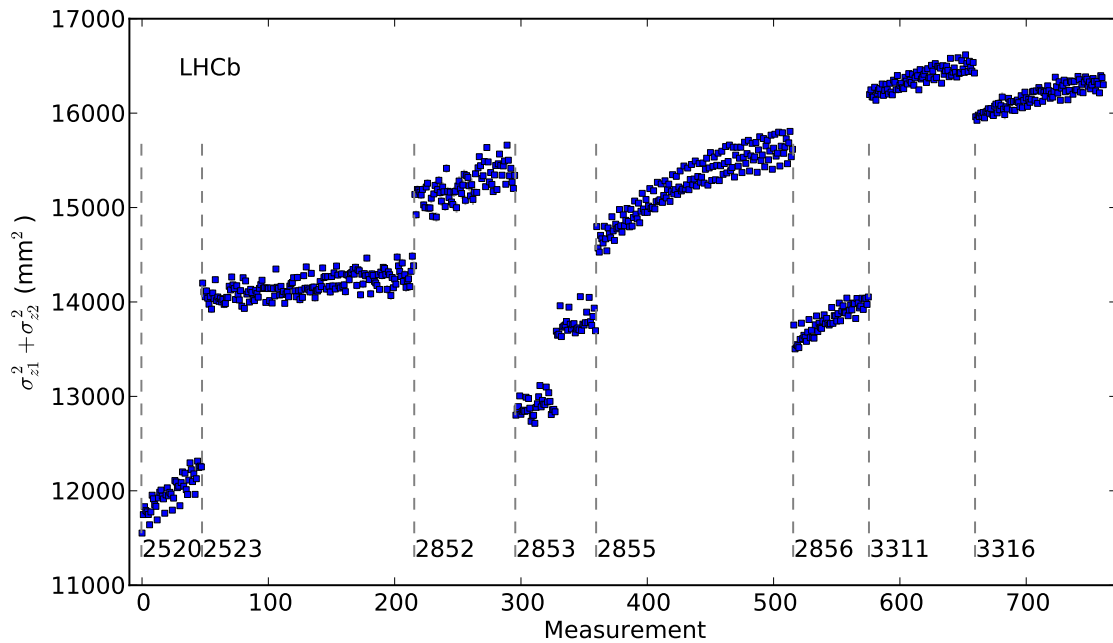


**Fig. D.8:** Convoluted bunch length  $\sigma_{z1}^2 + \sigma_{z2}^2$  measurement for all fills at 8 TeV. The statistical uncertainty is typically smaller than the marker. The measurements are sorted by time and BCID. The fill is indicated in the figure and the fill boundaries are denoted with a vertical dashed line.

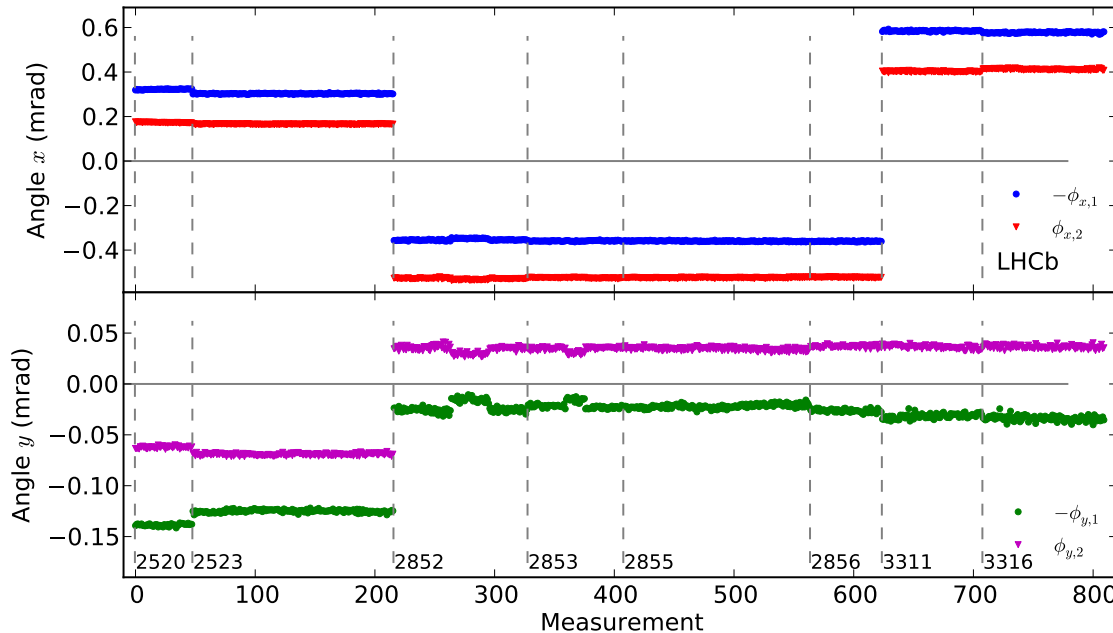


**Fig. D.9:** Beam crossing angles. The measurements are sorted by time and BCID. The fill is indicated in the figure and the fill boundaries are denoted with a vertical dashed line.

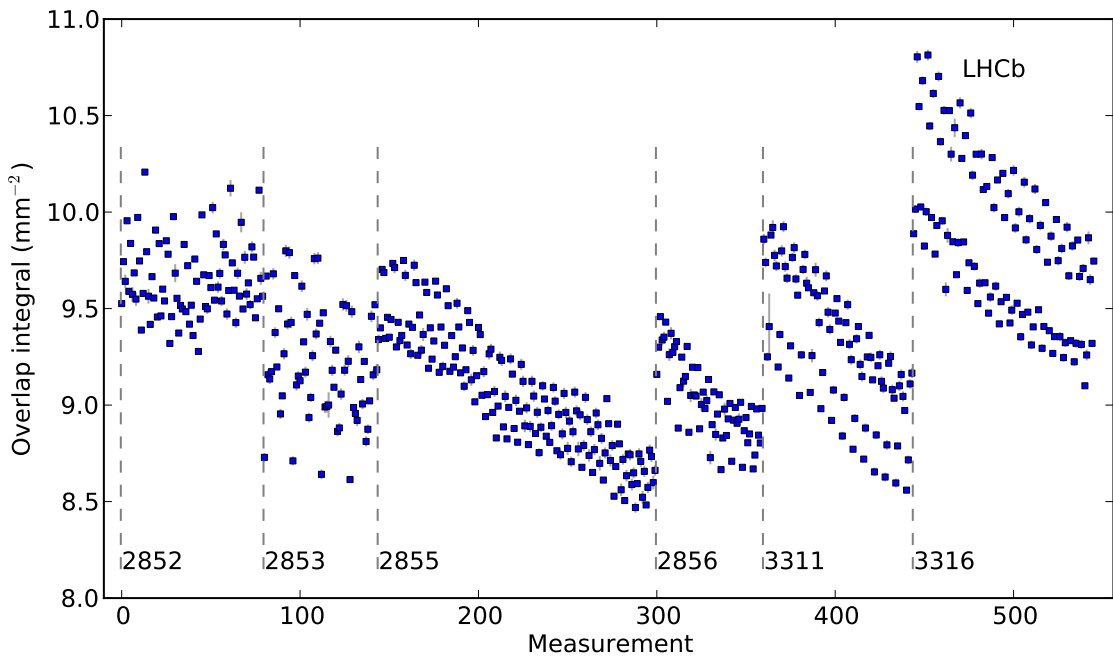


**Fig. D.10:** Overlap integral measurement. The measurements are sorted by time and BCID. The fill is indicated in the figure and the fill boundaries are denoted with a vertical dashed line.

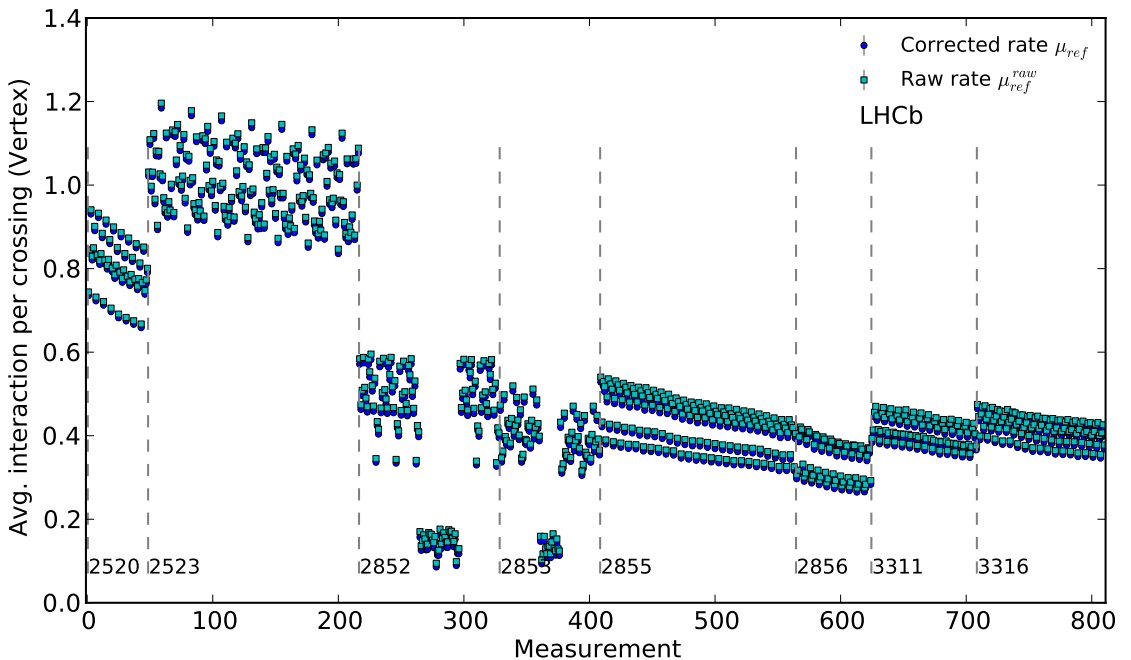


**Fig. D.11:** Average interaction rate per bunch crossing for the vertex counter. The background correction required for this counter is smaller than for the track counter.

**Table D.1:** Ghost charge (GC) fractions for fill 3562. The systematic (syst. ) uncertainty is fully correlated between beams. The gps time is at the center of the integration interval dt.

gps	dt (s)	GC (%)	Beam 1		GC (%)	syst. (%)	stat. (%)
			syst. (%)	stat. (%)			
1360778924	240	0.357	0.022	0.009	0.228	0.006	0.009
1360779164	240	0.378	0.024	0.009	0.235	0.006	0.009
1360779404	240	0.374	0.023	0.009	0.241	0.006	0.009
1360779644	240	0.425	0.026	0.010	0.250	0.006	0.010
1360779884	240	0.422	0.025	0.010	0.279	0.008	0.010
1360780124	240	0.445	0.027	0.010	0.277	0.007	0.010
1360780364	240	0.471	0.029	0.011	0.322	0.009	0.011
1360780604	240	0.499	0.030	0.011	0.336	0.009	0.011
1360780844	240	0.539	0.033	0.011	0.345	0.009	0.012
1360781084	240	0.553	0.033	0.012	0.365	0.009	0.012
1360781324	240	0.616	0.038	0.012	0.404	0.011	0.013
1360781564	240	0.647	0.039	0.013	0.427	0.011	0.013
1360781804	240	0.702	0.043	0.013	0.434	0.011	0.013
1360782044	240	0.732	0.044	0.013	0.471	0.012	0.014
1360782284	240	0.779	0.049	0.014	0.486	0.013	0.014
1360782533	240	0.809	0.051	0.014	0.530	0.014	0.015
1360782773	240	0.853	0.054	0.015	0.537	0.013	0.015
1360783013	240	0.893	0.054	0.015	0.567	0.014	0.015
1360783253	240	0.948	0.058	0.015	0.625	0.016	0.016
1360783493	240	0.987	0.061	0.016	0.667	0.016	0.017
1360783733	240	1.006	0.061	0.016	0.655	0.017	0.016
1360783973	240	1.082	0.067	0.017	0.666	0.017	0.017
1360784213	240	1.048	0.064	0.016	0.747	0.019	0.018
1360784453	240	1.102	0.068	0.017	0.772	0.020	0.018
1360784693	240	1.140	0.070	0.017	0.790	0.021	0.018
1360784933	240	1.154	0.072	0.017	0.828	0.021	0.019
1360785173	240	1.223	0.076	0.018	0.888	0.023	0.019
1360785413	240	1.235	0.076	0.018	0.886	0.023	0.020
1360785670	240	1.279	0.079	0.017	0.950	0.025	0.019

**Table D.2:** Ghost charge (GC) fractions for fill 3563. The systematic (syst. ) uncertainty is fully correlated between beams. The gps time is at the center of the integration interval dt.

gps	dt (s)	GC (%)	syst. (%)		GC (%)	syst. (%)	
			Beam 1	stat. (%)		Beam 2	stat. (%)
1360796200	240	0.543	0.034	0.011	0.419	0.010	0.012
1360796440	240	0.535	0.033	0.011	0.426	0.011	0.013
1360796680	240	0.555	0.033	0.011	0.423	0.011	0.013
1360796920	240	0.557	0.035	0.012	0.418	0.011	0.013
1360797160	240	0.584	0.036	0.012	0.443	0.012	0.013
1360797400	240	0.580	0.036	0.012	0.466	0.012	0.014
1360797640	240	0.600	0.038	0.012	0.459	0.012	0.014
1360797880	240	0.634	0.039	0.013	0.520	0.013	0.015
1360798120	240	0.623	0.038	0.012	0.472	0.012	0.014
1360798360	240	0.652	0.041	0.013	0.474	0.013	0.014
1360798600	240	0.686	0.042	0.013	0.503	0.013	0.014
1360798840	240	0.692	0.042	0.013	0.520	0.013	0.014
1360799080	240	0.718	0.044	0.013	0.534	0.014	0.015
1360799320	240	0.738	0.045	0.014	0.533	0.014	0.015
1360799557	240	0.746	0.045	0.014	0.557	0.015	0.015
1360799803	240	0.809	0.050	0.014	0.537	0.014	0.015
1360800043	240	0.822	0.050	0.014	0.581	0.015	0.015
1360800283	240	0.858	0.052	0.015	0.568	0.015	0.015
1360800523	240	0.871	0.054	0.015	0.625	0.016	0.016
1360800763	240	0.910	0.055	0.015	0.600	0.016	0.016
1360801003	240	0.898	0.054	0.015	0.652	0.017	0.016
1360801243	240	0.937	0.057	0.015	0.645	0.017	0.016
1360801483	240	0.933	0.059	0.015	0.680	0.018	0.017
1360801723	240	0.977	0.060	0.016	0.654	0.017	0.017
1360801963	240	0.980	0.061	0.016	0.696	0.018	0.017
1360802203	240	0.985	0.059	0.016	0.698	0.018	0.017
1360802443	240	1.071	0.066	0.017	0.716	0.018	0.017
1360802683	240	1.064	0.066	0.017	0.761	0.019	0.018
1360802923	240	1.076	0.065	0.017	0.770	0.020	0.018
1360803164	240	1.102	0.067	0.017	0.782	0.020	0.018
1360803413	240	1.108	0.068	0.017	0.804	0.021	0.019
1360803653	240	1.140	0.071	0.017	0.810	0.022	0.019
1360803893	240	1.189	0.072	0.018	0.837	0.022	0.019
1360804133	240	1.222	0.074	0.018	0.803	0.020	0.019
1360804373	240	1.226	0.075	0.018	0.880	0.023	0.020
1360804613	240	1.309	0.079	0.019	0.886	0.023	0.020
1360804853	240	1.342	0.084	0.019	0.903	0.023	0.020
1360805093	240	1.376	0.086	0.019	0.935	0.024	0.020
1360805333	240	1.444	0.090	0.020	0.978	0.026	0.021
1360805573	240	1.433	0.088	0.020	0.974	0.025	0.021
1360805813	240	1.481	0.092	0.020	0.997	0.026	0.021
1360806053	240	1.550	0.095	0.021	1.046	0.027	0.022
1360806293	240	1.567	0.096	0.021	1.017	0.027	0.022
1360806533	240	1.586	0.096	0.021	1.059	0.028	0.022
1360806774	240	1.650	0.102	0.021	1.107	0.029	0.022
1360807023	240	1.663	0.101	0.021	1.115	0.029	0.022
1360807263	240	1.678	0.104	0.022	1.150	0.031	0.023
1360807503	240	1.718	0.104	0.022	1.184	0.030	0.023
1360807743	240	1.767	0.109	0.022	1.228	0.032	0.024
1360807983	240	1.794	0.110	0.023	1.218	0.032	0.024
1360808223	240	1.871	0.115	0.023	1.251	0.033	0.024
1360808463	240	1.875	0.115	0.023	1.235	0.031	0.024
1360808703	240	1.942	0.119	0.024	1.270	0.032	0.024
1360808943	240	2.002	0.124	0.024	1.318	0.034	0.025
1360809183	240	2.006	0.123	0.024	1.292	0.034	0.024
1360809423	240	2.148	0.130	0.025	1.356	0.035	0.025
1360809663	240	2.132	0.131	0.025	1.415	0.037	0.026
1360809903	240	2.156	0.131	0.025	1.426	0.038	0.026
1360810143	240	2.182	0.135	0.025	1.480	0.038	0.026
1360810384	240	2.215	0.136	0.025	1.546	0.040	0.027
1360810633	240	2.283	0.142	0.026	1.448	0.037	0.026
1360810873	240	2.322	0.144	0.026	1.542	0.040	0.027
1360811112	240	2.325	0.143	0.026	1.592	0.041	0.028

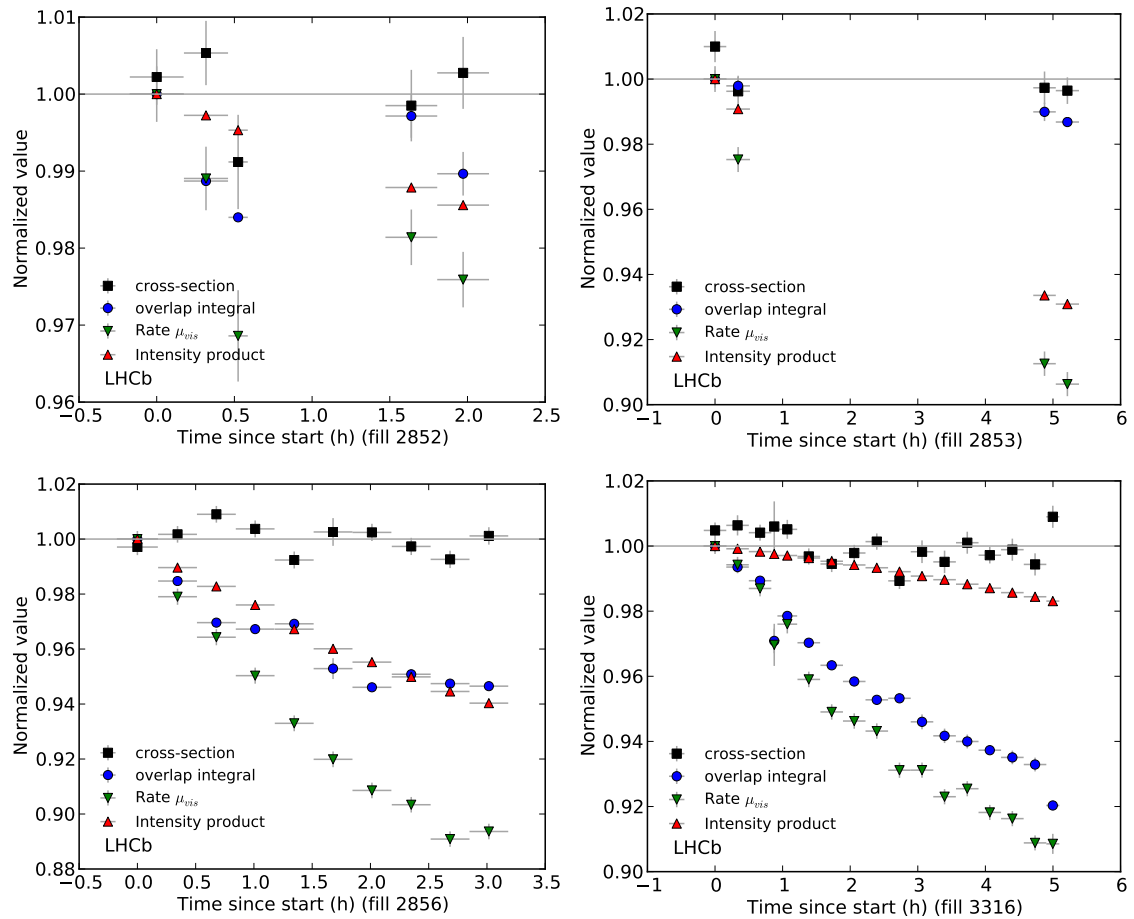


**Fig. D.12:** Normalized cross-section and related values evolution for a bunch pair in fills 2852, 2853, 2856 and 3316.

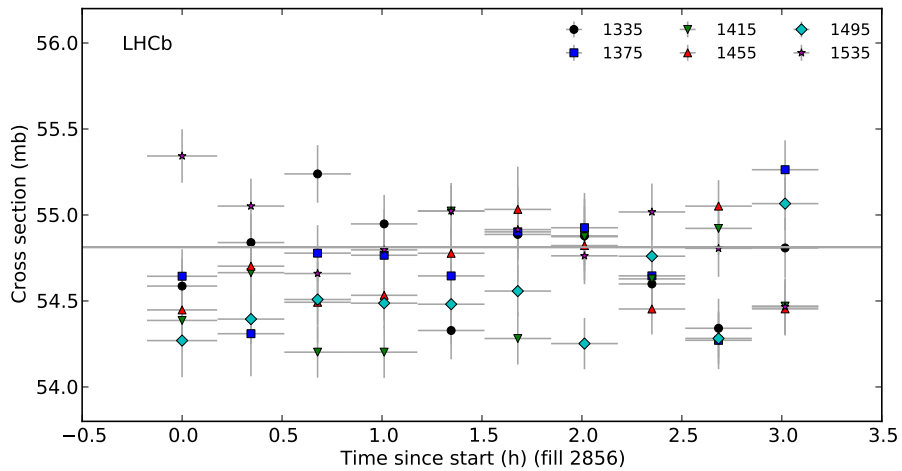


**Fig. D.13:** Cross-section trend of the six colliding bunches for fill 2856.

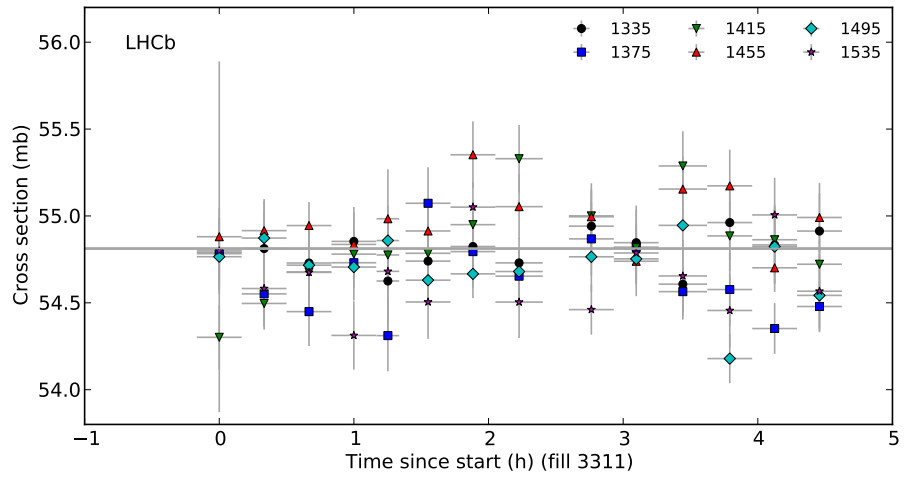


**Fig. D.14:** Cross-section trend of the six colliding bunches for fill 3311.

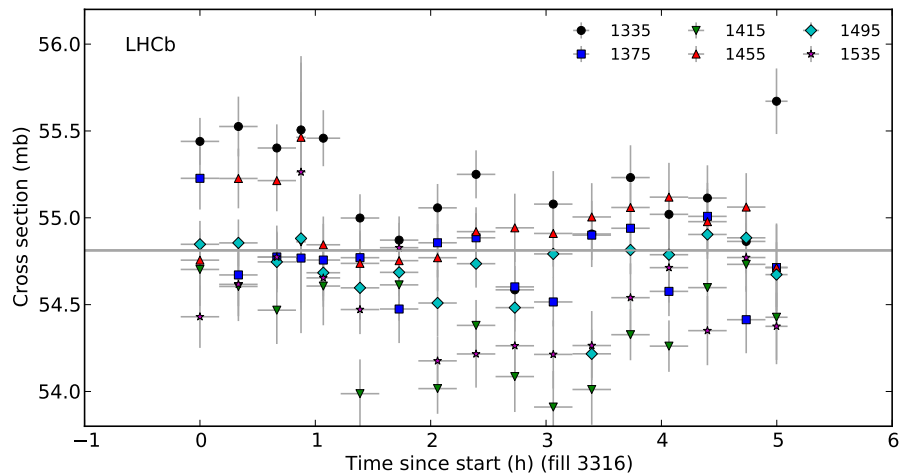


**Fig. D.15:** Cross-section trend of the six colliding bunches for fill 3316.

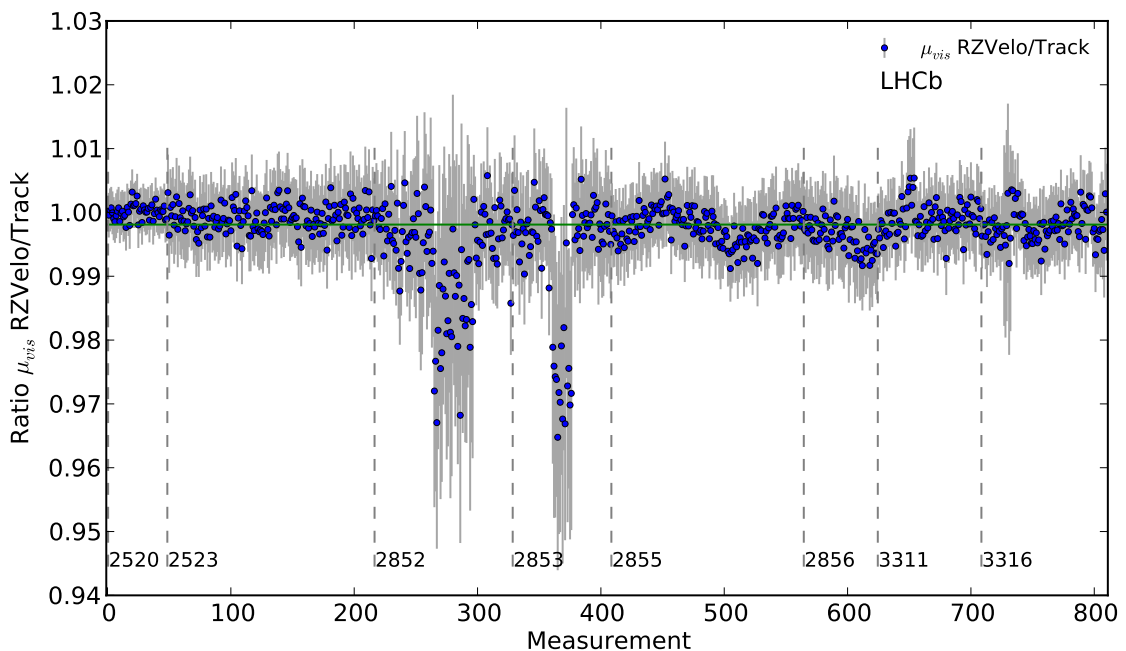


**Fig. D.16:** Ratio of RZVelo and Track counters after background correction.

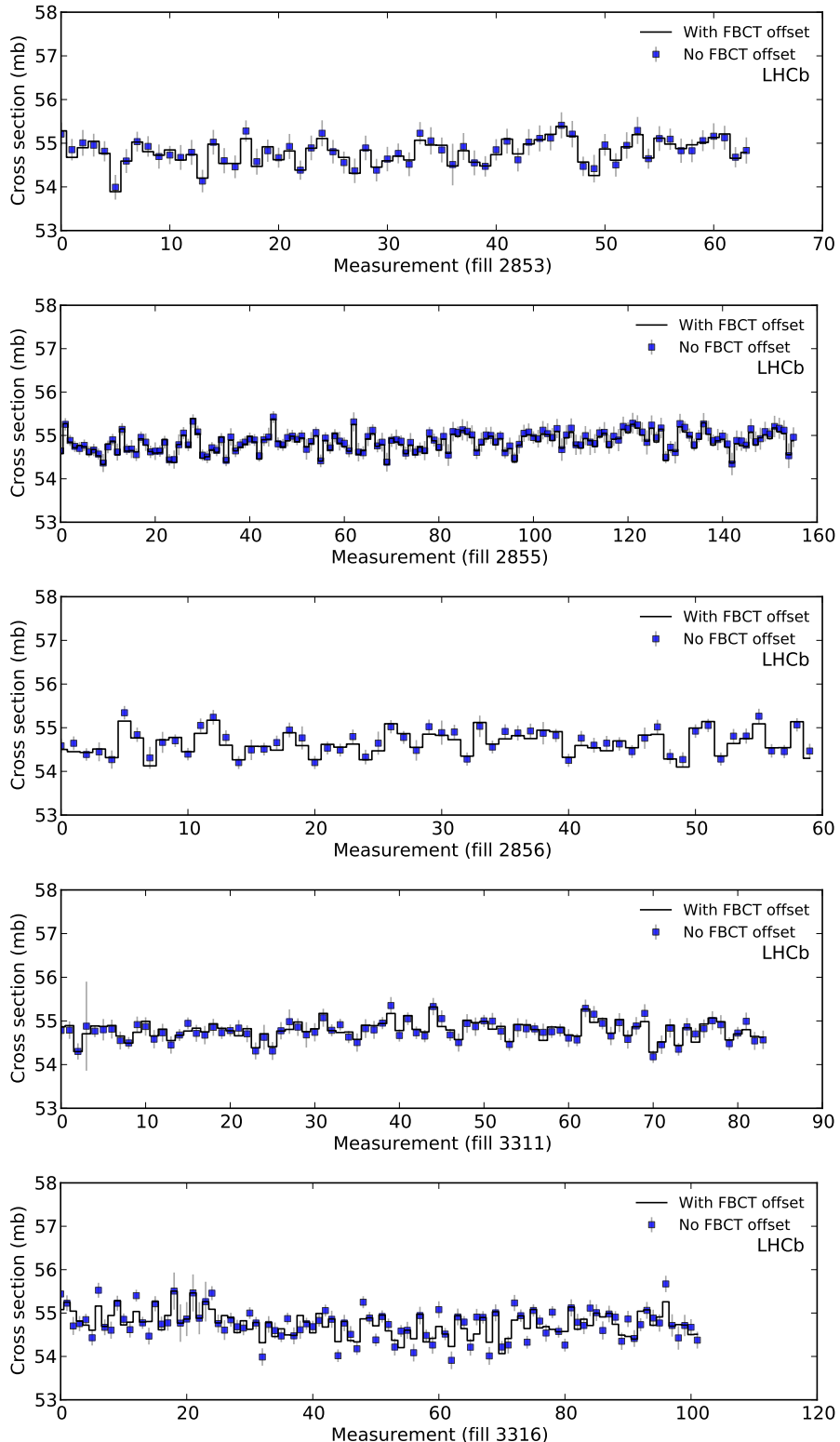


**Fig. D.17:** Cross-section with and without FBCT offset correction for fills 2853, 2855, 2856, 3311 and 3316 from panel to bottom panel, respectively.

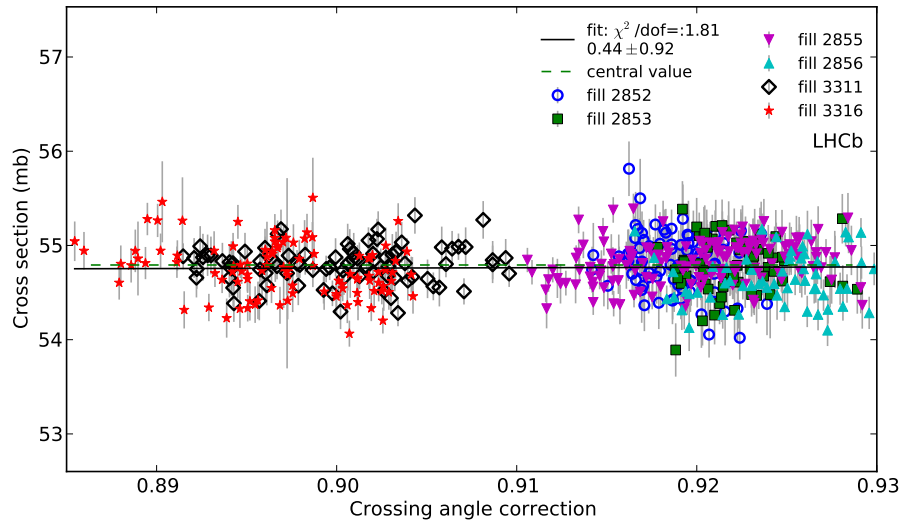


**Fig. D.18:** Correlation between the cross-section and crossing angle correction to the overlap integral. The central value is indicated as dashed horizontal line. A straight line fit through all data points is shown as solid black line.

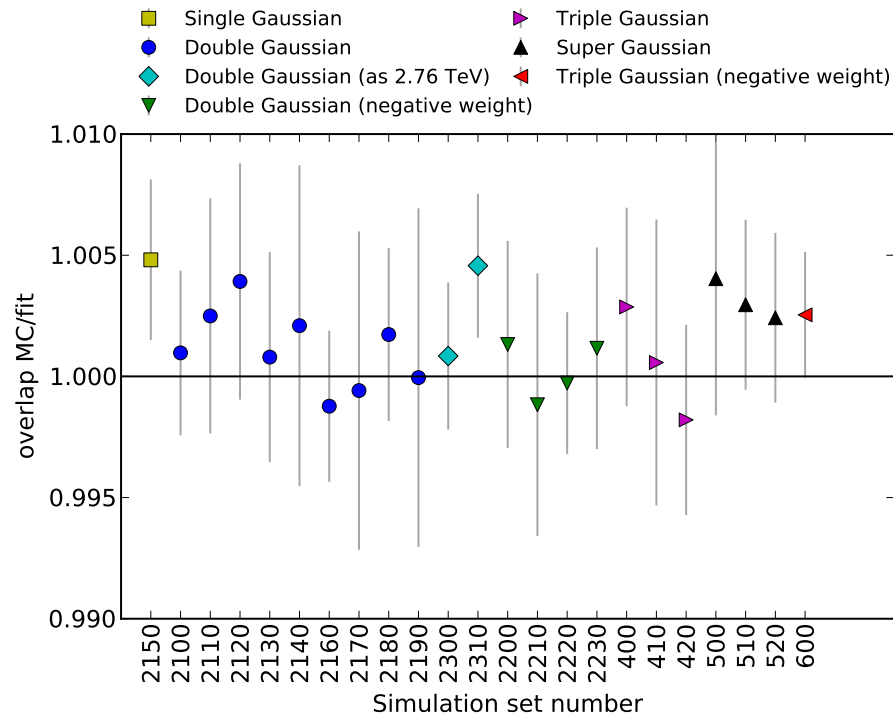


**Fig. D.19:** Evaluation of double Gaussian fit model applied to different simulation sets using single beam data only. Same plot as Fig. 7.14 (Sec. 7.2.5) but ignoring beam spot data.

## E GENERIC MONTE CARLO SIMULATION PARAMETERS

This Appendix contains the tables listing the generic simulation parameter sets used to generate datasets. The tables are referred to in the text.

**Table E.1:** Parameters for generic Monte Carlo sets with single and double Gaussian shape.

Set ID	beam	$w_x$	$\sigma_{x,n}$ ( $\mu\text{m}$ )	$\sigma_{x,w}$ ( $\mu\text{m}$ )	$\xi_x$ ( $\mu\text{m}$ )	$\alpha_x$ ( $\mu\text{rad}$ )	$w_y$	$\sigma_{y,n}$ ( $\mu\text{m}$ )	$\sigma_{y,w}$ ( $\mu\text{m}$ )	$\xi_y$ ( $\mu\text{m}$ )	$\alpha_y$ ( $\mu\text{rad}$ )
2150	1	0.5	95	95	0	-450	0.5	94	94	0	10
	2	0.5	93	93	0	550	0.5	96	96	0	10
2100	1	0.6	80	110	0	-450	0.45	60	110	0	10
	2	0.5	70	110	0	550	0.65	70	120	0	10
2110	1	0.6	85	110	0	-450	0.45	60	110	0	10
	2	0.5	75	110	0	550	0.65	70	120	0	10
2120	1	0.6	85	110	0	-450	0.45	70	110	0	10
	2	0.5	75	110	0	550	0.65	80	120	0	10
2130	1	0.6	75	115	0	-450	0.45	65	130	0	10
	2	0.5	65	115	0	550	0.65	75	135	0	10
2140	1	0.6	90	115	0	-450	0.45	80	110	0	10
	2	0.5	85	115	0	550	0.65	90	120	0	10
2160	1	0.6	70	115	0	-450	0.45	65	125	0	10
	2	0.5	60	110	0	550	0.65	70	130	0	10
2170	1	0.4	67	111	0	-450	0.4	58	118	0	10
	2	0.5	66	116	0	550	0.5	59	112	0	10
2180	1	0.45	80	160	0	-450	0.45	58	112	0	10
	2	0.35	66	110	0	550	0.35	57	110	0	10
2190	1	0.55	70	116	0	-450	0.55	70	125	0	10
	2	0.45	75	110	0	550	0.45	60	110	0	10
2300	1	0.88	153	219	0	-880	0.88	143	223	0	10
	2	0.86	133	217	0	880	0.86	133	146	0	10
2200	1	1.1	83	66	0	-450	1.15	80	55	0	10
	2	1.1	82	65	0	550	1.15	82	75	0	10
2210	1	1.2	83	66	0	-450	1.2	80	55	0	10
	2	1.2	82	65	0	550	1.2	82	75	0	10
2220	1	1.1	83	66	0	-450	1.1	80	55	0	10
	2	1.1	82	65	0	550	1.1	82	75	0	10
2230	1	1.05	87	50	0	-450	1.05	80	55	0	10
	2	1.05	89	51	0	550	1.05	80	46	0	10

---

**Table E.2:** Parameters for generic Monte Carlo sets with triple Gaussian shape.

Set	beam	$w_{x,n}$	$w_{x,m}$	$\sigma_{x,n}$	$\sigma_{x,m}$	$\sigma_{x,w}$	$w_{y,n}$	$w_{y,m}$	$\sigma_{y,n}$	$\sigma_{y,m}$	$\sigma_{y,w}$	$\xi_x; \xi_y$	$\alpha_x; \alpha_y$
ID		( $\mu\text{m}$ )	( $\mu\text{m}$ )	( $\mu\text{m}$ )			( $\mu\text{m}$ )	( $\mu\text{rad}$ )					
400	1	0.25	0.3	65	80	130	0.25	0.3	60	80	125	0;0	-450;10
	2	0.3	0.25	75	90	125	0.25	0.2	60	80	130	0;0	550;10
410	1	0.25	0.3	60	80	115	0.25	0.3	60	85	120	0;0	-450;10
	2	0.3	0.25	65	80	125	0.25	0.2	60	85	125	0;0	550;10
420	1	0.3	0.35	60	80	120	0.3	0.3	60	85	115	0;0	-450;10
	2	0.35	0.3	65	90	125	0.35	0.3	65	90	125	0;0	550;10
600	1	-0.1	0.45	50	70	100	-0.1	0.45	50	75	95	0;0	-450;10
	2	-0.15	0.5	55	80	105	-0.15	0.5	55	90	100	0;0	550;10

**Table E.3:** Parameters for generic Monte Carlo sets with super Gaussian shape.

Set	beam	$\epsilon_x$	$\sigma_x$	$\xi_x$	$\alpha_x$	$\epsilon_y$	$\sigma_y$	$\xi_y$	$\alpha_y$
ID			( $\mu\text{m}$ )	( $\mu\text{m}$ )	( $\mu\text{rad}$ )		( $\mu\text{m}$ )	( $\mu\text{m}$ )	( $\mu\text{rad}$ )
500	1	0.1	93	0	-450	0.1	90	0	10
	2	0.1	92	0	550	0.1	92	0	10
510	1	0.05	93	0	-450	0.05	90	0	10
	2	0.05	92	0	550	0.05	92	0	10
520	1	0.2	93	0	-450	0.2	90	0	10
	2	0.2	92	0	550	0.2	92	0	10

# F SMOG CHARACTERIZATION AND COMMISSIONING

## Contents

<b>F.1</b>	<b>Introduction</b>	144
<b>F.2</b>	<b>Laboratory setup</b>	145
<b>F.3</b>	<b>Evacuation and outgassing of SMOG</b>	145
F.3.1	Evacuation of SMOG only	146
F.3.2	Evacuation of the high pressure tube	147
F.3.3	Evacuation of the SMOG up to the high pressure gas bottle	148
<b>F.4</b>	<b>Gas injection and flow estimation</b>	149
F.4.1	Injection tests	149
F.4.2	Outgassing and flow rates	151
F.4.3	Estimation of Non-Evaporable Getter saturation	153
<b>F.5</b>	<b>Modifications performed to the SMOG</b>	154
F.5.1	Injections at different high pressures	154
F.5.2	Pressure loss with closed volume	157
F.5.3	Injections with NEG filter	158
F.5.4	Vacuum recovery after injection	160
<b>F.6</b>	<b>Installation and commissioning</b>	161

## F.1 Introduction

The BGI method relies on interaction vertices between the circulating beam and the residual gas present at the interaction point. This method was proposed in 2005 [37] and a device called SMOG<sup>1</sup> was developed to inject gas inside the beam vacuum at the interaction point [66, 67, 68, 69]. Before being able to operate the SMOG, a series of laboratory tests was required to assess its working principle and to characterize the flow of residual gases and of the injected gas. This document describes the various tests which were performed in the vacuum laboratory, the results of the SMOG commissioning in the LHCb experiment and the first gas injection tests.

A drawing of the main SMOG components and valve names is shown in Fig. F.1. The valves “Fill” and “Bypass” are electro-pneumatic valves (VAT series 57 all-metal) controlled by software, while the valves “HP” and “Pump” are manual. The SMOG is connected to the a vacuum vessel (called here pre-VELO), which precedes the VELO beam vacuum, with a 4 mm ID tube of a length of about 4 meters. The pre-VELO volume is evacuated with a 250  $\ell/\text{s}$  turbomolecular pump and is separated from the VELO beam vacuum by a gate valve. A high pressure gas bottle with pressure reducer is connected to the HP valve such that the gas pressure up to the Fill valve is about 1 to 4 bars. When the Fill valve is opened, the gas flows through the restriction that has a conductance of about  $10^{-8} \ell/\text{s}$  limiting the gas flow toward the VELO to about  $3 \cdot 10^{-5} \text{ mbar}\ell/\text{s}$ .

---

<sup>1</sup>System to Measure the Overlap integral with Gas.

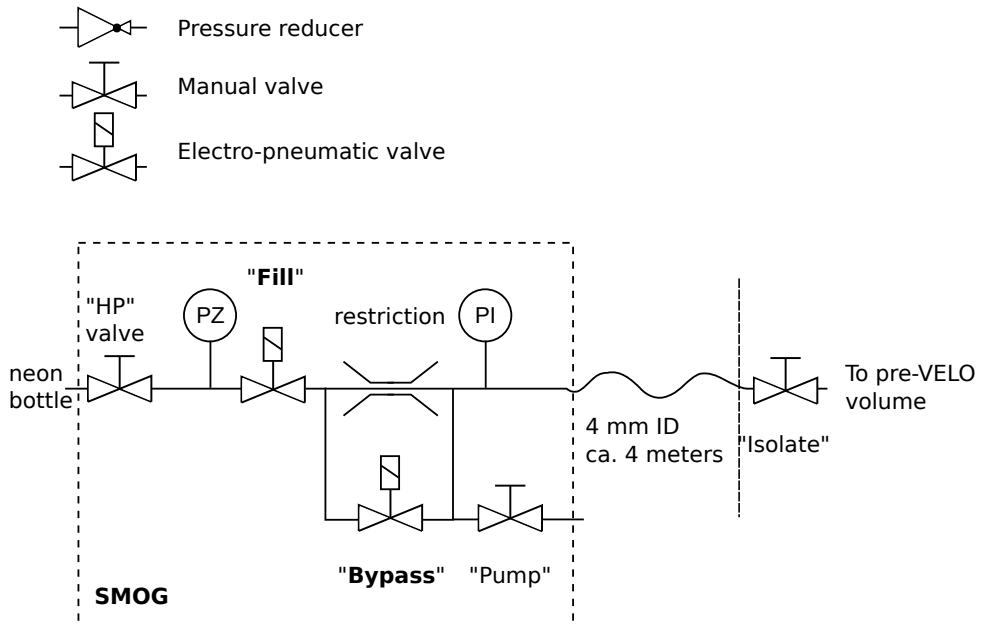


**Fig. F.1:** Scheme of stand-alone SMOG. The valves are named according to their use. The following pressure gauges are used: PZ=high pressure piezo, PI=Pirani.

## F.2 Laboratory setup

The SMOG system was installed in the vacuum laboratory in its original configuration including the 4 mm ID stainless steel tubes for the high and low pressure gas injection. Fig. F.2 shows a schematic view of the test setup. The pressure reducer and manual HP valve have been replaced due to leaks. The setup includes the SMOG panel and the pre-VELO test bench. The gas bottle is connected to the high pressure part of the SMOG with a 4 mm ID tube. The SMOG output is connected to the pre-VELO test bench with a 4 mm ID tube of about 4 meters. The pre-VELO test bench is evacuated with a Pfeiffer turbomolecular pump (model TMU 521P) which is identical to the one (TP301) installed in the experiment and used during the VELO evacuation. An Alcatel ACP28 dry pump is used as forepump.

The SMOG device is shown in Fig. F.3 and the SMOG connected to the test bench in the vacuum laboratory is shown in Fig. F.4. The different valve states used in the measurements are listed in Table F.1. The pre-VELO test bench vacuum is monitored with two Penning pressure gauges (PE1 and PE2) and a quadrupole mass analyzer (QMA) (Pfeiffer Prisma 200). This first setup is used to measure the time needed to evacuate the SMOG, evaluate the residual gases flowing from the SMOG and test the gas injection. An additional vacuum vessel will be installed to mimic the VELO beam vacuum volume as will be discussed in Sec. F.5.

## F.3 Evacuation and outgassing of SMOG

The SMOG and the 4 mm ID tubes are evacuated in three steps through the 4 mm ID tube: first, the SMOG is evacuated in *bypass* state (see Table F.1), which excludes all high pressure volumes left of the Fill valve. As a second step, in state *HP evacuate*, the high pressure tube excluding the reducer is pumped. Finally, the full volume up to the neon bottle is evacuated in the state *HPR evacuate*. The components are not baked-out. The outgassing rate can be estimated by measuring the pressure increase in the pre-VELO test bench when the Isolate valve is opened.

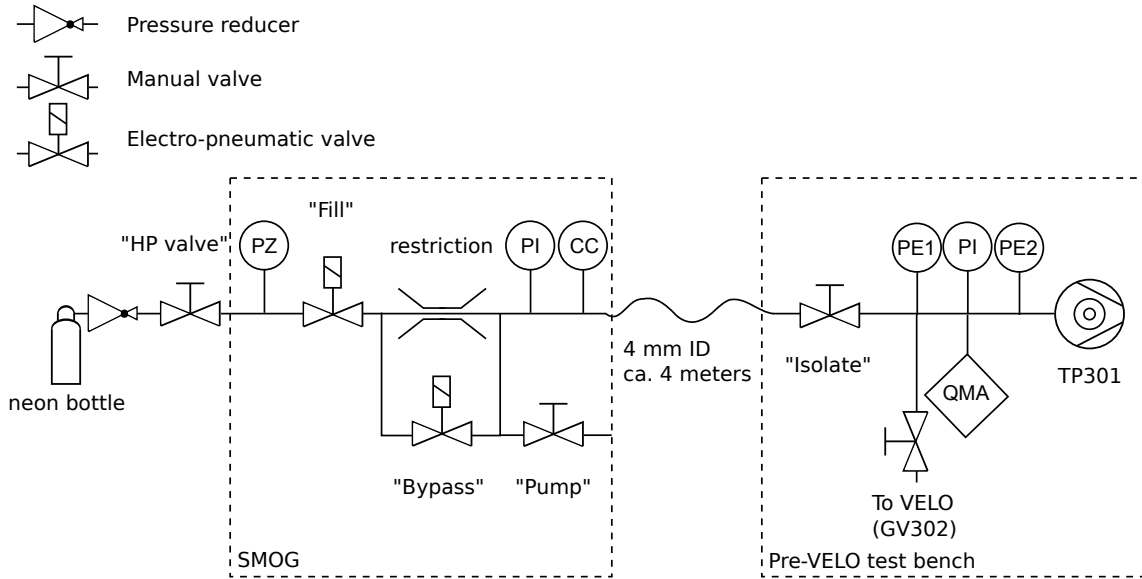


**Fig. F.2:** Scheme of the SMOG and test bench setup. The valves are named according to their use. The following pressure gauges are used: PZ=high pressure piezo, PI=Pirani, CC=Compact Capacitance, PE=Penning. The PE1 and PE2 gauges are placed at about 40 and 10 cm above the turbomolecular pump respectively. The QMA is a Pfeiffer Prisma 200.

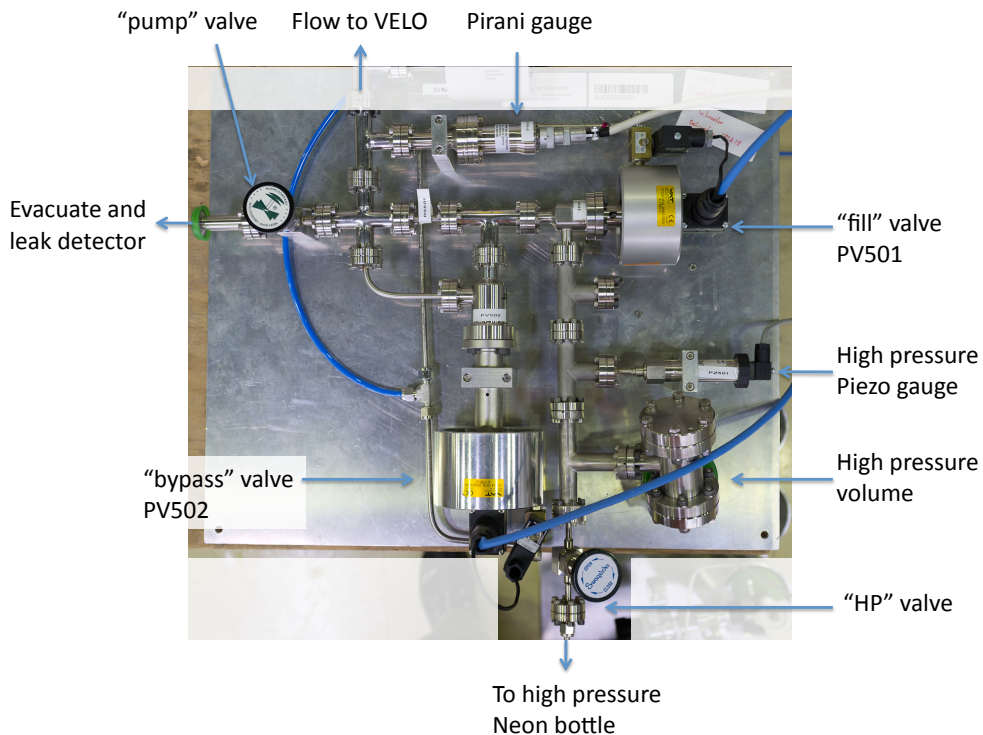


**Fig. F.3:** SMOG device in the laboratory. Components are indicated in the figure.

### F.3.1 Evacuation of SMOG only

The first measurement is performed without the high pressure tube. A blind flange is placed at the SMOG high pressure input. Table F.2 lists the pressures for each state after one day of pumping. The increase in ambient temperature can explain the higher pressure observed in the second “Isolated” state measured 2.5 hours later. The mass spectra for each state are shown in Fig. F.5. The mass spectra are similar and the peaks are consistent with the different pressures and reflect the residual gas expectations of an unbaked system. Note that the spectrum measured in the *Isolated* state shows

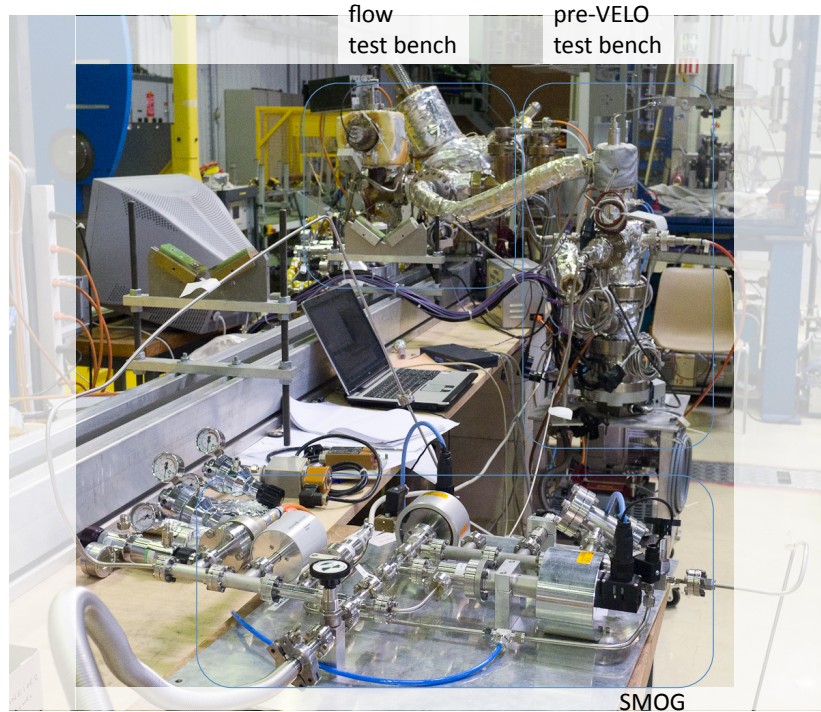


**Fig. F.4:** SMOG laboratory setup. The SMOG in the first plane is connected to the pre-VELO test bench (right). The pre-VELO is connected to the VELO (flow) test bench on the left. The pre-VELO and VELO test bench are baked-out.

**Table F.1:** Possible valve states. See Fig. F.2 for the valve placements. The Fill and Bypass valves are interlocked such that both valves can not be opened at the same time. Both “evacuate” states require to disconnect the interlock and to operate the valves manually. This state is only necessary to evacuate the high pressure line during the installation.

State name	“Fill”	“Bypass”	“Isolate”	“Pump”	“HP valve”
Isolated	-	-	closed	-	-
Injection off	closed	closed	open	closed	-
Injection on	open	closed	open	closed	-
Bypass	closed	open	open	closed	-
HP evacuate	open	open	open	closed	closed
HPR evacuate	open	open	open	closed	open

the base level of residual gases in the pre-VELO volume.

**Table F.2:** Pressures of different SMOG states. The high pressure tube is replaced by a blind flange.

Gauge (mbar)	Isolated	Injection off	Bypass	HP evacuate	Isolated
PE1	$1.8 \cdot 10^{-9}$	$3.2 \cdot 10^{-9}$	$3.4 \cdot 10^{-9}$	$3.9 \cdot 10^{-9}$	$2.4 \cdot 10^{-9}$
PE2	$6.6 \cdot 10^{-10}$	$1.2 \cdot 10^{-9}$	$1.3 \cdot 10^{-9}$	$1.5 \cdot 10^{-9}$	$9.0 \cdot 10^{-10}$
CC	$4.45 \cdot 10^{-2}$	$4.45 \cdot 10^{-2}$	$4.45 \cdot 10^{-2}$	$4.45 \cdot 10^{-2}$	$4.48 \cdot 10^{-2}$

### F.3.2 Evacuation of the high pressure tube

The second measurement is performed with the high pressure tube connected to the SMOG. The HP valve connecting the pressure reducer is kept closed. Table F.3 lists the pressures for each state.

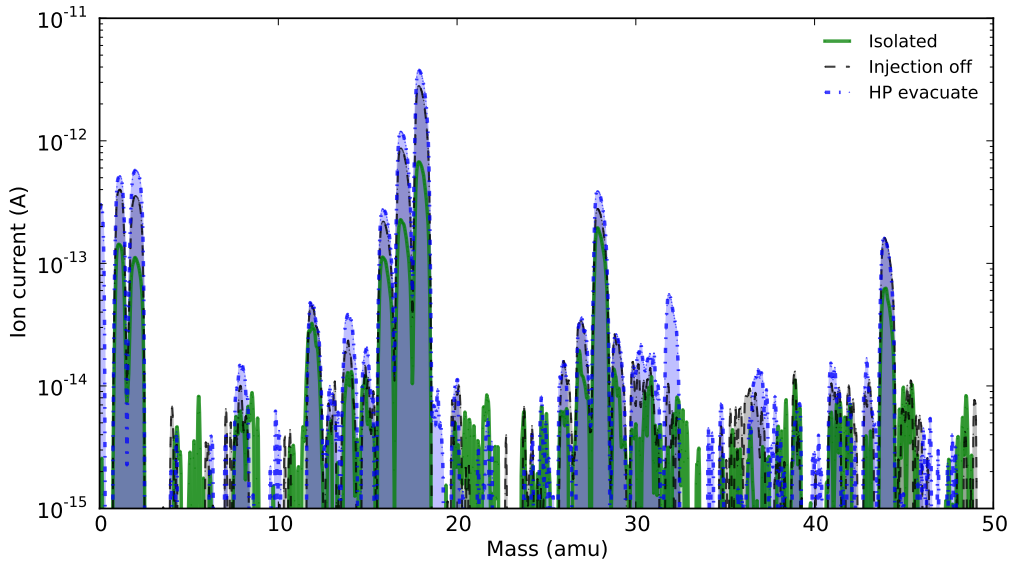


**Fig. F.5:** QMA spectra of SMOG output excluding the high pressure injection line (blind flange at SMOG high pressure input). The residual gas spectra are identical for all states and reflect an unbaked system. The *Isolated* state has lower peaks as expected.

The mass spectra for each state are shown in Fig. F.6. The state *HP evacuate* is measured again after 20 hours of pumping. The first measurement in the *HP evacuate* state reveals the presence of neon (mass peaks at 10, 11 and 20, 22 amu) and also air (mass peaks 40 and 32 amu). However, those peaks disappeared after 20 hours of pumping and the final residual gas spectrum is similar to the *Isolated* state.

**Table F.3:** Pressures of the different valve states. The high pressure 4 mm ID tube is connected to the SMOG input. The state *HP evacuate* has both valves Fill and Bypass opened to evacuate the part of the SMOG downstream of the restriction.

Gauge (mbar)	HP evacuate	Isolated	HP evacuate 20 hours later
PE1	$3.4 \cdot 10^{-6}$	$2.4 \cdot 10^{-10}$	$3.2 \cdot 10^{-9}$
PE2	$1.6 \cdot 10^{-6}$	$8.1 \cdot 10^{-10}$	$1.3 \cdot 10^{-9}$
CC	$5.4 \cdot 10^{-1}$	$4.3 \cdot 10^{-2}$	$4.3 \cdot 10^{-2}$

### F.3.3 Evacuation of the SMOG up to the high pressure gas bottle

The SMOG is evacuated in the state *HPR evacuate* with the HP valve and pressure reducer open. For comparison the state *Injection off* has both valves Fill and Bypass closed. The pressures of the different states are listed in Table F.4 after one day of pumping. The residual gas analysis (RGA) or the states are shown in Fig. F.7. The presence of neon (mass peaks at 10, 11 and 20, 22 amu) is visible in the *HPR evacuate* state (green line). This can be explained by a small leak in the bottle valve and is expected.

The buffer volume between the restriction and the Fill valve (called dead volume) is reduced mechanically to minimize the dead volume upstream of the restriction. This volume is filled with high pressure gas during SMOG operation. Since the dead volume reduces the flow conductance towards the high pressure part of the SMOG, the evacuation of the high pressure line requires a longer pumping time. The high pressure part is evacuated in two steps. First the high pressure line excluding the reducer is evacuated, the corresponding pressure decay is shown in (left) Fig. F.8. The

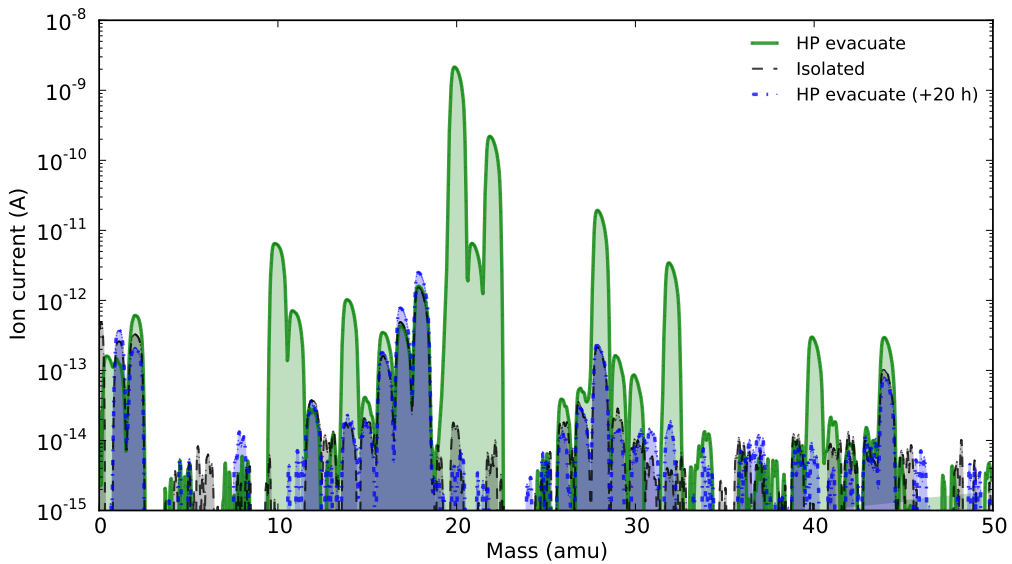


**Fig. F.6:** Residual gas spectrum of the SMOG output including the high pressure injection line. The HP valve is closed to isolate the pressure reducer and gas bottle. The first measurement of the *HP evacuate* state (dashed line) is taken at the beginning of the high pressure injection tube evacuation ( $P = 1.6 \cdot 10^{-6}$  mbar). The presence of neon (mass peaks at 10, 11 and 20, 22 amu) and air (mass peaks 40 and 32 amu) is clearly visible. After 20 hours of pumping the final residual gas spectrum is similar to the *Isolated* state.

**Table F.4:** Pressures of the different valve states with the high pressure line opened up to the gas bottle. In the *HPR evacuate* state, the HP valve and the pressure reducer are open.

Gauge (mbar)	HPR evacuate	Isolated	Injection off
PE1	$1.3 \cdot 10^{-8}$	$1.9 \cdot 10^{-9}$	$4.2 \cdot 10^{-9}$
PE2	$6.4 \cdot 10^{-9}$	$8.7 \cdot 10^{-10}$	$1.8 \cdot 10^{-9}$
CC	$4.38 \cdot 10^{-2}$	$4.20 \cdot 10^{-2}$	$4.27 \cdot 10^{-2}$

second step includes the evacuation of the pressure reducer and evacuates all parts up to the gas bottle, the pressure decay is shown in (right) Fig. F.8. In both cases, two pressure decays are visible in the pressure curves. A first rapid decrease is due to the evacuation of the high pressure line which is limited by the low conductance due to the filling of the dead volume upstream of the restriction. This first evacuation takes about 5 hours for the high pressure line and about 8 hours for the reducer. The first evacuation is followed by a slower pressure decrease similar to a normal outgassing decay. The pressure evolution in the *bypass* state over 23 days is shown in Fig. F.9. Ambient temperature variations influence the pressure below  $1 \cdot 10^{-9}$  mbar and are visible in the plot.

## F.4 Gas injection and flow estimation

### F.4.1 Injection tests

Four injection tests were performed with a Neon pressure of about 0.3 bar above atmospheric pressure (as indicated by the outlet gauge of the reducer). The pressure difference at the restriction is  $\approx 1.3$  bar. The injection procedure is divided in four states: *injection off*, *injection on*, *bypass* and *Isolated*. In the *injection off* state, the Isolate valve is open and the SMOG is pumped by the turbo pump; this is the normal stand-by state. The bypass state is used to evacuate the high pressure in the dead volume upstream of the restriction. The injection is started by opening the valve Fill and is stopped by opening the Bypass valve. Finally the Isolate valve is closed to stop the flow of impurities from the SMOG.

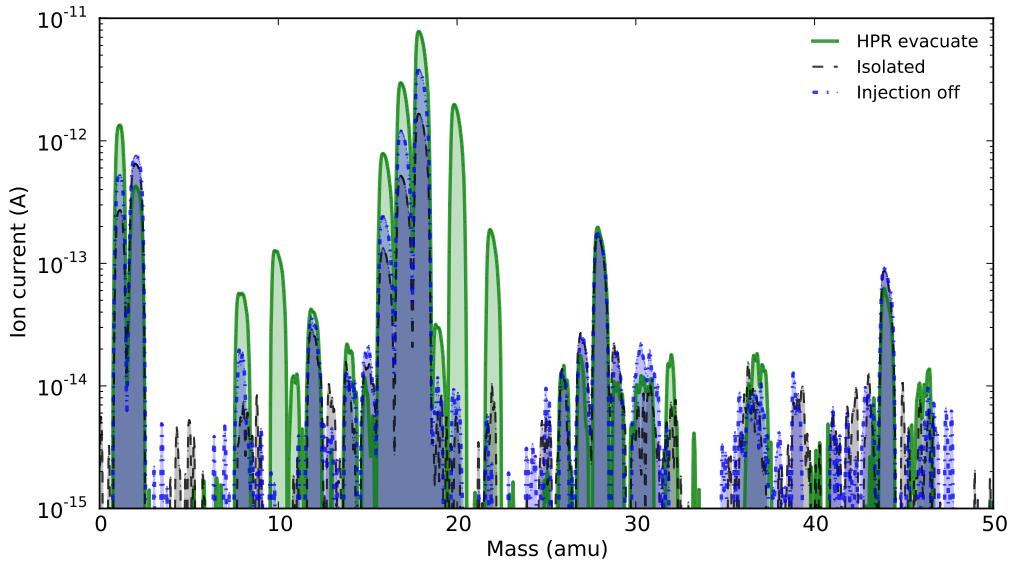


**Fig. F.7:** QMA spectrum of the SMOG output with vacuum path open up to the gas bottle (pressure reducer is open). In addition to the common residual gas peaks, the state *HPR evacuate* (green line) clearly shows the presence of neon (mass peaks at 10, 20 and 22 amu). The state *Injection off* has higher peaks compared to the *Isolated* state, but shows the same residual gas content.

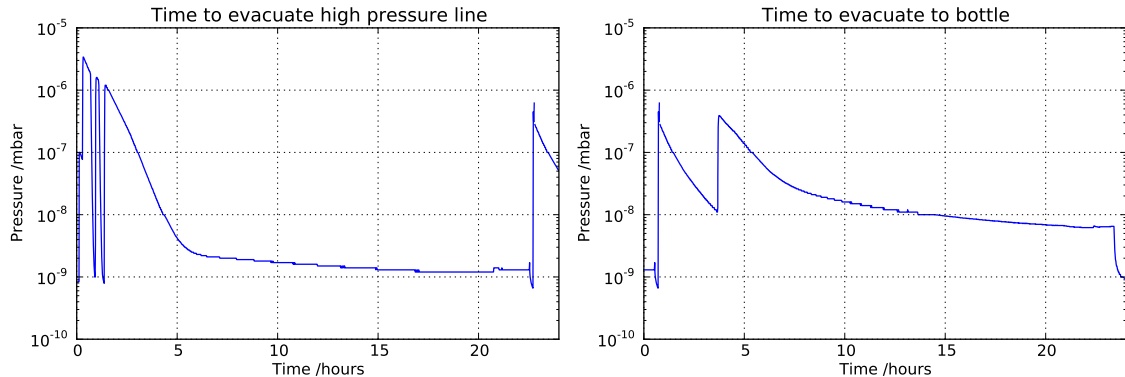


**Fig. F.8:** Pressure decay over time for the evacuation of the high pressure line. Left: pressure profile during the evacuation of high pressure line excluding the pressure reducer. The two pressure drops visible at the beginning are due to a change into state *Injection off* for testing. Right: pressure profile during the evacuation of high pressure line including the pressure reducer. At first the SMOG is evacuated through the Pump and the Isolate valve. After 3 hours the SMOG is evacuated through the Isolate valve only.

The pressure profile during the different injection states is shown in Fig. F.10 (showing the first measurement). Once the injection is started, a stable pressure is reached within about 5 minutes. When the injection valve Fill is closed, the bypass valve is used to evacuate the dead volume between the restriction and the Fill valve. The evacuation through the bypass requires about 10 minutes to stop the flow coming from the restriction. The Penning gauges in the pre-VELO test bench are turned off before opening the bypass valve due to the high pressure peak. After opening the bypass, the turbo pump current increases from 0.6 to 1.0 A during the first minute; however, the speed remains mostly constant ( $\pm 2$  Hz). The residual gas spectra of the injection states are shown in Fig. F.11. The pressures reached in the injection states are listed in Table F.5 for all measurements.

The pressure time profile for the evacuation of the “dead volume” between the Fill valve and restriction through the bypass is shown in Fig. F.12. With an unbaked system, a partial pressure of residual gases below  $\approx 5 \cdot 10^{-10}$  mbar is reached in 24 hours.

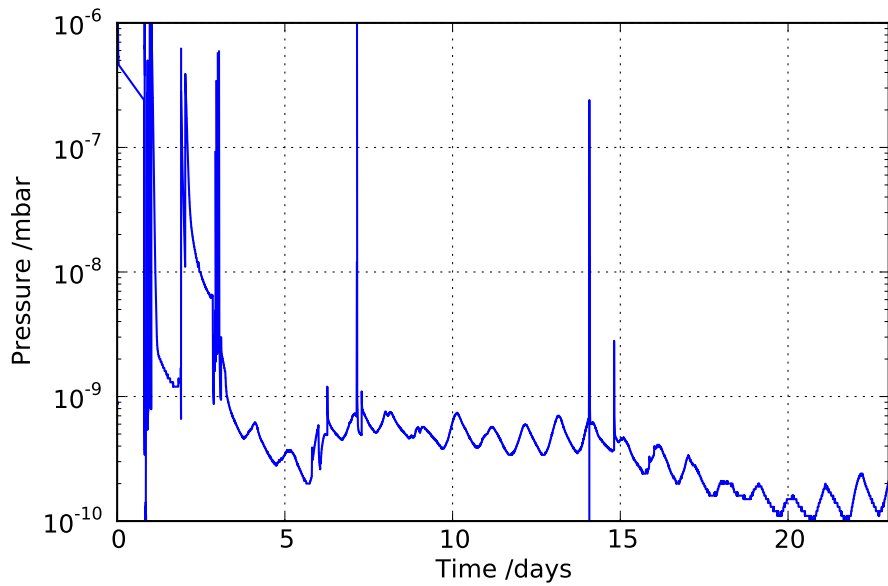


Fig. F.9: Pressure versus time during the first 23 days of pumping.

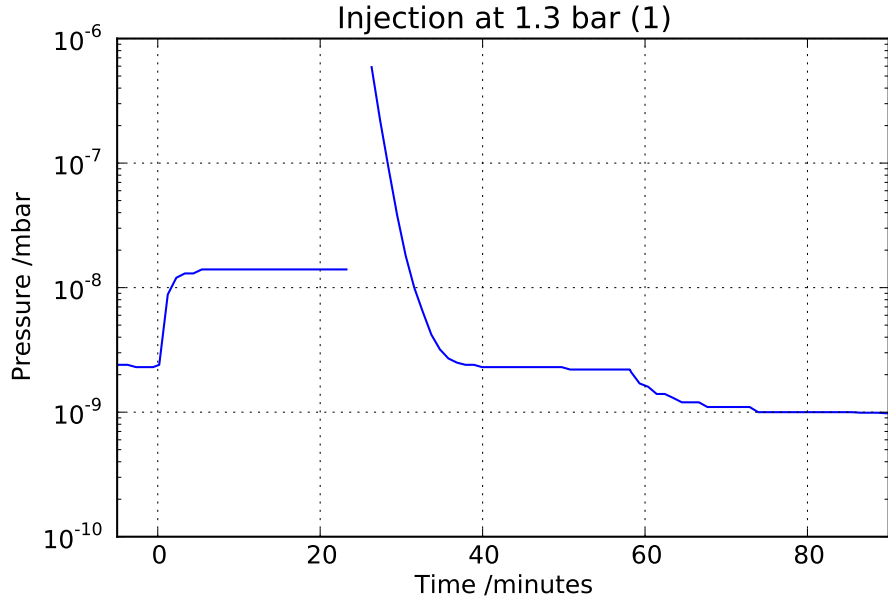


Fig. F.10: SMOG injection test at 1.3 bar. The measurement starts in the state *Injection off*. The injection is started at  $t = 0$  (state *Injection on*) and lasts for about 20 minutes. The bypass is opened after 25 minutes (state *bypass*). About 20 minutes later the pressure is constant and at the same level as in the starting state *Injection off*. The Isolate valve is closed at about 60 minutes bringing the SMOG in the state *Isolated*.

#### F.4.2 Outgassing and flow rates

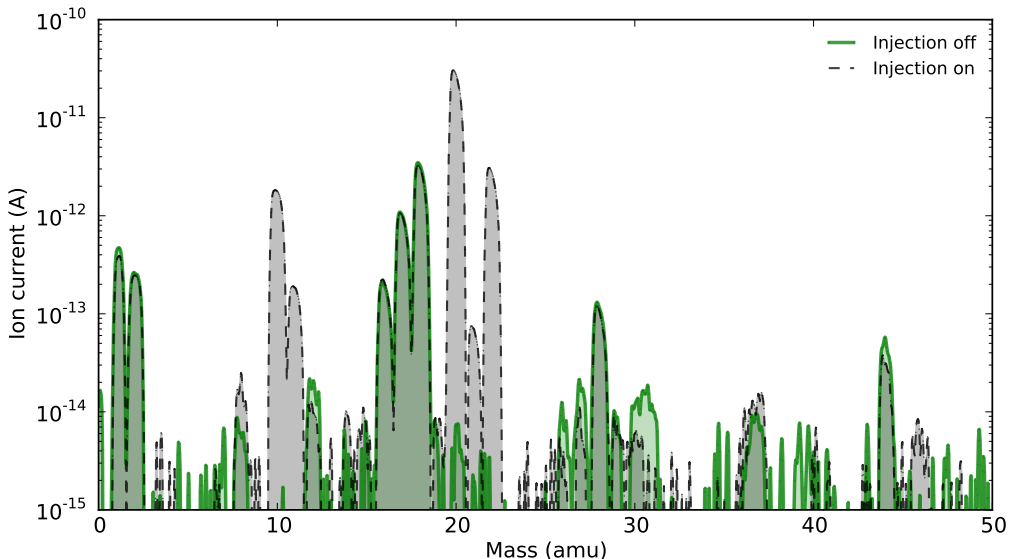
The end pressure of the states  $i$  reached in the pre-VELO test bench is dictated by the flow rate  $Q_i$  (in mbar  $\ell/s$ ) entering the volume and by the pumping speed  $S$  (in  $\ell/s$ ) of the turbomolecular pump

$$Q_i = p_i \cdot S. \quad (\text{F.1})$$

The rate  $Q_i$  of a state is composed of the sum of all flows from different residual gases entering the test bench volume. In the *Isolated* state (the valve to the SMOG is closed), the base pressure is a direct measurement of the background flow rate  $Q_{\text{isolated}}$  due to the outgassing of the test bench itself. During gas injection, the gas flow entering the test bench is composed of a neon flow  $Q_{\text{Neon}}$  and a flow of impurities  $Q_{\text{SMOG}}$ . The impurities are dominated by water and hydrogen and originate

**Table F.5:** Pressures during the different injection states.

Gauge (mbar)	Injection off	Injection on	Bypass	Isolated
Measurement 1 (3 days outgassing)				
PE1	$5.0 \cdot 10^{-9}$	$3.1 \cdot 10^{-8}$	$4.9 \cdot 10^{-9}$	$2.0 \cdot 10^{-9}$
PE2	$2.3 \cdot 10^{-9}$	$1.4 \cdot 10^{-8}$	$2.3 \cdot 10^{-9}$	$9.8 \cdot 10^{-10}$
CC	$4.40 \cdot 10^{-2}$	$5.04 \cdot 10^{-2}$	$4.44 \cdot 10^{-2}$	$4.42 \cdot 10^{-2}$
Measurement 2 (7 days outgassing)				
PE1	$1.4 \cdot 10^{-9}$	$2.6 \cdot 10^{-8}$	$1.5 \cdot 10^{-9}$	$1.0 \cdot 10^{-9}$
PE2	$6.9 \cdot 10^{-10}$	$1.2 \cdot 10^{-8}$	$7.8 \cdot 10^{-10}$	$5.1 \cdot 10^{-10}$
CC	$4.28 \cdot 10^{-2}$	$4.89 \cdot 10^{-2}$	$4.37 \cdot 10^{-2}$	$4.36 \cdot 10^{-2}$
Measurement 3 (14 days outgassing)				
PE1	$1.4 \cdot 10^{-9}$	$2.9 \cdot 10^{-8}$	$1.8 \cdot 10^{-9}$	$1.2 \cdot 10^{-9}$
PE2	$6.7 \cdot 10^{-10}$	$1.3 \cdot 10^{-8}$	$8.6 \cdot 10^{-10}$	$6.1 \cdot 10^{-10}$
CC	$4.21 \cdot 10^{-2}$	$4.90 \cdot 10^{-2}$	$4.33 \cdot 10^{-2}$	$4.31 \cdot 10^{-2}$
Measurement 4 (28 days outgassing)				
PE1	$8.3 \cdot 10^{-10}$	$2.8 \cdot 10^{-8}$	$1.9 \cdot 10^{-9}$	$9.7 \cdot 10^{-10}$
PE2	$4.0 \cdot 10^{-10}$	$1.2 \cdot 10^{-8}$	$9.1 \cdot 10^{-10}$	$5.0 \cdot 10^{-10}$
CC	$3.68 \cdot 10^{-2}$	$4.34 \cdot 10^{-2}$	$4.22 \cdot 10^{-2}$	$4.16 \cdot 10^{-2}$


**Fig. F.11:** Residual gas spectrum before, during and after injection. The pressure difference at the restriction is about 1.3 bar. The state “Injection on” (solid line) is dominated by neon (mass peaks 10, 11 and 20, 22 amu). The other peaks from hydrogen and water are identical to the state “Injection off” (dashed line).

from the outgassing of the SMOG and of the injection lines. The flow of impurities  $Q_{\text{SMOG}}$  from the SMOG is also present without gas injection in the states *Injection off* and *bypass* when the Isolate valve is open. The pressures of the states listed in Table F.5 are used to evaluate the individual gas flows. The pressure difference between the states *bypass* and *Isolated* is used to calculate  $Q_{\text{SMOG}}$ . The gauge PE2 is used as reference because it is placed directly above the turbomolecular pump similar to the VELO setup. The gas flow results are listed in Table F.6, assuming a pumping speed  $S$  of 250  $\ell/\text{s}$ . Uncertainties related to the Penning gauges, conductance estimation and pumping speed can be larger than 100% and those numbers should be understood as orders of magnitude.

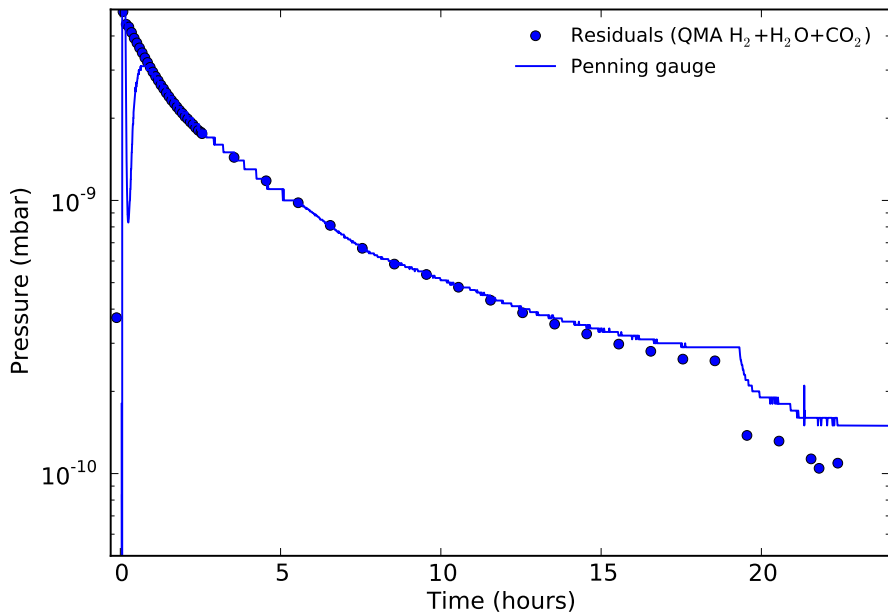


**Fig. F.12:** Partial pressure of residual gases during the evacuation of the “dead volume” through the bypass. About 24 hours are necessary to reduce the residual gases partial pressure below  $\approx 5 \cdot 10^{-10}$  mbar.

**Table F.6:** Gas flow rates.  $Q_{\text{isolated}}$  is the base background rate of the pre-VELO test bench.  $Q_{\text{SMOG}}$  is the base gas rate coming from the SMOG and is composed of impurities.  $Q_{\text{Neon}}$  is the neon rate injected with an inlet pressure of 1.3 bar.

Measurement number	$Q_{\text{Neon}}$ (mbar $\ell/\text{s}$ )	$Q_{\text{SMOG}}$ (mbar $\ell/\text{s}$ )	$Q_{\text{isolated}}$ (mbar $\ell/\text{s}$ )
1	$2.9 \cdot 10^{-6}$	$3.3 \cdot 10^{-7}$	$2.5 \cdot 10^{-7}$
2	$2.8 \cdot 10^{-6}$	$6.8 \cdot 10^{-8}$	$1.3 \cdot 10^{-7}$
3	$3.1 \cdot 10^{-6}$	$6.3 \cdot 10^{-8}$	$1.5 \cdot 10^{-7}$
4	$2.9 \cdot 10^{-6}$	$1.0 \cdot 10^{-7}$	$1.3 \cdot 10^{-7}$

### F.4.3 Estimation of Non-Evaporable Getter saturation

Some amount of Non-Evaporable Getter (NEG) surface on the beam pipe close to the VETO will be saturated by getterable gases (mostly water) coming from the SMOG during an injection. The amount of saturated surface depend on the injection time, the gas flow coming from the SMOG and the ratio entering into the VETO. As a conservative approach one can assume that the NEG around the VETO is mostly intact and the pumping speed is limited by the flange diameter towards the VETO. In this case one half of the SMOG getterable gases will be pumped by the turbo pump and the other half will be absorbed by the NEG.

In a first “pessimistic” approach, one can assume that the pre-VELO vacuum reaches a pressure of  $\approx 1 \cdot 10^{-9}$  mbar due to the outgassing flow. Furthermore, assuming a pumping speed of 250  $\ell/\text{s}$  in the pre-VELO volume, this results in an outgassing flow of  $1 \cdot 10^{-9} \cdot 250 \ell/\text{s} = 2.5 \cdot 10^{-7}$  mbar  $\ell/\text{s}$ . The total flow of molecules entering the VETO beam vacuum would be

$$Q = 1 \cdot 10^{-7} \text{ mbar } \ell/\text{s} \cdot 2.5 \cdot 10^{19} \frac{\text{molecules}}{\text{mbar } \ell} = 2.5 \cdot 10^{12} \text{ molecules/s.}$$

In 1000 hours of operation, this leads to a total of

$$3600 \text{ s/h} \cdot 1000 \text{ h} \cdot 2.5 \cdot 10^{12} \text{ molecules/s} \approx 1 \cdot 10^{19} \text{ molecules.}$$

Assuming a NEG capacity of  $10^{15}$  molecules/cm<sup>2</sup> [70], the total NEG surface saturated is in the order of

$$\frac{10^{19} \text{ molecules}}{10^{15} \text{ molecules/cm}^2} = 10000 \text{ cm}^2.$$

In a more “optimistic” (and more realistic) estimation, one can assume a gas flow of getterable gases in the order of  $1 \cdot 10^{-8}$  mbar  $\ell/s$  and a total injection time in the order of 100 hours. Those values lead to a saturation of  $100 \text{ cm}^2$  of NEG.

While a saturation of 100 to  $1000 \text{ cm}^2$  of NEG would be acceptable, the decision was taken to add a NEG filter at the end of the SMOG injection line to exclude any contamination by the SMOG and to not limit in time the usage of the SMOG.

## F.5 Modifications performed to the SMOG

Two modification were performed to the SMOG system to improve the operational security and reduce the residual gas flow. A small high-pressure volume has been added to the SMOG to replace the high-pressure neon gas bottle. The volume is visible on the SMOG picture in Fig. F.4. The total capacity is estimated at  $146 \text{ cm}^3$  comprising the tubing elements ( $\approx 62 \text{ cm}^3$ ) and the volume itself ( $\approx 84 \text{ cm}^3$ ). An uncertainty of  $\pm 5\%$  can be assumed on the total volume; however, a precise knowledge of the capacity is not necessary. Additionally a NEG filter was installed at the end of the 4 m injection line, its effect will be discussed in Sec. F.5.3. Furthermore, an additional vacuum vessel was added to the laboratory setup for the final injection measurements. The additional section permits to simulate the VELO beam vacuum and to estimate the gas flow entering the VELO volume with a calibrated conductance. The final setup used in the following measurements is depicted in Fig. F.13 with the VELO test bench shown on the bottom right. The VELO test bench is evacuated by an ion getter pump; two SVT gauges are placed on each side of the conductance. The calibrated conductance is an orifice with a diameter of 8.16 mm resulting in a conductance of  $6.06 \ell/s$  using the formula  $C = 11.6 \cdot A \cdot \ell/s$  with  $A$  in  $\text{cm}^2$  [71].

### F.5.1 Injections at different high pressures

Multiple injections are performed with different neon high-pressure between 0 and 4.5 bar in the added neon volume. The maximal pressure is limited by the SMOG valves (VAT series 57 all-metal) which can operate at a maximal pressure of 5 bar. Partial pressures of different gases are measured with the QMA Prisma 200 in the pre-VELO volume and with the QMA 400 in the VELO test bench. In both cases a linear dependence is assumed between the measured ion current of a spectrometer mass peak and the pressure. Furthermore, different gas ionization sensitivities are not taken into account in the measured ion current. The partial pressure of a gas is calculated with

$$P_{\text{gas}} = \frac{I_{\text{gas}} - O_{\text{gas}}}{C_{\text{gas}}} \quad (\text{F.2})$$

with  $I_{\text{gas}}$  the QMA ion current of a given mass peak (or sum of mass peaks),  $O_{\text{gas}}$  the ion current offset if not zero and  $C_{\text{gas}}$  the calibration constant. For residual gases, the offset and calibration constant values are measured at low pressure without neon injection. The neon calibration constant is measured during the neon highest injection pressure. Selected mass peaks assigned to residual gases and neon are listed in Table F.7. Measured calibration constants  $C_{\text{gas}}$  for the pressure gauges used in the setup are given in Table F.8. High vacuum gauges have different sensitivities depending on the gas type. The gauge sensitivity to neon pressure, compared to  $\text{N}_2$  gas, is reduced by a factor of 4.1 and 3.4 for the Penning and SVT gauges, respectively [72]. Consequently, the indicated pressure

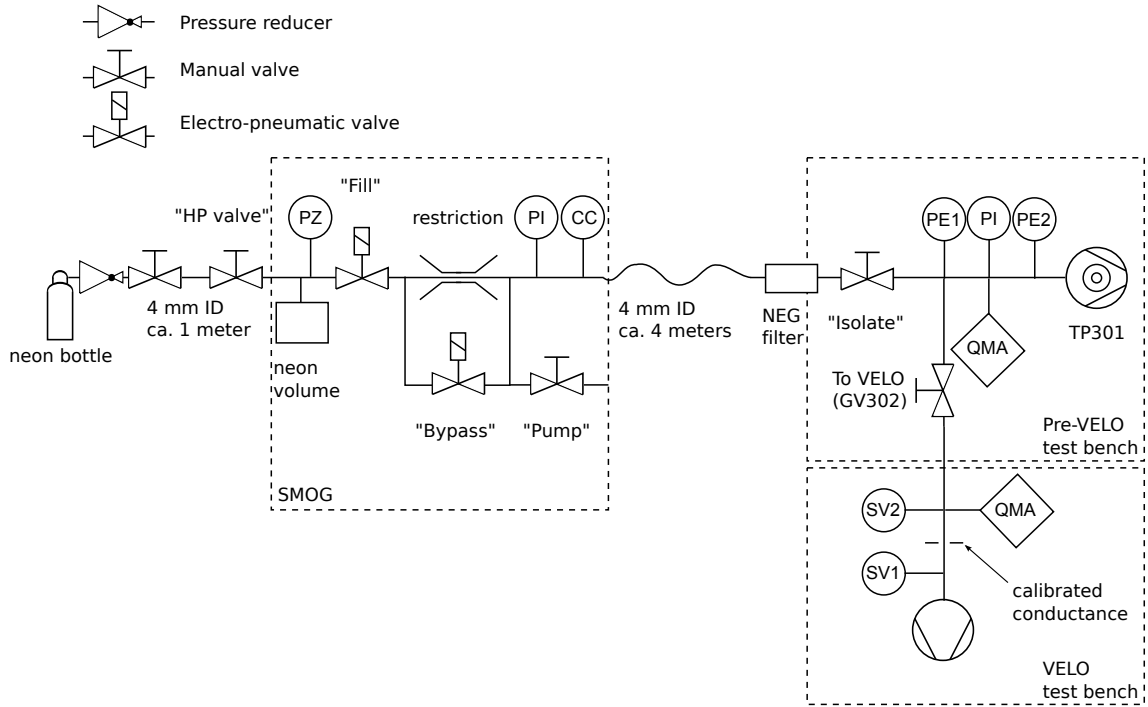


**Fig. F.13:** Final SMOG laboratory setup with high pressure volume (labeled neon volume in the SMOG panel). The SMOG fill and bypass valves are VAT series 57 all-metal and can operate up to  $\Delta P = 5$  bar. A QMA Prisma 200 is used to analyze the residual gas in the pre-VELO volume. A VELO test bench is connected to the pre-VELO volume with a flexible below. The VELO test bench is equipped with a residual gas analyzer QMA 400 (from Balzers).

**Table F.7:** Selected mass peaks for residual gases and neon.

	Mass number	Gas
Residual gases	1, 2	$H_2$
	16, 32	$CH_4/O_2$
	17, 18	$H_2O$
	28	$N_2/CO$
	40	Ar
Neon	44	$CO_2$
	10, 20	$^{20}Ne$
	11, 22	$^{22}Ne$

measured when the volume is dominated by neon has to be multiplied by those sensitivity factors. The calibration constants  $C_{\text{gas}}$  in Table F.8 include the gauge sensitivity correction.

Partial pressure measurements of neon and residual gases for different neon high pressure injections as measured in the pre-VELO volume are shown in Fig. F.14. The background level is measured in the state *Isolated* and the horizontal dashed line indicates the residuals partial pressure when the Isolate valve is open and the SMOG is in the state *injection off*. The residual gas pressure is almost constant at different injection pressures.

The gas flow  $Q_{\text{gas}}$  entering the pre-VELO and VELO vacuum vessels is evaluated with

$$Q_{\text{gas}} = P_{\text{gas}} S, \quad (\text{F.3})$$

with the partial pressure  $P_{\text{gas}}$  measured with Eq. (F.2) and  $S$  the pumping speed in the vessel. The value  $S$  is given by the pumping speed of  $S = 250 \text{ l/s}$  of the turbomolecular pump in the pre-VELO

**Table F.8:** Calibration of the QMA Prisma 200. If the offset is too close to the noise level of the QMAs, it is set to zero.

Gauge number	Gas	$C_{gas}$ (A/mbar)	$O_{gas}$ (A)
PE2	residuals	0.0030	$7.3 \cdot 10^{-13}$
PE2	neon	0.0026	0
SVT1	residuals	0.70	0
SVT1	neon	0.310	0
SVT2	residuals	0.14	0
SVT2	neon	0.070	0

volume, and by the calibrated conductance  $S = 6.06 \ell/s$  in the VELO test bench. The gas flows for residual gases and neon entering the pre-VELO and VELO test bench are shown in Fig. F.15. For the VELO test bench (right) Fig. F.15, one can see that the increase of residual gases from the SMOG, which is indicated by the horizontal dashed line (denoted SMOG open), is negligible and is below background level. The measured values of  $\Delta P \cdot C$  are indicated as a cross-check and should correspond to the neon flow measured with the QMA. The pressure difference  $\Delta P$  is evaluated with the gauges SV1 and SV2 (see Fig. F.13) and is corrected for the neon sensitivity. A good agreement is observed between the QMA and gauges flow estimation.

Measurements of residual gas spectrum acquired with and without neon injection are shown in Fig. F.16 for the pre-VELO volume (left plot) and the VELO test bench (right plot). The neon isotopes  $^{20}\text{Ne}$ ,  $^{21}\text{Ne}$  and  $^{22}\text{Ne}$  are clearly visible. A small increase in residual gases is visible during the neon injection, but could be attributed to an instrumental effect due to the higher pressure. Those injection measurements were performed with an unbaked system and without NEG filter.

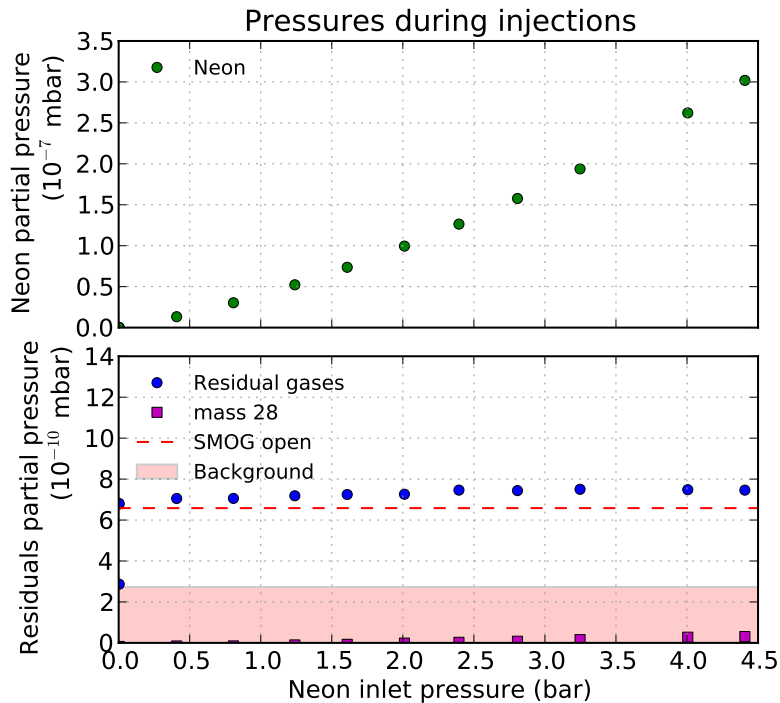


**Fig. F.14:** Partial pressure of residuals and neon measured in the pre-VELO volume during neon injection at different high pressures and without NEG filter. The background level is measured in the state *Isolated* and the horizontal dashed line indicates the residual background level when opening the Isolate valve, which connects the SMOG to the per-VELO volume. The partial pressure for  $\text{N}_2$  (mass peak 28 amu) is mostly constant with regard to the neon injection.

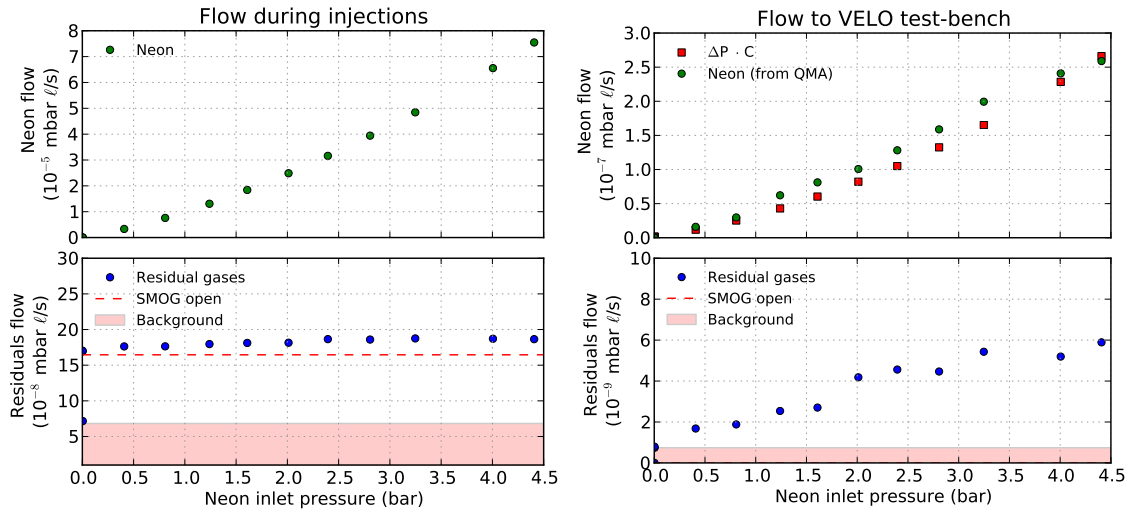


**Fig. F.15:** Residual gases and neon flows in the pre-VELO and VELO test bench volume during injection. Left: gas flows entering the pre-VELO volume assuming a pumping speed of 250  $\ell/\text{s}$ . Right: gas flows entering the VELO test bench.

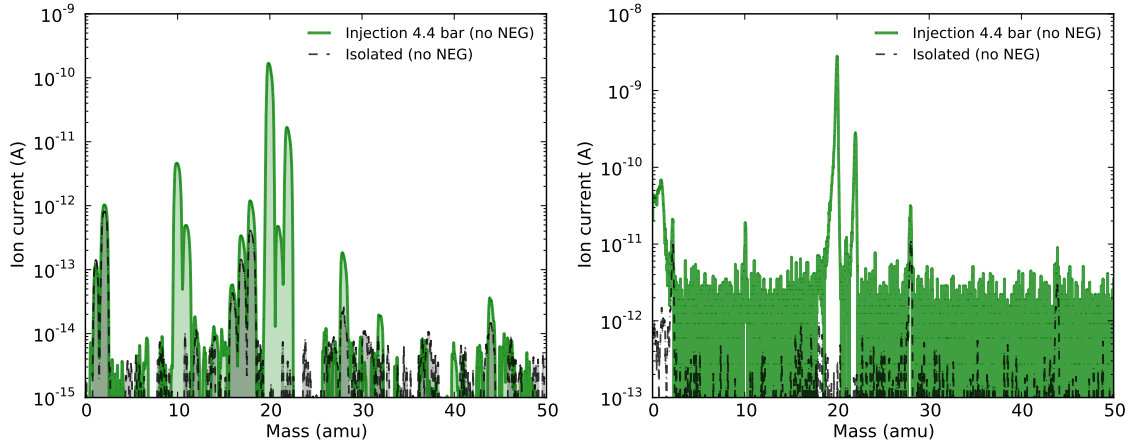


**Fig. F.16:** Residual gas analysis during injection without NEG filter. Left: RGA of the pre-VELO volume. Right: RGA of the VELO test bench.

## F.5.2 Pressure loss with closed volume

The neon volume has been added to decouple the high pressure neon bottle from the SMOG to increase the security. However, the finite amount of neon induces a pressure decay during the SMOG operation and will also limit the number of SMOG operations before a refill is required. The pressure evolution with time during neon injection has been measured over 7 days and is shown in Fig. F.17. Daily temperature cycles are visible in the neon high pressure (measured with the piezo gauge) and residuals. A pressure loss of about 265 mbar in the neon volume corresponds to about 38 mbar/24 hours, or about 1% pressure loss per 24 hours injection. While the gas loss will deplete the neon volume over multiple injections, the decay is negligible during a beam-gas imaging measurement.

The measured neon flow with a neon high pressure of about 4 to 4.5 bar is evaluated at about  $Q_{\text{Ne}} \approx 7 \cdot 10^{-5}$  mbar  $\ell/\text{s}$  or 6.1 mbar  $\ell/\text{day}$ . With an estimated neon volume of 0.146  $\ell$ , the expected pressure loss per day is then  $\Delta P_{\text{Ne}} \approx 6.1 \text{ mbar } \ell/\text{day} / 0.146 \ell \approx 41 \text{ mbar/day}$  which is close to the measured 38 mbar/day.

At each injection cycle, the volume between the restriction and the Fill and Bypass valves must be filled with neon. This gas will be lost when the high pressure neon is purged with the Bypass valve.

The neon pressure loss per fill (purge) cycle has been measured for different high pressure injections and is shown in Fig. F.18. The loss per SMOG injection amounts to about 2.3%. The procedure to refill the neon volume is described in reference [73].

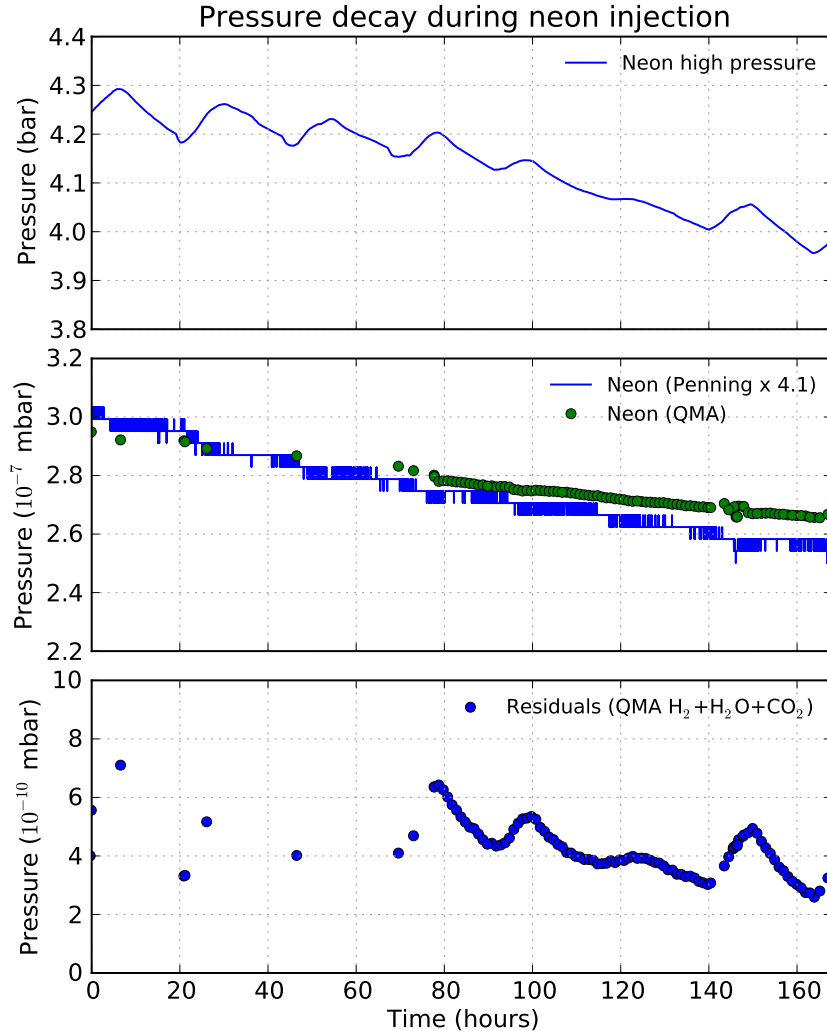


**Fig. F.17:** Pressure loss during long term injection. Top panel: high pressure measured with the piezo gauge. Note that the piezo gauge measures a force proportional to the pressure, and is therefore sensitive to temperature fluctuations. Middle panel: neon pressure measured with the Penning gauge (including a factor of 4.1 to account for the different neon sensitivity) and with the QMA. Note that both methods measure the gas density which is not sensitive to temperature. Bottom panel: measurement of residual gas pressure evaluated with the QMA. It can be seen that the ambient temperature influences the outgassing rate.

### F.5.3 Injections with NEG filter

To reduce or eliminate the residual gas flow from SMOG impurities, a NEG filter was installed at the end of the injection line, before entering the pre-VELO volume. The NEG filter precludes the use of getterable gases like  $\text{CO}_2$ , but ensures that the injected gas is free of residual gases which would be pumped by the NEG in the VELO beam vacuum. The NEG filter was activated at  $400^\circ\text{C}$  and the whole pre-VELO volume was baked-out. With a completed bake-out, the background pressure in the pre-VELO is about  $3 \cdot 10^{-10}$  mbar. Opening the Isolate valve does not increase the pressure as the outgassing from the SMOG is pumped by the NEG filter.

The same gas injection measurements as described in Sec. F.5.1 are repeated with the NEG filter installed. Partial pressure measurements of neon and residual gases for different neon high pressure

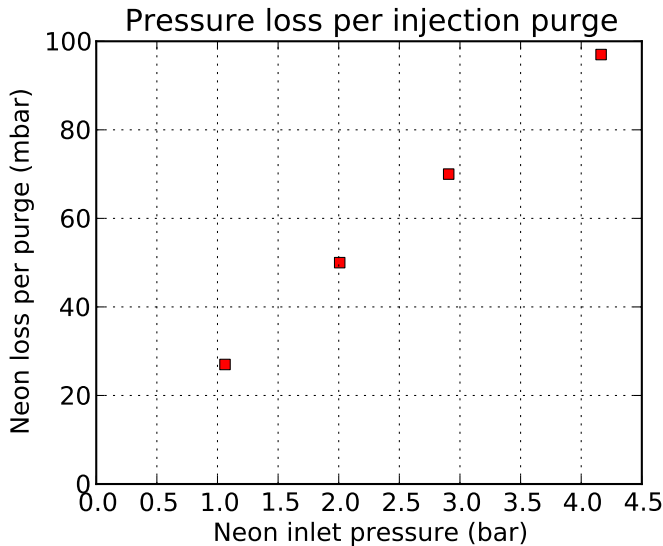


Fig. F.18: Pressure loss in the neon volume per injection cycle.

injections as measured in the pre-VELO volume are shown in Fig. F.19. No difference in the background level is observed in the states *Isolated* and *injection off* (SMOG open). The residual gas pressure is almost constant at different injection pressures and the small increase can be attributed to an instrumental effect of the QMA due to the higher pressure. The gas flows for residual gases and neon entering the pre-VELO and VEL0 test bench are shown in Fig. F.20. For the VEL0 test bench (right) Fig. F.20, the increase of residual partial pressures is to be attributed to QMA. Measurements of residual gas spectra acquired with and without neon injection are shown in Fig. F.21 for the pre-VELO volume (left plot) and the VEL0 test bench (right plot).

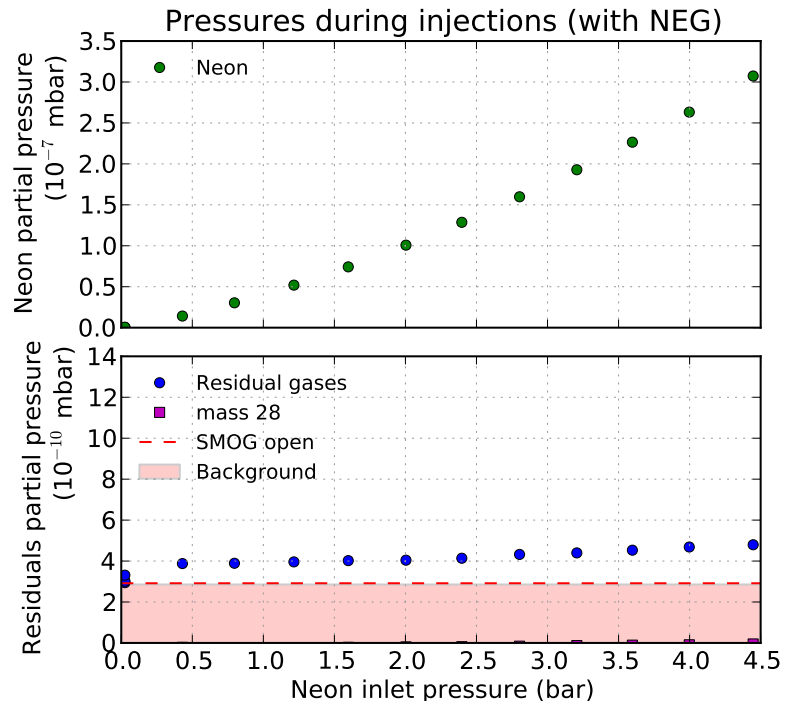
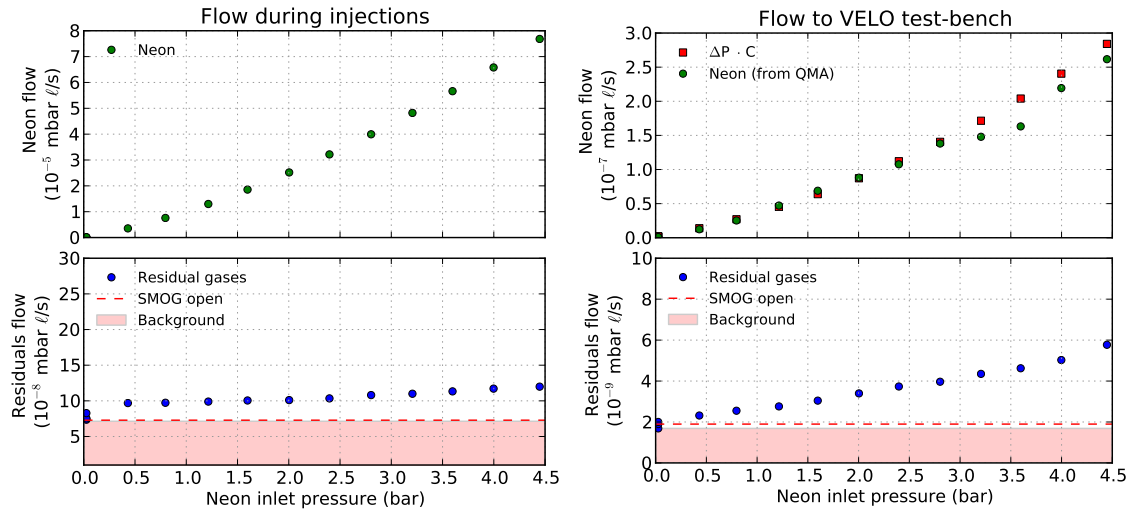
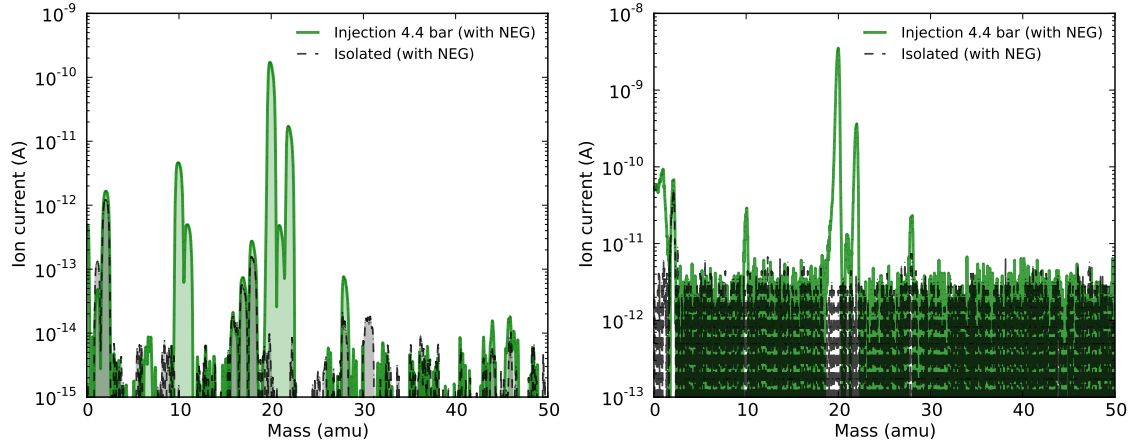


Fig. F.19: Partial pressure of residuals and neon measured in the pre-VELO volume during neon injection at different high pressures and with the NEG filter installed. The background level is measured in the state *Isolated* and the horizontal dashed line indicates the residual background level when opening the *Isolate* valve, which connects the SMOG to the per-VELO volume. The partial pressure for  $N_2$  (mass peak 28 amu) is mostly constant with regard to the neon injection and is similar in amplitude to the QMA noise level.



**Fig. F.20:** Residual gases and neon flows in the pre-VELO and VELO test bench volume during injection with NEG filter installed. Left: gas flows entering the pre-VELO volume assuming a pumping speed of 250 l/s. Right: gas flows entering the VELO test bench.



**Fig. F.21:** Residual gas analysis during injection with NEG filter. Left: RGA in the pre-VELO volume. Right: RGA in the VELO test bench.

#### F.5.4 Vacuum recovery after injection

The time required to evacuate the neon gas after an injection and to return to a nominal background pressure was measured with the QMA in the pre-VELO volume. The measurements are shown in Fig. F.22 for an injection without NEG filter (left plot) and with NEG filter (right plot). Once the Fill valve is closed, the “dead volume” between the Fill valve and the restriction has to be evacuated through the bypass to stop the injection. As seen in Fig. F.22, the neon partial pressure drops below the background level within 20 minutes.

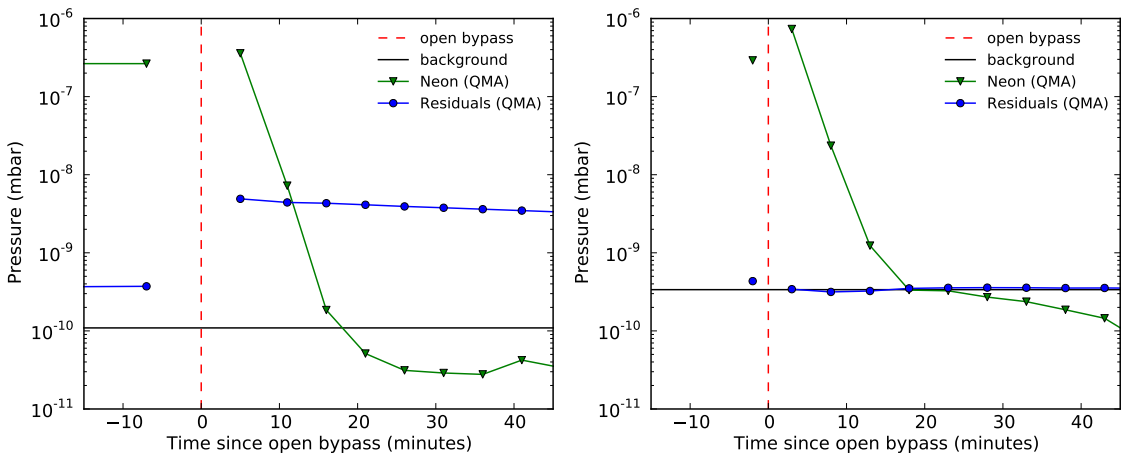


**Fig. F.22:** Residual gases and neon pressure during the bypass evacuation after a neon gas injection. Left: injection without NEG filter. Right: injection with NEG filter installed. The background level is indicated by an horizontal solid line, the vertical dashed line indicates the time at which the Bypass valve is opened. The first measurements of partial pressures for neon and residual gas during the injection (left of the vertical line) are performed during an injection steady state.

## F.6 Installation and commissioning

The SMOG system was installed in the LHCb environment during the technical stop No. 5 between 7 and 11 November 2011. A schematic drawing of the SMOG and VELO vacuum is shown in Fig. F.23. The valves PV501, PV502 and GV302 are controlled with the VELO vacuum control software, the Isolate MV502 valve is to be kept open. Two high vacuum Penning gauges PE411 and PE412 are located in the VELO and measure the beam vacuum pressure at the interaction point. The in-situ test procedure to test the control software and valve operation is described in Ref. [74] and the installation procedure is described in Ref. [75]. The installation and first injection test is documented in Ref. [76].

A first gas injection was performed in the scope of the test procedure in November 2011 after the installation. The pressure over time for this injection sequence is shown in Fig. F.24, the pressure is measured by the VELO valves PE411 and PE412 and acquired with the CERN common logging service. Before injection, the ion pumps located under the VELO are switched off, increasing the base pressure by a factor of about 5. The end pressure reached during the injection was about  $4.5 \cdot 10^{-8}$  mbar as measured by the Penning gauges. As the gauges have a sensitivity factor of 4.1 for neon, the measured pressure has to be multiplied by 4.1 to indicate real neon pressure. A residual gas analysis acquired with the VELO spectrometer is shown in Fig. F.25 for the injection sequence and for a selection of mass peaks, the different injection steps are indicated in the plot and marked with a vertical dashed line and are explained below.

Before injection (time = 0), the VELO ion pumps are switched off, the VELO valve GV302 is closed and the pressure is dominated by hydrogen. The presence of neon is already visible. Before the valve GV302 is opened, the SMOG is already injecting in the pre-VELO volume. To start the gas injection in the VELO beam vacuum, the valve GV302 is opened (at about 8 minutes in Fig. F.25). Most residual gases ( $H_2$ ,  $CH_4$ ,  $N_2$ ,  $Ar$ ) are now pumped by the pre-VELO turbomolecular pump TP301. Water (mass peak 18 amu) remains mostly constant as it is in equilibrium with the pre-VELO residual water pressure. Neon gas during the injection is dominating the pressure in the VELO. The VELO GV302 valve is closed at about T=23 minutes, the residual gases increase and the SMOG bypass is evacuated during this time. Note that the LHCb sector valves are closed during this measurement and the beam pipe is not pumped. The VELO valve is opened again at about T=38 minutes to evacuate the neon gas through the TP301 pump in the pre-VELO. At about T=45 minutes, the VELO valve GV302 is closed and the ion pumps are switched on.

A first gas injection with circulating beam was performed the 23 November 2011 as a test in fill 2297 with 358 Pb bunches per beam. For this test, only the calorimeters and some VELO sensors were powered in order to evaluate the detector occupancies. The triggered beam-gas rates and VELO pressure are shown in Fig. F.26. The beam-gas rate for beam 1 increased by a factor of 50 and the CALO rate for beam 1 increased by a factor of 100.

Following this successful commissioning tests, the SMOG was subsequently used during all luminosity calibration fills in 2012 and 2013.

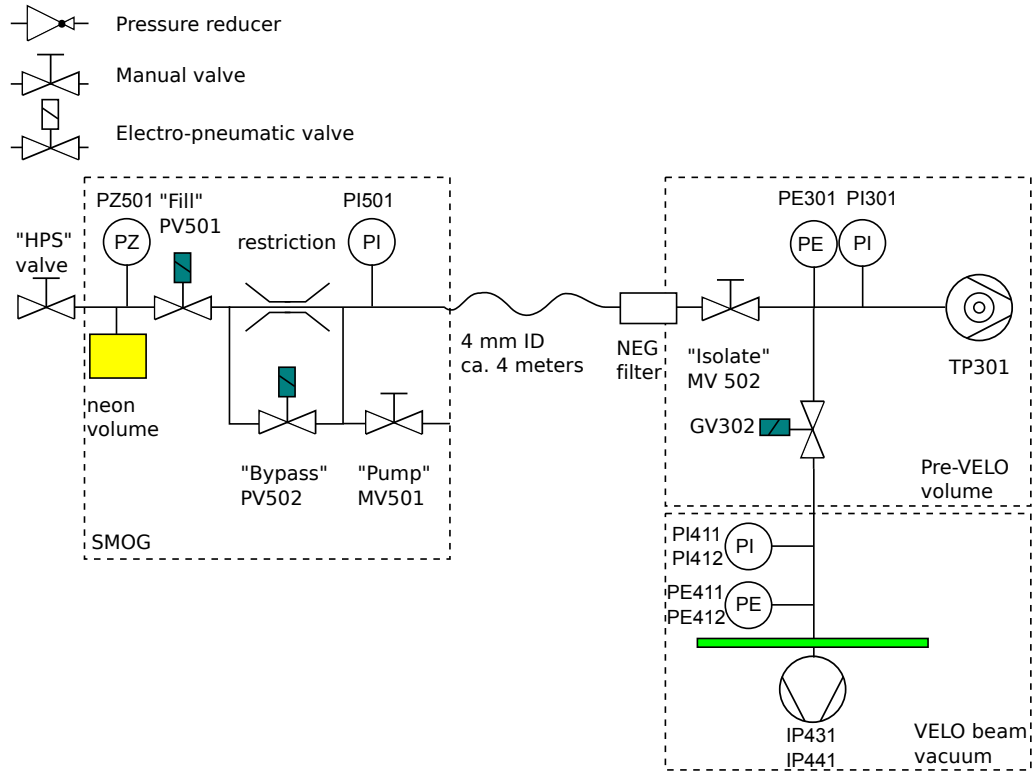


Fig. F.23: SMOG setup when connected to the VELO.

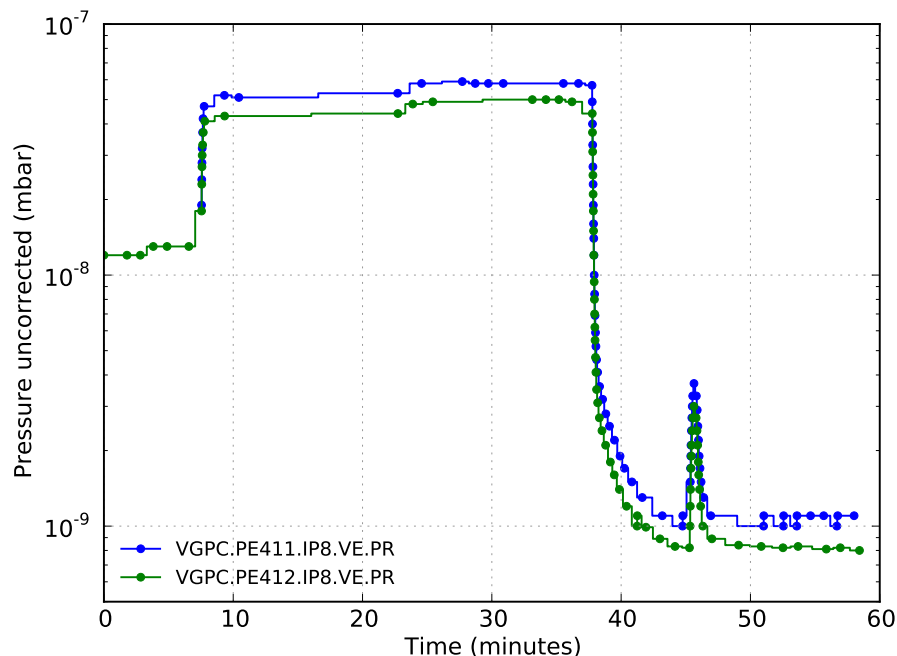
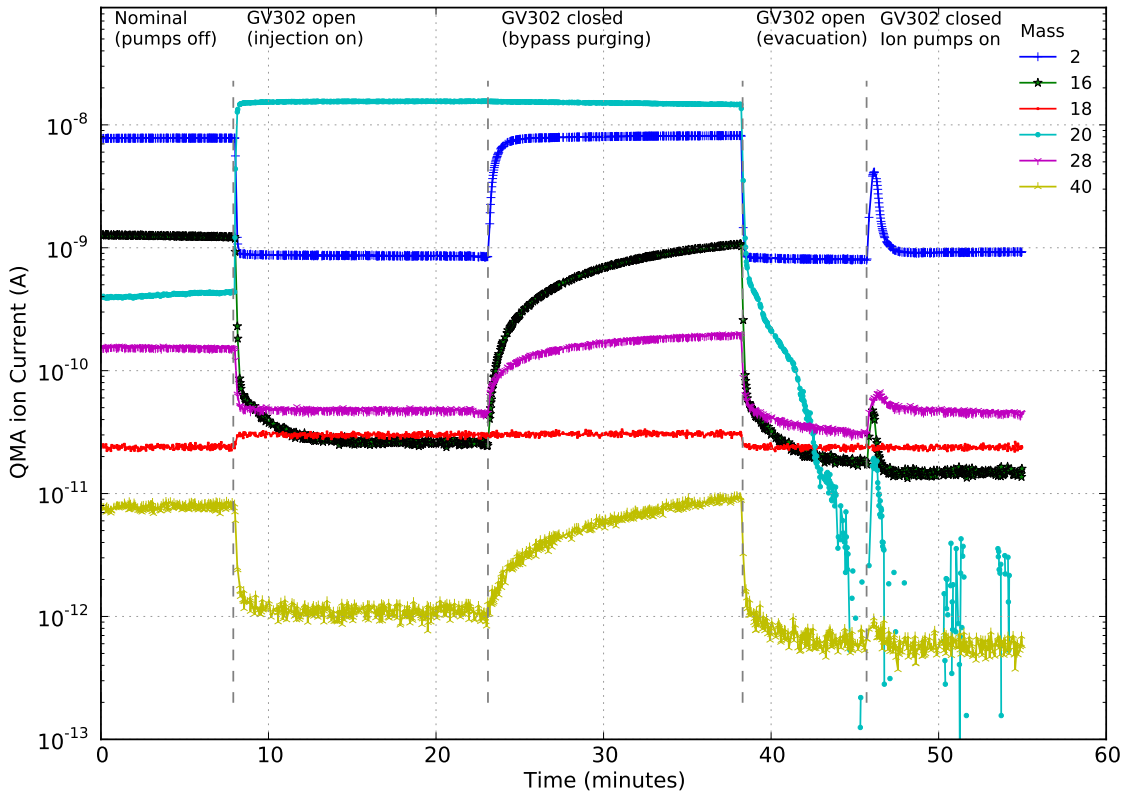
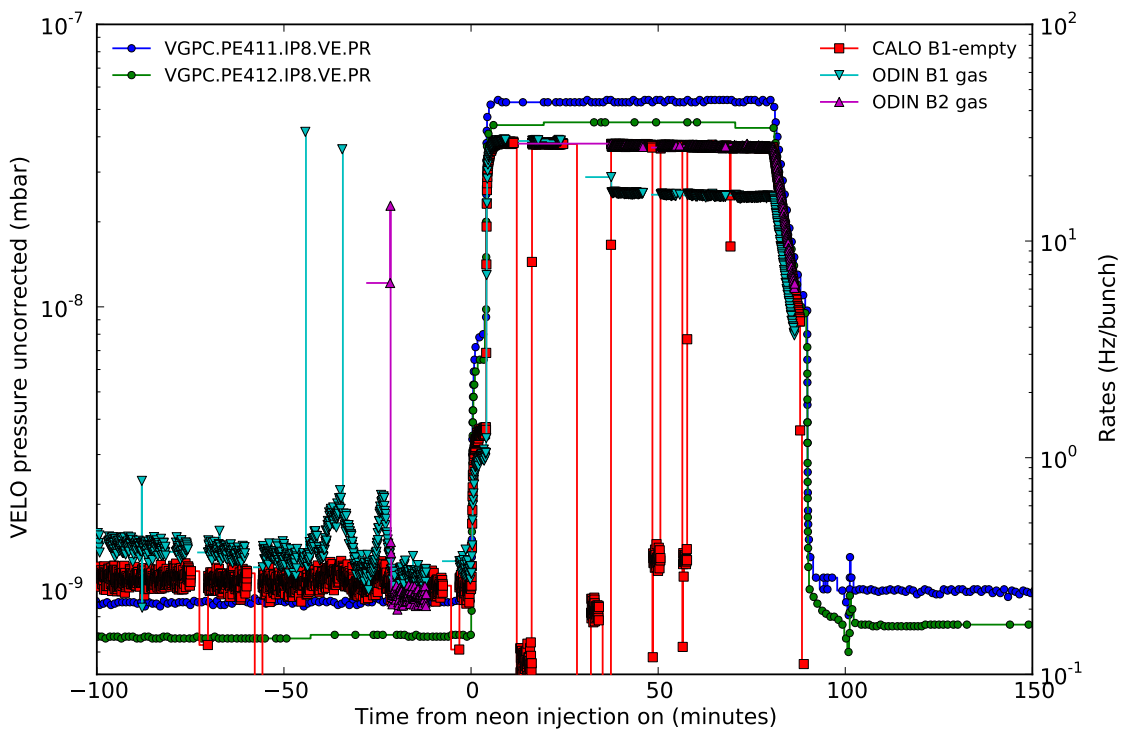


Fig. F.24: VELO pressure profile during first injection test.



**Fig. F.25:** VELO residual gas analysis during first injection test. The injection steps are indicated in the figure and separated with a vertical dashed line.



**Fig. F.26:** Pressure and beam-gas rates during first injection with beam. The ODIN B1 gas and ODIN B2 gas values are the hardware trigger rates dedicated to trigger on beam-gas interactions for beam 1 and beam 2, respectively.

## G RESULTS OF THE LHC DCCT CALIBRATION STUDIES

This work has been published in Ref. [56, 77] and is reproduced here in its entirety. Some typographic corrections have been made. The document has the following authors:  
C. Barschel, M. Ferro-Luzzi, J.J. Gras, M. Ludwig, P. Odier and S. Thoulet

The studies presented in this chapter were necessary to reduce the uncertainty on the beam intensity product and to make it possible to perform a precision luminosity measurement. My contribution to this work has been to devise, perform, analyse and document a set of measurements to cover possible sources of uncertainties related to the instrument including its acquisition chain. The measurements took place in the laboratory on a spare instrument or in-situ in the tunnel.

### Abstract

An important aspect of luminosity calibration measurements is the bunch population product normalization. In the case of the LHC, the treatment of this normalization can be split into three subjects: the total current measurement, the corrections from the non-perfect longitudinal distribution and the relative amplitude of the individual bunch populations. In this note, we discuss the first item in details and in the context of the 2010 and 2011 luminosity calibration measurements performed for each LHC Interaction Point. Effects Internal to the DCCT, the sensitivity to external factors, uncertainty related to the absolute calibration and comparison of two systems are all addressed. The DCCT uncertainty and numerical examples are given.

---

## Contents

<b>G.1</b>	<b>Introduction</b>	166
<b>G.2</b>	<b>Description of the DCCT system</b>	168
G.2.1	Layout	168
G.2.2	Principle	169
G.2.3	Implementation	170
<b>G.3</b>	<b>Instrumental stability and linearity</b>	171
G.3.1	Baseline subtraction method	171
G.3.2	Automatic baseline correction	174
G.3.3	Fourier analysis of the noise	175
G.3.4	In-situ tunnel measurements	177
G.3.4.1	Long term stability over 12 hours	178
G.3.4.2	Long term stability under load over 24 hours	184
G.3.4.3	DCCT Linearity	184
G.3.5	DCCT Linearity verified with alternate ADC	188
G.3.5.1	Reference response of NI ADC	188
G.3.5.2	DCCT Linearity compared with NI ADC	189
G.3.6	Absolute Scale	190
<b>G.4</b>	<b>Sensitivity to beam conditions and other external factors</b>	192
G.4.1	Cross talk between rings	192
G.4.2	Bunch pattern dependence	193
G.4.2.1	Laboratory measurements	194
G.4.2.2	Measurement with beam	198
G.4.2.3	Sensitivity to an injected RF sine wave	198
G.4.3	Bunch position dependence	203
G.4.4	Interference from Accelerator Systems	204
G.4.4.1	Interference from magnetic field	204
G.4.4.2	Interference from RF	205
<b>G.5</b>	<b>Calibration Method</b>	206
G.5.1	Current source accuracy	207
G.5.2	Position of the calibration rods	208
G.5.3	Methodology and current leak	208
<b>G.6</b>	<b>Difference between systems A and B</b>	210
<b>G.7</b>	<b>Summary of uncertainties affecting total-intensity measurements</b>	215
G.7.1	Example with a VDM fill	218
G.7.2	Example with a typical high intensity fill	219
G.7.3	Example with a low intensity fill	219
G.7.4	Outlook	220
<b>G.8</b>	<b>Appendices</b>	221
G.8.1	Noise and baseline correction	221
G.8.2	Long term stability over 12 hours	224
G.8.3	Linearity	228
G.8.3.1	Linearity measurements with 12-bit ADC	228
G.8.3.2	Linearity measurements with 24-bit ADC	230
G.8.4	Cross talk between rings	233
G.8.5	Calibration	233

## G.1 Introduction

Several luminosity calibration experiments were carried out in 2010 and 2011 at the LHC, with proton collisions ( $p$ - $p$ ) and with ion collisions (Pb-Pb), to obtain physics cross section normalizations at each Interaction Point (IP). Both the van der Meer (VDM) scan method and the beam-gas imaging (BGI) method were used. The experiments were carried out at the zero-momentum frame energies  $\sqrt{s} = 7$  and 2.76 TeV for  $p$ - $p$  and  $\sqrt{s} = 7 Z$  TeV for Pb-Pb. A summary of the most relevant conditions of each set of VDM scans are listed in table G.1.

The first measurements showed that one of the dominant uncertainties is introduced through the bunch population product normalization. As a consequence, a detailed bunch population analysis was carried out using data from the LHC Beam Current Transformers (BCTs) and from the LHC detectors (ALICE, ATLAS, CMS and LHCb). An analysis procedure was defined and bunch population uncertainties were quantified. The results of a first analysis for 2010 calibration measurements were documented in two bunch current normalization notes [46, 47] where a detailed description of the procedure used to determine the bunch populations and their associated uncertainties can be found. The precision was limited by the understanding of the BCT data at that stage. Since then, a number of additional tests were carried out which significantly improved the understanding of the bunch current measurements. The purpose of the present note and of two companion notes [48, 49] is to review the bunch population measurements and their accuracy in the light of these improvements.

**Table G.1:** VDM luminosity calibration series for the LHC (2010 and 2011). The number of bunches in brackets indicates the number of “pilot” proton bunches in addition to the number of “main” proton bunches. Here,  $\langle N \rangle$  is an indicative value of the main bunch charge in units of  $10^{10}$  elementary charges.

Period / beams	$\beta^*$ (m) IP1&5 / 2 / 8	Net angle $\alpha_{\text{net}}$ ( $\mu\text{rad}$ )	$\sqrt{s}/Z$ (TeV)	LHC fill	Nr of bunches	Colliding in IP1&5 / 2 / 8	scanned IPs	$\langle N \rangle$ ( $10^{10} e$ )
Apr-May 2010 <i>p</i> - <i>p</i>	2 / 2 / 2	0 / 0 / 0	7	1058	3	2 / 2 / 2	5	1.1
				1059	2	1 / 1 / 1	1, 8	1.1
				1089	2	1 / 1 / 1	1, 5	2.0
				1090	2	1 / 1 / 1	2	2.0
Oct 2010 <i>p</i> - <i>p</i>	3.5 / 3.5 / 3.5	200 / 500 / 340	7	1386	19	6 / 1 / 12	1, 5	8.0
				1422	16	3 / 1 / 12	2, 5, 8	8.0
Nov 2010 Pb-Pb	3.5 / 3.5 / 3.5	0 / 0 / -	7	1533	121	113 / 114 / 0	1, 2, 5	0.8
Mar 2011 <i>p</i> - <i>p</i>	11 / 10 / 10	0 / 710 / 1370	2.76	1653	72 (+4)	64 / 48 / 16	1, 2, 5, 8	9.0
				1658			1	10.5
May 2011 <i>p</i> - <i>p</i>	1.5 / 10 / 3	240 / 440 / 1040	7	1783	38 (+1)	14 / 16 / 22	1, 2, 5, 8	8.5
Jun 2011 <i>p</i> - <i>p</i>	1.5 / 10 / 3	240 / 440 / 1040	7	1875	1092 (+1)	1042 / 35 / 1008	5	12.0
Oct 2011 <i>p</i> - <i>p</i>	90 / 10 / 10	0 / 440 / 540	7	2234	36	4 / 16 / 16	2, 8	9.0
Dec 2011 Pb-Pb	1 / 1 / 3	240 / 120 / -	7	2335 2337	352	344 / 324 / 0	2 1, 5	1.0 1.0

As discussed in reference [46], the LHC is equipped with a number of Bunch Current Transformers (BCTs)<sup>1</sup>. Four independent Direct Current Current Transformers (DCCTs), two per ring (called

<sup>1</sup>Throughout this note, it is assumed that the measured charge for Pb beams is exactly proportional to the particle

system A and B), are used to measure the total beam current circulating in each LHC ring. The DCCT is designed to be insensitive to the time structure of the beam. Two Fast Bunch Current Transformers (FBCTs), one per ring, give a measure of the individual bunch charges. The FBCT is designed to produce a signal (one per 25 ns bunch slot) which is proportional to the charge in a slot, by integrating the charge observed inside a fast gate. The IP1 BPTX button pick-up was also used to measure the relative charge in nominally filled slots. Both the FBCT and BPTX devices are “blind” to a slot charge below a given threshold. Such beam charge, if present, will be measured by the DCCT but not by the FBCT/BPTX. This is called the “ghost” charge. It is defined as the total beam population outside the nominally filled 25 ns bunch slots. Other devices, such as the Longitudinal Density Monitor (LDM) or the LHCb detector, were also used, when available, to check the relative bunch populations.

The ghost charge was mainly measured by comparing the beam-gas rates from nominally empty bunch crossings with those of crossings in which only the slot of one beam was filled with a bunch. This technique was pioneered at IP8/LHCb (though efforts are now being made to deploy it at other LHC experiments). Given the nature of the LHCb detector readout electronics, the method was limited to a 25 ns granularity. Furthermore, within the 25 ns of a nominally filled slot the bunch occupies only one of the ten RF bins. Possible “satellite” bunches may populate the other nine RF bins. Such satellite charges were indeed observed and measured in different ways with the LHC detectors (by timing or vertex reconstruction) by monitoring longitudinally displaced collisions. The amount of satellite population is generally small compared to the main bunch population, but nevertheless needs to be quantified to obtain a precise measurement of the bunch population that actually participates in the luminosity signal. At some stage, the LHC LDMs were deployed and commissioned (one per ring). The LDM allows one to obtain a precise longitudinal distribution of the beam charge with a time resolution of about 90 ps. It is now used for constraining both the ghost charge and the satellite populations.

The bunch population normalization was decomposed in three tasks: (i) determination of the total beam charge, (ii) analysis of the relative bunch populations and (iii) corrections due to the ghost charge and satellite populations. The second and third items are discussed in detail in references [48] and [49], respectively. In the present note, we concentrate on the first item, namely the determination of the total beam intensity measurement and its uncertainties. The present report is structured as follows. Section G.2 provides a description of the DCCT systems and its working principle. The analysis of all factors contributing to the DCCT uncertainties are divided in the following three main categories. A schematic overview is given in Fig. G.1. Section G.3 reports on the analysis of effects internal to the DCCT system which may contribute to the total current uncertainty. Section G.4 discusses the sensitivity to external factors and beam conditions. Section G.5 focuses on uncertainties related to the absolute calibration. The difference between systems A and B observed throughout 2011 is given in Sec. G.6. The DCCT uncertainties are summarized in Sec. G.7 along with a few explicit numeric examples for calculating beam current uncertainties.

---

population, with 82 as proportionality factor.

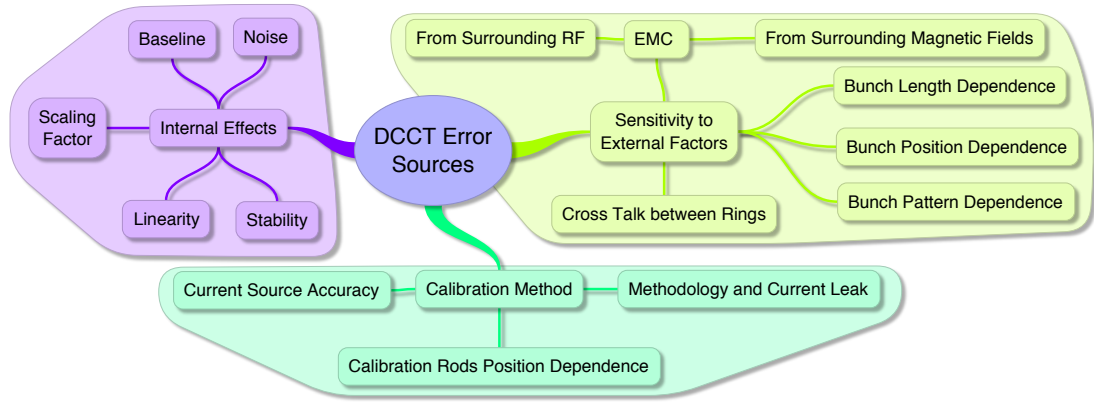


Fig. G.1: DCCT errors classification.

## G.2 Description of the DCCT system

### G.2.1 Layout

The DCCT which were designed and fabricated at CERN, are based on the principle of flux gate magnetometer and measure the mean intensity or current of the circulating beam. They can be used to measure the beam lifetime. In order to achieve the high levels of operational reliability required, two independent systems were installed on each ring (Fig. G.2). Each system consists of one monitor per ring [54], one front and one back end electronics per monitor as well as one Front End Computer (FEC), housed in a VME crate, for acquisition and control purpose. The monitors and the front end electronics are located in LSS4R 152 meters away from IP4, in a region where the vacuum chamber is at room temperature, while the back end electronics and the FEC are located in the surface building SX4, which is easily accessible for performing maintenance and calibration tasks.

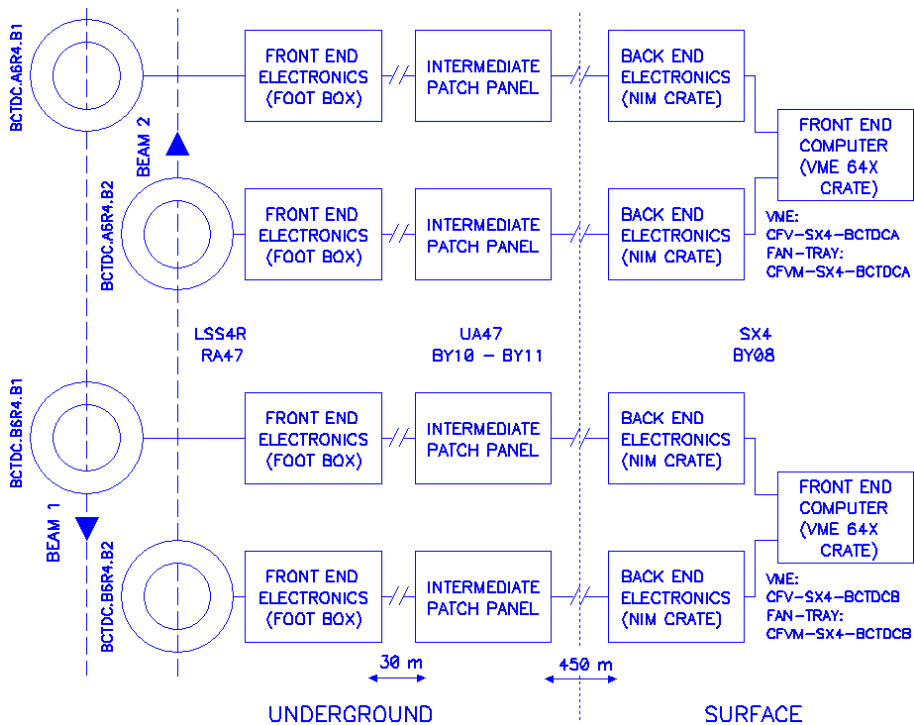


Fig. G.2: DCCT General Layout (source [54]).

### G.2.2 Principle

The DCCT exploits the non-linear magnetization curve of soft ferromagnetic material. Excitation coils of two cores are fed in opposite phase with a sinusoidal voltage at several 100 Hz (215Hz in this case) produced by the Modulator (Fig. G.3). The modulation current of each core is distorted when the magnetic flux of the core enters into saturation. The distortion creates odd harmonics in the frequency spectrum of the modulation current. However, with the anti-phase excitation, the difference of the modulation current between both cores is zero, provided the cores are well matched. The principle is illustrated in Fig. G.4. In the absence of current passing through the cores, both cores are in phase and driven simultaneously into saturation with opposing polarity. With the presence of a DC current, the core magnetization is biased with the same polarity in both cores, therefore, one core will reach its saturation before the other. In this case, the modulation current difference is not zero when one core is in saturation while the flux in the other core is still changing. A signal in the modulation current difference will appear at each polarity change i.e. at twice the modulation frequency, and the second harmonic of the modulator frequency appears in the modulation current as illustrated in Fig. G.4 (right). The detection of the second harmonic is performed by synchronous detection at twice the modulation frequency. To extend the DCCT bandwidth, the detected signal is combined with an AC signal produced by a fast current transformer made of a third core. The generated common feedback current passes through the cores and cancels the magnetic field produced by the calibration or beam current. Therefore, the feedback current is equivalent to the beam or calibration current. The DCCT calibration is established with a current generator sending a known current through a dedicated coil allowing the calibration of the whole acquisition chain, from the sensor to the calibrated intensities made available digitally in the API to the control system.

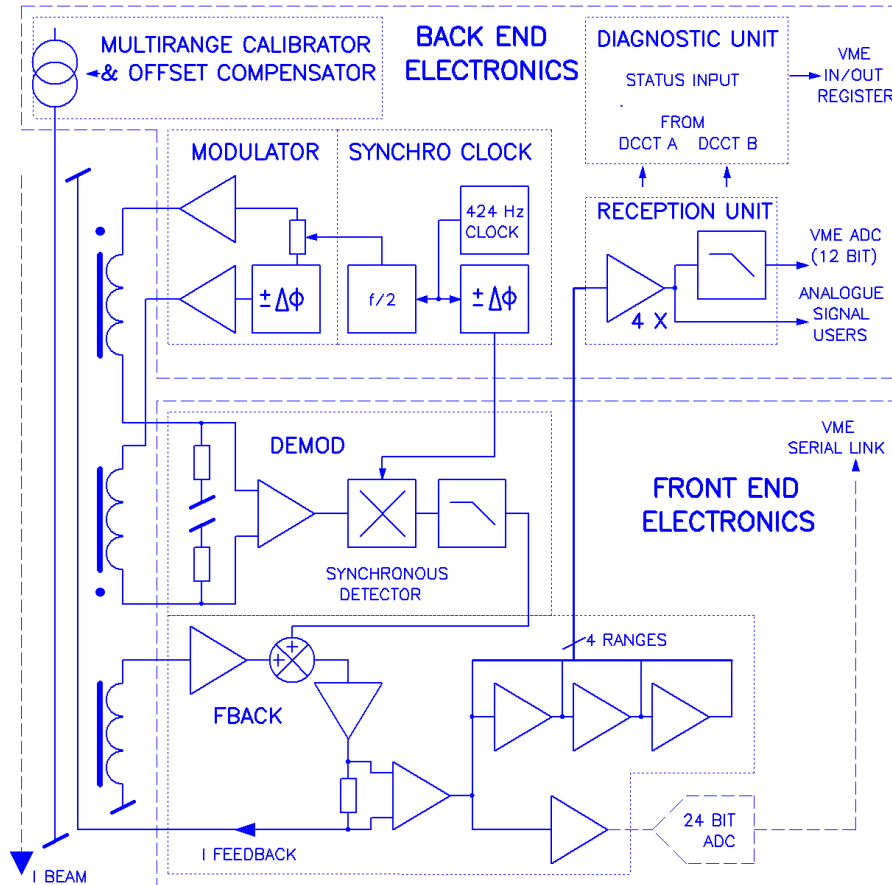
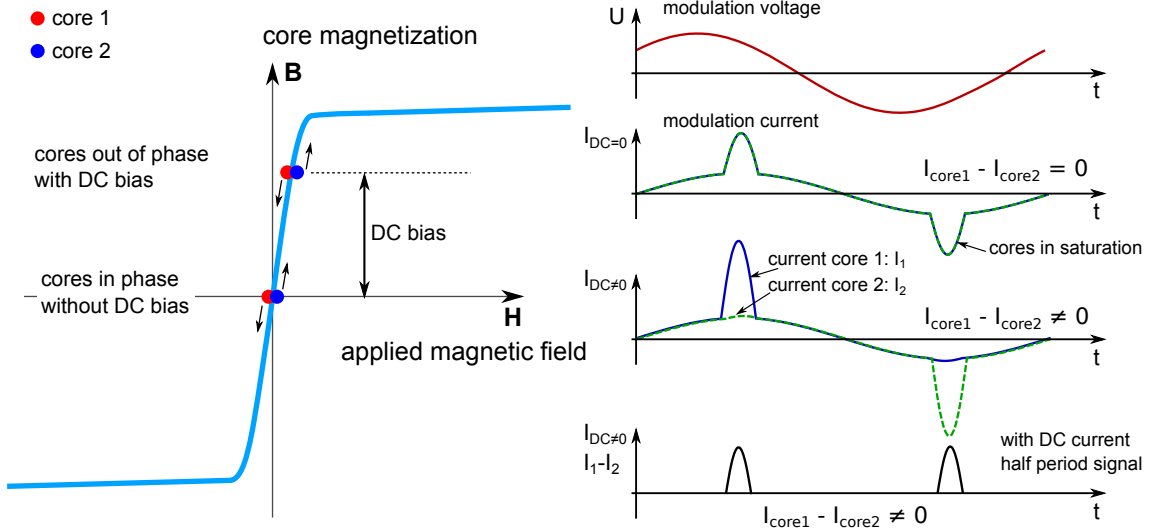


Fig. G.3: DCCT simplified schematics (source [54]).



**Fig. G.4:** (left) The non-linear response of the soft ferromagnetic cores permits to drive the cores into saturation. The presence of a DC current biases the magnetization of both cores with the same polarity. (right) The non-linear magnetization of the cores distorts the modulation current; the current is higher when the core is saturated. The modulation current difference between the cores is zero when the cores are in phase; however, a signal in the modulation current appears when the cores are out of phase due to a DC current flowing through the cores. The modulation current has a phase delay of about 45 degrees.

### G.2.3 Implementation

The total beam population  $N_{\text{tot}}$  is extracted (for each ring separately) from the measured (raw) DCCT signals  $S_{\text{DCCT}}^{\text{raw}}$  (in V) after correcting for the baseline offset  $S_{\text{DCCT}}^{\text{offset}}$ :

$$S_{\text{DCCT}} = S_{\text{DCCT}}^{\text{raw}} - S_{\text{DCCT}}^{\text{offset}} \quad (G.1)$$

$$N_{\text{tot}} = \alpha \cdot S_{\text{DCCT}} = N_{\text{DCCT}}.$$

Here,  $\alpha$  is the calibrated absolute scale factor of the DCCT (elementary charges/V) when fixing the absolute scale at 80% of the considered DCCT range with a precise current source. The measurement of the feedback current is made via four ranges (see Table G.2), provided simultaneously, to cover the entire beam dynamic ( $10^9$  to  $5 \cdot 10^{14}$  protons). The DCCT bandwidth

**Table G.2:** DCCT ranges. The scale factor for a Least Significant Bit (LSB) (charges/ADC bin) is calibrated for each range and DCCT, the last column shows the approximate value.

Range	Scaling factor (charges/V)	Full scale (charges)	LSB value (charges)
1	$1 \cdot 10^{14}$	$5 \cdot 10^{14}$	$2.5 \cdot 10^{11}$
2	$1 \cdot 10^{13}$	$5 \cdot 10^{13}$	$2.5 \cdot 10^{10}$
3	$1 \cdot 10^{12}$	$5 \cdot 10^{12}$	$2.5 \cdot 10^9$
4	$1 \cdot 10^{11}$	$5 \cdot 10^{11}$	$2.5 \cdot 10^8$

is limited, for noise reduction reason, to 20 Hz, even though the natural bandwidth is in the order of 20 kHz. The analogue signals of the four ranges are continuously acquired at 50Hz via a 12 bit ADC housed in a VME crate. The same ADC is used for both DCCT (beam 1 and beam 2) on one system. The choice of the pertinent range is performed by the real time program running at 10 Hz synchronously with the machine timing. The beam intensity, actually the number of circulating charges, after arithmetic averaging is published each second with a resolution of up to 20ms for all machine control and operation interfaces such as i.e. logging and fixed display. The beam intensity is also published at 10 Hz rate for the machine protection system. Before each LHC beam injection a

DCCT offset acquisition sequence is automatically launched. This sequence starts the acquisition in a hardware module of the four ranges offset for subsequent subtraction followed by the generation of four pulses of current, each lasting 100ms, used to check the calibration of the four ranges of the four DCCT's. Any result outside the given tolerance produces an explicit message sent to the LHC operators in charge and to the DCCT experts. At the end of the sequence the residual offset  $S_{\text{DCCT}}^{\text{offset}}$  is acquired and averaged for a period of 60 s by the real time program. The actual calibration adjustment is made manually by the DCCT experts during the technical stops.

A dependence on the filling pattern has been discovered during 2010 as described in Sec. G.4.2. The problem in the front-end electronic cards have been solved in the laboratory and a new improved version of the card has been reinstalled in the DCCT front-end during the winter shutdown in early January 2011. Additionally, the RF bypass has also been improved, see details in Ref. [51]. Except for the noise studies in Sec. G.3.1 and G.3.3, all in-situ measurements performed for this work are done with the new hardware which is in operation since 2011. Therefore the DCCT uncertainties presented in this work are also retroactively valid for the LHC 2011 run including the first van der Meer scans in March 2011. The new electronics have been tested up to intensities corresponding to the maximal number of 50 ns spaced bunches with nominal intensity.

## G.3 Instrumental stability and linearity

### G.3.1 Baseline subtraction method

The DCCT data as well as all measurements performed for this study are corrected for the baseline (offset) using the method defined Ref. [46]. The offset is measured in periods without beam before and after the analyzed fill. The value of the offset  $S_{\text{DCCT}}^{\text{offset}}$  during the fill is linearly interpolated with the two bounds and subtracted from the data as illustrated in Fig. G.5. Half of the largest peak-to-peak (P2P) variation in these two no-beam periods (before and after the fill) is taken as the uncertainty on the correction. A schematic example is shown in Fig. G.6.

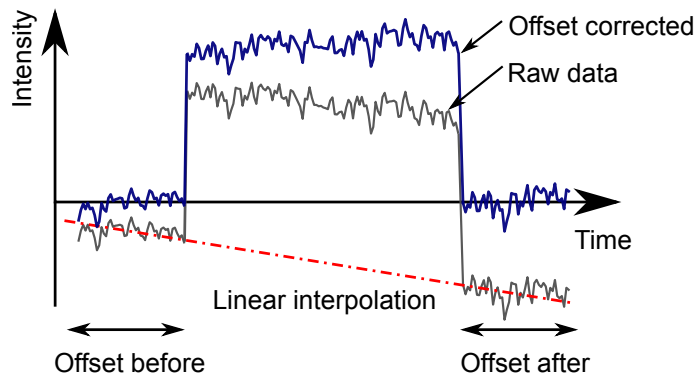


**Fig. G.5:** DCCT offset correction method. The offset  $S_{\text{DCCT}}^{\text{offset}}$  is linearly interpolated using no-beam periods before and after the fill and subtracted from the raw signal  $S_{\text{DCCT}}^{\text{raw}}$  to provide the final DCCT data  $S_{\text{DCCT}}$ .

A period of nine days of continuous noise have been acquired at the end of 2010 after the last beam dump. This data is used to verify the baseline correction method over a longer time period and also to detect possible periodic fluctuations in the noise. The full data for system A/beam 1 is shown in Fig. G.7, the data for the other three DCCT's is shown in Appendix G.8.1 (Figs. G.58 to G.60).

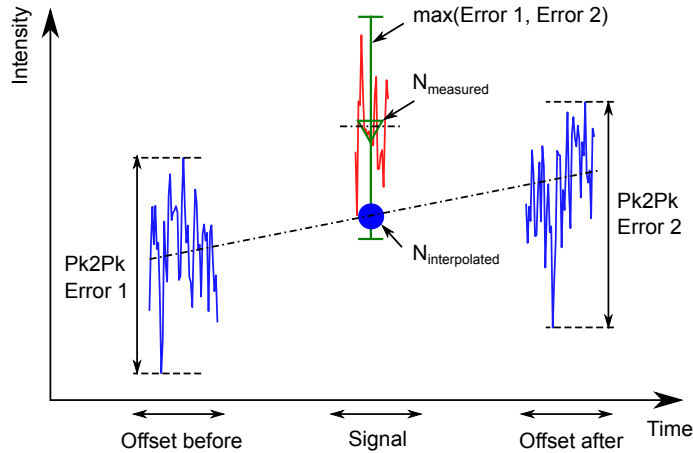


**Fig. G.6:** Offset uncertainty method. The largest peak-to-peak variation is taken as the uncertainty on the correction. The dot represents the interpolated offset, the triangle is the DCCT reading.

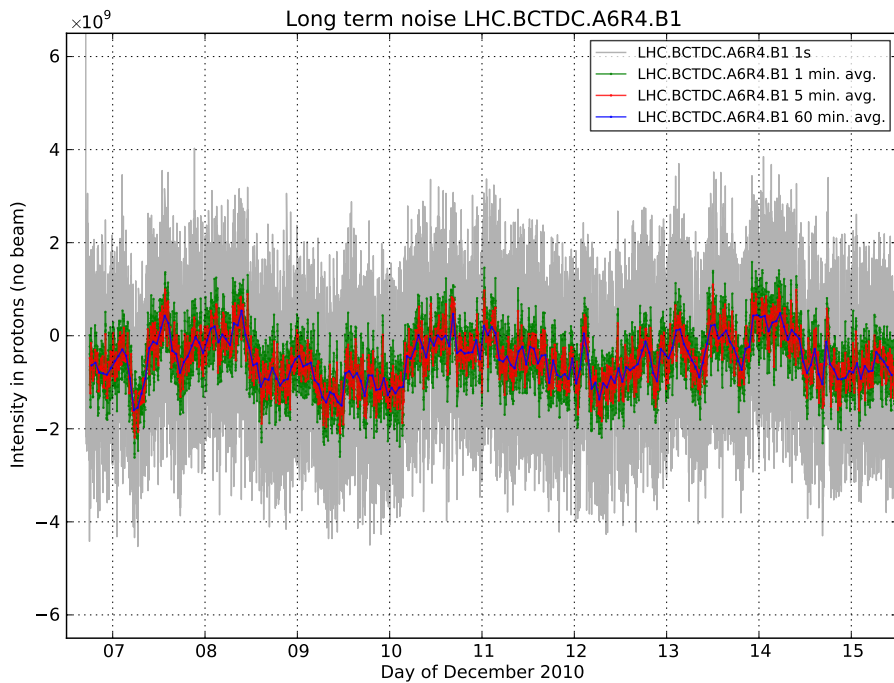


**Fig. G.7:** DCCT long term offset for system A/beam 1.

A verification of the baseline subtraction method is performed as follows (see also Fig. G.6). A random gap length between 1 hour and 40 hours is taken at a random time position within nine days of data. Periods of two hours before and after the selected gap are taken as offset bounds and used to interpolate the offset  $N_{\text{interpolated}}$  to the center of the gap with a linear function. The real offset  $N_{\text{measured}}$  is taken from the signal using a 1 hour average at the center of the gap and the largest peak-to-peak error from the offset bounds is taken as error for the interpolated offset. The interpolated offset  $N_{\text{interpolated}}$  is compared to the measured value  $N_{\text{measured}}$  to verify that the interpolated offset lies within the given error. The test is performed 500 times for each DCCT, totaling 2000 data points. Fig. G.8 shows the result for system A/beam 1 displaying only 50 out of the 500 points for better clarity. See Appendix G.8.1 (Fig. G.61) for the result of all DCCT's. The ratio  $|N_{\text{measured}} - N_{\text{interpolated}}| / (1/2 \text{ P2P error})$  for all tests and all DCCT's is combined in Fig. G.9. A histogram of the largest peak-to-peak errors from all tests is shown in Fig. G.10. In Ref. [46] the largest peak-to-peak error was assigned as a fixed error for all intensity measurements. As can be seen in Fig. G.9, 79% of the tested offsets fall within  $0.683 \cdot 1/2 \text{ P2P error}$ , which is better than for a Gaussian distribution; 8.2% are outside the expected peak-to-peak error.

In conclusion, the baseline correction method and error estimation described in [46] is valid. As seen in Fig. G.10, in general an envelope error of  $\pm 1 \cdot 10^9$  charges can be assumed if the baseline has been corrected manually or if the offset is already smaller than  $\pm 1 \cdot 10^9$  before and after the fill. A smaller error on the correction can be achieved by analyzing the offset manually which can be relevant for intensities acquired in range 4. For cases where the offset is not analyzed, a generic error can be used as discussed Sec. G.3.2.

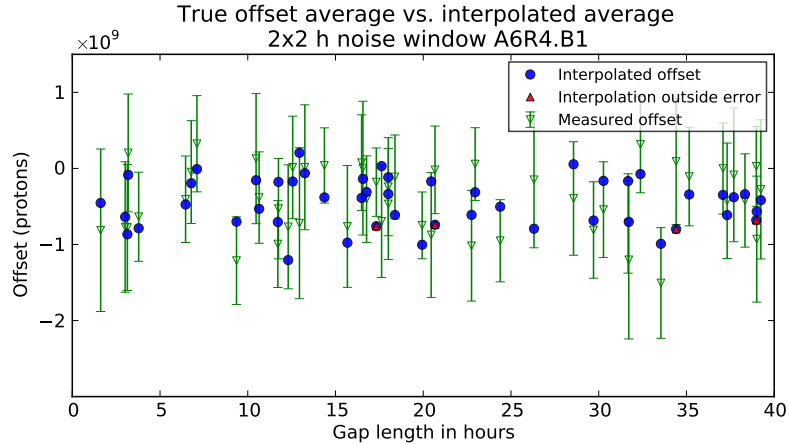


**Fig. G.8:** Offset box error test system A/beam 1 displaying 50 out of 500 points. Plain blue dots indicate an interpolated offset inside the error bar. A plain red triangle indicates an interpolated offset value outside of the expected error.

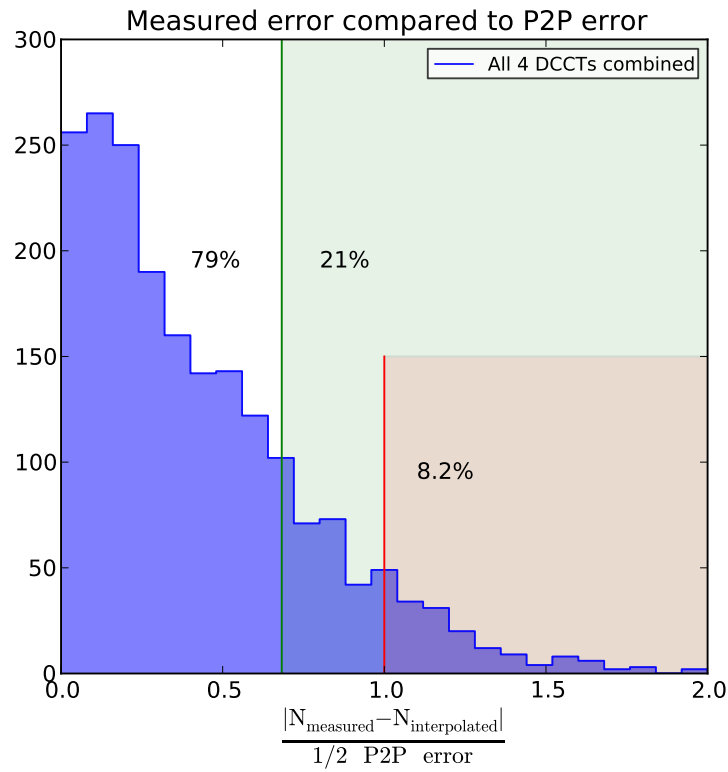


**Fig. G.9:** Offset box error histogram combining all 4 DCCT's. Entries with a ratio  $|N_{\text{measured}} - N_{\text{interpolated}}| / (1/2 \text{ P2P error}) < 1$  are tests where the interpolated offset lies within the peak-to-peak error. All values above one are tests where the measured offset lies outside the peak-to-peak error. From the 2000 tests, 79% have a ratio 0.683 indicated by the left vertical line. If the peak-to-peak error would be truly a Gaussian distribution, 68.3% of the tested offsets would lie below 0.683.

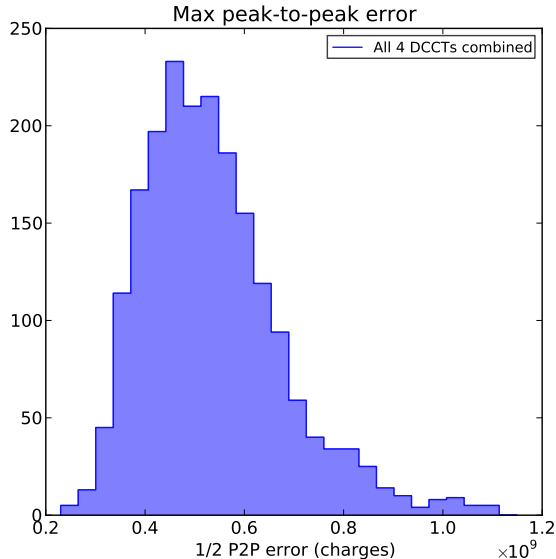


**Fig. G.10:**  $1/2$  P2P error observed within two hours or noise with samples of 5 minutes average. The histogram represents the expected distribution of the half peak-to-peak error attributed to the baseline correction.

### G.3.2 Automatic baseline correction

The baseline is automatically corrected before each fill in the preparation sequence of the DCCT's. A first rough correction using an 80 ms average is performed at the hardware level before the signal acquisition, a second correction using a 60 s average is performed in the acquisition software such that every range is set at zero at the beginning of each fill. If the baseline is not analyzed manually as described in Sec. G.3.1, a generic uncertainty of the baseline can be used which is based on the results of the following analysis.

An analysis has been performed to evaluate the offset deviation from zero at the end of fills. The baseline values for each range and DCCT were measured at the end of each fill in 2011<sup>2</sup>. The ADC raw data of every range is averaged over 10 minutes immediately after the beam dump and the offset correction which is measured automatically in the preparation sequence is applied to the average. Ideally the offset is zero when the beam is dumped. For each range, the absolute offset values of all DCCT's observed in 2011 are combined in a histogram as shown in Fig. G.11.

Based on the histograms in Fig. G.11, an error covering 68.3% and 99% offset deviations is provided in Table G.3. This systematic error due to the offset has to be added to the DCCT uncertainty if the baseline is not corrected or analyzed manually as described in Sec. G.3.1.

**Table G.3:** Observed offset deviation at the end of fills for each range. The indicated offset error includes 68.3% (left column) and 99% (right column) of the measured fills.

Range	Absolute offset	Absolute offset
	error (charges)	error (charges)
	68.3% of samples	99% of samples
1	$\pm 7.0 \cdot 10^9$	$\pm 6 \cdot 10^{10}$
2	$\pm 2.1 \cdot 10^9$	$\pm 7 \cdot 10^9$
3	$\pm 1.3 \cdot 10^9$	$\pm 4 \cdot 10^9$
4	$\pm 1.3 \cdot 10^9$	$\pm 4 \cdot 10^9$

<sup>2</sup>Only fills declared for physics were analyzed.

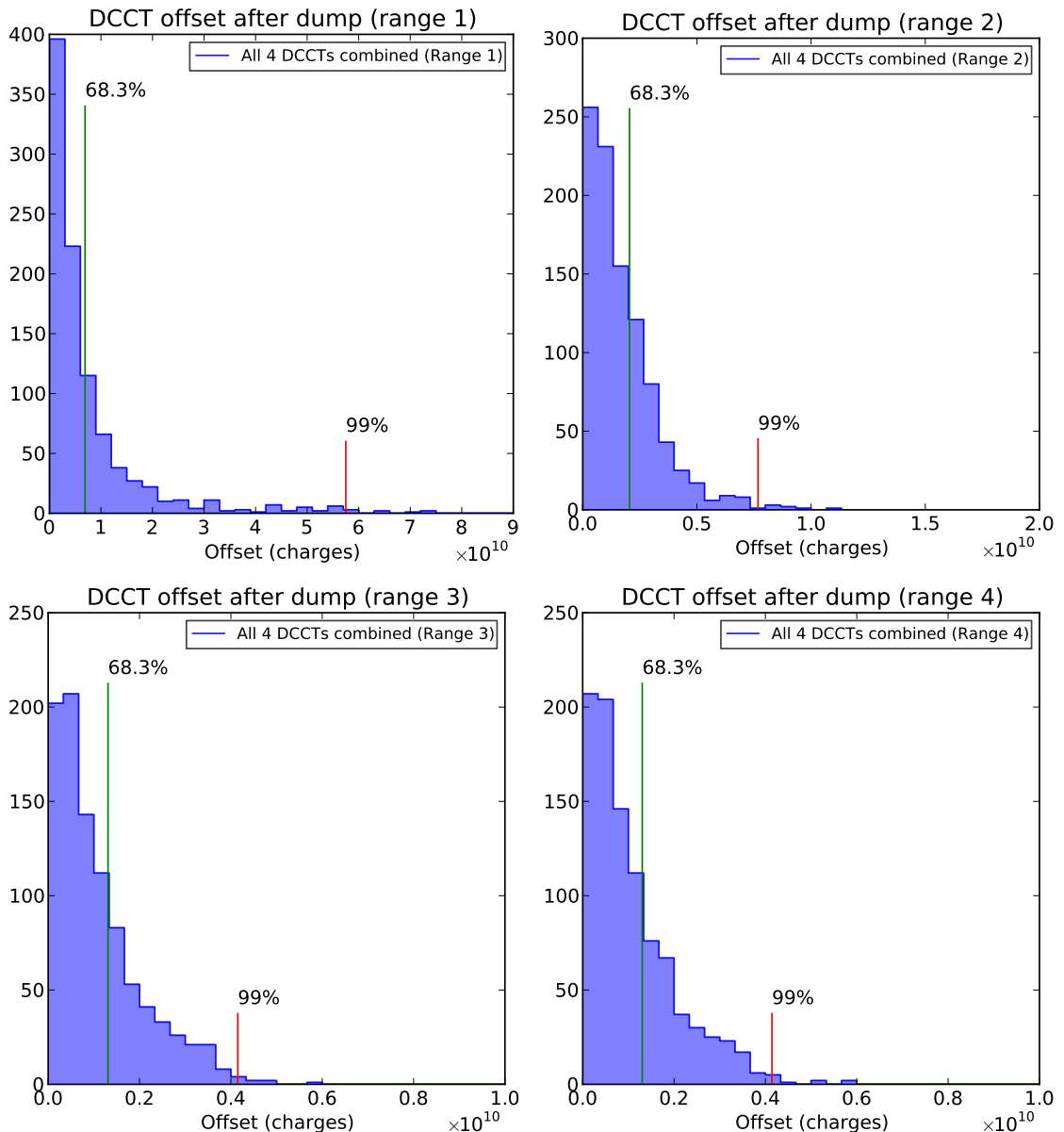


**Fig. G.11:** Measured offsets after a fill dump for all physics fills in 2011. The averaged offset over 60 seconds was automatically subtracted from the raw values in order to correct the baseline down to zero at the beginning of each fill. The deviation observed at the end of each fill was taken as a 10 minutes average starting 10 s after the dump.

### G.3.3 Fourier analysis of the noise

Periodic fluctuations of the noise can be detected with a Fourier analysis of the available data. A Fast Fourier Transform (FFT) of the nine days of data with a 60 s sampling average is shown on Fig. G.12 for the four DCCT's. The highest detectable frequency is  $2 \text{ min}^{-1}$  and the lowest detectable frequency is about  $3 \text{ days}^{-1}$  as a minimum of 3 periods are needed to detect a frequency. The power is highest at low frequencies  $< 24 \text{ h}^{-1}$  indicating a possible long term drift or a period longer than 9 days. There is, however, no frequency peak visible in the available range.

The FFT method used in Fig. G.12 was verified by analyzing a simulated signal with known frequencies. The raw signal and resulting FFT are shown in Fig. G.13. The simulated signal is a superposition of a linear function, 4 sine waves and random values as static. The points are generated with a 1 s resolution over 10 days and are averaged into 60 s time bins before the Fourier

transformation as with the DCCT noise. The linear function simulates a slow downward drift starting at 1 at  $T = 0$  and ending at -2 after 10 days. The four sine waves have a frequency of  $360^{-1}$  s,  $3600^{-1}$  s,  $24^{-1}$  h and  $30^{-1}$  days with amplitudes of 0.5, 1, 0.5 and 5 respectively. A random value between  $\pm 10$  is added to the final signal to simulate some static noise. The top plot shows the resulting signal over 10 days, the x axis is the time in s; the  $24^{-1}$  h is clearly visible and the  $30^{-1}$  days period is responsible for the long curvature. The peaks at 360 s, 3600 s and 24 h (86400 s) are clearly visible, however the long term period of  $30^{-1}$  days could not be detected with 10 days of data. The high power towards the low frequencies is due to the slow drift and  $30^{-1}$  days period.

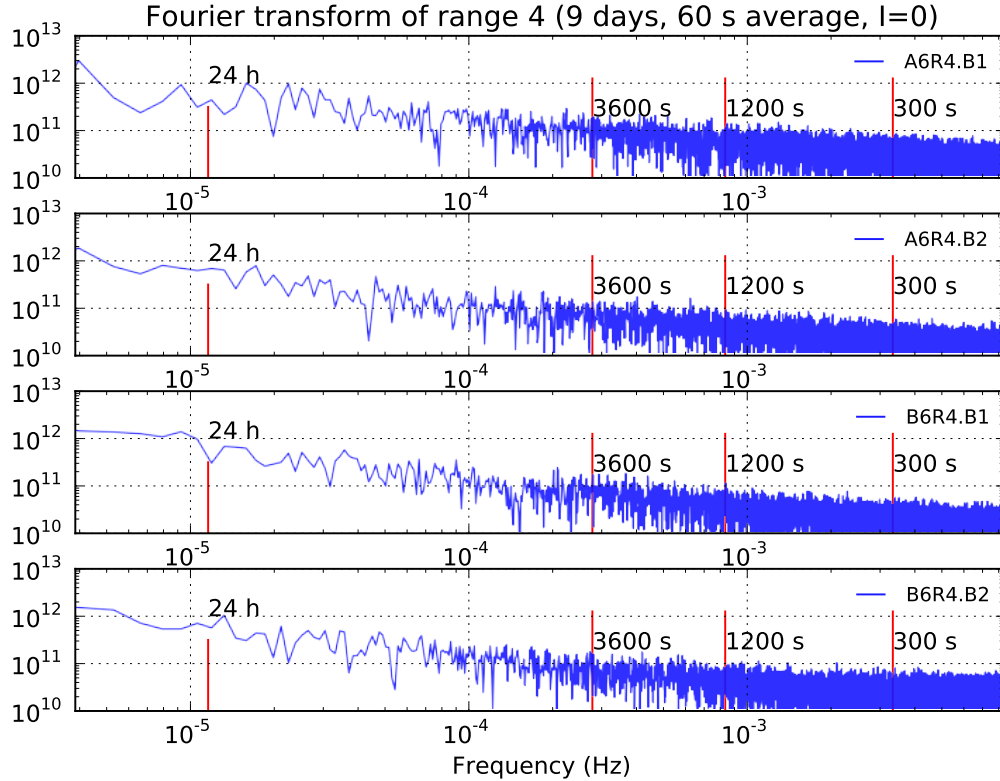


**Fig. G.12:** Fast Fourier transform of the DCCT noise. The DCCT signal was acquired with range 4 (the most sensitive). The x axis represents the frequency on a logarithmic scale. For reference, the frequency value for  $300^{-1}$ ,  $1200^{-1}$  and  $3600^{-1}$  seconds and of  $24^{-1}$  hours are indicated with a vertical line as example.

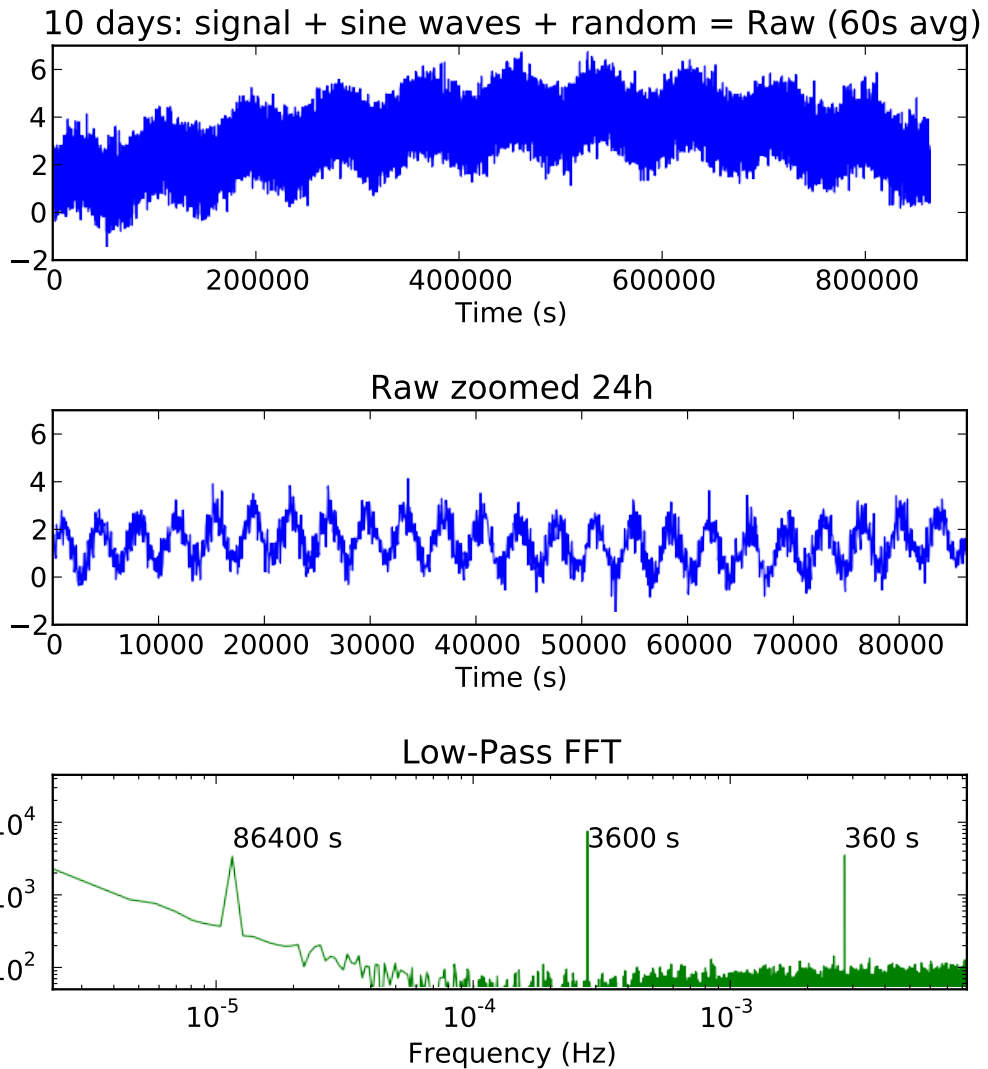


**Fig. G.13:** Fast Fourier transform of simulated noise. The first graph shows the raw signal over 10 days. The second plot shows a zoom in a 24 h period, here the  $3600^{-1}$  (1 h) period is clearly visible but not the  $360^{-1}$  period. The FFT of the raw signal is shown on the bottom plot, the highest detectable frequency is  $120^{-1}$  s due to the 60 s binning.

#### G.3.4 In-situ tunnel measurements

A set of measurements have been performed with the DC current source placed in the tunnel near the DCCT's. The aim was to evaluate the DCCT stability with and without current over a long term period of 12 hours, also the linearity away from the calibration point and the calibration method were analyzed in-situ. The setup is summarized in Fig. G.14. The current source<sup>3</sup> was controlled by a labview program which set the desired current in predefined time steps. The cable connected to the DC source passed through all four DCCT's in two loops, therefore the current seen by the DCCT's was twice larger than the injected current. A  $100 \Omega$  resistance (Sfernice RE3 RH50 5%, 50 W) was connected in series. Because the measurement were performed during an access-restricted period, the planned sequence could not be modified once started. The incentives to place the source near the DCCT's were the following:

- The DC current seen by the DCCT's is exactly the same at all times. Therefore, any difference between the DCCT's can not be due to the source.

<sup>3</sup>Yokogawa GS200 is also used for the precise calibration

- One measurement can be performed with all DCCT's at the same time. This was important for the long term measurements which required 5 days to test all ranges.
- A current leak in the 500 meter cables from the surface back-end electronics to the DCCT's in the tunnel can be excluded by comparing the calibrations with the source in the tunnel and on the surface.

The normal acquisition chain was used to record the DCCT values; however, an additional software feature has been added to the DCCT acquisition software to be able to record the raw ADC value of each DCCT range. The ADC values of each DCCT range were sampled at 50 Hz; however, only one value out of the 50 was sent to the logging database for diagnostic purposes. The special software flag computed a 1 Hz average of the 50 Hz DCCT values and wrote the averages in a file. The system was therefore independent of the central logging database and provided a 1 Hz average of the raw values from all ranges.

The absolute scale calibration was performed as a first measurement in the 7 days sequence. A known current was injected at about 80% of each range and was used to measure the value of 1 ADC Least Significant Bit (LSB) for each range from all DCCT's. This calibration was used throughout all subsequent measurements to convert the DCCT signal into charges.

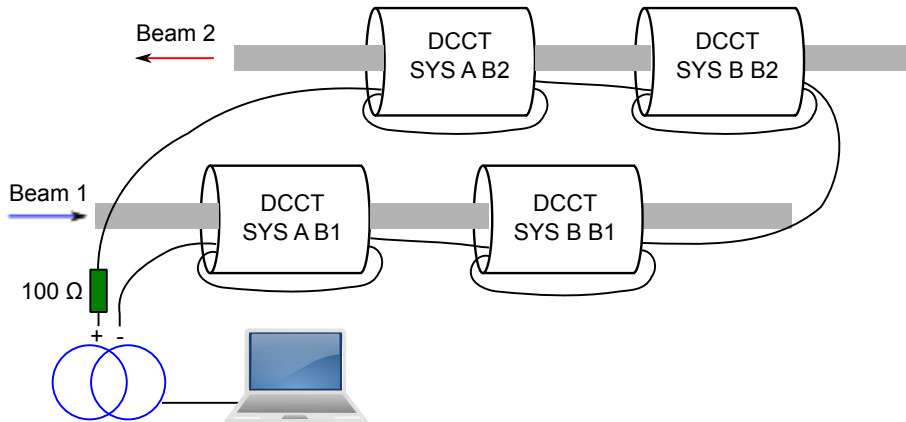


Fig. G.14: Tunnel setup.

#### G.3.4.1 Long term stability over 12 hours

The long term stability of the DCCT was verified with two measurements of 12 hours per range separated by 3.5 days using a constant current. Short term fluctuations within 12 hours are expected to be due to a variation of the baseline instead of the scale factor and depend on the averaging time. Furthermore, periods longer than 12 hours could yield larger fluctuations while shorter periods will reduce the fluctuations. Therefore the uncertainties deduced from this measurement are valid for fills of less than 12 hours and are provided for measurements averaged over 1 minute or 1 hour.

Each range was tested with a current near its full scale; the injected currents are listed in Table G.4. The time evolution of the DCCT response during both 12 hours measurements is shown in Fig. G.15 for system A/beam 1 range 3 and Fig. G.16 for system B/beam 1 range 1 as examples. The results for all DCCT's and all ranges are shown in Appendix G.8.2 (Figs. G.62 to G.65). In all cases, the measurements use the same calibration factors determined at the beginning of the tunnel sequence.

There is no visible systematic drift or long term daily fluctuation visible. An oscillation with a 30 minute period is visible on range 1 which is probably due to a digitalization artifact due to the low

noise of the signal for this range. The Fourier analysis for range 1 for all DCCT's is shown in Fig. G.17 and confirms the oscillation with a frequency of about  $1800^{-1} \text{ s}^{-1}$ , no other frequency is visible in the spectrum. The amplitude of the oscillation is  $< 0.02 \text{ ADC bin}$  and can be ignored. In all other ranges the current is stable and no pattern or daily effect can be observed.

For each DCCT and range, the raw ADC values are projected in a histogram to evaluate the spread of the signal over 12 hours at different currents. Each measurement, for a given range, taken during one of the 12-hour periods, is centered around its average during that period. An example histogram for system A/beam 1, range 3 is shown in Fig. G.18. The histograms for all ranges and different currents are grouped in Fig. G.19 for the DCCT system A/beam 1, the remaining DCCT's are shown in Appendix G.8.2 (Figs. G.66 to G.68). The histograms taken without current (bottom line) use 5 hours of data instead of the normal  $2 \times 12$  hours.

The current intensity flowing through the DCCT does not affect the spread of the signal. For a given range and using 1 minute and 1 hour time bins, the largest observed standard deviation and the largest half peak-to-peak value from any current and from all DCCT's are given in Table G.5. The conversion into charges is calculated before rounding and uses the calibration factor of the corresponding DCCT.

The RMS and largest observed deviation from the average taken from Table G.5 reflect the error induced by the baseline fluctuation even after baseline correction. The fluctuation depend on the averaging time: as expected, averaging the signal over a longer time period reduces both the RMS and peak-to-peak spread, therefore a 1 minute measurement will have a larger baseline induced uncertainty as a 1 hour measurement. In a typical precise van der Meer fill the DCCT signal is averaged over about 1 hour.

The intrinsic DCCT noise can improve the ADC resolution below  $1/\sqrt{12}$  LSB; this is probably the case for range 3, and possibly for range 2 (for range 4 the noise level exceeds the ADC resolution). This assumption, however, is not true for range 1 which has a low noise level and quantization effects are visible during the slow beam decay if the signal sampling is too short. An example demonstrating this effect is shown in Fig. G.20 where a step-like structure is visible in the beams intensity decay. This step wise decay can be observed in all fills with intensities covered by range 1. In this case the noise level is too low to improve the ADC resolution below  $1/\sqrt{12}$  LSB and the ADC is limiting the precision of range 1.

In conclusion, the uncertainty induced by the baseline fluctuation within a fill depends on the signal averaging time and acquisition range. A signal averaged over 1 hour or more will have smaller fluctuations compared to an average of 1 minute only. The corresponding absolute half peak-to-peak fluctuations are provided in Table G.5. Furthermore, the long term fluctuations are independent of the intensity within a range.

**Table G.4:** Injected currents per range used during the long term measurements of two times 12 hours. For range 1 the 200 mA maximal current or the source was used. The DCCT sees twice the current due to the two loops of the cable.

Range	Injected current (mA)	Equivalent charges	Relative range scale
1	400	$2.22 \cdot 10^{14}$	44.4 %
2	80	$4.44 \cdot 10^{13}$	88.8 %
3	8	$4.44 \cdot 10^{12}$	88.8 %
4	0.8	$4.44 \cdot 10^{11}$	88.8 %

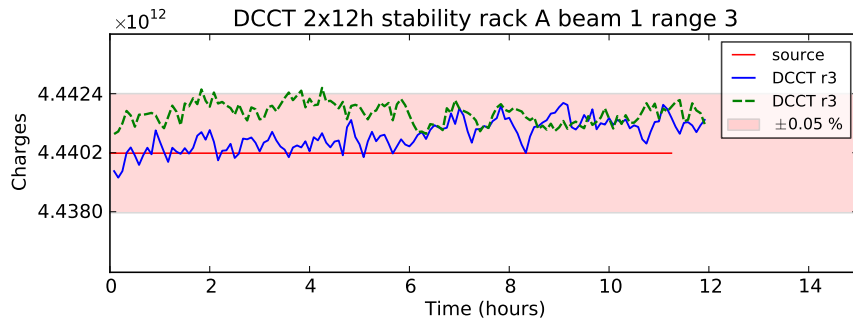


**Fig. G.15:** Long term stability under load for system A/beam1, range 3. The data is averaged in 300 s time bins. The first 12 hours measurement is plotted as a solid blue line, the second measurement taken 3.5 days later is plotted as a dashed green line.

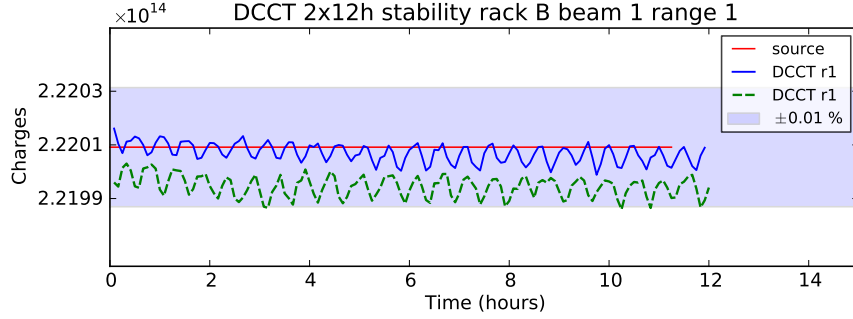


**Fig. G.16:** Long term stability under load for system B/beam1, range 1. A 30 minutes oscillation is clearly visible on range 1 and is probably due to digitalization and averaging effects with a low noise signal.

**Table G.5:** Observed standard deviation and largest half peak-to-peak deviation of 1 minute and 1 hour average over two periods of 12 hours. For each range, the largest RMS and half peak-to-peak deviation from any intensity and from all DCCT's is selected. The LSB conversion into charges is done before rounding.

Range	Averaging time	Absolute RMS (LSB)	Absolute RMS (charges)	Absolute P2P (LSB)	Absolute P2P (charges)
1	1 min.	$\pm 0.1$	$\pm 2.3 \cdot 10^{10}$	$\pm 0.4$	$\pm 1.1 \cdot 10^{11}$
2	1 min.	$\pm 0.1$	$\pm 2.2 \cdot 10^9$	$\pm 0.4$	$\pm 1.0 \cdot 10^{10}$
3	1 min.	$\pm 0.3$	$\pm 6.7 \cdot 10^8$	$\pm 0.9$	$\pm 2.4 \cdot 10^9$
4	1 min.	$\pm 2.5$	$\pm 6.3 \cdot 10^8$	$\pm 9.4$	$\pm 2.3 \cdot 10^9$
1	1 hour	$\pm 0.01$	$\pm 2.8 \cdot 10^9$	$\pm 0.03$	$\pm 7.3 \cdot 10^9$
2	1 hour	$\pm 0.02$	$\pm 5.2 \cdot 10^8$	$\pm 0.05$	$\pm 1.1 \cdot 10^9$
3	1 hour	$\pm 0.2$	$\pm 4.8 \cdot 10^8$	$\pm 0.4$	$\pm 1.1 \cdot 10^9$
4	1 hour	$\pm 1.9$	$\pm 4.7 \cdot 10^8$	$\pm 4.1$	$\pm 1.0 \cdot 10^9$

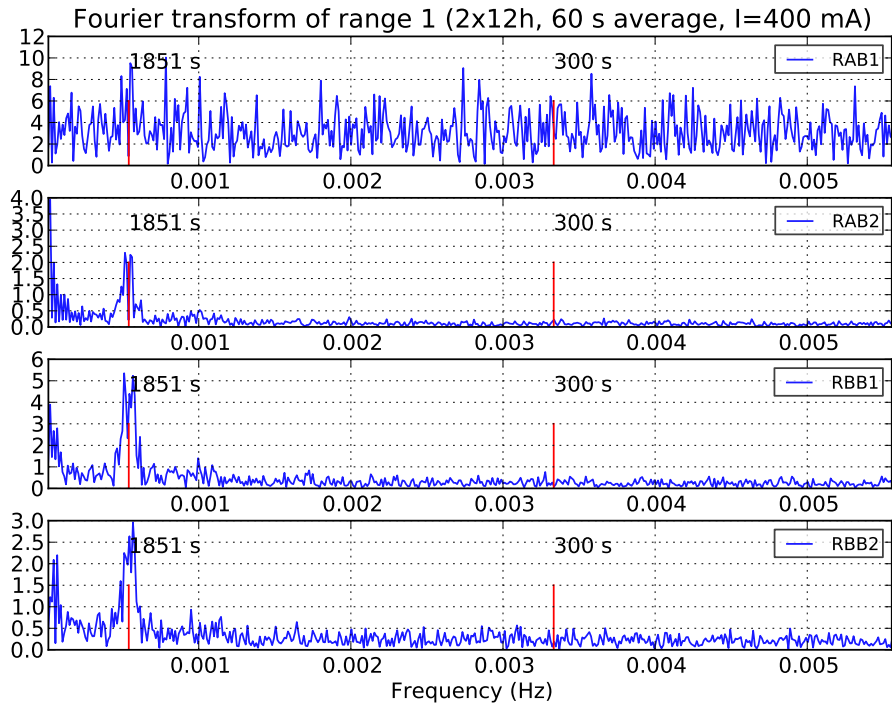


**Fig. G.17:** Fourier analysis of range 1. The small oscillation visible on range 1 is visible at a frequency of  $1851^{-1} \text{ s}^{-1}$ . As reference the frequency of  $300^{-1} \text{ s}^{-1}$  is indicated with a vertical line.

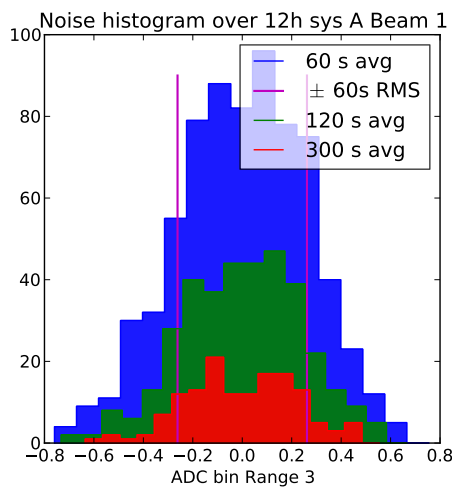


**Fig. G.18:** Histogram of ADC values for system A, beam 1, range 3 recorded during two 12-hour periods at 88% of the maximum intensity for that range. The zero ADC bin is set to the average of the 12-hour measurement; both periods are accumulated in the same histogram. The signal is averaged in time bins of 60 seconds (blue), 2 minutes (green) and 5 minutes (red). The two vertical lines indicate the RMS value of the 60 s time averages.

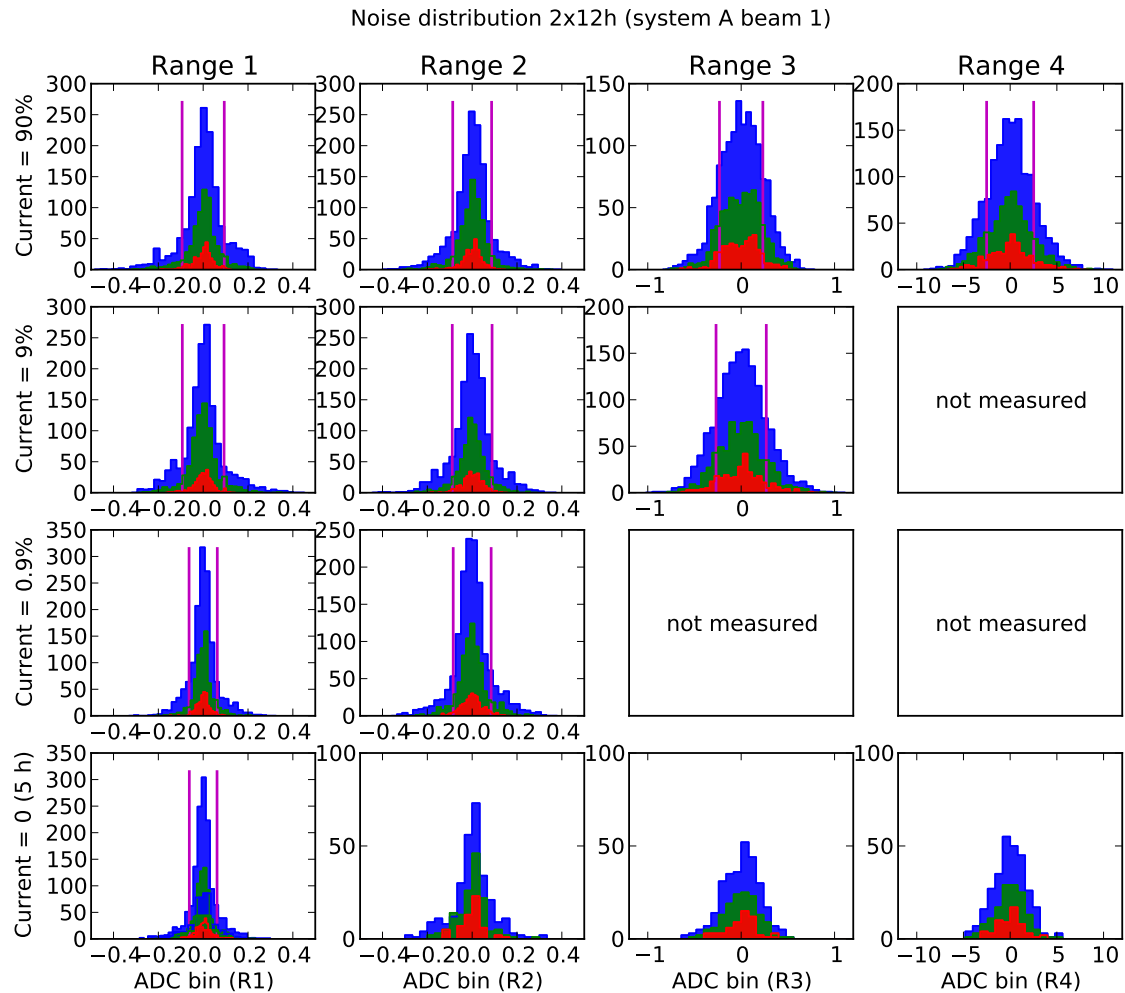


**Fig. G.19:** Histograms of  $2 \times 12$  hours of all ranges for system A/beam 1. The ranges are sorted per column, each row represents a current intensity relative to the total scale of the range. The first row is measured with a current intensity equivalent to 90% of the range and the lower row is measured without current. Due to time constraints the histograms without current contain only 5 hours of data instead of  $2 \times 12$  hours. For this reason the histogram for range 1 at zero current (bottom left frame) uses instead the current of range 4 at 90%, which corresponds to 0.09% of range 1. The lowest current used during the long term measurements corresponds to 90% of range 4; values below this intensity have therefore not been measured and the corresponding frames are marked accordingly.

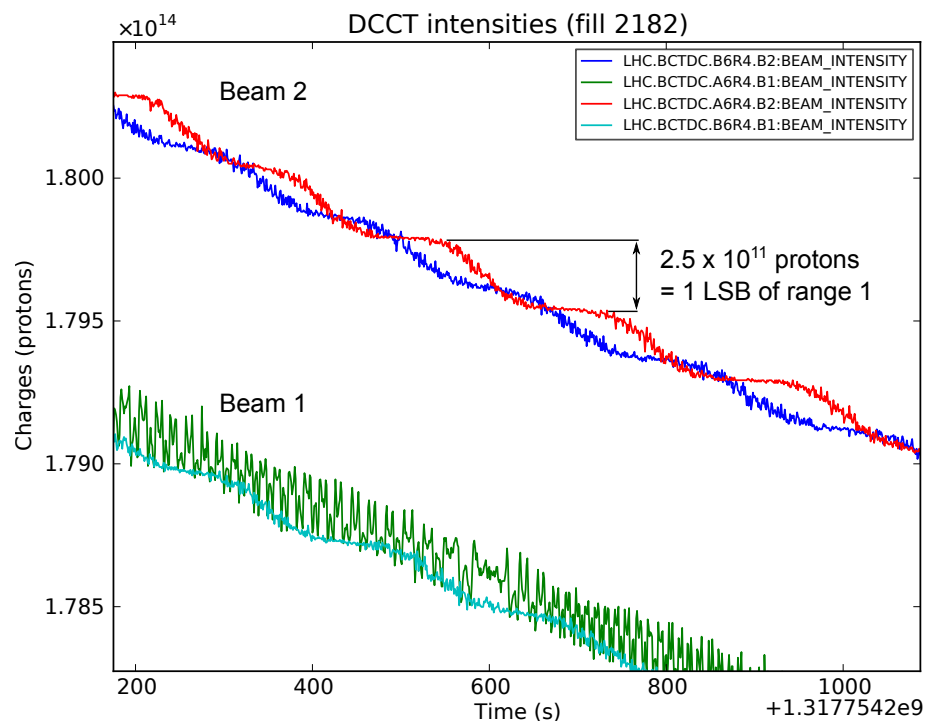


**Fig. G.20:** The quantization of the 12-bit ADC response is apparent on range 1 as the beam-2 intensity slowly decays. DCCT system A/beam 1 is more noisy and the step pattern is less visible. The difference between two steps corresponds to the scale factor of one ADC bin of range 1. The resolution of the DCCT 12-bit ADC is not improved by the noise for range 1.

### G.3.4.2 Long term stability under load over 24 hours

An additional long term measurement has been performed during 24 hours with a current of 400 mA to test for possible thermal effects in the front-end electronics. The DCCT injects a current equivalent to the measured intensity to cancel the total current; therefore, this generated current could warm up the electronic components over time and induce a slow drift. The DCCT response of range 1 during 24 hours averaged over 300 seconds time bins is shown in Fig. G.21 for all DCCT's. The small oscillation pattern observed in Sec. G.3.4.1 is also visible here. No thermal effect or systematic drift can be observed, only a slow downward drift on system A/beam 2 can be observed with a total amplitude of about 0.01% in 24 hours. Range 1 reaches about 890 ADC bins with a current of 400 mA, therefore, 1 LSB represents about 0.11% at this intensity.

In conclusion, no thermal or daily effect can be observed within 24 hours with a current intensity of 44% of range 1. The observed signal is within  $\pm 0.1$  LSB, therefore, the accuracy of the measurement is limited by the 12-bit ADC.

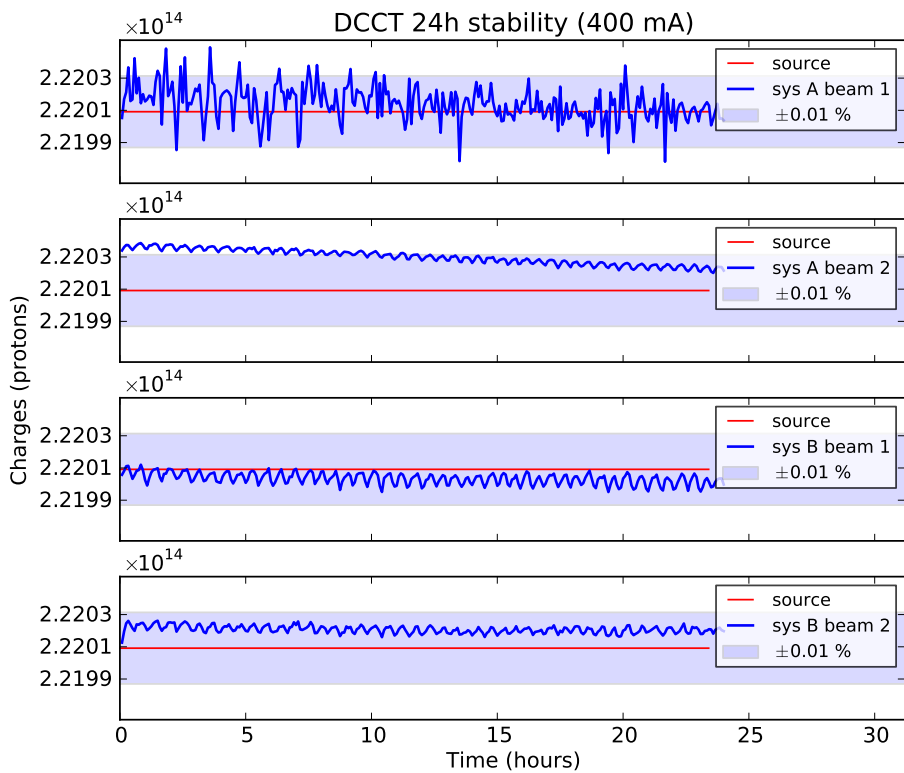


**Fig. G.21:** Long term stability under load for range 1. A current of 400 mA ( $2.22 \cdot 10^{14}$  charges, 44% of range 1) is injected during 24 hours. The data is averaged in 300 s time bins, the calibration was performed 48 hours before the measurement

### G.3.4.3 DCCT Linearity

The linearity of the DCCT response away from the calibration point was studied with three measurements performed in the tunnel. The first two measurements were spaced by 48 hours and took 5 minutes per step with 8 steps per range. The third measurement was performed 5 days later taking 2 minutes per step with 5 steps per range. Zero-current intervals separated one period from the next, in order to correct the offset with the method described in G.3.1. All values used the same calibration performed at the beginning of the tunnel measurements. All linearity measurements were done with the new 2011 front-end electronics which solved the bunch

pattern dependence observed in 2010 (see Sec. G.4.2). The acquisition chain together with the ADC remained unchanged from 2010. The 12-bit ADC is shared and multiplexed in a system, that is, the same ADC acquires all ranges for beam 1 and 2 for a given system. An example of the current sequence used to test the four ranges is shown in Fig. G.22. As an example, Fig. G.23 shows the DCCT response in all ranges for system A, beam 1.

The residual fraction  $1 - (N_{DCCT}/N_{source})$  (%) for each range is shown in Fig. G.24 for system A/beam 1. The plots for the remaining DCCT's are shown in Appendix G.8.3 (Figs. G.69 to G.71). Due to technical reasons, the second measurement was lost for system A.

A positive residual, i.e. the DCCT underestimates the actual current, is observed for the ranges 1, 2 and 3 of all DCCT's. The noise level of range 4 limits the accuracy of the measurement. This observed non-linearity, however, is within 1 LSB as indicated by the dashed line. A standard precise calibration performed at 14% of range 2 instead of the usual 80% is compared to the linearity measurements for range 2 in Fig. G.25. The green dots show the combined three linearity measurements according to the calibration performed in the tunnel. The red star shows the result of the standard precise calibration performed at 14% of range 2 and is in accordance with the expected non-linearity.

In conclusion a non-linearity of the DCCT response of the order of 1 LSB is observed for all ranges and DCCT's. The non-linearity measurement is inconclusive for range 4 due to the noise level; however, it is expected to be the same as for the other ranges as all ranges are acquired with the same ADC.

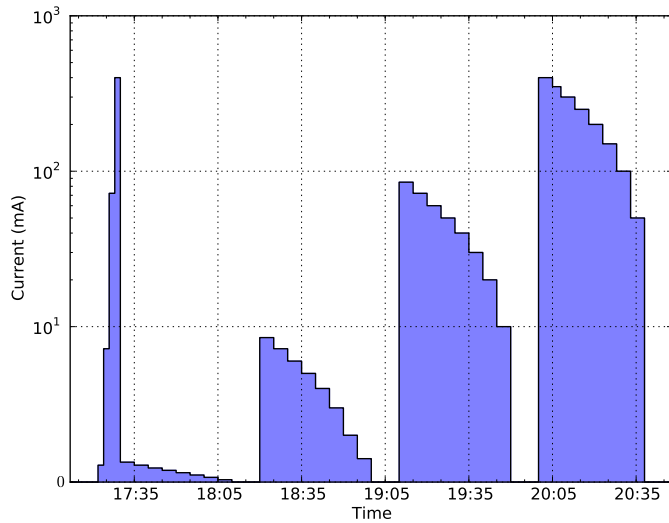


**Fig. G.22:** Current sequence used for the linearity measurement. A period of 10 minutes separated each sequence to correct the offset. The low intensity steps were also used in the less sensitive ranges. The first four steps were used for the calibration which were kept throughout all measurements in the tunnel.

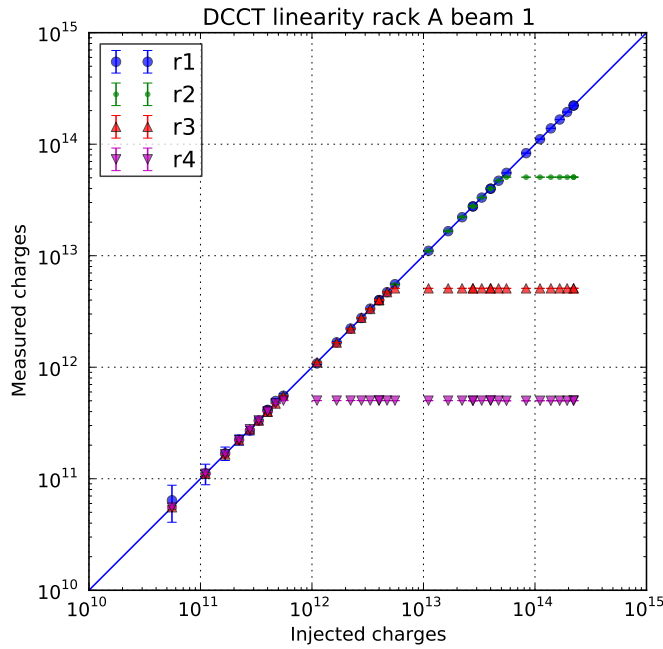


**Fig. G.23:** Injected current versus measured current for the DCCT system A/beam 1. With increasing intensity, the ranges 4, 3 and 2 enter in saturation and the response is constant.

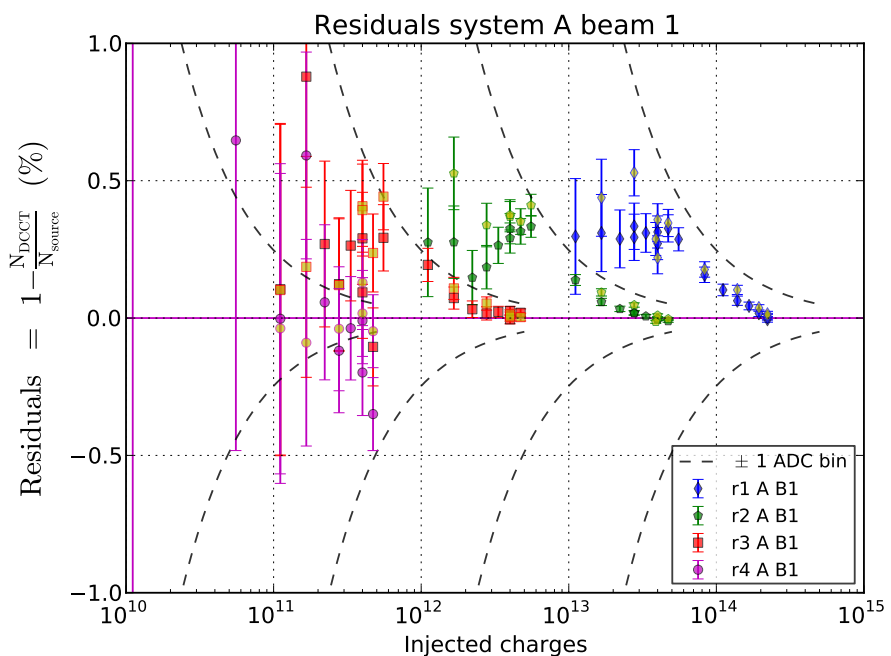


**Fig. G.24:** Linearity residuals for system A/beam 1 combining values from the first measurement (plain dots) and third measurement (yellow faced dots). Intensities below 2% of the range (about 40 ADC bins) are not shown. The residuals corresponding to  $\pm 1$  ADC bin are indicated by dashed lines.

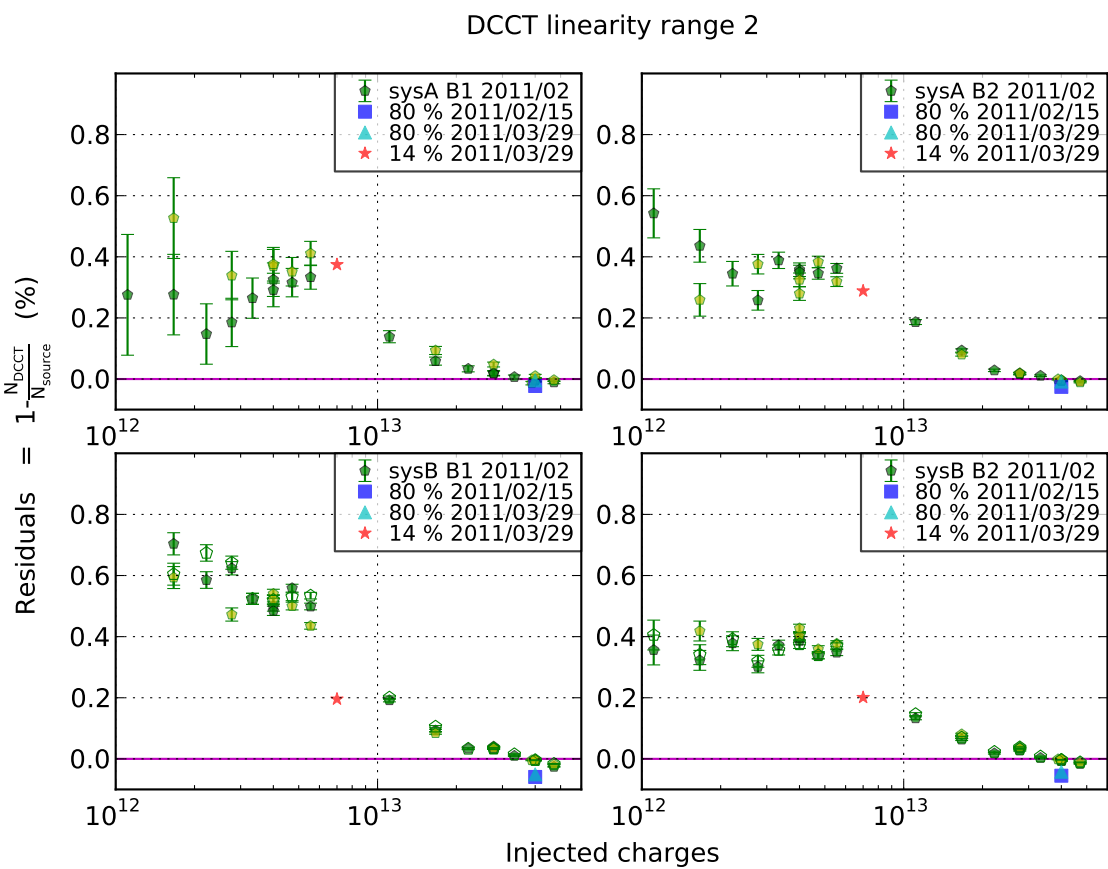


**Fig. G.25:** Linearity residuals for range 2 compared to standard calibrations.

### G.3.5 DCCT Linearity verified with alternate ADC

In an effort to disentangle the origin of the non-linearity between the DCCT and the acquisition chain, an additional linearity measurement was performed with an alternate ADC recording the DCCT signal in parallel to the normal acquisition. The second ADC from National Instruments was a 16 bit ADC model NI USB-9162 with a connector block NI 9215 with 4 BNC and was used in the bipolar range of  $\pm 10$  V.

#### G.3.5.1 Reference response of NI ADC

A reference response of the NI ADC has been measured in the laboratory with the same source and was used as a control reference. The goal was to generate a signal between 0 and 5 V by using four different ranges of the source by selecting an appropriate resistance. The voltages were acquired with the NI ADC for each range to quantify the residuals. To avoid any thermal effects, the maximal power dissipated was kept below 1% of the nominal power of the resistance configuration; furthermore, the measurement was performed twice, once with an increasing current and once with a decreasing current (see Fig. G.26). The resistances used to test each range are listed in Table G.6; the last column lists the current range used at the source. Each voltage generated from a current step was acquired during 20 s with a 10 Hz sampling.

The residual fraction  $1 - (N_{\text{ADC}}/N_{\text{source}}) (\%)$  for each range is shown in Fig. G.27. the source was used over its full range and the non-linearity pattern is similar for all ranges, therefore, the systematic negative non-linearity points towards a non linearity of the ADC instead of the source.

**Table G.6:** Resistance used to test the NI ADC. The symbol “//” means “parallel”.

Range	Resistance configuration	Measured resistance	Nominal power	Maximal power used	Resistance model	Current range used (A)
4	$4 \times 100 \text{ k}\Omega$ in //	25.05 $\text{k}\Omega$	1.4 W	1 mW	Philips MRS 25 0.4 W	$0 - 2 \cdot 10^{-4}$
3	$11 \times 26 \text{ k}\Omega$ in //	2.37 $\text{k}\Omega$	1.4 W	10 mW	Sfernice 25 k RS63Y 0.25 W	$0 - 2 \cdot 10^{-3}$
2	$4 \times 100 \Omega$ ; 2 in // 2 in series	250 $\Omega$	25 W	0.1 W	Sfernice 100 $\Omega$ RH50 5% 50 W	$0 - 2 \cdot 10^{-2}$
1	$4 \times 100 \Omega$ in //	25 $\Omega$	200 W	1 W	same as in 2	$0 - 2 \cdot 10^{-1}$

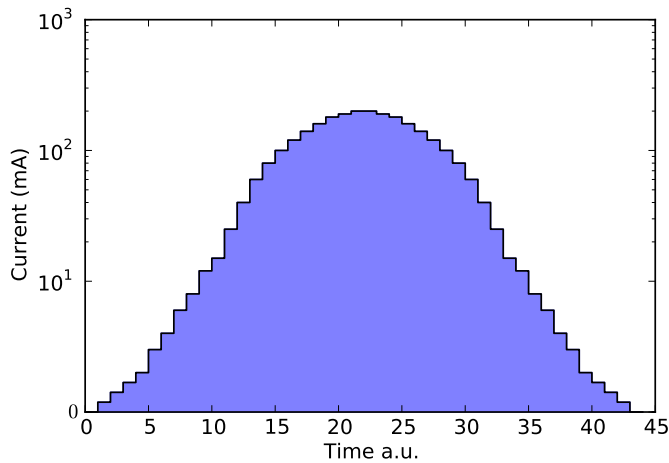


**Fig. G.26:** Current steps used to characterize the NI ADC. The pyramidal measurement permits to check for a possible thermal effect of the resistances. This sequence example with a maximal current of 200 mA used a similar current range as used to measure the linearity of range 1 of the DCCT.

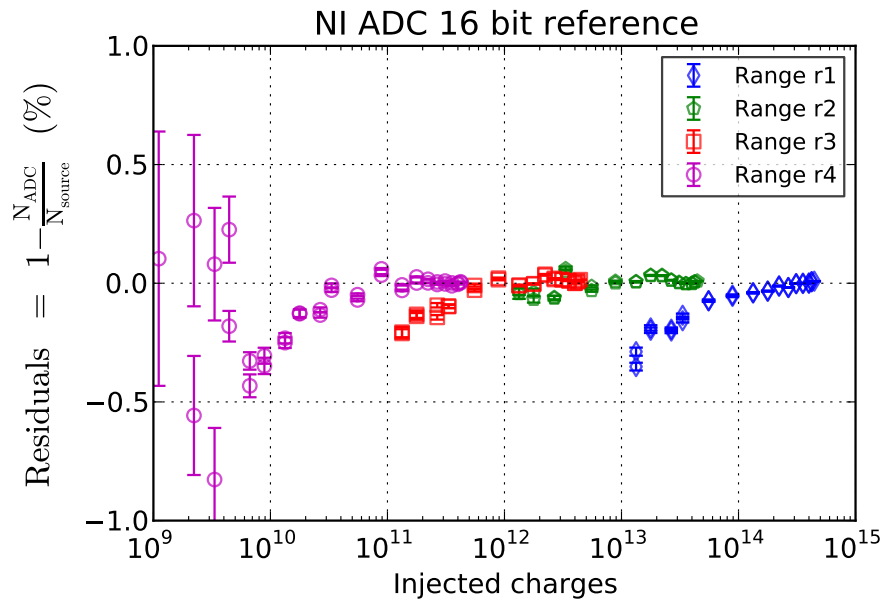


**Fig. G.27:** Reference response of the NI ADC.

### G.3.5.2 DCCT Linearity compared with NI ADC

The setup used to acquire the DCCT signal with the two ADC's is sketched in Fig. G.28. Each range of beam 1 and beam 2 of one system provided a signal between 0 and 5 V in the front-end electronics. The signals were send to the surface and decoupled with a unity gain module. The 12-bit ADC of a system acquired the 8 signals from the unity gain module with a multiplexer. The same signals were also acquired in parallel at the unity gain module with the 16 bit ADC.

The results of the linearity measurement acquired with both ADC's in parallel is shown in Fig. G.29 for system B/beam 2 range 1. The DCCT response measured with the NI ADC follows closely the laboratory reference of the NI ADC. As in the previous measurements, the 12-bit ADC shows a positive non-linearity. The same measurement performed on all DCCT's and all ranges is shown in Appendix G.8.3 (Fig. G.72).

In conclusion the observed non-linearity appears to originate from the acquisition chain, most probably from the 12-bit ADC and not from the DCCT itself. The ideal working point for a

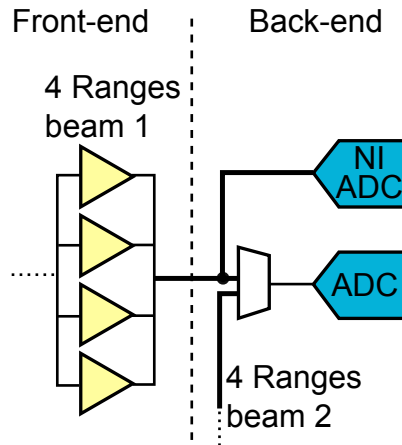


**Fig. G.28:** Setup with parallel ADC. Each DCCT range sends a signal between 0 and 5 V to the surface. The signals were acquired through a unity gain module by the normal 12-bit ADC and also a 16 bit ADC from NI. Therefore, both ADC's acquired the signal from the same source.

precise measurement of the beam intensity is close to calibration point. In addition to the above linearity measurements, a similar measurement has been performed one year later with the new single range 24-bit ADC. The results are shown in Appendix G.8.3.2 (Figs. G.73 to G.76) This new 24-bit acquisition system is still in a testing phase at this time; however, the results confirm that the DCCT is linear within the measured range. The noise level and baseline fluctuations limit the accuracy at low intensities below  $10^{11}$  charges.

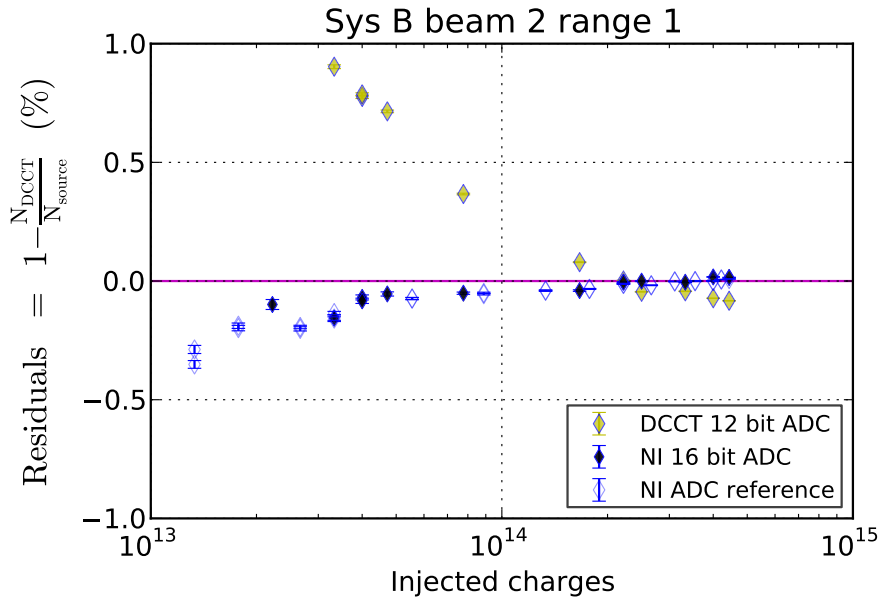


**Fig. G.29:** Linearity measurement with NI ADC acquired in parallel to the DCCT 12-bit ADC. The open dots are the reference response of the NI ADC measured in the laboratory. The filled blue dots are the DCCT response measured with the NI ADC and the filled yellow dots are the DCCT response measured with the 12-bit ADC. The DCCT response measured with the NI ADC follows the reference response of the ADC.

### G.3.6 Absolute Scale

The stability over time of the scale factor (Sec. G.2.3) was the main source of uncertainty affecting the measured beam intensities in 2010. A difference of up to 1.6% was observed between the two precise calibrations performed in 2010 at two different times. A precise calibration has been performed during all technical stops in 2011 to assert the stability of the scale factor over the year.

The history of the scale factors over nine month is shown in Fig. G.30. The scale factors for the ranges 1 to 3 are contained within an envelope of  $\pm 1$  ADC bin which corresponds to a relative error of  $\pm 0.06\%$ . The scale factors of range 4 are contained in an envelope of  $\pm 4$  ADC bins which corresponds to a relative error of  $\pm 0.24\%$ . The stability of range 4 is compatible with the intrinsic noise of the DCCT which is of the order of 4 ADC bins ( $10^9$  charges). The ranges 1 to 3 are probably limited by the ADC resolution similarly to the long term measurements in Sec. G.3.4.1.

The scale factor could be sensible to the temperature of the electronics or of the monitor, however, no seasonal fluctuation is visible over the full year. A view of the inlet ventilation temperature for different sections around the DCCT's is shown in Fig. G.32, the location of the section is provided in Fig. G.31. Fluctuations of  $\pm 2^\circ\text{C}$  are present, but there is no seasonal change in the tunnel or service sections.

In conclusion the scale factors are stable within  $\pm 1$  LSB for the ranges 1 to 3 and within the intrinsic noise level of range 4. Therefore, an uncertainty envelope of  $\pm 1$  LSB and  $\pm 4$  LSB has to be assumed for the ranges 1 to 3 and 4 respectively.

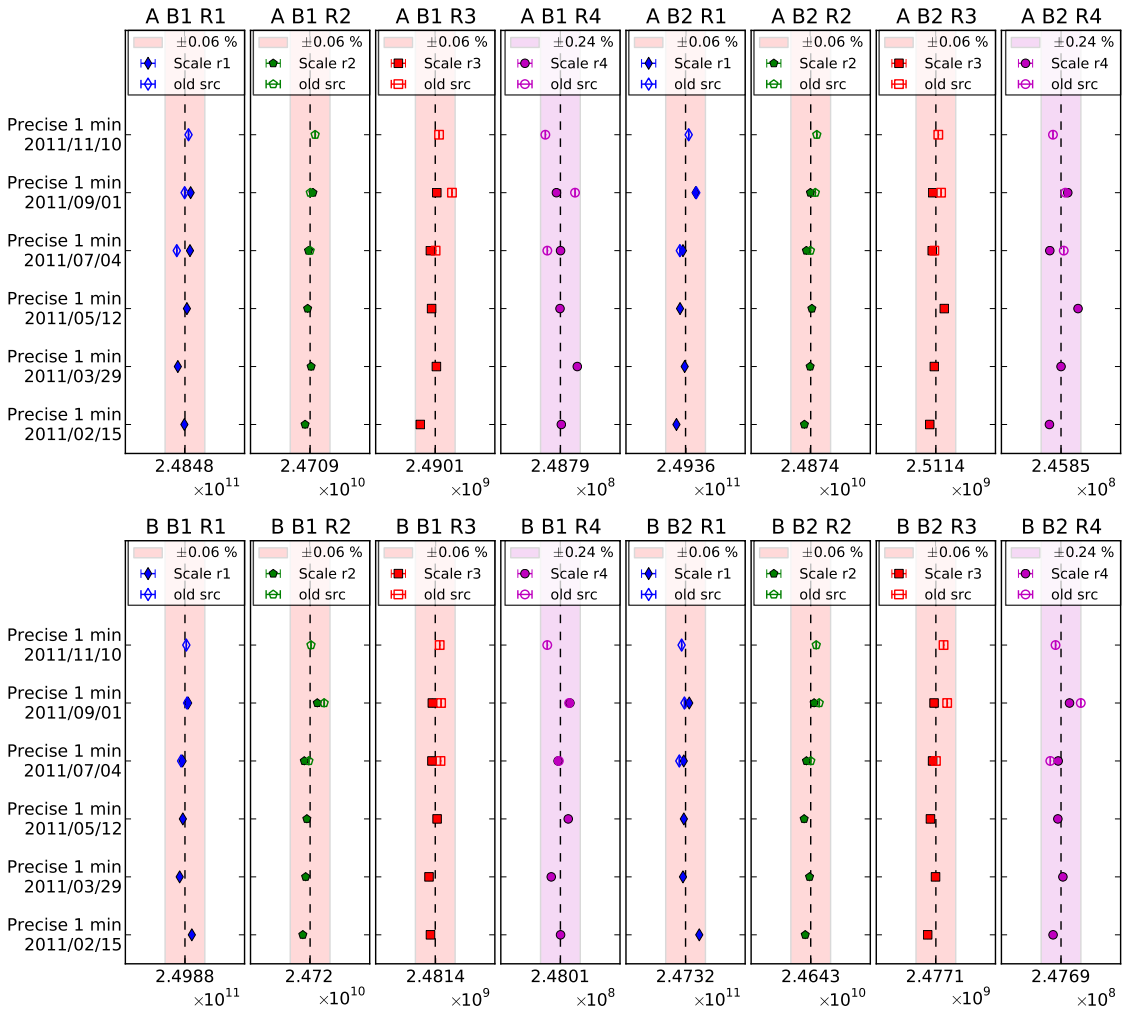


**Fig. G.30:** Precise calibrations preformed during the six technical stops in 2011 using the standard BI procedure. The top plot shows the scale factors for each range of system A, the bottom plot shows system B. The scale factor of a range is the value of charges for 1 LSB and is expressed in units of charges/ADC bin. The vertical dashed line is the average of all scale factors of the corresponding range. Most of the calibrations are done with the more recent source Yokogawa GS200 (see also Sec. G.5.1) and are indicated with plain markers. The last three measurements indicated with an empty marker are done with the old source Yokogawa 7651. The pink band shown in ranges 1 to 3 has a width of  $\pm 0.06\%$  (equivalent to  $\pm 1$  LSB), the magenta band shown in range 4 has a width of  $\pm 0.24\%$  (equivalent to  $\pm 4$  LSB)

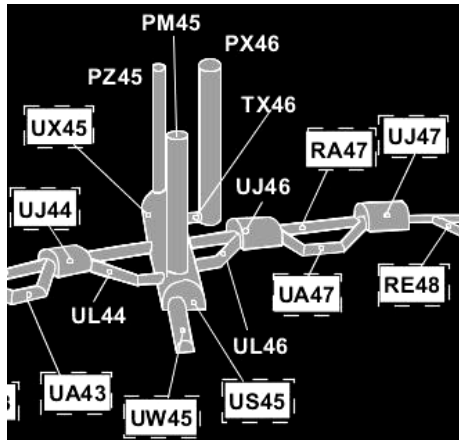


**Fig. G.31:** Synoptic of LHC point 4 shafts. The DCCT's are located in the section RA47.

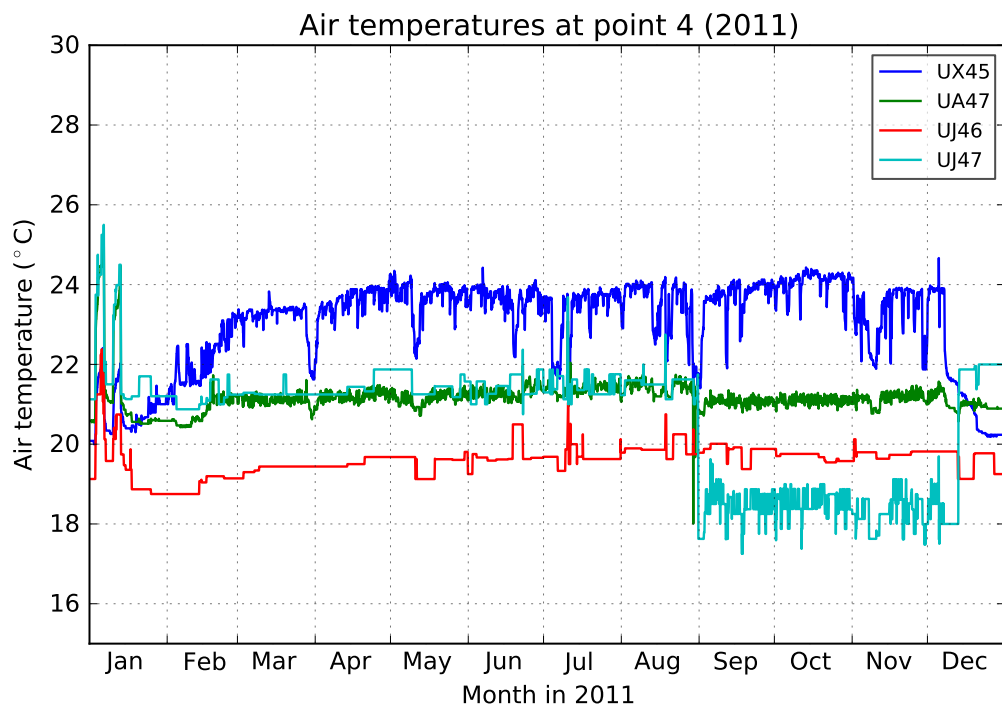


**Fig. G.32:** Air temperature around the straight section 4-5 at the LHC point 4 where the DCCT's are installed, see Fig. G.31. The values are taken at the ventilation inlet; the values for UX45 and UA47 are an average of 12 sensors. The temperature of UJ46 is probably the most representative of the values found in the tunnel section RA47 where the DCCT's are located.

## G.4 Sensitivity to beam conditions and other external factors

### G.4.1 Cross talk between rings

A possible cross-talk effect between the rings of beam 1 and beam 2 has been analyzed with special machine development (MD) fills. Five fills have been identified in 2010 where only one beam was circulating with a large intensity in the order of  $10^{13}$  protons, while the other ring was empty. The DCCT's of the empty ring were automatically set to range 4 and were therefore sensitive to a potential cross-talk effect when the other beam is dumped. The noise behavior of the empty ring before and after the dump time was analyzed. An example of a beam dump with only one beam is shown in Fig. G.33. The difference in noise levels recorded 60 s before and 60 s after the beam dump are shown in Fig. G.34 for the five fills. Detailed plots of the other fills are shown in Appendix G.8.4 (Fig. G.77).

In conclusion there is no evidence of a cross-talk effect between rings, the difference in noise before

and after the dump lies within  $\pm 0.5 \cdot 10^9$  charges for both system A and system B. Such spread is expected with a typical noise level of  $\pm 1 \cdot 10^9$  charges.

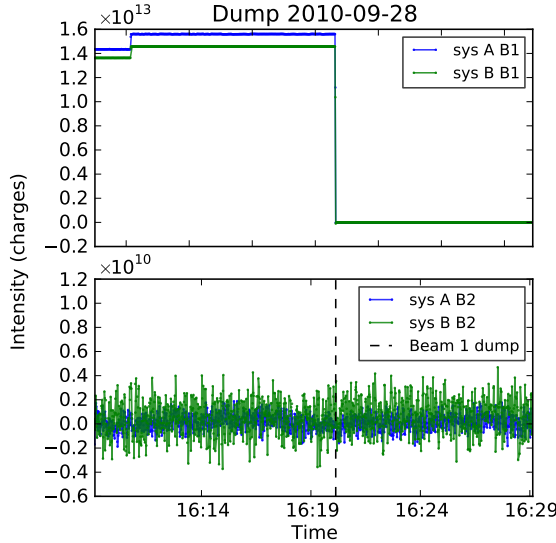


**Fig. G.33:** Crosstalk example. Beam 1 is circulating with  $\approx 1.5 \cdot 10^{13}$  protons (top plot) while beam 2 is empty (bottom plot). The noise level of beam 2 remains constant when beam 1 is dumped.

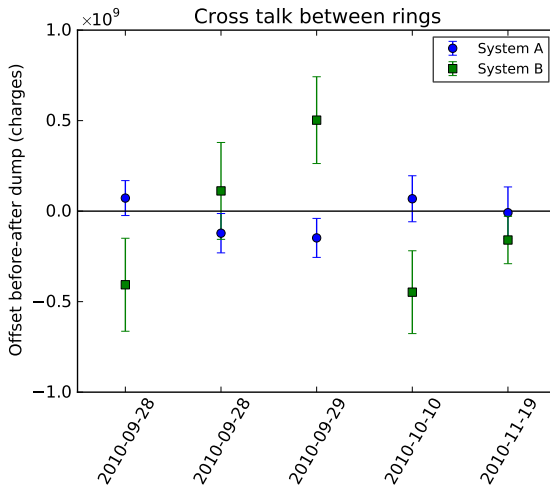


**Fig. G.34:** Crosstalk between both rings at dump time. For a given fill on the x axis, the data point shows the difference of the noise level  $|N_{\text{before}} - N_{\text{after}}|$  at the time of the dump. The indicated error is the standard deviation of the 60 points used for the average.

## G.4.2 Bunch pattern dependence

A misbehavior of the DCCT related to the filling pattern has been discovered in 2010. The problem was observed with bunch train fills with bunch spacings of 150 ns and 50 ns. The problem has been identified in the laboratory and corrected in the 2011 hardware [51]. The misbehavior was due to saturation effects in the front-end amplifiers. An example showing the effect of the bunch pattern dependence is provided in Fig. G.35. The left plot shows a fill for beam 1 in 2010 injected with bunch trains. The DCCT responses between systems A and B are inconsistent at each train injection and do not follow the FBCT signal. The right plot shows a bunch train injection in 2011 with the corrected hardware.

Three measurements have been performed to test the DCCT dependence on the bunch pattern. A laboratory measurement simulating high intensity bunch trains is given in Sec. G.4.2.1. A measurement with beam debunching is shown in Sec. G.4.2.2. Finally the sensitivity to an injected RF sine wave is presented in Sec. G.4.2.3.

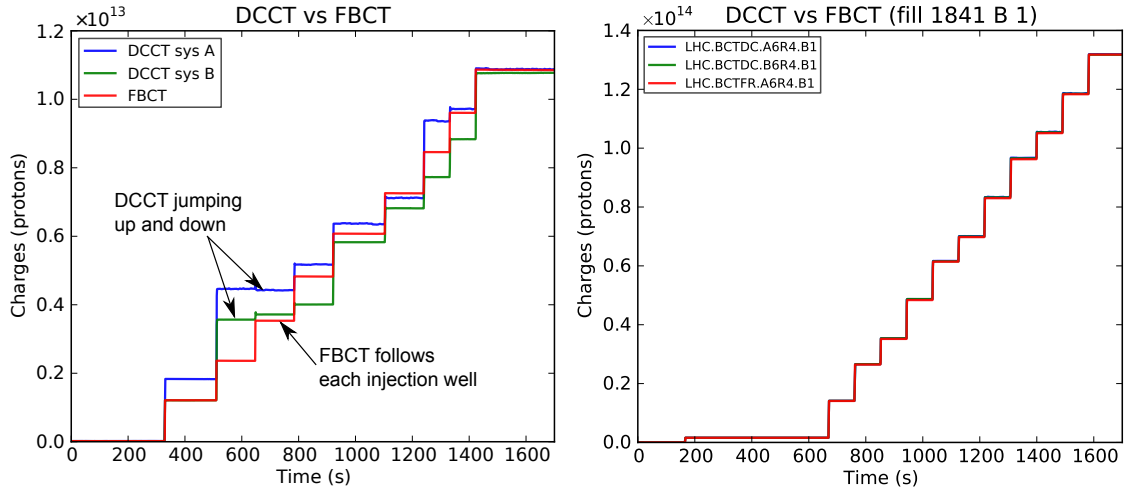


**Fig. G.35:** Example of difference between system A and B in 2010 (fill 1459, left) and 2011 (fill 1841, right). The DCCT misbehavior is clearly visible in 2010.

#### G.4.2.1 Laboratory measurements

The new front-end cards have been tested in the laboratory with a spare DCCT. The configuration in the laboratory was identical to that in the LHC tunnel including the beam pipe section and high-frequency (HF) bypass. However, the acquisition of the DCCT signal was different and used a portable 16 bit ADC. In 2010 the bunch trains used in the LHC filling scheme were composed of several close bunches with 150 ns or 50 ns spacing. One bunch occupied a 25 ns slot but had a width of 2.5 ns dictated by the LHC RF cavities (400 MHz). The generation of 2.5 ns or 25 ns high intensity pulses was not possible in the laboratory, only the shape of bunch trains could be simulated. However, the DCCT bunch pattern misbehavior was due to the presence of bunch trains combined with a high intensity. That is, the large mean intensity of a bunch train as a whole was the source of the problem, rather than the shape, the number of trains or the bunch structure within a train. The laboratory setup could therefore reproduce the faulty DCCT behavior and was a valid test for the new hardware.

The setup used to test the bunch pattern dependence is shown in Fig. G.36. A computer controlled scope generated a voltage pattern over time with a maximal amplitude of 1 V. The generated pattern, which represents one or more bunch trains simulating an LHC filling pattern, was repeated at a frequency of 11245 Hz. The different patterns tested are shown in Fig. G.37. The filling pattern signal from the pico scope was fed to a custom made “shaper” which amplified the signal up to 20 V. The amplified signal was carried through the DCCT via the beam pipe antenna and was terminated with a  $50\ \Omega$  - 200 W resistance. The repeated pattern created a net current flowing through the DCCT with the shape of the given pattern. The current intensity depends on the pattern shape and the amplification of the “shaper”. The voltage drop at the  $50\ \Omega$  resistance is a measure of the average current flowing through the DCCT; the signal was reduced with a 1/2 divider to stay within the acquisition range. The signals were acquired with a 16 bit ADC with a sampling rate of 1 s. A low-pass 1 Hz filter was used for each channel to smooth the signal before acquisition.

All measurements were averaged over 60 s. One measurement with zero current was used to correct the DCCT offset. The ratio between the injected current pattern ( $I_{pattern}$ ) and the DCCT response ( $I_{DCCT}$ ) must be constant for all tested patterns and intensities. A comparison of the DCCT response between the 2010 and 2011 hardware at low intensity is shown in Fig. G.38. The 2010 misbehavior is clearly visible (bottom plot), while the ratios taken with the new 2011 settings are constant within  $\pm 1\%$ . The accuracy of the measurement is limited by the low voltage drop at the  $50\ \Omega$  resistance and by the noise-induced fluctuations. The same measurement performed with the

maximal intensity is shown in Fig. G.39. The higher current intensity improved the measurement accuracy. The ratio  $I_{pattern}/I_{DCCT}$  is constant within a 0.1% band for all tested patterns. The DCCT range 2 is saturated for some measurements, the data points are therefore missing.

In conclusion the improved DCCT front-end electronics are stable for all tested patterns and the measurement accuracy is limited by the instrumentation and electronic components. While it is not feasible to test all possible patterns, this measurement confirms the correct DCCT behavior with bunch trains up to the tested intensities. Indeed the saturation effects on some amplifiers, responsible for the misbehavior, are visible as soon as a large mean intensity is grouped in a continuous train, regardless of its length, shape or number of bunches. High intensities worsen the misbehavior effect; this measurement simulates intensities of up to 1200 nominal bunches. Testing the bunch pattern ratio to simulate the higher intensities reachable with 25 ns trains will require a new dedicated experiment.

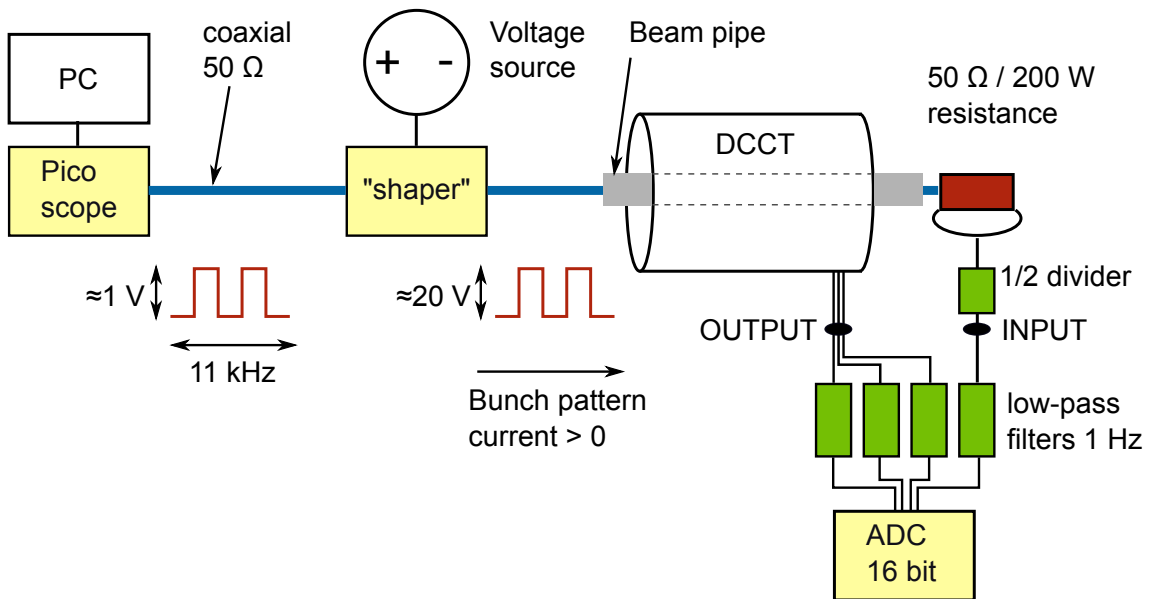


**Fig. G.36:** Setup in the laboratory to verify the bunch pattern dependence. A computer controlled scope generated a  $90\ \mu\text{s}$  filling pattern which was repeated at 11 kHz. The signal was amplified by a custom made “shaper” and fed through the DCCT. The resulting net current intensity was measured through the voltage drop of the  $50\ \Omega$  resistance terminating the circuit. The DCCT signals and the input current were acquired with a NI 16 bit ADC.

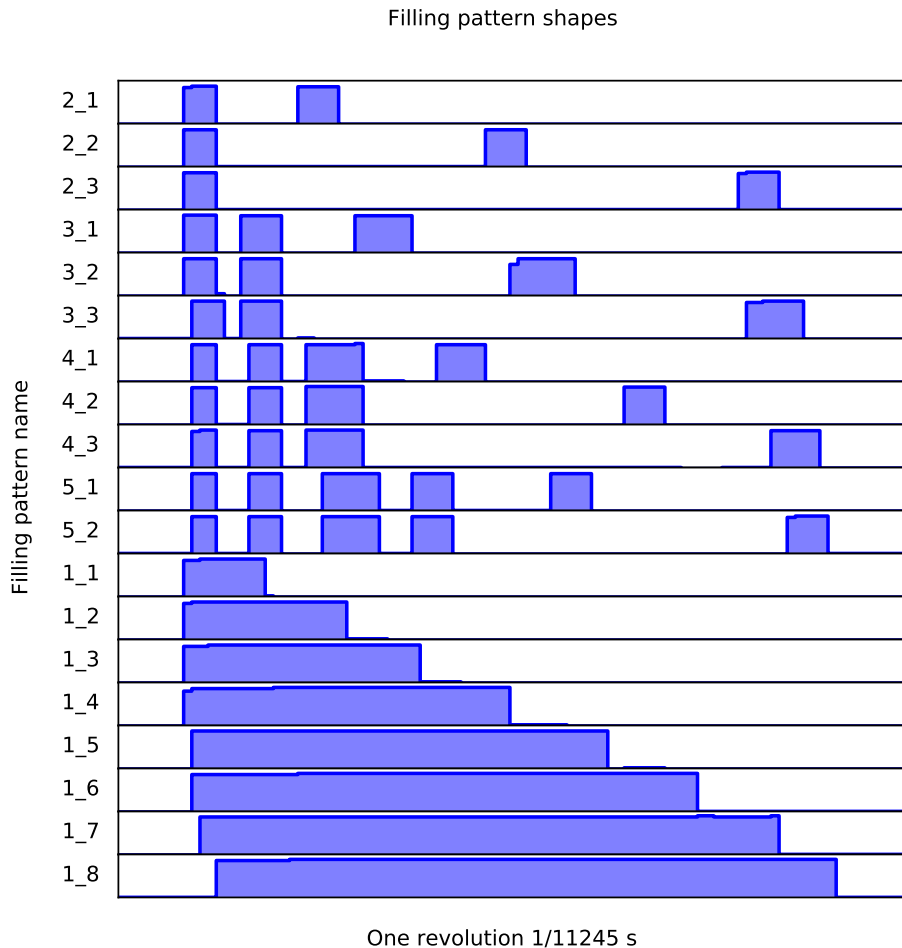


**Fig. G.37:** Bunch pattern used in laboratory tests of the DCCT. The shape was measured at the output of the Pico scope with an oscilloscope; each line represents a different pattern. The first number in the pattern name (y axis) is the total number of trains in the pattern, the second number enumerates the different positions or sizes of the trains. The x axis represents the time with a total length of one LHC revolution (90  $\mu$ s). The filled and empty regions are the time when the signal carries 1 V and 0 V, respectively. Within the hardware limitations, the shortest possible train is about 2.8  $\mu$ s (e.g. first train in 4)

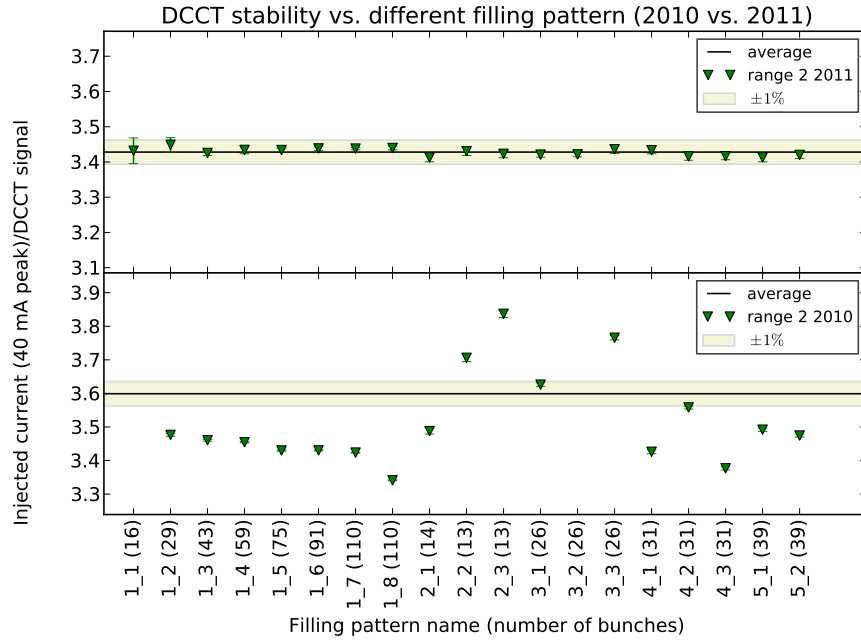


**Fig. G.38:** Comparison of the DCCT sensitivity to different bunch patterns at low beam intensity, in 2010 and 2011. The different filling pattern names are listed on the x axis with an estimation of the equivalent number of bunches with  $10^{11}$  protons indicated in parentheses. The y axis represents the ratio  $I_{pattern}/I_{DCCT}$ . For those measurements, the “shaper” amplified the signal to 2 V resulting in a peak current of 40 mA. The spread in the 2010 data points (bottom plot) is due to the bunch pattern dependence, the ratio for the 1\_1 pattern is off-scale. The indicated errors include only the noise fluctuations of the data within the 1 minute measurement.

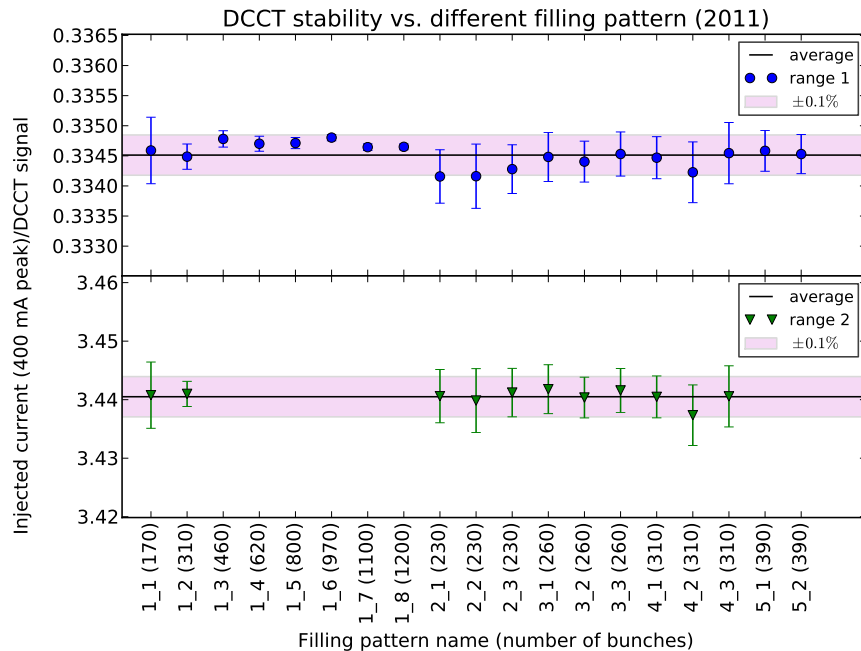


**Fig. G.39:** Bunch pattern dependence at high intensity. The “shaper” amplified the signal to 20 V resulting in a peak current of 400 mA. Some data points are missing on range 2 due to saturation, because the value is above the range maximum. The indicated errors include only the statistical fluctuation of the data within the 1 minute measurement.

#### G.4.2.2 Measurement with beam

The pattern-related misbehavior was only observed during fills with bunch trains and a large mean intensity. A bunch train generates different frequency harmonics compared to single bunches: the power spectrum is stronger at lower frequencies with a bunch train compared to a single bunch. High-frequency harmonics from single bunches are masked by the 80 kHz HF by-pass of the DCCT. In principle the DCCT is not affected by single bunch pattern.

A beam debunching measurement has been performed on 30 June 2011. Both beams were filled with five nominal bunches plus one pilot bunch before the RF was switched off. Without RF capture, the bunched protons quickly populated the whole beam circumference eventually forming an unbunched, continuous beam. The DCCT was therefore subjected to a continuously changing frequency pattern. Provided that the unbunched protons remain in the beam, the DCCT signal must be constant during the debunching process which takes less than 15 minutes. The results of the debunching measurement are shown in Fig. G.40. The debunching process is evidenced by the fall of the FBCT signal towards zero in the first 600 to 800 seconds after the RF was switched off. During this time the DCCT was stable within the noise level. On beam 2 an intensity decay is visible; however, the decay is starting before the RF was switched off and the FBCT signal is stable during this time. Therefore, the decay is probably due to a drift of the DCCT offset.

In conclusion the DCCT is not affected by the bunch length or the filling pattern; however, the low intensity of the beam limits the significance of the measurement.

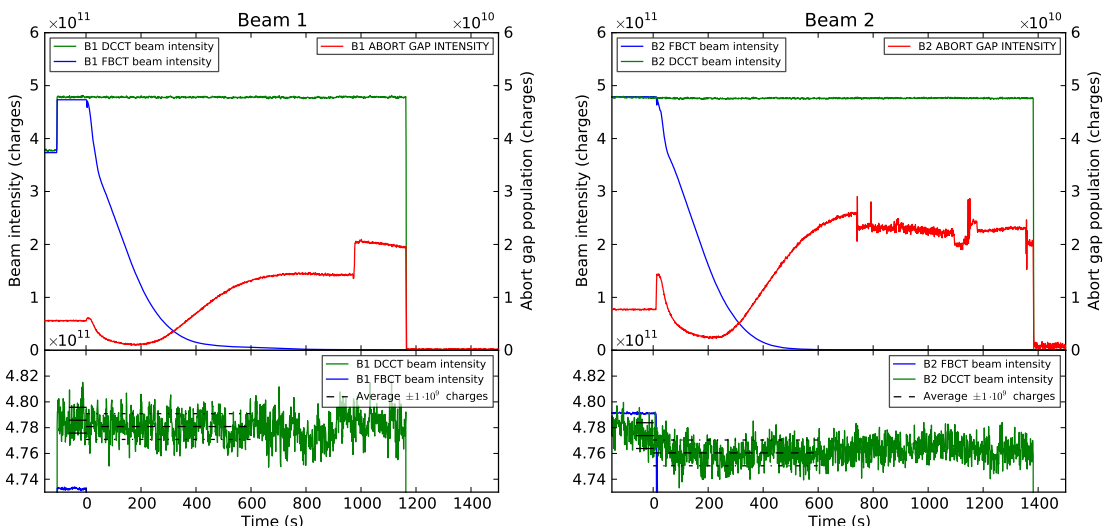


**Fig. G.40:** Stability of the DCCT during beam debunching for beam 1 (left) and beam 2 (right). The LHC RF was switched off at  $T=0$  at which point the FBCT signal dropped quickly. The beam was fully unbunched after about 12 minutes; at this time the FBCT signal reached zero and the abort gap population reached its maximum. The lower plot shows the DCCT intensity in a narrow intensity range. The average DCCT value taken 60s before and 600s after turning off the RF is indicated as an horizontal line. A boundary of  $\pm 10^9$  charges is shown as dashed lines. The stability of the DCCT during the debunching of the beam is compatible with the typical noise value of  $\pm 10^9$  charges.

#### G.4.2.3 Sensitivity to an injected RF sine wave

The DCCT is exposed to various frequency spectra depending on the number of circulating bunches and the filling pattern. A circulating bunch will create harmonics in the frequency domain; the amplitude of the harmonics are related to the beam intensity. The frequencies and number of

harmonics depend on the number of circulating bunches and their arrangement in trains. While it is not possible to reproduce in the laboratory the same spectrum and power generated by a 200 MJ beam, a single harmonic can be shown as an RF wave with high amplitude. In this measurement the DCCT was exposed to an RF sine wave which was swept over a wide frequency range to test if the DCCT is sensitive to a specific harmonic.

The Gaussian pulse created by a circulating bunch of  $N$  protons with a width  $\sigma_z$  at a revolution frequency  $\nu_{rev}$  is described in the time domain as

$$I(t) = Q \cdot \sum_{n=-\infty}^{\infty} \frac{1}{\sqrt{2\pi}\sigma_t} e^{-\frac{(t-nT)^2}{2\sigma_t^2}} \quad (G.2)$$

with

$$T = \frac{1}{\nu_{rev}}; \quad Q = N \cdot e; \quad \sigma_t = \frac{\sigma_z}{c}. \quad (G.3)$$

The Fourier transform of the pulse takes the form of a Dirac comb

$$I(\nu) = Q \cdot \nu_{rev} \cdot e^{-\nu^2 \cdot \sigma_t^2 \cdot 2\pi^2} \sum_{k=-\infty}^{\infty} \delta(\nu - k\nu_{rev}); \quad k = 0, \pm 1, \pm 2, \dots \quad (G.4)$$

The harmonics form a Dirac comb  $\sum_{k=-\infty}^{\infty} \delta(\nu - k\nu_{rev})$  with a Gaussian envelope  $e^{-\nu^2 \cdot \sigma_t^2 \cdot 2\pi^2}$  and the DC component  $Q \cdot \nu_{rev}$  as amplitude. An example of a bunch pulse and the resulting harmonics is shown in Fig. G.41. The pulse width of 2.25  $\mu$ s is arbitrarily large to demonstrate the effect of the Gaussian envelope which reduces the high frequency harmonics. A wide pulse has a stronger spectrum power at lower frequencies while a narrow pulse of 2 ns has a flat power spectrum with for example 97% intensity at 200 kHz. Therefore a nominal bunch creates a similar harmonic spectrum to an RF wave considering that the 80 kHz HF by-pass of the DCCT cuts the high-frequencies.

An RF wave with a frequency  $\nu_0$  can be described as

$$I_{RF}(t) = I_{peak} \cdot \cos(2\pi\nu_0 t). \quad (G.5)$$

The Fourier transform of the RF is

$$I_{RF}(\nu) = I_{peak} \cdot \frac{1}{2} (\delta(\nu - \nu_0) + \delta(\nu + \nu_0)). \quad (G.6)$$

The power of a single bunch pulse can be compared to an RF wave with (G.4) and (G.6):

$$Q \cdot \nu_{rev} \approx \frac{1}{2} I_{peak} \quad (G.7)$$

with the peak intensity of an RF wave defined as

$$I_{peak} = \sqrt{2} \cdot I_{RMS} = \sqrt{\frac{2P}{R}}. \quad (G.8)$$

The DCCT has been tested against the effect of radio frequencies (RF) using the setup depicted in Fig. G.42. An RF wave generated by a network analyzer was fed through the DCCT with a coaxial antenna. The net current produced by the RF, which is expected to be zero, was measured in parallel by the DCCT and with the  $50 \Omega$  resistance. The network analyzer scanned a given frequency range during 4000 seconds in a continuous logarithmic sweep, i.e. more time was spent at low frequencies. The ADC acquisition was sampled at 1 Hz and the data was offset corrected with a linear function taking a 5 minutes offset before and after the sweep using the same method as

described in Sec. G.3.1. The baseline correction of about 40 mV ( $\approx 2 \cdot 10^{10}$  charges) was substantial but not unexpected in the laboratory DCCT. Furthermore the large ambient temperature variation in the laboratory during the summer days influenced the offset during the measurement. The DCCT offset has an estimated temperature dependence of  $\approx 5 \mu\text{A}/^\circ\text{C}$  ( $\approx 2.5 \cdot 10^9$  charges/ $^\circ\text{C}$ ) [78]. The laboratory DCCT is uncalibrated, therefore, the DCCT signal conversion into charges was approximated with the theoretical scale of 1 V  $\approx 10^{11}$  charges.

The DCCT response signal during the frequency scan from 1 kHz to 250 kHz is shown in Fig. G.43. In this frequency range the RF signal was taken directly from the network analyzer without amplifier. The DCCT is unaffected by the RF and only the typical random noise pattern of range 4 is visible. Using equations (G.7) and (G.8), the equivalent bunch charge for this RF power is about

$$N_{30mW} \approx \frac{35 \cdot 10^{-3}}{2} \cdot \frac{1}{10^4} \cdot \frac{1}{1.6 \cdot 10^{-19}} \approx 10^{12} \text{ protons.} \quad (\text{G.9})$$

The measurement from 250 kHz to 110 MHz was performed with an additional amplifier resulting in an RF power of about 10 W. The scan was performed once without DC current as in Fig. G.43 and once with a 80 mA DC current passing through the DCCT. The results of both scans are shown in Fig. G.44. Without DC current (top plot) the DCCT 10 seconds average stays mostly above the expected zero line at a value of about  $10^9$  charges. Such deviation is however compatible with range 4 with a typical noise level of  $\pm 10^9$  charges. The bottom plot in Fig. G.44 shows the same measurement with the addition of an 80 mA DC current flowing through the DCCT. The acquisition was performed with range 2. The signal has less noise and remains within a  $\pm 0.1\%$  band around the expected value. Here with (G.7) and (G.8), the equivalent bunch charge for this 10 W RF power is about

$$N_{10W} \approx \frac{0.6}{2} \cdot \frac{1}{10^4} \cdot \frac{1}{1.6 \cdot 10^{-19}} \approx 1.6 \cdot 10^{14} \text{ protons.} \quad (\text{G.10})$$

In conclusion, the DCCT proved to be unaffected by all tested RF frequencies from 1 kHz to 110 MHz and no resonance has been found. In all measurements the DCCT signal is compatible with the noise of the selected range.

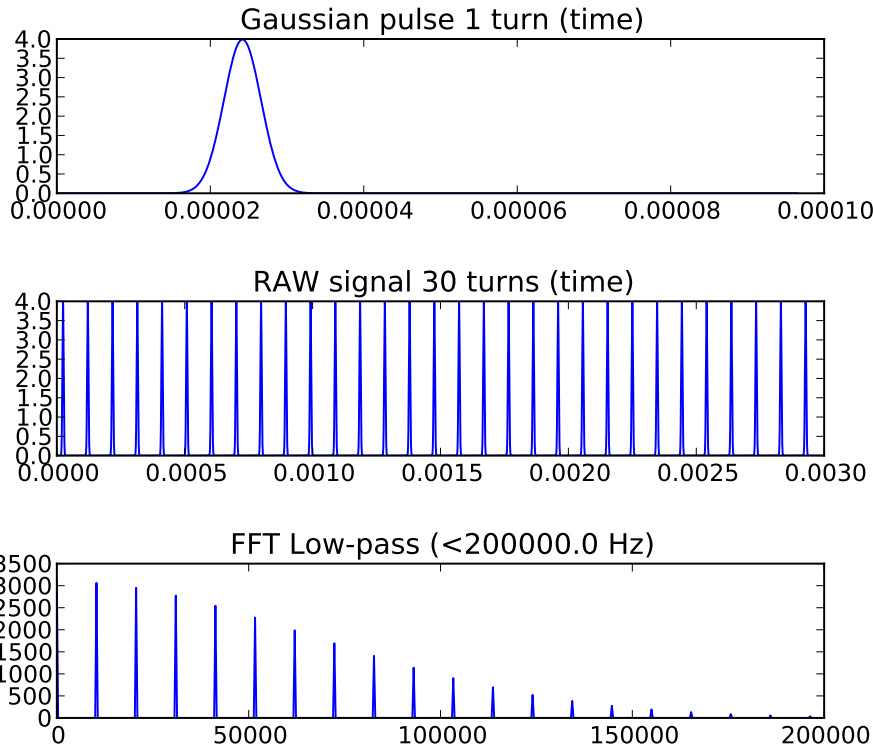


**Fig. G.41:** Fourier transform example with a wide Gaussian pulse. The first plot (top) shows a  $2.25 \mu\text{s}$  wide pulse in the time domain. The full width of the x axis represents  $100 \mu\text{s}$ , approximately one LHC revolution. The second plot shows the resulting signal of the pulse during 30 revolutions also in the time domain. The Fourier transform of this signal is shown in the bottom plot, the x axis represents the frequency. The harmonics are places at  $10 \text{ kHz}$  intervals. The effect of the Gaussian envelope is clearly visible for a wide pulse and the power is close to zero at  $200 \text{ kHz}$ .

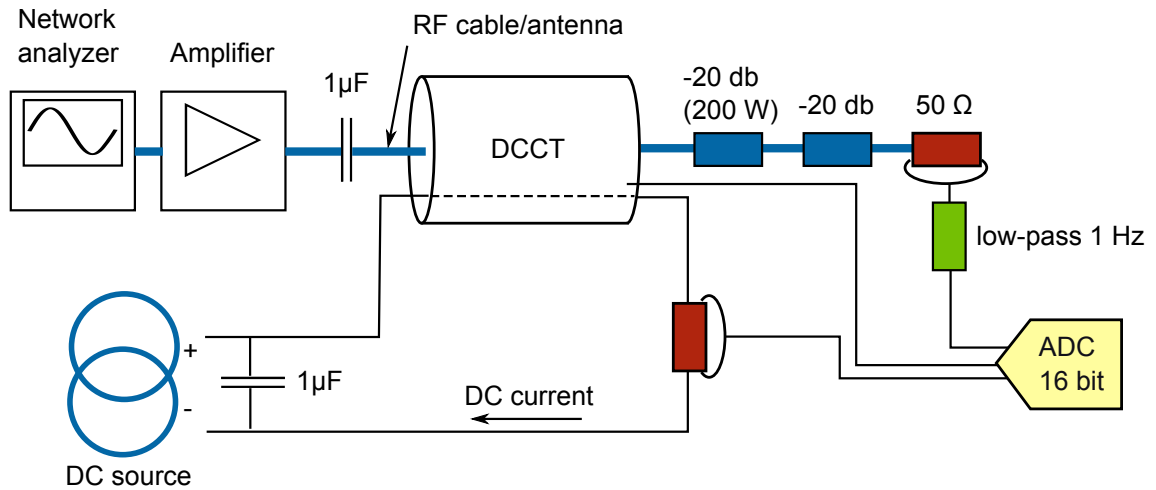


**Fig. G.42:** Sensitivity to RF setup. A network analyzer and an amplifier send an RF wave through the DCCT. The wave was guided through a coaxial cable and then through the beam pipe antenna and finally two  $-20 \text{ db}$  RF attenuators. The cable was terminated with a  $50 \Omega$  resistance; furthermore, a  $1 \mu\text{F}$  capacitance was placed after the amplifier to avoid any direct current flowing through the RF cable, for example due to a ground differential. The voltages at the resistances and from the DCCT were acquired with a 16 bit ADC. Additionally, for one measurement, a DC current was fed through the DCCT in parallel to the RF. The voltage drop in a  $14.7 \Omega$  resistance ( $3 \text{ W}; \pm 5\%$ ) was used to verify the DC current.

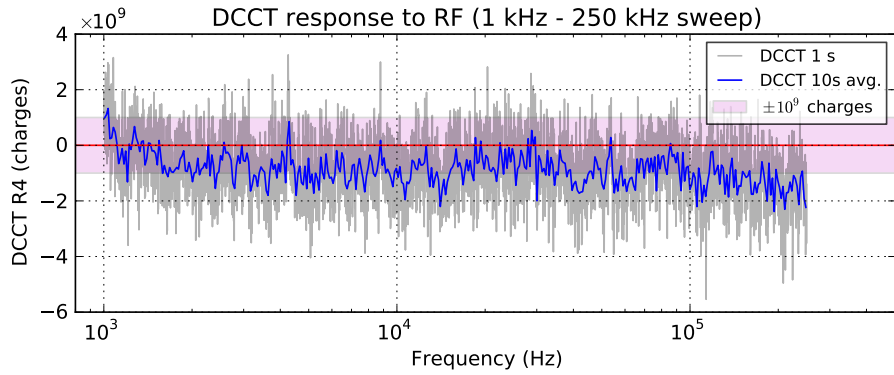


**Fig. G.43:** DCCT response to RF between 1 kHz and 250 kHz. The range was scanned in 4000 seconds in a logarithmic sweep. The average RF power was about 30 mW by using the network analyzer directly at its maximal output (signal unamplified).

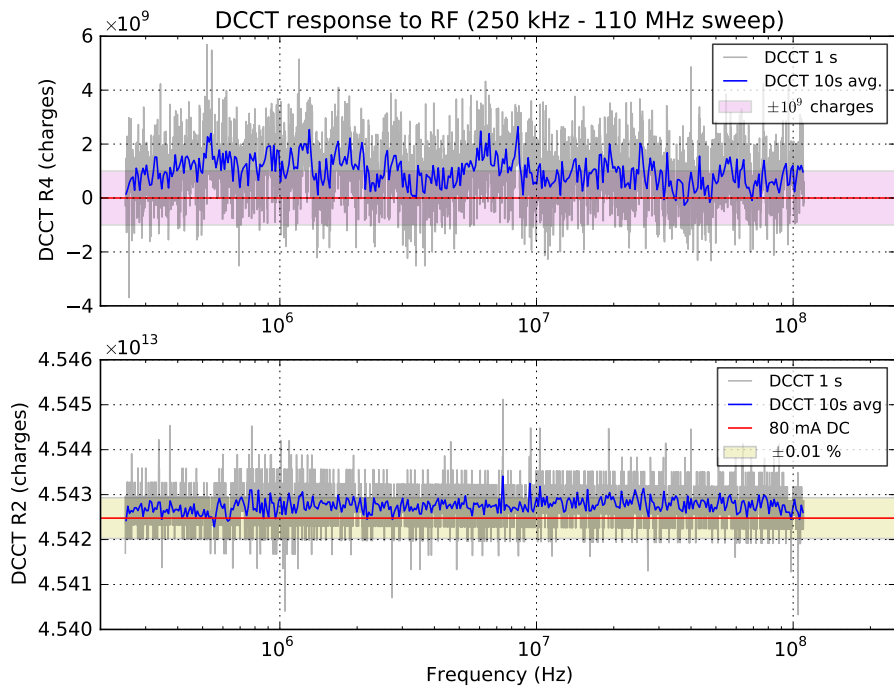


**Fig. G.44:** DCCT response to RF between 250 kHz and 110 MHz. The range was scanned in 4000 seconds in a logarithmic sweep. The RF was amplified with an RF amplifier ENI (Electronic Navigation Industries) 310L with a range of 250 kHz - 110 MHz resulting in an average RF power of about 10 W. The top plot shows the DCCT range 4 during the sweep, without an additional DC current. The bottom plot shows the DCCT range 2 during the sweep with an additional current of 80 mA passing through the DCCT.

### G.4.3 Bunch position dependence

The fast BCT's have a known sensitivity to the bunch position. The sensitivity of the DCCT with respect to the bunch position has been tested by moving each beams in the vertical and horizontal planes during a machine development (MD) fill<sup>4</sup>. The DCCT signal and beam position over time are shown in Fig. G.45 for beam 1 and Fig. G.46 for beam 2. No correlation with the beam position can be seen in the beam decay.

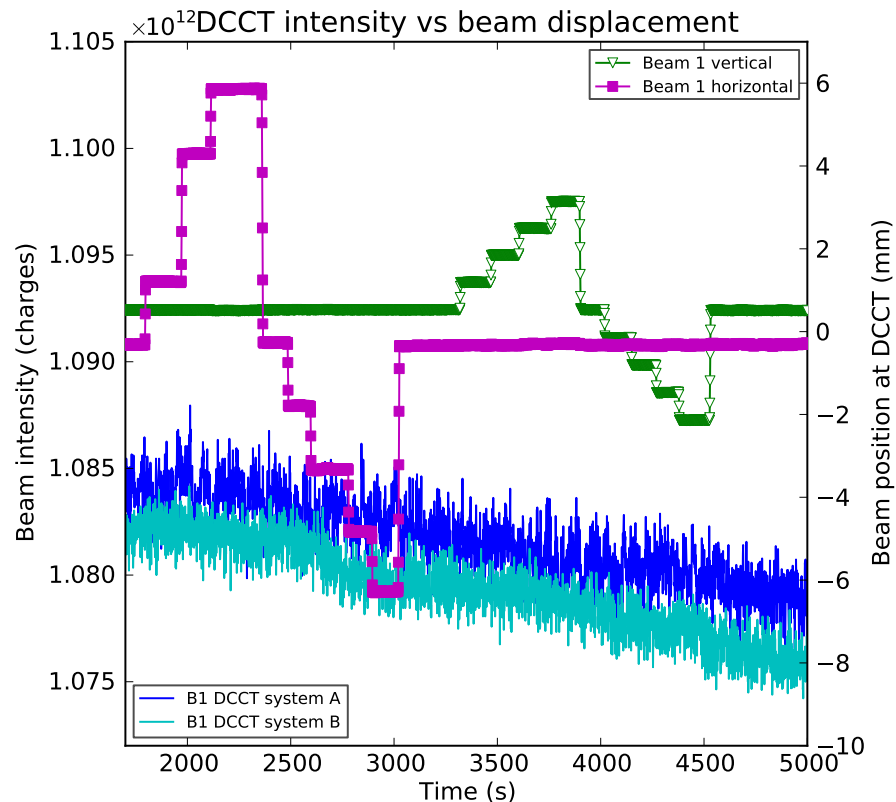


**Fig. G.45:** Bunch position dependence beam 1.

<sup>4</sup>Fill 1910 on 30 June 2011.

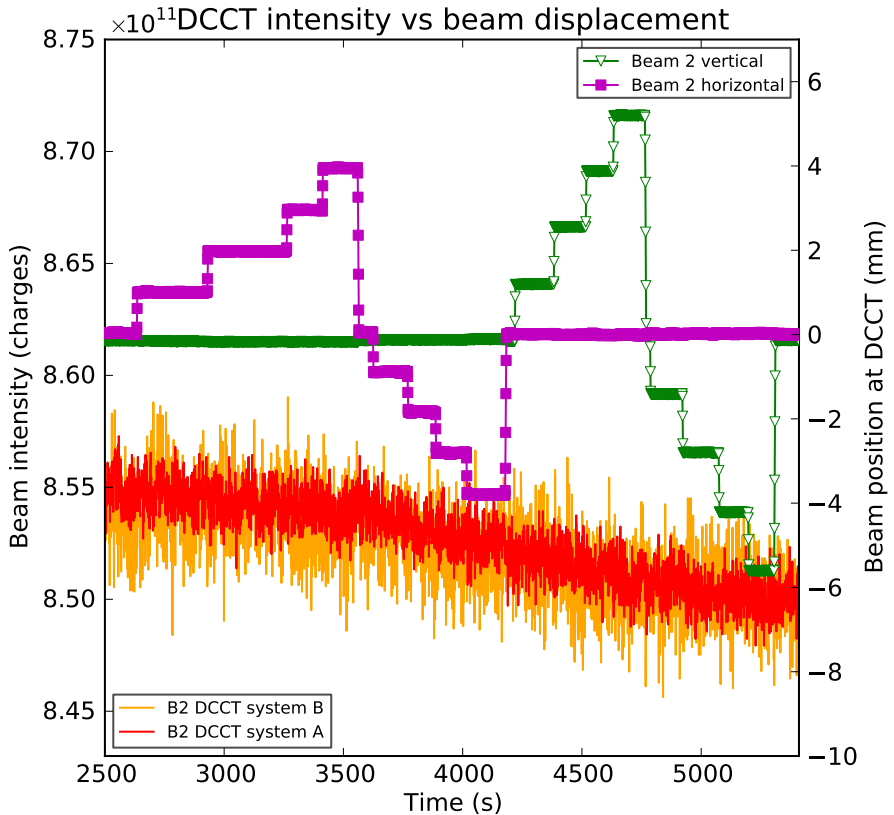


**Fig. G.46:** Bunch position dependence beam 2.

#### G.4.4 Interference from Accelerator Systems

##### G.4.4.1 Interference from magnetic field

A possible interference between the LHC magnetic fields present at high energy and the DCCT response has been analyzed for all physics fill in 2011. The DCCT's are placed in straight section 45 and the nearest magnet is located xx meters away (TODO: find numbers). During the energy ramp down, after a fill has been dumped, the DCCT is at its most sensitive range and the signal is expected to be zero or compatible with the typical offset of  $\pm 5 \cdot 10^9$  charges. For this verification, the correlation between the DCCT signal and the LHC energy has been analyzed for all physics fills in 2011. The DCCT signal and LHC energy are averaged over 60 seconds time bins during the ramp down period from 3500 GeV to 450 GeV followind the beam dump. The correlation between the LHC energy and the DCCT signal without beam is shown in Fig. G.47 for the four DCCT's. This analysis is biased by the fact that the energy is always ramped down from high to low energies, and the high energy data is therefore always taken shortly after the dump, while the low energy data is always taken 15 to 20 minutes later. A possible correlation with the time or an other time changing parameter can not be disentangled from the LHC energy with this method. However, the offset during the energy ramp down stays within  $\pm 5 \cdot 10^9$  charges for all DCCT's and is compatible with the typical offset drift as seen in Sec. G.3.2.

For system A/beam 1 the offset is systematically larger at 3.5 TeV compared to lower energies, while for system B/beam 1 the offset is often smaller at higher energies. This effect can be observed in some fills where, immediately after the beam dump, a downward drift for system A/beam 1 and a similar upward drift for system B/beam 1 can be observed. The full drift amplitude is typically of the order of  $2 - 5 \cdot 10^9$  charges over 10 minutes after which the signal is flattening out. This drift is not always present and is also observed when the LHC energy remains constant before the start of the ramp down, it is therefore not correlated with the LHC energy.

In conclusion, no correlation with the LHC energy is observed and the baseline is always within the  $\pm 5 \cdot 10^9$  charges as observed in Sec. G.3.2. A drift during the first 15 minutes following the beam dump is sometime observed in beam 1; the drift is downward for system A and upward for system B. The drift amplitude is smaller than  $5 \cdot 10^9$  charges and is not correlated with the LHC energy.

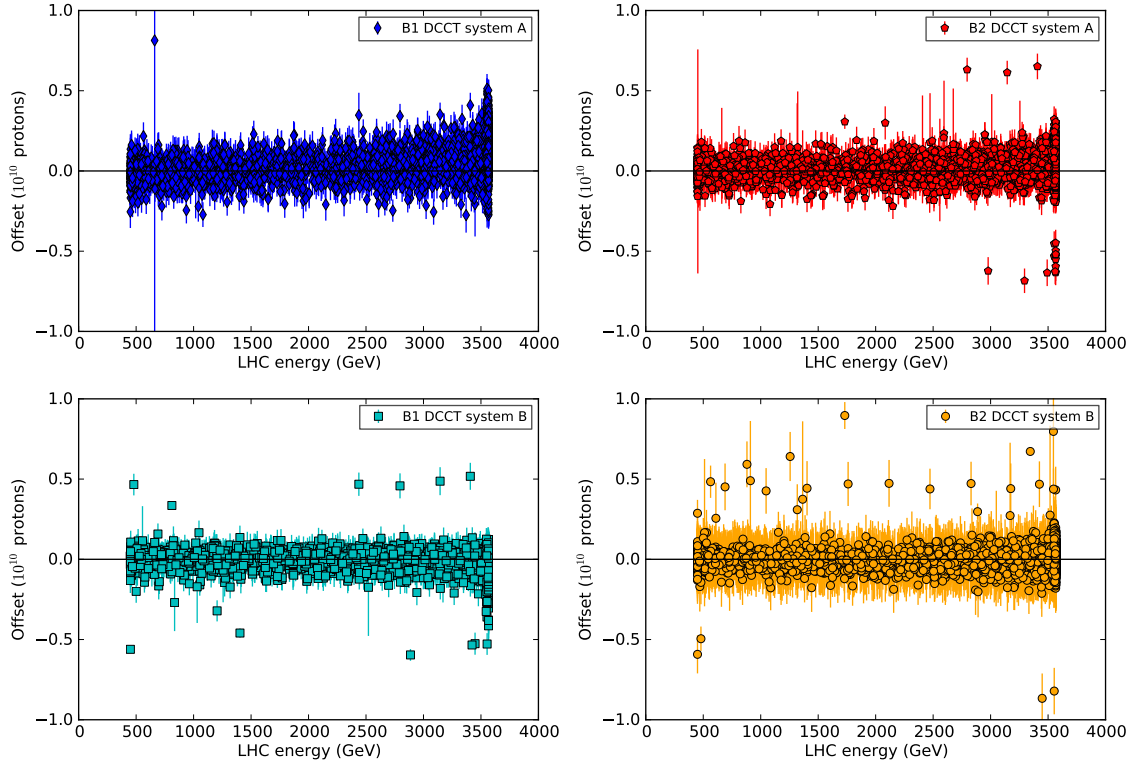


**Fig. G.47:** Offset versus LHC energy during ramp down for all physics fills in 2011. Each point is a DCCT average of 60 seconds placed at the average LHC energy for this time. The indicated error is the standard deviation of the 60 values.

#### G.4.4.2 Interference from RF

The LHC RF system is located on each side of the interaction point 4 (IP4), about 200 m away from the DCCT's. The accelerating cavities are composed of 8 single-cell cavities per ring operated at a constant frequency of 400 MHz. During a fill setup, and before the first beam injection, the field from each cavity is ramped up from 0.02 MV/m (RF<sub>off</sub>) to about 0.75 MV/m (RF<sub>on</sub>).

The following analysis evaluates a possible interference between the RF field variation and the DCCT signal by evaluating the DCCT offset over 120 seconds before and after the RF field is switched on. An example showing the RF cavity transition is provided in Fig. G.48. In the absence of interference from the RF system, the offset should remain constant regardless of the RF cavity field and the difference Offset(RF<sub>on</sub>) - Offset(RF<sub>off</sub>) must be zero within the noise level of range 4. The RF is not always switched off between fills, furthermore the automatic offset correction, which is part of the LHC setup sequence, can occur within the averaging time window, therefore not all fills can be used to verify the offset change. From all physics fills in 2011, 86 fills had a clear RF transition and could be used for this analysis. The offset difference observed between the time periods RF<sub>on</sub> and RF<sub>off</sub> is shown in the histograms in Fig. G.49 for beam 1 (left) and beam 2 (right), combining both systems A and B. The offset difference amounts to  $0.5 \cdot 10^8$  and  $-0.1 \cdot 10^8$  charges for beam 1 and 2 respectively.

In conclusion the DCCT's are unaffected by the cavity field of the RF accelerating system located at IP4, the DCCT offset in its most sensitive range is not sensitive to the LHC RF.

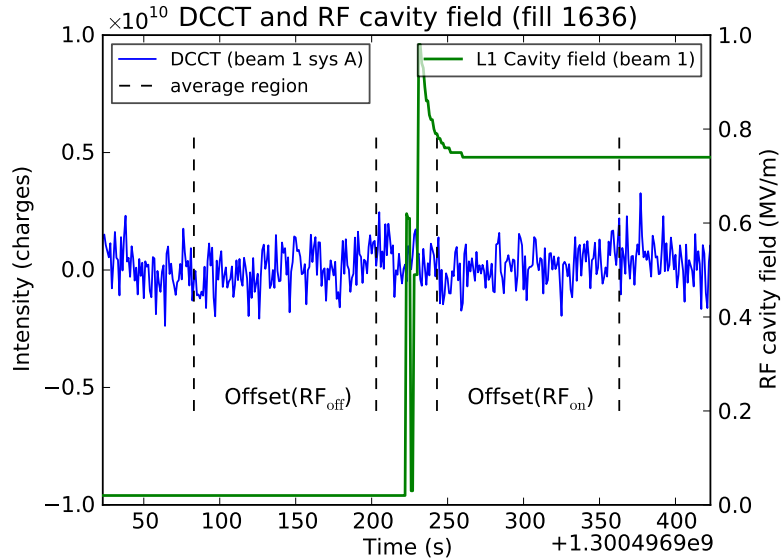


**Fig. G.48:** Example plot showing one DCCT (beam 1 system A) offset evolution when the RF cavity field is switched on. For better clarity, only 1 out of the 16 cavities is shown. The left y axis shows the beam intensity measured by the DCCT, the right y axis indicates the RF cavity field. The vertical dashed lines indicate the bounds used to average the DCCT offset before and after the RF field ramp.

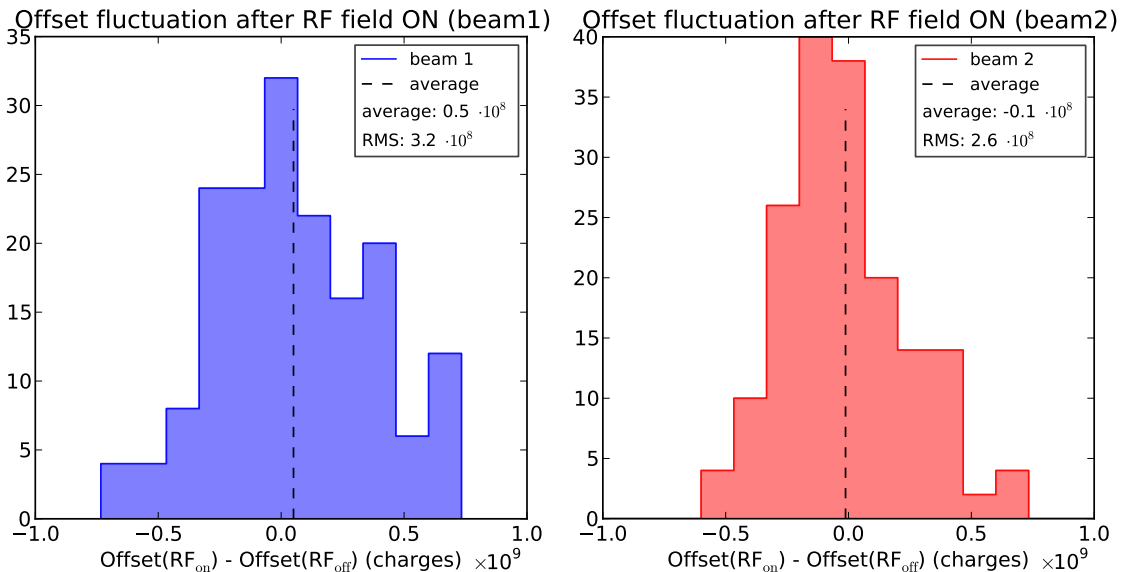


**Fig. G.49:** Offset versus LHC RF field. The offset is measured for 120 s before and after the RF field has been switched on. The offset difference  $\text{Offset}(\text{RF}_{\text{on}}) - \text{Offset}(\text{RF}_{\text{off}})$  is evaluated at each ramp up of the cavities in the pre-injection setup.

## G.5 Calibration Method

The stability of the scaling factor during the year seen in Sec. G.3.6 shows that the reproducibility of the calibration method combined with the stability of the scaling factor are limited by the resolution of the ADC only. The following sources of uncertainty related to the calibration itself are discussed below:

- The precision of the current source used for the calibration
- The position of the calibration rods
- The methodology of the standard BI calibration procedure

- Current leak between the surface and the tunnel

### G.5.1 Current source accuracy

The absolute scale for each transformer is calibrated with a precise DC current source. Two sources are available: the model Yokogawa 7651 was used for the 2010 calibrations and the model Yokogawa GS200 was used for the 2011 calibrations. The sources manufacturers quote a 90-day accuracy of 0.02%. Both sources have been tested with common laboratory multimeters or voltmeters. While the results are compatible with the expected uncertainties, those methods were not able to reach a precision of the order of a permille. The most precise measurement was reached by measuring the voltage drop across a known precise resistance. The measurement was performed with a soldered 4-wire (Kelvin) setup (Fig. G.50) to eliminate both wiring and contact resistances. This precise measurement could not reach the claimed accuracy of the sources; however, it can be used as systematic uncertainty for the calibration of the DCCT's. The following components were used:

- A  $100 \Omega$  precise foil resistance with a tolerance of  $\pm 0.01\%$ ,  $\pm 5 \text{ ppm}/^\circ\text{C}$  and power rating of 0.6 W. RS catalog number 201-9848.
- A Voltmeter Solartron / Schlumberger 7060 multimeter with a quoted accuracy of 0.002%. The lowest measurements of 0.1 mA and 0.18 mA were limited by the last digit of the voltmeter.

The measured currents for both sources are shown in Fig. G.51. For reference, the calibration currents used for the ranges 4 to 1 are: 0.18, 1.8, 18 and 120 mA, respectively. The 100 mA measurement dissipated 1 W of heat which is above the maximal power of the resistance quoted at 0.6 W. Therefore, the measurement was performed quickly as to avoid a temperature drift or damage to the resistance. The last digit of the voltmeter, equivalent to  $10 \mu\text{V}$ , limited the accuracy of the lowest measurement of 0.1 mA to  $\pm 0.1\%$ . At 0.18 mA, which is the current used to calibrate range 4, the uncertainty is still dominated by the last digit and amounts to 0.06 %.

In conclusion, the current used for the calibration of range 4 is verified with an accuracy of 0.06% which is dominated by the last digit of the instrument, the higher currents agree within an error of  $\pm 0.05\%$ . Therefore, an envelope error of  $\pm 0.05\%$  has to be taken for the total beam intensity. Because the same source is used for all DCCT's, the error is correlated between both beams. Furthermore, there is no precision advantage of using one source over the other.

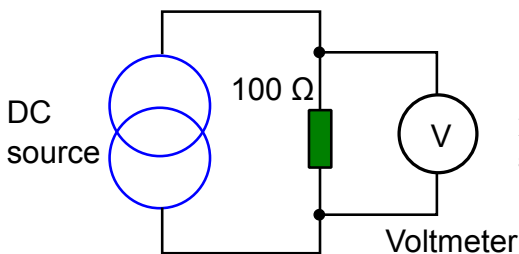
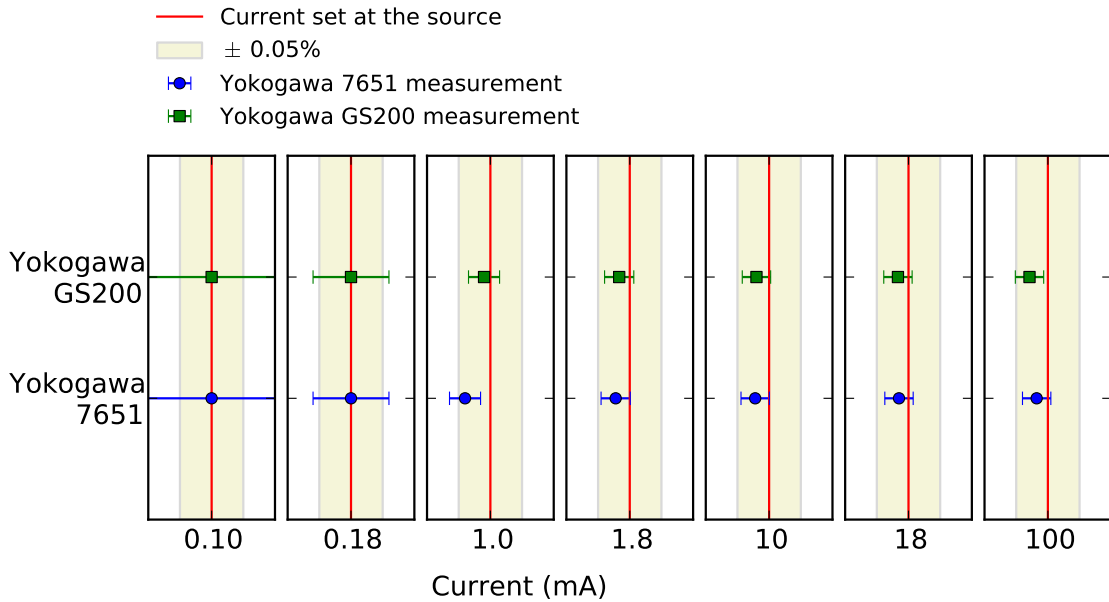


Fig. G.50: 4-wire (Kelvin) setup to measure the DC source accuracy. The resistance and wires are soldered.



**Fig. G.51:** Accuracy verification of the precise DC sources. The vertical lines indicate the current set at source; the measured current is indicated by a square for the GS200 source (top) and by a circle (bottom) for the 7651 source. The error bars include the resistance uncertainty of  $\pm 0.01\%$  plus a maximal temperature variation of  $40^\circ\text{C}$  and the voltmeter uncertainty of 20 ppm and last digit resolution. The vertical band shows an envelope of  $\pm 0.05\%$ . The uncertainty of the two smallest values (0.1 and 0.18 mA) are dominated by the last digit of the voltmeter.

### G.5.2 Position of the calibration rods

The calibration current is injected through 4 rods placed symmetrically around the internal opening of the DCCT for the beam pipe. The wiring configuration is such that the DCCT sees four times the current which is injected with the current source. Measurements in the laboratory confirmed that the position of the cable carrying the DC current has no influence on the DCCT response. The DCCT signal was identical regardless of the cable position inside the DCCT opening and the signal was exactly multiplied by four when injected through the calibration rods.

In conclusion, for a DC current, the DCCT is not sensitive to the cable position and no error is introduced by the fact that the calibration current is not injected at the center of the DCCT.

### G.5.3 Methodology and current leak

The standard precise calibration procedure which is regularly carried out during technical stops is performed in the following way. The current source is connected to the back-end electronic rack on the surface. The DCCT control software first acquires the offset for all ranges of the given DCCT while the source is set to zero current. For each range the calibration current (shown in Table G.7) is injected in the DCCT while the digital signal is acquired for 60 seconds. The scaling factor is the offset corrected average signal over 60 seconds divided by the equivalent charges specified by the operator.

To validate the standard procedure, a series of independent “self” calibrations has been performed using the measurements in the tunnel; in addition, one “self” calibration was carried with the source on the surface. For those independent calibrations, the source was controlled by a computer and the raw DCCT data was saved offline for analysis (as in Sec. G.3.4). The offset was subtracted using a period before and after the signal as described in Sec. G.3.1. The LSB value (i.e. the scaling factor)

**Table G.7:** Calibration currents used to measure the scaling factor of each range. The ranges 2 to 4 are calibrated at 80% of their range while range 1 is calibrated at 50% of its range due to the limited maximal current of the source.

Range	Injected current (mA)	Equivalent charges	Approximate LSB value (charges/bin)
4	0.18017	$4 \cdot 10^{11}$	$2.5 \cdot 10^8$
3	1.8017	$4 \cdot 10^{12}$	$2.5 \cdot 10^9$
2	18.017	$4 \cdot 10^{13}$	$2.5 \cdot 10^{10}$
1	112.61	$2.5 \cdot 10^{14}$	$2.5 \cdot 10^{11}$

is given by the ratio (Injected charges)/(measured ADC signal). The measurements dedicated to the linearity and 12 hour long term measurements were also used to calculate the scaling factor using the longer averaging time provided by the sequence. The results of the so called “self” calibrations compared to the standard calibrations performed in 2011 is shown in Fig. G.52 for the DCCT system A beam 1. The other DCCT’s are shown in the appendix Fig. G.78, G.79 and G.80.

In conclusion the scaling factors measured with both methods agree within an envelope of  $\pm 1$  LSB (equivalent to  $\pm 0.06\%$  at 80% of the range) for the ranges 1 to 3 and within  $\pm 4$  LSB ( $\pm 0.24\%$ ) for range 4. No difference can be seen between the two methods. Furthermore there is no difference between the calibrations performed with the source in the tunnel or on the surface excluding a possible current leak in the 500 meter cables and switches between the surface and the calibration rods in the tunnel.

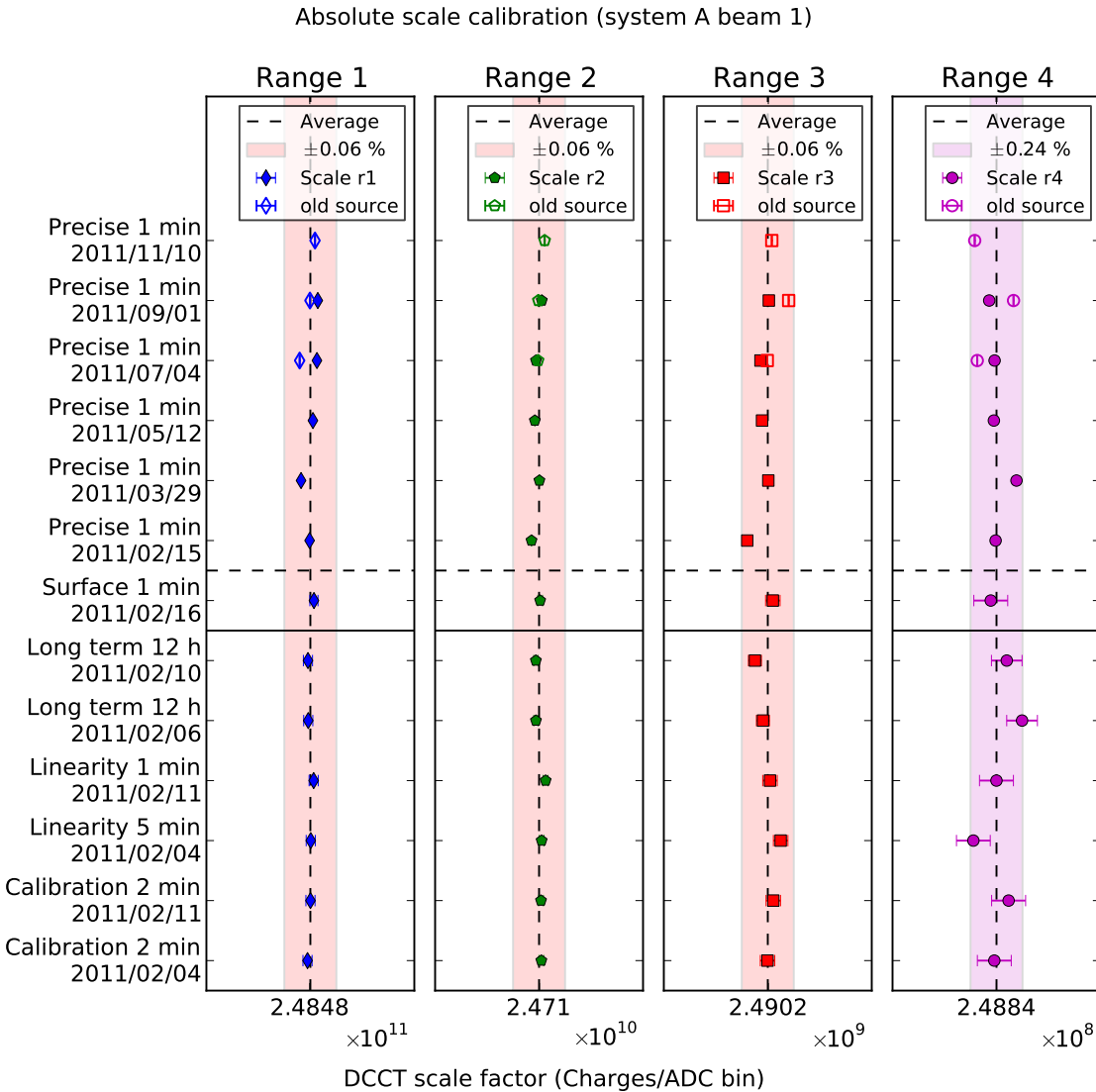


**Fig. G.52:** Long term stability of scaling factor. All points below the horizontal dashed line are so called “self” calibrations performed independently from the BI method and software. The points below the continuous horizontal line are calibrations performed with the source in the tunnel instead of on the surface.

## G.6 Difference between systems A and B

As shown in Sec. G.4.2, both systems A and B were behaving differently in 2010 due to a dependence on the bunch pattern. The difference can be seen on all train injections in 2010, but is not observed with the corrected hardware in 2011 as shown in Fig. G.35. A systematic study of all injections during 2010 and 2011 permits to assert the stability of the new hardware. Indeed the injections during 2011 are performed not only with high intensities up to  $2 \cdot 10^{14}$  charges in total, but also with different train length from 8 to 144 bunches per train. Furthermore, during a fill injection each additional train changes the filling pattern and thus the harmonics seen by the DCCT. Additionally, since no error source larger than  $\pm 1$  LSB has been discovered for the ranges 1 to 3, both DCCT systems must agree within  $\pm 1$  LSB in the absence of uncorrelated systematic error.

Each injection step was analyzed for all physics injections of 2010 and 2011, an example of the method used for all fills is shown in Fig. G.53 for fill 1459. On the left plot, each injection step of a given fill is detected and the intensity is measured by taking a 60 s average. The standard deviation of data is used as error. The relative difference at each step  $N(\text{sys A}) - N(\text{sys B}) / N(\text{average})$  (%) between system A and B is plotted over time on the right plot. While both systems happen to agree

at the end of injection, the erratic behavior during the injection unveil large discrepancies.

The relative difference between system A and B over the course of two years is shown in Fig. G.54 for all analyzed fills. A detailed view of all 2011 injections is shown in Fig. G.55. With some exceptions, the relative difference between both systems remains within  $\pm 0.5\%$  for the majority of the injection steps. On May 24 some points (all from fill 1804) with negative relative difference in beam 2 are clearly visible. The behavior of fill 1804 is not explained yet. The November injections are fills with lead ions. The same 2011 data plotted against the intensity on the x axis is shown in Figs. G.56 and G.56 for beams 1 and 2 respectively. A relative difference caused by a 1 ADC bin difference is indicated by a dashed line; the four ranges span from range 1 on the right to range 4 on the left. The lower right group of points from beam 2 belongs to fill 1804 which was identified in Fig. G.55. On the upper right, some points from beam 2 are above the 1 LSB line at the limit between range 1 and range 2. Those 9 points above 0.5% are spread around the year as can be seen in Fig. G.55. No study has been made to understand this rare effect which appears to occur at the range change. A possible explanation is that the switch from range 1 to 2 occurs at a slightly different time for both independent systems and the comparison is made between the high-end of range 2 and low-end of range 1. In all other injection steps throughout 2011, the relative difference between system A and B remains within  $\pm 1$  LSB. At low intensities covered by range 4, the difference is larger which is to be expected with a typical noise of  $\pm 3 - 4$  LSB; however, the difference remains within  $\pm 1$  LSB of range 3 which corresponds to  $\pm 10$  LSB of range 4.

In conclusion both independent DCCT systems A and B provided a consistent measurement throughout all physics injections in 2011 within the resolution of the 12-bit ADC or within the noise level of range 4. The DCCT accuracy is therefore at best limited by the 12-bit ADC; furthermore, no other uncorrelated systematic error has been revealed with this consistency check. An envelope error of  $\pm 1$  LSB is taken for the ranges 1 to 3 and of  $\pm 10$  LSB for range 4. However, this additional uncertainty is probably already included in the absolute scale and baseline fluctuations error. In absence of better knowledge, the difference is conservatively added to the total error.

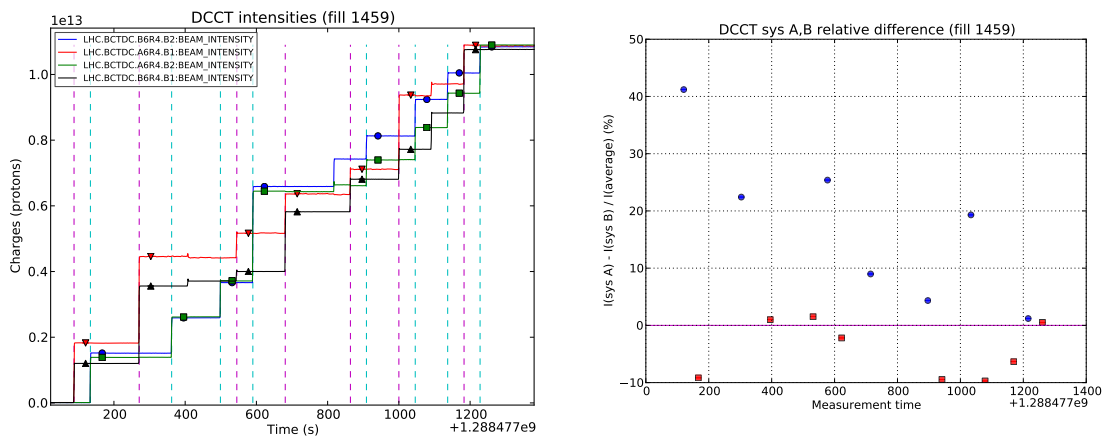


**Fig. G.53:** Example of injection steps (fill 1459 in 2010). Each train injection is seen as a step in the beam intensity. In 2010 the DCCT misbehavior can be clearly seen where the systems A and B indicate a different intensity for the same beam.

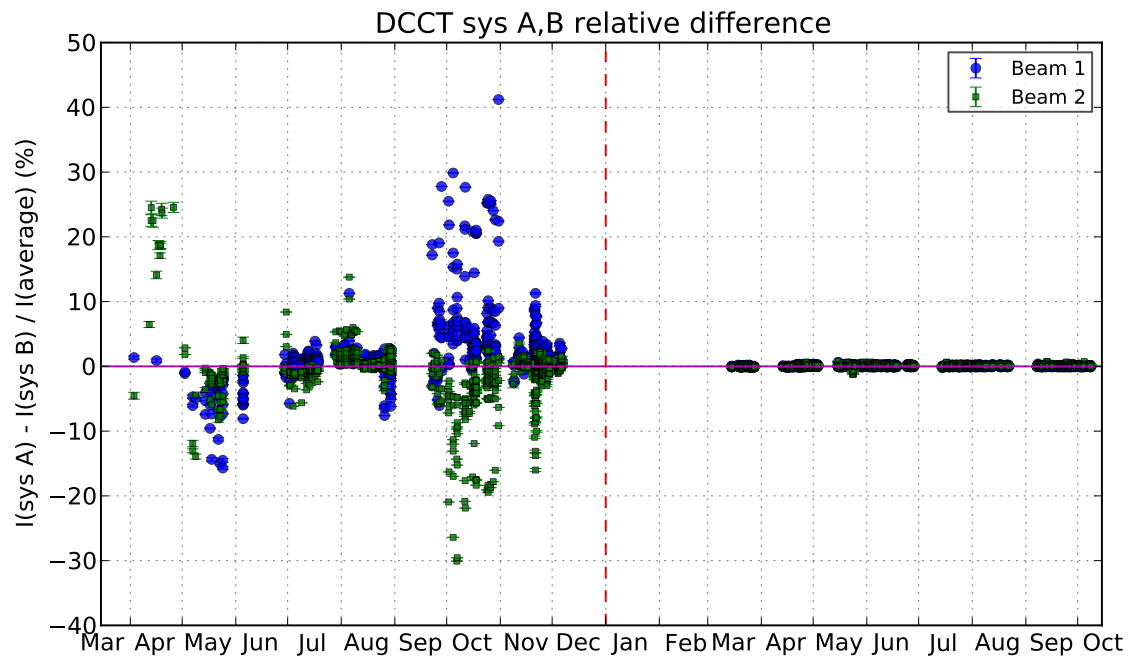


**Fig. G.54:** Relative difference between system A and B during all physics injections of 2010 and 2011 using a 60 s average per injection step. The DCCT misbehavior in 2010 is clearly visible.

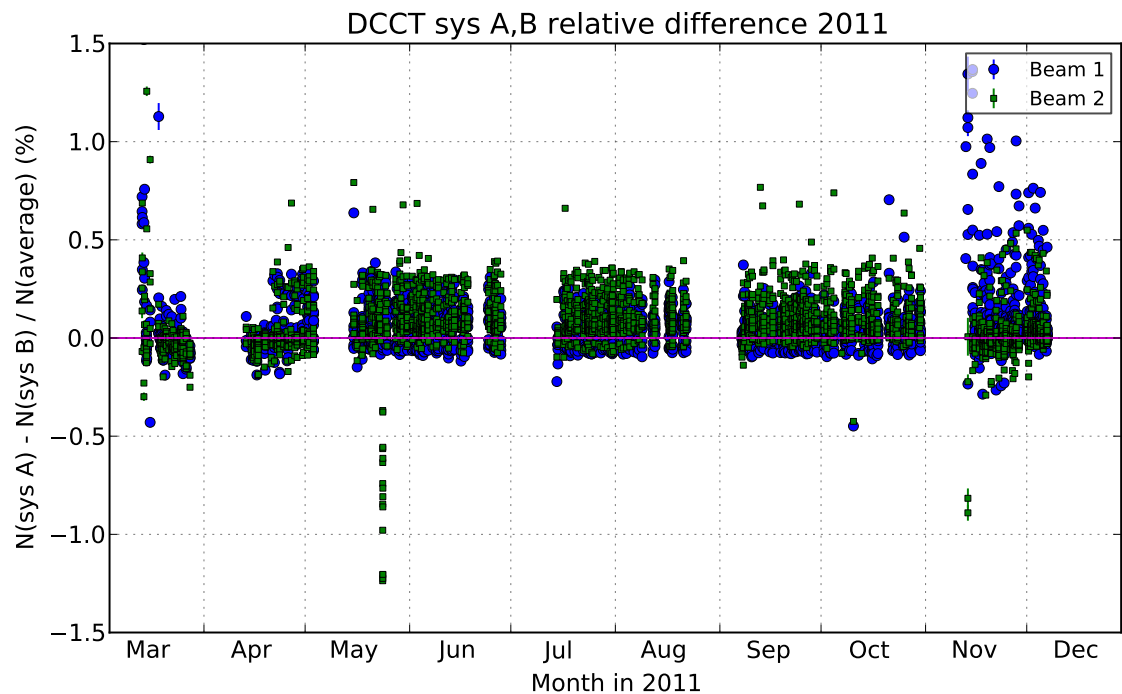


**Fig. G.55:** Relative difference between system A and B for 2011 using a 60 s average per injection step.

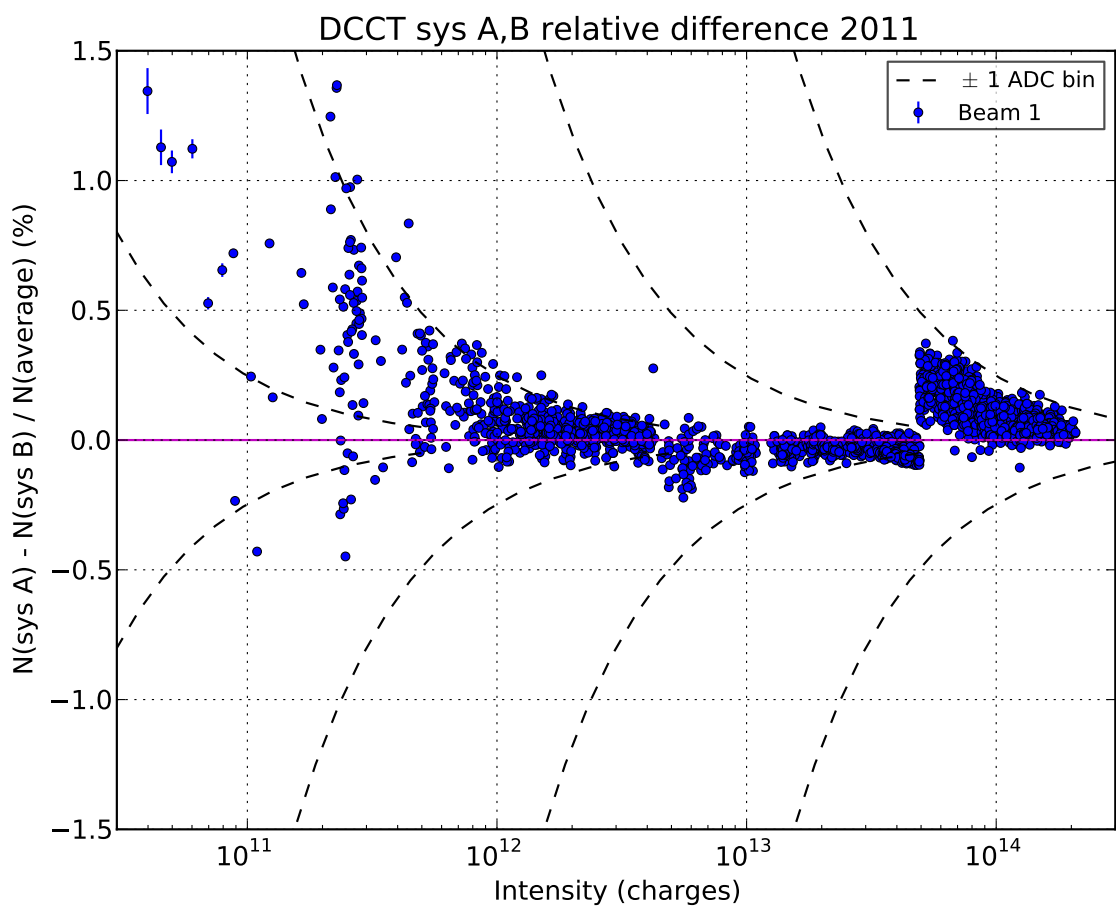


**Fig. G.56:** Relative difference between system A and B for 2011 vs. beam-1 intensity. Each point is a 60 s average of an injection step.

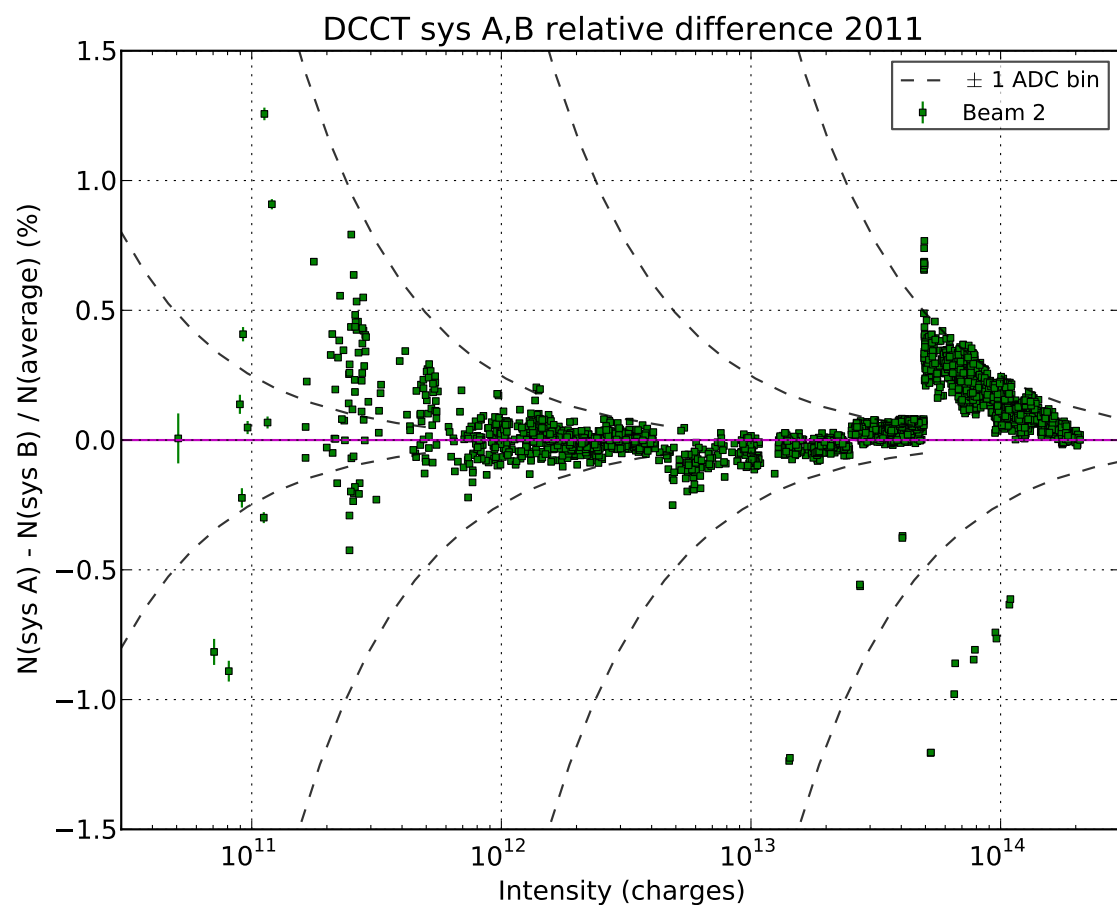


**Fig. G.57:** Relative difference between system A and B for 2011 vs. beam-2 intensity. Each point is a 60 s average of an injection step.

## G.7 Summary of uncertainties affecting total-intensity measurements

The DCCT system proved to be stable and consistent throughout all tests documented in this work. No sensitivity to external factor or to the beam conditions could be found. The uncertainty of 0.1% attributed to the laboratory measurement of the bunch pattern dependence is probably limited by the instrumentation and components used in the setup. For the DCCT internal effects, the acquisition chain with the 12-bit ADC is limiting the accuracy for the ranges 1 to 3, while the noise level is limiting range 4. No error could be found in the calibration method and the accuracy of both sources was tested down to 0.05% in the laboratory. This uncertainty reflects the limits of the laboratory instrumentation and components and is higher than the specifications provided by the manufacturer.

The source of uncertainties without any measurable effect are listed in Table G.8. The listed effects have been analyzed and the fluctuations are either compatible with the noise level or within one LSB. The summary of the DCCT uncertainties used for the final uncertainty on the beam intensities are listed in Table G.9. All uncertainties are given as an envelope error (100% confidence level). To interpret the envelope uncertainties below in terms of 68.3% confidence level, the numbers in Table G.9 and in the examples below should be multiplied by 0.683. The following errors should be considered as correlated between fills:

- The current source precision, because the same source is used for all calibrations throughout the year.
- The non-linearity of 12-bit ADC, because all fills are acquired with the same ADC.
- The bunch pattern dependence, because the laboratory measurement is applied to all DCCT's and it is not possible to exclude a systematic effect below 0.1%.

The other errors are related to random fluctuations and can be treated as uncorrelated between fills.

**Table G.8:** Summary of tested source of uncertainty without measurable effect.

Source of uncertainty	Range	Relative error (%)	Absolute error
Cross-talk between beams (Sec. G.4.1)			-
Noise change during dump of other beam			
Sensitivity to injected RF sine wave (Sec. G.4.2.3)			-
No resonance found between 1 kHz - 110 MHz			
Sensitivity to LHC energy (Sec. G.4.4.1)			-
No correlation observed with LHC energy			
Sensitivity to LHC RF system (Sec. G.4.4.2)			-
No correlation observed with LHC RF cavity field			
Thermal effect during 24 hours under load			< 0.01%
No systematic drift of day/night effect (Sec. G.3.4.2)			
Current leak during calibration from surface			-
No difference between the source on the surface or in the tunnel (Sec. G.5.3)			
Methodology of calibration procedure			-
No difference between “self” calibration and standard BI procedure (Sec. G.5.3)			
Seasonal fluctuations of calibration factors			-
Calibrations stable within expected ADC bit accuracy, verified over 9 month (Sec. G.3.6)			
Off-center position of calibration rods (Sec. G.5.2)			-
Bunch position dependence (MD)			-
No dependence found with beam movement during MD (Sec. G.4.3)			
Bunch pattern dependence (MD)			-
No dependence found during beam debunching with RF off (Sec. G.4.2.2)			

**Table G.9:** Source of uncertainties per beam. All numbers are given as envelope error (100% confidence level). For the baseline correction, the reduced error of  $\pm 1 \cdot 10^9$  charges can be used if the offset is corrected or smaller than  $\pm 1 \cdot 10^9$  e. Otherwise the more generic errors dependent on the range must be used. For the long term stability of the baseline, the indicated errors depend on the signal averaging time. A normalization of the beam intensity using a 1 hour average or more can use the lower errors provided in parenthesis. Low intensity fills acquired with range 4 will benefit from a longer averaging time, while the difference is negligible for the other ranges.

Source of uncertainty	Range	Relative error (%)	Absolute error	Correlated btw. beams
Current source precision accuracy limited by instrumentation (Sec. G.5.1)		$\pm 0.05\%$		yes
Baseline correction				
If data is manually baseline corrected (Sec. G.3.1)			$\pm 1 \cdot 10^9$ e	
If data is not baseline corrected (Sec. G.3.2)	1		$(\pm 6 \cdot 10^{10}$ e)	
	2		$(\pm 7 \cdot 10^9$ e)	
	3		$(\pm 4 \cdot 10^9$ e)	
	4		$(\pm 4 \cdot 10^9$ e)	
Non-linearity of 12-bit ADC (Sec. G.3.4.3) non-linearity due to acquisition chain beam 1, 2 and all ranges share same ADC			$\pm 1$ LSB	yes
Long term stability of baseline observed fluctuations within $2 \times 12$ hours if signal average $\geq 1$ minute (Sec. G.3.4.1)	1		$\pm 1.1 \cdot 10^{11}$ e	
	2		$\pm 1.0 \cdot 10^{10}$ e	
	3		$\pm 2.4 \cdot 10^9$ e	
	4		$\pm 2.3 \cdot 10^9$ e	
observed fluctuations within $2 \times 12$ hours if signal average $\geq 1$ hour (Sec. G.3.4.1)	1		$(\pm 7.3 \cdot 10^9$ e)	
	2		$(\pm 1.1 \cdot 10^9$ e)	
	3		$(\pm 1.1 \cdot 10^9$ e)	
	4		$(\pm 1.0 \cdot 10^9$ e)	
Long term stability of calibration factor envelope observed within 9 month (Sec. G.3.6)	1,2,3		$\pm 1$ LSB	
	4		$\pm 4$ LSB	
Bunch pattern dependence (laboratory test) accuracy limited by instrumentation (Sec. G.4.2.1)		$\pm 0.1\%$		yes
Difference between system A and B observed during all physics injections 2011 range 4 limited by noise (Sec. G.6)	1,2,3		$\pm 1$ LSB	
	4		$\pm 10$ LSB	

The final uncertainty on the beam intensity provided by the DCCT depends on the range used for the measurement and the total intensity relative to the full scale of the range. The range used for a given fill can be deduced from Table G.2. The acquisition system will select the most sensitive range such that the measurement is lower than the full scale of the range. For example a measurement of  $4 \cdot 10^{12}$  charges is acquired with range 3. In case of doubt, the selected range for a DCCT can be retrieved from the logging database using the variable “LHC.BCTDC.A6R4.B1:SELECTED\\_RANGE” as an example for system A/beam 1. The 12-bit ADC has a total resolution of  $2^{12} = 4096$  bins; due to the bipolar mode, only the positive range is used, limiting the full range to 2048 bins. In addition, the automatic offset correction can further reduce the range, therefore, it can be assumed in general that 2000 ADC bins are available to measure values covering the full dynamic of a range. In consequence, the absolute uncertainty corresponding to 1 LSB depends on the full intensity  $N_{\text{Full scale}}$  of the range used:

$$1 \text{ LSB} = \frac{N_{\text{Full scale}}}{2000}, \quad (\text{G.11})$$

Thus, for a beam intensity measured by the DCCT the relative uncertainty corresponding to 1 LSB is

$$\delta N_{\text{LSB}} = \frac{1 \text{ LSB}}{N_{\text{DCCT}}}. \quad (\text{G.12})$$

The full scale of the range and the corresponding LSB value are given in Table G.2.

The error on the baseline correction depends on whether the correction is applied or not: without any correction or verification, an absolute error of  $\pm 5 \cdot 10^9$  charges has to be assumed (see Sec. G.3.2). However, if the data is baseline-corrected, or if the absolute value of the baseline before and after the fill is smaller than  $10^9$  charges, the uncertainty of  $\pm 1 \cdot 10^9$  charges can be used.

### G.7.1 Example with a VDM fill

The following section is an example for the uncertainty calculation for the VDM fill 1783 on May 15 2011.

The fill started with an intensity of  $3.26 \cdot 10^{12}$  protons and ended with  $3.16 \cdot 10^{12}$  protons, and the DCCT was acquired with range 3. To be valid for the whole fill, the relative errors are based on the lowest intensity of  $3.16 \cdot 10^{12}$  protons, with (G.12), the relative error of 1 LSB is 0.08%. The acquisition was locked on range 3 during the whole fill including the periods without beam. The absolute value of the baseline before and after the fill is smaller than  $10^9$  protons, a manual correction is therefore not warranted and the smaller error of  $10^9$  protons can be used as if the baseline was manually corrected. The relative error of the baseline is  $10^9 / 3.16 \cdot 10^{12} = 0.03\%$ . If the normalization is done with a time average shorter than 1 minute, then the error from the long term stability of baseline for range 3 is  $2.4 \cdot 10^9$  protons corresponding to a relative error or 0.08%. The smaller error of  $1.1 \cdot 10^9$  can be used if the normalization is done over a period of 1 hour or more. The summary of all uncertainties for fill 1783 is presented in Table G.10. As with Table G.9, all uncertainties are given as an envelope error.

In conclusion the total uncertainty per beam is 0.20% and of 0.34% for the beam product taking into account that the first three listed errors are correlated between beams.

**Table G.10:** Summary of uncertainties for VDM fill 1783

Source of uncertainty (per beam)	Relative error (%)	Correlated btw. beams
Current source precision	± 0.05	yes
Bunch pattern dependence (laboratory test)	± 0.1	yes
Non-linearity of 12-bit ADC	± 0.08	yes
Baseline correction	± 0.03	no
Long term stability of baseline on range 3	± 0.08	no
Long term stability of calibration on range 3	± 0.08	no
Difference between system A and B on range 3	± 0.08	no
Total error per beam	± 0.20	
Correlated error per beam	(± 0.138)	yes
Uncorrelated error per beam	(± 0.143)	no
Total error on beam product	± 0.34	

### G.7.2 Example with a typical high intensity fill

The following section provides an example for the uncertainty calculation for a typical high intensity fill acquired in range 1 assuming an intensity of  $1.5 \cdot 10^{14}$  protons. Without any analysis of the offset, an error of  $\pm 6 \cdot 10^{10}$  protons has to be assumed for the baseline uncertainty, corresponding to a relative error of 0.04%. The long term stability of the baseline has an absolute error of  $1.1 \cdot 10^{11}$  protons corresponding to a relative error of 0.07%. The maximal intensity of range 1 is  $5 \cdot 10^{14}$  protons, with equation (G.12), the relative error of 1 LSB is  $\pm 0.17\%$ . The summary of all uncertainties given as an envelope error for such fill is presented in Table G.11.

**Table G.11:** Summary of uncertainties for a fill acquired with range 1

Source of uncertainty (per beam)	Relative error (%)	Correlated btw. beams
Current source precision	± 0.05	yes
Bunch pattern dependence (laboratory test)	± 0.1	yes
Non-linearity of 12-bit ADC	± 0.17	yes
Baseline correction	± 0.04	no
Long term stability of baseline on range 1	± 0.07	no
Long term stability of calibration on range 1	± 0.17	no
Difference between system A and B on range 1	± 0.17	no
Total error per beam	± 0.32	
Correlated error per beam	(± 0.20)	yes
Uncorrelated error per beam	(± 0.25)	no
Total error on beam product	± 0.53	

### G.7.3 Example with a low intensity fill

This section provides an example for the uncertainty calculation for a low intensity fill acquired in range 4 assuming an intensity of  $4 \cdot 10^{10}$  protons as example. Provided the offset has been either corrected or is smaller than  $1 \cdot 10^9$  protons, the reduced error of  $\pm 1 \cdot 10^9$  protons can be used as baseline error, which corresponds to a relative error of  $\pm 2.5\%$ . If the normalization is done with a time average of 1 hour or more, then the absolute error from the long term stability of the baseline

for range 4 is  $1.0 \cdot 10^9$  protons corresponding to a relative error or 2.5%. The maximal intensity of range 4 is  $5 \cdot 10^{11}$  protons, with equation (G.12), the relative error of 1 LSB is  $\pm 0.63\%$ . The summary of all uncertainties given as an envelope error for such a fill is presented in Table G.12. The resulting beam intensity error is valid for any period during the fill averaged over 1 hour or more. The error is dominated by the difference between system A and B ( $\pm 10$  LSB). A lower error can be achieved by comparing both systems for the same time period.

**Table G.12:** Summary of uncertainties for a fill acquired with range 4

Source of uncertainty (per beam)	Relative error (%)	Correlated btw. beams
Current source precision	$\pm 0.05$	yes
Bunch pattern dependence (laboratory test)	$\pm 0.1$	yes
Non-linearity of 12-bit ADC	$\pm 0.63$	yes
Baseline correction	$\pm 2.50$	no
Long term stability of baseline on range 4	$\pm 2.5$	no
Long term stability of calibration on range 4	$\pm 2.5$	no
Difference between system A and B on range 4	$\pm 6.25$	no
Total error per beam	$\pm 7.6$	
Correlated error per beam	$(\pm 0.63)$	yes
Uncorrelated error per beam	$(\pm 7.6)$	no
Total error on beam product	$\pm 10.8$	

#### G.7.4 Outlook

The laboratory measurement of the bunch pattern dependence is the dominating uncertainty and is probably limited by the instruments and components used in the setup. Furthermore the maximal intensity allowed by the setup could not test the high LHC intensities that can be reached with 25 ns bunch spacing. Therefore, further tests will be carried out in the laboratory to include all possible LHC intensities.

The remaining uncertainties are essentially originating from the noise level together with the baseline stability and the 12-bit limitation of the ADC acquisition. In conclusion, the ideal settings and conditions to minimize the DCCT uncertainties, for example during a van der Meer scan, are as follows.

- Low intensities acquired with range 4 should be avoided due to the dominating influence of the noise level and the baseline and scaling factor fluctuations. Ideally the beam intensities should lie within the ranges 1 to 3. The typical van der Meer scans performed in 2010 and 2011 were acquired in range 3.
- The total beam intensity should be close to the calibration point of the range which is normally set at 80% of each range (notice that range 1 is calibrated at 50% of its range). Therefore, the error induced by the non-linearity of the ADC is minimized near the calibration point; furthermore, at 80% of the range the relative error of 1 LSB is also reduced.
- The expected range should be blocked throughout the fill including periods without beam before and after the fill. Consequently the offset can be evaluated without analyzing the ADC raw values and the manual correction is simplified.

A new single range 24-bit ADC has been installed in the front-end electronics and will acquire the DCCT intensities in parallel to the actual setup starting with the 2012 LHC run. Once fully tested

and validated, this new higher resolution acquisition might further reduce the uncertainties quoted in this work. Because the 24-bit is installed directly in the front-end electronics, digital values are sent to the surface crates instead of analogue voltages; therefore, a better understanding of the DCCT intrinsic noise level, baseline fluctuations and linearity will be possible. Accordingly, the acquisition chain should not limit the DCCT's accuracy anymore in the future.

## G.8 Appendices

### G.8.1 Noise and baseline correction

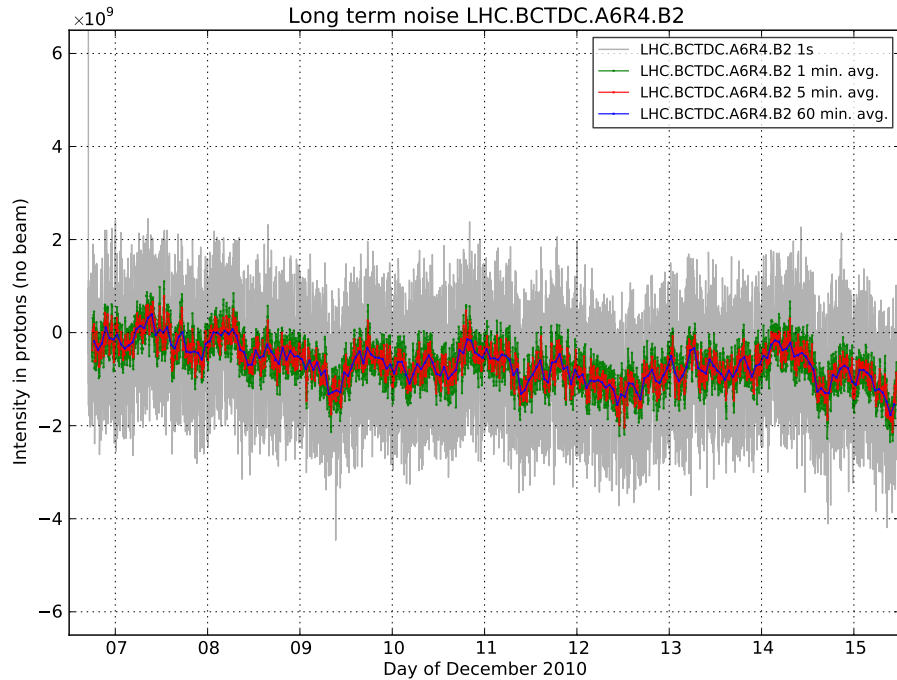


**Fig. G.58:** DCCT long term offset for system A/beam 2.

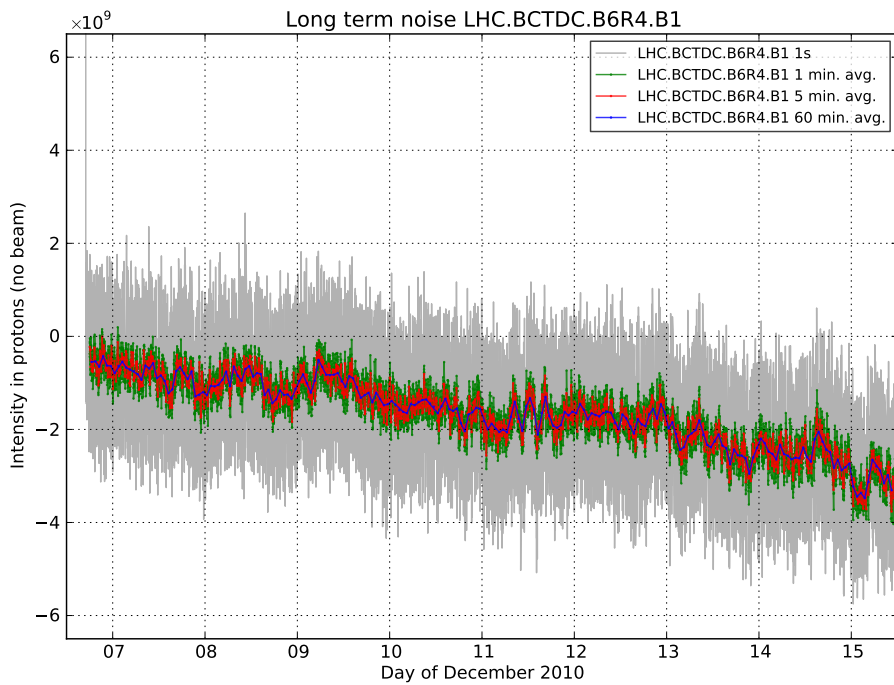


**Fig. G.59:** DCCT long term offset for system B/beam 1.

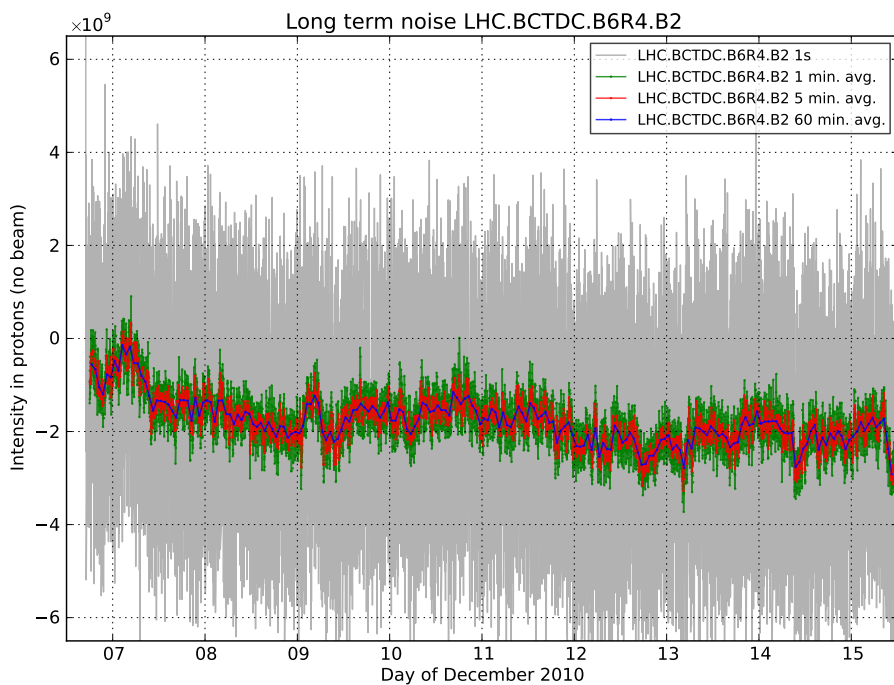


**Fig. G.60:** DCCT long term offset for system B/beam 2.

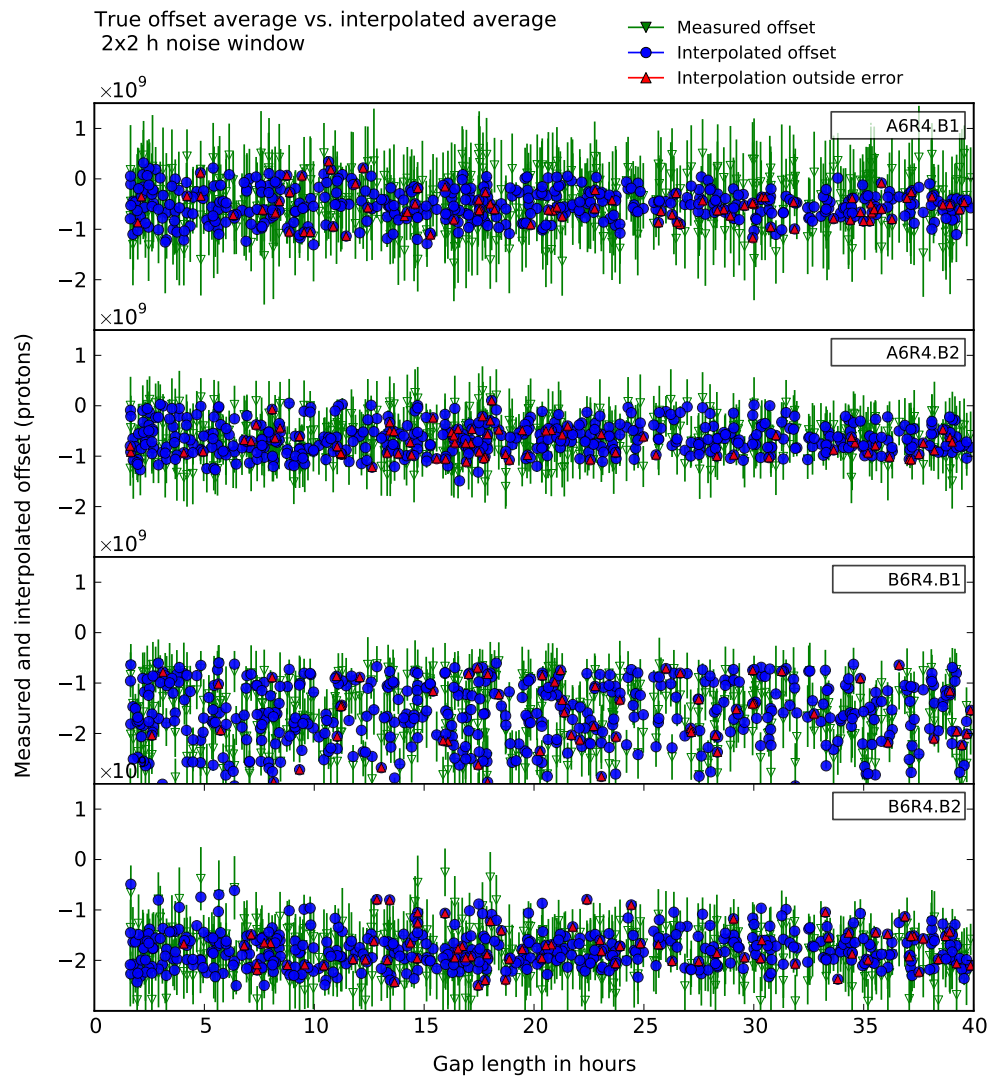


**Fig. G.61:** Offset box error test for all DCCT's. A random gap length between 1 h and 40 h is chosen at a random time position within the 9 days of available noise data. The true signal value taken at the center of the gap is compared to the interpolated value. A plain blue dot indicates an interpolated offset inside the error bar. A plain red triangle indicates an interpolated offset value outside of the expected error. 8.2% of the 2000 tests are outside of the peak-to-peak error.

### G.8.2 Long term stability over 12 hours

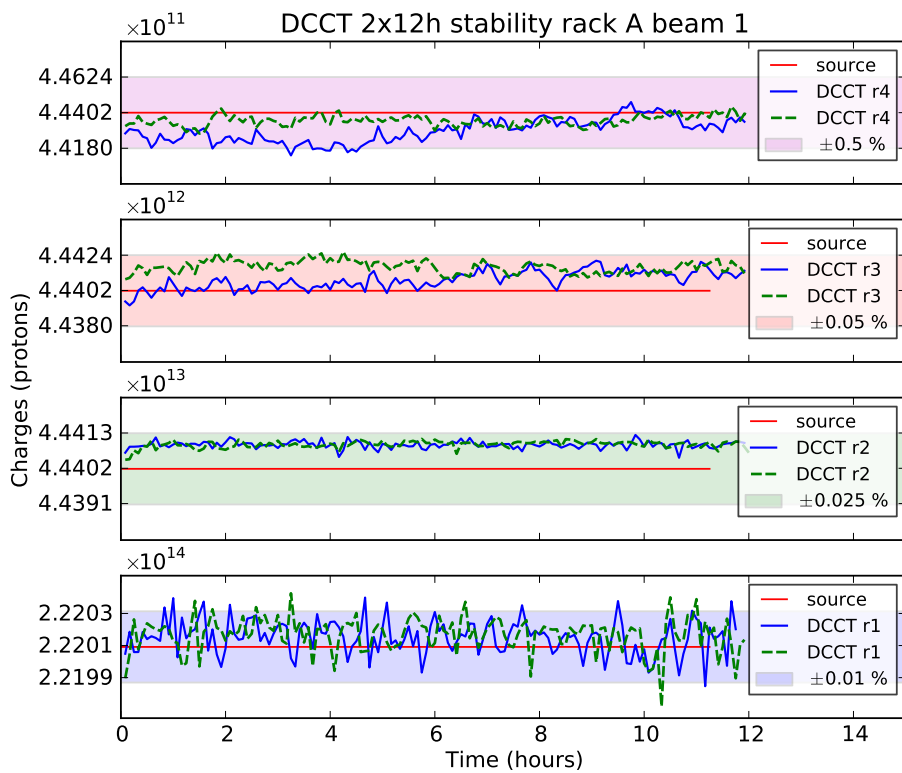


**Fig. G.62:** Long term stability under load for all ranges of system A/beam 1.

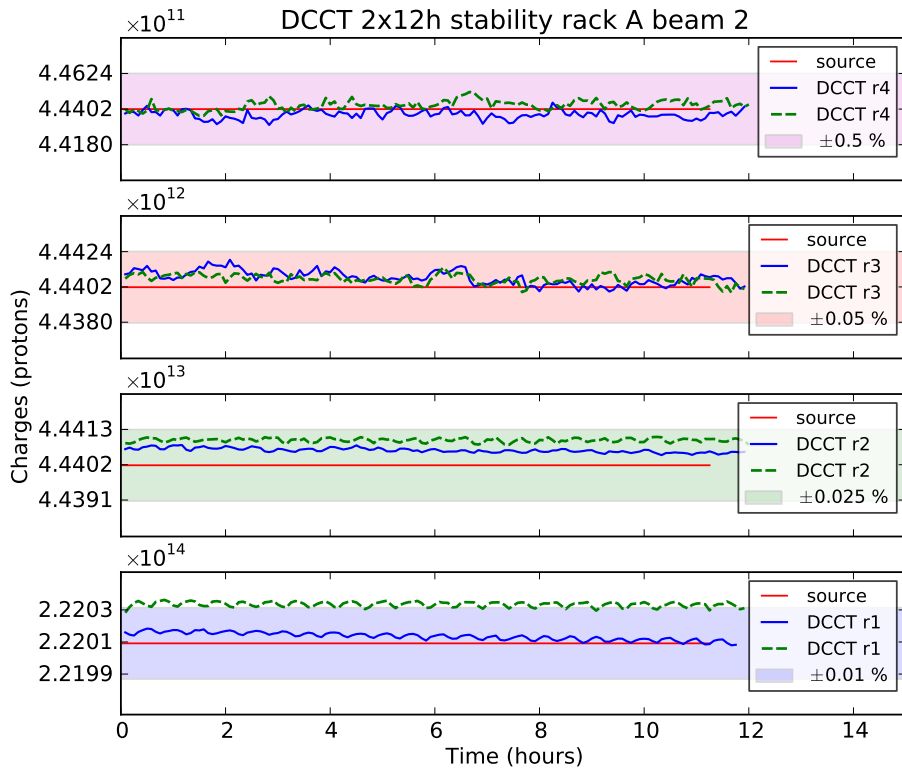


**Fig. G.63:** Long term stability under load for all ranges of system A/beam 2.

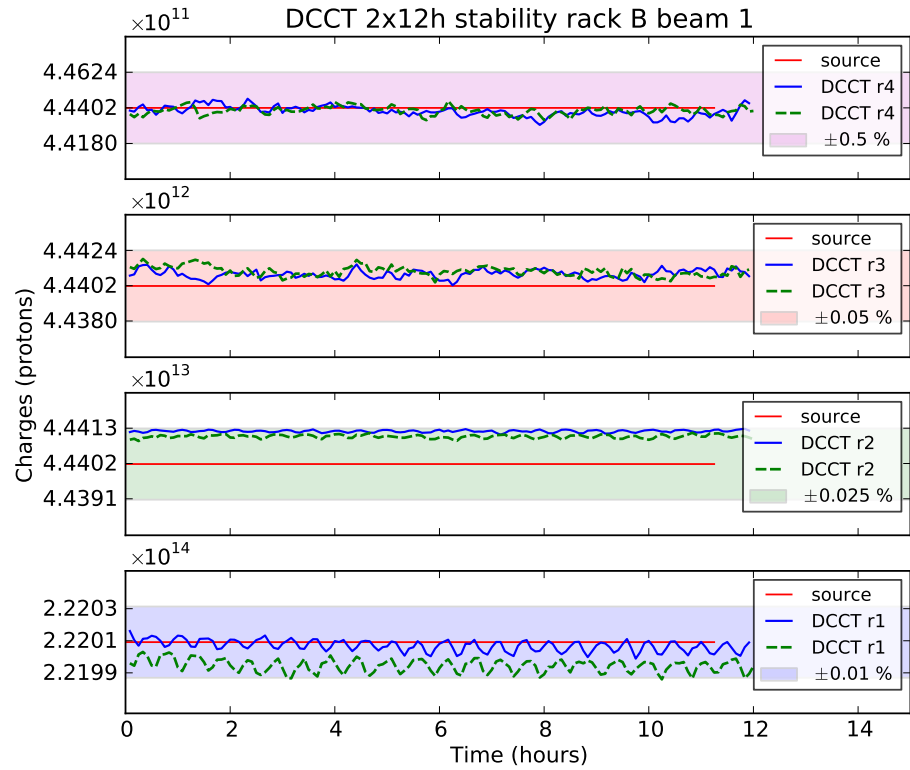


**Fig. G.64:** Long term stability under load for all ranges of system B/beam 1.

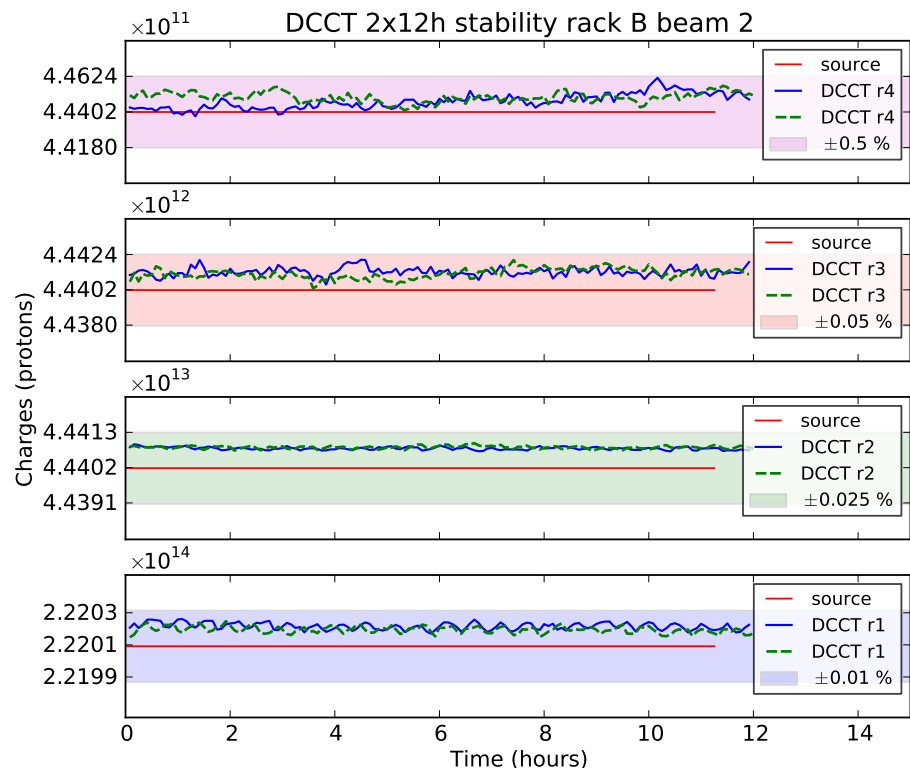


**Fig. G.65:** Long term stability under load for all ranges of system B/beam 2.

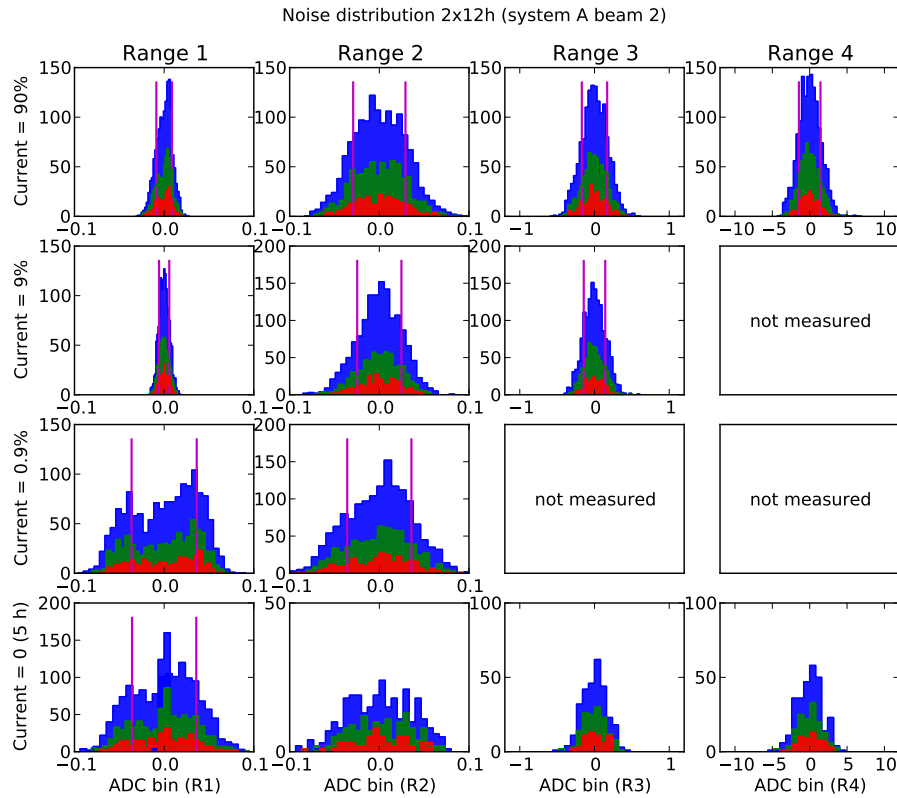


**Fig. G.66:** Histograms of  $2 \times 12$  hours of all ranges for system A/beam 2

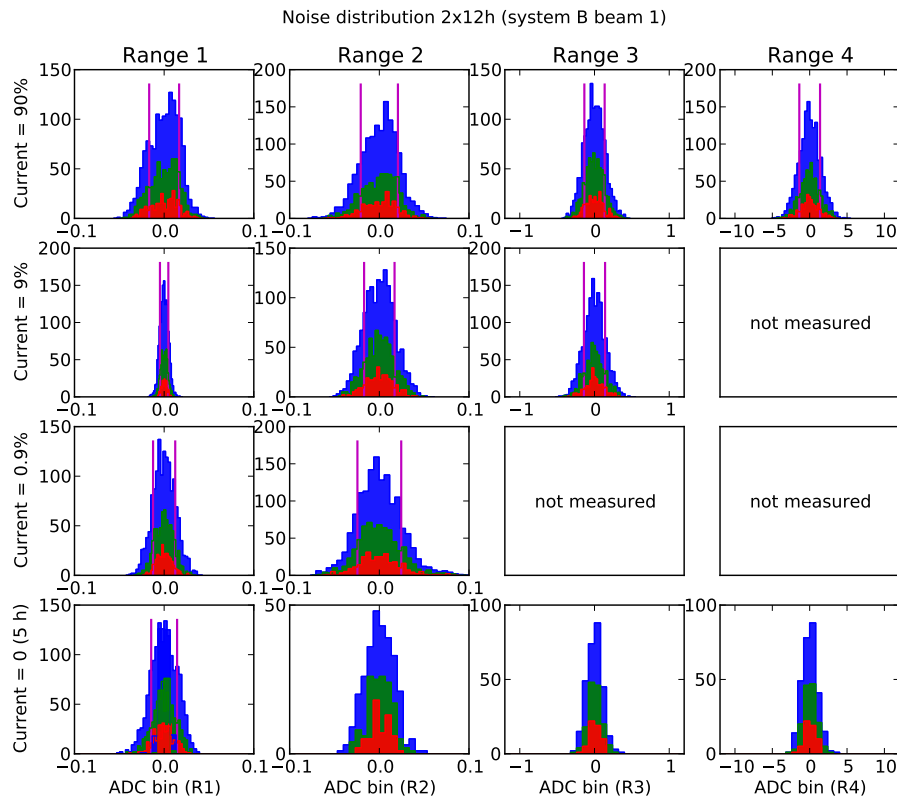


**Fig. G.67:** Histograms of  $2 \times 12$  hours of all ranges for system B/beam 1

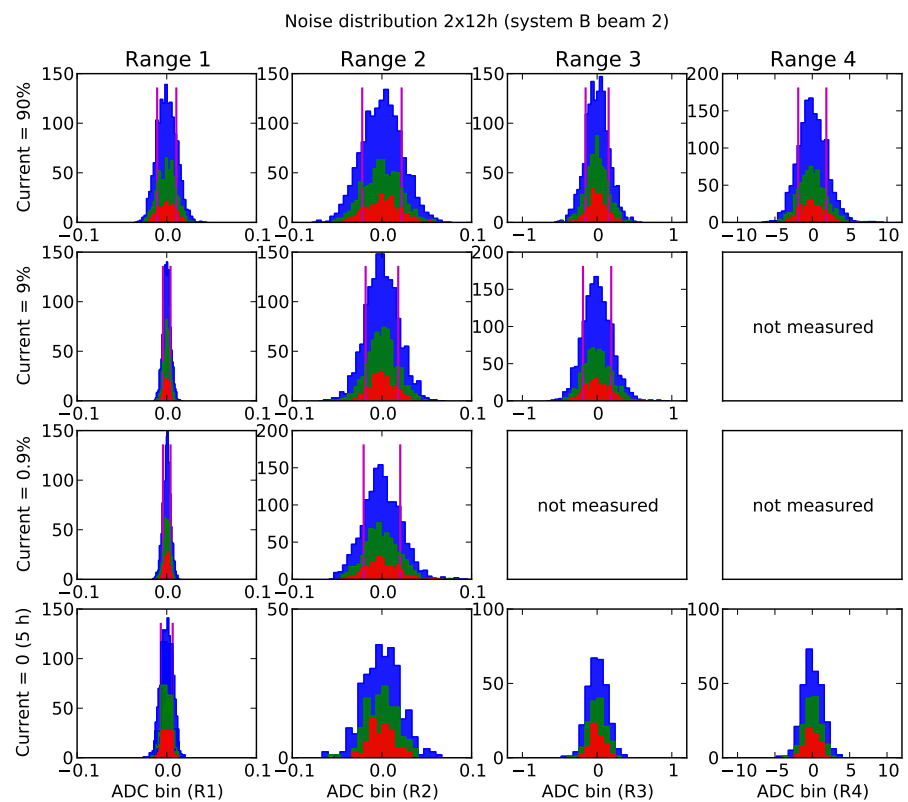


**Fig. G.68:** Histograms of  $2 \times 12$  hours of all ranges for system B/beam 2

### G.8.3 Linearity

#### G.8.3.1 Linearity measurements with 12-bit ADC

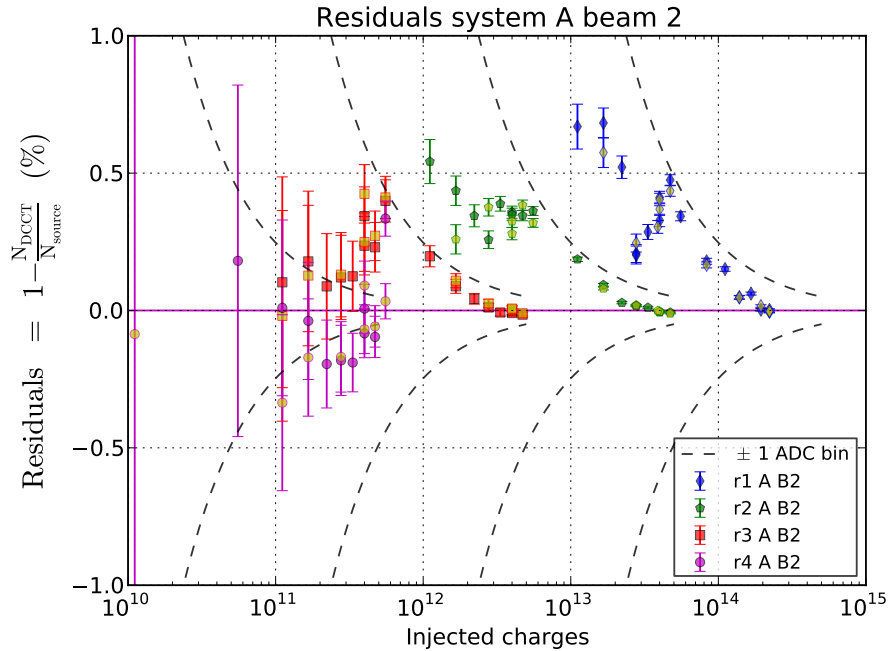


**Fig. G.69:** Linearity residuals for system A/beam 2 combining the values from the first measurement (plain dots) and the third measurement (yellow faced dots). Intensities below 2% of the range (about 40 ADC bins) are not shown.

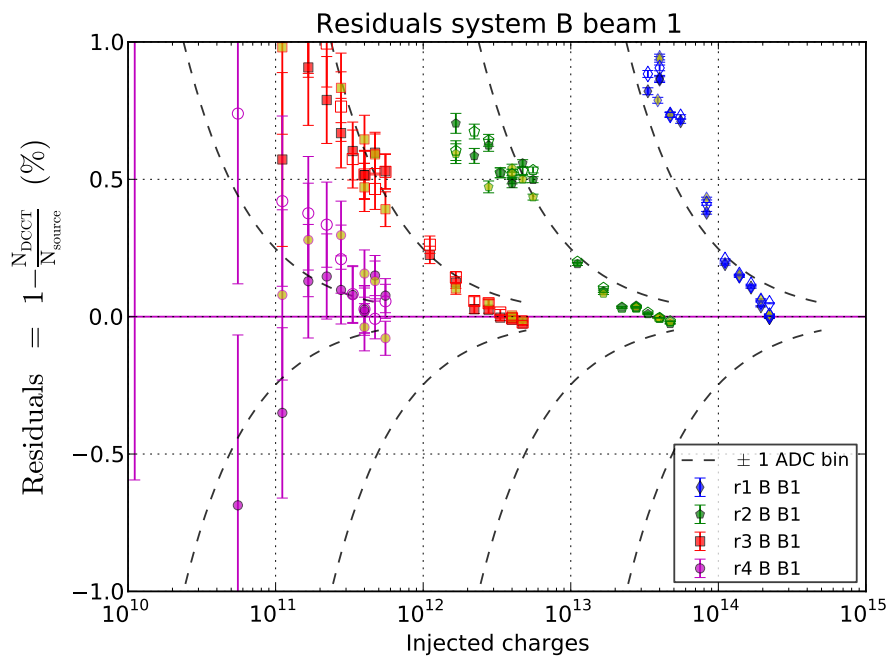


**Fig. G.70:** Linearity residuals for system B/beam 1 combining the values from the first measurement (plain dots), the second measurement (open dots) and the third measurement (yellow faced dots). Intensities below 2% of the range (about 40 ADC bins) are not shown.

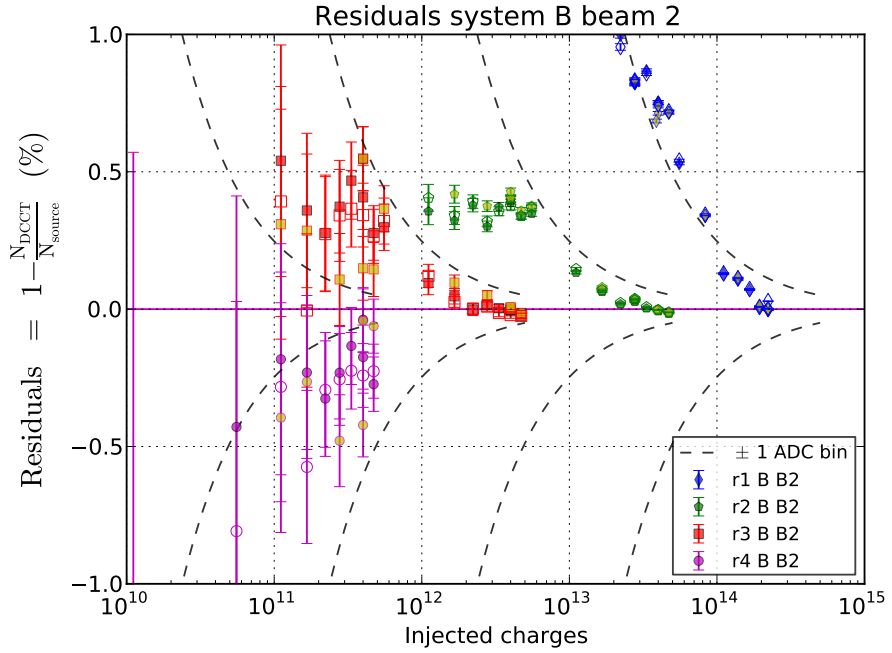


**Fig. G.71:** Linearity residuals for system B/beam 2 combining the values from the first measurement (plain dots), the second measurement (open dots) and the third measurement (yellow faced dots). Intensities below 2% of the range (about 40 ADC bins) are not shown.

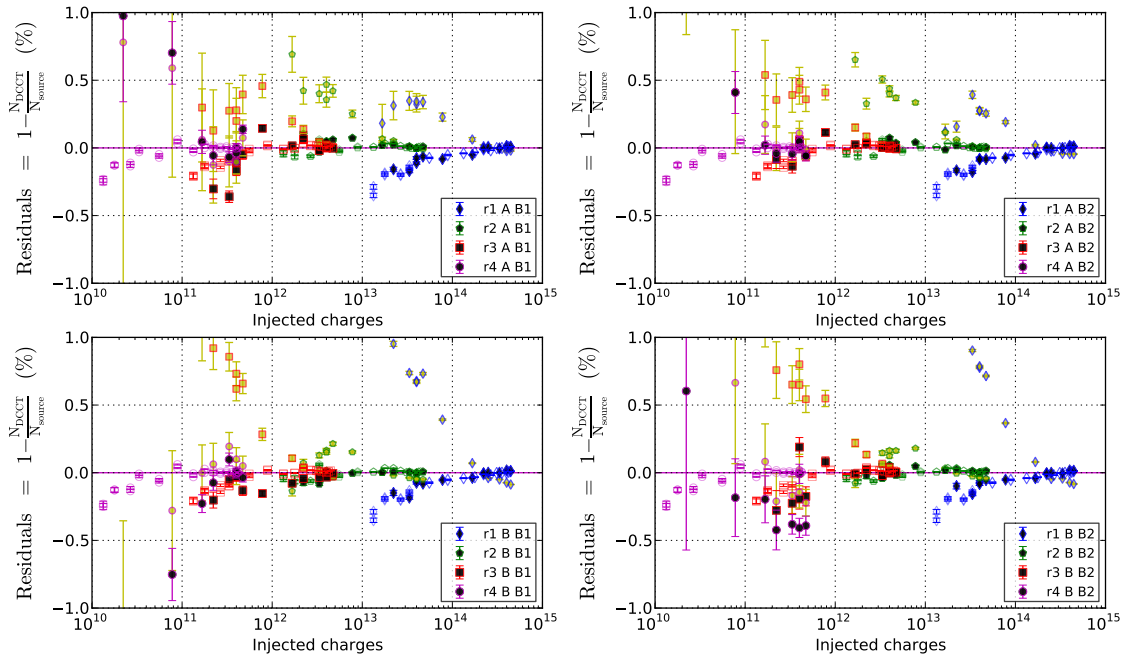


**Fig. G.72:** Linearity residuals measured with both ADC's. The empty markers are the laboratory reference response of the 16 bit NI ADC, the yellow filled markers are the DCCT response measured with the standard 12-bit ADC and the black filled markers are the DCCT response measured with the 16 bit NI ADC. With the ranges 1 and 2, the DCCT response measured with the NI ADC clearly follow the laboratory reference while the response measured with the 12-bit ADC shows the same positive residuals pattern as observed before (see above and Fig. G.24). The larger fluctuations on range 3 still allow to see that the 16 bit measurement tends to follow the reference; however, range 4 is too noisy and difficult to measure as before. The observed non linearity is therefore due to the acquisition chain and not due to the DCCT itself.

### G.8.3.2 Linearity measurements with 24-bit ADC

The scaling factors of the 24-bit acquisition were measured with a similar setup as used in Sec. G.3.4.3. The source Yokogawa 7651 was used to inject a current through the DCCT's in preprogrammed steps of 5 minutes. Due to the limited maximal output of 120 mA, the cable carrying the current passed one time through both systems A to test injections at low intensities and four times through both systems B to test injections at higher intensities. The maximal nominal current of the DCCT is 1 A. The measurement was performed three times within 24 hours and consisted of 31 steps of 5 minutes in a sequence similar to Fig. G.22 in Sec. G.3.4.3. The results are shown in Figures G.73 to G.76. The errors include the source uncertainty as specified by the manufacturer, the data fluctuations within one measurement step and the fluctuations due to the offset corrections.

The scaling factors are constant within  $\pm 0.1\%$  for intensities larger than  $5 \cdot 10^{11}$  protons. For lower intensities, the noise level and baseline fluctuations start to decrease the accuracy resulting in larger fluctuations as seen on both systems A. In general no systematic bias can be observed and the non-linearity measured in Sec. G.3.4.3 is not observed with the 24-bit ADC acquisition.

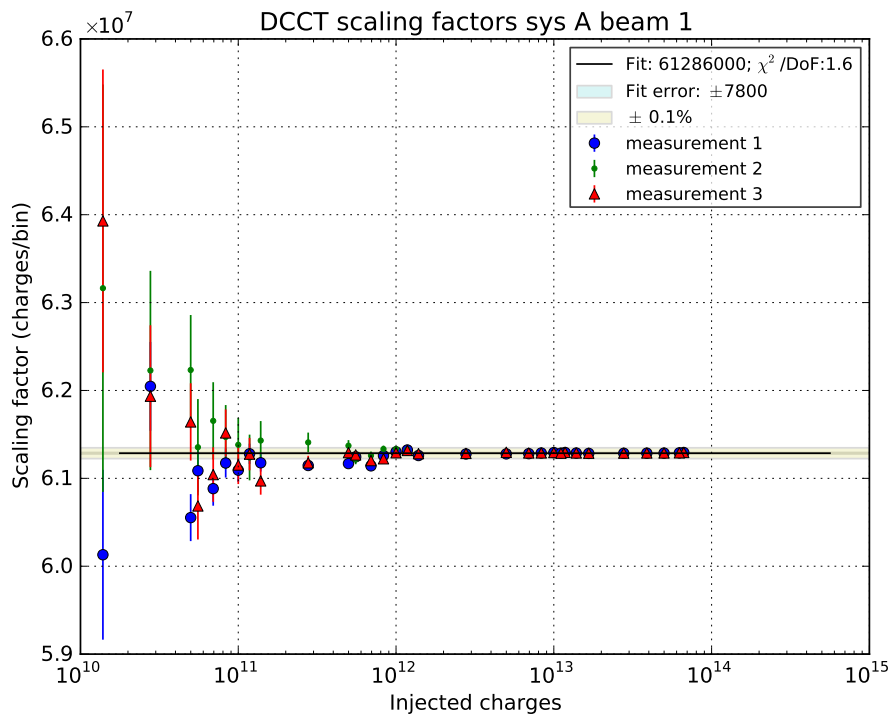


**Fig. G.73:** Scaling factor of 24-bit acquisition for system A/beam 1 combining the values from three measurements.

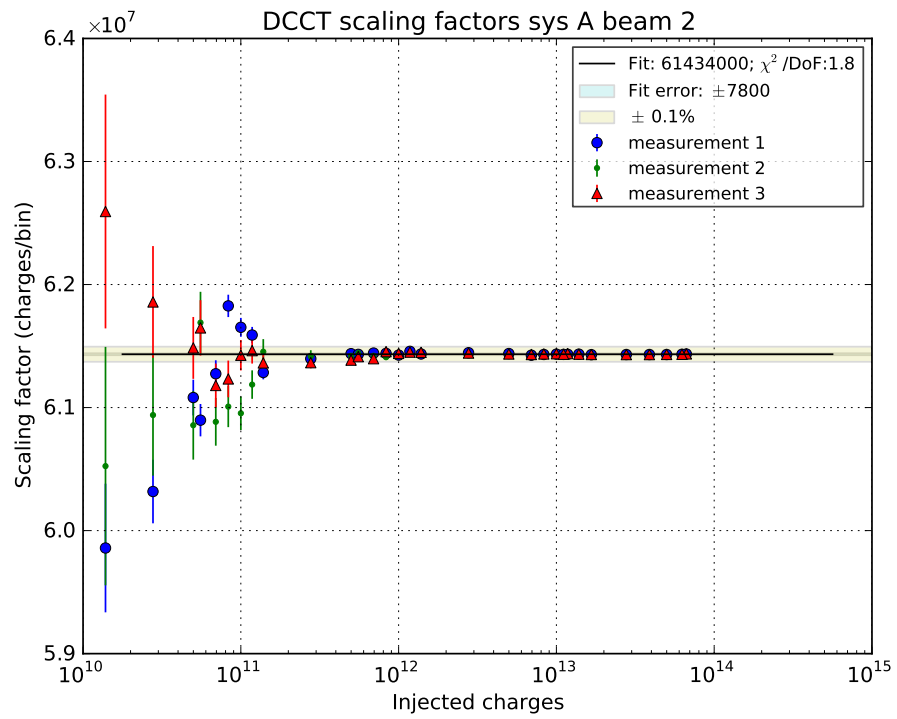


**Fig. G.74:** Scaling factor of 24-bit acquisition for system A/beam 2 combining the values from three measurements.

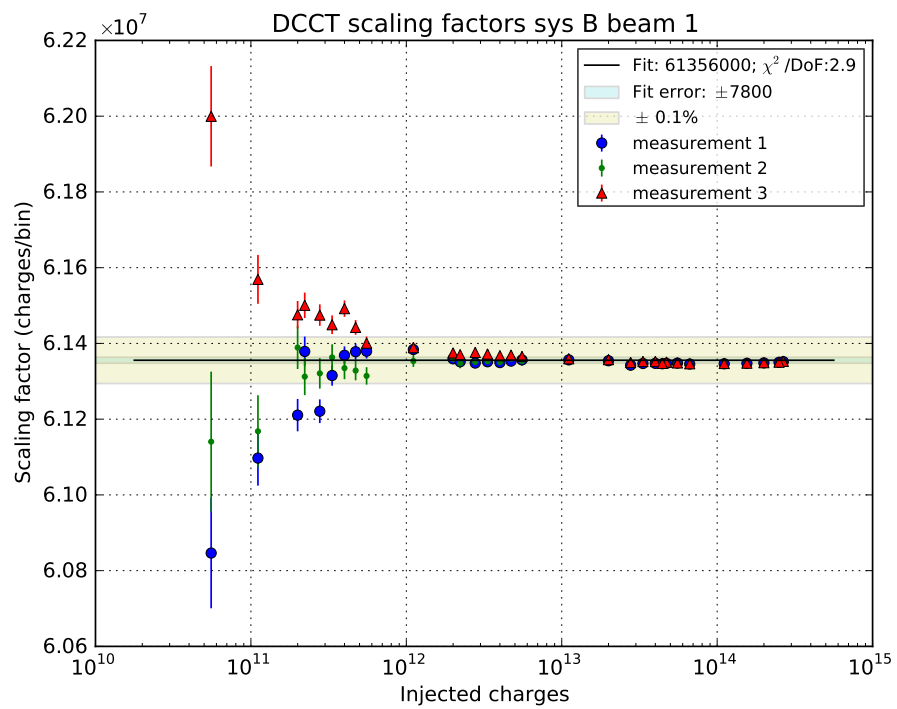


**Fig. G.75:** Scaling factor of 24-bit acquisition for system B/beam 1 combining the values from three measurements.

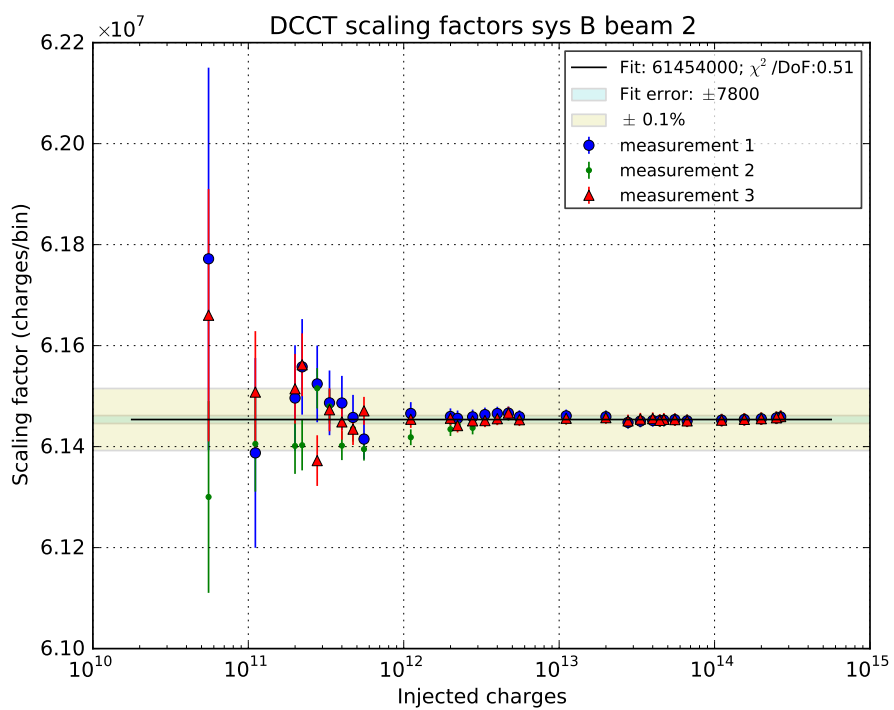


**Fig. G.76:** Scaling factor of 24-bit acquisition for system B/beam 2 combining the values from three measurements.

#### G.8.4 Cross talk between rings

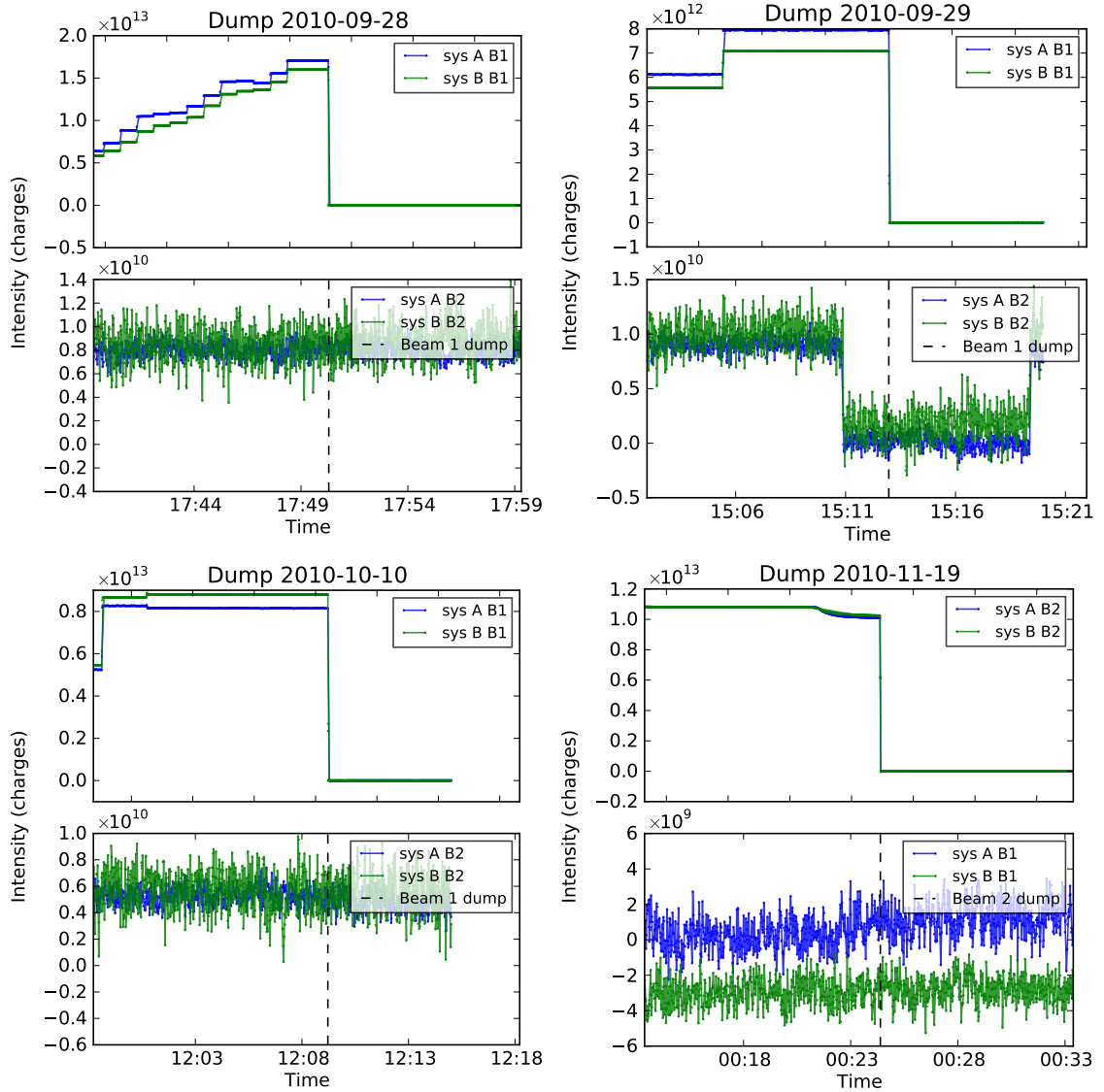
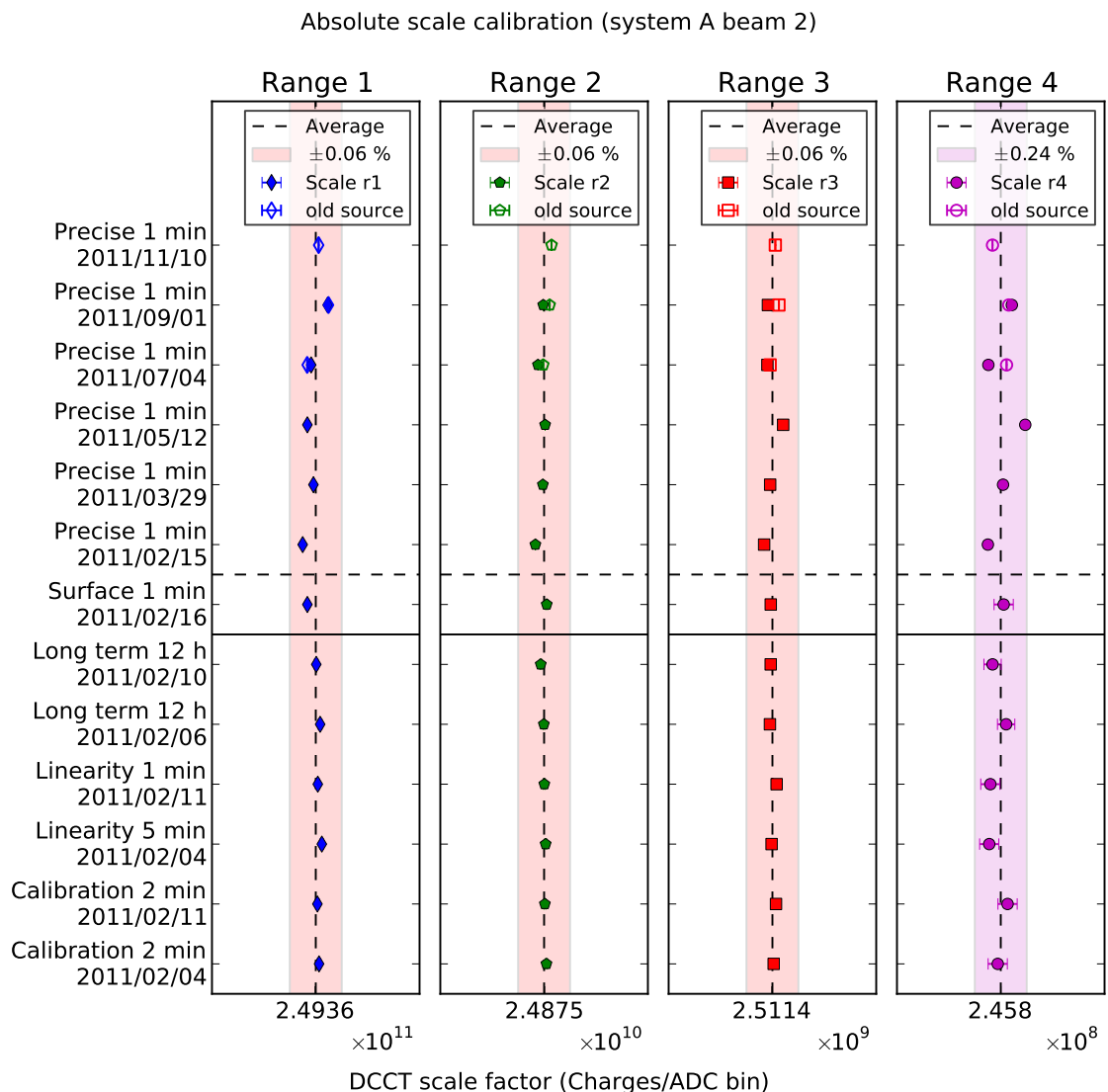
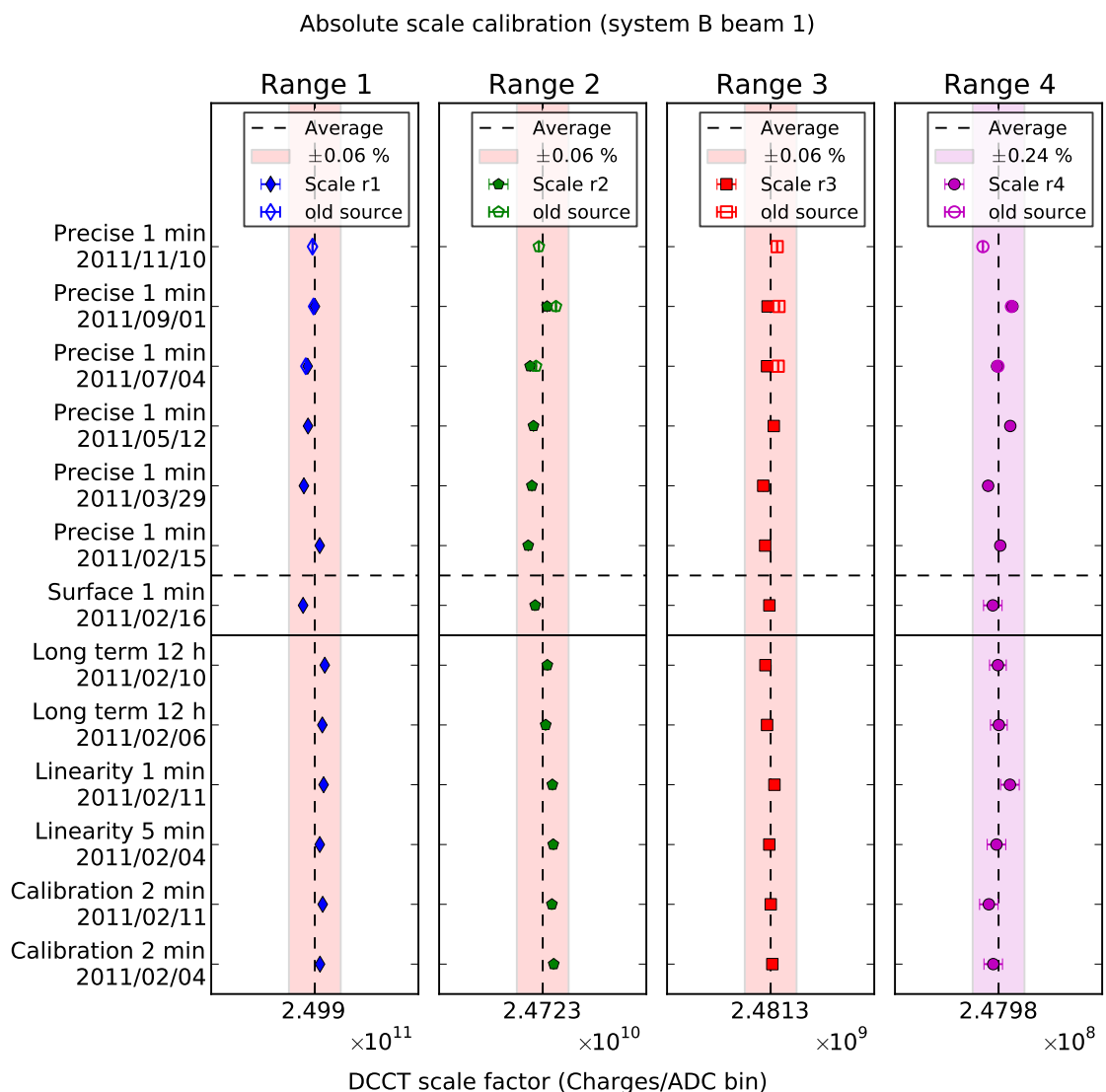


Fig. G.77: Cross talk between rings

#### G.8.5 Calibration



**Fig. G.78:** Calibration stability of all ranges of system A/beam 2.



**Fig. G.79:** Calibration stability of all ranges of system B/beam 1.

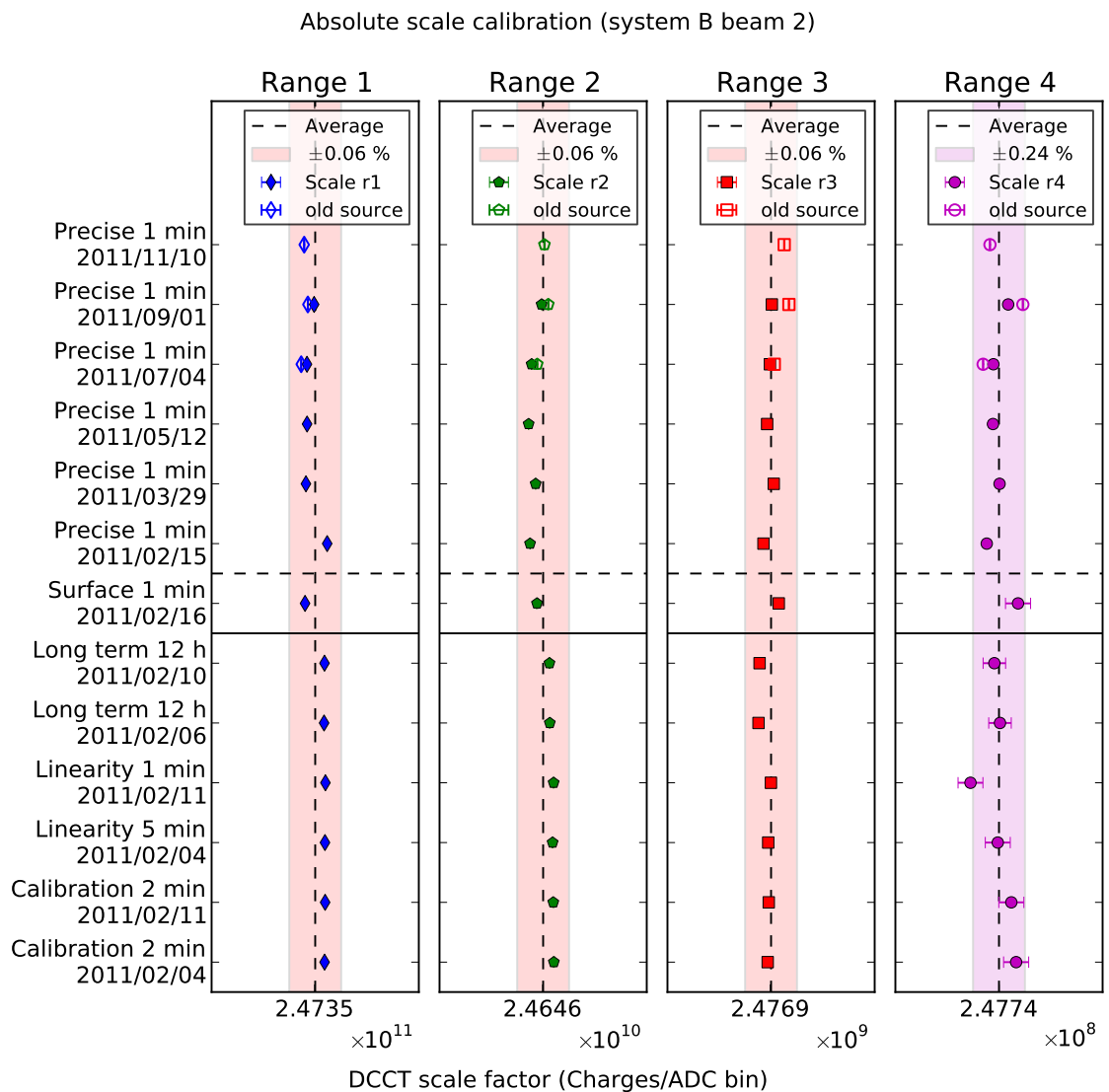


**Fig. G.80:** Calibration stability of all ranges of system B/beam 2.

# LIST OF FIGURES

1.1	Beam-gas interaction vertices visualized with the LHCb event display. . . . .	3
2.1	Vertical cross section through the LHCb detector. . . . .	4
2.2	Cross section of the VELO in the $(x,z)$ plane, at $y = 0$ . . . . .	5
2.3	Delivered integrated luminosity to the four LHC experiments . . . . .	6
2.4	Schematic view of the LHC. . . . .	7
3.1	Definition of coordinates and beam geometry. . . . .	10
4.1	Distribution of longitudinal $z$ -position vertices for the various bunch crossing types	19
4.2	Position of beam-gas vertices projected in the $xz$ and $yz$ planes . . . . .	20
4.3	Reconstructed beam-gas interaction vertices view in 3 dimensions . . . . .	20
4.4	Beam-gas event rate increase with SMOG injection . . . . .	22
4.5	Dedicated luminosity measurement fill with SMOG gas injection. . . . .	22
4.6	Selected beam-beam vertices for resolution measurement. . . . .	24
4.7	Measurement of the residuals between two split vertices from beam-beam interactions (fill 2520). . . . .	25
4.8	Beam-beam resolution as function of track multiplicity. . . . .	26
4.9	Residuals between direct resolution measurement and parameterization fit . . . . .	27
4.10	Beam-beam resolution $z$ -dependent correction factor. . . . .	28
4.11	Number of tracks per vertex distribution for different $z$ -bins. . . . .	29
4.12	Beam-gas vertex resolution parameterization for both beams and different $z$ -bins. .	30
4.13	Weighted residuals between the direct beam-gas resolution measurement and the parameterization. . . . .	30
4.14	Beam-gas resolution correction factors as function of $z$ -position. . . . .	31
4.15	Measurement of the single beam width along $z$ normalized to the width at $z = 0$ . .	34
4.16	Beam-gas resolution correction factors $f_z$ as function of $z$ -position. . . . .	35
4.17	Measurement of single beam width $\sigma_v$ along $z$ normalized to the width at $z = 0$ including resolution corrections. . . . .	36
4.18	Weighted resolution for dedicated luminosity calibration fills . . . . .	37
4.19	Resolution parametrization bias for dedicated luminosity calibration fills. . . . .	37
4.20	Crossing angle measurement. . . . .	39
4.21	Resolution distribution and effective resolution function $R(m)$ . . . . .	40
4.22	Resolution deconvolution examples . . . . .	41
4.23	Selected $z$ -regions for global fit . . . . .	43
4.24	Reconstructed beam-gas interaction vertices view in 3 dimensions for fill 2852 . .	43
4.25	Global fit results of a colliding bunch pair in 1-dimension. . . . .	44
4.26	Global fit results in 2-dimensions showing 1 single beam slice. . . . .	46
4.27	Global fit in 2-dimensions. . . . .	48
4.28	Global fit results of a colliding bunch pair in 2-dimensions. . . . .	49
4.29	Bunch length and $Z_{RF}$ fit . . . . .	51
4.30	Fit model test on simulated data with extreme non-realistic beam parameters . .	54
4.31	Fit model test on simulated data with realistic beam parameters . . . . .	54
4.32	Longitudinal $z$ position of the luminous region and beam offset. . . . .	57
4.33	Detector alignment corrections for fill 2852 . . . . .	58

4.34	Alignment offset correction improvement on the fit quality . . . . .	59
4.35	Orbit drift measurement during fill 2855. . . . .	60
4.36	Effect of beam factorizability seen on double-Gaussian 2-d transverse distribution. . . . .	61
4.37	Measurement of beam factorizability with simulated data. . . . .	61
4.38	Non-factorizable beam shape measurement in $x$ using a 1-d fit. . . . .	62
4.39	Measurement of beam factorizability on real data. . . . .	62
4.40	Measurement of beam factorizability with different beam parameters with simulated datasets. . . . .	63
4.41	Strength of double Gaussian beam shape. . . . .	64
4.42	Measurement of beam factorizability for all measurements performed in 2012 at $\sqrt{s} = 8$ TeV sorted by time and BCID. . . . .	64
4.43	Measurement of beam factorizability for all measurements performed in 2012 at $\sqrt{s} = 8$ TeV projected as histogram. . . . .	65
4.44	Difference in the overlap integral between 1-dimensional and 2-dimensional fits. . . . .	65
5.1	Average raw interaction rate per bunch crossing for fill 2855 . . . . .	70
5.2	Background rate per charge and beam for fill 2855 . . . . .	70
5.3	Background corrected average interaction rate per bunch crossing for fill 2855 . . . . .	71
5.4	Average interaction rate per bunch crossing. . . . .	71
5.5	Counter efficiency as function of $z$ . . . . .	72
5.6	Ratio of raw rates compared to background corrected rates. . . . .	73
5.7	Ratio of counters after background correction. . . . .	73
6.1	Total beam intensity measured with the DCCT (fill 2855). . . . .	76
6.2	Single bunch intensities measured with the FBCT (fill 2855) as function of time. . . . .	76
6.3	Example of a longitudinal profile measured with the LDM . . . . .	77
6.4	Distribution of selected beam-gas events along $z$ used for the ghost charge measurement. . . . .	79
6.5	Beam-gas $x$ - $z$ profile for ghost charge . . . . .	79
6.6	Transverse distribution of selected beam-gas events for ghost charge analysis. . . . .	80
6.7	Relative beam-gas trigger efficiency . . . . .	82
6.8	Ghost charge distribution over the ring circumference. . . . .	83
6.9	Correlation between ghost charge fractions measured by the LDM and LHCb. . . . .	83
6.10	Ghost charge distribution comparison with LDM. . . . .	84
6.11	Ghost charge distribution comparison with LDM (enlarged). . . . .	84
6.12	Ghost charge fraction for fill 2852. . . . .	85
6.13	Ghost charge fraction for fills 2855 and 3563. . . . .	86
6.14	Missing $ee$ events for 15 BCIDs . . . . .	86
7.1	Cross-section results for head-on beams with $\beta^* = 10$ m at $\sqrt{s} = 8$ TeV. . . . .	91
7.2	Normalized cross-section and related values evolution for a colliding bunch pair . . . . .	91
7.3	Cross-section trend of the six colliding bunch pairs for fill 2855. . . . .	91
7.4	Cross-section with and without FBCT offset correction for fill 2852. . . . .	93
7.5	Cross-section results for head-on beams and 10 m $\beta^*$ fills at $\sqrt{s} = 8$ TeV after FBCT offset correction. . . . .	93
7.6	Measurement of convolved bunch length $\sigma_{z1}^2 + \sigma_{z2}^2$ with displaced beam. . . . .	94
7.7	Cross-section correlation checks with the rate and intensity. . . . .	95
7.8	Cross-section correlation checks. . . . .	95
7.9	Cross-section dependence on beam-beam resolution compared to beam width. . . . .	98
7.10	Cross-sections measured with and without beam-gas resolution correction factors. . . . .	99
7.11	Cross-section overview for head-on periods with $\beta^* = 10$ m fills at $\sqrt{s} = 8$ TeV. . . . .	99
7.12	Effect of detector alignment on crossing angle and overlap uncertainty . . . . .	100
7.13	Overlap integral difference using two different alignments with the same data. . . . .	101

7.14	Evaluation of double Gaussian fit model applied to different simulation sets. . . . .	102
7.15	Bunch length and $Z_{RF}$ measurement with asymmetric tracks cut . . . . .	103
7.16	Fraction of vertices in the tails beyond the double-sided 99 percentile predicted by the fit. . . . .	104
7.17	Overlap integral and $z$ -crossing point measurements with displaced beams. . . . .	105
7.18	Cross-section measurement with displaced beams. . . . .	106
7.19	Measurement of pressure gradient in the VELO . . . . .	107
8.1	Average interaction rate per crossing $\mu_{\text{ref}}$ from counter <i>Tracks</i> in 2011. . . . .	111
8.2	Average interaction rate per crossing $\mu_{\text{ref}}$ from <i>Track</i> counter in 2012 for $pp$ collisions at $\sqrt{s} = 8$ TeV. . . . .	112
A.1	Average interaction rate and overlap integral for fills at $\sqrt{s} = 2.76$ TeV. . . . .	116
A.2	Strength of double Gaussian beam shape and beam factorizability for fills at $\sqrt{s} = 2.76$ TeV. . . . .	116
A.3	Bunch length and $Z_{RF}$ fit example at $\sqrt{s} = 2.76$ TeV. . . . .	117
A.4	Convolved bunch length and beam position for fills at $\sqrt{s} = 2.76$ TeV. . . . .	117
A.5	Luminous region position $\xi_{lz}$ and crossing point position $Z_{RF}$ . . . . .	118
A.6	Cross-section results for head-on beams and 10 m $\beta^*$ fills at $\sqrt{s} = 2.76$ TeV. . . . .	119
A.7	Uncertainties related to resolution for fills at $\sqrt{s} = 2.76$ TeV. . . . .	119
A.8	Number of vertices per measurement at $\sqrt{s} = 2.76$ TeV. . . . .	120
B.1	Detector response $I$ for single interaction for the <i>Track</i> counter . . . . .	123
B.2	Detector response spectrum during normal physics data taking with $\mu_{\text{ref}} = 1.7$ (fill 3034). . . . .	123
B.3	Detector response spectrum during normal physics data taking (bad agreement). .	123
C.1	Difference in transverse vertex position as seen from VELO left and right halves with default alignment in 2012. . . . .	125
C.2	Residuals between a straight line fit to the average beam position and the beam seen by a VELO half using the default alignment in 2012. . . . .	126
C.3	Difference in transverse vertex position as seen from VELO left and right halves with dedicated alignment in 2012. . . . .	127
C.4	Residuals between a straight line fit to the average beam position and the beam seen by a VELO half using the dedicated alignment in 2012. . . . .	128
D.1	Correction function describing the $z$ -dependence of the beam-beam resolution (fill 2855). . . . .	129
D.2	Correction factors $f_z$ to the beam-gas resolution as function of $z$ -position (fill 2855). .	130
D.3	Correction factors $f_z$ to the beam-gas resolution as function of $z$ -position (fill 3563). .	130
D.4	Measurement of single beam width along $z$ normalized to the width at $z = 0$ . . . .	131
D.5	Measurement of single beam width along $z$ normalized to the width at $z = 0$ including resolution corrections. . . . .	132
D.6	Number of vertices per measurement. . . . .	133
D.7	Fit $\chi^2/\text{dof}$ of the 2-d global fit. . . . .	133
D.8	Convolved bunch length $\sigma_{z1}^2 + \sigma_{z2}^2$ measurement. . . . .	134
D.9	Beam crossing angles. . . . .	134
D.10	Overlap integral measurement. . . . .	135
D.11	Average interaction rate per bunch crossing, counter vertex. . . . .	135
D.12	Normalized cross-section and related values evolution for a bunch pair for fills in fills 2852, 2853, 2856 and 3316 . . . . .	138
D.13	Cross-section trend of the six colliding bunches for fill 2856. . . . .	138
D.14	Cross-section trend of the six colliding bunches for fill 3311. . . . .	139

D.15	Cross-section trend of the six colliding bunches for fill 3316 . . . . .	139
D.16	Ratio of <i>RZVelo</i> and <i>Track</i> counters after background correction. . . . .	139
D.17	Cross-section with and without FBCT offset correction for fills 2853, 2855, 2856, 3311 and 3316 . . . . .	140
D.18	Correlation between the cross-section and crossing angle correction. . . . .	141
D.19	Evaluation of double Gaussian fit model applied to different simulation sets using single beam data only. . . . .	141
F.1	Scheme of stand-alone SMOG. . . . .	145
F.2	Scheme of SMOG and test bench setup . . . . .	146
F.3	SMOG device in the laboratory. . . . .	146
F.4	SMOG laboratory setup. . . . .	147
F.5	QMA spectra of SMOG output excluding the high pressure injection line. . . . .	148
F.6	Residual gas spectrum with HP injection line connected . . . . .	149
F.7	Outgassing RGA with injection line and high pressure reducer . . . . .	150
F.8	Pressure decay over time for the evacuation of the high pressure line. . . . .	150
F.9	Pressure versus time during first 20 days. . . . .	151
F.10	SMOG injection at 1.3 bar . . . . .	151
F.11	Residual gas spectrum of SMOG before and during injection . . . . .	152
F.12	Evacuation of “dead volume” through the bypass. . . . .	153
F.13	Final SMOG laboratory setup with high pressure volume. . . . .	155
F.14	Partial pressure in the pre-VELO volume during injection without NEG filter. . . . .	156
F.15	Residual gases and neon flows in the pre-VELO and VELO test bench volume during injection. . . . .	157
F.16	Residual gas analysis during injection without NEG filter. . . . .	157
F.17	Pressure loss during long term injection. . . . .	158
F.18	Pressure loss per injection cycle. . . . .	159
F.19	Partial pressure of residuals and neon measured in the pre-VELO volume during neon injection at different high pressures and with the NEG filter installed. . . . .	159
F.20	Residual gases and neon flows in the pre-VELO and VELO test bench volume during injection with NEG filter. . . . .	160
F.21	Residual gas analysis during injection with NEG filter. . . . .	160
F.22	Residual gases and neon pressure during the bypass evacuation. . . . .	161
F.23	SMOG setup when connected to the VELO. . . . .	162
F.24	VELO pressure profile during first injection test. . . . .	162
F.25	VELO residual gas analysis during first injection test. . . . .	163
F.26	Pressure and beam-gas rates during first injection with beam. . . . .	163
G.1	DCCT errors classification . . . . .	168
G.2	DCCT General Layout . . . . .	168
G.3	DCCT simplified schematics . . . . .	169
G.4	Narrow hysteresis and production of even harmonics . . . . .	170
G.5	DCCT offset correction method . . . . .	171
G.6	Offset uncertainty method . . . . .	172
G.7	DCCT long term offset (system A/beam 1) . . . . .	172
G.8	Offset box error tests . . . . .	173
G.9	Offset box error histogram . . . . .	173
G.10	1/2 P2P error histogram . . . . .	174
G.11	Measured offset after a fill dump in 2011 . . . . .	175
G.12	Fast Fourier transform of long term offset . . . . .	176
G.13	Fast Fourier transform of simulated noise . . . . .	177
G.14	Tunnel setup . . . . .	178

G.15 Long term stability under load system A/beam 1 range 3 . . . . .	180
G.16 Long term stability under load system B/beam 1 range 1 . . . . .	180
G.17 Fourier analysis of range 1 . . . . .	181
G.18 12-hour histogram of system A/beam 1 range 3 . . . . .	181
G.19 Histograms of $2 \times 12$ hours of all ranges for system A/beam 1 . . . . .	182
G.20 Quantization of the 12-bit ADC . . . . .	183
G.21 Long term stability under load of range 1 . . . . .	184
G.22 Current sequence used for the linearity measurement . . . . .	185
G.23 Injected current versus measured current . . . . .	186
G.24 Linearity residuals for system A/beam 1 . . . . .	186
G.25 Linearity residuals for range 2 compared to standard calibrations . . . . .	187
G.26 Current steps to test the NI ADC . . . . .	189
G.27 Reference response of the NI ADC . . . . .	189
G.28 Setup with parallel ADC . . . . .	190
G.29 Linearity measurement with NI ADC . . . . .	190
G.30 Precise calibrations during 2011 . . . . .	191
G.31 Synoptic of LHC point 4 shafts . . . . .	192
G.32 Air temperature around point 4 . . . . .	192
G.33 Crosstalk example . . . . .	193
G.34 difference at dump time . . . . .	193
G.35 Example of difference between system A and B . . . . .	194
G.36 Lab setup bunch pattern dependence . . . . .	195
G.37 Bunch pattern used in laboratory . . . . .	196
G.38 Bunch pattern dependence with low intensity . . . . .	197
G.39 Bunch pattern dependence at high intensity . . . . .	197
G.40 Beam debunching . . . . .	198
G.41 Fourier transform example with wide pulse . . . . .	201
G.42 Sensitivity to RF setup . . . . .	201
G.43 Sensitivity to RF: 1 kHz to 250 kHz . . . . .	202
G.44 Sensitivity to RF: 250 kHz to 110 MHz . . . . .	202
G.45 Bunch position dependence beam 1 . . . . .	203
G.46 Bunch position dependence beam 2 . . . . .	204
G.47 Offset versus LHC energy . . . . .	205
G.48 Example of DCCT offset during RF switch on . . . . .	206
G.49 Offset versus LHC RF field . . . . .	206
G.50 4-wire setup . . . . .	207
G.51 Verification of the precise DC source . . . . .	208
G.52 Long term stability of scaling factor . . . . .	210
G.53 Example of injection steps fill 1459 . . . . .	211
G.54 Relative difference between system A and B . . . . .	212
G.55 Relative difference between system A and B for 2011 . . . . .	212
G.56 Relative difference between system A and B for 2011 vs. beam-1 intensity . . . . .	213
G.57 Relative difference between system A and B for 2011 vs. beam-2 intensity . . . . .	214
G.58 DCCT long term offset (system A/beam 2) . . . . .	221
G.59 DCCT long term offset (system B/beam 1) . . . . .	222
G.60 DCCT long term offset (system B/beam 2) . . . . .	222
G.61 Offset box error tests for all DCCT's . . . . .	223
G.62 Long term stability under load system A/beam 1 . . . . .	224
G.63 Long term stability under load system A/beam 2 . . . . .	224
G.64 Long term stability under load system B/beam 1 . . . . .	225
G.65 Long term stability under load system B/beam 2 . . . . .	225
G.66 Histograms of $2 \times 12$ hours of all ranges for system A/beam 2 . . . . .	226

G.67 Histograms of $2 \times 12$ hours of all ranges for system B/beam 1 . . . . .	226
G.68 Histograms of $2 \times 12$ hours of all ranges for system B/beam 2 . . . . .	227
G.69 Linearity residuals for system A/beam 2 . . . . .	228
G.70 Linearity residuals for system B/beam 1 . . . . .	228
G.71 Linearity residuals for system B/beam 2 . . . . .	229
G.72 Linearity residuals measured with both ADC's . . . . .	229
G.73 Scaling factor of 24-bit acquisition for system A/beam 1 . . . . .	230
G.74 Scaling factor of 24-bit acquisition for system A/beam 2 . . . . .	231
G.75 Scaling factor of 24-bit acquisition for system B/beam 1 . . . . .	231
G.76 Scaling factor of 24-bit acquisition for system B/beam 2 . . . . .	232
G.77 Cross talk between rings . . . . .	233
G.78 Calibration stability system A/beam 2 . . . . .	234
G.79 Calibration stability system B/beam 1 . . . . .	235
G.80 Calibration stability system B/beam 2 . . . . .	236

## LIST OF TABLES

4.1	Dedicated luminosity measurement fills used for BGI analysis. . . . .	17
4.2	Hardware trigger channel definitions. . . . .	18
4.3	HLT requirements for dedicated luminosity measurement fills. . . . .	18
4.4	Beam-beam resolution parameters . . . . .	27
4.5	Resolution global correction factors . . . . .	37
5.1	Luminosity counters. . . . .	67
6.1	Summary of uncertainties for fill 2855 in July 2012 . . . . .	75
6.2	Relative beam-gas trigger efficiency for the ghost charge. . . . .	82
6.3	ghost charge results . . . . .	87
6.4	Summary of bunch population uncertainties. . . . .	89
7.1	FBCT offset fit . . . . .	93
7.2	Track multiplicity cuts used to change the resolution. . . . .	97
7.3	Systematic uncertainties on the luminosity calibration using the beam-gas imaging method. . . . .	108
8.1	Integrated luminosity for CEP analysis. . . . .	112
A.1	FBCT offset fit at $\sqrt{s} = 2.76$ TeV. . . . .	118
A.2	Beam-gas imaging systematic uncertainties on the visible cross-section at $\sqrt{s} = 2.76$ TeV. . . . .	120
D.1	Ghost charge results for fill 3562 at $\sqrt{s} = 2.76$ TeV . . . . .	136
D.2	Ghost charge results for fill 3563 at $\sqrt{s} = 2.76$ TeV . . . . .	137
E.1	Parameters for generic Monte Carlo sets with single and double Gaussian shape. . . . .	142
E.2	Parameters for generic Monte Carlo sets with triple Gaussian shape. . . . .	143
E.3	Parameters for generic Monte Carlo sets with super Gaussian shape. . . . .	143
F.1	Valve states . . . . .	147
F.2	SMOG outgassing without high pressure tube . . . . .	147
F.3	SMOG outgassing pressures with high pressure tube . . . . .	148
F.4	SMOG outgassing with high pressure tube up to gas bottle . . . . .	149
F.5	Pressures at the injection states . . . . .	152
F.6	Gas flow rates into the pre-VELO volume . . . . .	153
F.7	Selected mass numbers for residual gases and neon. . . . .	155
F.8	Calibration of the QMA Prisma 200 . . . . .	156
G.1	VDM luminosity calibration series for the LHC (2010 and 2011). The number of bunches in brackets indicates the number of “pilot” proton bunches in addition to the number of “main” proton bunches. Here, $\langle N \rangle$ is an indicative value of the main bunch charge in units of $10^{10}$ elementary charges. . . . .	166
G.2	DCCT ranges . . . . .	170
G.3	Offset variation at the end of fills . . . . .	174

G.4	Injected currents per range over 12 hours . . . . .	179
G.5	Standard deviation over 12 hours . . . . .	180
G.6	Resistance used to test the ADC . . . . .	188
G.7	Calibration currents . . . . .	209
G.8	Summary of uncertainties without measurable effect . . . . .	216
G.9	Summary of uncertainties . . . . .	217
G.10	Summary of uncertainties for VDM fill 1783 . . . . .	219
G.11	Summary of uncertainties for a fill acquired with range 1 . . . . .	219
G.12	Summary of uncertainties for a fill acquired with range 4 . . . . .	220

## BIBLIOGRAPHY

- [1] R. McNulty, *Potential PDF sensitivity at LHCb*, 2008, 0810.2550, arXiv:0810.2550.
- [2] F. De Lorenzi, Proceedings C10-04-19 (2010), 1011.4260, arXiv:1011.4260.
- [3] R. Thorne, A. Martin, W. Stirling, and G. Watt, *Parton Distributions and QCD at LHCb*, 2008, arXiv:0808.1847.
- [4] LHCb Collaboration, R. Aaij *et al.*, JHEP **06**, 058 (2012), 1204.1620.
- [5] LHCb Collaboration, R. Aaij *et al.*, JHEP **02**, 106 (2013), 1212.4620.
- [6] LHCb Collaboration, R. Aaij *et al.*, JHEP **1301**, 111 (2013), 1210.6289.
- [7] LHCb Collaboration, R. Aaij *et al.*, (2013), arXiv:1310.8197.
- [8] LHCb Collaboration, R. Aaij *et al.*, (2012), LHCb-CONF-2012-013.
- [9] M. Mangano, Proceedings lumi days CERN (2011).
- [10] J. Rojo and A. Vicini, (2013), 1309.1311, arXiv:1309.1311.
- [11] G. Montagna, O. Nicrosini, and F. Piccinini, Riv. Nuovo Cim. **21N9**, 1 (1998), arXiv:hep-ph/9802302.
- [12] S. Jadach, Proceedings C03-02-28.1 , 85 (2003), arXiv:hep-ph/0306083.
- [13] I. Brock *et al.*, Nucl. Instrum. Meth. **A381**, 236 (1996).
- [14] A. Shamov and V. I. Telnov, Nucl. Instrum. Meth. **A494**, 51 (2002), hep-ex/0207095.
- [15] P. Jenni, M. Nordberg, M. Nessi, and K. Jon-And, *ATLAS Forward Detectors for Measurement of Elastic Scattering and Luminosity* (CERN, Geneva, 2008).
- [16] LHCb Collaboration, A. A. Alves *et al.*, JINST **3**, S08005 (2008).
- [17] LHCb Collaboration, R. Antunes-Nobrega *et al.*, *LHCb reoptimized detector design and performance: Technical Design Report* (CERN, Geneva, 2003).
- [18] L. Evans and P. Bryant, JINST **3**, S08001 (2008).
- [19] O. S. Brüning *et al.*, *LHC Design Report* (CERN, Geneva, 2004).
- [20] The ATLAS Collaboration, G. Aad *et al.*, JINST **3**, S08003 (2008).
- [21] The CMS Collaboration, S. Chatrchyan *et al.*, JINST **3**, S08004 (2008).
- [22] The ALICE Collaboration, K. Aamodt *et al.*, JINST **3**, S08002 (2008).
- [23] W. C. Middelkoop and A. Schoch, *Interaction rate in colliding beam systems*, 1963, CERN-AR-Int-SG-63-40.
- [24] C. Møller, *General Properties of the Characteristic Matrix in the Theory of Elementary Particles I* (I kommission hos E. Munksgaard, 1945).
- [25] J. P. Quesnel, *Géométrie Du LHC : Points Caractéristiques, Formules De Transformation*, 1997, LHC-Project-Note-95.

- [26] M. Ferro-Luzzi, *Luminosity and luminous region shape for pure Gaussian bunches*, 2012, LHCb-PUB-2012-016.
- [27] T. Suzuki, *General Formulas of Luminosity for Various Types of Colliding Beam Machines*, 1976, KEK-76-3.
- [28] W. Herr and B. Muratori, CERN Accelerator School (2003).
- [29] K. Wille, *The physics of particle accelerators : an introduction* (Oxford University Press, Oxford New York, 2000).
- [30] S. White, *Determination of the Absolute Luminosity at the LHC*, PhD thesis, Orsay, Universit   Paris-Sud 11, Orsay, 2010.
- [31] S. van der Meer, *Calibration of the effective beam height in the ISR*, 1968, CERN-ISR-PO-68-31.
- [32] C. Rubbia, *Measurement of the luminosity of  $p\bar{p}$  collider with a (generalized) Van der Meer Method*, 1977.
- [33] S. White, R. Alemany-Fernandez, H. Burkhardt, and M. Lamont, Proceedings of IPAC, Kyoto, Japan , 3 p (2010).
- [34] V. Balagura, Nucl. Instrum. Meth. **A654**, 634 (2011).
- [35] LHCb Collaboration, R. Aaij *et al.*, JINST **7**, P01010 (2012).
- [36] W. Herr, Proceedings of LHC Lumi Days 2012 (2012), LHC Lumi Days.
- [37] M. Ferro-Luzzi, Nucl. Instrum. Meth. **A553**, 388 (2005).
- [38] J. Panman *et al.*, *Absolute luminosity measurements for the  $p$ - $Pb$  pilot run*, 2012, LHCb-ANA-2012-093.
- [39] LHCb Collaboration, R. Aaij *et al.*, JINST **8**, P04022 (2013), 1211.3055.
- [40] P. Bromiley, *Products and Convolutions of Gaussian Distributions*, 2003, tina-vision 2003-003.
- [41] A. W. Chao and M. Tigner, *Handbook of Accelerator Physics and Engineering* (World Scientific, Singapore, 1999).
- [42] G. Vanbavincckhove, *Optics measurements and corrections for colliders and other storage rings*, PhD thesis, Amsterdam U., 2013, Presented 16 Jan 2013.
- [43] M. Ferro-Luzzi, *private communication*.
- [44] O. Callot, *FastVelo, a fast and efficient pattern recognition package for the Velo*, 2011, CERN-LHCb-PUB-2011-001.
- [45] R. Matev, PhD thesis, Sofia University, to be published.
- [46] G. Anders *et al.*, CERN-ATS-Note-2011-004 PERF (2011), (BCNWG note1).
- [47] G. Acli   *et al.*, CERN-ATS-Note-2011-016 PERF (2011), (BCNWG note2).
- [48] G. Anders *et al.*, CERN-ATS-Note-2012-028 PERF (2012), (BCNWG Note 3).
- [49] A. Acli   *et al.*, CERN-ATS-Note-2012-029 PERF (2012), (BCNWG Note 4).
- [50] C. Fischer and R. Schmidt, *On the Measurements of the Beam Current, Lifetime and Decay Rate in the LHC Rings*, 2005, LHC-BCT-ES-0001-10-00.
- [51] P. Odier *et al.*, Proceedings of DIPAC11, Hamburg, Germany (2011).
- [52] D. Belohrad, S. Longo, P. Odier, and S. Thoulet, *Mechanical Design of the Intensity Measurement Devices for the LHC*, 2007, CERN-AB-2007-026.

[53] D. Belohrad *et al.*, *Implementation of the Electronics Chain for the Bunch by Bunch Intensity Measurement Devices for the LHC*, 2009, CERN-BE-2009-018.

[54] P. Odier *et al.*, Proceedings of DIPAC09, Basel, Switzerland. (2009).

[55] D. Belohrad *et al.*, Proceedings of IPAC10, Kyoto, Japan , 3 p (2010).

[56] C. Barschel *et al.*, *Results of the DCCT Calibration Studies*, 2012, CERN-ATS-Note-2012-026.

[57] P. Hopchev, *Absolute luminosity measurements at LHCb*, PhD thesis, University of Grenoble, 2011, CERN-THESIS-2011-210.

[58] A. Boccardi, E. Bravin, M. Ferro-Luzzi, and S. Mazzoni, *LHC Luminosity calibration using the Longitudinal Density Monitor*, 2013, CERN-ATS-Note-2013-034 TECH.

[59] F. J. Decker, SLAC-PUB-95-6684 (1994).

[60] LHCb Collaboration, R. Aaij *et al.*, J.Phys. **G40**, 045001 (2013), 1301.7084, arXiv:1301.7084.

[61] LHCb Collaboration, R. Aaij *et al.*, *Central Exclusive Dimuon Production at  $\sqrt{s} = 7$  TeV*, 2011, LHCb-CONF-2011-022.

[62] V. Balagura, *Analysis methods for luminosity data*, 2009, LHCb-INT-2009-001.

[63] M. Gersabeck *et al.*, Nucl. Instrum. Meth. **A596**, 164 (2008).

[64] S. Viret, C. Parkes, and M. Gersabeck, Nucl. Instrum. Meth. **A596**, 157 (2008).

[65] V. Blobel and C. Kleinwort, Proceedings of CASTPP, Durham, UK (2002), hep-ex/0208021.

[66] M. Ferro-Luzzi, *Design considerations for controlling the pressure in the VELO beam vacuum to perform beam-gas imaging*, 2011, CERN EDMS 1148364.

[67] M. Ferro-Luzzi, *Test of SMOG control and monitoring*, 2011, CERN EDMS 1148366.

[68] M. Ferro-Luzzi, *Specification for SMOG control and monitoring*, 2011, CERN EDMS 1148367.

[69] V. Balagura, C. Barschel, M. Ferro-Luzzi, and J. Panman, *Proposed measurement programme to test beam-gas imaging in LHCb enhanced with gas injection*, 2011, CERN EDMS 1166432.

[70] C. Benvenuti, *Molecular surface pumping: the getter pumps*, 1999, CERN-OPEN-2000-265.

[71] Leybold, *Fundamentals of Vacuum Technology* (Vakuum GmbH, 2007).

[72] CERN/TE/VSC, *Ecart-types ges jauges*, 2000.

[73] C. Barschel and G. Schneider, *SMOG Buffer volume refill procedure*, 2011, CERN EDMS 1166107.

[74] C. Barschel and G. Schneider, *SMOG in-situ test procedure in the VELO environment*, 2011, CERN EDMS 1166122.

[75] C. Barschel and G. Schneider, *SMOG installation procedure in the LHCb VELO environment*, 2011, CERN EDMS 1166114.

[76] C. Barschel and G. Schneider, *SMOG Installation and Test Report*, 2011, CERN EDMS 1170989.

[77] C. Barschel, Proceedings of LHC Lumi Days 2012 (2012), LHC Lumi Days.

[78] P. Odier, *DCCT Technology Review*, in *2nd meeting in the framework of the CARE-HHH-ABI networking*, 2004.

## ACKNOWLEDGMENT

Looking back on those years I realize how little I knew about the hurdles lying ahead and it comes with no surprise that this work has only been made possible with the help and collaboration of many persons, all of whom I cannot mention here. And so my gratefulness goes to everyone who helped in one way or another to make this work possible.

First of all I would like to thank Prof. Thomas Hebbeker for supporting my thesis outside of the institute and on a different experiment; a sign of trust, so I believe, which I hope to comply with. I also would like to thank Monica Pepe-Altarelli for giving me the chance to work on the LHCb experiment, to be part of the collaboration and to offer me a pleasant work atmosphere.

I am deeply indebted to Massimiliano Ferro-Luzzi for giving me the opportunity to work on this new project. He always provided valuable insights and guidance, while leaving me full freedom to organize all activities required to reach my goal. It has been a real pleasure to work together and I would like to express my gratitude for his trust and also for proof reading my thesis.

I am particularly grateful to Jaap Panman for the helpful discussions throughout the years, for sharing his knowledge and keeping a critical and constructive eye on my work. I also would like to thank him for proof reading some important parts of this document.

I would like to offer my special thanks to Rosen Matev, not only for the countless discussions about various aspects of the analysis and physics in general, but also for his constructive suggestions and help in a true collaborative spirit. I also would like to thank Plamen Hopchev for helping me to start working with the LHCb framework and its many algorithms.

The assistance provided by Richard Jacobsson to operate the detector in special conditions required for this work, was greatly appreciated.

Also advices given by Silvia Borghi and Wouter Hulsbergen for the detector alignment has been of great help.

I wish to thank Paula Collins for the interesting discussions about central inclusive production.

Special thanks go to Gerhard Schneider for his help commissioning the SMOG system, for his guidance during the laboratory measurements, and for the first SMOG operations. Here I would also like to thank Giulia Lanza and Didier Calegari for their readiness to help with the SMOG operation, which often occurred during night time or on week-ends.

I am grateful to Jean-Jacques Gras, Patrick Odier, Sebastien Thoulet and Micheal Ludwig from the beam instrumentation group for their help during the DCCT studies; they accepted me in their laboratory and with the special operation of the DCCT instrument.

Finally, I would like to thank the members of the online and trigger group who always managed to push the detector boundaries a little further for those special measurements.

And of course I would like to thank our kind and helpful secretaries Nathalie Grüb, Lalaine Barbon Strelbel and Anu Liisa Saarelainen without whom nothing would work.

Last, I would like to express my gratitude to my parents, Monique and Eike, for their continuous positive motivation, support and foremost trust.

## DECLARATION

Hiermit erkläre ich eidesstattlich, dass ich die vorliegende Doktorarbeit selbständig erarbeitet und alle in Anspruch genommenen Hilfen in der Dissertation angegeben habe. Alle Quellen und Zitate sind als solche kenntlich gemacht, und die Literaturangaben sind nach meinem besten Wissen und Gewissen korrekt und vollständig wiedergegeben.

Ich versichere eidesstattlich, dass ich diesen Promotionsantrag erstmalig einreiche und keine früheren Versuche einer Promotion unternommen habe.

Hiermit erkläre ich, dass durch die Veröffentlichung als Dissertation der RWTH-Aachen bestehende Schutzrechte – insbesondere Urheberschutzrechte – nicht verletzt werden.

# CURRICULUM VITAE

## Colin Barschel

---

CONTACT INFORMATION	Colin Barschel 301 chemin du Crêt 01170 Gex France	<i>Tel:</i> +41 325127259 <i>Mobile:</i> +41 768222615 <i>E-mail:</i> colin@barschel.com <i>WWW:</i> colin.barschel.net
BORN	January 5, 1975, Brockville, Canada	
NATIONALITY	German, Swiss, Canadian	
EDUCATION	<b>CERN</b> , Switzerland	<b>2010 to 2014</b>
	Doctoral student in Experimental particle physics (graduation: March 2014)	
	<ul style="list-style-type: none"><li>• Thesis: Precision luminosity measurement at LHCb with beam-gas imaging</li><li>• Advisors: Prof Dr T. Hebbeker (RWTH Aachen) and Dr Massimiliano Ferro-Luzzi (CERN)</li></ul>	
	<b>RWTH Aachen University</b> , Aachen, Germany	<b>2001 to 2010</b>
	Diploma in physics (graduation: February 2010)	
	<ul style="list-style-type: none"><li>• Thesis Topic: Calibration of the Breit-Rabi polarimeter for the PAX-Spin filtering experiment at COSY/FZJ and AD/CERN</li><li>• Advisors: Prof Dr T. Hebbeker (RWTH Aachen) and Prof Dr H. Ströher (IKP, Jülich)</li><li>• Principle fields of Study: Experimental particle physics, semiconductor technology</li></ul>	
	<b>University of Stuttgart</b> , Germany - Aerospace Engineering	<b>1997-2000</b>
	<b>EPFL</b> , Switzerland - Mechanical Engineering	<b>1994-1996</b>
	<b>Baccalauréat</b> , Lausanne, Switzerland - (natural sciences)	<b>1994</b>
PROFESSIONAL EXPERIENCE AND RESEARCH	<b>CERN, LHCb collaboration</b> , Switzerland	<b>2010 to 2014</b>
	<i>Doctoral student, CERN fellow since January 2014</i>	
	<b>IKP, Forschungszentrum Jülich</b> , Jülich, Germany	<b>February 2009 to Mai 2010</b>
	<i>Diploma student</i>	
	<b>Ericsson GmbH</b> research unit, Aachen, Germany	<b>March 2002 to 2010</b>
	<i>Researcher and developer</i>	
	<b>Institute of Jet Propulsion and Turbomachinery</b> RWTH Aachen, Germany	<b>2001 to 2002</b>
	<i>Research assistant and Fortran programmer</i>	
	<b>Institute for Statics and Dynamics</b> , Stuttgart, Germany	<b>1997 to 2001</b>
	<i>Research assistant</i>	
	<b>Contraves Space SA</b> , Zürich, Switzerland	<b>October 1999 to March 2000</b>
	<i>Research intern</i>	